Die approbierte Originalversion dieser Dissertation ist an der Hauptbibliothek der Technischen Universität Wien aufgestellt (http://www.ub.tuwien.ac.at).

The approved original version of this thesis is available at the main library of the Vienna University of Technology (http://www.ub.tuwien.ac.at/englweb/).

DISSERTATION

Synthesis and Characterization of Hybrid Inorganic-Organic Core-Shell Nanoparticles by a Grafting-from Approach of Polymers from Metal and Metal Oxide Cores

ausgeführt zum Zwecke der Erlangung des akademischen Grades
eines Doktors der technischen Wissenschaften
unter Anleitung von

Ao. Univ.-Prof. Dr. G. Kickelbick

Institut für Materialchemie
E 165
eingereicht an der Technischen Universität Wien
Fakultät für Technische Chemie

von

Dipl. Ing. Dieter Holzinger
Matr. Nr. 9625736

A-1200 Wien, Lorenz-Müller-Gasse 1A/5406

Wien, am 30. September 2004

THESIS

Synthesis and Characterization of Hybrid Inorganic-Organic Core-Shell Nanoparticles by a Grafting-from Approach of Polymers from Metal and Metal Oxide Cores

Ao. Univ.-Prof. Dr. G. Kickelbick

By

Dipl. Ing. Dieter Holzinger

Matr. Nr. 9625736

Vienna University of Technology

at the Institute of

Materials Chemistry

(165)

A-1060 Vienna

Acknowledgments

I am very grateful to *Ao. Univ. Prof. Guido Kickelbick* for giving me the opportunity to undertake my thesis in his research project and for his guidance and support during the last years and last but not least for offering me the possibility to spend three month at the University of Vigo, Spain. Furthermore, I want to thank *Guido* for reviewing the original drafts of the chapters of this thesis and for performing X-ray single crystal analyses of my not always perfect crystals.

My sincere thanks go to *Prof. Ulrich Schubert* for the possibility to undertake my thesis in his working group.

I also want to express my gratitude to *Prof. Luis Liz-Marzán* from the Department of Physical Chemistry of the University of Vigo and to the members of this department (especially to *Ana, Moi and Celia*) for making my time in Vigo an enjoyable experience, both academically and socially.

I would like to thank *Liesi* and *Oliver*, who also reviewed parts of the thesis.

My thanks go to all my colleagues from the working group; *Beatrice, Bogdan, Christian, Christina F., Christina R., Claudia, Didi, Dini, Doris B., Helmut, Isa, Isabella, Ivan, Jorge, Josef, Melitta, Nico, Olga, Patricia, Ralf, Renè, Rutzi, Silvia, Susan, Thomas Ga., Thomas Gi. Thomas J., Viki, Uli, Urska,* and *Wolfgang* for the pleasant working atmosphere. A big "thank you" goes to *Silvia, Uli* and *Christina F.* for sharing the laboratory with me. A special thanks to my friends *Beatrice, Christina R., Uli, Slavi* and *Silvia* for enjoyable times outside to university.

Further thanks go to *Horst* who repaired my broken glassware, *Harald* who solved numerous computer problems for me, *Doris E.* who ordered chemicals in record time, *Rupert* who repaired everything beginning from my roller blades to the vacuum pump for me and *Michael* for his help in NMR spectroscopy.

I also want to thank *Dr. Johannes Bernardi* and *Dr. Gerhard Rumplmair* for their support on the electron microscopy, *Dr. Kurt Mereiter* and *Ralf Supplit*, who helped me recording the X-

ray powder diffractograms, *Andreas Rief* who helped me with the interpretation of the obtained diffraction patterns and *Dr. E. Füglein* from Netsch Gerätebau GmbH, who performed several TG-FTIR experiments for me.

Further thanks go to *Dr. O. Diwald, S. Stankic, A. Riss* and *T. Berger* for their support with photoluminescence spectroscopy.

I also want to thank *T. Giesenberg* and *E. Eitenberger* for several SEM measurements and *V. Kessler* for the donation of various iron alkoxides.

I gratefully acknowledge the financial support by the Fonds zur Förderung der wissenschaftlichen Forschung (FWF), Austria, and by the Österreichischer Akademischer Dienst (ÖAD), (Acciones Integradas; Austria-Spain), which founded my stay in Vigo.

My final and greatest debt is, of course to my mother. Without her financial support it would not have been possible to study at the Technical University of Vienna.

Kurzfassung der Arbeit

Das Ziel dieser Arbeit war die Herstellung von Hybrid Kern-Schale Nanopartikeln, wobei der Kern aus einem Metall oder Metalloxid bestand, während die organische Schale aus einem Polymer aufgebaut war.

Im ersten Teil der Arbeit wurde die Herstellung von metallischen und oxidischen Nanopartikeln unter der Nutzung unterschiedlicher Synthesewege beschrieben. Während Gold- und SiO_2 Nanopartikel in freier Lösung mittels Stabilisierung durch Ionen hergestellt wurden, wurden andere oxidische Nanopartikel ($Ti_xO_y(OH)_z$, $Fe_xO_y(OH)_z$, $Zr_xO_y(OH)_z$, $Zn_xO_y(OH)_z$, $V_xO_y(OH)_z$, $Y_xO_y(OH)_z$ und $Al_xO_y(OH)_z$) mit Durchmessern von 1 – 600 nm in Mikroemulsion synthetisiert. Der Einfluss unterschiedlicher Parameter auf die Morphologie der Nanopartikel wurde untersucht. Mittels β-Diketonaten wurde die Oberfläche der Partikel *in situ* mit Polymerizationsinitiatoren funktionalisiert. Weiters wurde die Initiatorkapazität dieser neuartigen β-Diketonaten in ATRPs untersucht.

Im zweiten Teil der Arbeit wurden nicht funktionalisierte Nanopartikel, die aus Metallsalzen hergestellt wurden, mit neuartigen silan- oder thiol-hältigen Kupplungsagenzien umgesetzt um organische Gruppen (z. B. Polymerisationsinitiatoren) auf der Oberfläche der Nanopartikel kovalent zu binden, wobei Funktionalisierungsgrade bis zu 1.5 mmol/g erzielt wurden. Das Aggregationsverhalten von oberflächenfunktionalisierten Partikel wurde an zwei Arten modifizierter SiO_2 Partikeln (93 nm Durchmesser) als Modellsystem untersucht. Abhängig vom pH-Wert wurde das Auftreten von elektrostatischen Wechselwirkungen und/oder Wasserstoff-Brücken-Bindungen beobachtet, wobei Menge und Größe der Aggregate mittels DLS untersucht wurden.

Die Initiierung der Polymerisation der Polymer-Hülle erfolgte direkt an der Oberfläche der funktionalisierten Nanopartikel. Abhängig vom gebundenen Initiatormolekül wurden unterschiedliche Polymerisationsmechanismen, wie freie radikalische Polymerisation, thermisch- oder photo-initiiert, oder kontrollierte radikalische Polymerisation (ATRP), eingesetzt. Es wurde gezeigt, dass die Verwendung von ATRP das Einstellen der Polymer-Schalendicke ermöglicht. Als Monomere kamen MMA, Styrol, Isopren und Methacrylsäure-trimethoxysilyl-propylester zum Einsatz. Kinetik Studien bestätigten, im Fall der untersuchten ATRPs, den annähernd linearen Verlauf des Größenwachstums der Kern-Schale-Partikel und die lineare Steigerung des Molekulargewichtes der Polymerketten, in Abhängigkeit vom Umsatz. Die Untersuchung der hergestellten Hybrid-Nanopartikel bestätigte deren Kern-Schale Aufbau.

Abstract

The aim of the work was the controlled synthesis of inorganic-organic hybrid core-shell nanoparticles, where the core consisted of a metal or a metal oxide, covered by an organic shell consisting of an organic polymer.

In the first part of the work metal and metal oxide nanoparticles were synthesized using various approaches. While gold and silica nanoparticles were synthesized in free solution, other amorphous and crystalline oxidic nanoparticles ($Ti_xO_y(OH)_z$, $Fe_xO_y(OH)_z$, $Zr_xO_y(OH)_z$, $Zn_xO_y(OH)_z$, $V_xO_y(OH)_z$, $Y_xO_y(OH)_z$ and $Al_xO_y(OH)_z$) with diameters between 1 nm and 660 nm were prepared using the microemulsion technique. In case of the metal oxide nanoparticles, the influence of various parameters, such as water content, precursor content and pH value was investigated. Using β-diketonate functionalized metal alkoxides as precursors allowed for an *in situ* functionalization of the metal oxide surface with polymerization initiators. Novel β-diketonates were developed for this approach, which were studied in more detail for their ATRP initiation capabilities.

In a second step, another route to surface-functionalized nanoparticles, i.e. the post modification of metal oxide nanoparticles, was studied. For this purpose, metal salts were used as precursor molecules. The received particles were surface functionalized with novel silane and thiol coupling agents, allowing the covalent attachment of organic groups directly onto the particles surface, such as polymerization initiator and molecules that support aggregation, with a degree of functionalization up to 1.5 mmol/g. Furthermore, systematic studies of the aggregation behavior of surface modified particles were presented, using two types of functionalized silica particles with a diameter of 93 nm as a model system, which supported electrostatic interactions and hydrogen-bridge bonds, depending on the pH value of the suspension, as demonstrated via characterization of the amount of aggregates and their size.

The formed surface-functionalized nanoparticles were used in "grafting from" polymerizations. Depending on the used initiator molecule, different polymerization mechanisms, such as free radical polymerization (thermal- and photo-initiated) and controlled radical polymerization (ATRP), were applied. It was demonstrated that the usage of ATRP enabled adjustment of the thickness of the polymer shell, using several monomers such as MMA, styrene, isoprene and methacrylic acid trimethyloxysilyl propylester. In case of ATRP, kinetic investigations proved a nearly linear dependence of the diameter increase of the core-shell nanoparticles and the molecular weight of the polymer chains on conversion. The formed nanoparticles were proved to show a clear core-shell character.

Some part of the work has already been published:

1) Hybrid inorganic-organic core-shell metal oxide nanoparticles from metal salts, Dieter Holzinger, Guido Kickelbick, *Journal of Materials Chemistry*, **2004**, *14*, 2017.

2) Preparation of Amorphous Metal-Oxide-Core Polymer-Shell Nanoparticles via a Microemulsion-Based Sol-Gel Approach, Dieter Holzinger, Guido Kickelbick, *Chemistry of Materials*, **2003**, *15*, 4944.

3) Modified cubic spherosilicates as macroinitiators for the synthesis of inorganic-organic starlike polymers, Dieter Holzinger, Guido Kickelbick, *Journal of Polymer Science, Part A: Polymer Chemistry*, **2002**, *40*, 3858.

List of Symbols of Abbreviations

^{13}C NMR	Carbon Nuclear Magnetic Resonance Spectroscopy
^{1}H NMR	Proton Nuclear Magnetic Resonance Spectroscopy
^{29}Si NMR	Silicon Nuclear Magnetic Resonance Spectroscopy
A@B	Core-Shell particle consists of A (core) and B (shell)
Ac	Acetyl group
AcacH	Pentane-2,4-dioen
AOT	Sodium bis(2-ethylhexyl)sulfosuccinate
APS	Aminopropyltrimetoxysilane
BET	Brunauer, Emmet, Teller
Br-AcacH	3-Bromo-pentane-2,4-dione
Bu	Butyl group
Cl-AcacH	3-Chloro-pentane-2,4-dione
CP	Cross Polarisation
CTAB	Cetyltrimethylammonium bromid
DLS	Dynamic Light Scattering
EDX	Energy Disperse X-ray Spectrometry
Et	Ethyl group
EtOH	Ethanol
FTIR	Fourier Transform Infrared Spectroscopy
GC/MS	Gas Chromatography / Mass Spectroscopy
GPC	Gel Permeation Chromatography
h	Hour
M	Metal
MAS-MNR	Magic Angle Spinning Nuclear Magnetic Resonance
Me	Methyl group
Me_6Tren	Tris(2-(dimethylamino)ethyl)amine
MeOH	Methanol
MeX	Metal salt
min	Minute
MMA	Methyl methacrylate
M_n	Number average molecular weight
MWD	Molecular weight distribution

NMR	Nuclear Magnetic Resonance
OBu	Butoxide group
OEt	Ethoxide group
OH	Hydroxyl group
O^iPr	Isopropoxide group
OMe	Methoxide group
pmdeta	N,N,N′,N′,N′′-pentamethyldiethylenetriamine
PMMA	Polymethyl methacrylate
Pr	Propyl group
PS	Polystyrene
R_T	Room temperature
s	Second
SDS	Sodium dodecylsulfate
SP	Single Pulse
TEM	Transition Electron Microscopy
TEMPO	2,2,6,6-Tetramethylpiperidin-1-yloxy
TEOS	Tetraethoxy silane
TG	Thermogravimetric
TGA	Thermogravimetric Analysis
TTAB	Tetradecyltrimethylammoniumbromide
TTAB	Tetradecyltrimethylammonium bromide
UV/VIS	Ultraviolet / Visual Spectroscopy
XRD	X-ray Diffraction

NMR-analysis:

d	Doublet
m	Multiplet
q	Quartet
s	Singlet
t	Triplet

FTIR-analysis:

δ	bending vibration
γ	rotating vibration

Table of Contents

1.	**Introduction**	8
1.1.	**Core-Shell nanoparticles**	10
1.2.	**Inorganic-organic core-shell nanoparticles**	10
1.2.1.	Production of inorganic nanoparticles	11
1.3.	**Chemical functionalization of the particle surface**	21
1.4.	**Polymerization of the organic shell**	23
1.4.1.	Free radical polymerization	25
1.4.2.	Atom Transfer Radical Polymerization (ATRP)	26
1.5.	**Formation of ordered structures**	29
2.	**Aim of the work**	33
3.	**Synthesis of nanoparticles**	35
3.1.	**Synthesis of nanoparticles without microemulsion technique**	35
3.1.1.	Synthesis of SiO_2 nanoparticles	35
3.1.1.1.	Stability of SiO_2 nanoparticles without ammonia	36
3.1.1.2.	Kinetics of the SiO_2 nanoparticle synthesis	39
3.1.1.3.	Thermal analysis of SiO_2 nanoparticles	40
3.1.2.	Synthesis of gold nanoparticle	41
3.1.3.	Synthesis of larger gold nanoparticles	44
3.1.4.	Synthesis of Au@SiO_2 nanoparticles	47
3.1.5.	Synthesis of metal oxide nanoparticles via the precipitation from solvents	50
3.1.5.1.	Synthesis of TiO_2 nanoparticles	50
3.1.5.2.	Usage of ethylenglycol to reduce the activity of titanium alkoxides	51
3.2.	**Synthesis of nanoparticles from metal alkoxide derivatives**	53
3.2.1.	Synthesis of various pentane-2,4-dione derivatives	54
3.2.1.1.	Coordination of 3-chloro-pentan-2,4-dione	54

3.2.1.2.	Synthesis of 3-bromo-pentane-2,4-dione	56
3.2.1.3.	Coordination of 3-bromo-pentane-2,4-dione to titanium isopropoxide	57
3.2.1.4.	Synthesis of 1-acetyl-2-oxopropyl 2-bromo-2-methylpropanoate	59
3.2.1.5.	Coordination of 1-acetyl-2-oxopropyl 2-bromo-2-methylpropanoate	60
3.2.1.6.	Synthesis of 3-acetyl-5-bromo-5-methylhexane-2,4-dione	62
3.2.1.7.	Coordination of 3-acetyl-5-bromo-5-methylhexane-2,4-dione	63
3.2.1.8.	Synthesis of 2-bromo-1,3-diphenylpropane-1,3-dione	65
3.2.1.9.	Synthesis of 2-chloro-1,3-diphenylpropane-1,3-dione	67
3.2.1.10.	Synthesis of 2,2-dichloro-1,3-diphenylpropane-1,3-dione	68
3.2.1.11.	Coordination of 2-bromo-1,3-diphenylpropane-1,3-dione to titanium isopropoxide	70
3.2.2.	Synthesis of nanoparticles using pentane-2,4-derivates without additives	74
3.2.2.1.	Short summery	77
3.2.3.	Synthesis of nanoparticles using pentane-2,4-derivates applying a microemulsion approach	78
3.2.3.1.	Synthesis of functionalized titanium oxide nanoparticles from alkoxide precursors	78
3.2.3.2.	Synthesis of functionalized zirconium oxide nanoparticles from alkoxide precursors	90
3.2.3.3.	Synthesis of functionalized vanadium oxide nanoparticles from modified alkoxides	99
3.2.3.4.	Synthesis of functionalized yttrium oxide nanoparticles from modified alkoxides	104
3.2.3.5.	Synthesis of functionalized tantalum oxide nanoparticles from modified alkoxides	107
3.2.3.6.	Synthesis of functionalized iron oxide nanoparticles from modified alkoxides	110
3.2.3.7.	Synthesis of crystalline TiO_2 nanoparticles in a microemulsion approach at increased temperature and pressure	113
3.2.4.	Short summary	120

3.3.	**Synthesis of nanoparticles from metal salts**	123
3.3.1.	Synthesis of iron oxide nanoparticles	123
3.3.2.	Synthesis of titanium oxide nanoparticles	125
3.3.3.	Synthesis of zirconium oxide nanoparticles	128
3.3.4.	Synthesis of zinc oxide nanoparticles	130
3.3.5.	Synthesis of aluminum oxide nanoparticles	133
3.3.6.	Short summary	135
4.	**Functionalization of nanoparticles**	135
4.1.	**Functionalization of SiO_2 nanoparticles**	136
4.2.	**Functionalization of gold nanoparticles**	139
4.2.1.	Synthesis of 2-sulfanylethyl-2-bromo-2-methylpropanoate	139
4.2.2.	Functionalization of gold nanoparticles with 2-sulfanylethyl-2-bromo-2 methylpropanoate	141
4.3.	**Functionalization of Au@SiO_2 nanoparticles**	141
4.3.1.	Synthesis of 2-bromo-2-methyl-propionic acid allyl ester and hydrosilation	142
4.3.2.	Functionalization of the Au@SiO_2 nanoparticles with 2-bromo-2-methyl-propionic acid propane-(3´-triethoxy-silyl)-ester	143
4.4.	**Functionalization of the metal oxide nanoparticles**	143
4.4.1.	Synthesis of the asymmetric azo initiator containing a triethoxy-silane group	143
4.4.2.	Synthesis of the photo initiator containing a triethoxy-silane group	145
4.4.3.	Synthesis of hydrosilated 4-vinyl-benzyl-chloride	146
4.4.4.	Functionalization of the different metal oxide nanoparticles	147
4.4.4.1.	Functionalization of the iron oxide nanoparticles	148
4.4.4.2.	Functionalization of the titanium oxide nanoparticles	150
4.4.4.3.	Functionalization of the zirconium oxide nanoparticles	153
4.4.4.4.	Functionalization of the zinc oxide nanoparticles	155
4.4.4.5.	Functionalization of the aluminum oxide nanoparticles	158
4.5.	**Photoluminescence spectroscopy of different types of TiO_2 nanoparticles**	159
4.6.	**Photoluminescence spectroscopy of different types of**	

	ZrO_2 nanoparticles	163
4.7.	**Short summary**	165
5.	**Aggregation of SiO_2 particles**	166
5.1.	**Investigation of influence of solvent effects on the redispersion of unmodified and surface functionalized silica nanoparticles**	167
5.2.	**Investigation of the aggregation behavior of the two types of functionalized silica nanoparticles**	172
5.3.	**Short summary**	178
6.	**Polymerization of the organic shell**	179
6.1.	**Polymerization of the organic shell around Au- and Au@SiO_2 nanoparticles**	179
6.1.1.	Copolymerization of a second polymer-shell onto Au@SiO_2@PS particles	184
6.1.2.	GPC analyses of the obtained Au and Au@SiO_2 core-shell systems	184
6.1.3.	Eliminating the silica shell of Au@SiO_2@PS particles	186
6.1.4.	Kinetic investigation of the polymerization process	186
6.2.	**Formation of core-shell nanoparticles from modified alkoxides**	188
6.2.1.	Investigation of the polymerization capacities of 3-bromo-pentane-2,4-dione and 3-chloro-pentane-2,4-dione	188
6.2.1.1.	Investigation of the polymerization activity	204
6.2.2.	Synthesis of titanium oxide core-shell nanoparticles	209
6.2.3.	Synthesis of zirconium oxide core-shell nanoparticles	214
6.2.4.	Synthesis of tantalum oxide core-shell nanoparticles	217
6.2.5.	Synthesis of vanadium oxide core-shell nanoparticles	218
6.2.6.	Synthesis of yttrium oxide core-shell nanoparticles	221
6.2.7.	Synthesis of iron oxide core-shell nanoparticles	222
6.3.	**Grafting of a polymer shell from particles that were synthesized from metal salts**	224
6.3.1.	Synthesis of iron oxide core-shell nanoparticles	224
6.3.2.	Synthesis of titanium oxide core-shell nanoparticles	230

6.3.3.	Synthesis of zirconium oxide core-shell nanoparticles	232
6.3.4.	Synthesis of zinc oxide core-shell nanoparticles	234
6.3.5.	Thermal investigation of the obtained hybrid materials	236
6.3.6.	TG-FTIR analyses of representing core-shell nanoparticles performed at Netzsch-Gerätebau GmbH	241
6.4.	**Short summary**	244
7.	**Experimental part**	245
7.1.	**General techniques**	245
7.2.	**Materials**	245
7.3.	**Analytical techniques**	245
7.4.	**Synthesis procedures**	250
7.4.1.	Synthesis of SiO_2 nanoparticles	250
7.4.2.	Synthesis of gold nanoparticles	250
7.4.3.	Increasing the diameter of preformed gold nanoparticles	251
7.4.4.	Synthesis of gold@SiO_2 nanoparticles	251
7.4.5.	Synthesis of TiO_2 nanoparticles	251
7.4.6.	Utilization of ethylenglycol to reduce the activity of titanium alkoxides for the synthesis of titanium oxide nanoparticles	252
7.4.7.	General procedure for the coordination of 3-chloro-pentane-2,4-dione	252
7.4.8.	Synthesis of 3-bromo-pentane-2,4-dione	255
7.4.9.	Coordination of 3-bromo-pentane-2,4-dione to titanium isopropoxide	256
7.4.10.	Synthesis of 1-acetyl-2-oxopropyl 2-bromo-2-methylpropanoate	256
7.4.11.	General procedure of the coordination of 1-acetyl-2-oxopropyl 2-bromo-2-methylpropanoate	257
7.4.12.	Synthesis of 3-acetyl-5-bromo-5-methylhexane-2,4-dione	260
7.4.13.	Coordination of 3-acetyl-5-bromo-5-methylhexane-2,4-dione	261
7.4.14.	Synthesis of 1,3-diphenylpropane-1,3-dione derivatives	263
7.4.15.	Coordination of 2-bromo-1,3-diphenylpropane-1,3-dione to titanium isopropoxide	270
7.4.16.	Synthesis of TiO_2 nanoparticles with the coordination product of titanium isopropoxide and 3-chloro-pentane-2,4-dione	

	(without additives)	273
7.4.17.	Formation of TiO_2 nanoparticles using the coordination product of titanium isopropoxide and 3-acetyl-5-bromo-5-methylhexane-2,4-dione (without additives)	273
7.4.18.	General procedure for the synthesis of metal oxide nanoparticles from modified metal alkoxides in microemulsion	274
7.4.19.	General procedure for the synthesis of crystalline TiO_2 nanoparticles in a microemulsion approach at increased temperature and pressure	278
7.4.20.	General procedure for the synthesis of metal oxide nanoparticles using metal salts	278
7.4.21.	General procedure for the functionalization of the surface of the SiO_2 particle	279
7.4.21.1.	Hydrolysis of methoxy-ester group of the functionalized silica nanoparticles	280
7.4.22.	Synthesis of 2-Sulfanylethyl 2-bromo-2-methylpropanoate	280
7.4.23.	Functionalization of gold nanoparticles with 2-sulfanylethyl-2-bromo-2-methylpropanoate	282
7.4.24.	Synthesis of 2-bromo-2-methyl-propionic acid allyl ester	282
7.4.25.	Hydrosilation of 2-bromo-2-methyl-propionic acid allyl ester	283
7.4.26.	Functionalization of the $Au@SiO_2$ nanoparticles with 2-bromo-2-methyl-propionic acid propane -(3´-triethoxy-silane)-ester	283
7.4.27.	Synthesis of the asymmetric azo-initiator	283
7.4.28.	Hydrosilation of the asymmetric azo initiator	285
7.4.29.	Etherification of 2-hydroxy-1-[4-(2-hydroxyethoxy)phenyl]-2-methyl-1-propanone with allyl bromide	286
7.4.30.	Hydrosilation of the modified photo-initiator	287
7.4.31.	Hydrosilation of 4-vinyl-benzyl-chloride with triethoxysilane	287
7.4.32.	General procedure for the functionalization of metal oxide nanoparticles	288
7.4.33.	General procedure for atom transfer radical polymerization	289
7.4.33.1.	Au- and $Au@SiO_2$-particles	290
7.4.33.2.	General procedure for free radical polymerization	291
7.4.33.3.	Polymerizations initiated by halo-pentane-2,4-diones	291
7.4.33.4.	General procedure of the investigation of the activation rate of	

	3-bromo-pentane-2,4-dione and 3-chloro-pentane-2,4-dione	292
7.4.33.5.	Synthesis of pmdeta-complexes	293
7.4.33.6.	Metal oxide particles synthesized from modified metal alkoxides	294
7.4.33.7.	Metal oxide particles synthesized from metal salts	298

8. Summary 300

9. Literature 314

1. Introduction

In recent years considerable effort has been devoted to the investigation and fabrication of nanostructured materials with functional properties. The large interest in nanosized materials is based on the fact that their properties (optical, chemical, electrical, thermal, etc.) depend on their size, composition and structural order.[1] New effective strategies to built nanomaterials which have predictable properties are investigated with high effort to meet the increasing industrial demands, such as structural and compositional complexity. [2-4]

Nanoparticles show a large specific surface area compared to their volume, which results in the presence of many atoms located at their surface. These surface atoms show a higher energetic state because they have, compared to atoms that are located in the interior of a nanoparticle, a decreased number of neighbor atoms. Very small nanoparticles consist only of a few atoms, which reduces the amount of delocalized electrons significantly compared to extended macromolecular structures, resulting in a larger gap between the discrete energy levels. When the energetic structure of such nanoparticles is investigated no quasi continuous state can be assumed, which has direct influence on their optoelectronic properties. Such physical properties are of great importance for the synthesis of future electronic devices.[5]

The aim of material science is the development of materials which can be adapted to various demands depending on the required properties. A new material class which achieves that kind of requirements are inorganic-organic hybrid materials that combine the properties of inorganic and organic moieties.[6-8] In principle inorganic-organic hybrid materials are divided in two groups: (i) Materials where the phases are interacting by weak forces like van der Waals interactions or hydrogen bridge-bonding (class 1 materials). (ii) Materials where the different phases are linked by strong covalent or ionic bondings (class 2 materials). Because of the different character of the moieties, phase separation is a serious problem in the preparation of the materials. A possibility to overcome this problem is the covalent or ionic linkage between the phases for the formation of a homogenous system.[9-14]

Another important point in the preparation of such materials are the various shapes of the precursors. In figure 1, possible morphologies for the inorganic moieties are presented. The "In" groups are molecules that are bond to the inorganic structure which have the ability to interact with polymer chains. They can represent polymerization initiator molecules [15], groups which can interact with functionalities delivered by the polymer chains [16] or

polymerizable groups.[17] Depending on the morphology of the used building blocks the properties of the resulting composite materials can differ enormously.

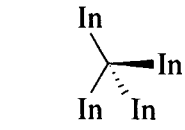

isolated molecules

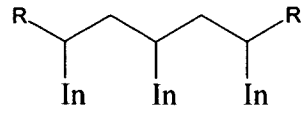

oligo- or polymer chains

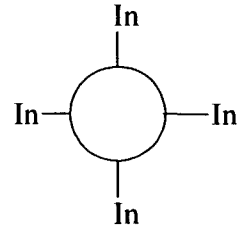

rings

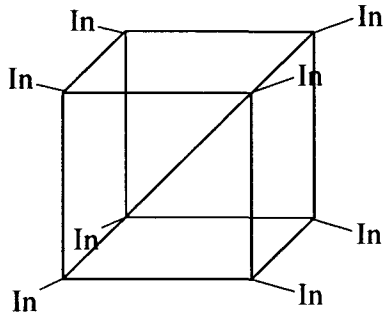

complex polyedric structures

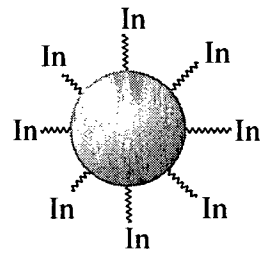

nanoparticles

Figure 1: Possible multifunctional inorganic building blocks for the production of inorganic-organic hybrid materials.

Side chain functionalized polymers, cyclosiloxane rings, spherosilicates or polyhedral silsesquioxanes as well as functionalized nanoparticles were used as inorganic building block for the formation of hybrid material.[15-17]

Inorganic surface functionalized nanoparticles have recently been more intensively studied as building blocks. The major issues in their synthesis are a reproducible formation of the inorganic core with a high size and shape selectivity as well as their stable organic surface modification. A lot of work was done in the field of silica nanoparticles because a simple reproducible synthesis is available and the surface functionalization can be carried out via the reaction of nucleophilic silanol groups with the surface OH-groups. For example, *Blaadern et al.* demonstrated that silica nanoparticles, which were surface-modified with silane coupling agents, remained functionalized after the dispersion in various solvents.[18]

1.1. Core-shell nanoparticles

Core-shell particles can be defined by their different core and shell composition.[19] Usually the core shows an interesting property typical for its composition , e. g. semi conducting or magnetic characteristics. In return the shell can stabilize the core, create compatibility between the core and the environment, or can change the charge, functionality, or reactivity of the surface. Core-shell nanoparticles can be divided according to their chemical composition:[19]

- Inorganic-inorganic nanoparticles. This category mainly covers metallic, magnetic or semi conductor cores which are covered by a semiconductor, insulating, or metal shell.[20-24]
- Inorganic-organic nanoparticles. These nanoparticles consist of an inorganic core like a metal or a metal oxide and an organic shell, which is built by a layer of organic molecules or by a polymer shell.[25-29]
- Organic-organic nanoparticles. Recent examples for this morphology are PMMA-PS [30], polypyrrole-PS [31], PS-poly(*p*-vinylphenol) [32], and poly(dimethylsiloxane)-poly(butadiene).[33] Normally cross linking building blocks have to be inserted to guarantee the linkage of two different polymer entities.[34]
- Organic-inorganic nanoparticles. In this case organic polymer cores are combined with inorganic shells (e. g. metal oxides).[35-39]
- Inorganic-biomolecule nanoparticles. The inorganic core is covered with biologically active substances like receptor molecules or DNA sequences.[40-43]

1.2. Inorganic-organic core-shell nanoparticles

Inorganic nanoparticles that are covered by a polymer layer are of special interest in this category. Polymer-coated particles offer a wide range of industrial applications ranging from catalysis, where the inorganic core deploys a stable phase for the catalytic active groups, to the manufacture of cosmetics, inks, and paints.[12, 13]

The synthetic routes for the production of polymer coated core-shell nanoparticles can be divided into two main classes: polymerization of the organic shell directly on the surface of the inorganic core via grafting from or grafting to techniques, and incorporation of surface-bond monomer molecules into polymer chains.[44-48]

In figure 2 the necessary steps for the production of hybrid materials containing nanoparticles are given.

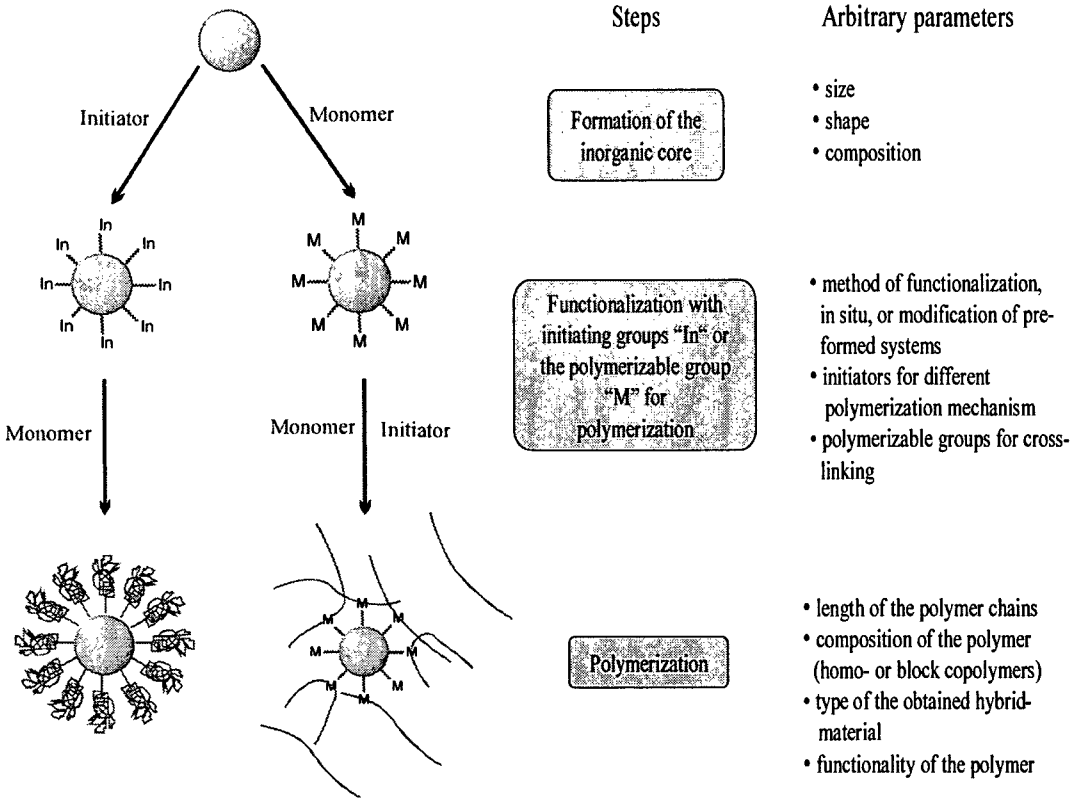

Figure 2: Synthesis of inorganic-organic hybrid materials containing nanoparticles.

1.2.1. Production of inorganic nanoparticles

Inorganic nanoparticles have received considerable attention because of their size-dependent specific physical and chemical properties which led to the development of many different methods for their synthesis and the evaluation of their characteristics. However, if used in suspension, these nanoparticles agglomerate very easily and show very poor dispersion capacity in organic solvents and oils. Therefore the possible applications for unmodified nanoparticles are strongly limited.[49] It is necessary to stabilize the nanoparticles during the formation process to avoid agglomeration. Such stabilizing effects can either be introduced by electrostatic repulsion by charged surfaces (e.g. negatively charged OH-groups), by added salts (like citrates that stabilize gold colloids) or by organic groups that are either adsorbed or covalently attached to the particle surface. If organic groups are used for stabilizing the

particle dispersion, chemical functionalities can be included which broadens the range of possible applications.

As one of many examples, *Li et al.* managed to bond oleic acid groups through esterification on the surface of SiO_2 particles which allowed them to redisperse the functionalized nanoparticles in many organic solvents.[50]

Another way to prevent agglomeration of the nanoparticles during the synthesis is the use of water-in-oil microemulsion. The micelles, which are stabilized by a surfactant and a co-surfactant, serve as nanoreactors for the nanoparticle formation whereby in theory in each micelle just one nanoparticle is formed. The resulting particles are equal in size and composition which makes microemulsion approaches an ideal technique for the production of monodisperse particles.[51] In consideration of the mechanism for the production of well-defined particles, it is necessary to distinguish between two stages, which often overlap, e.g., the formation of nuclei in a homogenous environment and their subsequent growth to particles of larger size.[52] Most of the original concepts for the preparation of "monodispersed" colloids are based on the *LaMer model*,[53] which was developed to explain the formation of uniform spherical sulfur particles. Figure 3 shows a schematic representation of molecularly dissolved sulfur before and after nucleation as a function of time.

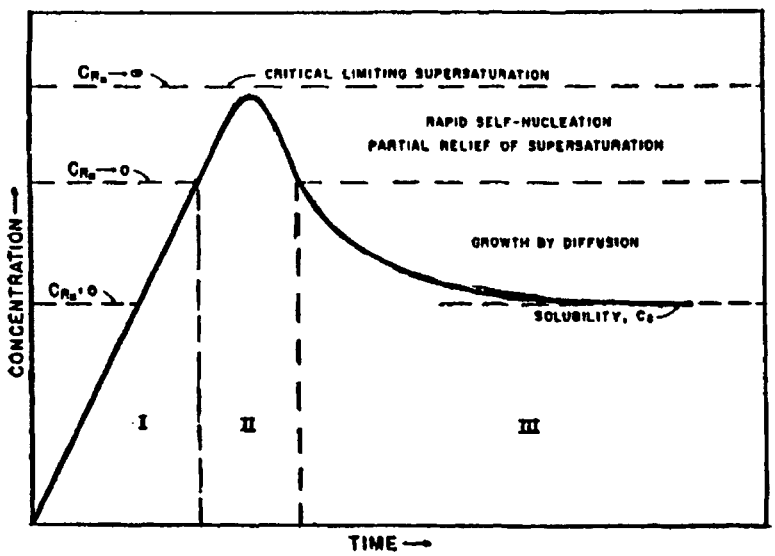

Figure 3: LaMer model for particle formation as a function of time with (I) as concentration phase, (II) as nucleation phase and (III) as growth phase of the nanoparticles; c_s stands for the solubility of the used salt and c_{R^*} stands for the nuclei concentration. [53, 54]

In essence, this model implies that monodisperse particles are formed, if the process in a homogenous solution is conducted in a kinetically controlled manner, so that the concentrations of constituent species reach critical super saturation resulting in a short single burst of nuclei. The latter are then allowed growing by diffusion of solutes to the so produced dispersed solids. Recently, it has been amply demonstrated that LaMer's model is applicable to a limited number of specific cases and often only to the initial stages for the precipitation process. With respect to the nucleation stage, the concept of a short burst has been shown inadequate both in solution of simple and complex species. [55] *Sugimoto* developed a theory of the nucleation process for monodispersed sparingly colloidal particles in an open system, which is based on the assumption that stable nuclei are produced through a kind of Ostwald ripening of originally unstable nuclei. A continuous nucleation/growth has been introduced as well to explain the formation of uniform spherical silica particles by the hydrolysis of tetraethoxysilane (TEOS) developed by *Stöber et al.*[56]

Many different techniques are available for the production of the inorganic core whereby probably the most common methods are: (i) formation of particles via precipitation from a metal salt solution, and (ii) the synthesis of particles in microemulsions.

a) Production of the inorganic nanoparticles via precipitation from metal salt solutions

There is a large variety of different metal and metal oxide nanoparticles which can be manufactured applying this approach. The chemical composition and the morphology of the resulting particles depend on a number of parameters like pH value, concentration of the reactants, temperature, anions, method of mixing, reducing agent etc., which often have to be changed only slightly in order to alter the nature of such precipitates.

A prominent route to generate metal oxide nanoparticles is the hydrolysis and precipitation of defined precursors under basic conditions. It is impossible to generate monodisperse metal oxide nanoparticles just by the addition of a strong base into a solution of a metal salt.
Controlling the kinetic of metal ion hydrolysis that will eventually result in uniform particles, can be achieved using three different mechanisms: 1) forced hydrolysis; 2) controlled release of hydroxide ions; 3) hydrolysis of defined precursors such as metal alkoxides.

1) Forced hydrolysis: In this procedure metal salts are aged at increased temperatures for a certain period of time. For example, aluminum hydrous oxide particles (660 nm in diameter) [57], chromium hydrous oxide particles (diameter 320 nm) [58], hematite particles (diameter 570 nm) [59] or zinc oxide particles (diameter 210 nm) were synthesized using this approach.

2) Controlled release of hydroxide ions: The hydrolysis of cations can be controlled by a slow release of hydroxide ions into a metal salt solution. The decomposition of certain organic compounds, such as urea or formamide, has been extensively used for this purpose. Exemplarily Y_2O_3 nanoparticles [60] with a diameter of 80 nm and CuO particles [61] with a diameter of 110 nm are mentioned here. With such an approach not only oxides but also sulfides and carbonates can be formed.[62]

3) Hydrolysis of defined precursors such as metal alkoxides: The most common starting compound used in the preparation of metal oxide nanoparticles are alkoxides. Silica particles were the first type of oxidic particles that were produced from alkoxides. A prominent route to obtain dense monodisperse SiO_2 nanoparticles is the so called "Stöber" process where in an ethanol ammonia mixture SiO_2 particles are formed via a hydrolysis and condensation route of tetraethoxysilane.[56] Since 1969, when the process was discovered, large efforts were put into optimizing the process. *Park et al.* managed to produce SiO_2 nanoparticles with diameters in the range from 10 to 350 nm revealing a very small size distribution.[63]

Other metal alkoxides can be used as well as precursors but these substances usually show higher hydrolysis rates which leads to the formation of non-spherical particles with a size distribution that is not monodisperse if no stabilizing additives are used. Metal alkoxides can be functionalized for example with β-diketones, ethylene glycol, carboxylic acids, etc, to overcome this problem. For example, *Jiang et al.* prepared monodisperse colloids of titania from titanium butoxide that was functionalized with ethylene glycol in aqueous solution.[64] With this approach the diameter of the resulting particles could easily be tuned by varying the precursor concentration.

Often additives are present during the particle synthesis to enhance the stability of the formed particle dispersion. The most prominent example for the usage of additives is the synthesis of gold nanoparticles which are commonly produced by reduction of gold salts and stabilized with citrate ions in aqueous solution. With such approaches gold nanoparticles in the range of

a few nanometer up to 60 nm can be manufactured.[65, 66] Other metals nanoparticles, which are produced in a similar way are cobalt[67, 68], and iron[69, 70] that can provide magnetic properties or silver[71, 72] and nickel[73, 74] nanoparticles, which offer conductive and in the case of nickel magnetic properties as well. Furthermore, binary systems were also synthesized with this approach. For example, *Toshima et al.* have produced Pd/Pt nanoparticles which were used for catalytic applications.[75, 76]

In the case of more sensitive non noble metals special precautions have to be taken to protect the nanoparticles against environmental influences. Either the surface of the system is protected by a capping layer of another material (e.g. polymer, silica) or less reactive binary compositions (e.g. oxides, sulfides, selenides) are chosen as basic materials. Exemplarily the results of *Danek et al.* are presented here, who manufactured CdSe cores which they covered with a layer of ZnSe.[77] In this case the attachment of a second layer fulfilled two different purposes. New properties were induced to the obtained hybrid-material as they showed that the deposition of a semi conductor with a larger bandgap than the one of the core led to enhanced luminescence due to the suppression of radiation less recombination; furthermore, the sensitive core was protected by the added layer of ZnSe.

b) Production of inorganic nanoparticles with microemulsion techniques

It is crucial to obtain in a first step well defined nanoparticles, which can serve as the core, for the synthesis of defined core-shell systems. Only small salt concentrations can be used, if the formation of the nanoparticles takes place via precipitation from solution to prevent agglomeration during the nanoparticle formation. If large quantities of nanoparticles shall be synthesized, large amounts of solvents would be necessary.
An elegant way to avoid that drawback in the nanoparticle synthesis is the usage of the microemulsion techniques. In particular water-in-oil microemulsions, also called reverse micro-emulsion, play here a major role. They consist of a continuous organic phase and water droplets, which are stabilized by a surfactant and in some cases by a cosurfactant as well (figure 4).

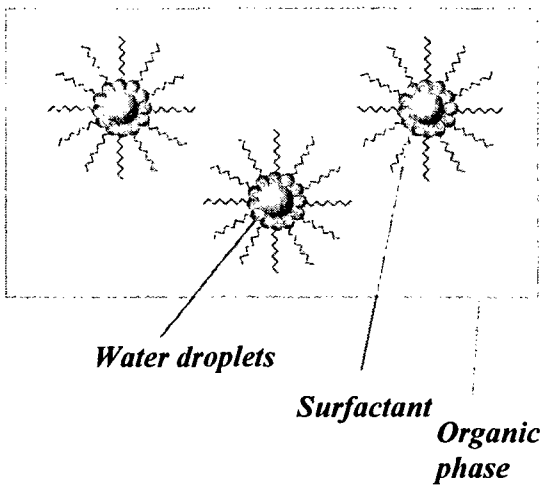

Figure 4: Scheme of a water in oil microemulsion.

In this approach, in which the stabilized water droplets can be considered as nanoreactors, the size, shape, and curvature of the droplets determine the shape of the nano-objects obtained.[78-82] The main idea behind this technique is that by appropriate control of the experimental parameters one can use these nanoreactors to produce tailor-made products down to the nanoscale level. It is stressed that particle formation in nanoreactors takes place in a highly parallel fashion, i.e. the synthesis is performed in nanocompartments, which are separated from each other by a continuous phase.[83, 84]

The properties of the particles depend not only on the surfactant type and the thermodynamic conditions but also on the presence of additives like alcohols, electrolytes, and block copolymers that can reduce the polarity diversity between aqueous solution and organic phase.

The exact size of the droplets can be selectively adjusted by the type and amount of surfactant used for stabilization. In scheme 1 the most common surfactants used in water-in-oil microemulsions are presented.

Scheme 1

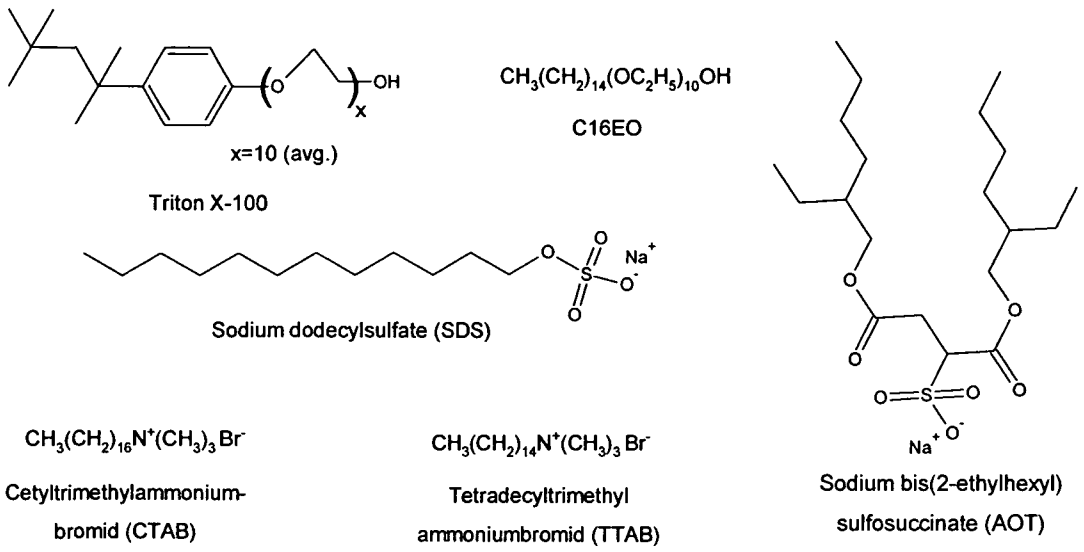

Triton X-100[85] and C16EO[86] are nonionic surfactants while SDS[87, 88] and AOT[89] are negatively and CTAB[90], CTAC[91], and TTAB[92] are positively charged.

The type of the used surfactant has a great influence on the obtained micelle structure. Anionic and cationic surfactants allow the formation of monodisperse droplets between 30 and 200 nm; nonionic oligomeric or polymeric surfactants are suitable for the formation of droplets between about 100 nm and 800 nm. Furthermore, it was shown that the mobility of water molecules near the surfactant layer is increased if ionic surfactants are used, which has strong influence on occurring diffusion processes.[93]

If metal oxide nanoparticles should be produced via a microemulsion approach, there are two possible routes: (i) hydrolytical unstable precursors which penetrate into the water droplets are mixed with the emulsion that can already contain a water-soluble reactive; (ii) the precursor and a reactive solution are prepared in two microemulsions which are subsequently unified. In the formed microemulsion a dynamic exchange of molecules from different micelles occurs.

The particle formation from precursors that diffuse from the organic phase through the surfactant layer into the water droplets is shown in figure 5.

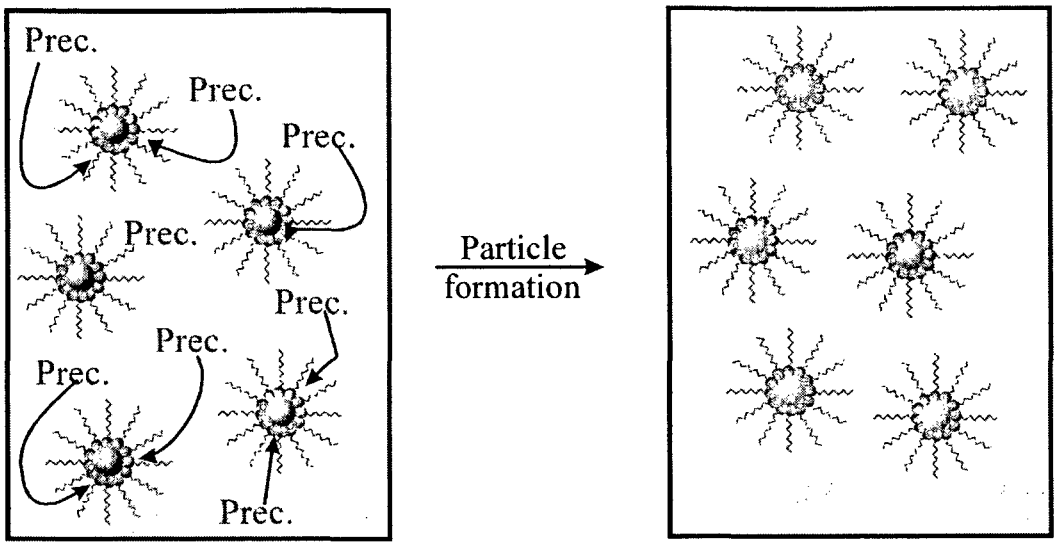

Figure 5: Particle formation if one microemulsion is utilized.

In this case a precursor which has the ability to undergo hydrolysis and condensation reactions with water can be chosen. The particle formation depends strongly on the diffusion coefficient of the chosen precursor through the surfactant layer. The preconditions of this approach are the solubility and reactivity of the precursor in the organic phase.

An important process for the formation of metal oxide nanoparticles is the sol-gel process, which is based on hydrolysis and condensation reactions of metal precursors and is shown in scheme 2.[94] In particular metal alkoxides $M(OR)_x$ (M = Si, Ti, Zr, VO, Al, Zn, Sn, Ce, Mo, W, lanthanides, etc. R = alkane or aromate) are often used that are hydrolyzed through the addition of water and react from a sol to a gel in organic solvents.[95]

Scheme 2

Hydrolysis:

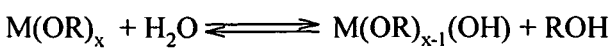

Condensation:

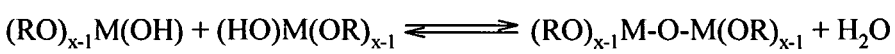

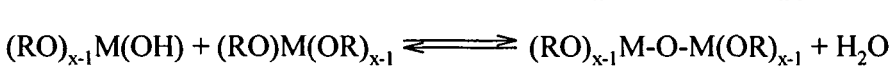

Oleation:

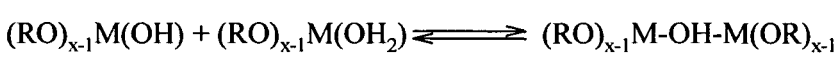

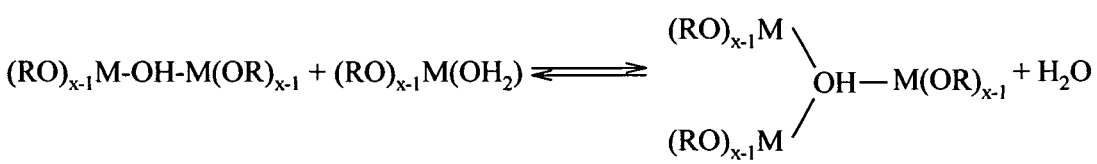

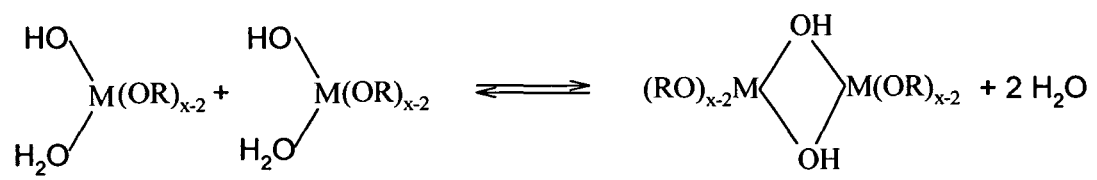

The hydrolysis is catalyzed either by acid or base. The nature of the metal and the ligands has great influence on the reactions described above.[96-100] Applying this method, for example, organically modified silica nanoparticles can be produced in a reverse microemulsion.[101, 102] A variety of trialkoxysilane molecules with vinyl, thiol, amino, or methacryloxy functionalities were introduced into a AOT microemulsion along with TEOS to produce hydrophobic functionalized silica particles.

Contrary to the often used silicon alkoxides, metal alkoxides show a higher reactivity with water. This effect is caused by the lower electronegativity and the higher Lewis-acidity of the metal center on the one hand and by the possibility of the increase of the coordination number on the other hand. The reaction velocity of the metal alkoxides has to be slowed down for a better control of the hydrolysis, which can be achieved, for example, by the coordination of bidentate ligands instead of the commonly used alkoxides.[103]

For example, *Berkovich et al.* used the coordination product of pentane-2,4-dione and aluminum isopropoxide as precursor in a water-in-oil microemulsion with octanol as organic phase and nonionic Silwet L-7607 as surfactant, whereby they gained globular, amorphous aluminum oxide-hydroxide nanoparticles with a diameter of 3 nm.[104]

With this approach it is also possible to produce crystalline nano structures. For example, *Andersson et al.* managed to produce crystalline TiO_2 nano-rods from titanium butoxide.[105] The alkoxide was dissolved in 5 M HCl or HNO_3 and added to a microemulsion containing Triton X-100 as surfactant. This mixture was heated to 120 °C for several hours. Depending on the used acid both anatase and rutile nano structures were obtained.

(ii) The second possible approach towards the formation of metal oxide nanoparticles is the use of two water-in-oil microemulsions A and B, one containing a precursor while the second contains a reactive solution, which are unified (figure 6).

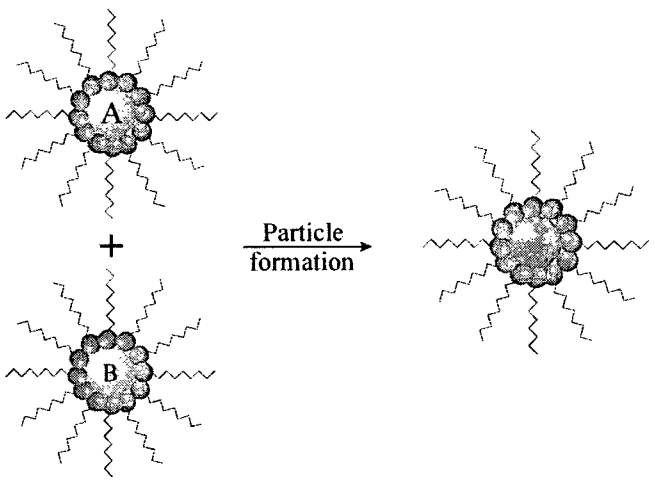

Figure 6: Synthesis of nanoparticles with a two microemulsion approach.

Particle formation takes place via droplet collision and rapid intermicellar exchange of their water content. Typically these particles do not carry functional groups and have to be functionalized afterwards. With this approach metal oxide nanoparticles, such as SiO_2[81, 106-108], TiO_2[50, 109-111], ZrO_2[112], and magnetite [113, 114] can be synthesized.

He et al. produced CeO_2 nanoparticles from cerium nitrate and methyl oxalate with a diameter of 58 nm in a microemulsion consisting of cyclohexane as continuous phase, cetyl trimethylamine bromide (CTAB) as surfactant, and 1-hexyl alcohol as cosurfactant.[90] *Tai et al.* investigated the influence of operation variables on the properties of hydrous-zirconia particles using positively charged CTAB as surfactant.[115] Depending on the water-to-CTAB and water-to-hexanol ratio, zirconia particles with a diameter between 20 – 60 nm and 20 –

250 nm were synthesized. By decreasing the water-to-hexanol ratio, *Tai et al.* were able to reduce the size distribution of the zirconia particles. With this approach not only metal oxide nanoparticles but also other binary nanoparticles such as CdS[116] and metal nanoparticles can be produced. For example, *Ingelsten et al.* reported the synthesis of nano-sized platinum particles in water-in-oil microemulsion using anionic and nonionic surfactants or a mixture of the two.[117] In another example, monodisperse gold colloids were prepared by the reduction of $HAuCl_4$ in CTAB/octane + butanol/H_2O reverse micelle system with $NaBH_4$ as the reducing agent.[118]

1.3. Chemical functionalization of the particle surface

Controlling the surface properties of nanoparticles is of outstanding importance from both a theoretical and a practical point of view. Functionalization of the surface makes it possible to fine-tune the suspension behavior in various solvents, to incorporate chemical functionalities, and is of fundamental interest for a better understanding of the stabilization mechanism of colloids. In principle there are two different approaches for the functionalization of nanoparticles:

- Post synthetic functionalization
- *In situ* functionalization

In the post synthetic route the particles are formed in a first and the surface is modified in a second step. The surface atoms of metal oxide nanoparticles often carry reactive O^- or OH groups, which can be applied for the functionalization with suitable organic groups by nucleophilic substitution or by electrostatic interactions. Organically substituted silane molecules with the general formula R_nSiX_{4-n}, where X is a hydrolysable group (i.e., halogen, amine, alkoxy, acyloxy) and R represents a nonhydrolyzable organic substituent, have widely been used to alter the surface characteristics of inorganic oxides.[119, 120] The X substituents of these silanes undergo substitution reactions with surface OH groups present on the inorganic support. Applying these so called silane coupling agents, specific surface properties can be induced which are often important for further modification, depending on the organic substituent. This type of surface modification was extensively investigated using SiO_2 nanoparticles but in general all particles that have OH groups at the surface can be modified in that way. Depending on the functional group, different properties can be induced, for example, the surface can turned from hydrophilic to hydrophobic by the functionalization

with alkyl groups. Several groups published the functionalization of SiO_2 nanoparticles with modified silane alkoxides.[123] For example, *Blaaderen et al.* functionalized silica particles with the commercially available silane coupling agent 3-aminopropyltriethoxysilane and obtained a surface coverage of 7 groups per nm^2.[18] Similar results were reported by *Philipse et al.* who covered the same kind of silica with the coupling agent methacryloxypropyltrimethoxysilane and published a surface coverage of 10-20 groups per nm^2.[121] Reactions with other nanoparticles that contain hydroxy groups were also carried out such as alumina[122], or Fe_3O_4[19], whereby the silane coupling agents were used to allow the encapsulation via a silica shell.

Not only silane coupling agents but also metal alkoxides that are modified with a bidentate ligand can be used for the surface functionalization of metal oxide particles. For example, *Chang et al.* used diisopropyl methacryl isostearoyl titanate for the functionalization of TiO_2 nanoparticles.[124]

Such modifications of the surface not only induce additional functionalities but also can change the physical properties of the inorganic nanoparticles as well. One example is the complexation of surface metal atoms by bidentate ligands. Enediols form charge-transfer complexes with the surface metal atoms of metal oxide nanoparticles, which result in a change of the optical absorption spectra and the effective band, which were found to be proportional to the density of delocalized π electrons and the dipole moment of surface-bound titanium enediol ligand complexes.[125] Not only optical but also magnetic properties can be influenced via a surface functionalization. For example, *Lui et al.* used emulsifier to cover iron oxide nanoparticles with a shell of different polymers.[126] The composite microbeads showed magnetic properties which are strongly related to the size of the produced core-shell systems.

Not only metal oxide nanoparticles but also metal nanoparticles can be surface functionalized after their formation. One of the most prominent metal particle systems that is utilized as a model for particle properties are gold particles, which have been studied for centuries and used for many applications, e.g., for the coloring of windows. During the synthesis these particles are stabilized with weakly surface-bound citrate molecules that can easily be replaced by thiol groups.[66] These thiol groups can act as anchor groups on the particle surface for many organic molecules. Applying this approach it is, for example, possible to functionalize the particle surface with initiator molecules for atom transfer radical

polymerization (ATRP) which contain thiol anchor groups and polymerization initiators. In addition, several groups reported the use of phosphines, phosphine oxides, amines, carboxylates and isocyanides for the modification of gold nanoparticles.[127-131] The obtained functionalized gold nanoparticles are highly interesting due to physical (e.g. surface plasmons band, fluorescence, electrochemistry), chemical, supramolecular, and recognition properties which enable many different applications (e.g. chemical sensors, catalysis).[132]

The most elegant way to receive surface-functionalized nanoparticles is an *in situ* modification during the microemulsion process. Pentane-2,4-dione is a compound that offers a lot of possibilities for chemical functionalization due to its chemical structure. β-Diketones dispose acid H-atoms that allow easy substitution at the C-atom, which is situated between the two carboxylic groups. Furthermore, the methyl group atoms can be functionalized as well. β-Diketones have often been used in sol-gel processing as a chemical additive to reduce the reactivity of metal alkoxides.[133-135] Stable TiO_2-based colloids have been prepared by using a new precursor, $Ti(O^iPr)_3acac$, derived from the modification of titanium isopropoxide by acetylacetone.[136, 137] NaH or other bases can be used for the functionalization of β-diketones depending on the functional group that should be attached and the electronical structure of the β-diketone. For example, *Shono et al.* performed different alkylations at the 3-position with alkyl halides in the presence of NaH.[138] Hydroxybenzylations of 1,3-diketones do not even require the use of an additional base. *Poss et al.* bonded p-hydroxybenzoyl alcohol just by rising the temperature in an aqueous medium.[139]

Not only metal oxide but also metal nanoparticles (e.g. Au, Ni) can be functionalized *in situ* during the formation process. For example, *Brust et al.* synthesized gold nanoparticles that were stabilized and *in situ* functionalized with sodium 3-mercaptopropionate showing a diameter between 1.5 and 5.2 nm.[140]
Green et al. used nickel acetylacetonate for the synthesis of nickel nanoparticles that were alkylphosphine passivated during the synthesis by the reduction with Lewis bases like tri-*n*-octylphosphine.[141]

1.4. Polymerization of the organic shell

The attachment techniques of polymers onto the surface of inorganic particles can be divided into two basic types, the "grafting from" and the "grafting to" method. Through a prior

functionalization, polymerization initiators can be covalently bonded onto the particle surface which leads to polymer chains that grow directly from the particle surface in a "grafting from" approach.[140] Different groups described recently coverage of silica nanoparticles in a "grafting from" approach via controlled radical polymerization.[142-144] For example, *von Werne et al.* deposited bromo-isobutyric acid derivatives on the surface of silica particles and polymerized a layer of polystyrene.[145]

If the polymer chains are synthesized prior and attached afterwards via functional groups on the particle surface, the "grafting to" method is performed. Another possibility would be to pre-functionalize the particle surface either with functional groups that can bind to polymer chains or with monomer molecules that can be incorporated in the polymer chains during the polymerization process. For example, *Yoshinaga et al.* synthesized series of polymeric silane coupling agents and subsequently attached them to colloid silica beads.[146, 147] These functional polymers contained anhydride maleic moieties and were designed to allow molecular recognition for the immobilization of certain enzymes. The drawback of this approach is the limited surface coverage due to diffusion restrictions.

A convenient way to elaborate organic-inorganic colloids is through heterophase polymerization which leads to direct nucleation and growth of the polymer particles on the inorganic surface by simple adsorption of the main ingredients of polymerization namely, the monomer, the surfactant or the initiator molecule.[78] *Bourgeat-Lami et al.* showed that steric stabilizers, such as poly-vinyl-pyrrolidone, have a positive impact on the formation of the polymer-shell in case of inorganic-organic silica/polystyrene colloids.[47]

Miniemulsion polymerization is a further type of polymerization to encapsulate inorganic entities. Here an effective surfactant/hydrophobic system is used, in combination with a high shear source, to stabilize very small monomer droplets containing the nanoparticles, typically 50-500 nm in diameter. Titanium dioxide[148, 149], calcium carbonate[150], iron oxide[151], carbon black[152], silica[153] and phtalocyanine blue pigments[154] have been encapsulated by this technique.

Another way for producing hybrid materials is the utilization of polymer gel colloids (also called microgels) as reactors for the controlled precipitation of minerals. For example,

Saunders et al. used poly(N-isopropylacrylamide) hydrogels to trap iron salts and form iron oxide nanoparticles embedded in the polymer gel.[155]

The polymerization of the polymer-shell can be applied via several polymerization mechanisms. Radical, ionic, and ring-opening metathesis polymerizations (ROMP) are described in literature.[19] For example, *Tsubokawa et al.* used anionic polymerization to graft polyesters from various inorganic particles such as silica, titania, and ferrite.[156] The drawback of ionic polymerization is the sensibility towards impurities, which have to be avoided for a controlled polymerization reaction. ROMP was exemplarily applied by *Skaff et al.* from the surface of cadmium selenides nanoparticles that were stabilized by functional phosphine oxides.[157]

As the polymerization of the polymer-shell in this work was applied via radical polymerization, this type of polymerization is discussed in more detail. All radical polymerization methods can be divided into controlled and free radical polymerizations. The advantage of the controlled polymerization mechanisms is that polymer chains with a predetermined molecular weight and a low polydispersity are obtained and therefore the thickness and the composition of the polymer shell can be perfectly controlled.

1.4.1. Free radical polymerization

Free radical polymerization can be induced by various processes, depending on the initiator. Commonly UV-light induced and thermal sensitive initiators that form radicals upon decomposition are used, which afterwards can initiate polymerization.[17] The initial obtained radical concentration is very high which leads to various termination reactions that lead to uncontrolled polymerization. Furthermore, the so called "Trommsdorf-effect" also contributes to uncontrolled growth of the polymer chains due to auto-acceleration of the ongoing polymerization through exothermic effects.[158] Due to diffusion problems, locally very high radical concentrations are achieved which broaden the molecular weight distribution of the resulting polymer. The usage of solvents can minimize this effect as the auto-acceleration of the process can be reduced.

If this polymerization mechanism is utilized for the encapsulation of nanoparticles in a "grafting from" approach, a further drawback arises. The surface attached free radical

polymerization initiators often form two radicals upon decomposition. Therefore, polymerization also occurs in solution. In this case a further purification step is necessary to separate core-shell particles from the homo-polymer. Several methods were applied for the grafting from free radical polymerization. For example, *Tsubokawa et al.* converted the surface OH groups of SiO_2 particles to peroxy groups, which were polymerized afterwards with methacrylic acid (scheme 3).[159] 6 % of the used monomer reacted with 44 % of the theoretical accessible surface peroxy groups.

Scheme 3

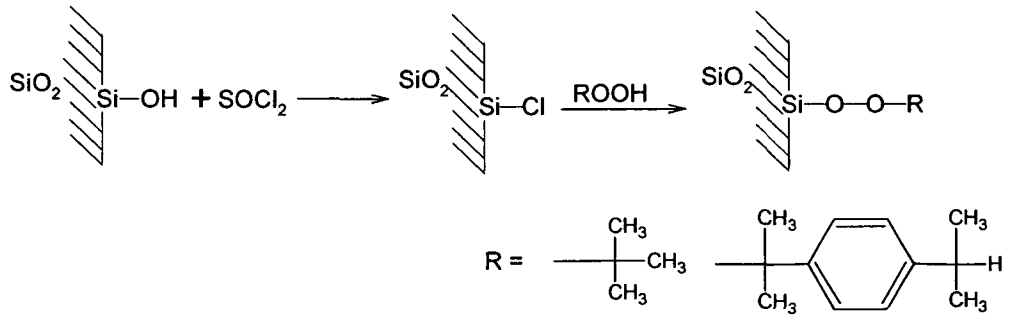

Prucker et al. recently described the synthesis of an asymmetric diazo-initiator that contained a silane for the coupling with the particle surface.[160] The azo compound contained a cleavable ester group to facilitate degrafting of the polymer chains after polymerization for analytical purposes and was configured with one anchor group, to control self assembly of the chlorosilane azo initiators on the silica surface. Polymerization was performed in toluene at 60°C and delivered grafted and free polymer chains. *Bai et al.* prepared polymer-inorganic hybrid nanoparticles through radical photo-polymerization of methyl methacrylate initiated by *N,N*-diethyldithiocarbamyl surface functionalized silica nanoparticles under UV irradiation at ambient temperature.[161]

1.4.2. Atom Transfer Radical Polymerization (ATRP)

In contrast to free radical polymerization, where polymerization also occurs in solution, this is not the case if controlled radical polymerization, such as transition metal mediated atom transfer radical polymerization (ATRP) is applied.[142, 143, 162] In ATRP a halogen atom is transferred from a carbon-halogen bond to a metal complex via homolytical bond cleavage. The addition of the halogen radical to the metal complex increases its oxidation state by one

and an organic radical, which is able to start a polymerization process, is formed. A number of transition metals that can increase and decrease their oxidation state reversely by one can serve as metal center of the catalyst complex. The salts of the following metals have already successfully been used as metal centers: Cu[163], Mo[164], Cr[165], Re[166], Ru[167], Fe[168], Rh[169], Ni[170], and Pd[171]. The main role of the ligand is to solubilize the transition-metal salt in the organic media and to adjust the redox potential of the metal center to the appropriate reactivity and dynamics for the atom transfer. Nitrogen ligands are mainly used for copper and iron mediated ATRP in monodentate and bidentate form.[172] Phosphorus-based ligands are used to coordinate most other transition metals used in ATRP.[173]

Miscellaneous ligands like cyclopentadienyl, indenyl[174, 175], and 4-isopropyl-toluene[173] were recently used in ruthenium-based ATRP to obtain more reactive catalysts than ruthenium complexed by phosphorus alone.

Initiators that are used for ATRP have to be able to form stable radicals as the number of initiator molecules determines the number of growing polymer chains. If initiation is fast and transfer and termination negligible, then the number of growing chains is constant and equal to the initial concentration. As initiators manly halogenated alkanes [176], benzylic halides [177], α-haloketones [178], α-halonitriles [179], and sulfanyl halides [180] are used.

In ATRP an equilibrium where the metal bound halogen can react again with the radical to form the so called dormant species is formed. The mechanism of ATRP is shown in scheme 4. The equilibrium normally is situated on the left hand side because k_d is much larger than k_a which keeps the radical concentration very small and reduces the occurrence of termination reactions, therefore, the polymerization is controlled and quasi living. The ratio between k_d and k_a depends on the utilized metal core and ligand that form the catalytically active complex.

Scheme 4

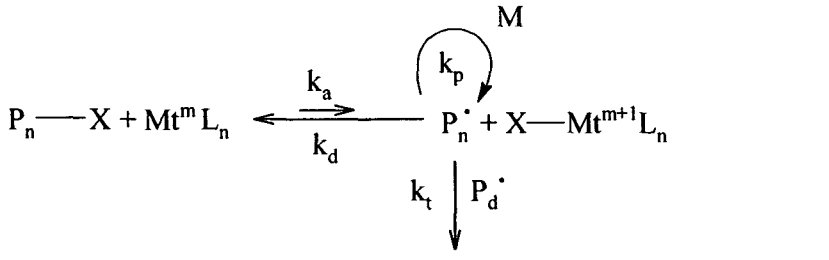

Termination reactions + 2 X— Mt^{m+1} L_n

Coupling

Elimination

Disproportion

If functionalized nanoparticles shall be used as macroinitiators in an ATRP initiator, molecules have to be attached to the particles surface as described before. For example, *Pyun et al.* functionalized silica particles with 2-bromo isobutyrate groups and polymerized methyl methacrylate (MMA), styrene, and n-butyl acrylate directly from the surface.[181] The core-shell particles were treated with hydrofluoric acid to dissolve the silica core to enable characterization of the cleaved polymer chains. The received polymer and copolymer chains showed polydispersities of the molecular weight between 1.2 and 1.5 and conversion from 10 to 50 % which is typical for ATRP. A similar approach was applied by *von Werne et al.* who used 2-(4-chloro-methylphenyl)ethylendimethylethoxysilane to attach initiating groups on the SiO_2 particles surface.[182] Similarly, (11′-dimethylsilylundecyl)-2-chloro-2-phenylacetate was attached to a silica surface to initiate the ATRP of styrene by *Böttcher et al.*[183]
Wang et al. used oleic acid stabilized Fe_2O_3 nanoparticles where the ligand was exchanged with 2-bromo-2-methylpropionic acid (Br-MPA). These Fe_2O_3 nanoparticles were dispersed in styrene and used as macroinitiators for solvent-free ATRP.[184] Furthermore, CdS@SiO_2 nanoparticles were synthesized by *Farmer et al.*, functionalized with ATRP initiators via silane coupling agents, and polymerized with methyl methacrylate.[28] The films which were manufactured from these hybrid inorganic-inorganic-organic nanoparticles still showed the typical photoluminescence for CdS.

Besides ATRP, several other controlled radical polymerization methods are investigated which are all based on establishing a rapid dynamic equilibrium between a small amount of growing free radicals and a large majority of the dormant species.[163] The dormant chains can

be alkyl halides as in ATRP or formed by degenerative transfer (DT)[185], thioesters, as in reversible addition fragmentation chain transfer processes (RAFT)[186], alkoxyamines, as in nitroxide mediated polymerization (NMP)[187] or stable free radical polymerization (SFRP)[188], and potentially even organometallic species.

1.5. Formation of ordered 3D-structures

Surface functionalization not only plays an important role if active sites for chemical reactions should be attached to the surface of nanoparticles but also if self aggregation should be obtained. The organizing and patterning of nanoparticles into two- or three-dimensional superstructures opens a route to chemical, optical, magnetic, and electronic devices with outstanding properties.[189-191] The production of ordered macroscopic structures can be physically induced via solvent evaporation, filtration, sedimentation, or centrifugation techniques. Three different strategies are available to obtain ordered 3D-structures. (i) Ordering of nanoparticles without surface functionalization; (ii) ordering of surface functionalized nanoparticles; (iii) ordering of functionalized nanoparticles due to interactions between the functionalities (hydrogen-bondings, ionic forces).

As an example for the ordering of particles which do not carry surface functionalities, polystyrene particles are presented. *Park et al.* recently presented a cell which is based on a square frame of a photoresist to order polystyrene particles, which had a diameter from 60 nm to 3 μm, in an ultrasonic bath.[192] With this approach they were able to crystallize polystyrene beads of 0.48 μm in diameter into a 25 layer assembly over an area of 1 cm^2 in 48 hours to produce tunable optical filters. Depending on the diameter of the utilized particles each crystalline assembly effectively rejects a narrow wavelength interval (as determined by the Bragg condition) in the spectral region ranging from ultraviolet to near-infrared.

Furthermore, it was shown that ordered structures deliver outstanding optical properties. For example, *Xia et al.* have fabricated three-dimensional photonic crystals for the use in the spectral region from ultraviolet to near-infrared.[4] They describe a self-assembly approach of colloid particles from 150 nm to 50 μm in diameter into cubic-close-packed lattices over larger macroscopic areas. Not only organic particles were organized in 3D arrays but also inorganic systems. As an example of many, *Kang et al.* organized silica nanoparticles with a

diameter of 200 nm into 3D arrays using a combination of ultrasonic treatment and centrifugation.[2]

Also the controlled assembling of metal nanoparticles was described in literature. For example, *Taleb et al.* directed silver nanocrystals into ordered aggregates or quantum dots superlattices.[193] They observed that the optical behavior of the Ag particles strongly depends on the kind of organization. In a 2D hexagonal network, the plasmons peak was shifted towards low energy and an increase in the bandwidth was observed, whereas in 3D superlattices the self-organization induced an increase of the dielectric constant, which provoked a larger shift toward low energy compared to the 2D superlattice. If the metal nanoparticles show magnetic properties, external magnetic fields can be used to induce the self-assembling as well. For example, *Hilgendorff et al.* used magnetophoric deposition to obtain large areas of symmetric multi-dimensional structures based on monodispersed cobalt nanoparticles.[194] The intensity of the magnetic field seemed to be crucial for the obtained lattice. Whereas low magnetic field intensities like 0.8 T led to two dimensional structures, higher intensities like 6 T provided 3 dimensional arrays.

As mentioned before surface functionalization can be used to support the self-assembling process. Self ordering is supported by several intermolecular forces: covalent, electrostatic, van der Waals interactions, and hydrogen bondings. Although van der Waals interaction is one of the most common intermolecular or interparticular forces responsible for the formation of ordered arrays in evaporated nanoparticles[195], particles held together by such a non-specific force are not fully controllable or chemically and mechanically stable on the macroscopic scale. In contrast, chemically specific binding (e.g., covalent or H-bonding) could overcome the weakness, though observations of large domains of highly ordered organizations are very limited.[196] For example, *Beck et al.* functionalized the surface of silica nanoparticles with (trimethoxy-silyl)-propyl-dihydrofurane-2,5-dione, hydrolyzed the anhydride and saponified the ester groups with NaOH. These highly charged nanoparticles were dispersed in aqueous solution and ordered via solvent evaporation from a single drop.[197] Not only metal oxide nanoparticles can be arranged with such an approach. For example, *Han et al.* used a hydrogen-bonding mediated pathway to obtain control over the aggregation of gold nanoparticles via alkanethiols.[198]

Recently, it was shown in literature that biomoleculare substances can be used to support the ordering process of nanoparticles. For example, *Brust et al.* arranged randomly dispersed DNA-coated gold particles into 3D-arrays by manipulating the particles with DNA-processing enzymes.[196]

The attachment of DNA on the surface of nanoparticles not only can be used to order the particles in a 3D-array but also to arrange them around a DNA helix such as *Storhoff et al.* published recently.[199] They managed to prepare ordered structures consisting of two or three DNA modified gold nanoparticles attached to a complementary DNA template, using phosphine-stabilized 1.40 nm particles modified with a single thiol-capped oligonucleotide and two different DNA template length and sequences.

Another possibility to gain ordered arrays are chemical interactions which can be tuned to provide donor/acceptor or ionic interactions between particles that carry different functionalities. With such an approach layer-by-layer deposition of nanoparticles can be achieved if the nanoparticles that are equipped with two different surface functionalities are deposited layer-by-layer like shown in figure 7.

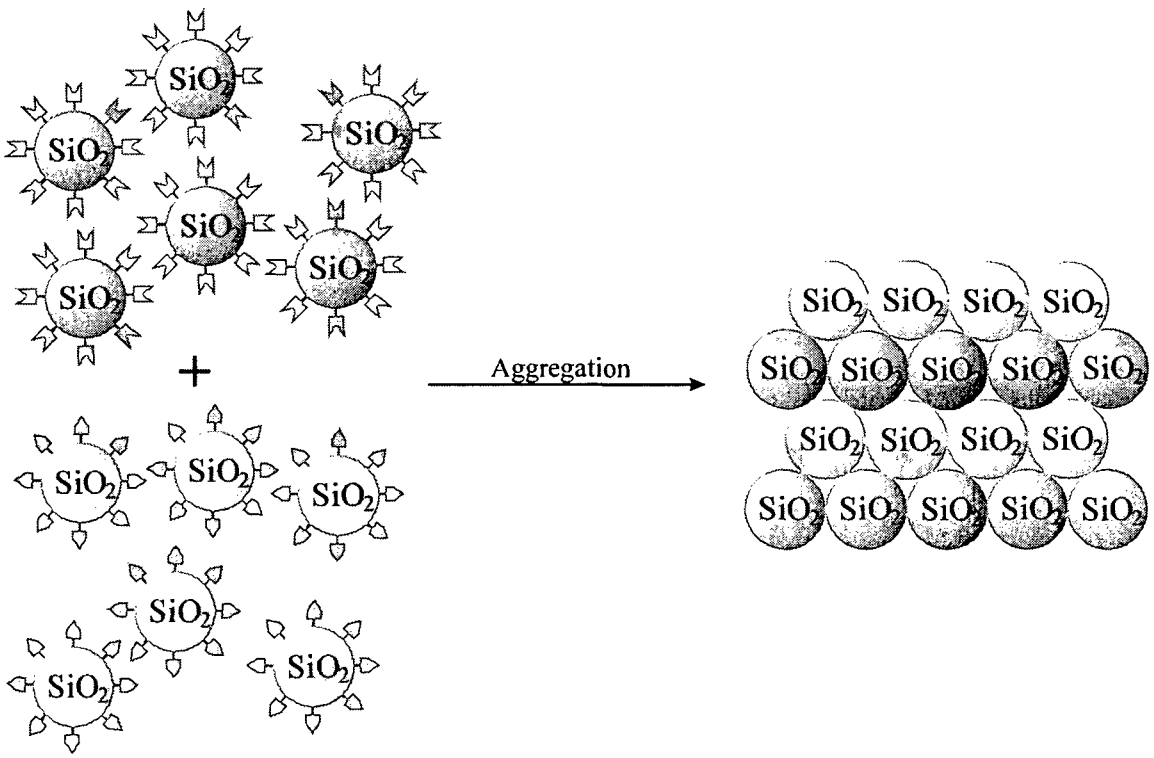

Figure 7: Controlled aggregation of SiO_2 particles with different surface functionalities.

For example, *Philipse et al.* used various chloro- and alkoxy silanes to obtain donor and acceptor functionalities on the surface of silica particles.[121]

Often additives like polyelectrolytes are added to enhance the ordering process of functionalized particles. For example, *Boal et al.* have recently demonstrated the self-assembly of colloid gold particles (~ 2 nm) by a "bricks and mortar" approach, in which complementarity between colloid and polymer was achieved using the diaminotriazine-thymine three-point hydrogen-bonding interaction.[200] *Mori et al.* covered silica nanoparticles with tertiary amine containing alkoxy-silanes that allowed the complexation of a weak acidic polyelectrolyte in order to form 3D-arrays.[201]

A similar approach can be used for the for the layer-by-layer deposition of ionic polymers. *Lee et al.* used poly(sodium 4-styrenesufonate) as polyanion and polyacridine as a polycation to reveal an photoactive polymer which is sensible to metal ions and, therefore can be used as sensor.[10]

2. Aim of the work

The synthesis of polymer modified inorganic nanoparticles is a great challenge consisting of various steps that have to be accurately controlled. In this work a microemulsion-based sol-gel process was used for metal oxide nanoparticles, while gold nanoparticles were stabilized via additives during the synthesis. Functionalization of the particle's surface was either performed *in situ* or via an additional step using silane coupling agents or thiol functionalities. The polymer shell was formed via "grafting from" polymerization applying free radical polymerization and controlled radical polymerization.

The following aspects of the production of core-shell systems were investigated in detail in this work:

1. Exploring a general route to synthesize different metal oxide nanoparticles via a microemulsion approach.

2. Synthesis of novel functionalized pentane-2,4-diones, which are able to initiate several types of radical polymerization and can serve as ligand for the coordination to various metal alkoxides. Additionally, investigation of the efficiency values of the new formed initiators and the properties of the resulting particles was performed.

3. Synthesis of polymerization initiators based on literature-known systems that can bond to metal or oxidic surfaces via a thiol functionality or silane coupling agents, respectively.

4. Comparison of the methods of nanoparticle surface functionalization, during or after their formation, with polymerization initiators for different polymerization mechanisms.

5. Investigation of the aggregation behavior of organically surface-functionalized silica nanoparticles in various solvents.

6. Polymerization of an organic shell by a grafting from approach from the surface of the modified inorganic nanoparticles using different monomers and free radical as well as controlled radical polymerization.

7. Investigation of the kinetic aspects of the ATRP using functionalized nanoparticles as macroinitiators.

3. Synthesis of nanoparticles

3.1. Synthesis of nanoparticles without microemulsion technique

A broad variety of metal and metal derivate nanoparticles can be synthesized without additives that stabilize the dispersion. In case of metal and metal oxide particles the most common precursors are metal salts and organometallic compounds which are reduced or hydrolyzed, respectively. Metal alkoxides allow hydrolysis at low temperatures which makes them perfect educts in the nanoparticle synthesis if organic functionalities should be incorporated. Probably, the most extensively investigated process deals with the synthesis of silica by the hydrolysis of tetraethoxysilane, first described by *Stöber et al.*[56]
Because of the well-known control over their size and the possibilities to functionalize these particles with silane coupling agents, which can be easily produced by modification of unsaturated compounds, these systems were chosen as model compounds in our studies.

3.1.1. Synthesis of SiO_2 nanoparticles

SiO_2 nanoparticles were produced according to the so called "Stöber" process in which the particles were formed in an ammonia containing ethanol solution.[56] As precursor tetraethoxysilane (TEOS) was utilized like shown in scheme 5.

Scheme 5

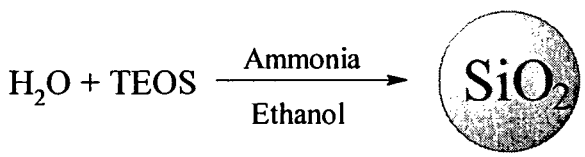

The resulting SiO_2 nanoparticles were isolated via centrifugation and washed with water and ethanol. In figure 8 a transition electron microscopy (TEM) image and a dynamic light scattering (DLS) study of the synthesized SiO_2 nanoparticles are shown.

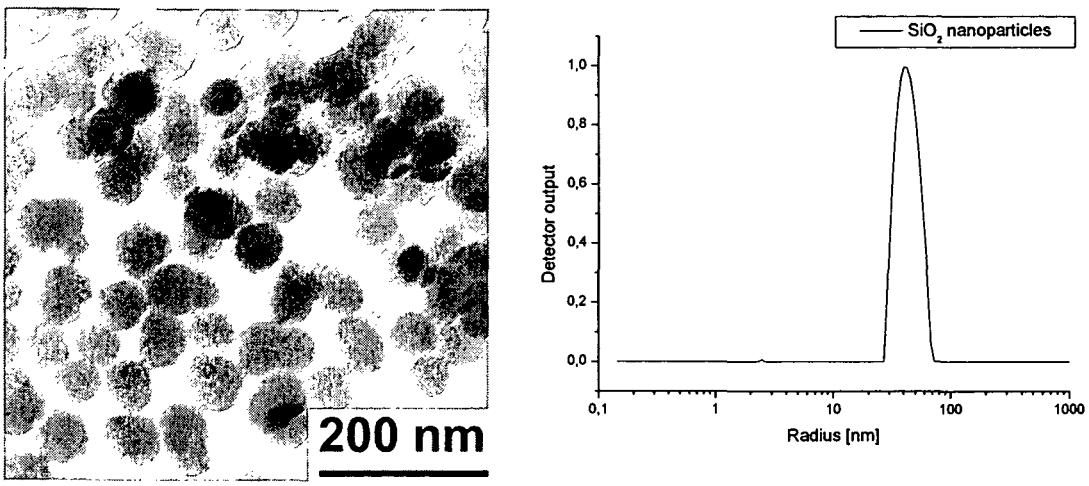

Figure 8: TEM image and DLS study (recorded in ethanol) of SiO_2 nanoparticles with a diameter of 92 ± 15 nm.

The particles had a diameter of 94 nm and were uniform in morphology and size which was necessary for further applications. The small size distribution was also shown in the DLS diagram where just one signal corresponding to one diameter with the mean peak position at 92 ± 15 nm was found. The observed size distribution is in the same range as observed by *Philipse et al.*[202] In this sol-gel reaction the amount of ammonia, which served as catalyst, was crucial for the morphology of the resulting particles. If higher pH values are adjusted during the particle synthesis, larger particles are gained because the OH^- ions have a strong influence on the equilibrium between the formation of the nuclei and their subsequent growth.[203] Particles with this diameter were chosen because the synthesized metal oxide nanoparticles (chapter 3.2. and 3.3.) had comparable diameters.

The specific surface area of the SiO_2 nanoparticles was investigated via nitrogen sorption, which resulted in 117 m^2/g. Comparison with literature is difficult to perform, as very different values ranging from 18 m^2/g to more than 1000 m^2/g for silica particles depending, of course, on the diameter and the induced pore structure are published.[204, 205]

3.1.1.1. Stability of SiO_2 nanoparticles without ammonia

SiO_2 sols prepared via the "Stöber process" are stable over months because of their highly charged surfaces that lead to rejection of particles.[56] The particles were washed with ethanol and water to remove excessive ammonia to obtain uncharged particle surfaces and then stored

in ethanol to investigate the influence of a charged surface. In figure 9 the aging process of SiO_2 nanoparticles is shown.

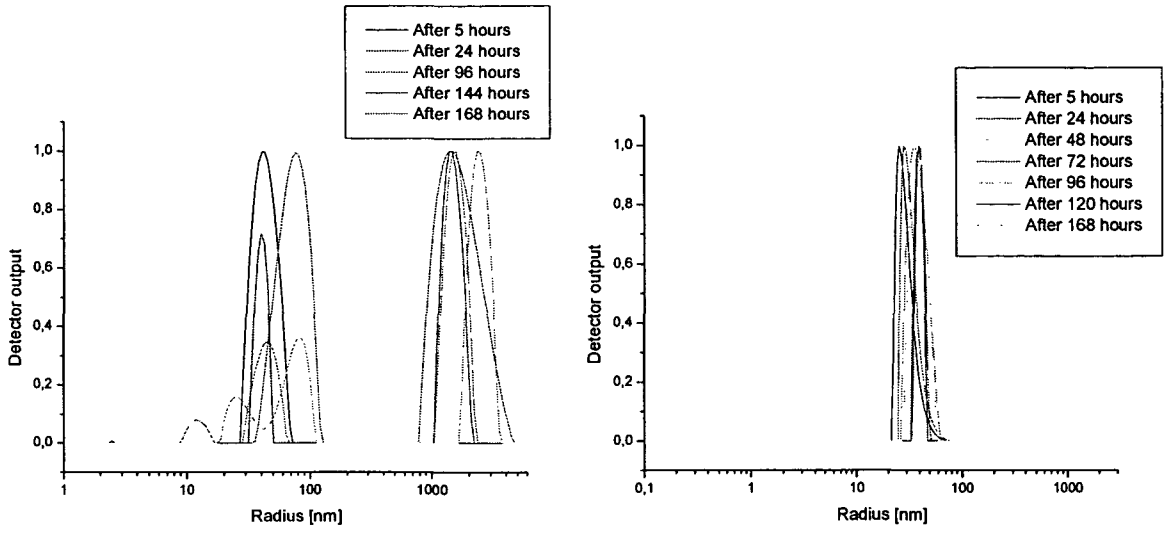

Figure 9: DLS study of SiO_2 nanoparticles after different time periods recorded in ethanol compared to ammonia stabilized SiO_2 particles.

When the particles were redispersed directly after the synthesis and the washing procedure, they had a monodisperse size distribution which was shown by the black curve in figure 9. In the following days the lack of stabilizing ammonia became visible which led to the formation of large agglomerates with a radius of about 2 µm. The agglomeration process occurred rather quickly because after one day the agglomerates already showed a radius about 1.5 µm. In the following days the amount of non agglomerated nanoparticles decreased continuously which is shown in table 1.

Table 1: Shares of aggregated and non aggregated SiO_2 nanoparticles after different time periods.

Time [h]	**Share of non aggregated SiO_2 nanoparticles [%] (radius [nm])**	**Share of aggregated SiO_2 nanoparticles [%] (radius [µm])**
5 hours	100 (43 nm)	0
24 hours	40.8 (10/76 nm)	57.4 (1.4 µm)
96 hours	27.5 (47 nm)	72.5 (1.6 µm)

144 hours	31.6 (40 nm)	68.3 (1.4 µm)
168 hours	24.3 (25/82 nm)	75.2 (2.1 µm)

The shares of aggregated and non-aggregated species were obtained via integration of the area below the curves. These aggregates showed only weak interactions as shaking of the sample vials led to partial dispersion of the aggregates. After 144 hours the amount of non aggregated nanoparticles was higher than after 96 hours which indicated that there was an equilibrium between aggregation to larger structures and the entropic favored disaggregation. Furthermore, it was observed that all aggregates required a certain size to gain stability. It is noticeable that the existing aggregates either had a size up to approximately 100 nm which corresponded to two or three aggregated particles or up to 2 µm which corresponded to very large aggregates consisting of hundreds of particles. Surprisingly in the DLS study signals that were smaller than the original particles were found after 24 hours and 168 hours. A possible explanation might be the appearance of a partial decomposition process.
Compared to ammonia stabilized particles the influence of charged surface groups is obvious. Comparable results were obtained by *Kallay et al.* who managed to describe the aggregation behavior of hematite and rutile nanoparticles.[206-208]

Considering the stability of nanosystems, the particle concentration is a very important parameter. The consequences of different concentrations can easily be shown by comparing two systems with the same mass concentration but different in particle, assuming a difference in particle size by the factor of 10 would result in a 1000 times higher concentration of nanoparticles. Since the aggregation rate is proportional to the square of the particle concentration, the collision frequency in the nanosystem would be a million times higher. Thus, the aggregation rate would be a million times higher while the aggregation half-time would be reduced by a factor of 1000. So, a nanoparticle suspension can hardly form a stable dispersion without additives because their aggregation is fast due to both, low stability coefficient and high particle number concentration.

To clarify this concept two types of silica nanoparticles were synthesized, one with a radius of 12.5 ± 0.6 nm and another one with a radius of 78.5 ± 5 nm. Nitrogen sorption obtained a specific surface area of 220 m^2/g and 51 m^2/g for the two types, respectively. TGA analyses revealed a weight loss of 16.5 % and 14 % for the two different types of SiO_2 particles. Up to

200 °C the mass loss was caused by adsorbed water. At 200 °C the curve of the mass loss flattened.

Both types were measured in the original suspension containing the stabilizing ammonia, afterwards washed, isolated, and dried. 0.01 g of both types were suspended in 3 ml of ethanol and sonicated for several hours. The obtained dispersions were rested for 2 days and measured via DLS. In figure 10 a comparison of the obtained DLS plots is presented.

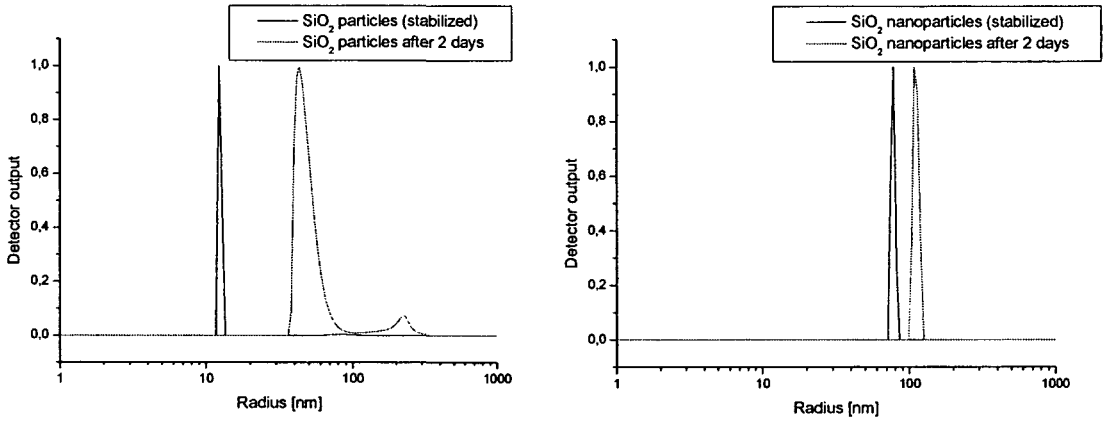

Figure 10: Comparison of DLS plots (recorded in ethanol) of silica nanoparticles directly after synthesis and two days later.

The DLS analyses demonstrate the influence of the number of particles that were redispersed in ethanol. Despite the same mass concentration the aggregation behavior was totally different. In case of the smaller particles massive aggregation occurred that led to the formation of unities with a radius of 43.5 ± 11 nm. A second signal in the DLS plot suggests the appearance of larger aggregates as well. The larger silica particles aggregated as well but the relative change of the radius was much smaller. The formed aggregates had a radius of 110 ± 10 nm.

3.1.1.2. Kinetics of the SiO_2 nanoparticle synthesis

The kinetic of the SiO_2 particle formation process was investigated via DLS. The ratios between the different components are as mentioned in the experimental part (chapter 7.4.1.). Samples were drawn for the DLS measurements from the stirred mixture and returned afterwards to keep the entire amount of particles relatively constant for further investigations.

The measurements were carried out at room temperature. The resulting kinetic curve is shown in figure 11.

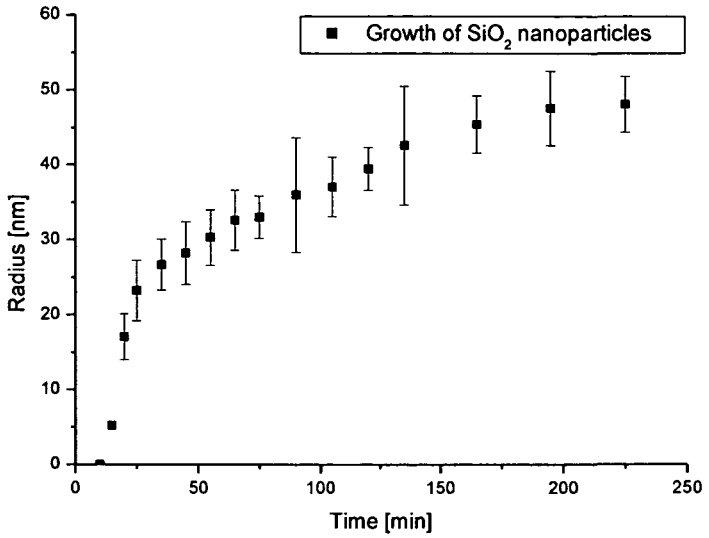

Figure 11: Kinetics of the SiO_2 nanoparticle formation in ethanol.

The nucleation process seemed to be completed ten minutes after the initiation and the growing phase began. In the first 15 minutes after the nuclei formation, the particles increased their radius by 25 nm. Then the growing process slowed down and resulted in a nanoparticle radius of 47 ± 11 nm after 250 minutes. Comparison with literature proofed that various groups found the same formation kinetic as presented above. For example, *Green et al.* published a similar kinetic evolution measuring the soluble silica concentration using ^{29}Si NMR.[209]

3.1.1.3. Thermal analysis of SiO_2 nanoparticles

Thermal gravimetric analysis (TGA) was utilized to investigate the thermal properties of SiO_2 nanoparticles up to 800 °C. Before the measurement the nanoparticles were dried in vacuo for several hours. The temperature was raised with a rate of 5 °C per minute which led to a weight loss of 16 % at 800 °C. Up to 200 °C the weight loss processed fairly linear and most likely, the remaining water was eliminated. At 200 °C the rate of the weight reduction slowed down. Up to 600 °C the surface OH groups were cleaved from the particle surface, afterwards the weight loss was very small.

Björnström et al. observed the same effect applying Raman spectroscopy.[210] They annealed porous silica gels, consisting of small silica nanoparticles, at 500 °C and observed a significant decrease of the signature of OH-vibrations between 3100 and 3700 cm^{-1}. As a controlling experiment the silica particles were deposited under ambient conditions after the TGA analysis for 24 hours. Afterwards the TGA analysis was repeated, which led to an overall weight loss of 11 %. The form of both obtained weight loss curves was equal which led to the following assumptions: (i) no alkoxide groups remained unhydrolyzed during the formation process; (ii) during the 24 hours at ambient conditions rehydration occurred which was also observed by *Björnström et al.*[210]

3.1.2. Synthesis of gold nanoparticle

Inorganic metal nanoparticles like silver, gold and copper colloids have been the major focus of interest because of their unique optical properties determined by the collective oscillations of electron density termed plasmons.[52] As metal nanoparticles do not have stabilizing surface OH-groups the usage of additives to obtain boosted stabilization is inevitable. For example, *Brust et al.* reduced a gold chloride solution with sodium borohydride in the presence of dodecanethiole to stabilize the obtained nanoparticles which had a diameter of 1-3 nm.[140] *Nuss et al.* used organic molecules that contained thiol functionalities and α-bromoester to prevent on the one hand aggregation of the 4 nm particles during the synthesis process and to allow on the other hand initiation of ATRP.[211] Other groups used organic salts like sodium citrate to stabilize the nanoparticle dispersion which led to particles with a diameter of 15 nm.[65, 212]

Gold nanoparticles were used as model metal system because their optical properties make them highly interesting and the synthesis and functionalization process of their surface are easy to perform.

According to a literature procedure[65], tetrachloroaureate trihydrate was dissolved in distilled water, reduced and stabilized with sodium citrate solution which led to a change in color from the original yellow to colorless, black, and finally to red. The reaction equation is shown in scheme 6. The citrate ions that stabilize the gold particles are symbolized with 'R'.

Scheme 6

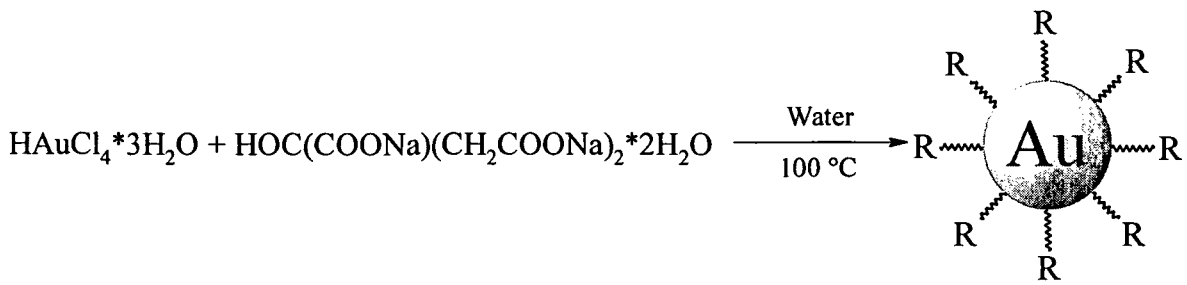

A TEM image of the resulting particles is presented in figure 12.

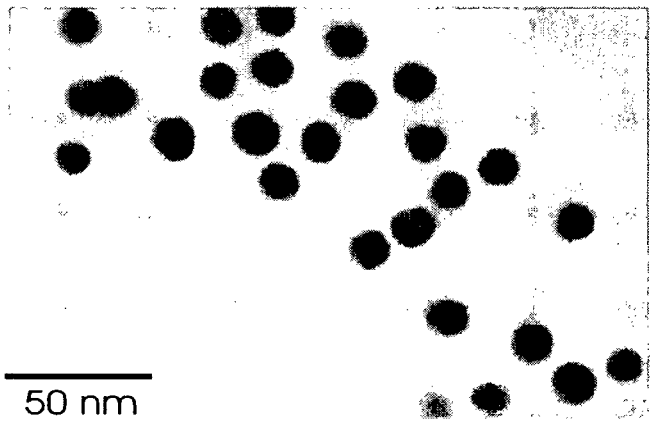

Figure 12: TEM picture of gold nanoparticles with a diameter of 15 nm.

The synthesized gold nanoparticles had a diameter of 15 nm and were uniform in morphology and size. UV/VIS spectroscopy and DLS were applied to characterize the obtained gold nanoparticles. In case of noninteracting spheres, Mie theory describes quantitavely the absorption and scattering of light by spherical particles in a non absorbing medium.[213] Numerous approximations are available, especially for small particles compared to the incident radiation. If one considers only dipole absorption processes, this leads to the equation for the spectrum of nanoparticles:

$$\varepsilon(M^{-1}cm^{-1}) = \frac{18\pi 10^{-3} V_m \varepsilon_m^{3/2}}{2.303\lambda}\left[\frac{\varepsilon''}{(\varepsilon'+2\varepsilon_m)^2+\varepsilon''^2}\right]$$

Here ε_m is the dielectric constant of the solvent, $\varepsilon(\omega) = \varepsilon' + i\varepsilon''$ is the dielectric function of the particles, and V_m is the molar volume of the material, constituting the particles. The

mentioned equation makes UV/VIS spectroscopy an excellent method for investigating the monodispersity of the size distribution of small particles.
The obtained spectra and the measured DLS plot of the sample are shown in figure 13.

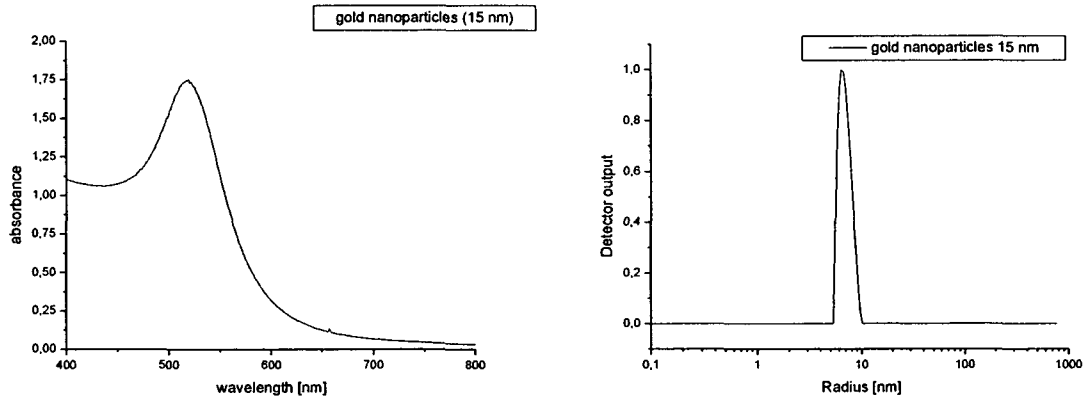

Figure 13: UV/VIS spectrum and DLS plot of gold nanoparticles with a diameter of 15 ± 2 nm. The DLS spectrum was recorded in water at room temperature.

Both, the UV/VIS spectrum and the DLS plot, showed only one absorption band and one signal, respectively, which both revealed a Gaussian distribution that stood for a monodisperse distribution of the particle diameter. The gold nanoparticles showed an absorption maximum at a wavelength of 520 nm, which corresponded to the results that were obtained by *Liz-Marzan et al.*[213]

The DLS plot in figure 13 represents the gold nanoparticles directly measured after the synthesis without any further purification. A single dominant signal appeared at a diameter of about 15 nm. Both results, i.e. of the DLS analysis and the UV/VIS spectroscopy, confirmed the diameter of the nanoparticles received from the TEM analysis. FTIR-spectroscopy confirmed the presence of citrate ions on the particles surface as several characteristic bands were found (e.g. 3452 ν(C-H);1587 ν(C-C) + ν(C-O); 1069 ν(C-O); 830 γ(CHR) cm^{-1}).

Via TGA the thermal properties of the obtained nanoparticles were investigated. In figure 14 the obtained TGA curves of a measurement in air and under a nitrogen atmosphere are shown.

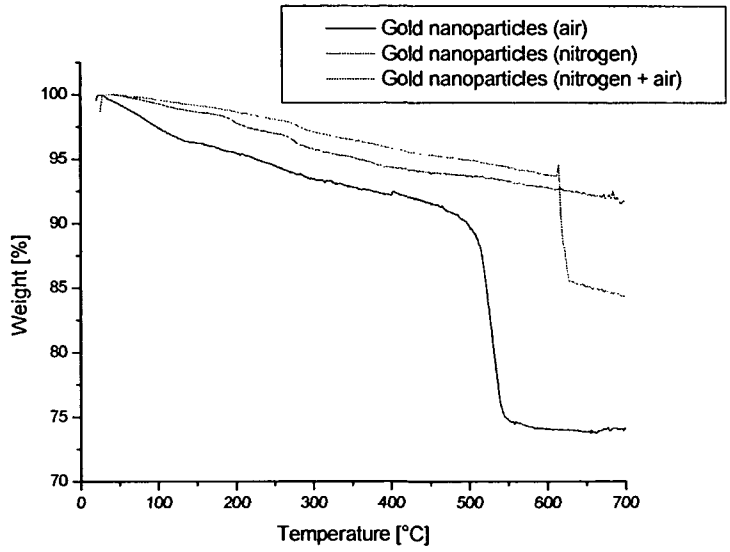

Figure 14: Comparison of the TGA curves of citrate stabilized gold particles measured (i) in air, (ii) under a nitrogen atmosphere up to 700 °C, and (iii) under a nitrogen atmosphere up to 615 °C and then in air up to 700 °C.

Heating the sample up to 700 °C under nitrogen resulted in mass loss of 8.5 %. In air the obtained results were very different. Up to 500 °C the mass reduction of the gold nanoparticles was linear and resulted in a loss of 10 %. From 500 °C to 550 °C about 15 % of the mass were lost caused by oxidation of organic components. Afterwards the mass remained constant until 700 °C which resulted in a summarized mass loss of 26 %. One explanation for this different combustion behavior might be a pyrolysis of the organic citrate molecules, which possibly resulted in a layer of carbon. The gold-particles were heated under a nitrogen atmosphere up to 616 °C to verify if pyrolysis occurred or not. Then the gas supply was switched to air which caused immediate combustion of the organic components. An overall reduction of weight of 18 % was obtained. As not all of the initially used gold salt forms nanoparticles and so not all of the sodium citrate is attached to the surface, it is impossible to estimate the ratio between gold and citrate. Nitrogen sorption obtained a specific surface area of 39 m^2/g.

3.1.3. Synthesis of larger gold nanoparticles

If larger gold nanoparticles shall be synthesized, it is not sufficient just to increase the gold salt concentration during the synthesis. If the original gold concentration is too high, the

synthesized nanoparticles would exhibit a broad size distribution which makes them worthless for further applications. Larger gold nanoparticles are synthesized based on nanoparticles with lower diameter as seed crystals. In this work a literature-known procedure was used.[214]

In a first step the original gold particles were reacted with a solution of tetradecyltrimethylammoniumbromide (TTAB) which replaced the stabilizing citrate groups. After the addition of ascorbic acid, gold chloride trihydrate solution was added very slowly to make sure that the added gold salt did not create new gold cores but enlarge the diameter of the already existing particles. The reaction is shown in scheme 7.

Scheme 7

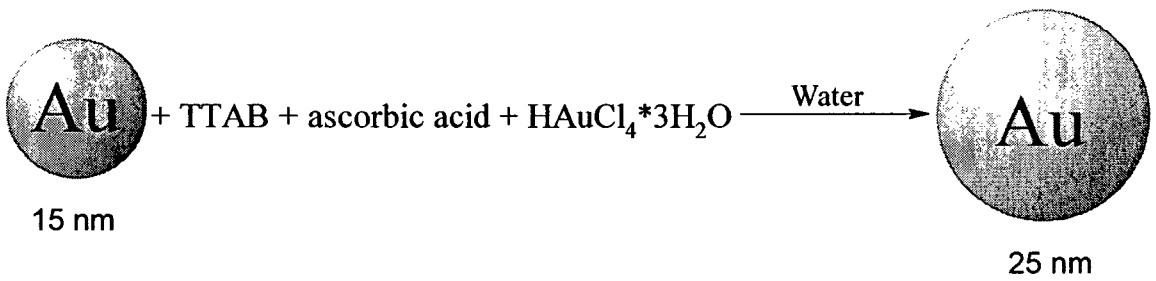

It was crucial for this process to keep the salt concentration below the critical super saturation concentration of the nucleation. According to the following equation the resulting particle diameter was estimated.[215]

$$r = r_{original} * \left(\frac{c_{(HAuCl_4)_{final}} + c_{particle}}{c_{particle}}\right)$$

$r_{original}$: original radius of the used nanoparticles

$c_{(HAuCl4)}$: final concentration of $HAuCl_4$ when all components are added

$c_{particle}$: final concentration of gold particles when all components are added

r: final radius of the gold particles

The particle radius has a direct relation to the salt concentration and increases with the latter. Depending on the original nanoparticle concentration the diameter was increased about 10 nm. In figure 15 a TEM image of the gold nanoparticles with the larger diameter of 25 nm is shown.

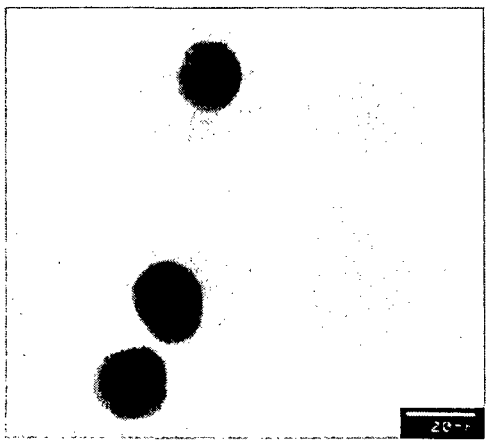

Figure 15: Gold nanoparticles with a diameter of 25 nm.

The growth of the gold shell was controlled via UV/VIS spectroscopy and DLS. The UV/VIS spectrum and the DLS plots of the original nanoparticles and the enlarged ones are shown in figure 16.

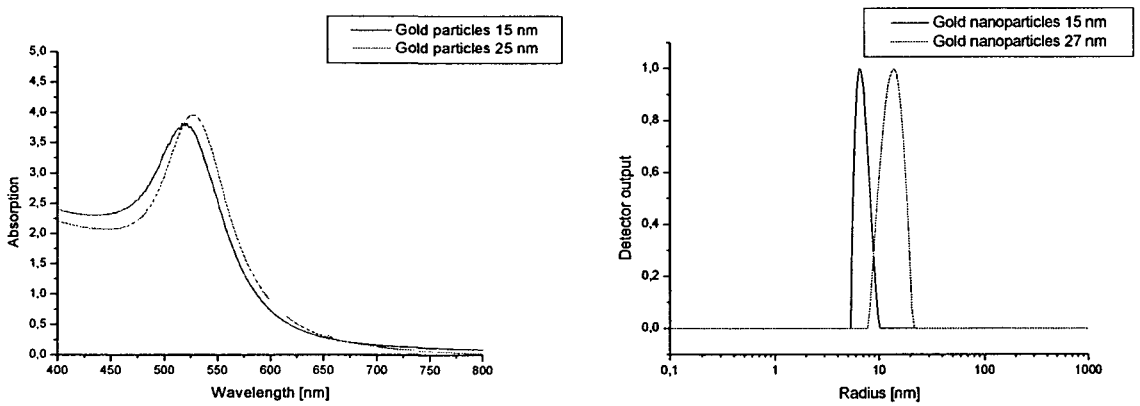

Figure 16: UV/VIS spectra and DLS plots of gold nanoparticles with a diameter of 15 ± 2 nm and 27 ± 5 nm. The DLS spectra were recorded in water at room temperature.

The gold nanoparticles with diameters of 15 nm and 25 nm differed in the wavelength of the absorption maximum which was shifted from 520 nm to 528 nm. Furthermore, the dispersion containing the larger particles showed a higher gold concentration which resulted in a higher extinction coefficient of the measured dispersion. Both curves showed a Gaussian distribution that was the result of a uniform morphology which was already observed before.[214]

The received diameter differed slightly from the value received by TEM measurements. The gold nanoparticles with a diameter of 15 nm, according to TEM analysis, had their dominant

peak at a diameter of 15 nm, which matched the TEM result perfectly well. DLS measurements of the larger nanoparticles resulted in a diameter about 27 nm compared to the 25 nm, received by TEM and the estimation given by the presented equation. The size distribution was like expected slightly broader in case of the particles with a diameter of 25 nm due to the additional growing step. TGA analysis obtained a weight loss of 24 % which is 2 % less compared to the gold particles with a diameter of 15 nm. The specific surface of the gold nanoparticles was determined by nitrogen sorption and resulted in an effective surface of 32.9 m^2/g. Compared to the smaller gold nanoparticles which revealed a specific surface of 39.0 m^2/g, the surface was decreased about 16 %. The reduced specific surface of gold nanoparticles compared to, for example, silica particles was caused by their denser surface.

3.1.4. Synthesis of Au@SiO_2 nanoparticles

As already mentioned, there are several good reasons for covering core materials with a shell of a different chemical composition. The most important ones are on the one hand to change physical (optical, magnetic, conductive, etc.) and chemical properties of the particles via the coating material, on the other hand to protect the core material from environmental influences. Furthermore, the stability of the dispersed particles in various solvents can be increased. Many different core materials, such as gold [216, 217], hematite, chromia, and titania were coated with a shell of silica or aluminum hydroxide.[218] Furthermore, it was demonstrated that it is possible to cover an inorganic core with layers of different chemical composition including yttrium [219], chromium (hydrous) oxide [220], zirconium (hydrous) oxide [221], or silica.[222]

The main motivation to cover gold nanoparticles with a silica layer is the altered stability of dispersions of the obtained Au@SiO_2 particles compared to uncovered gold nanoparticles.
Several methods to cover Au nanoparticles with a SiO_2 layer were published in literature.[12, 214, 223, 224]

In our approach the Au@SiO_2 nanoparticles were produced according to the procedure which was published by *Liz-Marzan et al.*[223] who used aminopropyltrimethoxysilane to form the first silica mono-layer.
The citrate stabilized gold particles with a diameter of 15 nm were produced in a first step. The citrate ions were replaced by aminopropyltrimethoxysilane (APS) which served as

linking bridge to the first silica monolayer that was built up by sodium silicate. This first silica monolayer required a very careful synthetic procedure because the nucleation of new silica cores had to be prevented and an even surface coverage of the gold particles had to be guaranteed. After 6 days of stirring the particles were isolated via centrifugation and redispersed in ethanol. Afterwards, TEOS was added stepwise to generate a thicker silica layer (scheme 8).

Scheme 8

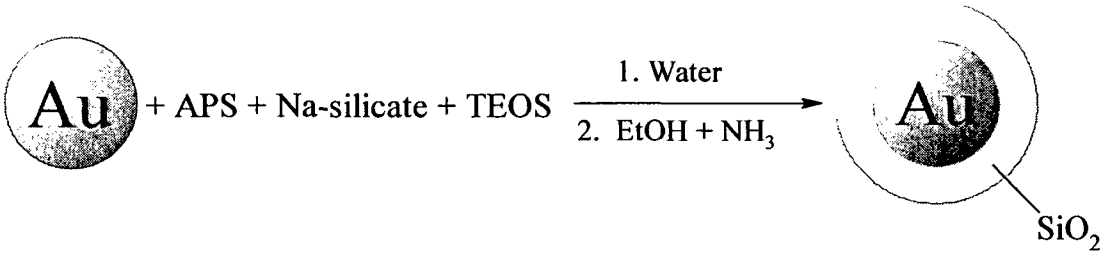

The growing process of the silica layer was monitored by UV/VIS spectroscopy (Figure 17).

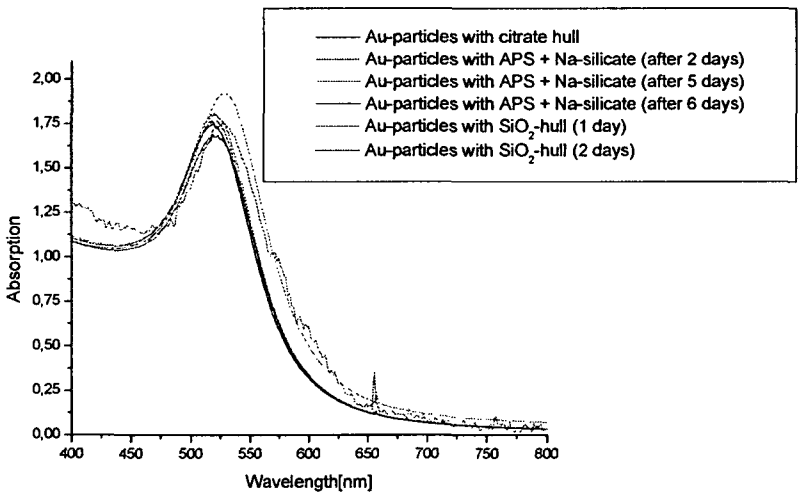

Figure 17: UV/VIS-spectra of the Au@SiO_2 synthesis.

The UV/VIS-spectra of figure 17 shows the nanoparticle dispersion with a different shell thickness. The black curve represents the unmodified gold nanoparticles with a size of 15 nm in diameter with an absorption maximum at a wavelength of 520 nm. After the addition of APS and sodium silicate a shift of the intensity of the absorption signal was observed. This was caused by the replacement of the protecting citrate hull with APS and the attachment of a silica monolayer. After the isolation of the particles and the redispersion in ethanol the intensity could not be compared any more due to a change in the particle concentration.

After the addition of TEOS a shift of the wavelength of the absorption maximum was observed. The $Au@SiO_2$ particles with a shell thickness of 14 nm showed an absorption maximum with a wavelength of 528 nm.
In figure 18 a TEM image and the corresponding curve from DLS analysis are shown.

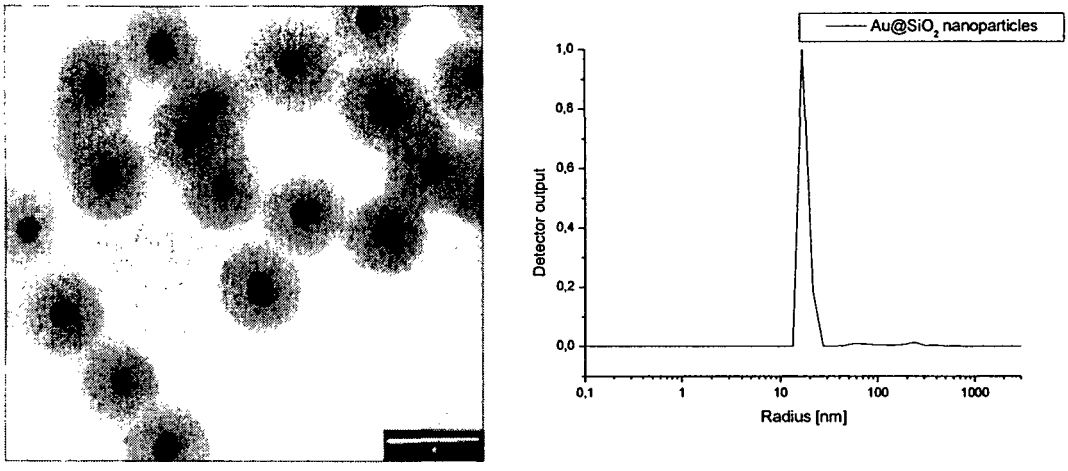

Figure 18: TEM picture and DLS curve of $Au@SiO_2$ nanoparticles with a diameter of 43 nm (TEM). The DLS analysis was performed in ethanol at room temperature.

The DLS analysis showed only one maximum at a diameter of 38 ± 3 nm which resulted nearly in the same diameter estimated from the TEM image being 43 nm. Both methods approved the monodispersity in shape and size of the produced $Au@SiO_2$ nanoparticles. The shoulder that is visible in the DLS plot might have been caused by partial aggregation. The specific surface of the $Au@SiO_2$ nanoparticles was measured by nitrogen sorption and determined 45.2 m^2/g. Despite the larger diameter these particles nearly had the double effective surface, compared to the gold nanoparticles, due to their porous structure.

The $Au@SiO_2$ nanoparticles were analyzed thermally via TGA. Between 100 and 400 °C 12 % of the particles mass were lost. In this temperature area the OH groups of the SiO_2 shell probably underwent condensation reactions and water was released. Up to 540 °C further 15 % of the particles mass were lost. The overall mass reduction upon 800 °C therefore was about 40 % of the $Au@SiO_2$ mass as already observed in case of Stöber and uncovered gold particles.

Efforts have been made to replace TEOS with other alkoxy-silanes like vinyl-triethoxysilane, methyl-triethoxysilane, and phenyl-trimethoxysilane to incorporate organic entities. While the latter did not form any shell around the gold core, vinyl-triethoxysilane led to uncontrolled precipitation. During the addition of the silane the hydrolyzed form already flocculated. Methyl-triethoxysilane did not lead to the formation of regular particles, i.e. as aggregation and precipitation were observed. Possibly the reduced amount of charged surface OH-groups prevented the stabilization of the growing particles in ethanol.

3.1.5. Synthesis of metal oxide nanoparticles via the precipitation from solvents

Metal oxide nanoparticles show unique properties (optical, magnetic, electrical) depending on their composition and size which makes them highly interesting for materials science. Furthermore, they provide, compared to non noble metal nanoparticles, boosted chemical stability against environmental influences. The most common starting compounds used in the preparation of metal (hydrous) oxides are metal salts and various alkoxides, which readily hydrolyze at low temperatures by the addition of water or aqueous ammonia. The low reacting temperature is of great importance if organic groups should be incorporated into the metal oxide nanoparticles.

The size of the resulting nanoparticles can be controlled by the concentration of the alcoholic alkoxide solutions, the amount of water, and the addition rate of the latter.[120] The nature of the products very strongly depends on the type of metal alkoxide and the presence of a ligand. According to the procedure described by *Stöber et al.* it was tried to implement the so called Stöber process for other metal oxides.

3.1.5.1. Synthesis of TiO_2 nanoparticles

Similar to the Stöber process, titanium isopropoxide was added dropwise to a mixture of ethanol and ammonia and stirred over night to guarantee complete conversion of the used metal alkoxide. The resulting particles were analyzed by TEM where they showed neither a spherical morphology nor a monodisperse size distribution. A TEM image of the obtained particles is presented in figure 19.

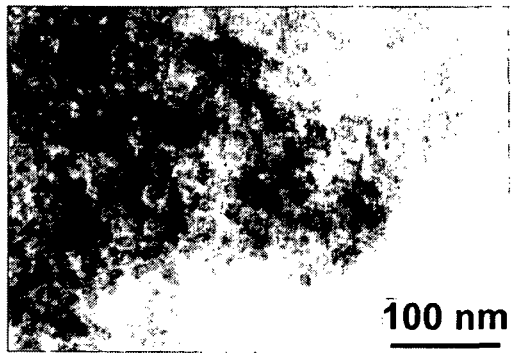

Figure 19: TEM-image of the obtained TiO_2 particles.

Because of the higher reactivity, the sol-gel process probably proceeded too quickly for the formation of uniform nanoparticles.

The reaction velocity can be slowed down using two different approaches. Either a less reactive metal alkoxide is utilized like in the work of *Jean et al.* who used titanium ethoxide as precursor and obtained large spherical particles with a diameter between 450 nm and 500 nm depending on the utilized water to alkoxide ratio [225], or the titanium alkoxide is functionalized, e.g., with ethylene glycol [64] or a pentane-2,4-dione derivate[226]. For example, *Sanchez et al.* produced anatase nanoparticles by reacting titanium n-butoxide with pentane-2,4-dione and by the addition of an acid at different temperature levels. By analyzing the obtained xerogels it was shown by solid state NMR that pentane-2,4-dione was still coordinated after the hydrolysis.[226]

3.1.5.2. Usage of ethylenglycol to reduce the activity of titanium alkoxides [64]

As the use of titanium isopropoxide as precursor did not lead to the formation of spherical nanoparticles with a narrow size distribution, the reactivity of the alkoxide was reduced via coordination. According to *Jiang et al.* [64] it has been tried to produce TiO_2 nanoparticles by reducing the chemical activity of titanium butoxide through the coordination of ethylene glycol. Ethylene glycol was mixed under a nitrogen atmosphere with titanium isopropoxide and stirred over night. The resulting mixture was poured into vigorously stirred acetone that contained 0.3 % water as shown in scheme 9.

Scheme 9

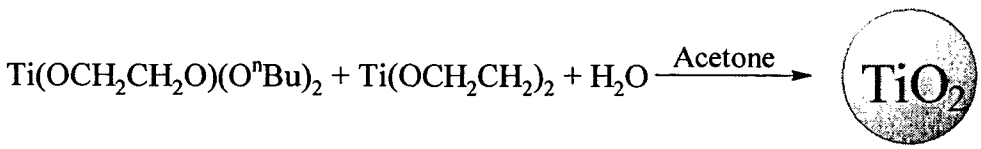

The particles were centrifuged and washed with water and ethanol several times to remove absorbed ethylene glycol from the surface. A TEM image and the corresponding DLS plot of the titanium oxide nanoparticles are shown in figure 20.

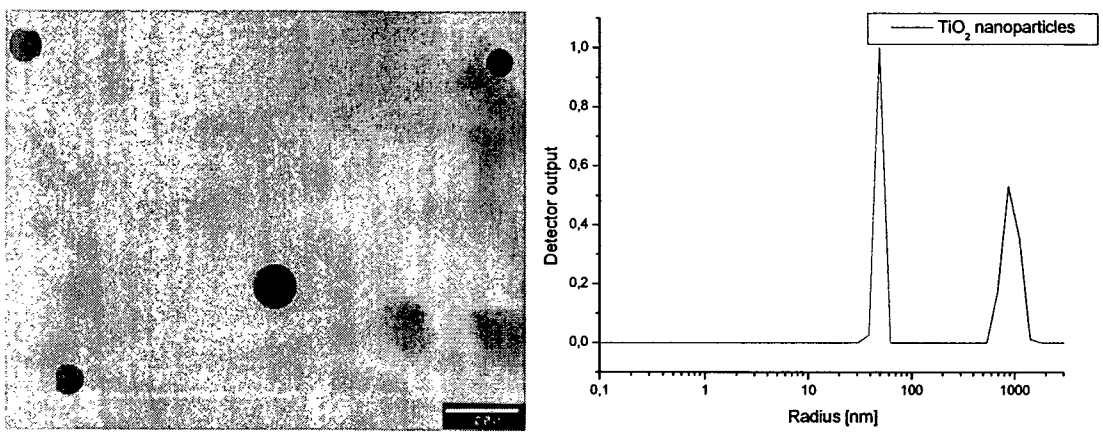

Figure 20: TEM image and DLS plot (recorded in ethanol) of TiO_2 nanoparticles.

The TEM image showed that the TiO_2 nanoparticles have a spherical morphology but a size distribution with diameters from 95 nm to 110 nm. DLS analysis revealed a diameter of 101 ± 7 nm. The second dominant peak was probably caused by aggregated species. A further drawback of this preparation technique was the incorporation of ethylene glycol into the material which could only be removed thermally and made further functionalization more difficult.

The particles were investigated via solid state ^{13}C CPMAS NMR which led to a broad signal of the incorporated ethylene groups at 66 ppm. A second signal was observed at 10 ppm that was assigned to the CH_3-groups of coordinated ethoxy groups. TGA showed a weight loss of 41.5 % and nitrogen sorption resulted in a specific surface area of 412 m^2/g. The relatively high weight loss that was obtained from the TGA analysis was caused by the evaporation of absorbed water (up to 200 °C) and from the decomposition of coordinated ethylenglycol.

The BET-surface is relatively high compared to functionalized TiO_2 nanoparticles that are presented in chapter 4, possibly, due to a less dense surface caused by the incorporation of organic entities.

3.2. Synthesis of nanoparticles from metal alkoxide derivatives

A novel approach for the synthesis of surface functionalized nanoparticles is the use of modified metal-alkoxides in a sol-gel based process. In particular we were interested in the surface attachment of initiator molecules for "grafting" from polymerizations or functional groups that act as charge carrier to prevent aggregation of the nanoparticles. In this chapter the modification of different metal alkoxides with polymerization initiators is presented including the synthesis of the latter. In a first step the initiating groups were linked to a molecule that could act as a bidentate ligand for the coordination like pentane-2,4-dione, which already proofed its ability to reduce the reaction rate of metal alkoxides in the sol-gel process and therefore allows a better control in the formation of the colloidal particle as well.[226, 227] An additional advantage of this ligand is its rather simple functionalization in the 3-position via deprotonation and C-C bond formation.[228] The used pentane-2,4-dione based initiators are presented in table 2.

Table 2: Overview of the used pentane-2,4-dione based initiators.

Initiator	Formula	Type of Polymerization
3-Chlor-pentane-2,4-dione	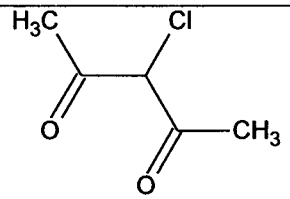	(i) Free radical polym. thermally initiated (ii) ATRP
3-Bromo-pentane-2,4-dione	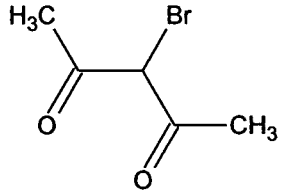	(i) Free radical polym. thermally and photo initiated (ii) ATRP

1-Acetyl-2-oxopropyl 2-bromo-2-methylpropanoate	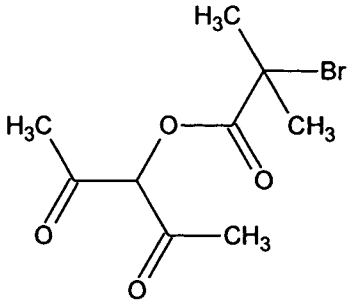	(i) ATRP
3-Acetyl-5-bromo-5-methylhexane-2,4-dione	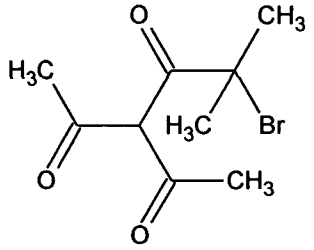	(i) ATRP

3.2.1. Synthesis of various pentane-2,4-dione derivatives

FTIR analysis showed that all pentane-2,4-diones occurred both in keto- and enol-form. The phenomena of the occurrence of tautomeric keto- and enol-form in case of pentane-2,4-dione are literature-known.[137] The ratio depends of course very strongly on the used solvent and on attached functional groups. Nevertheless, to avoid confusing complexity, all structure formulas in the reaction equations will be shown in keto-form.

3.2.1.1. Coordination of 3-chloro-pentane-2,4-dione

3-Chloro-pentane-2,4-dione is an acetylacetone derivate that can, due to its rather labile halogen-carbon bond, be used either for the initiation of a free radical polymerization or of an ATRP. The pentane-2,4-dione derivate was coordinated to the following metal alkoxides: titanium isopropoxide, zirconium isopropoxide, tantalum ethoxide, yttrium ethoxymethoxide, iron ethoxide, and vanadium oxo-ethoxide via an alkoxide exchange mechanism. 3-Chloro-pentan-2,4-dione was cooled below 0 °C using an ice-bath and a metal alkoxide was added under an argon atmosphere as shown in scheme 10.

Scheme 10

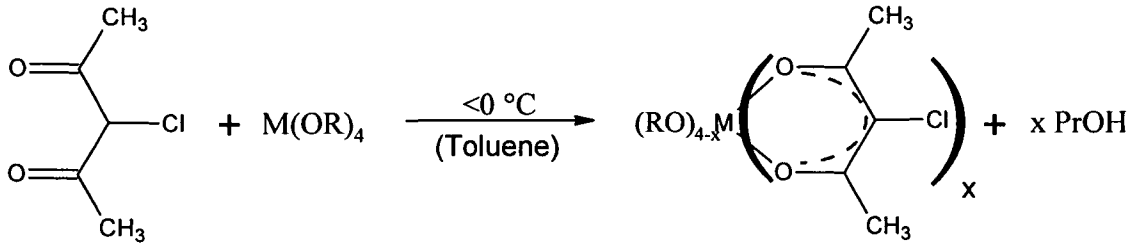

In case of tantalum ethoxide, iron ethoxide, and vanadium oxo-ethoxide toluene was used as solvent.

After several hours a mixture of different coordination products has been obtained. It was difficult to investigate the synthesized products via NMR experiments, because coordination to various titanium species (dimeres, oligomeres) occurred which led to a lower mobility than in molecular species.[226] This phenomenon generally increases relaxation times and thus broadens the NMR lines of the corresponding species whose characteristic resonance becomes unobservable. Furthermore, it has to be mentioned that the chloro-carbon bond is not very stable which led to the creation of additional by-products.

Nevertheless, in ^{13}C NMR some broad entities for the coordinated CO group about 190 ppm, the C-atom which is situated between the two CO-groups at 111 ppm, and the methyl-groups about 26 ppm were observed. In the ^{1}H NMR experiments the expected signals for the methyl and alkoxide protons were observed. It has to be admitted that from the obtained NMR spectra no conclusion about the completeness of the coordination process could be drawn.

The occurring problems using NMR spectroscopy for controlling the coordination state led to the utilization of FTIR-spectroscopy to analyze the coordination process.

In figure 21 the FTIR-spectra of uncoordinated and coordinated 3-chloro-pentane-2,4-dione are shown.

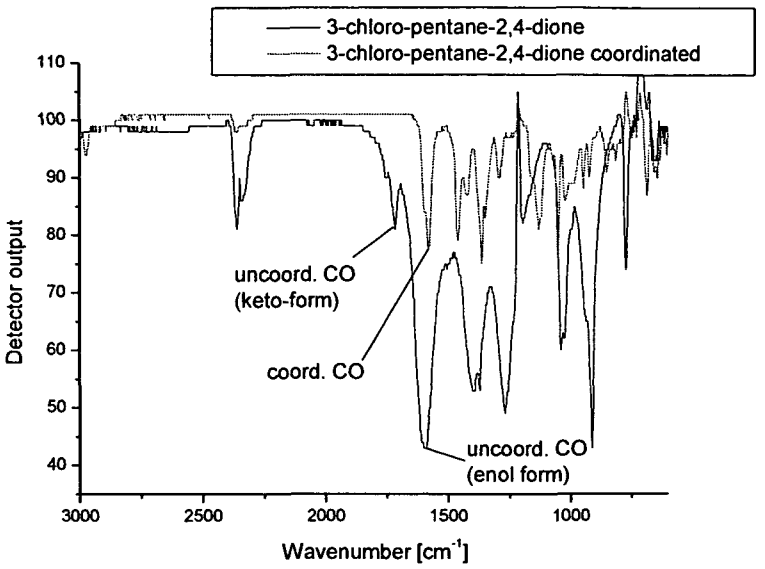

Figure 21: FTIR-spectra of uncoordinated and coordinated 3-chloro-pentane-2,4-dione.

The two bands caused by the CO-groups of the uncoordinated form at 1717 cm^{-1} and 1599 cm^{-1}, which were attributed to the ν(CO) vibration of the keto- and enol-form of the pentane-2,4-dione derivate, were not longer present in the spectrum of the coordinated 3-chloro-pentane-2,4-dione. A new band of the coordinated ν(CO) vibration appeared at 1576 cm^{-1}. These results correspond to the results that were obtained from *Léaustic et al.* who coordinated pentane-2,4-dione to titanium isopropoxide and assigned a new formed band at 1590 cm^{-1} to ν(CO) vibration of coordinated pentane-2,4-dione.[137] If zirconium n-butoxide was used the band of the coordinated ν(CO) vibration was observed at 1586 cm^{-1}, in case of yttrium methoxy-ethoxide at 1589 cm^{-1}, for tantalum ethoxide at 1583 cm^{-1}, for iron ethoxide at 1564 cm^{-1}, and for vanadium oxo-ethoxide at 1574 cm^{-1}. The assignment of all observed bands is presented in the experimental part (chapter 7.). Elemental analyses were performed for all obtained coordination products which showed only small differences between the calculated and the measured carbon content.

3.2.1.2. Synthesis of 3-bromo-pentane-2,4-dione

3-Bromo-pentane-2,4-dione is a polymerization initiating group that is capable of performing different initiating mechanisms like thermal- and photo-induced free radical polymerization and ATRP due to its rather labile halogen-carbon bond. The synthesis of the pentane-2,4-dione derivative was carried out via a brominating reaction. Pentane-2,4-dione was dissolved

in chloroform, cooled to 0 °C and reacted with bromine in a stoichiometric 1 : 1 ratio (scheme 11).

Scheme 11

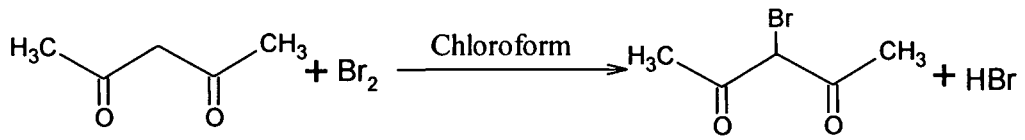

After drying the organic phase over $MgSO_4$ and removal of the solvent in vacuo, the product was obtained as a colorless liquid in a yield of 83.3 %.

FTIR analysis showed that, contrary to 3-chloro-pentane-2,4-dione (ν(CO) = 1720 cm^{-1}, 1610 cm^{-1}), the compound existed primarily in its diketone form that was associated to a band at 1713 cm^{-1}. A band at 1599 cm^{-1} appeared as well which could be attributed to the ν(CO) vibration of the enol-form. Due to different electronical influences, a shifting of the measured bands occurred; i.e. in case of unmodified pentane-2,4-dione the keto and enol signals of the ν(CO) vibrations are situated at 1710 cm^{-1} and 1605 cm^{-1}, respectively.

^{1}H NMR experiments resulted in a signal for the methyl group at 2.22 ppm. The performed ^{13}C NMR analysis indicated the CO group at 190.1 ppm which was slightly shifted compared to 3-chloro-pentane-2,4-dione where a signal at 189.2 ppm was observed. Compared to pentane-2,4-dione where two signals for the keto and the enol-form at 202.1 ppm and 191.1 ppm were observed, the peaks were slightly shifted due to the electron drawing effect of the bonded halogens. Elemental analysis revealed a discrepancy of 2.3 % between the theoretical and the measured bromine content, possibly caused by cleavage of the labile bromine-carbon bond during transportation.

3.2.1.3. Coordination of 3-bromo-pentane-2,4-dione to titanium isopropoxide

3-Bromo-pentane-2,4-dione was cooled below 0 °C and titanium isopropoxide was added dropwise without using a solvent. The reaction mixture was stirred until the product became solid (scheme 12).

Scheme 12

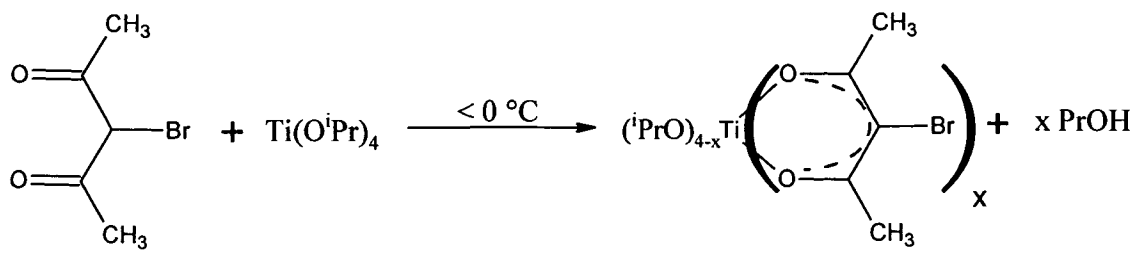

The coordination product was an orange solid substance which was used without removing the resulting propanol. NMR analysis was limited by the same facts that were mentioned in case of the coordination of 3-chloro-pentane-2,4-dione in the previous section 3.2.1.2.

^{13}C NMR revealed a small signal at 190 ppm corresponding to coordinated CO-groups, a signal at 100 ppm that was assigned to the carbon situated between the two carboxy-groups, two signals at 80 and 77 ppm that were assigned to CH-groups of isopropoxide and 6 signals between 29 and 22 ppm that corresponded to CH_3 of the isopropoxide and the 3-bromo-pentane-2,4-dione. All other signals could not have been assigned to a certain species due to the occurrence of side-reaction caused by the weakness of the carbon halogen bond.

The coordination product was analyzed via FTIR-spectroscopy. The spectra of the uncoordinated and the coordinated acetylacetone derivate are shown in figure 22.

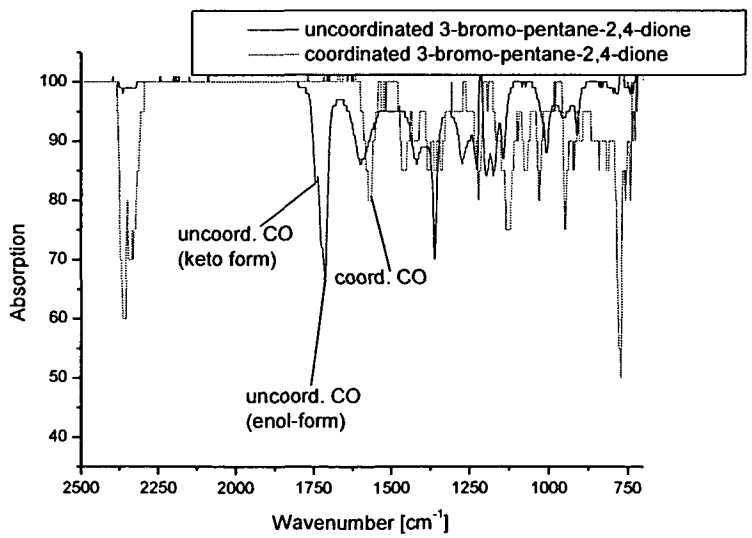

Figure 22: FTIR-spectra of uncoordinated and coordinated 3-bromo-pentane-2,4-dione.

A complete coordination of 3-bromo-pentane-2,4-dione to titanium isopropoxide was obtained after long reaction times. The ν(CO) vibration band at 1713 cm^{-1} disappeared completely like in case of the coordination of 3-chloro-pentane-2,4-dione. A new band at 1568 cm^{-1} was assigned to coordinated ν(CO) vibrations. The observed band was slightly shifted compared to the measured ν(CO) vibrations in case of the coordinated 3-chloro-pentane-2,4-dione (1576 cm^{-1}) which could be explained with the different electronical influences in case of the bromine and chlorine derivates. A discrepancy of 1.5 % between the theoretical and the measured carbon content was observed in the performed elemental analysis, possibly caused by cleavage of the labile carbon-bromine bond. A further purification and separation of the products was not necessary because the obtained mixture of coordination compounds could already be used as a precursor for the particle formation.

3.2.1.4. Synthesis of 1-acetyl-2-oxopropyl 2-bromo-2-methylpropanoate

1-Acetyl-2-oxopropyl 2-bromo-2-methylpropanoate contains a typical ester group to initiate ATRP and is not as sensitive as the presented halo-pentane-2,4-diones to ambient conditions. 2-Bromo-2-methylpropionic acid and the phase transfer catalyst $(N(Bu)_4)HSO_4$ were dissolved in 2 M NaOH, stirred for 30 minutes, and the reaction mixture was extracted with dichloromethane. The separated organic phase was reacted with 3-chloro-pentane-2,4-dione. After drying the organic phase over $MgSO_4$ and evaporation of the solvent, the received product was an orange oil in a yield of 78.3 % (scheme 13).

Scheme 13

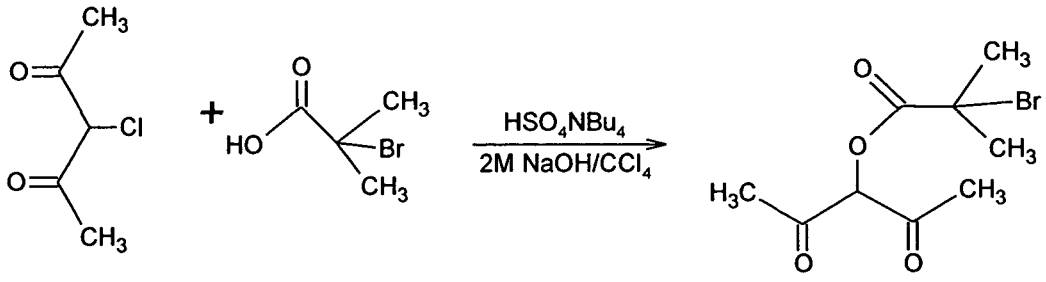

FTIR-spectroscopy showed that 1-acetyl-2-oxopropyl 2-bromo-2-methylpropanoate appeared in keto- and enol-form. The ν(CO) vibration of both forms were assigned to bands at 1730 cm^{-1} (keto) and 1609 cm^{-1} (enol), respectively, which is fairly similar to the bands that have been found in case of 3-chloro-pentane-2,4-dione (1720 cm^{-1}, 1609 cm^{-1}), possibly due

to similar electron withdrawing effects of both substituents. Further bands are discussed in the experimental part. ^{1}H NMR revealed the expected signals for the two types of methyl groups at 2.10 ppm and 1.97 ppm, respectively. ^{13}C NMR showed that the signal of the CO-group was slightly shifted from 190.1 ppm to 192.5 ppm compared to 3-bromo-pentane-2,4-dione, due to the presence of the ester group which was assigned to a signal that was found at 182.3 ppm.

3.2.1.5. Coordination of 1-acetyl-2-oxopropyl 2-bromo-2-methylpropanoate

As mentioned in chapter 3.2.1.1. and 3.2.1.2., 3-chloro-pentane-2,4-dione and 3-bromo-pentane-2,4-dione are rather instable compounds because the halogen carbon bond can be cleaved easily. So 1-acetyl-2-oxopropyl 2-bromo-2-methylpropanoate as a more stabile molecule was chosen to serve as "model"-ligand for coordination to various different metal alkoxides like $Ti(O^{i}Pr)_4$, $Zr(O^{n}Bu)_4$, $Y(OEtOMe)_3$, $Ta(OEt)_5$, $VO(OEt)_3$ and $Fe(O^{i}Pr)_3$ via an exchange reaction. Furthermore, 1-acetyl-2-oxopropyl 2-bromo-2-methylpropanoate shows a structural similarity to known ATRP initiators which allows comparison of the obtained polymerization efficiencies.

The acetylacetone derivate was dissolved in absolute THF or toluene and mixed with the metal alkoxide under an argon atmosphere. Toluene was used as solvent in case of $Zr(O^{n}Bu)_4$ and $Fe(O^{i}Pr)_3$ because the alkoxides showed an enhanced solubility in this solvent. The resultant mixture was refluxed over night. After the solvent was removed in vacuo, high yields above 90 % were obtained (scheme 14).

Scheme 14

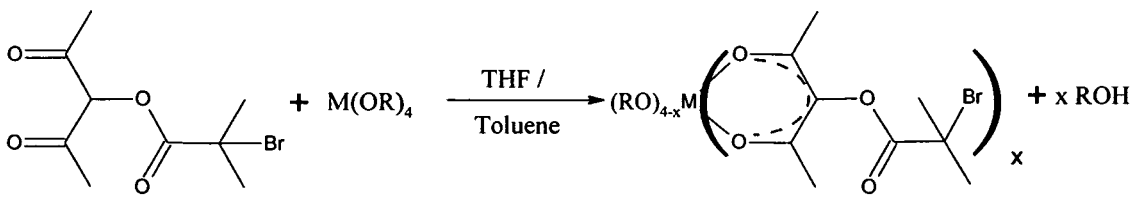

The resulting NMR spectra became very complex but most of the signals could have been assigned. ^{1}H NMR allowed the assignment of the different methyl-groups and the alkoxide groups. ^{13}C NMR showed two signals at 188 ppm and 187 ppm for the coordinated CO-groups and the COO-group, respectively and a broad peak at 110 ppm assigned to the carbon

atom between the two coordinated CO-groups. Between 69 and 58 ppm, 5 signals were obtained which could have been assigned to remaining alkoxy-groups and the carbon atom, which is connected to the bromine. From 28 ppm to 13 ppm the signals for the methyl-groups have been found. FTIR-spectroscopy was also used for the characterization. Exemplarily the FTIR-spectra of the uncoordinated 1-acetyl-2-oxopropyl 2-bromo-2-methylpropanoate and the coordination product with titanium isopropoxide are shown in figure 23.

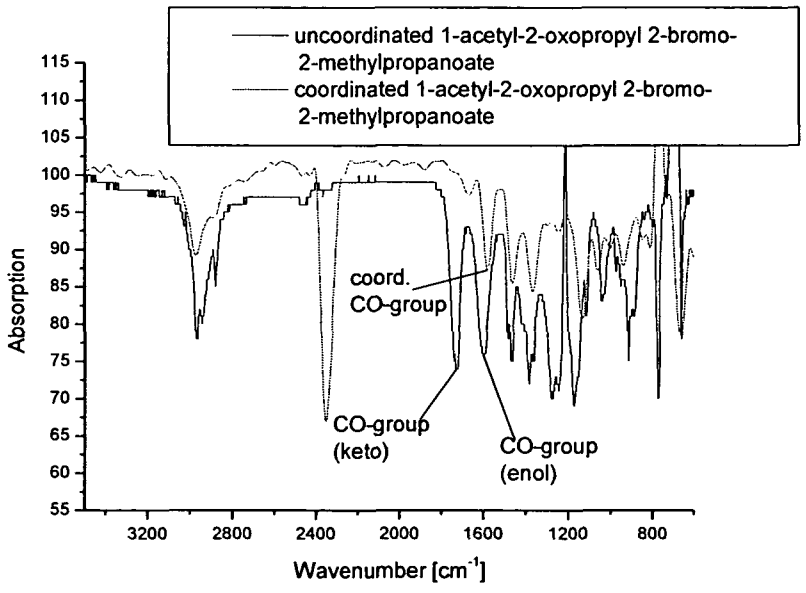

Figure 23: FTIR-spectra of 1-acetyl-2-oxopropyl 2-bromo-2-methylpropanoate in the uncoordinated state and coordinated to titanium isopropoxide.

Total coordination was obtained if titanium alkoxide was utilized as metal alkoxide. The keto- and enol-bands of the uncoordinated species disappeared completely and a new band of the coordinated CO group appeared at 1567 cm^{-1}. In case of zirconium butoxide full coordination was obtained as well which resulted in a band at 1588 cm^{-1}. Comparison to literature data showed a shift of the ν(CO) vibration to smaller wavelength in case of titanium and zirconium alkoxide as an effect of the modification of the C3 carbon atom.[137] When vanadium oxo-ethoxide was used, not all of pentane-2,4-dione derivate was coordinated possibly due to sterical hindrance. The ν(CO) vibration band of the keto-form at 1739 cm^{-1} was still visible and a new band at 1574 cm^{-1} appeared.. With yttrium ethoxymethoxide, and iron isopropoxide entire coordination was obtained. New bands were found at 1529 cm^{-1} and 1585 cm^{-1}, respectively. If tantalum ethoxide was coordinated, two bands were visible in the obtained spectrum; the first at 1720 cm^{-1} which complied to the uncoordinated species and one at

1650 cm^{-1} for the coordinated one. Eventually the "soft character" of tantalum prevented total coordination of the "hard" pentane-2,4-dione derivate. Furthermore, sterical hindrance might have made coordination more difficult.

Elemental analysis has been performed for all obtained coordination products which corresponded well to the calculated values. Just in case of the coordination product of yttrium ethoxymethoxide the elemental analysis showed a carbon content of 29.3 % instead of 41.5 %. This different carbon content might have been caused by partial condensation reaction of the modified yttrium alkoxide via condensed air moisture during transportation.

3.2.1.6. Synthesis of 3-acetyl-5-bromo-5-methylhexane-2,4-dione

3-Acetyl-5-bromo-5-methylhexane-2,4-dione is a polymerization initiator for ATRP which is supposed to have the same ability to form stable radicals as 1-acetyl-2-oxopropyl 2-bromo-2-methylpropanoate. The direct linkage of the three CO-groups via a single carbon atom and not via an oxygen atom should cause stronger coordination to metal centers because less electron density is withdrawn.

2-Bromo-2-methylpropanoyl bromide was mixed with pentane-2,4-dione and solid K_2CO_3 as base, which was used to attract the acid H-atom, and stirred over night in absolute acetone. After the removal of the K_2CO_3 and the evaporation of the solvent, 3-acetyl-5-bromo-5-methylhexane-2,4-dione was obtained in form of a yellow oil with a yield of 77.1 % (scheme 15).

Scheme 15

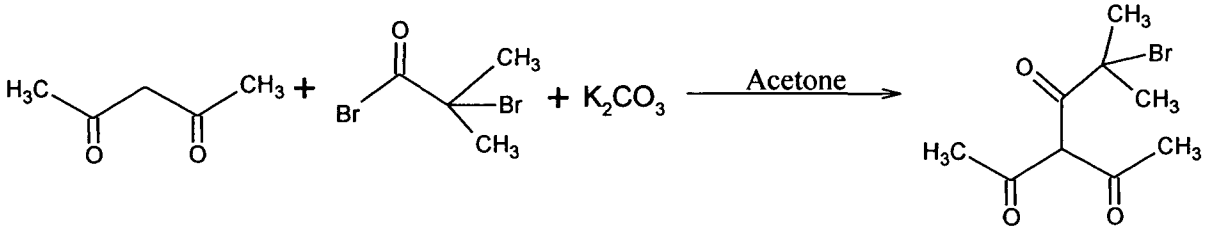

NMR analysis and FTIR spectroscopy were performed to characterize the obtained product. ^1H NMR analysis revealed 2 signals at 2.10 ppm and 1.97 ppm, which were assigned to the two types of methyl-groups. The signals for the CO-groups and methyl-groups that were obtained by ^{13}C NMR analysis were all assigned, except one signal at 171 ppm which suggested the formation of a by-product. A possible side reaction would have been the

formation of an ester instead of bonding in position 3 via a nucleophile substitution of the bromine atom. These results correspond with the results that were obtained by FTIR-analysis, where at 1238 cm^{-1} a small band was observed that could correspond to a ν(CO) absorption of an ester-group. The signals that were assigned to the keto and the enol-form of the ν(CO) vibration were found at 1730 cm^{-1} and 1589 cm^{-1}. The final product was used without further purification.

3.2.1.7. Coordination of 3-acetyl-5-bromo-5-methylhexane-2,4-dione

The coordination of the bidentate ligand was performed in absolute toluene under reflux over night with $Ti(O^iPr)_4$, $Zr(O^nBu)_4$, and $Fe(O^iPr)_3$. After the evaporation of the solvent an orange oil was obtained, which was not purified any further, in high yields (Scheme 16).

Scheme 16

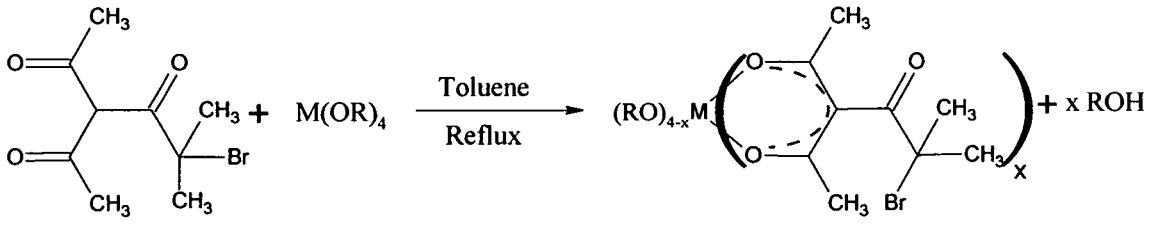

In the ^1H NMR experiments the expected signals for the methyl and alkoxide protons were observed. ^{13}C NMR analysis obtained signals of coordinated and uncoordinated CO-groups between 190 and 171 ppm, a further signal at 101 ppm which was assigned to the carbon atom between the CO-groups. Signals of the quaternary carbon atom and the alkoxide groups were found between 70 and 58 ppm and the signals corresponding to the different methyl-groups were observed between 31 ppm and 20 ppm.

Exemplarily the FTIR-spectrum of 3-acetyl-5-bromo-5-methylhexane-2,4-dione coordinated to titanium isopropoxide is compared to the uncoordinated form in figure 24.

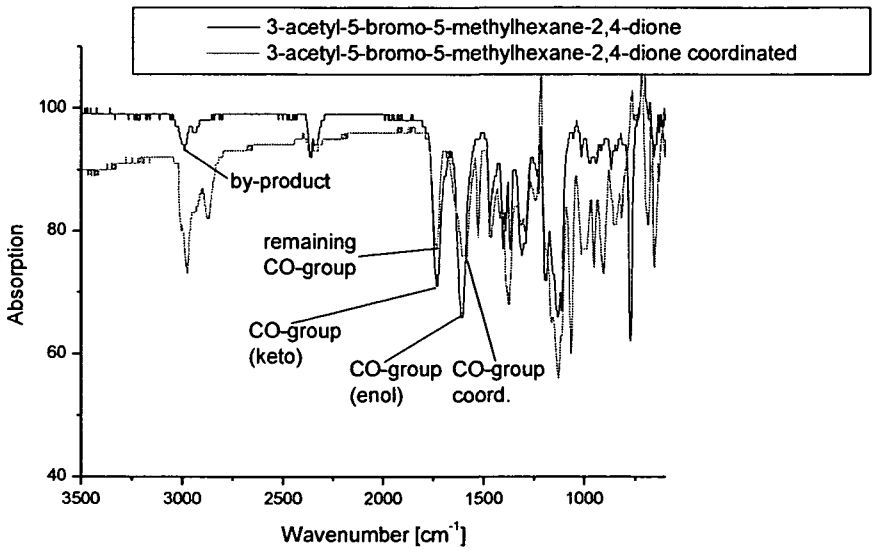

Figure 24: FTIR-spectra of uncoordinated and coordinated 3-acetyl-5-bromo-5-methylhexane-2,4-dione.

In case of titanium isopropoxide the band of the ν(CO) vibration of the keto-form at a wavelength 1730 cm^{-1} was still visible after the coordination due to CO-group of the acetyl fragment that could not coordinate. The band of the ν(CO) vibration of the enol-form at 1612 cm^{-1} disappeared completely after the coordination and was replaced by a band at 1582 cm^{-1}. Compared to the coordination of the ester derivative (ν(CO) = 1577 cm^{-1}) the band was shifted to higher wave-length due to different electronical influences. If zirconium butoxide was utilized the band of the ν(CO) vibration of the keto-form was measured at 1738 cm^{-1} whereas the coordinated CO-group resulted in a band at 1584 cm^{-1}. A slight shift to lower wavelength was observed for this band, compared with the band of the ν(CO) vibration in case of the coordination of the ester derivative at 1588 cm^{-1}.

In the case of iron isopropoxide, 3-acetyl-5-bromo-5-methylhexane-2,4-dione was coordinated completely according to FTIR-spectroscopy. The obtained coordination product showed the band of the ν(CO) vibration of the keto-form at 1738 cm^{-1} and the band of the coordinated species at 1571 cm^{-1}. Iron alkoxide revealed the most significant band shift compared to the coordination of the ester derivative as the ν(CO) vibration band was shifted from 1585 cm^{-1} to 1571 cm^{-1}. All assigned bands are shown in the experimental part in chapter 7.4.

Elemental analyses were performed for all obtained coordination products which all resulted in good agreement with the calculated values.

Other groups were bound to the two carbonyl-groups to induce different chemical properties. 1,3-diphenyl-propane-1,3-dione is a substance that has already been coordinated to various metal alkoxides such as titanium isopropoxide and zirconium isopropoxide [229] in defined ratios and allows, like pentane-2,4-diones, the functionalization of the 2-position via deprotonation. Chemical modification of the phenyl-entities would allow the introduction of functional groups in additional positions. Further on, the two phenyl-rings could favor the crystallization process.

3.2.1.8. Synthesis of 2-bromo-1,3-diphenylpropane-1,3-dione

1,3-Diphenylpropane-1,3-dione was dissolved in water and chloroform, cooled to 0 °C and was reacted with a bromine chloroform mixture (scheme 17).

Scheme 17

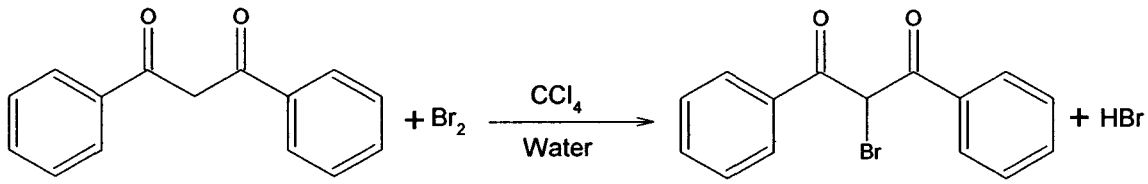

The phases were separated and the organic phase was dried over chloroform. After the elimination of the solvent in vacuo, the colorless, crystalline product was obtained in a yield of 92.4 %. FTIR- and NMR-spectroscopy were performed to analyze the keto-enol equilibrium of the substance. Both methods showed that 2-bromo-1,3-diphenylpropane-1,3-dione only exists in the diketo form. The typical band of the ν(CO) vibration was detected at 1671 cm^{-1}. The shift of the band of the CO-groups compared to the bromo-acetylacetone derivate (1717 cm^{-1} to 1579 cm^{-1}) was caused by the replacement of the methyl groups by phenyl groups. ^{1}H NMR analyses showed 2 signals at 7.98 ppm and 7.45 ppm, which both were assigned to the phenyl-rings. The CO groups were assigned to a signal at 188.9 ppm obtained by ^{13}C NMR. The high-field shift compared to 3-bromo-pentane-2,4-dione (CO groups at 190.1 ppm) probably was caused by the + M effect of the phenyl rings. The carbon atom that was linked to the bromine atom was assigned to a signal at 52.6 ppm. As mentioned before the product was obtained in crystalline form and a single crystal X-ray analysis was

performed. In figure 25 the molecular structure of 2-bromo-1,3-diphenylpropane-1,3-dione is shown.

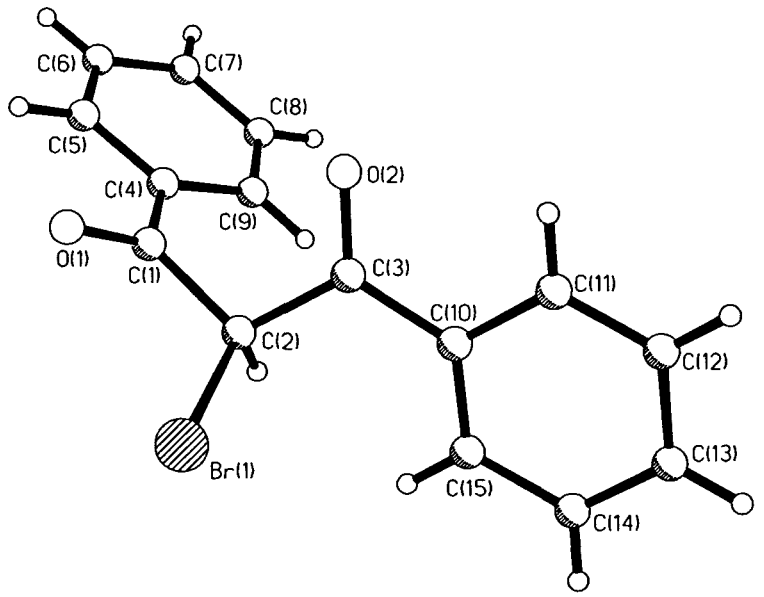

Figure 25: Molecular structure of 2-bromo-1,3-diphenylpropane-1,3-dione.

The molecular structure revealed that one of the acid H-atoms in position 3 was replaced by a bromine atom. The crystal data of 2-bromo-1,3-diphenylpropane-1,3-dione are discussed in the experimental part.

In case of the 2-bromo-1,3-diphenylpropane-1,3-dione, the C-O bond-length was reduced to 121(6) pm compared to 1,3-diphenylpropane-1,3-dione where a C-O bond-length of 130(4) pm was observed. The Br-C bond had a length of 195(5) pm. The length of the bond between C(2) and C(3) was increased to 155(6) pm in the bromine derivative compared to bromine free derivate where this bond had a length of 141(5) pm. The distance between the carboxyl group and the phenyl ring was in both molecules 148(7) pm.

In case of the bromine-derivate the bond angle between C(4)-C(1)-C(2) was slightly decreased to 120(4) °, compared to the bromine free species where this bond angle had a value of 122(6) °. In case of the bromine derivate, the O(1)-C(1)-C(4) bond angle was increased to 121(5) ° compared to 115(7) °.

In case of the bromine derivative a torsion angle of the phenyl-rings to the CO groups of -5(8) ° was observed while 1,3-diphenylpropane-1,3-dione showed a torsion angle of 17(2) °.

3.2.1.9. Synthesis of 2-chloro-1,3-diphenylpropane-1,3-dione

2-chloro-1,3-diphenylpropane-1,3-dione was synthesized from 1,3-diphenylpropane-1,3-dione via a chlorination reaction using SO_2Cl_2 as chlorine donor. 1,3-Diphenylpropane-1,3-dione was dissolved in toluene and reacted with dropwise added SO_2Cl_2 over night at room temperature under continuous stirring. After the addition of water the mixture was stirred for 24 hours. After evaporation of the solvent in vacuo a colorless, crystalline product was obtained in a yield of 93 % (scheme 18).

Scheme 18

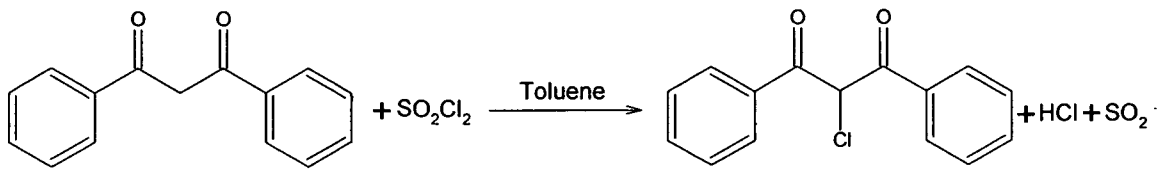

Both, FTIR and NMR analysis showed that 2-chloro-1,3-diphenylpropane-1,3-dione only occurs in its diketo-form. The band of the ν(CO) vibration was observed at 1690 cm^{-1} which was only slightly shifted compared to the bromine-derivative.

^1H NMR analyses revealed three signals at 7.98 ppm, 7.45 ppm and 6.45 ppm. While the first two signals corresponded to typical phenyl-ring signals the latter was assigned to the hydrogen atom that is bond to the carbon atom, which is situated between the CO-groups. This signal was not found in case of the bromine derivate. Compared to the bromine derivative ^{13}C NMR showed shifts of the CO-groups from 188.9 ppm to 185.4 ppm and of the CH-halogen group from 56.2 ppm to 78.3 ppm due to different electronical structure of the halogen atoms.

Single crystal X-ray analysis was performed after recrystallisation in toluene. In figure 26 the obtained crystal structure is shown.

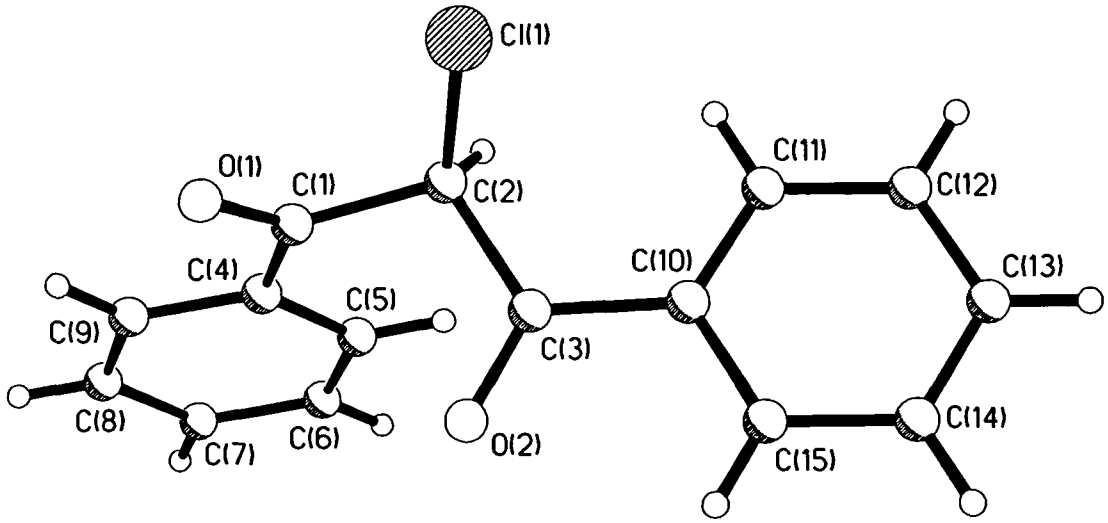

Figure 26: Molecular structure of 2-chloro-1,3-diphenylpropane-1,3-dione.

The molecular data of 2-chloro-1,3-diphenylpropane-1,3-dione are shown in the experimental part. Compared to the Br-C distance of 195(5) pm in the bromine derivate, the Cl-C bond length was with 178(2) pm much shorter due to different radii of the atoms and their different electronic behavior.

In case of the 2-chloro-1,3-diphenylpropane-1,3-dione the C-O bond length was slightly reduced to 120(3) pm compared to 2-bromo-1,3-diphenylpropane-1,3-dione where a C-O bond length of 121(6) pm was observed. In case of the chlorine-derivate the bond angle between C(4)-C(1)-C(2) was slightly decreased to 117(3) ° compared to the bromine containing species where this bond angle had a value of 120(4) °, while the O(1)-C(1)-C(4) bond angle in both cases was 122(4) °. The angle between the carbon-carbon-halogen bonds, both for the chlorine and the bromine derivate was 109(3) °.

The phenyl rings showed a torsion angle of 10(3) compared to -5(8) in case of the bromine derivate. All other structural data were similar to the data obtained for the bromine derivate.

3.2.1.10. Synthesis of 2,2-dichloro-1,3-diphenylpropane-1,3-dione

Efforts were made to attach 2 chlorine atoms in the C2 position to investigate the difference between the coordination mechanisms of mono- and bi-substituted 1,3-biphenylpropane-1,3-dione to titanium isopropoxide. 1,3-Diphenylpropane-1,3-dione was dissolved in toluene and reacted with dropwise added SO_2Cl_2 at room temperature. After the hydrolysis with water the organic phase was dried over $MgSO_4$ and the solvent was evaporated in vacuo. The product was obtained in its crystalline form in a yield of 92 % (scheme 19).

Scheme 19

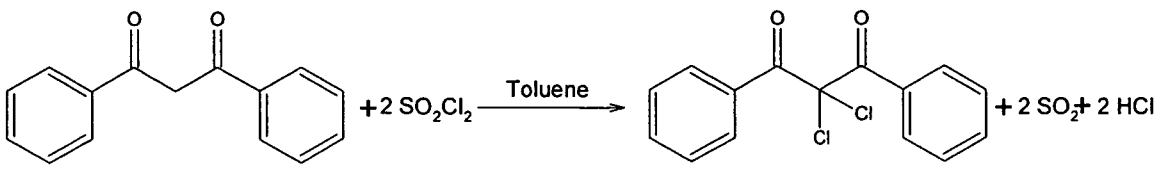

Both, NMR-analysis and FTIR-spectroscopy approved that the molecule exists only in its keto form. The band of the ν(CO) vibration was observed at 1694 cm^{-1}, which was slightly shifted compared to 2-bromo-1,3-diphenylpropane-1,3-dione. ^{1}H NMR analysis obtained 2 signals at 7.98 ppm and 7.45 ppm which were assigned to the phenyl-rings. Compared to the mono-chloro derivate, ^{13}C NMR showed a shift of the signal of the carbon atom situated between the CO groups from 78.3 ppm to 87.6 ppm. The signal of the CO-groups was in both cases found at 185.4 ppm.

The molecular structure of the synthesized compound was investigated via single crystal X-ray diffraction and (figure 27).

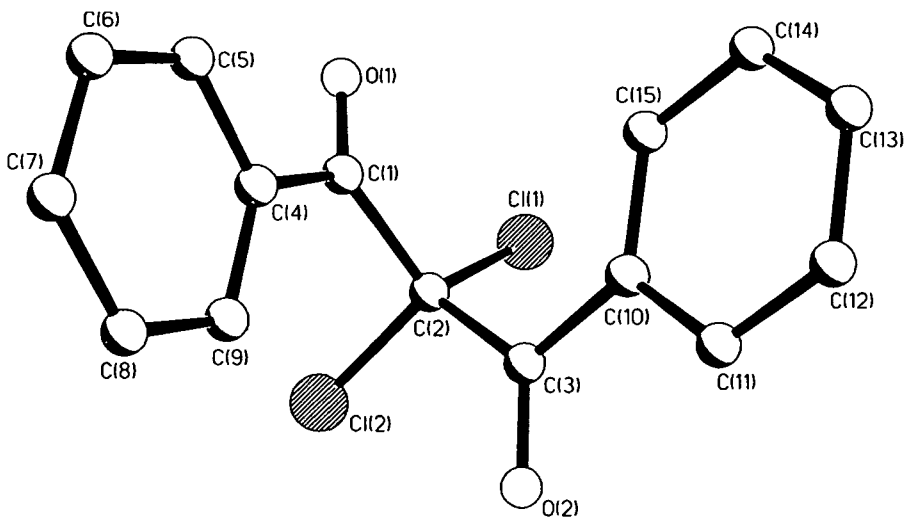

Figure 27: Molecular structure of 2-dichloro-1,3-diphenylpropane-1,3-dione

As shown in figure 27, the two acid hydrogen atoms were replaced by two chlorine atoms. The crystal data of 2,2-chloro-1,3-diphenylpropane-1,3-dione are presented in the experimental part. The bond lengths of C-Cl in the mono-chloro and the dichloro derivate

were equal with a length of 178(7) pm. The C-O bond length and the distance to the phenyl ring remained constant with 120(2) pm and 148(3) pm. The bond angle between Cl-C-Cl was with 107(10) ° slightly smaller than in case of H-C-Cl where an angle of 109(0) ° was obtained. The phenyl rings showed a torsion angle of -13(3) ° compared to the mono-chloro derivate where a torsion angle of 9(3) ° was observed. The other bond length angles were similar to the ones that were measured in case of the mono-chlorine derivate.

3.2.1.11. Coordination of 2-bromo-1,3-diphenylpropane-1,3-dione to titanium isopropoxide

2-Bromo-1,3-diphenylpropane-1,3-dione was dissolved in toluene and mixed with dropwise added titanium isopropoxide. After stirring overnight the solvent was removed in vacuo. This reaction showed a surprising result. A mixture of different products was obtained. It was possible to obtain crystals of one of the products via recrystallisation in toluene. The crystal structure of the gained crystals is shown in figure 28.

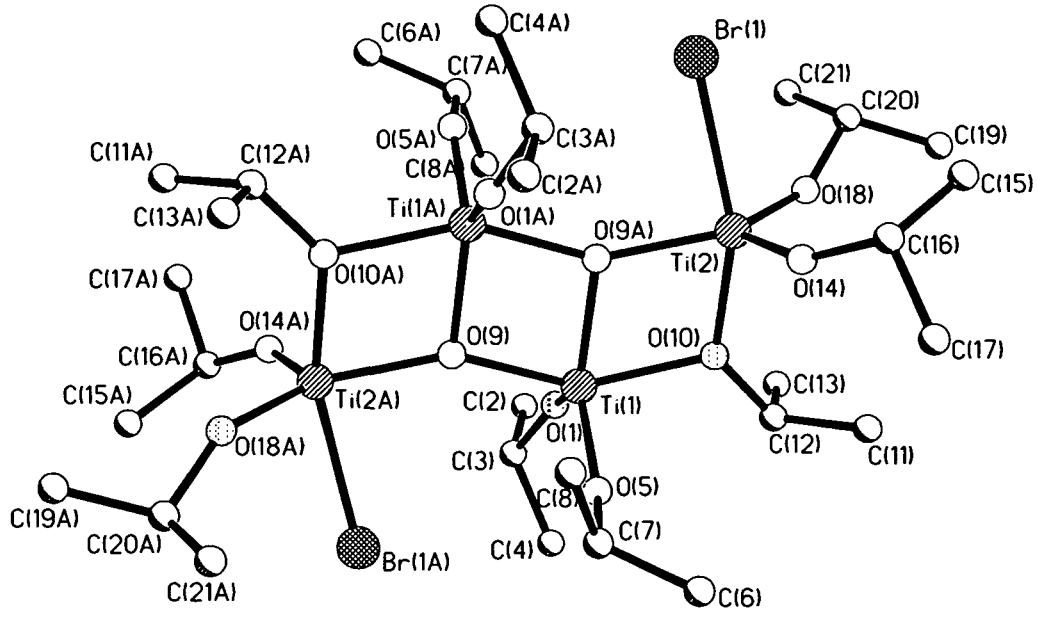

Figure 28: Molecular structure of the crystals.

Not the intended coordination of the entire ligand was obtained but bromine atoms were directly bond to the metal centre itself. The shown cluster (figure 28) contained four titanium atoms that were surrounded by five ligands in a trigonal bipyramidal arrangement. Three titanium atoms were linked over a μ_3-oxygen atom. All titanium atoms were connected via

bridging isopropoxide group and one of the two μ_3-oxygen atoms. Every titanium atom was also connected to two terminal isopropoxide groups.

A structural similar cluster was published by *Moraru et al.* where the cluster core consisted of four crystallographic independent titanium atoms, linked together by two μ_3-oxygen atoms but six bridging methacrylate ligands.[230] The structure was completed by six terminal isopropoxide groups.

As shown in figure 28, the four titanium atoms have a rhombic arrangement with an equal bond length between the μ_3-oxygen atom and the titanium atom of 195(14) pm, which is different compared to the cluster published by *Moraru et al.* where bond lengths of 191 pm and 208 pm were measured. The other oxygen titanium distances are between 176(16) pm and 201(15) pm while *Moraru et al.* has found Ti-O bond length up to 209(4) pm. The obtained titanium bromine distance has a length of 254(5) pm.

The measured Br-Ti-O angles are between 88(4) ° and 159(5) °. The Ti-μ_3O-Ti angles are 150(8) ° and twice 39(4) °, respectively. *Moraru et al.* published angels of 127(18) °, 132(19) ° and 102(15) °. In the experimental part (chapter 7.4.) selected data of the X-ray single crystal analysis are presented.

In figure 29 a magnified detail of the 2D-NMR spectrum shows the isopropoxide groups of the titanium cluster.

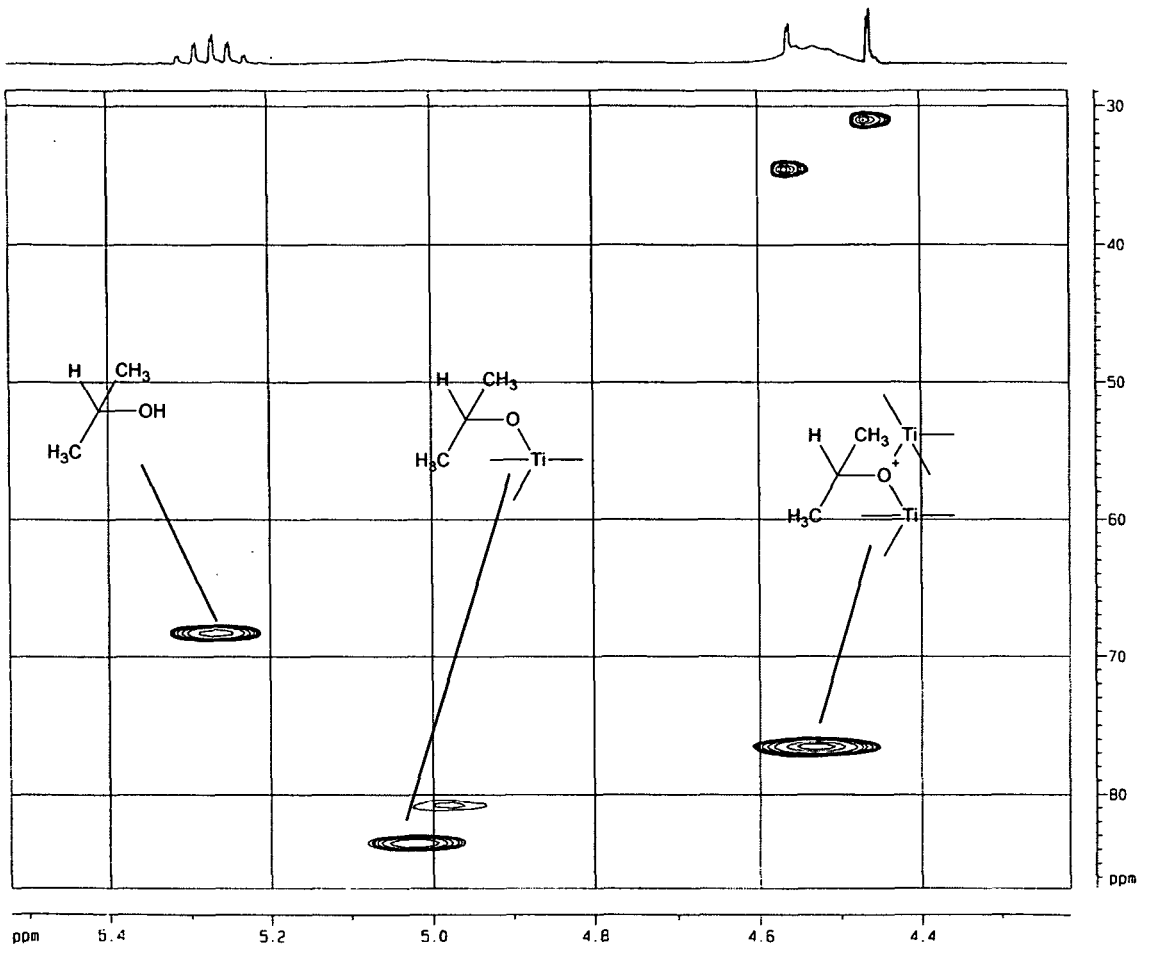

Figure 29: 2D NMR spectrum of the titanium cluster.

Via 2 D NMR-spectroscopy it was possible to differ between the occurring isopropoxide groups. As shown above, isopropanol was observed at a chemical shift at 5.3 ppm and 68 ppm in the ^{1}H NMR and the ^{13}C NMR, respectively. The signals of the isopropoxide groups that were bound to one titanium atom were detected at 5.0 ppm (^{1}H NMR) and 81-83 ppm (^{13}C NMR). The signal of bridging isopropoxide groups was detected at 4.5 ppm and 77.5 ppm in the ^{1}H- and ^{13}C-NMR, respectively.

The entire 2D NMR spectrum is shown in figure 30.

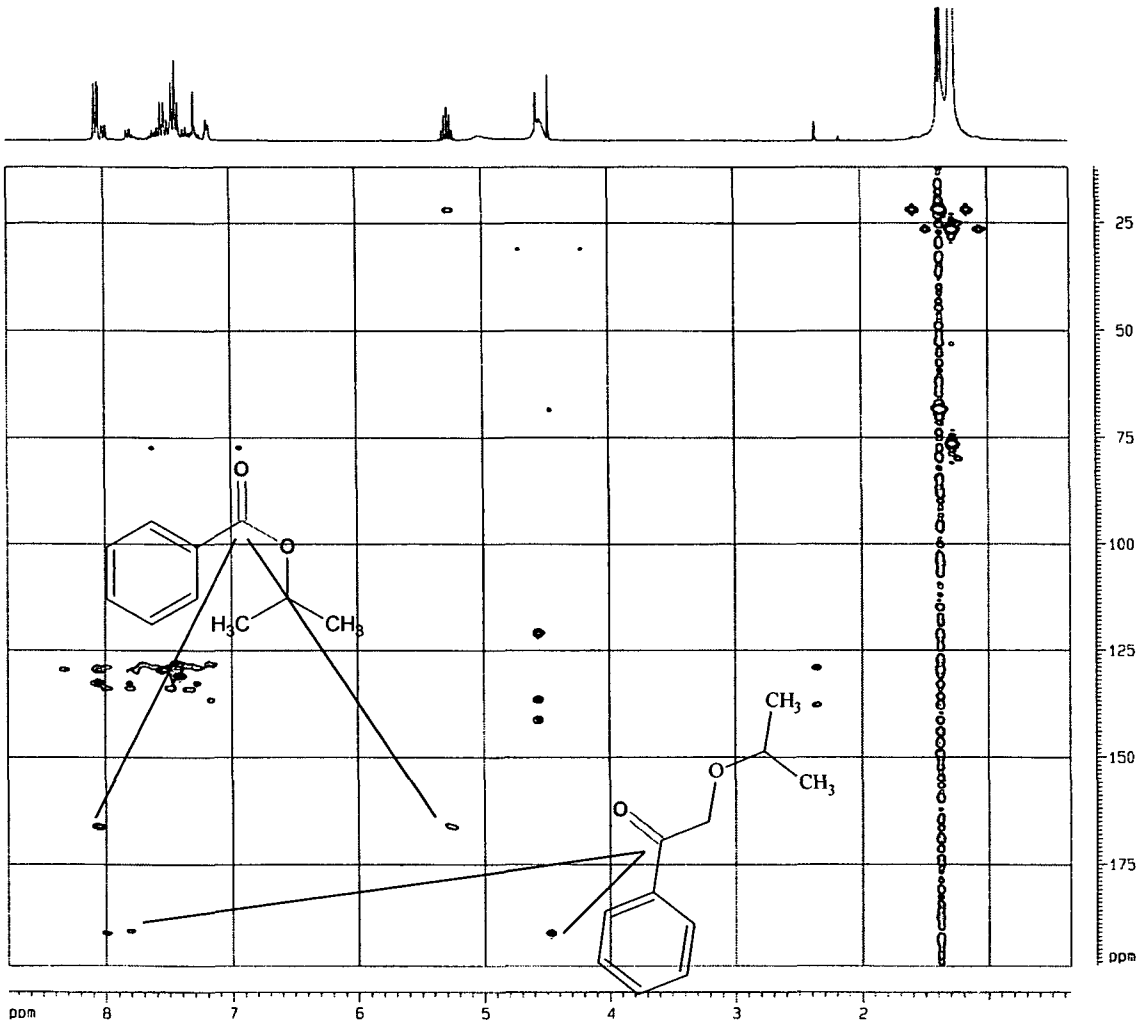

Figure 30: 2 D NMR-spectrum of obtained mixture.

Taking in account the observed NMR and crystallographic data, the following mechanism of the decay of 2-bromo-1,3-diphenylpropane-1,3 dione was postulated (scheme 20).

Scheme 20

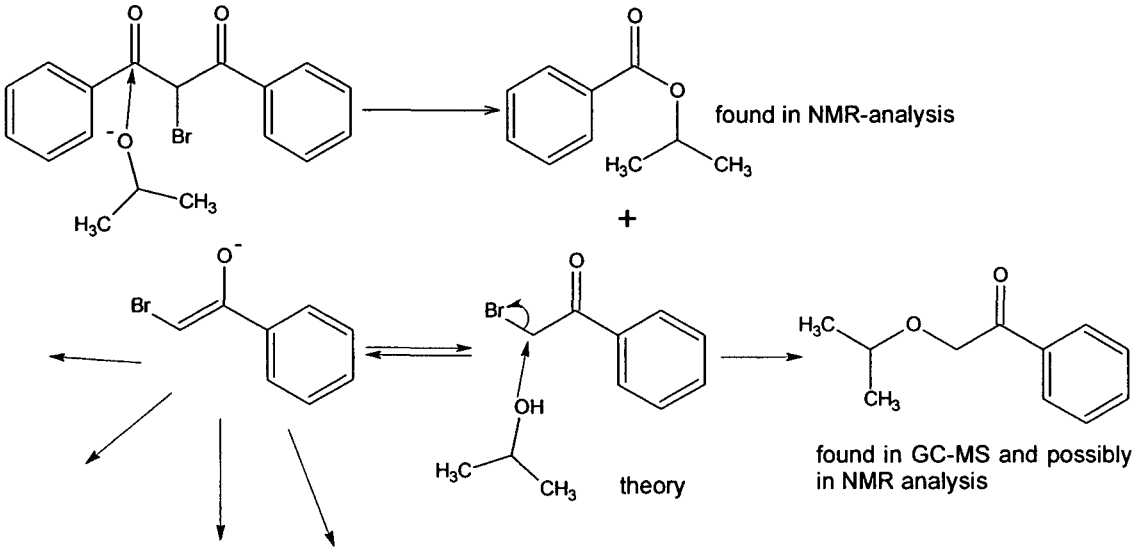

A separated isopropoxide molecule that carried a negatively charged oxygen atom attacked the electropositive carbon atom of the CO group which led to the cleavage of the carbon-carbon bond and the formation of an ester structure. The obtained isopropyl benzoate was identified via NMR analysis by a signal of the COO-group at 164 ppm. The emerging 2-bromo-phenyletnanone seemed to be an intermediate product which was not found via NMR-analysis. An observed secondary reaction of 2-bromo-phenyletanone was the conversion with a further isopropoxide group, which led to the elimination of the bromine atom and formation of 1-isopropoxy-1-phenylethanone. This was observed in the GC-MS analysis with a molecular peak of 179 g/mol and possibly in ^{13}C NMR spectroscopy with a signal at 186 ppm. Considering the NMR spectra, the existence of further decay and condensation products can be assumed. Despite intensive search in literature, such a formation mechanism was not encountered elsewhere.

3.2.2. Synthesis of nanoparticles using pentane-2,4-derivates without additives

The coordinated 3-chloro-pentane-2,4-dione was used for the formation of nanoparticles in a sol-gel-like approach as mentioned in chapter 1.2.1. Ethanol was mixed with ammonia to catalyze the following sol-gel reaction of the isopropoxide groups of the precursor molecule like shown in scheme 21.

Scheme 21

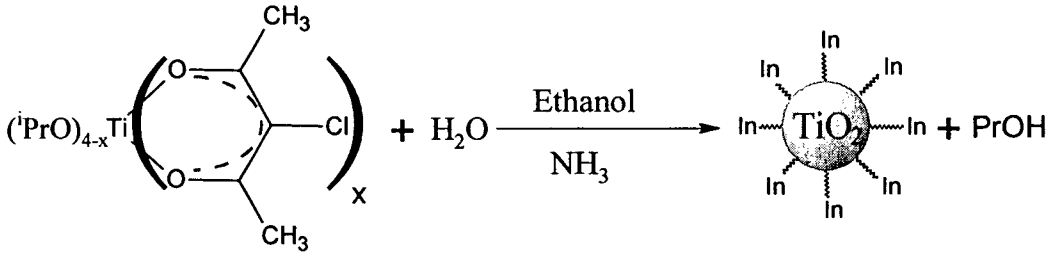

The obtained titania particles were stirred over night, isolated by centrifugation, and washed various times. In figure 31 a TEM image of the functionalized TiO_2 nanoparticles is shown.

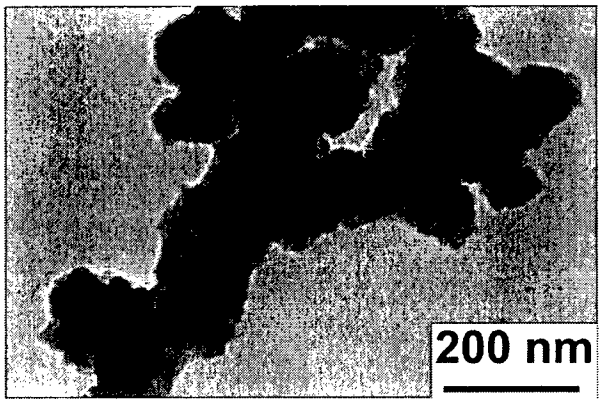

Figure 31: TEM image of TiO_2 nanoparticles produced without microemulsion technique.

The diameter of the particles shown in figure 31 is about 85 nm. They are aggregated and do not show a spherical morphology. A possible explanation is the high reaction velocity due to the high activity of the utilized precursor. Because of the non-spherical form and the large size-distribution no DLS investigation was performed.

FTIR analysis showed the typical band of the ν(CO) vibration at 1580 cm^{-1} which confirmed that 3-chloro-pentane-2,4-dione remained attached to the particle surface. Due to the non-spherical form of the nanoparticles no elemental analysis was performed.

This experiment was repeated using 3-acetyl-5-bromo-5-methylhexane-2,4-dione which was coordinated to titanium isopropoxide. The utilized precursor was added dropwise to a mixture of ethanol and ammonia under vigorous stirring as shown in scheme 22.

Scheme 22

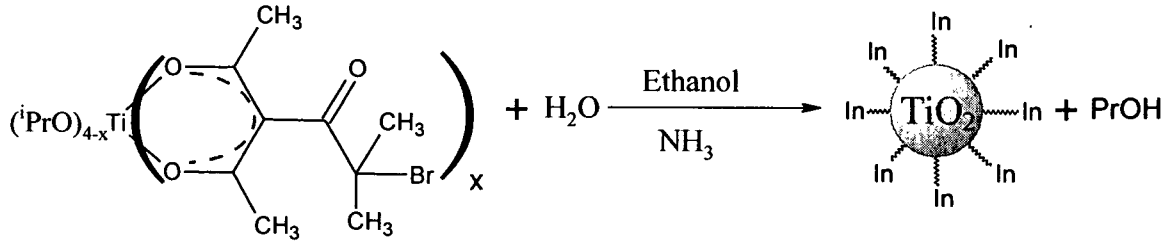

The particles were centrifuged, washed and analyzed via TEM and DLS as shown in figure 32.

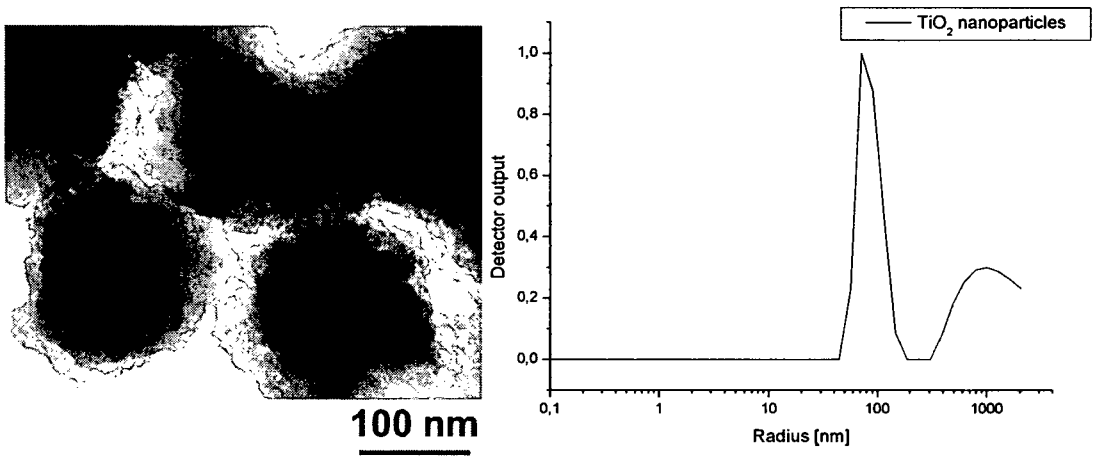

Figure 32: TEM image and DLS plot (recorded in ethanol) of the obtained TiO_2 nanoparticles.

The functionalized TiO_2 nanoparticles shown in figure 32 had a diameter of about 185 nm according to the TEM image and a non-spherical morphology with a rough surface. The DLS analysis revealed a diameter of 172 ± 38 nm and that most of the particles were aggregated. FTIR analysis revealed the typical band of the ν(CO) vibration at 1582 cm^{-1}.

For further applications homogeneity in size and morphology are of great importance for example for the synthesis of ordered 3D structures. Hence the microemulsion technique was used to get more homogenous particles.

3.2.2.1. Short summery

In this chapter the preparation of different types of nanoparticles, without using microemulsion technique, and the synthesis of precursor molecules that contain functional groups, which can initiate polymerization, were presented. As initiator molecules various pentane-2,4-dione derivatives were synthesized and characterized. These molecules were coordinated to different metal alkoxides to obtain bifunctional precursor molecules that can undergo sol-gel reactions and after the particle synthesis initiate a polymerization process. The coordination process was difficult to observe via NMR analysis because a mixture of different products was obtained. Various 1,3-diphenyl-propane-1,3-dione derivatives were synthesized and characterized to overcome this problem and allow further functionalization. With these derivatives it was not possible to obtain coordination to metal alkoxides.

In table 3 significant data of the nanoparticles are summarized.

Table 3: Data of the synthesized nanoparticles.

Nanoparticles	**Diameter TEM [nm]**	**Diameter DLS [nm]**	**Weight loss TGA [%]**	**Specific surface area [m^2/g]**
SiO_2	93	85 ± 15	16.0	117
	---	25 ± 1	16.5	220
	---	157 ± 10	14.0	51
Au	15	15 ± 2	26.0	39
	25	27 ± 5	24.0	33
$Au@SiO_2$	43	38 ± 3	40.0	45
TiO_2 functionalized with ethylene glycol	80-120	101 ± 7	41.5	412
TiO_2 functionalized with 3-Chloro-pentane-2,4-dione	≈ 85	---	---	---
TiO_2 functionalized with 3-acetyl-5-bromo-5-methylhexane-2,4-dione	≈ 185	172 ± 38	---	---

3.2.3. Synthesis of nanoparticles using pentane-2,4-derivates applying a microemulsion approach

The substituted alkoxides were used as precursors for the sol-gel process in a water-in-oil microemulsion with cyclohexane as continuous phase, the commercially available Triton X-100 as non-ionic surfactant, and 1-hexanol as cosurfactant based on a literature-known procedure.[110] If not otherwise mentioned, the amount of metal alkoxide and the water to alkoxide ratio was kept constant. ***All percentage contents are weight-percents.***
All amorphous particles that are presented in this chapter showed due to the high organic content a specific surface area below 2 m^2/g and are therefore not discussed in detail.

3.2.3.1. Synthesis of functionalized titanium oxide nanoparticles from alkoxide precursors

Cyclohexane was mixed with n-hexanol, Triton X-100 and water under vigorous stirring until no more turbidity was visible. Afterwards, the different modified titanium alkoxides, coordinated with 3-chloro-pentane-2,4-dione, 3-bromo-pentane-2,4-dione, 1-acetyl-2-oxopropyl 2-bromo-2-methylpropanoate, and 3-acetyl-5-bromo-5-methylhexane-2,4-dione, were added and stirred overnight at room temperature. The received nanoparticles were centrifuged and purified by several washing procedures.

The highest yield was obtained using 3-chloro-pentane-2,4-dione modified titanium isopropoxide as precursor for the titania particles resulting in 0.15 g (84.2 %) nanoparticles. Application of 1-acetyl-2-oxopropyl 2-bromo-2-methylpropanoate and 3-bromo-pentane-2,4-dione modified titanium isopropoxide resulted in 0.14 g (63.3 %) and 0.13 g (69.1 %) modified titanium oxide nanoparticles. The lowest yield was received, if 3-acetyl-5-bromo-5-methylhexane-2,4-dione modified titanium isopropoxide was used, which led to the formation of 0.11 g (49.7 %) nanoparticles. The observed yields suggested losses during the purification and an incomplete conversion of the isopropoxide residues.

FTIR investigation showed that only coordinated species were incorporated in the nanoparticles. Exemplarily the obtained FTIR-spectra of nanoparticles synthesized from a precursor containing 3-chloro-pentane-2,4-dione compared with the FTIR-spectrum of the precursor molecule are shown in figure 33.

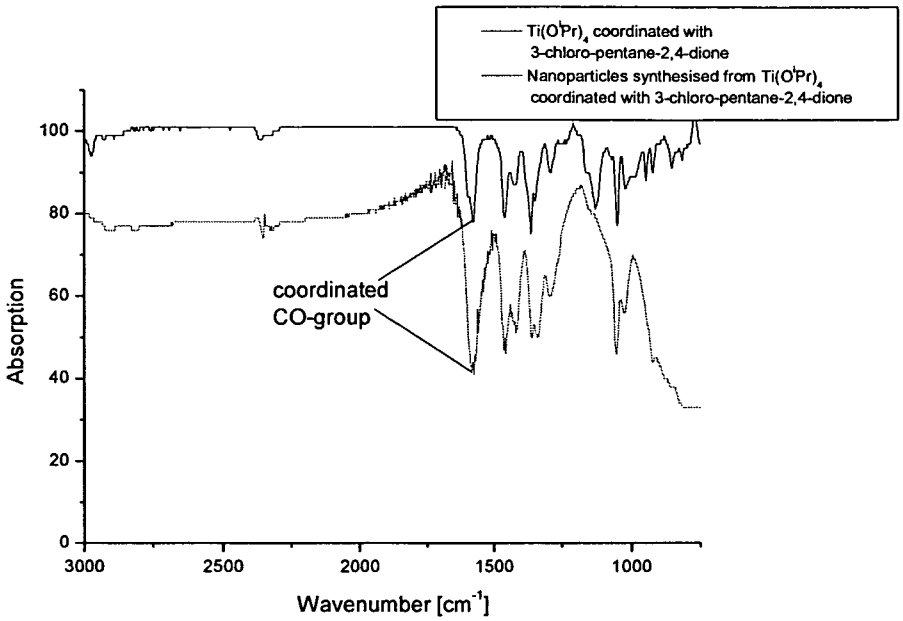

Figure 33: Comparison of the FTIR-spectra of $Ti(O^iPr)_4$ coordinated with 3-chloro-pentane-2,4-dione and the obtained nanoparticles.

The spectra shown in figure 33 demonstrated that during the particle formation no shift of the CO-band, which could have been caused by a cleavage of the coordinated ligand, occurred. Both spectra showed the ν(CO) vibration band of the CO-group at 1576 cm^{-1}. The results were similar for all other ligands. In case of 3-bromo-pentane-2,4-dione, 1-acetyl-2-oxopropyl 2-bromo-2-methylpropanoate and 3-acetyl-5-bromo-5-methylhexane-2,4-dione the band of the CO-group was measured at 1568 cm^{-1}, 1576 cm^{-1} and 1582 cm^{-1}, respectively.

The carbon contents of the obtained nanoparticles, received by elemental analysis were between 27 % in case of the 3-chloro-pentane-2,4-dione containing precursor and 35 % in case of the 3-acetyl-5-bromo-5-methylhexane-2,4-dione containing precursor depending, of course, on the used initiating group. The measured halogen contents were between 4.1 % and 7.2 %. From the observed carbon contents it should be possible to calculate the theoretical halogen content as well under the assumption that all alkoxide groups were hydrolyzed during the particles formation. But the calculated values for the halogen content proved to be much higher than the measured ones, which might have been caused by several reasons: (i) unreacted alkoxide groups on the surface and inside the nanoparticles and (ii) the quite labile carbon-halogen bond which probably led to a loss of halogen atoms. If the cleaving of these

bonds played an important role, the initiating capacity during polymerization would have dropped enormously, which was not observed as shown in chapter 6.2.2. (iii) In addition, halogen functionalized ligands and transition metal complexes are known to be connected with the formation of compounds which are highly volatile and can so falsify the results of elemental analysis. According to the Institute of Analytical Chemistry of the University of Vienna such reactions can falsify the obtained results within 0.5 %.

Excluding the latter two reasons for causing the observed discrepancy in the halogen content, it has to be assumed that unhydrolyzed isopropoxide groups were present in the produced nanoparticles. In case of the 3-chloro-pentane-2,4-dione containing particles this hypothesis led to the assumption that approximately 25 % of the carbon content were consumed by isopropoxide groups. If bromo-pentane-2,4-dione was used the amount of isopropoxide groups increased to approximately 30 %. In case of the two other ligands about 40 % of the carbon content was caused by isopropoxide groups. This estimation is only acceptable assuming that both, unfunctionalized particles and functionalized particles show the same water content and the same amount of condensation reactions. TGA analysis proved that all synthesized nanoparticles showed weight losses between 12 % and 15 % up to 200 °C.

In case of the 3-chloro-pentane-2,4-dione ligand, it was tried to raise the degree of condensation during the synthesis by ageing the microemulsion for one week at 60 °C. The obtained particles were analyzed via elemental analysis which showed both reduced carbon content and reduced chlorine content. It seemed as if increased temperature had negative impact on the stability of the carbon chlorine bond. Elemental analysis revealed a carbon content of 17.7 % and a chlorine content of < 0.2 %.

The titanium and halogen content was measured via an EDX-detector at the used transmission electron microscope. The obtained values were compared to calculated halogen contents using the amount of volatile substances obtained by TGA. The results are shown in table 4.

Table 4: Comparison of the metal and halogen content of the different modified TiO_2 nanoparticles measured by EDX with the results revealed via TGA.

		EDX			TGA	
TiO_2 nanoparticles functionalized with the following polymerization initiators	Weight ratio titanium-halogen	Titanium [%]	Halogen [%]	Volatile compounds up to 800 °C [%]	TiO_2 [%] *Ti [%]*	Halogen [%] (calculated)
---	---	---	---	26.3	73.7 *45.3*	---
3-chloro-pentane-2,4-dione	86:14	56.0	8.7	36.2	63.8 *39.2*	9.4
3-bromo-pentane-2,4-dione	62:38	32.6	20.3	37.0	63.0 *38.7*	14.0
1-acetyl-2-oxopropyl 2-bromo-2-methylpropanoate	92:8	51.3	4.3	32.5	67.5 *41.5*	6.6
3-acetyl-5-bromo-5-methylhexane-2,4-dione	95:5	56.3	3.5	36.6	63.4 *39.0*	7.0

In the EDX analysis the highest halogen content was obtained, if 3-bromo-pentane-2,4-dione was used as polymerization initiator which resulted in a titanium to bromine ratio of 62:38. The chlorine containing precursor showed the second highest halogen content, which resulted in a titanium to chlorine ratio of 86:14. The 1-acetyl-2-oxopropyl 2-bromo-2-methylpropanoate and the 3-acetyl-5-bromo-5-methylhexane-2,4-dione containing nanoparticles had the smallest titanium to bromine ratio of 92:8 and 95:5, respectively. A drawback of the EDX analysis was that it only covered a small sector of the sample, which could further lead to wrong results as well, while TGA and elemental analysis delivered results that are representative for the entire sample. The EDX measurements were repeated at least five times and the obtained average was utilized to compensate this effect. Furthermore, it has to be mentioned that the accuracy of EDX of the calculated contents is ± 5 %.

TGA analysis demonstrated that all nanoparticles had a volatile fraction between 63 and 67.5 % depending on the utilized initiator molecule. The percentages of TiO_2 and halogens were obtained by comparing the modified particles with unmodified ones under the assumption that all of them had the same amount of moisture and residues of organic solvents. Furthermore, the presence of remaining isopropoxide groups, observed from elemental analysis, was taken into account via reducing the "effective" carbon content caused by coordinated pentane-2,4-dione derivates.

Compared to the results obtained from EDX, the resulting titanium content from TGA analysis was much lower. This might have been caused by the influence of the conditions during the TEM analysis on the sample, such as on the one hand ultra high vacuum, which led to different moisture contents and on the other hand destruction of the sample, i.e. mainly the organic contents, by the electron beam. The evaporation of organic content would have led to an enrichment of the sample with titanium.

In general, the discrepancy between the halogen content obtained by TGA and EDX was below 3.5 % except for the 3-bromo-pentane-2,4-dione containing species, which revealed a higher halogen content in the EDX analysis which is inside the confidence interval of EDX.

The obtained nanoparticles were not crystalline which was proved by X-ray powder diffraction. However, crystallinity is highly desired because many interesting properties like the refractive index or mechanical stability are associated with the different crystalline modifications. In case of titanium oxide, different crystalline phases are known. Anatase and brookite are low temperature modifications which can be transformed to rutile at increased temperature. The crystal system of brookite shows an orthorhombic structure with the space group *Pbca* while anatase and rutile have a tetragonal crystal system with the space group $I4_1/amd$ and $P4_2/mnm$, respectively. Depending on the used condition, during the synthesis the mentioned phase can be synthesized.

For example, *Zhang et al.* [231] and *Gribb et al.* [232] observed that the synthesis of ultrafine titania by the sol-gel method resulted in anatase and/or brookite, which transformed to rutile after reaching a certain particle size. They analyzed the phase stability of anatase and rutile thermodynamically to conclude that anatase became more stable than rutile for a particle size < 14 nm. *Hwu et al.* [233] showed that the modification of TiO_2 strongly depends on the preparation method. In case of small particle size (< 50 nm) anatase seemed more stable and transformed to rutile at ≈ 973 K. *Wiggins et al.* studied the onset temperature of the

crystallization process of mainly amorphous titania films and observed that heating to 350 °C resulted in a substantial increase in crystallinity.[234]

X-ray powder diffraction patterns were recorded from 50 °C to 1200 °C to investigate the onset temperature of the crystallization temperature of the observed nanoparticles. The titanium oxide nanoparticles were deposited on a platinum heating band, heated to the selected temperature, and rested there for 20 minutes before the measurement began. In figure 34 the obtained diffractograms and the comparison with diffractograms from the ICSD database are shown.

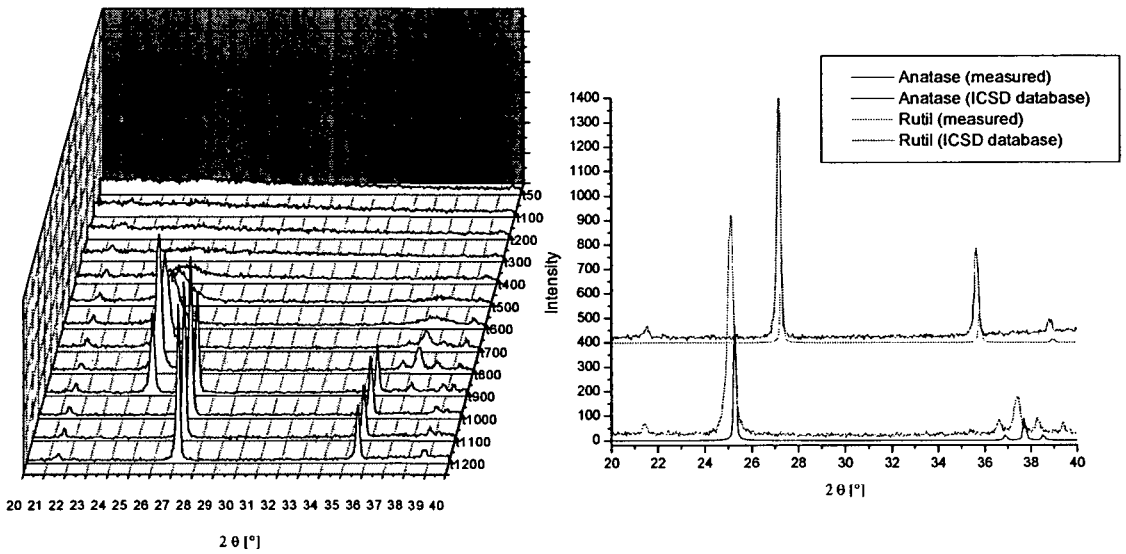

Figure 34: X-ray powder diffractograms of functionalized titanium oxide nanoparticles at different temperatures and comparison with ICDS database-diffractograms (800 °C for anatase [235] and 1200 °C for rutile [236]).

At room temperature the samples were X-ray amorphous. The beginning of the development of the anatase structure was observed at 400°C. The anatase reflections became sharper until 900 °C where the intensity started to decrease to be replaced by reflections assigned to rutile. At 1000 °C the reflections that corresponded to the anatase structure totally disappeared. The small discrepancy between the measured 2θ angles and the ones obtained from the database was caused by a displacement of the platinum band at high temperatures. *Lim et al.* calcinated amorphous titanium oxide nanoparticles with a diameter between 10-15 nm three hours at 300 °C and obtained reflections that were assigned to anatase.[237] The different transformation temperatures were probably caused by the shorter annealing times of 20

minutes at each temperature level. Furthermore, size effects possibly also had an influence on the crystallization behavior. This assumption is supported by *Zhai et al.*, who recently reported the observation of a strong influence of the anatase particles size on the phase transformation kinetic.[238]

Identification of the shape, size, and unity of the synthesized nanoparticles, was achieved via TEM. One drop of a suspension of the particles in ethanol was deposited on a Formvar coated copper grid for the preparation of the TEM-sample. In figure 35 TEM images of the modified TiO_2 nanoparticles are shown.

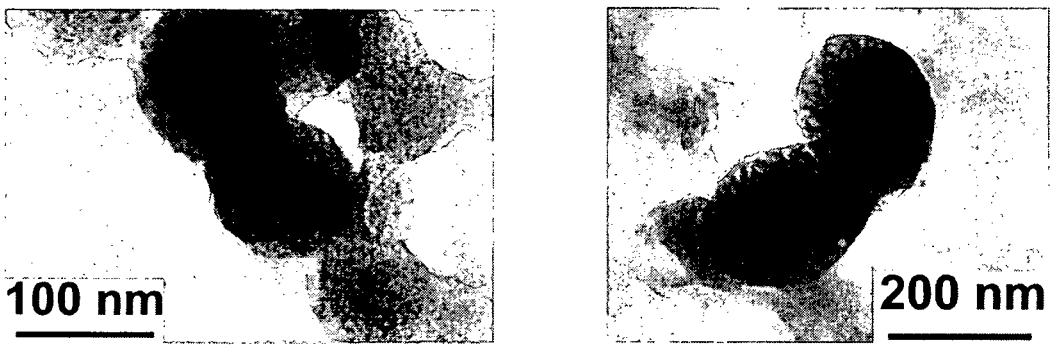

Figure 35: TEM images of TiO_2 particles prepared from a 3-chloro-pentane-2,4-dione containing precursor (diameter of 80 nm) and a 3-acetyl-5-bromo-5-methylhexane-2,4-dione containing precursor (diameter of about 200 nm).

The ligand used for the coordination of the titanium alkoxides had a great influence on the morphology and the size of the obtained nanoparticles. TiO_2 nanoparticles that contained 3-chloro-pentane-2,4-dione as organic functionality had a diameter of about 80 nm and a fairly homogenous structure. A DLS plot of these functionalized TiO_2 nanoparticles is presented in figure 36.

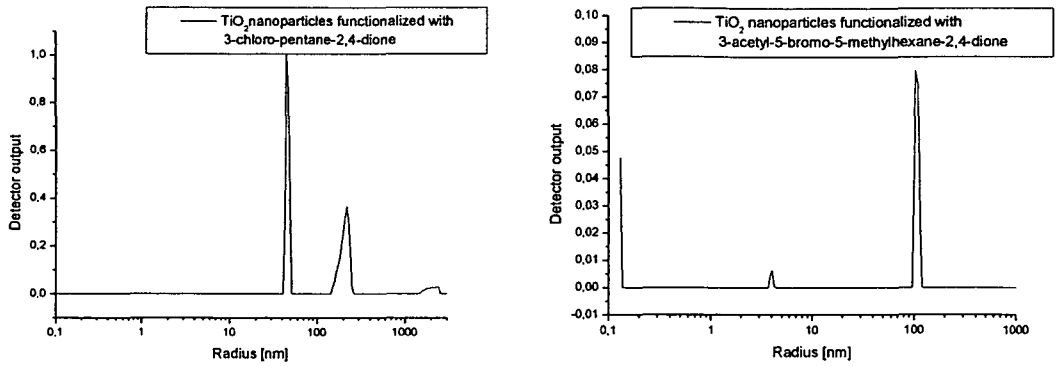

Figure 36: DLS plot of TiO_2 nanoparticles functionalized with 3-chloro-pentane-2,4-dione having a diameter of 92 ± 4 nm and with 3-acetyl-5-bromo-5-methylhexane-2,4-dione having a diameter of 210 ± 4 nm measured in ethanol.

The DLS plot showed, in case of the 3-chloro-pentane-2,4-dione functionality, that only a part of the obtained nanoparticles was non-aggregated while most of them seemed to have agglomerated to larger structures. Although efforts were made to separate the agglomerates via a treatment under ultrasound for several hours, it was not possible to obtain total redispersion.

If 3-acetyl-5-bromo-5-methylhexane-2,4-dione was used to functionalize titanium isopropoxide, the obtained nanoparticles showed a totally different size compared to the 3-chloro-pentane-2,4-dione functionalized ones. The received particles had a diameter of about 210 nm and a monodisperse size distribution (figure 36). The peak at 4 nm might have been caused by partially reacted precursor molecules which did not form nanoparticles but small oligomeres.

The morphology of the synthesized particles was very different as well. No homogenous particles but agglomerates of smaller particles were obtained. Hence, it can be suggested concerning the TEM images that the precursor had a strong influence on the mechanism of the particle formation process in the micelles of the microemulsion. In case of the 3-chloro-pentane-2,4-dione containing particles, the particle growth seemed to be the determining process rather than the nucleation of cores. This means that in a micelle just one or a few nucleation centers developed, which grew during the propagation phase and formed the nanoparticle. If 3-acetyl-5-bromo-5-methylhexane-2,4-dione was used as functional group, it seemed that many nucleation centers were established within one micelle which formed the developing nanoparticle by agglomeration and ripening.

The kinetic of the formation process using the precursors, which contain 3-chloro-pentane-2,4-dione, 3-acetyl-5-bromo-5-methylhexane-2,4-dione, 3-bromo-pentane-2,4-dione and $Ti(O^nBu)_4$ without a ligand, was analyzed via DLS.

In figure 37 the DLS plot of the particle growth versus time is shown. The radius of the shown particles was normalized to allow better comparison of the obtained curves.

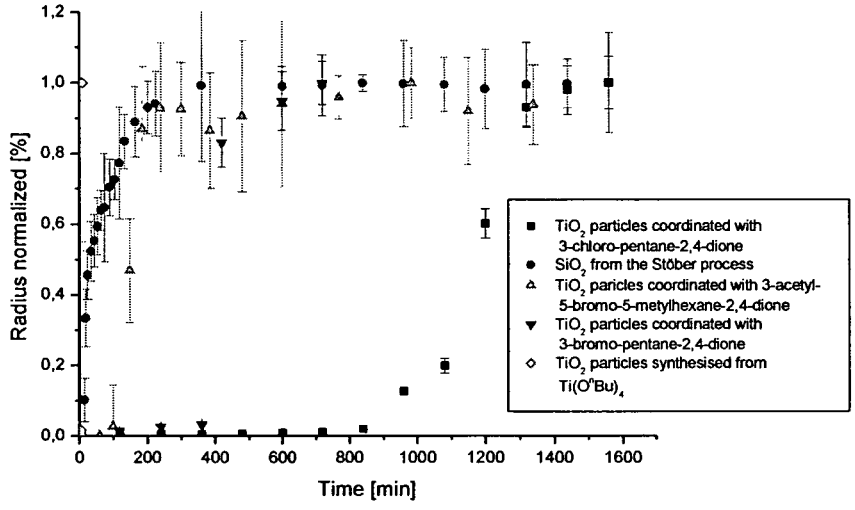

Figure 37: DLS plots of the growth of TiO_2 nanoparticles depending on the utilized precursors compared to the growth of SiO_2 nanoparticles from the Stöber process. The following diameters were obtained for the various functionalized TiO_2 particles: + 3-chloro-pentane-2,4-dione: 92 ± 4 nm; + 3-bromo-pentane-2,4-dione: 210 ± 4 nm; + 3-acetyl-5-bromo-5-methylhexane-2,4-dione: 156 ± 25 nm. The silica particles had a diameter of 92 ± 15 nm while the TiO_2 particles produced from $Ti(OBu)_4$ had a diameter of about 1500 ± 450 nm.

Compared to the synthesis of SiO_2 nanoparticles according to the Stöber process, the initiating phase of the synthesis of TiO_2 nanoparticles was much longer except if $Ti(O^nBu)_4$ without ligand was used. There were several reasons for the longer initiation phase of the coordinated isopropoxide derivatives. TiO_2 nanoparticles were synthesized in the micelles of a microemulsion whereas the SiO_2 nanoparticles were produced in free solution. Hence, in case of the TiO_2 nanoparticles, the precursor had to penetrate the surfactant layer which caused the slower initiation of the reaction because of different interaction with the surfactant. The differences in the reaction velocity of the three titanium isopropoxide derivates were explained by different hydrolysis activities of the obtained coordination products and the

different permeability of the precursors through the Triton X-100 surfactant layer. In case of 3-chloro-pentane-2,4-dione, particles were detected after a period of 600 minutes. The 3-acetyl-5-bromo-5-methylhexane-2,4-dione containing precursor already showed the presence of nanoparticles after 100 minutes, while 3-bromo-pentane-2,4-dione containing precursor led to particle formation after 400 minutes.

$Ti(O^nBu)_4$ had a very high reaction rate and could pass the surfactant layer without hindrance which led to a particle formation within minutes resulting in a large size distribution (about ± 450 nm). The usage of titanium isopropoxide and titanium n-propoxide caused instantaneous particle formation. The even higher reaction rate of these unmodified alkoxides led to the formation of large aggregates which could not be measured by DLS.

In case of the coordination product of titanium isopropoxide and 3-chloro-pentane-2,4-dione or 1-acetyl-2-oxopropyl 2-bromo-2-methylpropanoate, the influence of different parameters like amount of precursor, amount of water, and influence of the pH value on the particle formation process was analyzed. These two ligands were chosen because they represent the two types of polymerization initiator molecules with different amount of organic substituents; i.e. 1-acetyl-2-oxopropyl 2-bromo-2-methylpropanoate, which is the derivate of bromo-isobutyric acid that is a well known ATRP initiator and 3-chloro-pentane-2,4-dione that is the more stable acetylacetone derivative.

a) Influence of the amount of precursor on the formation of functionalized TiO_2 nanoparticles

Systematic studies of the influence of the amount of precursor were carried out to obtain information on the formation mechanism of nanoparticles using a microemulsion with the ratio of cyclohexane, n-hexanol, Triton X-100, and water as mentioned in the experimental part (chapter 7.4.18).

Various amounts of precursor were added to samples of this standard microemulsion and stirred overnight to complete the reaction. Depending on the precursor content, different TiO_2 particle sizes were expected due to the obtained degree of hydrolysis and nucleation.[239]

In figure 38 the resulting DLS plots are shown.

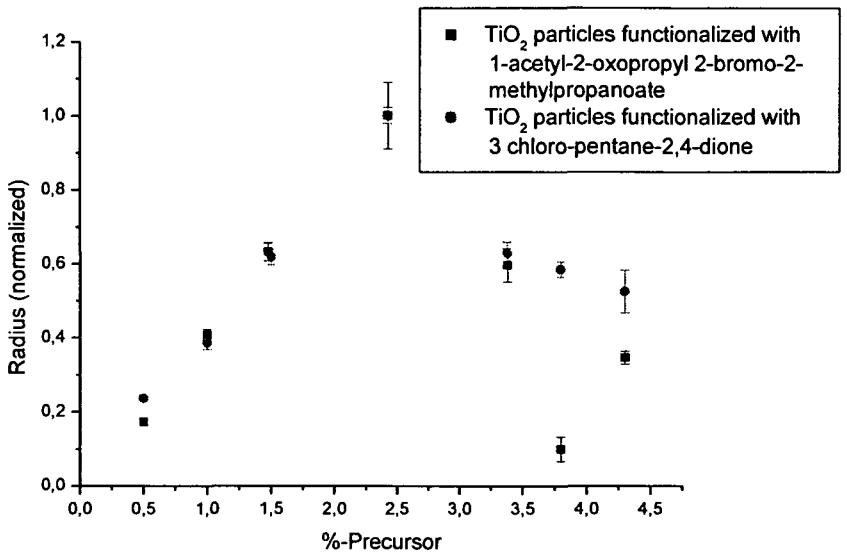

Figure 38: DLS plot of the influence of the amount of precursor on the nanoparticle growth in case of 3-chloro-pentane-2,4-dione and 1-acetyl-2-oxopropyl 2-bromo-2-methylpropanoate modified titanium isopropoxide. The diameter of the particles at a precursor content of 2.5 % was in case of the 3-chloro-pentane-2,4-dione functionality 97.2 ± 5 nm and in case of the 1-acetyl-2-oxopropyl 2-bromo-2-methylpropanoate 453 ± 77 nm.

It is important to mention that it was assumed that the number of obtained micelles in the microemulsion was not influenced by the amount of added precursor, hence, the quantity of micelles that were present in the system depended only on the water to surfactant ratio. As shown in figure 38 the diameter of the obtained nanoparticles obtained from both precursors had a maximum at a precursor content of 2.5 %. If the amount of the functionalized titanium isopropoxide was lower, the entire precursor seemed to form nanoparticles. With growing content of precursor the diameter of the obtained nanoparticles decreased which might have been caused by partially incomplete hydrolysis and condensation reactions of the precursor. *Arriagada et al.* analyzed the effect of the water to precursor ratio in case of silica particles.[81] They obtained a maximum diameter of the obtained nanoparticles at a water to TEOS ratio of 19.9 which became smaller if more TEOS was present in the system. The same effect was observed by *Van Helden et al.* who investigated the effect of the TEOS content in Stöber-like systems.[240] *Wang et al.* synthesized anatase and rutile particles (5-100 nm) in a hydrothermal sol-gel approach and observed at high water-to-alkoxide ratios a reduced crystallite size.[241]

$Ti(O^nBu)_4$ was also utilized as precursor but the high reaction rate during the hydrolysis of the butoxy-groups led to the immediate precipitation of hydrolyzed alkoxide and not to the formation of uniform nanoparticles.

b) Influence of the amount of water on the formation of functionalized TiO_2 nanoparticles

Systematic studies were performed to obtain information about the influence of the amount of water on the particle diameter. It was expected that, beginning from low water content, increasing the amount of water should increase the diameter of the obtained particles until a certain level. Additional water was estimated to lead to a decrease of the diameter as nucleation is favored over particle growth.[239, 241]

The three substances Triton X-100, cyclohexane and n-hexanol were mixed together in the same ratio as mentioned above and stirred for 5 minutes. Then equal samples of the solution were taken, mixed with different amounts of water, and stirred until no turbidity was present. Each of the microemulsions was mixed with 1.50 % of the 3-chloro-pentane-2,4-dione or 1-acetyl-2-oxopropyl 2-bromo-2-methylpropanoate modified titanium isopropoxide. This amount of precursor was chosen to guarantee the formation of stable emulsions. All samples were stirred overnight and the received nanoparticles were measured by DLS. The obtained data are shown in figure 39. The obtained radii were normalized to allow better comparison of the obtained data.

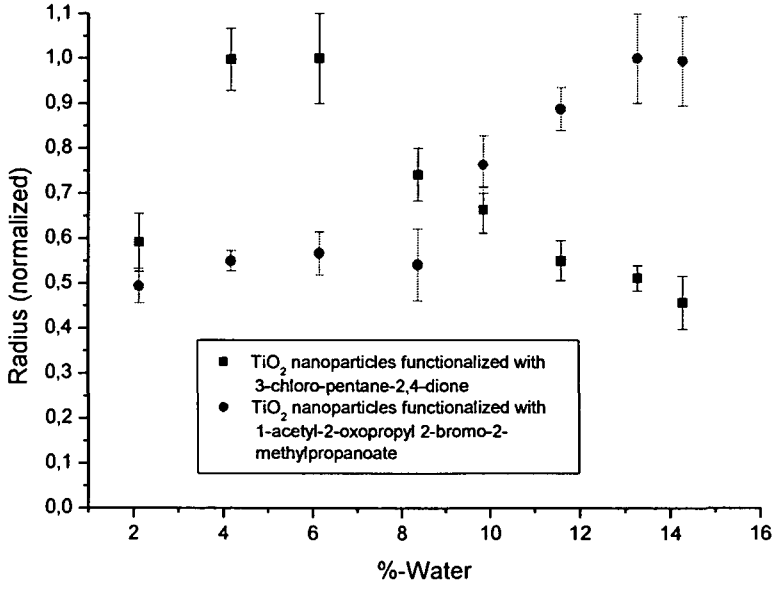

Figure 39: Influence of the water content on the growth of TiO_2 nanoparticles functionalized with 3-chloro-pentane-2,4-dione and 1-acetyl-2-oxopropyl 2-bromo-2-methylpropanoate. Maximum diameter in case of the 3-chloro-pentane-2,4-dione functionality 677 ± 73 nm at a water content of 4 % and in case of 1-acetyl-2-oxopropyl 2-bromo-2-methylpropanoate 310 ± 45 nm at a water content of 13 %.

In case of precursors that contain 3-chloro-pentane-2,4-dione, increasing the water content up to 6.0 % led to an increase of the radius, while it decreased nearly linearly at higher water content. *Arrigada et al.* observed the same effect in case of silica particles when they used polyoxyethylen (5) nonylphenyl ether as surfactant.[81] If a low quantity of water was present in the microemulsion, particle formation was not favored because most of the water molecules were bound to the surfactant molecules and were therefore blocked for any hydrolysis reaction. Sterical effects of the organic ligands even might have enhanced this inhibition of hydrolysis. If the water content was raised above a certain level, hydrolysis and condensation (nucleation) was favored because most of the water molecules were not bound by the surfactant molecules. Therefore, at higher water contents a larger number of nuclei was formed. *Arrigada et al.* postulated that, if nucleation occurred in the reverse micellar system over a limited period of time, the final particle size decreases continuously as the water to surfactant ratio is raised.[81]

If 1-acetyl-2-oxopropyl 2-bromo-2-methylpropanoate was used as ligand, a development of the particle radius with increasing water content was observed as follows; at 6.0 % water content a small local maximum of the radius was followed by a radius decrease until 8.0 % water content and a further almost linear increase of measured particle radius with increasing water percentage. The increase of the particle radius after the local minimum was explained by *Arrigada et al.*, who used TEOS as precursor by the effects of intermicellar interactions on the particle formation process.[81] As mentioned before, *Wang et al.* explained the decrease of the diameter of TiO_2 particles at high water contents with favourized nucleation.[241]

Efforts were made to repeat these analysis with unmodified alkoxides but the high velocity rate, which led to instantaneous precipitation, prevented controlled particle growth.

c) Influence of the pH value on the formation of functionalized TiO_2 nanoparticles

The pH value is one of the most important parameters in the sol-gel process as the proceeding reactions are catalyzed either by H^+ or OH^- ions and so a strong influence on the size of the formed particles is expected.[94]

Again, the standard solution consisting of Triton X-100, cyclohexane and n-hexanol was prepared, stirred for 5 minutes, and divided into several parts which were mixed with water of varied pH values. All of these samples were stirred until no turbidity was visible and then mixed with 1.3 % precursor produced from titanium isopropoxide and 3-chloro-pentane-2,4-dione and 1-acetyl-2-oxopropyl 2-bromo-2-methylpropanoate, respectively. Compared to the investigation of the water content, the precursor amount was slightly reduced are larger systems were expected at low and high pH values. The mixtures were stirred overnight to complete the hydrolysis and condensation reactions and then analyzed by DLS. The obtained plot is shown in figure 40. The obtained radii were normalized to allow easy comparison between the different curves.

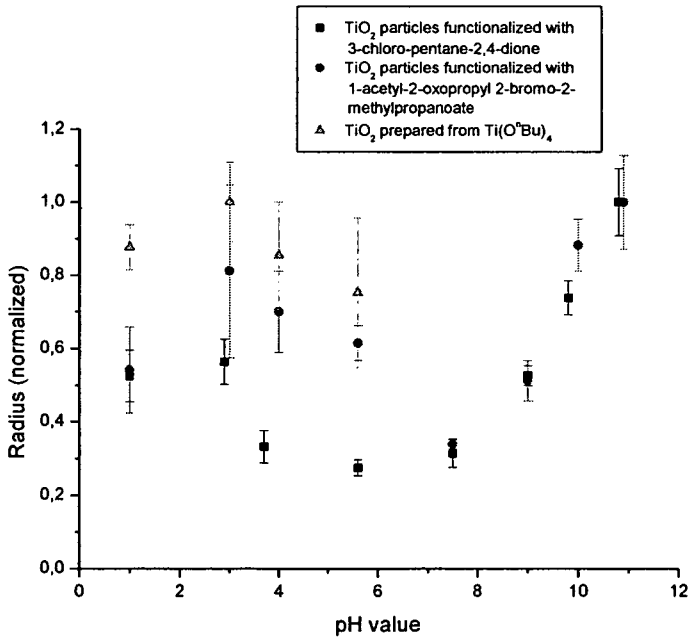

Figure 40: DLS plot of the particle growth of functionalized TiO_2 nanoparticles as a function of the utilized pH value. The obtained maximum diameters were in case of TiO_2 particles prepared from $Ti(OBu)_4$ (at pH > 6) > 1.5 µm; in case of TiO_2 functionalized with 3-chloro-pentane-2,4-dione (at pH 10.8) 1133 ± 210 nm; in case of TiO_2 functionalized with 1-acetyl-2-oxopropyl 2-bromo-2-methylpropanoate (at pH 10.9) 543 ± 163 nm;

In case of the production of silica particles in homogenous alcohol solution (Stöber process), the increase of the diameter of the nanoparticles at high pH value is related to the ability of the OH^- ions to catalyze both the hydrolysis and condensation reactions and the tendency for siloxane bonds to break in highly alkaline solution.[94, 240] This literature-known increase of the diameter of the silica nanoparticles was also observed in case of titanium oxide nanoparticles, which led to the assumption that OH^- ions catalyze hydrolysis and condensation reactions of titanium alkoxides, too. The presence of H^+ ions seemed to catalyze the nanoparticle formation as well but not as good as OH^- ions, which was visible in the smaller increase of the diameter of the obtained nanoparticles. *Wang et al.* also reported a smaller catalytic activity of H^+ and they remarked that the addition of acids is a necessity for the preparation of small TiO_2 particles.[241] At high pH values the hydrolysis rate of $Ti(O^nBu)_4$ was too high for controlled particle growth which led to the formation of larger aggregates.

3.2.3.2. Synthesis of functionalized zirconium oxide nanoparticles from alkoxide precursors

Triton X-100 (19 %), n-hexanol (15 %) and cyclohexane (58 %) were mixed and stirred to homogenize the mixture. Then the water phase (8 %) was added and stirred for 20 minutes to form the micelles. The different zirconium alkoxide precursors, containing 3-chloro-pentane-2,4-dione, 1-acetyl-2-oxopropyl 2-bromo-2-methylpropanoate, and 3-acetyl-5-bromo-5-methylhexane-2,4-dione, were added and stirred overnight. The obtained nanoparticles were isolated by centrifugation and washed several times with water and organic solvents.

The highest yield was obtained for particles prepared of 3-chloro-pentane-2,4-dione modified precursor followed by the precursor containing 1-acetyl-2-oxopropyl 2-bromo-2-methylpropanoate and 3-acetyl-5-bromo-5-methylhexane-2,4-dione.
FTIR analysis showed that just coordinated species was incorporated because uncoordinated CO-groups (from the pentane-2,4-dione derivate) were not detected. Exemplarily, the obtained spectrum of $Zr(O^iPr)_4$ coordinated with 3-chloro-pentane-2,4-dione is compared to the spectrum of the synthesized nanoparticles in figure 41.

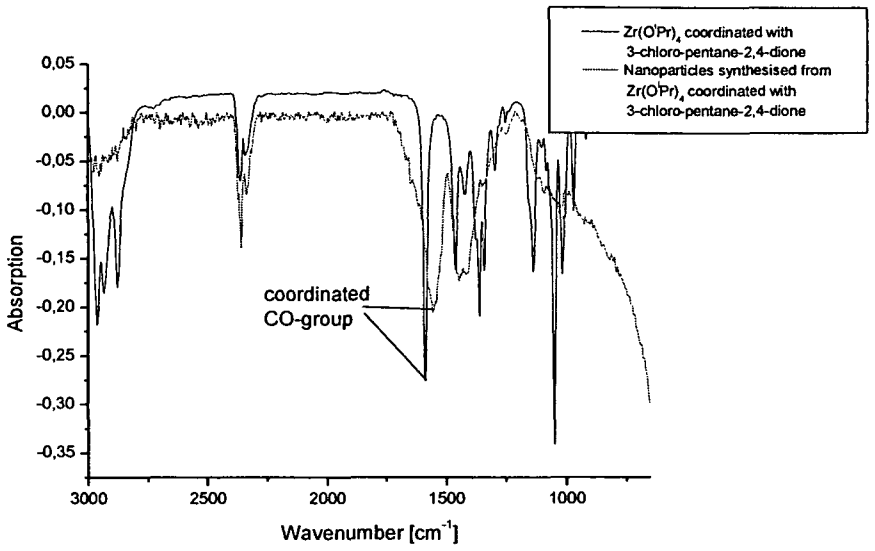

Figure 41: FTIR-spectra of $Zr(O^iPr)_4$ coordinated with 3-chloro-pentane-2,4-dione and the obtained functionalized ZrO_2 nanoparticles.

In both spectra only the ν(CO) vibration band of coordinated species was observed at 1586 cm^{-1} in case of the precursor and at 1550 cm^{-1} for the functionalized nanoparticles.
If 1-acetyl-2-oxopropyl 2-bromo-2-methylpropanoate was used as ligand, the band of the coordinated CO-group was observed at 1588 cm^{-1} and, in case of 3-acetyl-5-bromo-5-methylhexane-2,4-dione, the band of the coordinated CO-group was found at 1591 cm^{-1}, respectively. These results showed that, in case of functionalized ZrO_2 and TiO_2 nanoparticles no uncoordinated pentane-2,4-dione derivates were found in the synthesized systems.

Elemental analysis revealed that all particles had halogen contents between 2.6 and 3.0 %. From the observed discrepancy between the carbon and the halogen content it was possible to estimate the amount of unhydrolyzed alkoxide groups that were present after the nanoparticles formation. In case of the chlorine-containing particles an isopropoxide content of approximately 30 % was estimated, while results in case of the two isobutyric acid derivatives showed that approximately 40 % of the alkoxide groups were not hydrolyzed. This estimation was possible because both unfunctionalized and functionalized ZrO_2 particles showed nearly the same amount of hydrolysable groups up to 200 °C (between 10 and 13 %). It was not possible to perform EDX analysis for all particles which are presented further on as the EDX detector was not longer available on the used TEM.

TGA analysis was performed for all obtained nanoparticles. The results are summarized in table 5.

Table 5: TGA results of the obtained zirconium oxide nanoparticles.

ZrO_2 nanoparticles functionalized with the following polymerization initiators	**Volatile compounds [%]**	**ZrO_2 [%]**	**Halogen [%]**
---	26.8	73.2	---
3-Chloro-pentane-2,4-dione	41.0	59.0	7.6
1-Acetyl-2-oxopropyl 2-bromo-2-methylpropanoate	43.7	56.3	8.5
3-Acetyl-5-bromo-5-methylhexane-2,4-dione	39.3	60.7	7.6

The estimated halogen content of all functionalized nanoparticles was determined to be between 8.5 and 7.6 %, taking in account the presence of unreacted alkoxide groups, which was much higher than the values received from the elemental analysis. The reasons for this discrepancy were the same as in case of the functionalized TiO_2 nanoparticles, such as cleaving of the labile carbon-halogen bond, presence of unreacted alkoxide groups, and formation of volatile halogen-transition metal complexes during the elemental analysis.

The characterization of the morphology and the size distribution of the particles was performed via TEM and DLS.

In figure 42 a TEM image of the obtained zirconium oxide nanoparticles functionalized with 1-acetyl-2-oxopropyl 2-bromo-2-methylpropanoate, and the corresponding DLS plot are shown.

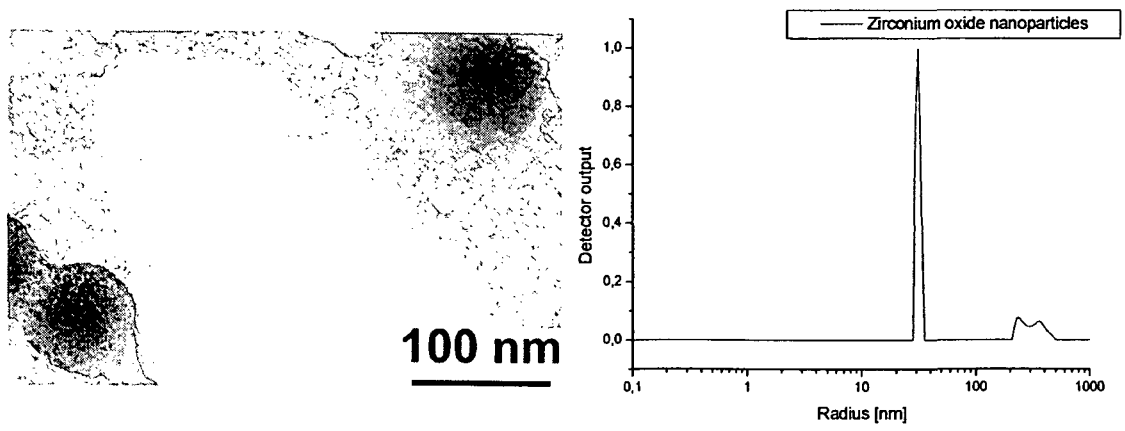

Figure 42: TEM image and DLS plot (in ethanol) of zirconium oxide nanoparticles functionalized with 1-acetyl-2-oxopropyl 2-bromo-2-methylpropanoate.

The particles shown in figure 42 had a diameter of 70 nm according to the TEM image, whereas the DLS plot revealed a diameter of 65 ± 7 nm.

If 3-chloro-pentane-2,4-dione was used as functional group, spherical zirconium oxide nanoparticles with irregular surface were obtained. A TEM image and the corresponding DLS-plot are shown in figure 43.

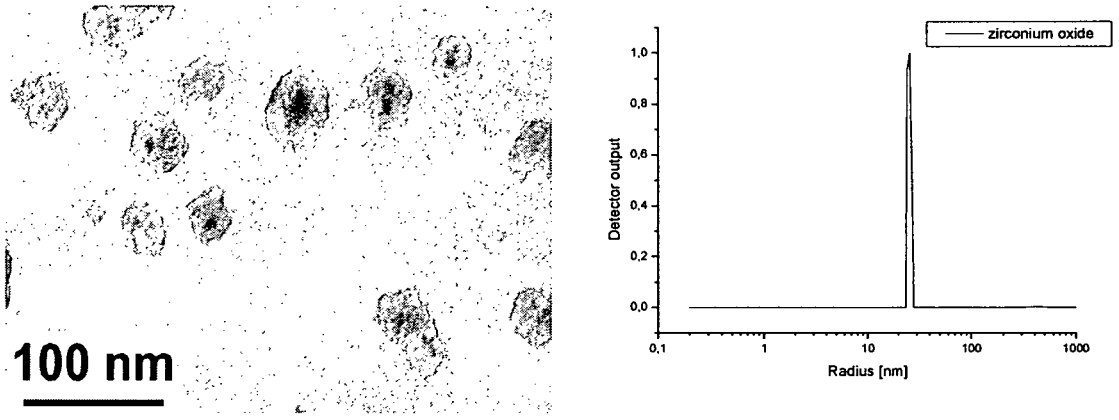

Figure 43: TEM image and DLS plot (in ethanol) of zirconium oxide nanoparticles functionalized with 3-chloro-pentane-2,4-dione.

According to the TEM image, the particles had a diameter of 44 nm while the DLS analysis resulted in a diameter of 49 ± 7 nm. *Li et al.* obtained crystalline ZrO_2 nanoparticles (between 20 and 60 nm) by using a hydrothermal synthesis with modified zirconium oxo-chloride as precursor and with nonyl phenylether as non-ionic surfactant.[242] Contrary to *Li et al.*, no crystalline product was obtained in the presented method because of the organic content of the used precursor and because of performing the synthesis at room temperature.

In figure 44 a TEM image of zirconium oxide nanoparticles, obtained from the 3-acetyl-5-bromo-5-methylhexane-2,4-dione containing precursor, is shown. From the TEM image the diameter of the particles is not measurable as the particles are very small and no automatic detection system was available.

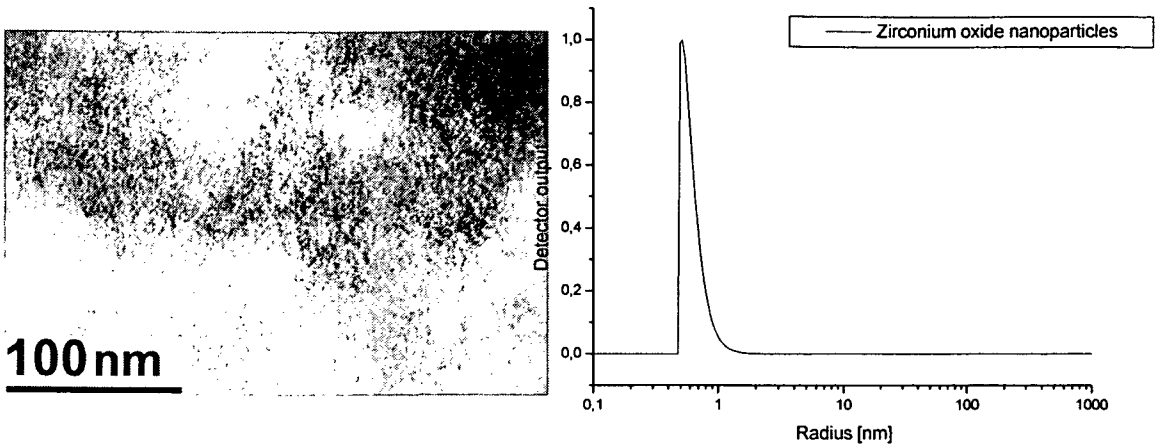

Figure 44: TEM image and DLS plot of zirconium oxide nanoparticles functionalized with 3-acetyl-5-bromo-5-methylhexane-2,4-dione are shown.

From DLS investigation a radius of 0.6 ± 0.1 nm was obtained. The TEM images of the three different zirconium alkoxide precursor showed the tremendous influence of the utilized ligand on the obtained particles morphology concerning size and form, caused by different growing mechanisms.

All prepared ZrO_2 particle samples were totally X-ray amorphous at room temperature. Zirconia exists in three crystalline phases: monoclinic, tetragonal and cubic. The monoclinic phase is thermodynamically stable at room temperature, while tetragonal and cubic phase exist at higher temperature (>1170 °C and >2380 °C respectively).[242]
The onset temperature of the crystallization process was measured via X-ray powder diffraction to investigate the beginning of the crystallization. The obtained diffractograms and a comparison with a diffractogram from ICSD database are shown in figure 45.

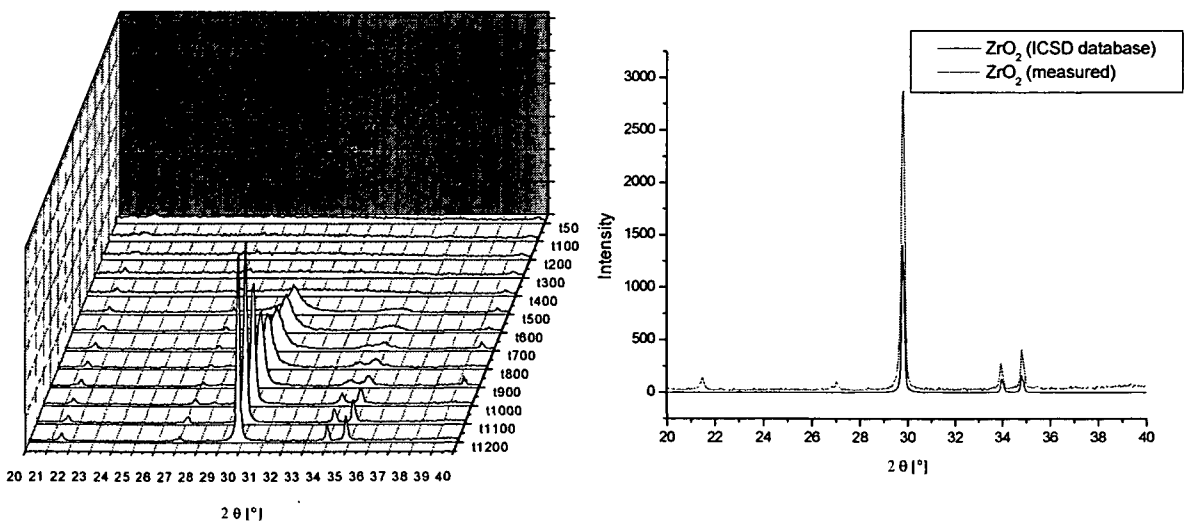

Figure 45: X-ray powder diffractograms of functionalized zirconium oxide nanoparticles at different temperatures and comparison with the tetragonal ZrO_2 [243] from the ICSD database.

The X-ray powder diffraction was performed for all three obtained functionalized nanoparticle types but no differences were observed between the different ligands. Below 500 °C no crystallized fraction was observed. At 500 °C the crystallization process of the tetragonal phase started with broad reflections that became sharper at higher temperature. In figure 45 on the right hand side the obtained diffractogram at 1200 °C was compared with a diffractogram from the ICSD database and identified as tetragonal ZrO_2. The two small reflections at a 2θ angle of 21.5 ° and 27 ° were eventually caused by a contamination of the used alkoxide with a small amount of alkaline or alkaline earth metal.
Petrunin et al. precipitated amorphous $ZrO(OH)_2$ particles from various zirconium salts as precursor and ammonia. After the amorphous particles, with a diameter of about 20 nm, were calcinated at 350-375 °C. X-ray diffraction obtained reflection, which were assigned to cubic and tetragonal phases of zirconia.[244]

The kinetic of the particle formation was analyzed with DLS to investigate the growth process of the different obtained precursors. The 3-chloro-pentane-2,4-dione and the 1-acetyl-2-oxopropyl 2-bromo-2-methylpropanoate containing precursor were chosen for this investigation because the initiating group of the latter represents a well known class of ATRP initiators and the chlorine derivate does have less problems with the thermal stability compared to 3-bromo-pentane-2,4-dione.

In the DLS plots shown in figure 46, the particle growth is compared to the formation process of silica particles produced according to the Stöber process.

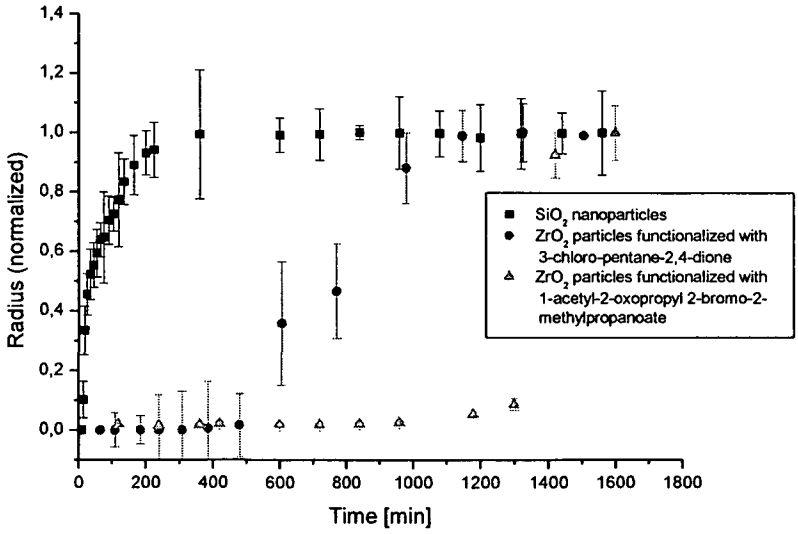

Figure 46: DLS-plots of the kinetic of the particle growth of SiO_2 nanoparticles, synthesized according to the Stöber process and ZrO_2 nanoparticles, functionalized with 3-chloro-pentane-2,4-dione (diameter 49 ± 7 nm) and 1-acetyl-2-oxopropyl 2-bromo-2-methylpropanoate (diameter 65 ± 7 nm). The silica particles had a diameter of 92 ± 15 nm.

Compared to the growth of the SiO_2 nanoparticles, the functionalized zirconium oxide particles started to grow after an initiating phase of about 400 and 1200 minutes, respectively, depending on the time to raise the concentration of the precursor inside the micelles above the critical nucleation concentration. When the nucleation centers were formed, they grew to the final particle size, on the one hand by reacting with other precursor molecules and on the other hand by aggregating with other nuclei situated in the same micelle. In case of the chlorine containing precursor, the final particle size was obtained after 1200 minutes, while the particles that are functionalized with 1-acetyl-2-oxopropyl 2-bromo-2-methylpropanoate required 1600 minutes to reach their final diameter.

There were efforts to use zirconium butoxide in this kinetic investigation, but the high reaction rate under the used conditions prevented controlled particle formation, and instantaneously precipitation from the microemulsion occurred.

3.2.3.3. Synthesis of functionalized vanadium oxide nanoparticles from modified alkoxides

The microemulsion was prepared like described above. As precursor the coordination product of $VO(OEt)_3$ with 3-chloro-pentane-2,4-dione and 1-acetyl-2-oxopropyl 2-bromo-2-methylpropanoate were utilized, respectively. The precursor was added under vigorous stirring and the emulsion was stirred overnight. The nanoparticles were isolated and washed with different organic solvents several times. From 0.25 g precursor molecules a yield of 0.14 g (67.3 %) in case of the 3-chloro-pentane-2,4-dione functionality and 0.16 g (74.6 %) for the second precursor was obtained.

TGA analysis showed that the particles functionalized with 1-acetyl-2-oxopropyl 2-bromo-2-methylpropanoate contained 44.1 % volatile components, while the rest remained as oxidized residue. Functionalization with 3-chloro-pentane-2,4-dione led to a mass loss of 35.7 %. Unmodified vanadium oxide particles showed a mass loss of 22.3 % if they were heated up to 800 °C. Elemental analysis obtained halogen contents between 1.2 % and 3.1 %. The comparison between measured and theoretical halogen content (according to the carbon content) led to an estimated ratio of unreacted alkoxide groups of about 25 % and 30 % for the two used precursors aware that both, functionalized and unfunctionalized particles lost between 11 and 13 % of their mass up to 200 °C.

The absorption of the coordinated CO group was investigated by FTIR spectroscopy. In figure 47 the FTIR-spectra of the nanoparticles functionalized with 1-acetyl-2-oxopropyl 2-bromo-2-methylpropanoate and the used precursor are shown.

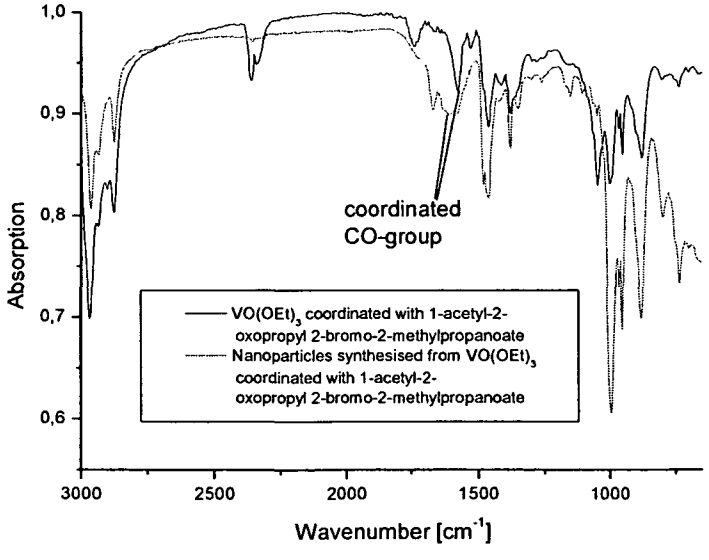

Figure 47: FTIR-spectra of the vanadium oxide nanoparticles that were functionalized with 1-acetyl-2-oxopropyl 2-bromo-2-methylpropanoate and of the synthesized precursor were compared.

As shown in the FTIR-spectra, the absorption band of the coordinated CO-group was shifted from 1575 cm^{-1} to 1610 cm^{-1}. The band of uncoordinated CO-groups (1730 cm^{-1}) that was visible in the spectrum of the precursor did not disappeare entirely after the nanoparticle formation as a small shoulder remained visible. An additional band was observed at 1672 cm^{-1} assigned to a δ(O-H) vibration, which was also observed by *Van Der Voort et al.* who produced supported vanadium oxides by adsorption of acetylacetone.[245] In case of the nanoparticles that were functionalized with 3-chloro-pentane-2,4-dione, the absorption band of the ν(CO) vibration of the coordinated CO-groups was shifted from 1574 cm^{-1} to 1627 cm^{-1}. Elemental analysis showed a bromine content of 3.1 % and a chlorine content of 2.2 % depending on the functionality.

The morphology and the size distribution of the obtained nanoparticles were investigated using TEM and DLS analyses. In figure 48 a TEM image and the DLS plot of the obtained functionalized vanadium oxide nanoparticles are shown.

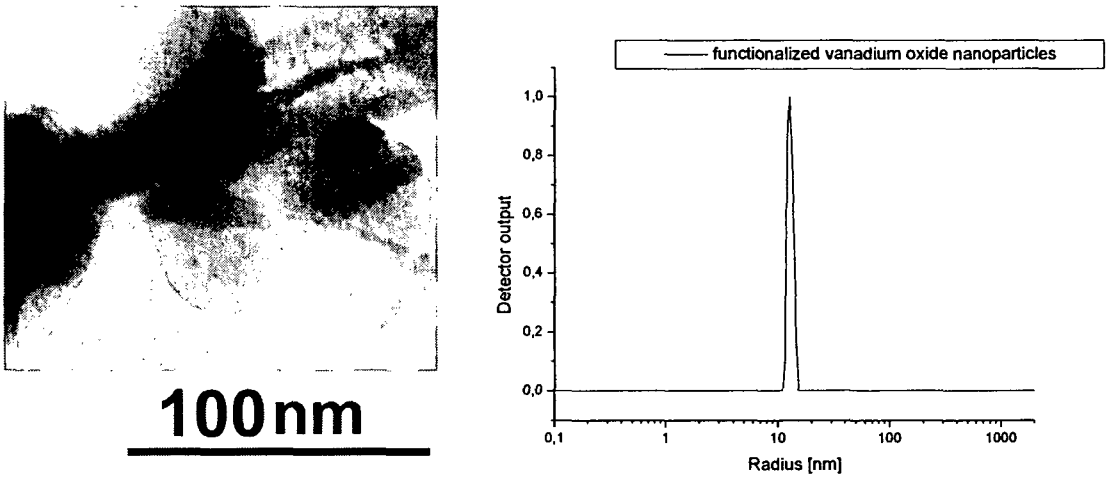

Figure 48: TEM image and DLS plot (in ethanol) of vanadium oxide nanoparticles functionalized with 1-acetyl-2-oxopropyl 2-bromo-2-methylpropanoate.

According to DLS measurement, the particles shown in figure 48 had a diameter of 25.0 ± 2.0 nm. The TEM image suggested a slightly larger diameter of approximately 35 nm, which

was difficult to estimate as the edges of the particles are difficult to recognize. Such a deviation might have been caused by not positioning the TEM sample exactly in the eucentric position, which might have led to a different magnification factor.

The same synthesis was performed with double the amount of precursor. A TEM image and the corresponding DLS plot of the obtained nanoparticles are shown in figure 49.

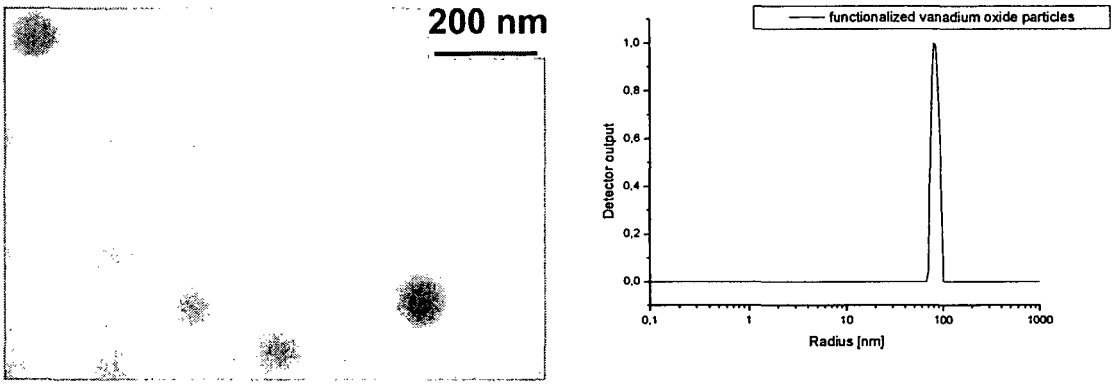

Figure 49: TEM image and DLS plot (in ethanol) of vanadium oxide nanoparticles functionalized with 1-acetyl-2-oxopropyl 2-bromo-2-methylpropanoate.

According to the DLS analysis, the particles shown in figure 49 had a diameter of 160 ± 31 nm. Compared to the smaller vanadium oxide particles the relative size distribution nearly doubled. The diameter obtained from TEM analysis was, being around 144 nm, within the full width at half maximum of the signal obtained from DLS investigation.
The increase of the diameter could not only be explained by the higher amount of utilized precursor. It seemed that the precursor concentration also had an influence on the formation mechanism of the vanadium oxide nanoparticles. With the higher precursor concentration in the continuous organic phase, the precursor concentration inside the micelle seemed to rise much quicker which could have led to an increased particle growth instead of core nucleation. The particles that were functionalized with 3-chloro-pentane-2,4-dione are discussed in more detail in chapter 6.

A TEM image and the corresponding DLS plot of these particles are shown in figure 50.

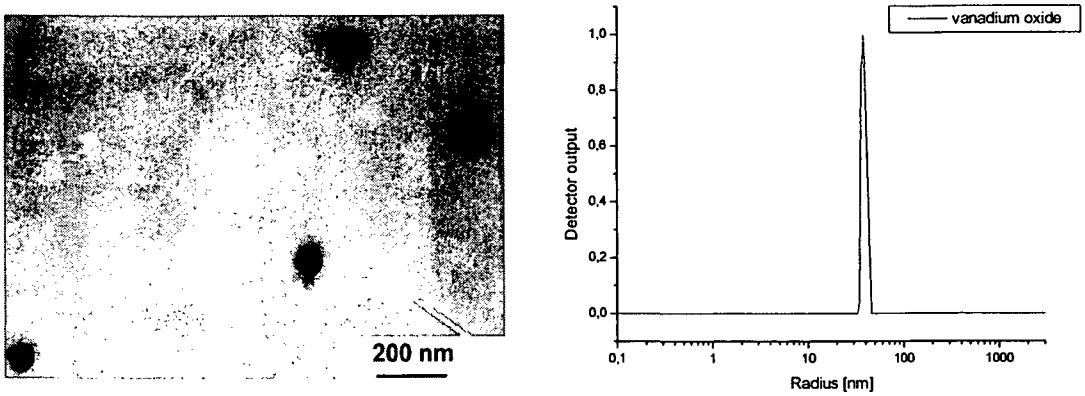

Figure 50: TEM image and DLS plot (in ethanol) of vanadium oxide nanoparticles that were functionalized with 3-chloro-pentane-2,4-dione.

According to the TEM image, the shown particles had a diameter of 80 nm. DLS analysis resulted in a diameter of 76 ± 5 nm. The obtained system showed a rather small size distribution of the diameter and revealed a spherical morphology.

The vanadium oxide system consists of many different, stoichiometric defined phases. Their composition depends highly on the temperature and the partial pressure of oxygen. In figure 51 the phase diagram of the V-O system is presented.

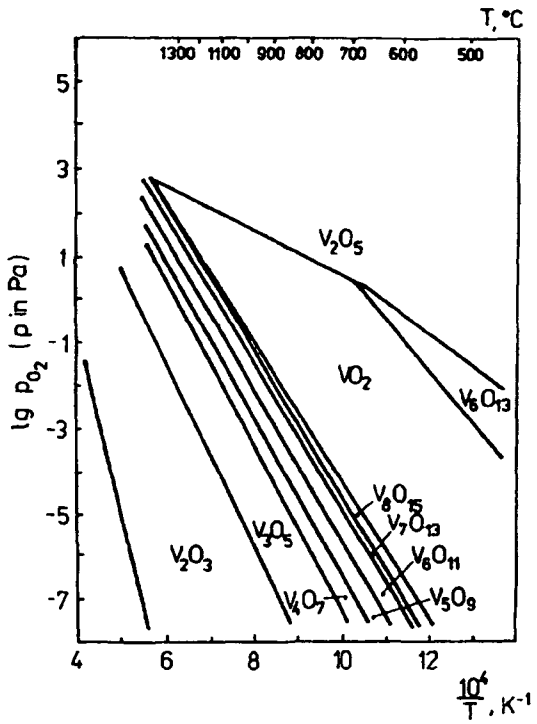

Figure 51: Phase diagram of the V-O system showing the equilibrium oxygen pressures over two coexisting vanadium oxide phases as a function of temperature.[246]

Depending on the oxygen partial pressure and the selected temperature, different V-O phases can be obtained because of the many stable oxidation states of the vanadium atom.[246] At room temperature V_2O_5 is the most stable phase.

As the synthesized vanadium oxide particles were completely X-ray amorphous at room temperature, the onset temperature of the crystallization process was measured via X-ray powder diffraction. The obtained diagrams and the identification of the obtained reflections are shown in figure 52.

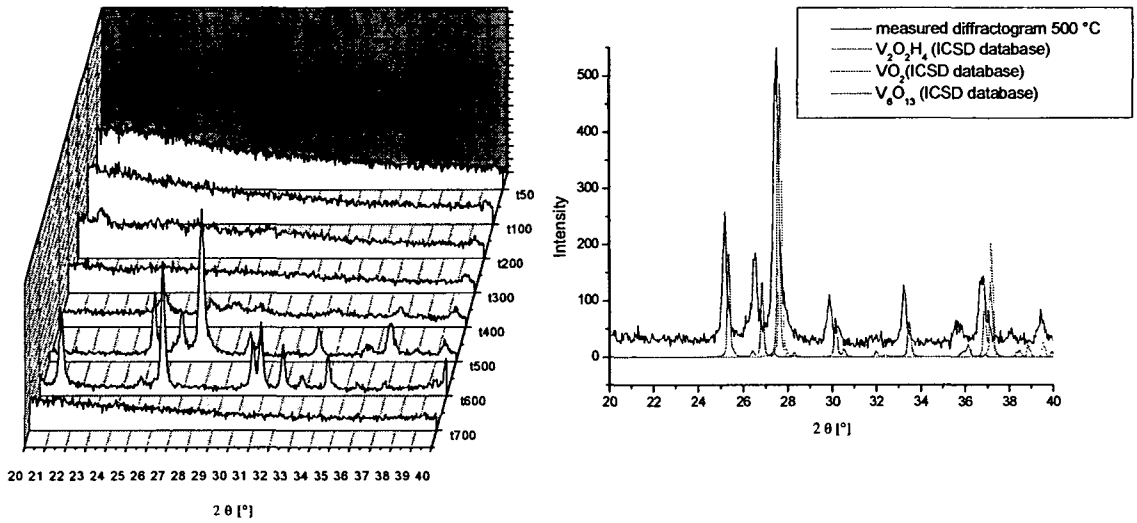

Figure 52: X-ray powder diffraction spectra of the manufactured vanadium oxide nanoparticles compared to $V_2O_2H_4$ [247], VO_2 [248], and V_6O_{13} [249] from the ICSD database.

Up to 400 °C only X-ray amorphous particles were observed. At 400 °C the first reflections were recorded, which became sharper at 500 °C. This diffractogram was used for the identification of the synthesized V-O phases. Comparison with data from the ICSD database revealed that the particles consisted of a mixture of 12 % $V_2O_2H_4$, 43 % VO_2 and 44 % V_6O_{13}. At higher temperatures the phases began to oxidize to V_2O_5 and started to evaporate. The offset of the measured diffractogram compared to the data from the database resulted from a displacement of the platinum heating band at higher temperature.

3.2.3.4. Synthesis of functionalized yttrium oxide nanoparticles from modified alkoxides

The coordination products of yttrium ethoxymethoxide with 1-acetyl-2-oxopropyl 2-bromo-2-methylpropanoate and 3-chloro-pentane-2,4-dione, respectively, were used in a microemulsion approach, which was performed as described before. The isolated particles were analyzed via TEM, DLS, FTIR spectroscopy, elemental analysis and TGA. In figure 53 the recorded FTIR-spectra of the particles functionalized with 1-acetyl-2-oxopropyl 2-bromo-2-methylpropanoate are presented.

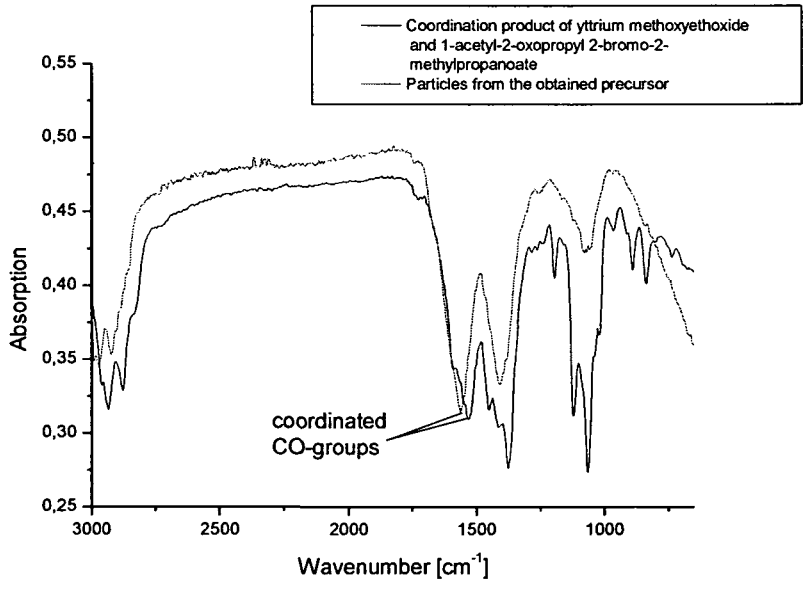

Figure 53: FTIR spectra of the synthesized yttrium oxide nanoparticles that were functionalized with 1-acetyl-2-oxopropyl 2-bromo-2-methylpropanoate and the precursor.

In case of the yttrium oxide nanoparticles that were functionalized with 1-acetyl-2-oxopropyl 2-bromo-2-methylpropanoate, the band of the coordinated CO group was slightly shifted from 1529 cm^{-1} to 1560 cm^{-1} after the particle formation, while the 3-chloro-pentane-2,4-dione containing precursor led to a small shift from 1589 cm^{-1} to 1594 cm^{-1}. Elemental analysis obtained a halogen content of 3.6 % in case of particles functionalized with 1-acetyl-2-oxopropyl 2-bromo-2-methylpropanoate, and 13.4 % in case of particles functionalized with 3-chloro-pentane-2,4-dione.

All particles showed a mass loss between 14 % and 17 % due to evaporated water and ongoing condensation reactions up to 200 °C. Afterwards the mass loss differed depending on the organic functionality. The weight loss up to 800 °C obtained by TGA was 47.9 %, which

was in the range of the other nanoparticles functionalized with 1-acetyl-2-oxopropyl 2-bromo-2-methylpropanoate. Modification with 3-chloro-pentane-2,4-dione led to a mass loss of 59.5 %. Unmodified yttrium oxide particles showed a weight loss of 41 %. Elemental analysis led to an estimated ratio of unreacted alkoxide groups of 20 % in case of 3-chloro-pentane-2,4-dione, and 28 % in case of the second precursor. TEM and DLS were used to analyze the morphology and the size distribution of the nanoparticles. In figure 54 a TEM image and a DLS plot of the obtained nanoparticles are shown.

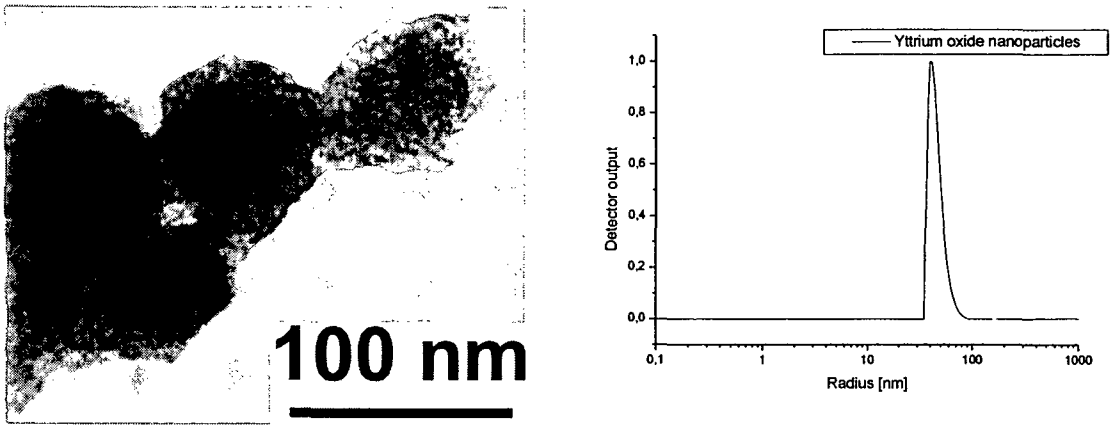

Figure 54: TEM image and DLS plot of yttrium oxide nanoparticles functionalized with 1-acetyl-2-oxopropyl 2-bromo-2-methylpropanoate.

A diameter of the single particle of approximately 70 nm was estimated from the TEM image whereas DLS analysis delivered a particle diameter of 80 ± 11 nm. The shoulder on the right side could be explained with the presence of aggregated species. A possible reason for the different diameters obtained from the two analyzing methods might be a partial aggregation of the received nanoparticles. Furthermore, the influence of the ultra high vacuum in the TEM combined with the electron beam might have induced further shrinking of the particle diameter due to the evaporation of solvent residues and proceeding of condensation reactions. The TEM image suggested that the nanoparticles did not exist in an isolated state. Polymerization experiments, which are presented in chapter 6 showed that the particles exist in a non aggregated state. Possibly the conditions in the electron microscope led to an aggregation of the particles via ripening.

The particles, which were functionalized with 3-chloro-pentane-2,4-dione, are discussed in more detail in chapter 6. A TEM image and the corresponding DLS plot of these particles are presented in figure 55.

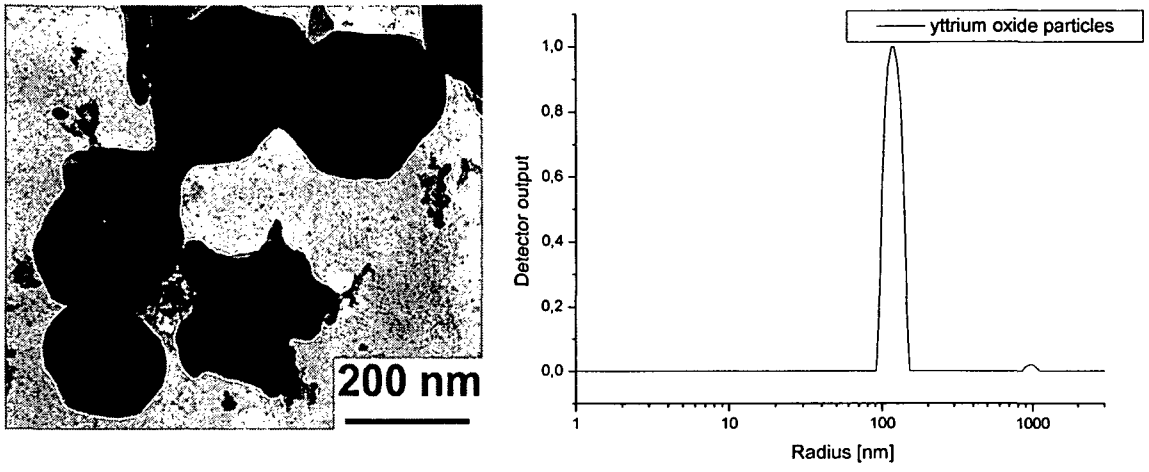

Figure 55: TEM image and DLS plot (in ethanol) of yttrium oxide nanoparticles functionalized with 3-chloro-pentane-2,4-dione.

The TEM image suggested a diameter of 215 nm while the DLS plot revealed a diameter of 222 ± 25 nm. Beside the spherical particles, remaining alkoxide and surfactant residues are visible.

Crystallinity has an influence on many material characteristics like electrical conductivity or the refractive index and is therefore a highly desired property of nanoparticles. Y_2O_3 occurs in a body-centered, cubic structure.[250]

At room temperature the obtained nanoparticles were in a totally X-ray amorphous. The samples were heated to temperatures between 50 ° and 1200 ° to obtain crystalline nanoparticles.

In figure 56 the obtained diffractograms and a comparison to data from the ICSD database are shown.

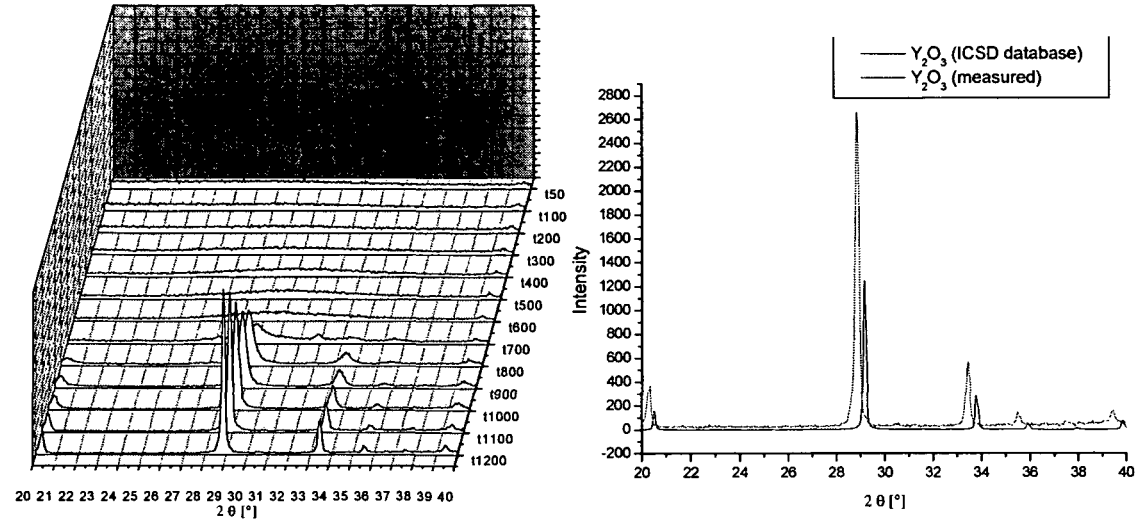

Figure 56: Diffractograms of the obtained yttrium oxide nanoparticles recorded at different temperatures and compared to cubic Y_2O_3 [250] from the ICSD database.

The crystallization process began at a temperature of about 700 °C where the first reflections were recorded. The diffractogram that was obtained at 1200 °C was identified as cubic Y_2O_3. The offset of the reflections between the two diffractograms was caused by a displacement of the platinum heating band at high temperatures.

3.2.3.5. Synthesis of functionalized tantalum oxide nanoparticles from modified alkoxides

The tantalum oxide nanoparticles were prepared using the coordination product of tantalum ethoxide and 1-acetyl-2-oxopropyl 2-bromo-2-methylpropanoate as a precursor in a microemulsion process, which led to a yield of 68.5 % and the coordination product with 3-chloro-pentane-2,4-dione that delivered a yield of 91.0 %. Elemental analysis showed a halogen content of 1.2 % and 1.3 %, respectively.

The coordination state of 1-acetyl-2-oxopropyl 2-bromo-2-methylpropanoate in the precursor and the particles was investigated via FTIR spectroscopy (figure 57).

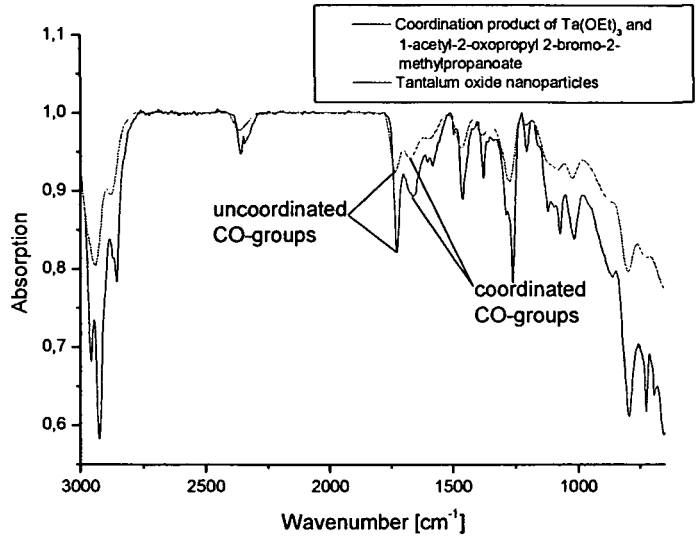

Figure 57: FTIR spectra of the tantalum-precursor containing 1-acetyl-2-oxopropyl 2-bromo-2-methylpropanoate and the obtained nanoparticles.

Both FTIR-spectra revealed several bands of CO-groups that referred to different CO species; bands at a wavelength of 1723 cm^{-1} and 1734 cm^{-1} in case of the precursor and the nanoparticles, respectively, that can be assigned to physically adsorbed initiator molecules; at a wavelength of 1659 cm^{-1} and 1666 cm^{-1} bands were found that are the result of coordinated species, in case of the precursor and the nanoparticles, respectively. If 3-chloro-pentane-2,4-dione was used as ligand, the ν(CO) vibration of the coordinated species was detected at 1583 cm^{-1}.

TGA analysis of the particles that were functionalized with 1-acetyl-2-oxopropyl 2-bromo-2-methylpropanoate showed a weight loss of 36.4 %, while functionalization with 3-chloro-pentane-2,4-dione led to a weight loss of 16 % up to 800 °C. Unmodified tantalum oxide nanoparticles lost 13.8 % of their mass if they were heated up to 800 °C. Elemental analysis led to an estimated ratio of unreacted alkoxide groups of 25 % and 30 % for the two used precursors. This estimation was possible because all synthesized tantalum oxide particles revealed mass losses about 7 % up to 200 °C in the TGA analysis, which was a result of the evaporation of adsorbed solvent and ongoing condensation reaction.

TEM and DLS analyses were performed to analyze the size distribution and morphology. In figure 58 a TEM image and a DLS plot of the obtained nanoparticles are shown.

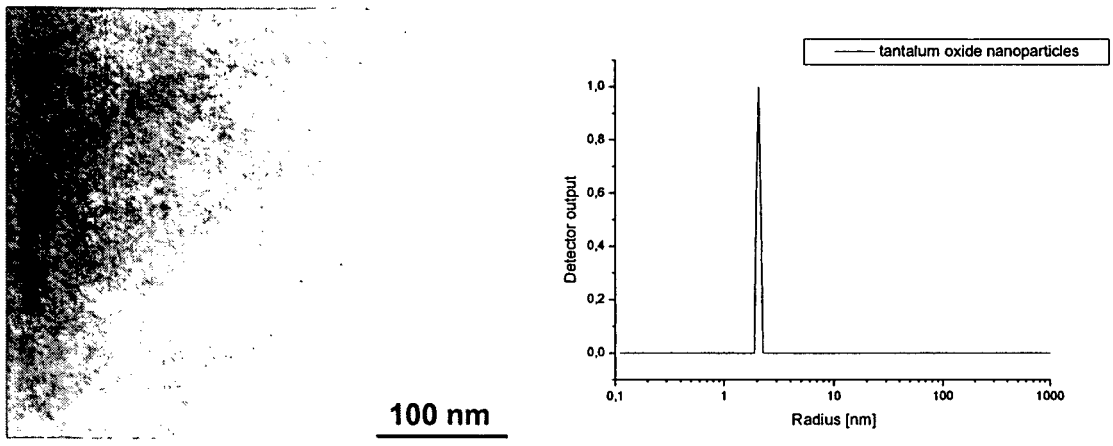

Figure 58: TEM image and DLS plot of the obtained functionalized tantalum oxide nanoparticles.

From the TEM image a particle diameter of approximately 6 nm was estimated while DLS analysis revealed a diameter of 4 ± 0.2 nm. The different results of the two methods were explained by inaccurate measuring of the particle diameters in the TEM image.

Crystalline Ta_2O_5 is a material with a very complex phase system. At room temperature several monoclinic and triclinic phases are literature-known. These phases are transformed to orthorhombic Ta_2O_5 at a temperature of 670 °C.[251]

As the produced particles were completely X-ray amorphous at room temperature, the onset temperature of the crystallization process was investigated via X-ray powder diffraction. The obtained diffractograms and a comparison with ICSD database data are shown in figure 59.

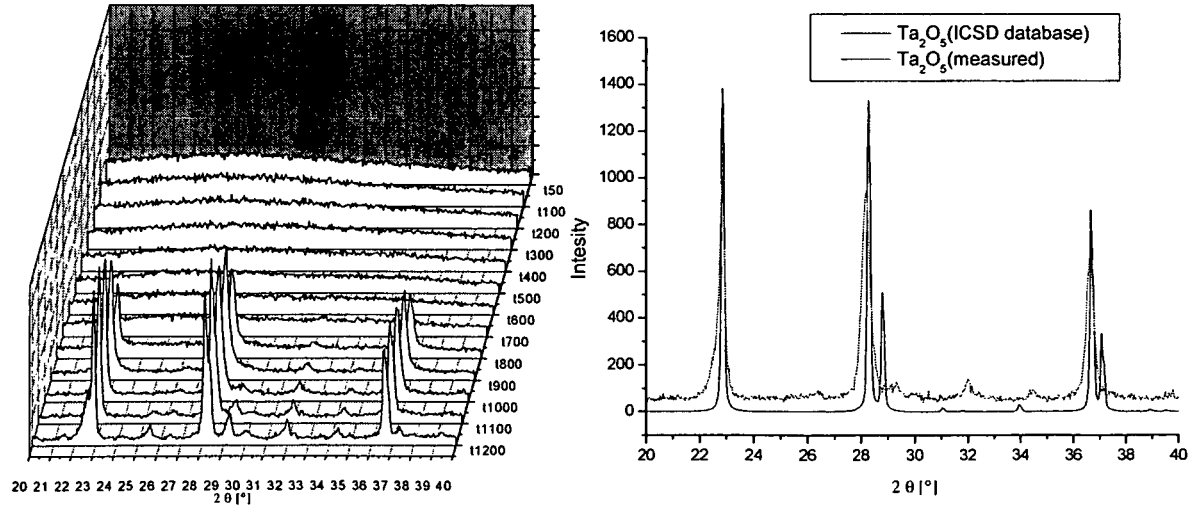

Figure 59: Diffractograms of the obtained tantalum oxide nanoparticles recorded at different temperature levels and comparison with orthorhombic Ta_2O_5 [310] from the ICSD database.

Up to 800 °C only X-ray amorphous species was obtained. The crystallization process started at 800 °C, where three reflections were observed that were assigned to orthorhombic Ta_2O_5. Compared to literature data, the transition temperature was about 100 °C higher which might have been caused by the rapid heating rate and the short hold time of 20 minutes at each temperature level before the diffractogram was recorded. At higher temperatures the obtained reflections of Ta_2O_5 became sharper.

3.2.3.6. Synthesis of functionalized iron oxide nanoparticles from modified alkoxides

The iron oxide nanoparticles were synthesized using the coordination product of iron isopropoxide and 3-acetyl-5-bromo-5-methylhexane-2,4-dione as precursor with a yield of 79.3 %. FTIR-analysis was performed to investigate the type of coordination of the pentane-2,4-dione derivate in the functionalized nanoparticles. In figure 60 the measured FTIR-spectra of the precursor and the functionalized nanoparticles are compared.

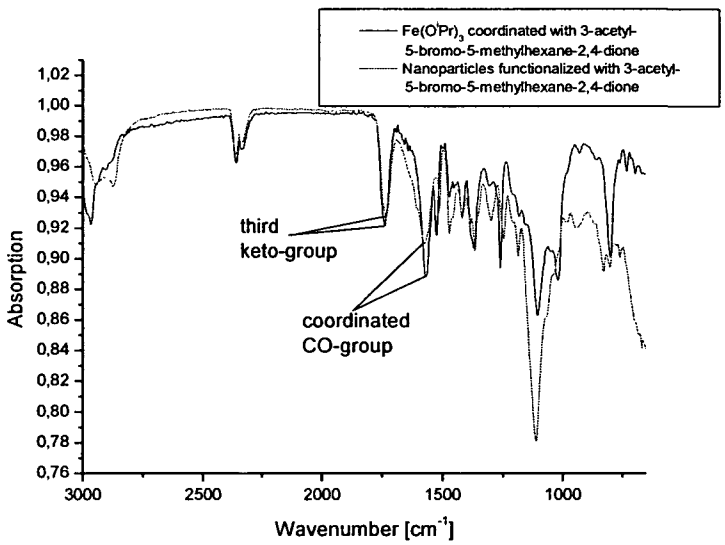

Figure 60: Comparison of the FTIR-spectra of the used iron-precursor and the obtained nanoparticles.

3-Acetyl-5-bromo-5-methylhexane-2,4-dione is a molecule that offers three CO-groups that can potentially coordinate to a metal center, but only two of these carbonyl groups actually

coordinate, which explained the strong band of ν(CO) both in the spectrum of the precursor and the obtained nanoparticles at 1731 cm^{-1}. The coordinated CO-groups were assigned to band at 1573 cm^{-1}. Elemental analysis obtained a halogen content of 1.9 %.

Via TGA analysis a weight loss of 34.3 % was received. Unmodified iron oxide particles showed a weight loss of 32 %. Elemental analysis led to an estimated ratio of unreacted alkoxide groups of 23 % for the used precursor. This estimation was possible as both unfunctionalized and functionalized iron oxide particles revealed the same mass loss of about 12 % up to 200 °C in the TGA analysis due to solvent evaporation and condensation reactions.

The obtained functionalized particles were analyzed via TEM and DLS to investigate the morphology, size, and size distribution. In figure 61 a TEM image and the DLS plot of the particles are shown.

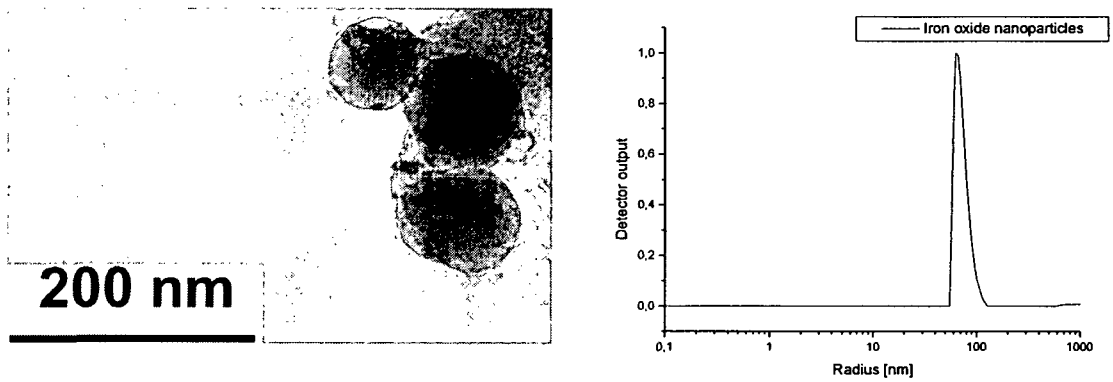

Figure 61: TEM image and DLS plot of the obtained functionalized iron oxide nanoparticles.

Analyzing the TEM image, a diameter of 95 nm was obtained while the DLS measurement resulted in a particle diameter of 120 ± 17 nm. The slightly different results that were obtained from the two analyzing methods might have been caused by particle aggregation. The shoulder at the right side of the DLS curve was a strong hint that aggregation occurred. Interaction of the particles with solvent molecules that could lead to a swelling process, which possibly was enabled by the high organic content, would also be a possible explanation of the different results. There were efforts to use iron ethoxide, which was modified with 3-chloro-pentane-2,4-dione, as precursor for the synthesis of nanoparticles but after one week still no formation of particles took place.

Fe_2O_3 is known in two different crystal structures at room temperature: α-Fe_2O_3, which crystallizes in the korund-type and occurs as hematite in nature, and γ-Fe_2O_3, which

crystallizes in a spinel structure and is ferrimagnetic. Above 300 °C γ-Fe_2O_3 is transformed to α-Fe_2O_3.[253]

As the received nanoparticles were completely X-ray amorphous at room temperature, the onset temperature of the crystallization process was measured via X-ray powder diffraction. The obtained diffractograms and a comparison with data from the ICSD database are shown in figure 62.

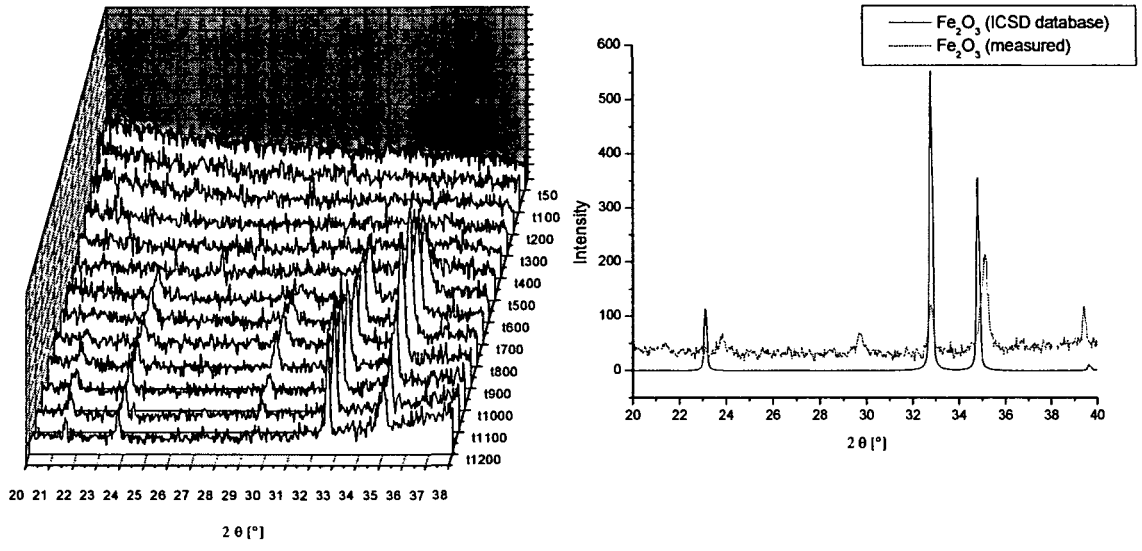

Figure 62: Diffractograms of functionalized iron oxide nanoparticles recorded at different temperature levels and comparison with hematite [311] from the ICSD database.

Up to 600 °C only amorphous structure was observed. At 600 °C the transformation to α-Fe_2O_3 (hematite) began. The observed crystal structure did not change up to a temperature of 1200 °C. Two reflections were observed at 2θ angles of 21.1 ° and 29.5 °, which were assigned to a spinel phase with an iron to oxygen ratio between Fe_2O_3 and Fe_3O_4.

Liao et al. synthesized amorphous Fe_2O_3 nanoparticles with a diameter between 3-5 nm and observed transformation at 400 °C.[255] The larger diameter of the presented Fe_2O_3 nanoparticles seemed to shift the onset temperature of the crystallization process to higher temperatures.

All different metal oxide particles that were presented in this chapter were obtained with an amorphous structure as the high organic content and the used reaction conditions prevented the formation of crystalline particles.

3.2.3.7. Synthesis of crystalline TiO_2 nanoparticles in a microemulsion approach at increased temperature and pressure

As already mentioned, all synthesized nanoparticles were obtained in the X-ray amorphous form. Crystalline particles from functionalized metal alkoxides can be synthesized using different routes. *Andersson et al.* used hydrothermal treatment for the production of crystalline nanoparticles.[105] They utilized respectively hydrochloric and nitric acid to stabilize titanium butoxide in an aqueous solution, which was then added to mixture of a surfactant and an organic solvent. In the formed microemulsion the particle formation was initiated by raised temperature (120 °C) and pressure. *Andersson et al.* did not stir the microemulsion during the nanoparticle formation, which led to the formation of tubular structures (80-1000 nm) containing of rutile and anatase that grew directly from the glass tube of the reaction vessel.

In the presented approach, efforts were made to modify the method presented by *Andersson et al.*, to synthesize spherical nanoparticles with a monodisperse size distribution, by stirring the microemulsion during the titanium oxide formation.
According to *Andersson et al.* titanium n-butoxide was dissolved in 5 M HNO_3 and added dropwise to a mixture of cyclohexane, n-hexanol and Triton X-100 inside a reactor. The obtained microemulsion was stirred until the mixture was totally clear and heated up to 120 °C under continuous stirring for 18 hours. The stirring during the nanoparticle formation led to the development of monodisperse nanoparticles with a diameter of 21 nm. A TEM image and the corresponding DLS plot are shown in figure 63.

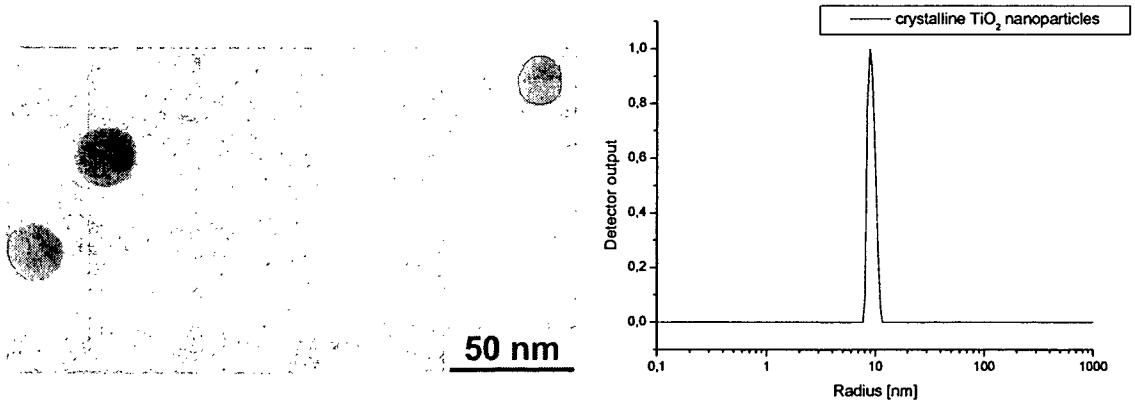

Figure 63: TEM image and DLS plot (in ethanol) of crystalline TiO_2 nanoparticles.

DLS analysis revealed a diameter of 19 ± 1.5 nm, being very similar to the result received from TEM measurement.

TGA analysis showed that heating up the nanoparticles to 800 °C led to a mass loss of 20.6 %. The specific surface was measured via nitrogen sorption and resulted in 260 m^2/g. In figure 64 the X-ray diffractogram of the obtained titanium oxide nanoparticles and a comparison with the database are shown.

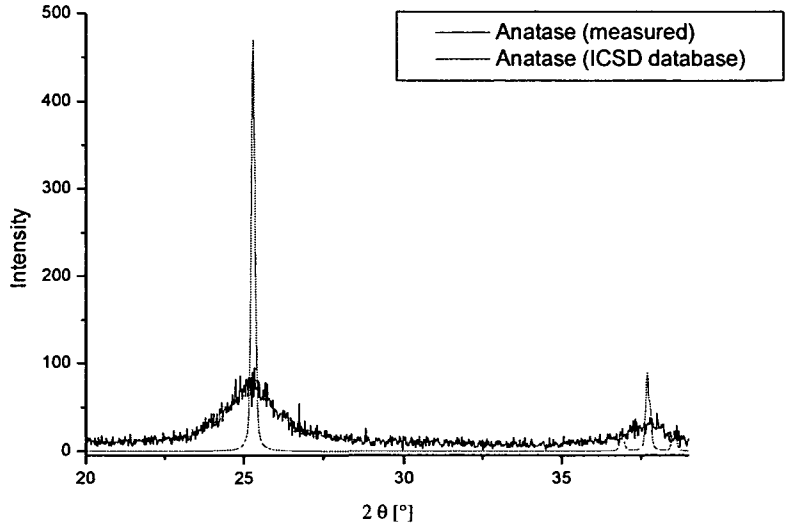

Figure 64: X-ray diffractogram of the obtained TiO_2 nanoparticles compared to anatase [235] from the ICSD database.

Through the comparison with the ICSD database data the obtained diffractogram was identified as anatase. This spectrum was recorded at room temperature. Due to the small crystallite size, the measured reflections are much broader than in the diffractogram obtained from the ICSD database. This broadening of the reflections was also observed by *Anderson et al.*[105]

The same synthesis was performed utilizing the coordination product of 3-bromo-pentane-2,4-dione and titanium isopropoxide as precursor in the synthesis of the nanoparticles. The obtained nanoparticles are shown in figure 65.

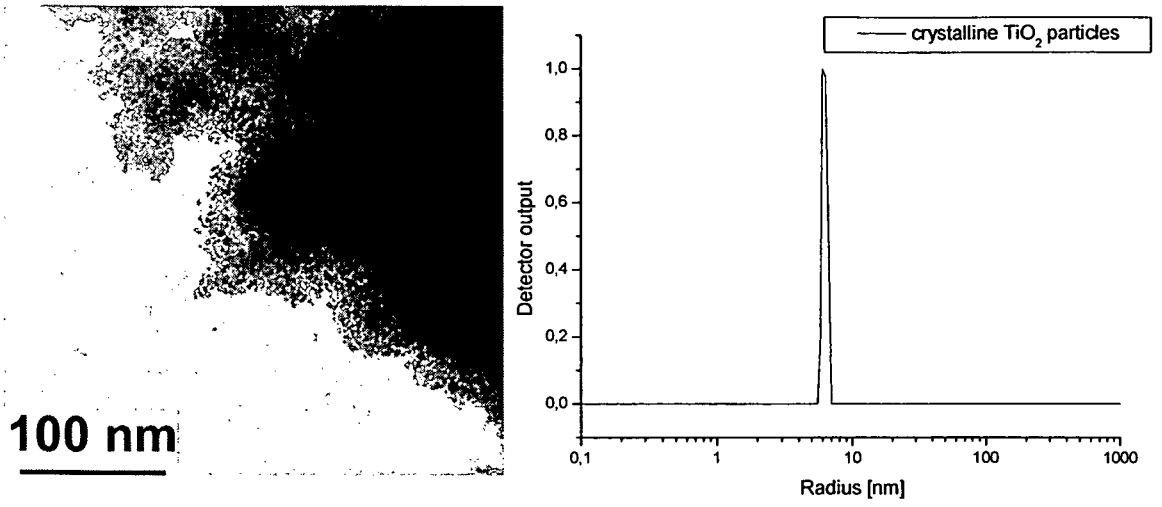

Figure 65: TEM image and DLS plot (in ethanol) of TiO_2 nanoparticles synthesized using the coordination product of titanium isopropoxide and 3-bromo-pentane-2,4-dione.

The diameter of the nanoparticles estimated from the TEM image in figure 65 was about 5 nm, while the diameter of particles obtained via DLS was about 12 ± 0.6 nm. One explanation for these different results might be occurring aggregation. This assumption is supported by a shoulder of the peak on the left side of the DLS plot, which possible represents non aggregated particles. The using of other solvents, such as methanol or water, could not improve the obtained result.

The mass loss which was measured by TGA was 14.7 %, which was even smaller than the mass loss of the particles that were prepared from titanium n-butoxide. Several reasons can be the source for the smaller mass loss; on the one hand the n-butoxide groups showed a lower reaction rate in hydrolysis reaction than isopropoxide groups, which may have led to a higher organic content as shown before; on the other hand decomposition of the functionalized alkoxide could have taken place as well, which may have decreased the amount of organic groups.

The specific surface area of the obtained particles was measured via nitrogen sorption and was estimated at 308 m^2/g. One reason for the higher specific surface of the particles, prepared from functionalized alkoxides, could have been the smaller diameter, while on the other hand the pentane-2,4-dione derivatives should have decreased the BET-surface dramatically. The higher hydrophobicity caused by functional groups normally reduces the absorption capacity of the surface.[256]

The observed increase of the specific surface area suggested that a total degradation of the functional groups, which should have been incorporated in the nanoparticle, took place. Elemental analysis delivered a carbon content of 3.6 % and a halogen content below 0.2 %, which suggested that most of the ligand was cleaved from the surface.

FTIR measurements obtained that no bands, which could have been assigned to a ν(CO) vibration of coordinated CO groups, were detected, which led to the assumption that the organic functionality was destroyed or cleaved from the surface during the synthesis. It was possible to assign the following bands that correspond to methyl groups: 1714 cm^{-1} ν(C-H), 1691 cm^{-1} ν(C-H), 1394 cm^{-1} $\delta(CH_3)$, 1044 cm^{-1} $\gamma(CH_3)$ and 3683 cm^{-1} ν(O-H) which correspond to OH-groups.

In figure 66 the X-ray diffractogram of the particles and a comparison to data from the ICSD database are shown.

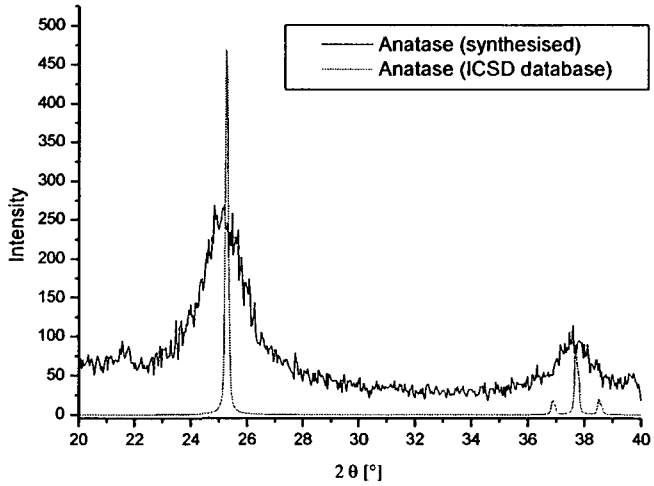

Figure 66: X-ray diffraction pattern of the titanium oxide nanoparticles compared to anatase[235] from the ICSD database.

The obtained diffractogram was identified as anatase. Compared to the anatase diffractogram from the ICSD database the measured reflections were broad due to a small crystallite size. The synthesized particles did not initialize a polymerization process, which led to the assumption that no surface functionalization was obtained.

The same approach was repeated with 3-chloro-pentane-2,4-dione as ligand because 3-bromo-2,4-pentane-dione was a very instable compound at ambient conditions.
The obtained nanoparticles and the corresponding DLS plot are shown in figure 67.

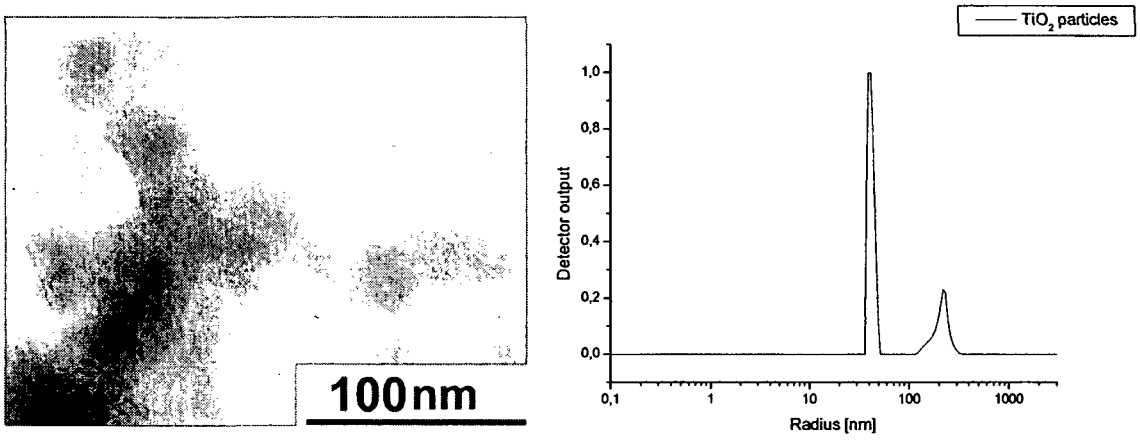

Figure 67: TEM image and DLS plot (recorded in ethanol) of the obtained nanoparticles.

The TEM image showed fairly spherical agglomerates of smaller particles with a diameter between 25 nm and 30 nm. Partially, these agglomerates formed larger aggregates. It was not possible to obtain the diameter of the single particles via DLS analysis although the sample was treated over long times in the ultrasound bath. The DLS analysis that was performed in ethanol resulted in a diameter of 82 ± 7 nm.

TGA analysis showed a mass loss of 31.5 %, which was much higher than the mass loss of the particles that were functionalized with 3-bromo-pentane-2,4-dione. Elemental analysis resulted in a carbon content of 4.9 % which was slightly higher than the values that were obtained in case of the bromine derivate. FTIR-spectroscopy revealed the same results as in case of the bromine derivate, where no bands of coordinated CO-groups were observed. The bands that were identified are listed in the experimental part (chapter 7.4.19.). Nitrogen sorption resulted in a specific BET surface area of 183 m^2/g.

X-ray powder diffraction was performed to analyze the obtained crystal phase of the sample, which is shown in figure 68.

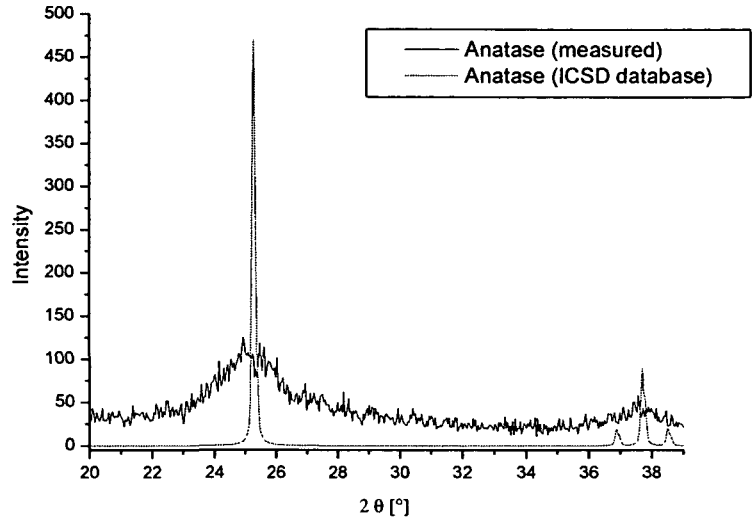

Figure 68: X-ray diffractogram of the obtained TiO_2 nanoparticles compared to anatase [235] from the ICSD database.

The obtained diffractogram was assigned to the anatase structure. Again the broad reflections are caused by the small crystallite size.
The received results suggested that the usage of the precursor that consists of $Ti(O^iPr)_4$ and 3-chloro-pentane-2,4-dione did not lead to surface functionalized nanoparticles as they did not initialize polymerization.

3-Acetyl-5-bromo-5-methylhexane-2,4-dione was utilized as coordinative species in the same reaction approach to overcome the thermal instability of the halo-pentane-2,4-diones. The obtained particles and the corresponding DLS plot are shown in figure 69.

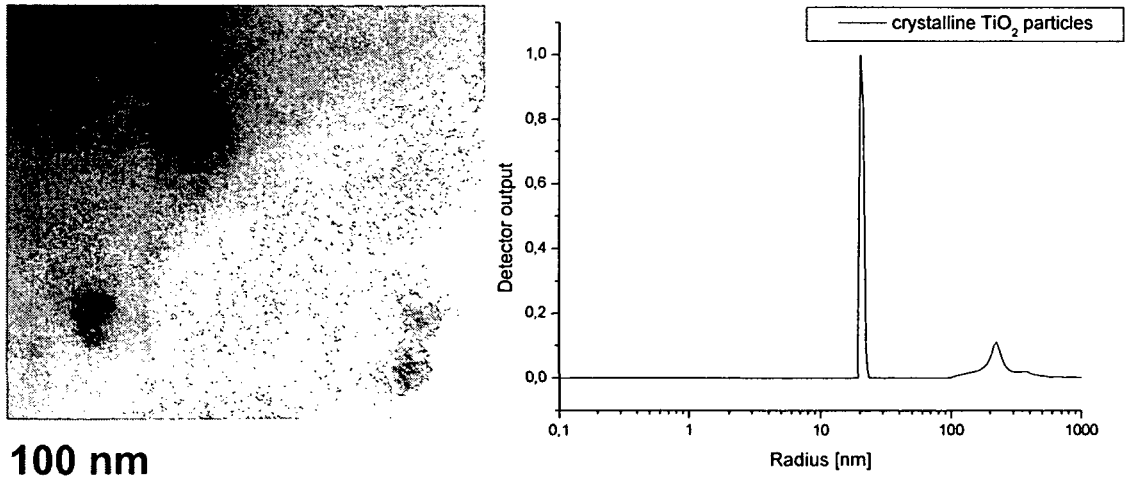

Figure 69: TEM image and DLS plot (in ethanol) of TiO_2 nanoparticles synthesized from the coordination product of titanium isopropoxide and 3-acetyl-5-bromo-5-methylhexane-2,4-dione.

The TEM image showed that the particles were spheroid with a diameter between 40 and 50 nm. The form of the particles was very irregular which led to the assumption that the structure of the particles was not stable. The DLS investigation resulted in a particle diameter of 42 ± 1 nm. In the DLS plot a second signal at a diameter of 460 nm was visible which might have been caused by aggregation of the obtained particles. TGA analysis suggested a mass loss of 29.8 %, which was slightly less than in case of the particles which were functionalized with 3-chloro-pentane-2,4-dione. Up to 200 °C the evaporation of absorbed solvent and ongoing condensation reactions led to a mass loss of 12 %. A carbon content of 5.8 % and a halogen content < 0.2 % via elemental analysis.

FTIR analysis showed no bands, which could have been assigned to ν(C-O) vibrations groups. These results suggested that the initiator was chemically changed during the synthesis. The specific surface of the nanoparticles was measured via nitrogen sorption and resulted in 163 m^2/g. Due to the higher amount of organic groups, which remained on the particle surface, the specific surface area was lower compared to the other crystalline titanium oxide nanoparticles, which were presented before. It was not possible to initiate a polymerization process with the obtained nanoparticles.

The X-ray diffractogram of the obtained particles is shown in figure 70.

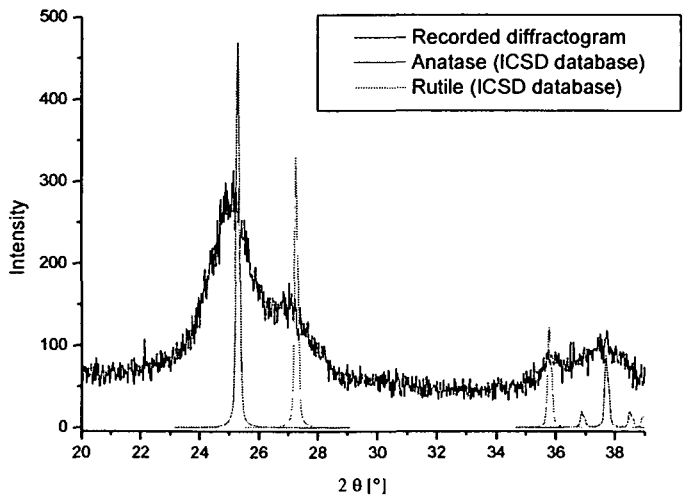

Figure 70: X-ray powder diffractogram of the obtained titanium oxide nanoparticles compared to anatase [235] and rutile [236] from the ICSD database.

In the diffractogram shown in figure 70 four reflections were found which were assigned to the anatase and to the rutile structure via the ICSD. The ratio between rutile and anatase structure was 33:66 as calculated via PCPDFWIN version 2.2 software. Possibly, the organic groups that remained attached to the nanoparticles had, in this case, an influence on the obtained crystal type, which supported the formation of rutile.

Because of their instable structure these particles were insufficient for the production of inorganic-organic core-shell nanoparticles.

3.2.4. Short summary

In this chapter the synthesis of different functionalized metal oxide nanoparticles from modified metal alkoxides, was presented. Both amorphous and crystalline nanoparticles were produced. While the amorphous particles were synthesized at room temperature, the crystalline particles were synthesized at increased temperature, which led to the destruction of the surface functionality. As shown in this chapter, there were discrepancies between the results that were obtained from DLS and TEM, concerning the size of the synthesized nanoparticles, caused by the occurrence of aggregation of the particles in the organic phase or swelling. In chapter 5 the influence of different solvents on the size of the nanoparticles in DLS measurements is discussed in more detail. Furthermore, the ultra high vacuum in the TEM, the destructive influence of the electron beam, and occurring deviation from the eucentric position during the investigation in the TEM might have been reasons for different results.

The following amorphous, functionalized metal oxide nanoparticles were synthesized: titanium oxide, zirconium oxide, vanadium oxide, tantalum oxide, yttrium oxide and iron oxide. In case of the titanium oxide nanoparticles the influence of certain synthesis parameters and the kinetic of the particle growth were investigated in more detail.
In table 6 the most important results were summarized.

Table 6: Results of the synthesized metal oxide nanoparticles

$Ti_xO_y(OH)_z$	Yield [%]	Weight loss [%]	Halogen content [%]	FTIR [cm^{-1}]
---	75.3	26.9	---	---
+ 3-chloro-pentane-2,4-dione	84.2	63.8	5.1	1576
+ 3-bromo-pentane-2,4-dione	69.1	63.0	7.2	1568
+ 1-acetyl-2-oxopropyl 2-bromo-2-methylpropanoate	63.3	67.5	4.9	1576
+ 3-acetyl-5-bromo-5-methylhexane-2,4-dione	49.7	63.4	4.1	1582

$Zr_xO_y(OH)_z$	Yield [%]	Weight loss [%]	Halogen content [%]	FTIR [cm^{-1}]
---	76.3	26.8	---	---
+ 3-chloro-pentane-2,4-dione	79.5	41.0	3.0	1550
+ 1-acetyl-2-oxopropyl 2-bromo-2-methylpropanoate	53.2	43.7	2.7	1598
+ 3-acetyl-5-bromo-5-methylhexane-2,4-dione	54.2	39.3	2.6	1591

$V_xO_y(OH)_z$	Yield [%]	Weight loss [%]	Halogen content [%]	FTIR [cm^{-1}]
---	77.1	22.3	---	---
+ 3-chloro-pentane-2,4-dione	74.6	35.7	2.2	1610
+ 1-acetyl-2-oxopropyl 2-bromo-2-methylpropanoate	67.3	44.1	3.1	1627

$Y_xO_y(OH)_z$	Yield [%]	Weight loss [%]	Halogen content [%]	FTIR [cm^{-1}]
---	81.3	41.0	---	---
+ 3-chloro-pentane-2,4-dione	79.3	59.7	13.4	1594
+ 1-acetyl-2-oxopropyl 2-bromo-2-methylpropanoate	62.3	47.9	3.6	1560

$Ta_xO_y(OH)_z$	Yield [%]	Weight loss [%]	Halogen content [%]	FTIR [cm^{-1}]
---	85.3	13.8	---	---
+ 3-chloro-pentane-2,4-dione	91.0	16.0	1.3	1583
+ 1-acetyl-2-oxopropyl 2-bromo-2-methylpropanoate	68.5	36.4	1.2	1723/1659

$Fe_xO_y(OH)_z$	Yield [%]	Weight loss [%]	Halogen content [%]	FTIR [cm^{-1}]
---	78.9	32.0	---	---
+ 1-acetyl-2-oxopropyl 2-bromo-2-methylpropanoate	79.3	34.3	1.9	1731/1573

3.3. Synthesis of nanoparticles from metal salts

If metal salts were utilized as precursors for the production of nanoparticles, two microemulsions were used, one containing the metal salt, the other containing a reaction partner for hydrolysis and condensation reactions. With this approach, various kinds of nanoparticles were manufactured such as SiO_2 [81, 106-108], TiO_2[50, 109-111], ZrO_2[112] and magnetite[113, 114]. The obtained nanoparticles carried surface OH-groups, which could be used for additional reactions, for example with modified alkoxides, and thus provide functionalized particles for various applications.[123, 124] If polymers should be grafted from the surface, initiator molecules can be attached covalently.

The general viability of the method was investigated using various metal salts such as $TiCl_4$, $ZrO(NO_3)_2$, $ZnBr_2$, $FeCl_2*4H_2O$ and $AlCl_3*3H_2O$, which were commercially available. The oxide formation took place in the micelles of a water in oil microemulsion via hydrolysis of the corresponding metal salts with an aqueous ammonia solution. After 24 hours of stirring the particles were isolated via centrifugation and washed several times.

3.3.1. Synthesis of iron oxide nanoparticles

In case of the iron oxide nanoparticles $FeCl_2*4H_2O$ was used as metal salt whereby red-brown particles in a yield of 26 % were obtained. The concentration of the ammonia solution was 0.6 M to achieve good stability of the iron oxide particles, which did not precipitate at low pH values. The particles were calcinated at 800 °C for 24 hours to investigate the condensation reactions and their influence on the diameter of the particles. A TEM image and the DLS plot of the iron oxide particles are shown in figure 71.

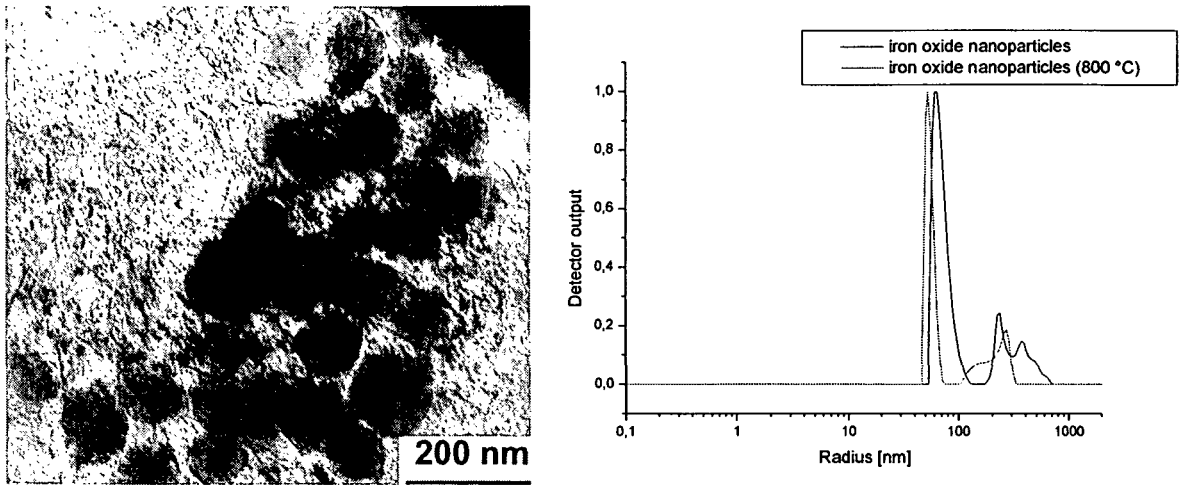

Figure 71: TEM image and DLS plot (measured in ethanol) of the obtained iron oxide nanoparticles.

The particles shown in figure 71 had a diameter of 103 nm according to estimations from the TEM image. The obtained particles were very homogeneous compared to the particles that were received in case of modified alkoxides as precursors. DLS investigations resulted in a diameter of 112 ± 18 nm. The second signal at a higher radius is caused by aggregated particles, which did not disperse after the isolation and washing procedure. The diameter was reinvestigated after calcinations at 800 °C via DLS and a reduction of the diameter to 106 ± 10 nm was observed. This shrinking process was caused by evaporation of adsorbed water and ongoing condensation reaction that resulted in the decay of water.

The diameter of the micelles of microemulsion A before mixing with the ammonia containing emulsion was measured by DLS and resulted in 540 nm, which was much larger than the particles diameter. It was not possible to measure the diameter of the micelles after the addition of microemulsion B because particle formation started instantaneously and so only the particles were measurable. TGA analysis resulted in a mass loss of 19 % if the particles were heated up to 800 °C. This mass loss was most probably caused by absorbed water until 200 °C and further on by condensation reactions of OH groups that led to the evaporation of water. The specific surface of the nanoparticles is 351 m^2/g as measured by nitrogen sorption. As the obtained iron oxide nanoparticles were X-ray amorphous at room temperature, the crystallization temperature of the particles was investigated via X-ray powder diffraction at elevated temperatures. The different possible crystalline phases of the iron oxide system were

presented in chapter 3.2.3.6. In figure 72 the obtained diffractograms and a comparison to ICSD database data are shown.

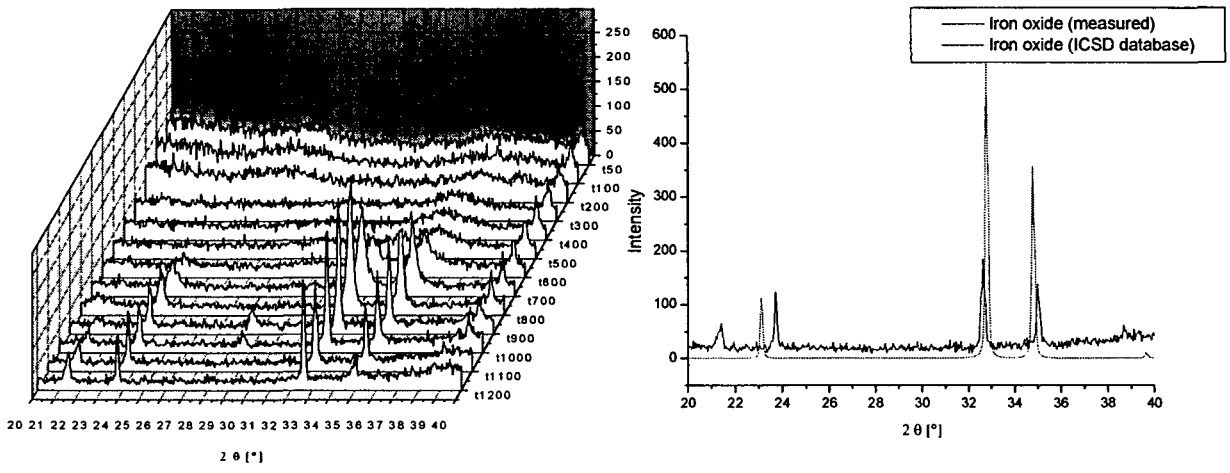

Figure 72: X-ray powder diffraction patterns of the obtained iron oxide nanoparticles at different temperature levels compared with α-Fe_2O_3 [311] from the ICSD database.

Up to 300 °C only amorphous structure was observed. At 300 °C the crystallization process began and broad reflections were measured. Up to 1200 °C the reflections sharpened and were assigned to α-Fe_2O_3 (hematite). This initiation temperature of the crystallization process corresponds to results published by *Liao et al.*[255], which were presented before (chapter 3.2.3.6.). Two reflections were observed at 2θ angles of 21.1 ° and 29.5 ° at 900 °C and 1000 °C, which were assigned to a spinel phase with an iron to oxygen ratio between Fe_2O_3 and Fe_3O_4. Compared to the nanoparticles that were synthesized from modified iron alkoxide, the crystallization process started at lower temperatures. The intermediate phase was also observed in the diffraction patterns of the iron oxide particles obtained from modified iron alkoxides where the intermediate phase did not disappear at higher temperatures.

3.3.2. Synthesis of titanium oxide nanoparticles

For the synthesis of titanium oxide nanoparticles $TiCl_4$ was used as metal salt, which had to be dissolved in concentrated HCl to prevent immediate hydrolysis and condensation reactions that occurred if the chloride was simply dissolved in distilled water. In microemulsion B a 3.4 M ammonia solution was used. In this case, the concentration had to be higher because the used HCl had to be neutralized to allow particle formation. 113 mg $TiCl_4$ delivered about

12 mg titanium oxide nanoparticles which corresponded to a yield of 25%. TEM and DLS analysis were performed to analyze size and morphology of the particles. A TEM image of the obtained particles and the corresponding DLS plot are shown in figure 73.

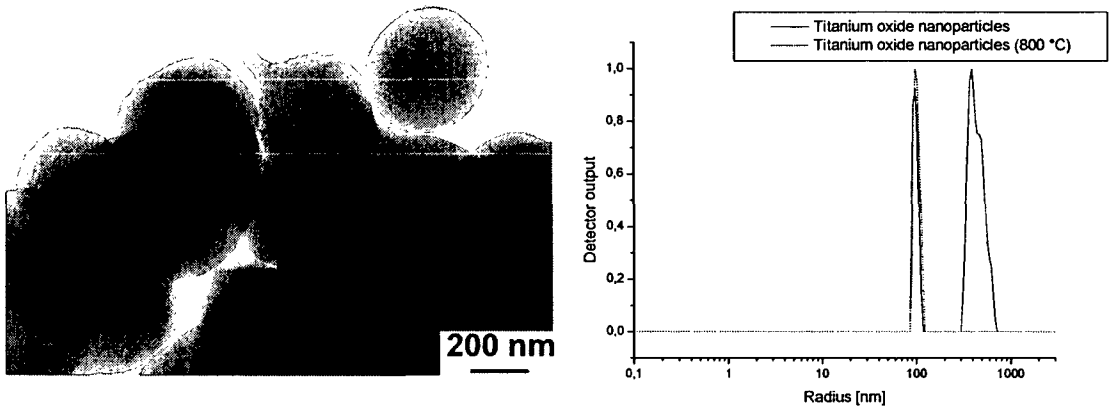

Figure 73: TEM image and DLS plot (measured in ethanol) of the produced titanium oxide nanoparticles.

From the TEM image a diameter of the particles of 245 nm was estimated. The particles had a rather homogenous shape which suggested that during the synthesis no aggregation of emerging particle cores was taking place. The diameter obtained from DLS investigations was 210 ± 15 nm. A reason for the different results might have been the estimation of the diameter obtained from the TEM image, where only a small part of the sample was analyzed, compared to DLS analysis, where the based on all scattering particles. The second peak in the DLS plot was probably caused by particles which were not redispersed in the supersonic bath. The particles were calcinated at 800 °C and the DLS analysis was repeated to observe the shrinking process caused by bound water and ongoing condensation reactions. A diameter of 205 ± 8 nm was observed.

The size of the micelles that contained the salt solution was investigated by DLS as well. The measured diameter was 170 nm which was smaller than the observed particle diameter. These results showed the dependence of the micelle diameter of the used salt, its concentration, and the pH value. *Förster et al.* have discovered that the stability of micelles of poly(2-vinylpyridine)-polyethylenoxide copolymers depend very strongly on the pH value and the salt concentration.[257] After unifying both microemulsions, the micelle size could be investigated because particle formation took place immediately and so covered the signal of the micelles in the DLS investigation. TGA analysis resulted in a weight loss of 24 % due to

evaporation of absorbed water, which was finished at about 200 °C and condensation reactions that took place at higher temperatures. The specific surface of the obtained nanoparticles was measured via nitrogen sorption, which led to a specific surface area of 459 m^2/g. Compared to the presented iron oxide particles the specific surface area of the produced titanium oxide particles was higher despite their larger diameter. This effect was attributed to the different pore structure of the received materials. In figure 74 the cumulative pore volume depending on the pore diameter of both particle types is compared.

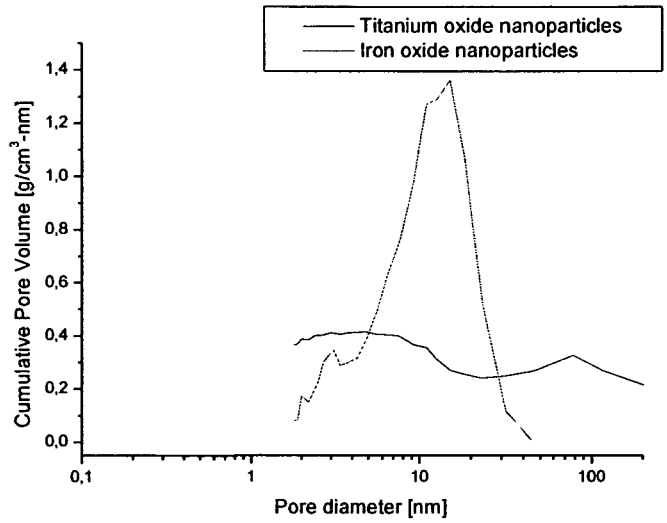

Figure 74: Comparison of the cumulative pore volume depending on the pore diameter of iron oxide and titanium oxide nanoparticles.

According to figure 74, both materials showed different cumulative pore volume dependence of the pore diameter. While the iron oxide nanoparticles showed a maximum cumulative pore volume at the weighted pore diameter of 13 nm, the titanium oxide nanoparticles had a broad maximum at a smaller pore diameter, which resulted in higher specific BET surface area despite the larger diameter.

The various crystal phases of TiO_2 and their formation temperature were presented in chapter 3.2.3.1. As the obtained particles were X-ray amorphous at room temperature, the onset temperature of the crystallization process of the titanium oxide nanoparticles was measured by temperature dependent X-ray powder diffraction. The obtained diffraction patterns and a comparison with data from the database are shown in figure 75.

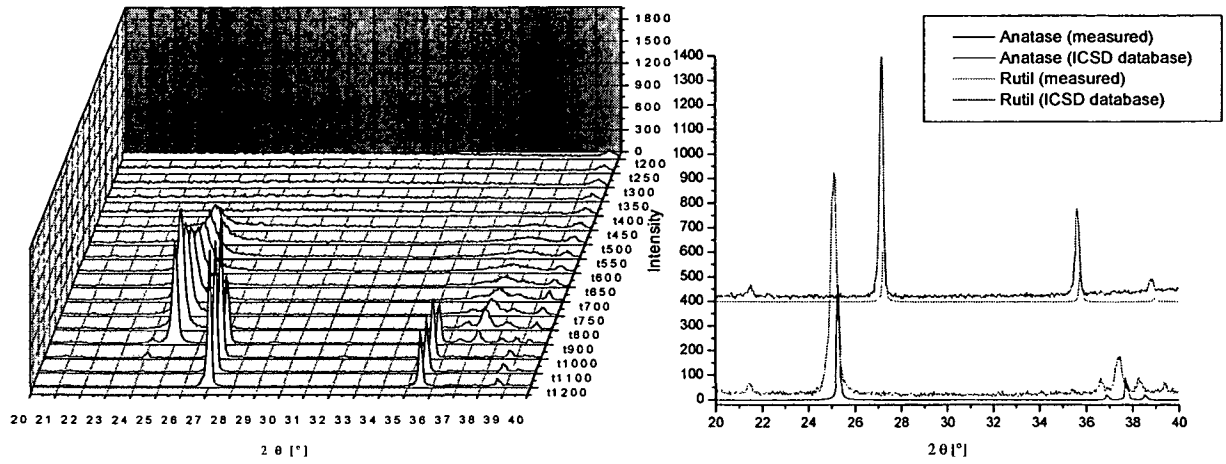

Figure 75: X-ray powder diffractograms of functionalized titanium oxide nanoparticles at different temperatures and comparison with ICDS database-diffractograms (800 °C for anatase [235] and 1200 °C for rutile [236]).

At room temperature the samples were X-ray amorphous. The evolvement of the anatase structure started at 400°C. The anatase crystals kept growing until 900 °C where the intensity of the reflections started to decrease in favor of reflections assigned to rutile. At 1000 °C the reflections that corresponded to the anatase structure had totally disappeared. No differences of the transformation temperatures between the particles that were synthesized from metal salts and titanium alkoxide derivates were observed.

3.3.3. Synthesis of zirconium oxide nanoparticles

As precursor for the production of the zirconium oxide nanoparticles, $ZrO(NO_3)_2$ dissolved in HNO_3 was used, which was diluted with distilled water. A 1.6 M ammonia solution was used in microemulsion B to obtain precipitation. From 138 mg $ZrO(NO_3)_2$ an amount of 11 mg zirconium oxide nanoparticles was obtained that corresponded to a yield of 13 %, which was much lower than the yields in case of the other presented metal salts. The usage of other zirconium salts like $ZrOCl_2$ was described by *Matsui et al.* They obtained higher yields but lost the spherical morphology and the monodisperse size distribution of the diameter of the obtained nanoparticles.[258] The described particles had a diameter between 20 nm and 200 nm.

The morphology and the size distribution of the synthesized nanoparticles were analyzed via TEM and DLS analysis. As condensation reactions at increased temperatures might influence

the particle diameter, the particles were calcinated at 800 °C and investigated via DLS. A TEM image and the corresponding DLS plot of the particles are shown in figure 76.

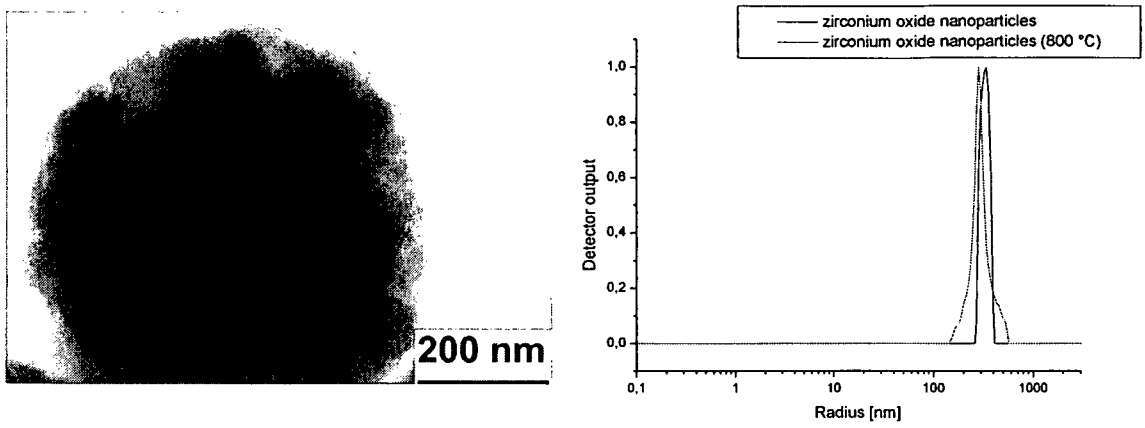

Figure 76: TEM image and DLS plot (measured in ethanol) of the obtained zirconium oxide nanoparticles.

The particle which was shown in figure 76 had a diameter of 642 nm according to the TEM image. The structure of the received particles was fairly inhomogeneous suggesting many condensation cores grew simultaneously inside the water droplet, kept steadily growing, and finally formed the particle by agglomeration. From DLS analysis a diameter of 658 ± 71 nm was received which was very close to the result obtained by TEM. The DLS analysis was repeated after the particles were calcinated at 800 °C for 24 hours. The observed decrease of the diameter to 570 ± 85 nm was caused by evaporation of absorbed water and ongoing condensation processes.

The diameter of the micelles of the microemulsion that contained the salt was measured by DLS which resulted in a diameter of 1460 nm. The size of the micelles is influenced by many parameters such as temperature, ratios of water to surfactant and cosurfactant, type and amount of dissolved salt, pH value, method of stirring, etc.[257] Compared to the synthesis of TiO_2 nanoparticles, the micelle size in microemulsion was larger, possibly due to the pH value and the used salt. Structures above 1500 nm were out of the guaranteed range of the photomultiplier, therefore DLS results near this limit should be treated with caution. TGA analysis showed a mass loss of 25.8 % up to 800 °C, caused by the desorption of absorbed water up to 200 °C and thermally initiated condensation reactions at higher temperatures. The specific surface area of the zirconium oxide nanoparticles resulted in 396 m^2/g, which was

between the specific surfaces of the titanium oxide and the iron oxide nanoparticles. As the obtained zirconium oxide nanoparticles were X-ray amorphous at room temperature, the onset of crystallization was investigated by X-ray powder diffraction at different temperatures. The obtained diffraction patterns and a comparison with data from the ICSD database are shown in figure 77.

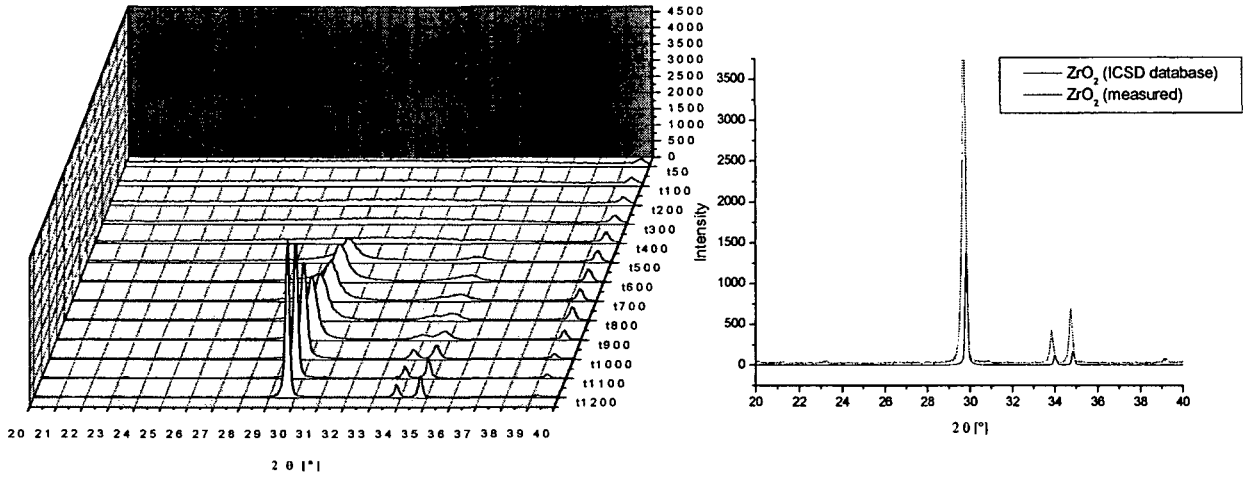

Figure 77: X-ray powder diffraction patterns of the obtained zirconium oxide nanoparticles at different temperatures and comparison with tetragonal ZrO_2 [243] from the ICSD database.

Below 500 °C no crystallized fraction was observed. At 500 °C the crystallization process of the tetragonal phase started with broad reflections that became sharper at higher temperatures. In figure 77 on the right hand side the obtained diffractogram at 1200 °C was compared with a diffractogram from the database and identified as tetragonal ZrO_2. Compared to the zirconia nanoparticles that were synthesized from modified alkoxides, the onset temperature of the crystallization process was equal. The two small reflections at a 2θ angle of 21.5 ° and 27 ° were not observed in case of the particles that were synthesized from metal salts. The obtained patterns did not correspond to the diffractogram that was presented by *Petrunin et al.*, who observed beside the tetragonal phase cubic structures as well.[244]

3.3.4. Synthesis of zinc oxide nanoparticles

$ZnBr_2$ was used as metal salt in microemulsion A for the production of the zinc oxide nanoparticles. From 135 mg $ZnBr_2$ an amount of 10 mg zinc oxide nanoparticles was obtained which corresponded to a yield of 17 %. TEM and DLS analyses were performed to investigate

the particle morphology and the monodispersity of the size distribution. The particles were heated to 800 °C for 24 hours to investigate the condensation reactions and their influence on the diameter of the particles at increased temperatures. A TEM image of the particles and the corresponding DLS plot are shown in figure 78.

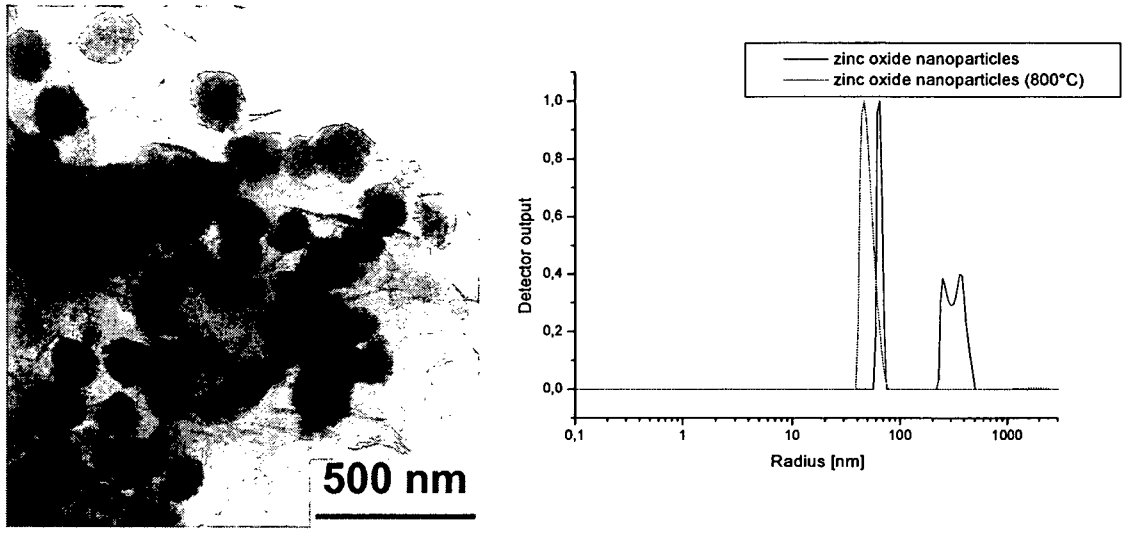

Figure 78: TEM image and the corresponding DLS plot (measured in ethanol) of the obtained zinc oxide nanoparticles.

The diameter of the zinc oxide particles was about 156 nm estimated from the TEM image. The particles did not have a homogenous appearance but a morphology as if many nucleation cores emerged in a single micelle, then steadily grew and aggregated to form a single particle. DLS measurements resulted in an average diameter of 135 ± 6 nm. The second signal in the DLS plot was caused by aggregated zinc oxide particles after isolation and redispersion. Although the suspension was treated in an ultrasonic bath, it was not possible to obtain a totally dispersed suspension. The diameter of the particles was measured again after calcination at 800 °C to observe a possible particle shrinkage via condensation processes. The diameter of the particles decreased after the calcination to 104 ± 11 nm.

The micelles of microemulsion A, which contained the zinc salt, were measured by DLS and a diameter of 520 nm was obtained. As shown before, the type of utilized salt and the pH value had a strong influence on the size of the received micelles.

From the TGA analysis a weight loss of 18.5 % was obtained if the sample was heated up to 800 °C. Up to 200 °C about 12 % of the weight were lost, at higher temperatures the weight-

loss curve flattened. Above 500 °C the mass remained constant. Nitrogen absorption / desorption measurements resulted in a specific surface of 41 m^2/g, which was much smaller than the values obtained in case of the other unfunctionalized metal oxide nanoparticles. A possible reason for this low specific surface might have been a different pore structure of the zinc oxide nanoparticles. Similar results were obtained by *Singhal et al.*, who synthesized zinc oxide particles from zinc nitrate with a diameter of 13 nm and obtained a BET surface of 83 m^2/g, which was comparable to the presented particles taking in account their larger diameter.[259]

ZnO is a system that crystallizes in the wurzite type. Above 450 °C the white ZnO changes its color reversible to yellow due to defects in the crystal structure caused by separation of oxygen atoms. That causes a small excess of Zn atoms, which occupy the octahedral holes in the crystal structure.

As the obtained particles were X-ray amorphous at room temperature, the onset temperature of the crystallization process was investigated by X-ray powder diffraction. The obtained diffraction patterns and a comparison with data from the ICSD database are shown in figure 79.

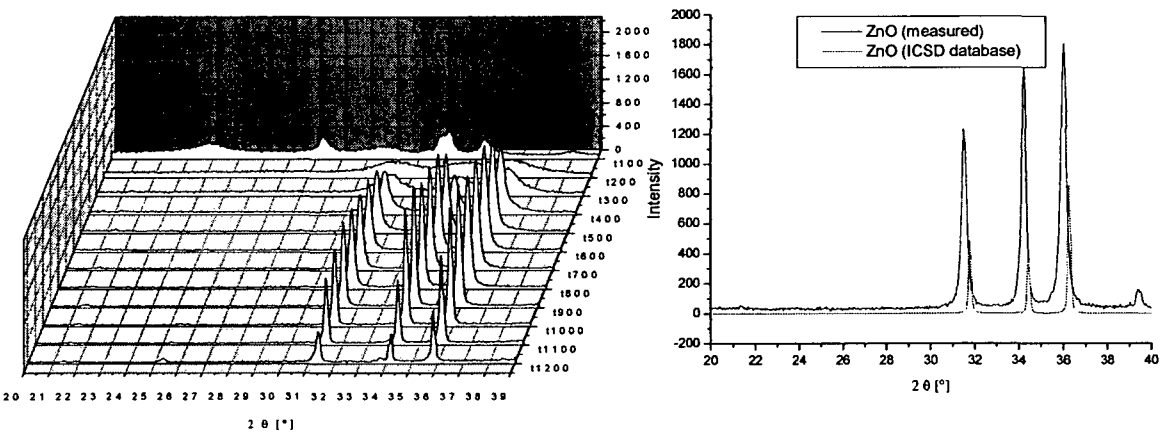

Figure 79: X-ray powder diffraction patterns of the obtained zinc oxide nanoparticles and comparison with hexagonal zinc oxide [260] from the ICSD database.

At 200 °C the crystallization process started, which was shown by the emerging of three broad reflections. At higher temperatures the reflections sharpened and were assigned to hexagonal ZnO. The small offset between the measured data and the database was caused by a thermal instability of the sample holder.

3.3.5. Synthesis of aluminum oxide nanoparticles.

$AlCl_3*3H_2O$ was used in microemulsion A as metal salt. From 482 mg aluminum chloride, 111 mg aluminum oxide nanoparticles were received, which corresponds to a yield of 84 %. As too low salt concentrations did not lead to particle formation, the salt concentration in microemulsion A was increased compared to the other presented metal oxide nanoparticles. In microemulsion B an ammonia concentration of 4.6 M was used to keep the pH value in the unified microemulsion high enough for the particle precipitation. If the pH value was lower than 5 the aluminum oxide particles were not stable. Morphology and the particle size distribution were investigated via TEM and DLS. DLS measurements were repeated after calcination at 800 °C to observe occurring shrinkage due to condensation reactions. A TEM image and the corresponding light scattering plot are shown in figure 80.

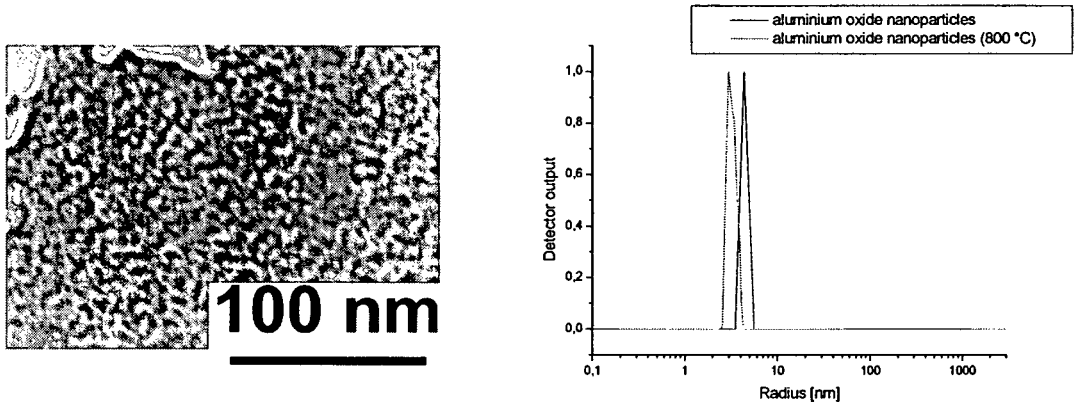

Figure 80: TEM image and DLS plot (measured in ethanol) of the obtained aluminum oxide nanoparticles.

The particle diameter obtained from the TEM image was about 6 nm. DLS analysis delivered a diameter of 8 ± 0.4 nm. It is remarkable that total redispersion was obtained. It might be possible that in case of the aluminum oxide nanoparticles the nucleophile character of the OH-groups on the particles surface had a stabilizing effect on the gained dispersion. *Zhou et al.* investigated the zeta-potential and the isoelectric point of various nanoparticles in water.[254] They observed that the isoelectric point of Al_2O_3 particles is with 8.70 much higher than in case of TiO_2 particles (5.26) and ZrO_2 particles (6.05), which might be the reason for this different behavior. The specific surface of the aluminum oxide nanoparticles was investigated by nitrogen sorption and resulted in 200 m^2/g. The mass loss obtained via TGA

analysis was about 45 %, caused by the evaporation of adsorbed water up to 250 °C and ongoing condensation reactions at higher temperatures.

Various crystal structures of Al_2O_3 are known from literature. The low temperature modification is γ-Al_2O_3 that crystallizes in a spinel-like structure, where a part of the octahedron places are statistically empty. At 1000 °C γ-Al_2O_3 is transformed to α-Al_2O_3 that is called corundum. In the crystal lattice of corundum the oxygen atoms form a hexagonal, dense structure. 2/3 of the hexagonal holes are filled with Al^{3+} ions. Furthermore, γ-, δ-, and θ-modification are literature-known.[261]

As the synthesized Al_2O_3 particles were X-ray amorphous at room temperature, the onset temperature of the crystallization process was measured via X-ray powder diffraction. The obtained diffraction patterns and a comparison with data from a database are shown in figure 81.

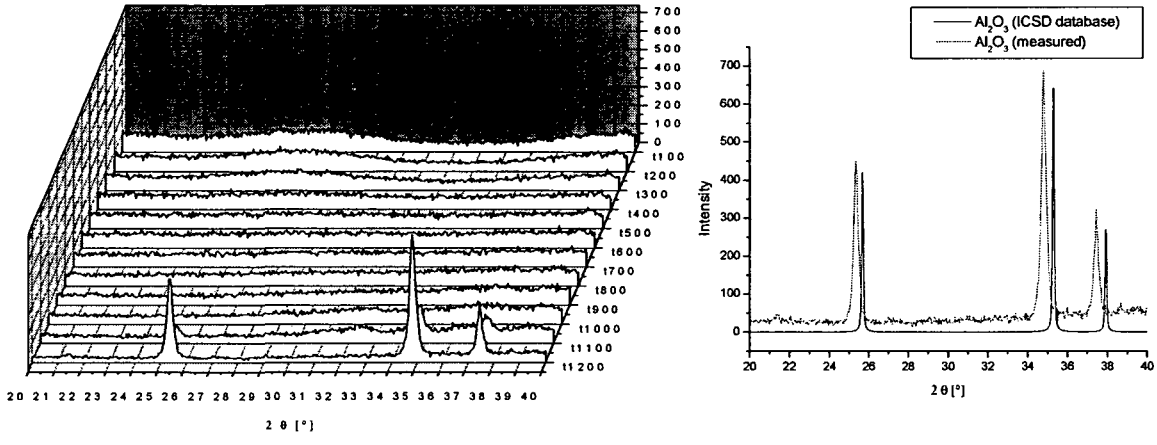

Figure 81: X-ray diffraction patterns of the obtained aluminum oxide nanoparticles compared with α-Al_2O_3 [252] from the ICSD database.

Up to 1100 °C the obtained nanoparticles were X-ray amorphous. At 1100 °C the first reflections were detected, which became sharper at higher temperatures. They were assigned to α-Al_2O_3 via database. The small offset between the measured data and the data obtained from the database was caused by a thermal instability of the sample carrier. These results correspond to the results that were published by *Sun et al.*, who observed phase transition to α-Al_2O_3 if the particles were heated up to 1100 °C for several hours.[261]

3.3.6. Short summary

In this chapter the synthesis of unfunctionalized metal oxide nanoparticles outgoing from metal salts with a microemulsion approach was presented. In table 7 the obtained results are summarized.

Table 7: Results of the nanoparticles obtained from metal salts.

	Yield [%]	Weight loss TGA [%]	Specific BET-surface [m^2/g]	Diameter (TEM) [nm]	Diameter DLS [nm]
$Ti_xO_y(OH)_z$	25	24.0	459	245	210 ± 15
$Zr_xO_y(OH)_z$	13	25.8	396	642	658 ± 71
$Fe_xO_y(OH)_z$	26	19.0	351	103	112 ± 18
$Zn_xO_y(OH)_z$	17	18.5	41	156	135 ± 6
$Al_xO_y(OH)_z$	84	45.0	200	6	8 ± 0.4

Compared to the nanoparticles that were synthesized from modified metal alkoxides, the observed specific surface areas were much larger due to the lack of organic groups on the surface. Furthermore, similar to the obtained diameters, in case of alkoxide precursors a wide range of different sizes was observed if metal salts were used as precursors due to different hydrolysis and condensation reactions.

4. Functionalization of nanoparticles

Modification of the surface fulfils, depending on the introduced functionality, different purposes. For example, functionalities which stabilize the suspension of the particles in a specific medium or which allow the initiation of a polymerization can be bond directly onto the surface of the particles. It is also possible to attach monomers or reactive sites that can bond polymer chains to the particles. Furthermore, such organic groups can protect the inorganic core from environmental influences. It is also possible to attach organic groups onto the particle surface, which support and control the aggregation process.[19]

The covalent linkage between the different components is of great importance for the construction of inorganic-organic hybrid materials, in order to prevent phase separation during the synthesis or utilization of the produced systems.

4.1. Functionalization of SiO_2 nanoparticles

The silica particles were surface-modified with two different functionalities to investigate the aggregation behavior of these two types depending on the pH value.

The nucleophile character of the surface OH-groups of the SiO_2 nanoparticles was utilized for the functionalization process. For this purpose, primary amines and ester-groups containing molecules which could, depending on the pH value, interact with each other via hydrogen bonds or ionic complexation were attached to the surface. In figure 82 the reactions of the functionalization process are shown.

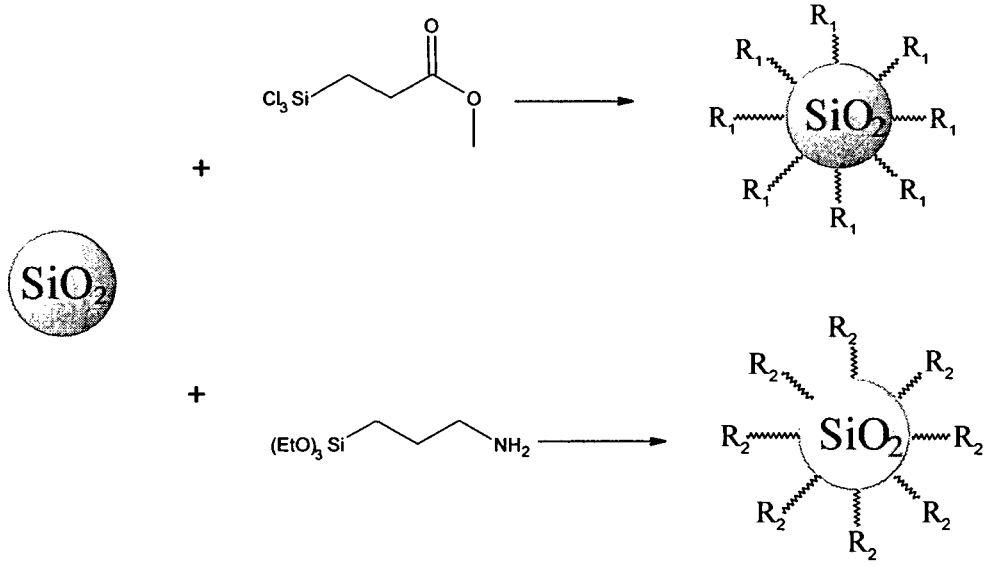

Figure 82: Functionalization of the SiO_2 nanoparticles with amino- and carboxyl-containing silanes.

Silica particles with a diameter of 93 nm were synthesized via the Stöber process. The particle dispersion was directly mixed with an excess of 2-(carbomethoxy)ethyltrichlorosilane and 3-amino-propyltriethoxysilane, respectively, which were both commercially available and stirred at increased temperature for several days. The particles were isolated and washed with ethanol.

In scheme 23 the assumed effect of different pH values on the attached molecules is shown.

Scheme 23

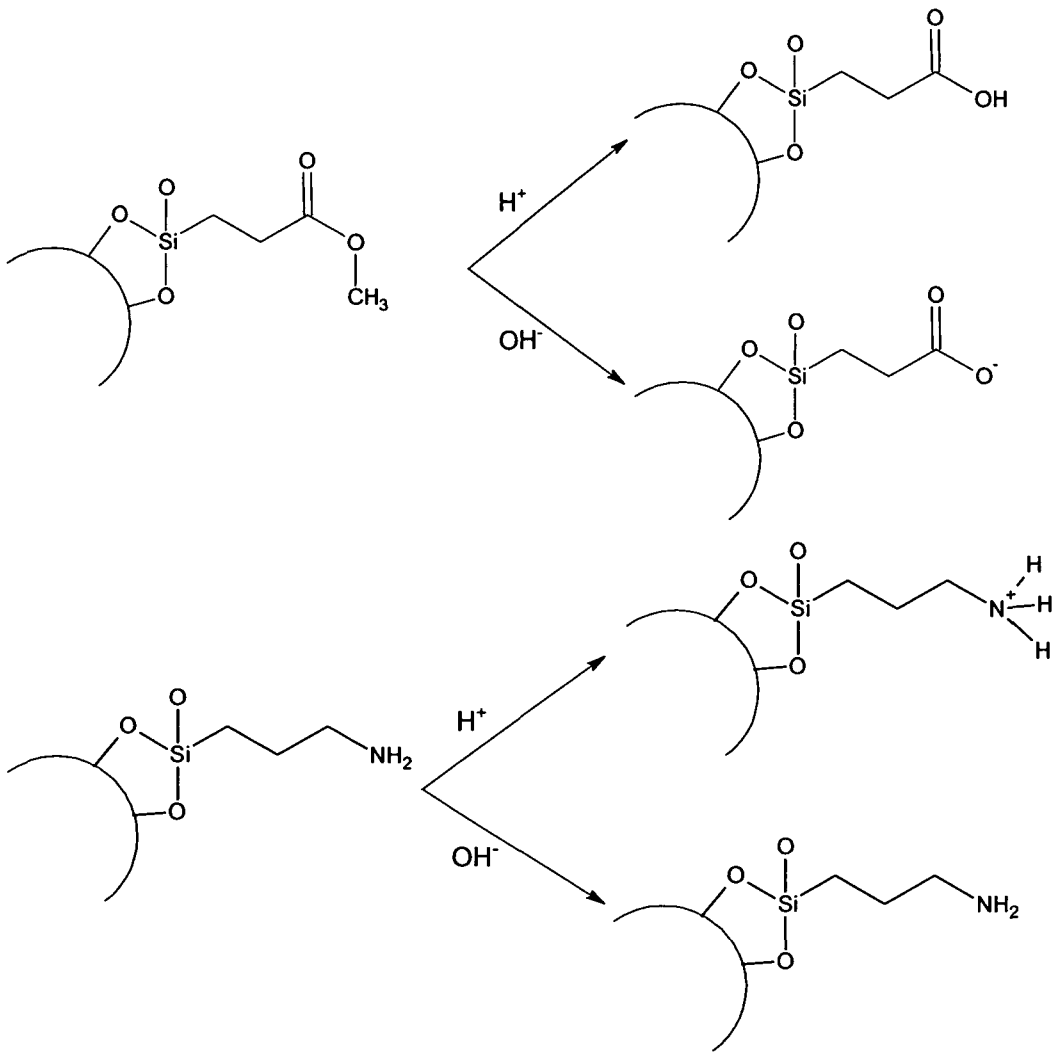

Depending on the pH value, the organic molecules became ionized, which led to ionic interactions and/or formation of hydrogen bonds if the functionalized particles were mixed.[201] In figure 83 the DLS spectra of the unmodified and the modified particles are presented.

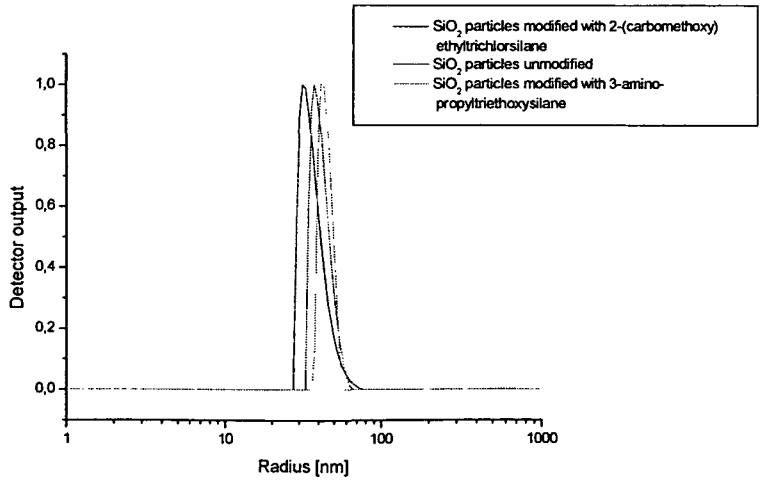

Figure 83: DLS plot of the unmodified and the surface functionalized SiO_2 nanoparticles recorded in ethanol.

As shown in figure 83 the unmodified SiO_2 particles had a diameter of 93 ± 15 nm. In case of the modification with 2-(carboxymethoxy)ethyltrichlorosilane a diameter of 90 ± 17 nm was obtained. The observed shrinking of the particles might have been caused by ongoing condensation reactions at increased temperatures during the functionalization process. Functionalization with 3-amino-propyltriethoxysilane led to an increase of the measured diameter to 102 ± 8 nm. The larger hydro-dynamical diameter might be caused be different interaction between the ethanol and the bond amino derivative as the hydrophobic amino functionalities possibly showed less interactions with the hydrophilic OH-groups. These results were obtained directly after the functionalization process before the particles were isolated, washed and dried.

^{13}C CPMAS NMR and ^{29}Si CPMAS NMR were performed for both types of functionalized particles. In case of the ^{13}C CPMAS all signals caused by the carbon atoms of the surface functionalities were assigned. ^{29}Si CPMAS NMR showed the presence of two T- and three Q-units (-67 / -76 ppm and -101 / -110 / -119 ppm). According to *Lippmaa et al.* the Q-units were assigned to the SiO_2 particle core and the T-units to the Si-atoms at the particle surface as the exchange of one Si-O bond with a Si-C bond leads to a chemical shift of about 45 ppm.[262]

The mass loss of the functionalized particles was measured by TGA up to 800 °C and resulted in a residue of 74.5 % for the particles that were functionalized with 2-(carbomethoxy)ethyltrichlorosilane and 78.5 % for the silica particles that were functionalized with 3-amino-propyltriethoxysilane. These results corresponded to a surface coverage of 0.9 mmol/g and 0.7 mmol/g, respectively, taking in account that the unfunctionalized particles had a mass loss of 16 %. The obtained surface coverage can be compared with results published by *Van Blaadern et al.*, who obtained a surface coverage of 5-10 groups/nm^2 with APS.[18] The specific surface of the particles was measured via nitrogen sorption. The specific surface of the SiO_2 nanoparticles functionalized with 2-(carbomethoxy)ethyltrichlorosilane resulted in 23.3 g/m^2, while the specific surface of the SiO_2 particles functionalized with 3-amino-propyltriethoxysilane resulted in 26.5 m^2/g. The obtained results show a tremendous decrease in BET surface area compared to the unmodified particles with a specific surface area of 117 m^2/g.

4.2. Functionalization of gold nanoparticles

In the case of gold nanoparticles surface modification (for example by polymerizable groups, stabilizing agents or initiating groups) is usually carried out using thiols as anchor groups. In this chapter the functionalization of the surface of gold particles with polymerization initiators is presented which allows a "grafting from" ATRP. Contrary to various published examples, efforts were made to use a thiol containing initiator with a short carbon chain. For example, *Brust et al.* functionalized the surface of gold nanoparticles with long-chained thiols that allow a stabilization of the particles in organic solvents like toluene.[140] *Nuß et al.* presented a method to attach an α-bromo-ester group that can serve as initiator in an atom transfer radical polymerization (ATRP) via a dodecanethiole bridge.[211]

4.2.1. Synthesis of 2-sulfanylethyl-2-bromo-2-methylpropanoate

2-Sulfanylethyl-2-bromo-2-methylpropanoate is a molecule that can initiate ATRP via the α-bromo-ester group and that can be directly connected to the surface of gold nanoparticles via the thiol groups.

In a first synthetic approach sulfanylethanol and 2-bromo-2-methyl-propionic acid bromide were reacted with a molar ratio of 1 : 1.2.
In the presence of triethylamine sulfanylethanol was cooled below 0 °C with an NaCl-ice bath and reacted with 2-bromo-2-methyl-propionic acid bromide. The resulting product was hydrolyzed with water and extracted with diethyl ether. Via vacuum distillation it was possible to separate a mixture of 2-sulfanylethyl-2-bromo-2-methylpropanoate and S-(2-hydroxyethyl) 2-bromo-2-methylpropanethioate at a temperature of 80 °C (5 mm Hg) from 2-[(2-bromo-2-methylpropanoyl)sulfanyl]ethyl 2-bromo-2-methylpropanoate (123 °C, 5 mm Hg). The two substances that formed the fraction at 80 °C were identified via NMR. The fraction at 123 °C consisted only of 2-[(2-bromo-2-methylpropanoyl)-sulfanyl]ethyl 2-bromo-2-methylpropanoate, which was proven by NMR and elemental analysis.

Because of the two nucleophilic reaction sites of sulfanylethanol, this approach did not only lead to the synthesis of 2-sulfanylethyl-2-bromo-2-methylpropanoate but also to the formation of a mixture of 2-[(2-bromo-2-methylpropanoyl)sulfanyl]ethyl 2-bromo-2-methylpropanoate,

2-sulfanylethyl-2-bromo-2-methylpropanoate and S-(2-hydroxyethyl) 2-bromo-2-methylpropanethioate as shown in scheme 24.

Scheme 24

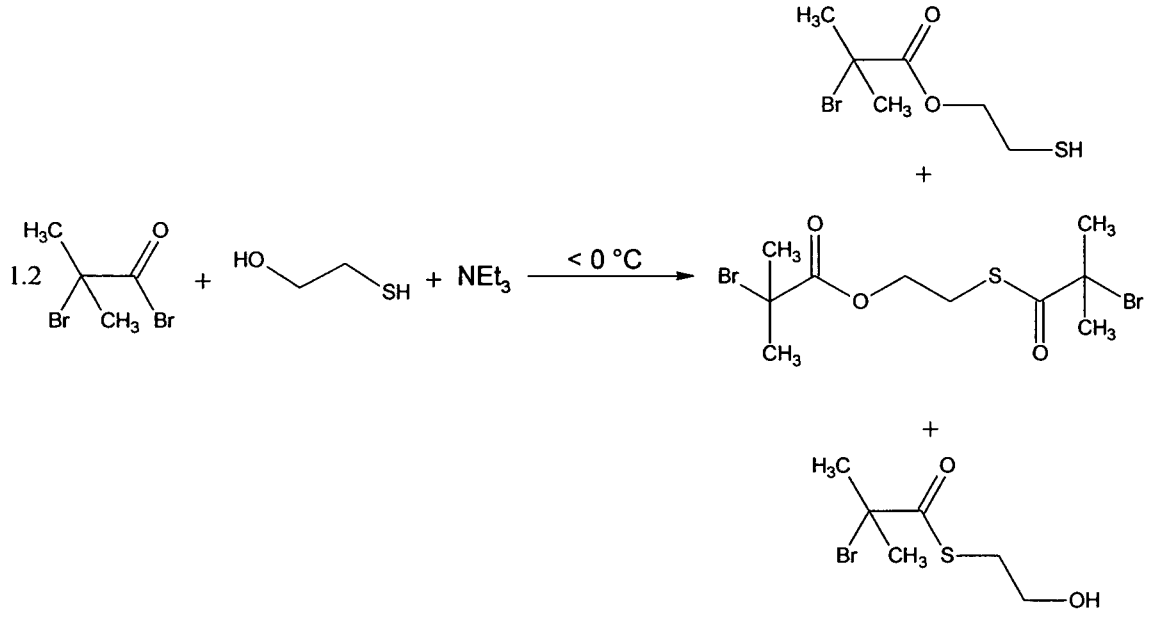

The approach was performed in a solvent and the molar ratio between sulfanylethanol and 2-bromo-methyl-propionic acid bromide was changed to overcome the side reactions. A five time molar excess of thio-alcohol and diethyl ether as solvent were used to obtain a pure fraction of 2-sulfanylethyl-2-bromo-2-methylpropanoate(Scheme 25).

Scheme 25

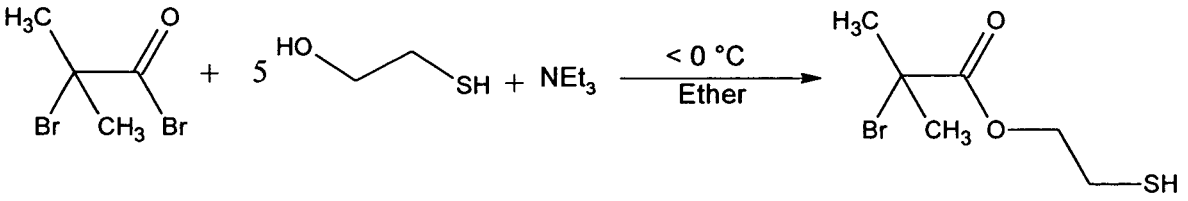

After the slow addition of the bromide the solution was stirred over night, hydrolyzed with water and extracted with diethyl ether. 2-Sulfanylethyl-2-bromo-2-methylpropanoate was isolated at 108 °C (7 mm Hg) in a yield of 83.1 % by fractionated distillation.

4.2.2. Functionalization of gold nanoparticles with 2-sulfanylethyl-2-bromo-2 methylpropanoate

The functionalization of the gold nanoparticles with a diameter of 15 nm (chapter 3.1.2.) with 2-sulfanylethyl-2-bromo-2 methylpropanoate was performed in aqueous solution directly after the isolation of the gold particles that were produced. The thiol was added in large excess to make sure that a maximum coverage of the gold nanoparticles was obtained. Immediately after the addition of the polymerization initiator the color changed from red to black due to aggregation of the nanoparticles. This aggregation was caused by the substitution of the stabilizing citrate ions by the thiol. As the bromo-methylpropanoate part was more hydrophobic and not charged compared to citrate ions, the particles were not longer stabilized in aqueous media. The now modified particles were isolated by centrifugation, and washed with water and ethanol in a supersonic bath to eliminate only adsorbed initiator molecules.

The surface area of the modified particles was analyzed via nitrogen sorption. The results of the nitrogen sorption analysis showed a significant decrease of the measurable surface after the functionalization with 2-sulfanylethyl-2-bromo-2 methylpropanoate from 32.9 m^2/g to 22.9 m^2/g. Thermal analysis was carried out by TGA. Compared to the citrate stabilized nanoparticles, which lost 27 % of their mass, the 2-sulfanylethyl-2-bromo-2 methylpropanoate functionalized showed a larger mass loss of 46 % that could be explained by the presence of additional organic groups. These mass losses led to an estimated surface coverage of 0.88 mmol/g under the assumption that all citrate groups were substituted.

4.3. Functionalization of Au@SiO_2 nanoparticles

As mentioned in the introduction, the Au@SiO_2 show improved stability and are easier to disperse in various solvents compared to pure Au particles. They still show the interesting physical characteristics which makes them interesting for various technical applications. The SiO_2-shell of the Au@SiO_2 nanoparticles carries silanol groups on the particle surface, which can be used for surface functionalization, commonly applied via silane coupling agents. For example, *Philipse et al.* managed to functionalize silica particles with the silane coupling agent 3-methacryloxypropyltrimethoxysilane.[121] Applying the same approach, it should be possible to attach polymerization initiators to the surface of Au@SiO_2 particles. *Perruchot et*

al. used methyl-silane modified bromo-isobutyric acid derivates that can initiate aqueous ATRP to functionalize silica nanoparticles.[263]

4.3.1. Synthesis of 2-bromo-2-methyl-propionic acid allyl ester and hydrosilation

The allyl alcohol was mixed with triethylamine, cooled down to 0 °C, and the 2-bromo-2-methyl-propionic acid bromide was added dropwise (scheme 26).

Scheme 26

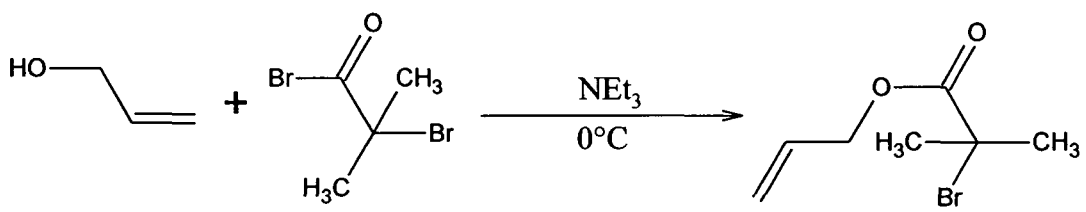

The mixture was stirred overnight whereby a white substance precipitate appeared that was hydrolyzed afterwards with water. The solution was extracted with diethyl ether; the resulting organic phase was washed with saturated $NaHCO_3$ solution and water, afterwards dried over $mgSO_4$, and distilled in vacuum at 55 °C (4 mm Hg) obtaining a yield of 61.9 % of a yellow oil.

The resulting 2-bromo-2-methyl-propionic acid allyl ester was directly hydrolsilated with triethoxy-silane by dissolving it in toluene and adding a few drops of Karstedt catalyst in xylene under vigorous stirring. Afterwards the mixture was heated under reflux over night (scheme 27).

Scheme 27

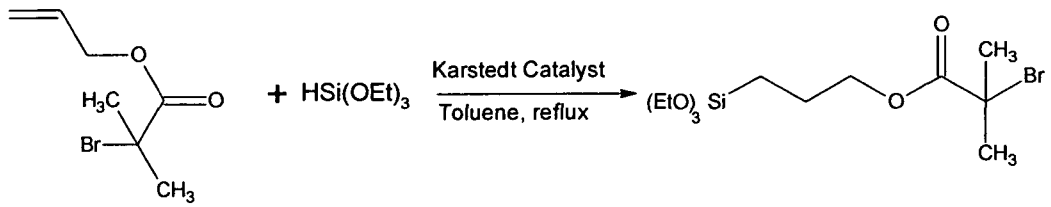

The excess of triethoxy-silane and the solvent were removed in vacuo and a yield of 98 % was obtained. The remaining oil was characterized by NMR and elemental analysis. In the ^{13}C NMR spectrum the signals of the vinyl protons at 131.6 ppm and 118.7 ppm disappeared totally. The ^{29}Si NMR spectrum showed only one peak at -46.8 ppm which confirmed that all

excessive triethoxy-silane was removed. The elimination of the excessive silane was of great importance because it also could react with the surface OH groups, which would have decreased the coverage of the polymerization initiator.

4.3.2. Functionalization of the Au@SiO_2 nanoparticles with 2-bromo-2-methyl-propionic acid propane-(3′-triethoxy-silyl)-ester

The isolated Au@SiO_2 nanoparticles were dispersed in absolute toluene, mixed with an excess of 2-bromo-2-methyl-propionic acid propane-(3′-triethoxy-silyl)-ester and heated under reflux over night under an argon atmosphere. Afterwards the particles were isolated via centrifugation and repeatedly washed with absolute toluene. TGA analysis revealed an increased mass loss after the functionalization of 55.0 % compared to 38.1 % in case of the unfunctionalized Au@SiO_2 particles, which led to an estimated surface coverage of 1.1 mmol/g. The specific surface was measured via nitrogen sorption and resulted in a decrease of the specific surface area from 45.2 m^2/g before the functionalization to 35.6 m^2/g afterwards.

4.4. Functionalization of the metal oxide nanoparticles.

Similar to previously described functionalizations of silica and Au@SiO_2 systems, OH-groups at the surface of the metal oxide nanoparticles were used for the modification via the reaction with triethoxy-silane derivatives of four different polymerization initiators, either for thermal and UV-light induced free radical polymerization or ATRP.[264] One of the ATRP initiators was already discussed in the functionalization of the Au@SiO_2 particles. The other initiator molecules will be discussed below.

4.4.1. Synthesis of the asymmetric azo initiator containing a triethoxy-silane group

Free radical polymerization initiators were used for the functionalization of metal oxide particles to demonstrate the differences in yield and MWD due to different polymerization mechanisms. The usually applied symmetric azo initiator for free radical polymerization of the type X-R-N=N-R-X, where X symbolizes an anchor group that allows a covalent attachment to a reaction site, offers several possibilities for an attachment either with two OH-groups at the same particle or by cross linking reactions with the surface of different particles.

Asymmetric azo initiators with only one coupling group were used to avoid the latter reaction. *Prucker et al.* were able to immobilize such an azo initiator onto the surface of SiO_2 particles and polymerize styrene from their surface.[16]

In a first step the asymmetric azo initiator was synthesized based on a literature-known procedure (scheme 28).[16]

Scheme 28

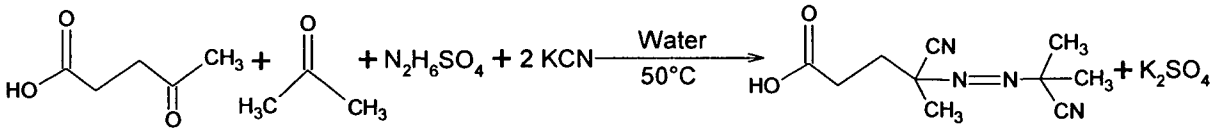

The sodium salt of the laevulin acid was reacted with acetone and hydrazine sulfate in the presence of KCN. The obtained yield was about 4.1 % of the theoretical. In the literature procedure a yield of 12 % was reached. The reason for this discrepancy between the yields could be that contrary to the procedure published by *Prucker et al.*, the organic phase was not used further on, to prevent contamination with symmetric azo initiator that was described as by-product.[16]

In a second step the acid chloride of the obtained acid was synthesized (scheme 29).

Scheme 29

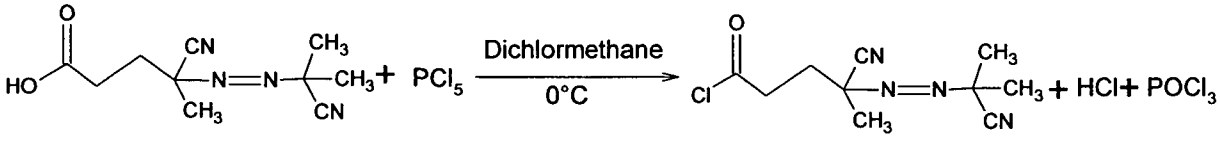

The compound that was received in the first part was reacted with PCl_5 in dichloromethane to the acid chloride in a yield of 40.6 %. The obtained powder was very unstable to moisture due to hydrolysis to the corresponding acid.

The next step was the esterification of the obtained acid chloride with allyl alcohol (scheme 30).

Scheme 30

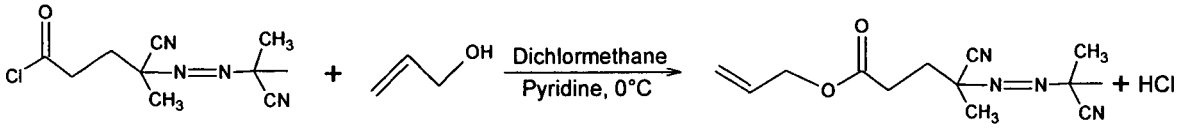

In the presence of pyridine as base, the acid chloride was esterified with allyl alcohol in dichloromethane with a yield of 95 %. ^{13}C NMR data showed the total conversion of the acid chloride by a shift of the CO group peak from 172.6 ppm to 169.9 ppm. In the FTIR spectrum the CO group vibration band was shifted from 1715 cm^{-1} to 1713 cm^{-1}.

The overall yield of the three step synthesis was only 1.6 %. All peaks of the final product were assigned according to *Prucker et al.*[16]

The asymmetric azo initiator was hydrosilated with triethoxy silane in the presence of Karstedt catalyst in absolute toluene at 40 °C (scheme 31).

Scheme 31

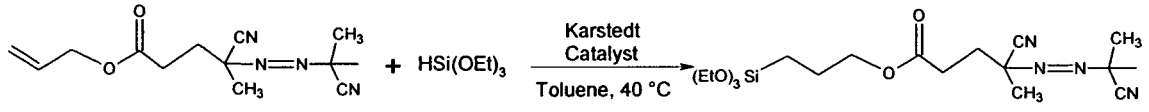

The yield of the hydrosilation was analyzed by $^{1}H^{NMR}$ after a four day reaction time. Because of the thermal instability of azo compounds, the solution was not heated over 40 °C to avoid decomposition. At such low temperatures the hydrosilation was not completed which led to traces of unreacted double bonding signals in the ^{1}H NMR spectrum at 5.85 and 5.28 ppm.

4.4.2. Synthesis of a photo initiator containing a triethoxy-silane group

Recently, this synthesis was published by us to obtain of POSS-silsesquioxanes containing photo-initiating groups.[264] In a first step the primary OH group of 2-hydroxy-1-[4-(2-hydroxyethoxy)phenyl]-2-methyl-1-propanone (Irgacure 2959, Ciba Spezialchemikalien) was etherified with allyl bromide in the presence of NaOH and tetraoctylammonium bromide as phase transfer catalyst (Scheme 32).

Scheme 32

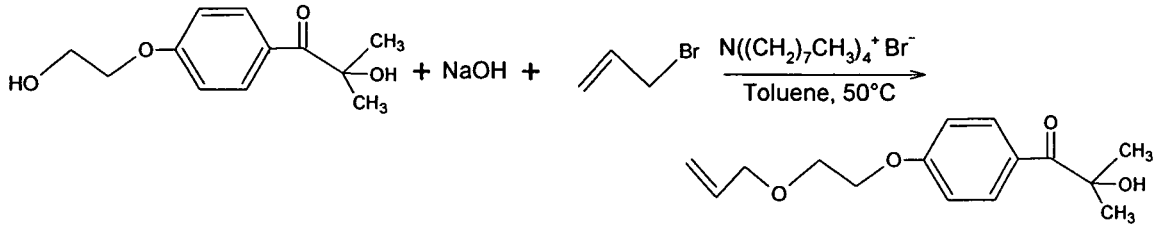

After the removal of the solvent in vacuo, a yellow oil was obtained in a yield of 81.2 %. In the ^{1}H NMR and ^{13}C NMR no signals of allyl bromide were detected after a reaction time of 24 hours. In the next step the modified photo initiator was hydrosilated with triethoxy-silane in the presence of Karstedt catalyst.

The hydrosilation was performed in absolute toluene under an argon atmosphere at a temperature of 40 °C in the presence of Karstedt catalyst for four days (Scheme 33).

Scheme 33

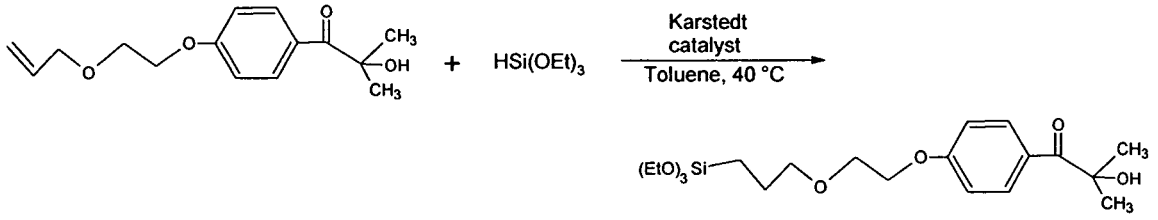

A yellow oil was obtained in a yield of 90 %. The synthesized photo initiator was very unstable at room temperature and in visible light. Therefore no elemental analysis was performed. Both, ^{1}H and ^{13}C NMR confirmed the completeness of the hydrosilation.

4.4.3. Synthesis of hydrosilated 4-vinyl-benzyl-chloride

As benzyl-chloride is known to act as ATRP initiator, [163] 4-vinyl-benzyl-chloride was chemically modified with trialkoxysilane groups. The double bond of the molecule was hydrosilated with triethoxy-silane in the presence of Karstedt catalyst (scheme 34).

Scheme 34

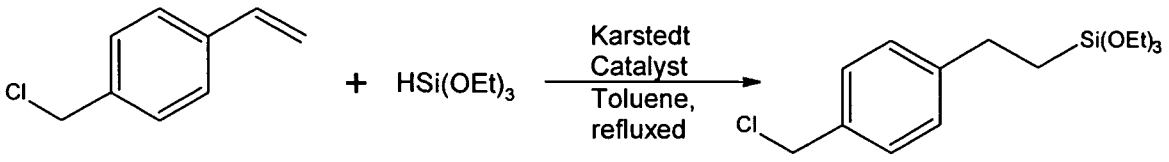

After the elimination of toluene and excessive silane, a yield of 87.2 % was obtained. NMR spectra indicated that a complete hydrosilation of the double bond occurred because neither in the ^{1}H NMR nor in the ^{13}C NMR spectrum signals of unreacted vinyl groups were detected.

Further on the modified azo initiator will be called initiator (A), the photo initiator will be shortened as initiator (B) and the ATRP initiator that contains a chlorine atom will be abbreviated as initiator (D). The synthesis of a second ATRP initiator (2-bromo-2-methyl-propionic acid propane (-3'-triethoxy-silane)-ester), which will be named initiator (C), was discussed in chapter 4.3.1.

4.4.4. Functionalization of the different metal oxide nanoparticles

The previously presented initiator molecules were attached on the particle surface to allow "grafting from" polymerization, initiated directly on the particle surface. The functionalization of the nanoparticles was performed by stirring a nanoparticle/ethanol suspension with the different initiator molecules. Depending on the thermal stability of the particular initiator, different reaction conditions were selected. While the ATRP-initiator/nanoparticle/ethanol mixture was refluxed for 48 hours, the photo- and azo initiator were only stirred at room temperature for four days due to their thermal instability. The attachment to the nanoparticle surface happened via condensation reactions of surface OH-groups with the silane alkoxide-modified initiators, probably catalyzed via residues of ammonia, absorbed on the surface of the metal oxide particles.

DLS investigations after the surface functionalization with the different initiators and redispersion in ethanol revealed only small enlargement in the particle size, based on the organic functionalization attached to the surface and will therefore not be discussed in detail. ^{13}C CPMAS NMR analyses of particles that were functionalized with initiator (A) and (B) led

to broad signals which did not allow distinct assignment of the obtained signals and will therefore not be discussed in detail.

4.4.4.1. Functionalization of the iron oxide nanoparticles

The obtained nanoparticles were washed several times to eliminate absorbed initiator molecules. In figure 84, exemplarily, a TEM image of iron oxide nanoparticles functionalized with initiator (C) is shown.

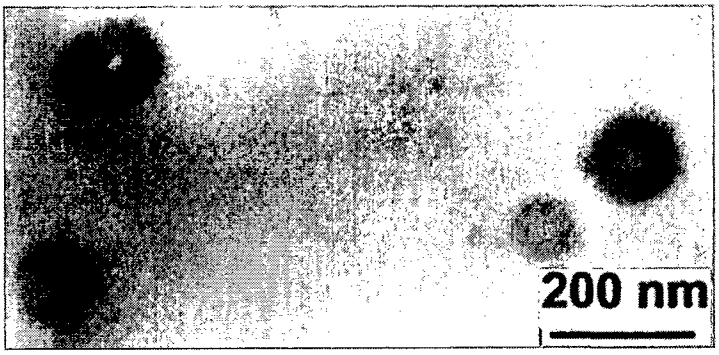

Figure 84: TEM image of iron oxide nanoparticles functionalized with initiator (C).

The particles had the same homogenous morphology like the unmodified ones. The diameter of the obtained particles, functionalized with initiator (C), is about 105 nm. From elemental analysis very different results for the four types of functionalized particles were obtained. The carbon content of the particles that were functionalized with initiator (A) was lowest with 2.8 % C, followed by initiator (C) with a carbon content of 10.9 %. High carbon contents were observed for the particles that were functionalized with initiator (B) and (D) where 15.4 % and 18.2 % carbon were measured, respectively.

^{13}C CPMAS NMR-analysis was performed on iron oxide nanoparticles that were functionalized with initiator (D). The plot of the ^{13}C CPMAS NMR analysis of the modified nanoparticles is compared with the ^{13}C NMR of initiator (D) in figure 85.

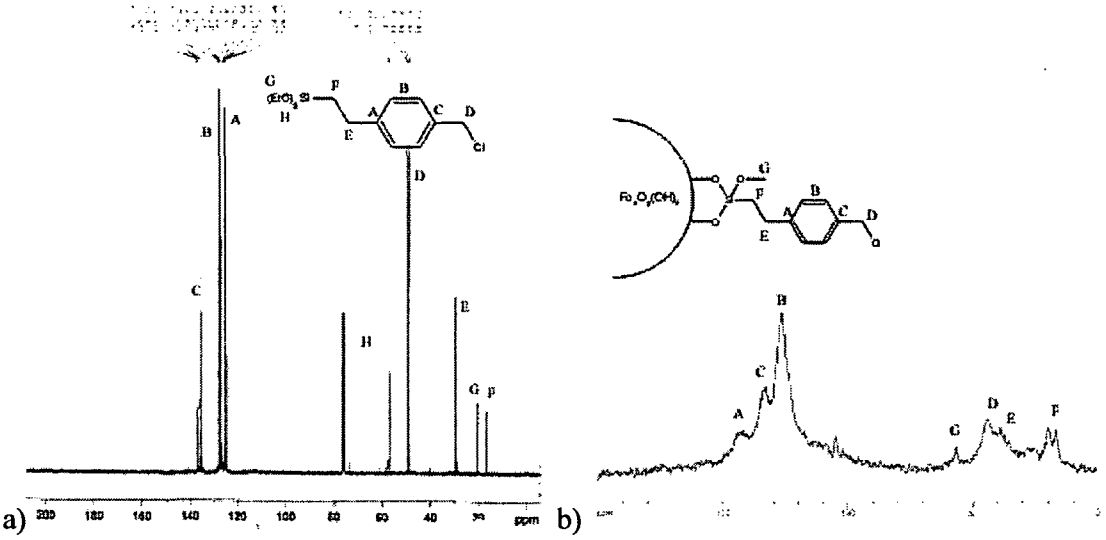

Figure 85: ^{13}C NMR spectra of a) initiator (D) and b) functionalized iron oxide particles.

Additional to the expected signals of the bound initiator molecule small signals of the remaining alkoxide or absorbed ethanol groups were identified at a chemical shift of 58.5 ppm and 17.3 ppm. The three phenyl ring signals were identified corresponding to the signals that were recorded in solution for the free initiator. All CH_2-groups were identified as well.
TGA measurements obtained similar results. In table 8 the received TGA results and the calculated surface coverage are given.

Table 8: TGA results of the functionalized iron oxide nanoparticles and the calculated surface coverage.

Nanoparticle	**TGA Residue [%]**	**Modified Nanoparticle**	**TGA Residue [%]**	**Surface Coverage [mmol/g]**
$Fe_xO_y(OH)_z$	81.0	$Fe_xO_y(OH)_z$ + Subst. A	80.6	0.03
		+ Subst. B	65.4	0.59
		+ Subst. C	65.3	0.78
		+ Subst. D	70.5	0.59

The unmodified iron oxide nanoparticles revealed a TGA mass loss of 19 %, so compared to the azo modified particles that lost 19.4 % of their mass nearly no difference was measured. This hardly increased mass loss corresponded to a surface coverage of 0.03 mmol/g. The

particles that were functionalized with initiator (B), (C) and (D) lost 34.6 %, 34.7 % and 25.9 % of their mass which corresponded to a surface coverage of 0.59 mmol/g, 0.78 mmol/g and 0.59 mmol/g, respectively. These results confirmed the results that were obtained in elemental analyses.

The particles were analyzed via nitrogen sorption where the unmodified particles obtained a specific surface of 351 m^2/g. The functionalization with initiator (A) led to a decrease of the specific surface to 263 m^2/g. The bonding of initiator (B) reduced the measurable surface to 247 m^2/g. After modification with the ATRP initiators (C) and (D), the specific surface decreased to 155 m^2/g and to 193 m^2/g respectively. *Armatas et al.* showed the direct relation between the obtained BET-surface and the obtained surface coverage in case of silica particles covered with silano-(trimethoxy)-propyl-imidazole groups.[265]
From these results it was concluded that the degree of functionalization of the iron oxide nanoparticles depended very much on sterical phenomena. Particles that were functionalized with the azo initiator, which was the most sterical demanding initiator had the lowest carbon content, the lowest surface coverage and the lowest reduction of specific surface after the functionalization. The ATRP initiators that were much smaller obtained a much higher degree of functionalization. Furthermore, it had to be taken into account that the functionalization process with ATRP initiators was performed via heating the mixture under reflux. The higher temperature, compared to the functionalization with free radical initiators, could also cause a higher degree of functionalization. The obtained discrepancies of the results from TGA and BET might be caused by different interactions of the absorbed nitrogen with the attached initiator molecules.[256] Furthermore, if the attached molecules have a high molecular weight, elemental analysis and TGA obtain high carbon contents, despite a possibly lower surface coverage, compared to smaller molecules.

4.4.4.2. Functionalization of the titanium oxide nanoparticles

The particles were isolated and redispersed in ethanol for the TEM analysis. In figure 86 a TEM image of titanium oxide nanoparticles that were functionalized with initiator (D) is shown.

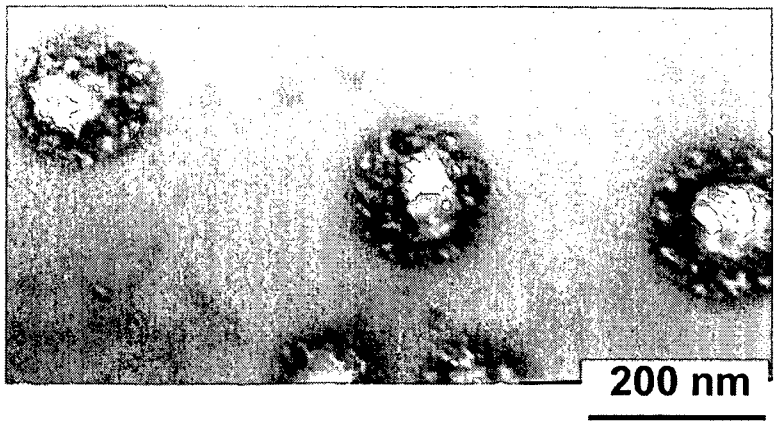

Figure 86: TEM image of titanium oxide nanoparticles that were modified with initiator (D).

The particles shown in figure 86 had a diameter of 210 nm with a different morphology compared to the unmodified particles. Considering the bright spot in the center of the particles, the electron beam of the electron microscope seemed to have interacted somehow with the particles. Elemental analysis showed similar results like the investigation of the iron oxide particles. In case of the functionalized titanium oxide particles, modification with initiator (A) led to a carbon content of only 3.3 %. The bonding of the photo-initiator (B) resulted in a carbon content of 9.3 % that was slightly reduced compared to the functionalized iron oxide nanoparticles. The ATRP initiators (C) and (D) led, after the bonding to the particle surface, to a carbon content of 15.2 % and 12.0 %, respectively.

In case of the titanium oxide nanoparticles, the functionalized systems with initiator (C) and (D) were measured via ^{13}C CPMAS NMR. The obtained ^{13}C CPMAS NMR spectrum of particles that were functionalized with initiator (C) is compared to the ^{13}C NMR spectrum of initiator (C) in figure 87.

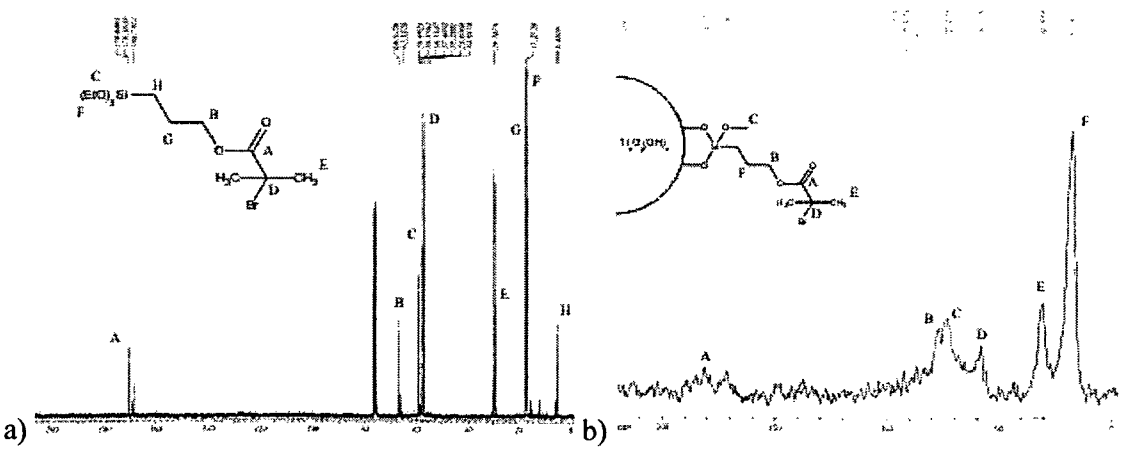

Figure 87: Comparison of the ^{13}C NMR spectra of a) initiator (C) and b) TiO_2 nanoparticles that were functionalized with initiator (C).

In case of the modification with initiator (C) a broad signal between 181 and 171 ppm of the carboxylate-group was found. Between 77 and 73 ppm a broad CH_2-signal was detected caused by the groups B and C. At 59 ppm a single peak emerged that was assigned to the tertiary carbon atom. The corresponding CH_3-groups were identified at a chemical shift of 30 ppm. At 17 ppm methyl groups of alkoxide groups and/or absorbed ethanol were detected. The signal of the Si-CH_2-group was not found, possibly due to too short scanning time. The solid state spectrum that was recorded from the particles that were functionalized with initiator (D) obtained rather broad signals compared to the spectrum that was obtained in case of the iron oxide particles. Without doubt the phenyl-ring was identified at a shift of 127 ppm. Absorbed ethanol or bound alkoxide groups were found at chemical shifts of 58 and 17 ppm. The benzylic CH_2-group was found at 27 ppm. The Si-CH_2-group resulted in a very small signal at about 20 ppm. Although long scanning times were applied it was not possible to find the CH_2 group that is bond to the chlorine atom.
The obtained TGA results and the estimated surface coverage of the titanium oxide nanoparticles are presented in table 9.

Table 9: TGA results of the functionalized titanium oxide nanoparticles and the calculated surface coverage.

Nanoparticle	**TGA Residue [%]**	**Modified Nanoparticle**	**TGA Residue [%]**	**Surface Coverage [mmol/g]**
$Ti_xO_y(OH)_z$	76.0	$Ti_xO_y(OH)_z$ + Subst. A	74.9	0.05
		+ Subst. B	69.3	0.31
		+ Subst. C	68.3	0.49
		+ Subst. D	70.2	0.42

Again, the additional mass loss after the functionalization with initiator (A) was very small. In case of the titanium oxide particles, the mass loss was just increased about 1.1 % from 24 % to 25.1 %, which corresponded to a surface coverage of 0.05 mmol/g. The modification of the

particle surface with initiator (B) led to a mass loss of 30.7 % which corresponded to a surface coverage of 0.31 mmol/g. Both ATRP initiators (C) and (D) obtained the highest surface coverage with 0.49 mmol/g and 0.42 mmol/g, respectively, deduced from mass losses of 31.7 % and 29.8 %. The obtained results corresponded to the carbon contents that were obtained via elemental analysis. Compared to the functionalized iron oxide particles, the surface coverage was slightly reduced, possibly due to worse interactions of the surface OH-groups with the silane groups.

The specific surface of the titanium oxide particles was measured with nitrogen sorption, whereby the unmodified particles had a surface of 459 m^2/g. This specific surface dropped after the functionalization with initiator (A) and (B) to 382 m^2/g and 399 m^2/g, respectively. The decrease of specific surface was more eminent if the ATRP initiators (C) and (D) were utilized for modifying the surface. After these functionalizations specific surfaces of 219 m^2/g and 184 m^2/g were measured.

These results showed that attachment of functional groups at increased temperatures resulted in a higher degree of functionalization. Furthermore, the influence of different sterical hindrances of the initiator molecules on the functionalization process and the obtained surface coverage was visible.

4.4.4.3. Functionalization of the zirconium oxide nanoparticles

A TEM image of zirconium oxide particles that were functionalized with initiator (D) is shown in figure 88.

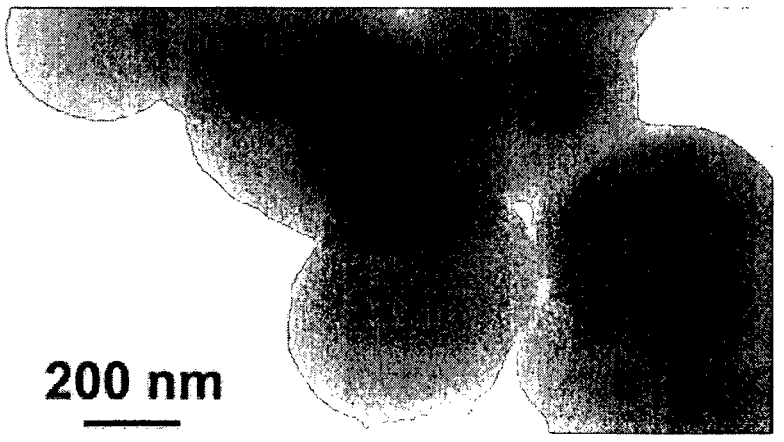

Figure 88: TEM image of zirconium oxide nanoparticles functionalized with initiator (D).

The appearance of functionalized zirconium oxide particles differed slightly from the unmodified particles. The surface became much smoother as an effect of the functionalization, while the diameter remained constant with 640 nm. The smallest carbon content in elemental analysis was obtained for the functionalization with initiator (A), where a value of 4.2 % carbon was measured. After modification of the surface with initiator (B), a carbon content of 13.9 % was observed. Functionalization with initiator (C) and (D) led to carbon contents of respectively 8.4 % and 13.0 %. The obtained results confirmed the presented data in case of the other functionalized nanoparticles.

^{13}C CPMAS NMR was performed on particles that were functionalized with initiator (C). The obtained spectrum and a comparison with the free initiator are shown in figure 89.

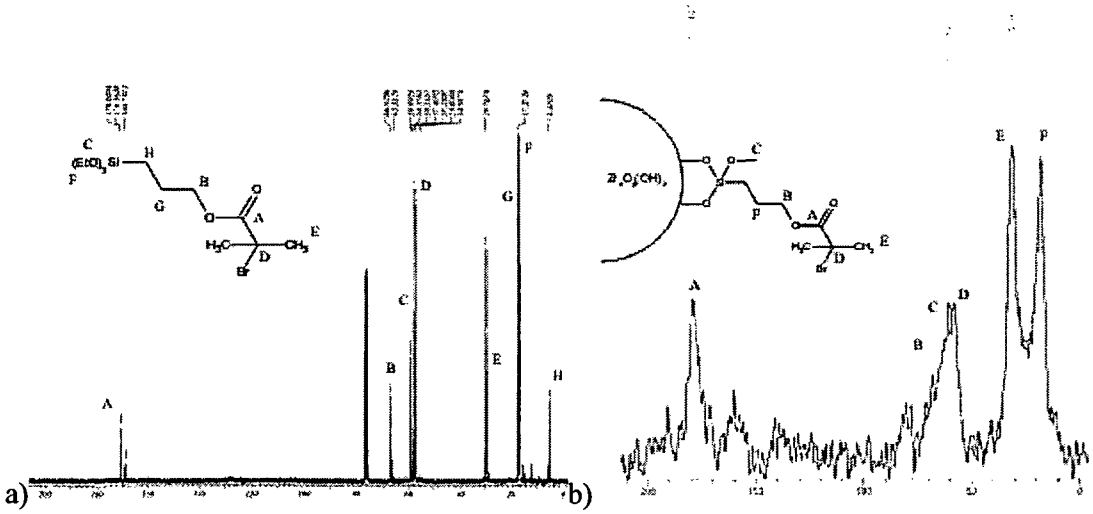

Figure 89: Comparison of the ^{13}C NMR spectra of a) initiator (C) and b) zirconium oxide nanoparticles that were functionalized with initiator (C).

The observed signal at 179 ppm in the solid state ^{13}C CPMAS NMR was assigned to the carboxylate carbon atom. A broad peak was detected between 70 and 50 ppm that was most likely caused by an overlap of (OCH_2CH_2), ($C(CH_3)_2Br$) and ($SiOCH_2CH_3$) groups. At 31 ppm the methyl-groups belonging to the tertiary carbon atom were detected. At 17 ppm the methyl-groups of absorbed ethanol or remaining alkoxide groups were observed.

The TGA results and the calculated surface coverage are shown in table 10.

Table 10: TGA results of the functionalized zirconium oxide nanoparticles and the calculated surface coverage.

Nanoparticle	TGA Residue [%]	Modified Nanoparticle	TGA Residue [%]	Surface Coverage [mmol/g]
$Zr_xO_y(OH)_z$	74.2	$Zr_xO_y(OH)_z$ + Subst. A	73.1	0.05
		+ Subst. B	56.2	0.83
		+ Subst. C	64.3	0.6
		+ Subst. D	59.3	1.13

In case of particles that were functionalized with the azo initiator (A), the mass loss increased just about 1.1 % from 25.8 % of the unmodified particles to 26.9 %, which suggested a very poor degree of functionalization corresponding to a surface coverage of 0.05 mmol/g. Modification with the photo initiator (B) led to a mass loss of 43.8 % if the particles were heated up to 800 °C, which corresponded to a surface coverage of 0.83 mmol/g. As in case of the functionalized iron oxide particles, initiator (B) revealed the second highest surface coverage. The bonding of the ATRP initiators (C) and (D) resulted in a mass loss of 35.7 % and 40.7 %, which revealed a surface coverage of 0.6 mmol/g and 1.13 mmol/g. The obtained results corresponded with the presented elemental analyses.

Nitrogen sorption analysis resulted in a specific surface of 396 m^2/g for the unfunctionalized zirconium oxide nanoparticles. The specific surface decreased to 341 m^2/g if the azo initiator was used for surface modification and to 345 m^2/g in case of the photo initiator. The bonding of the ATRP initiators (C) and (D) led to a reduction of the specific surface to 281 m^2/g and 198 m^2/g. The discrepancies between mass losses received from TGA and reduction of the specific surface area might be caused by the different molecule sizes. They resulted in a different number of attached molecules due to different sterical demands. So the surface areas that are accessible for nitrogen molecules depended not only on the degree of functionalization but also on the sterical demands of the attached molecules.

4.4.4.4. Functionalization of the zinc oxide nanoparticles

The TEM image of zinc particles that were functionalized with initiator (C) is shown in figure 90. The dried particles were redispersed in ethanol and directly used as TEM sample.

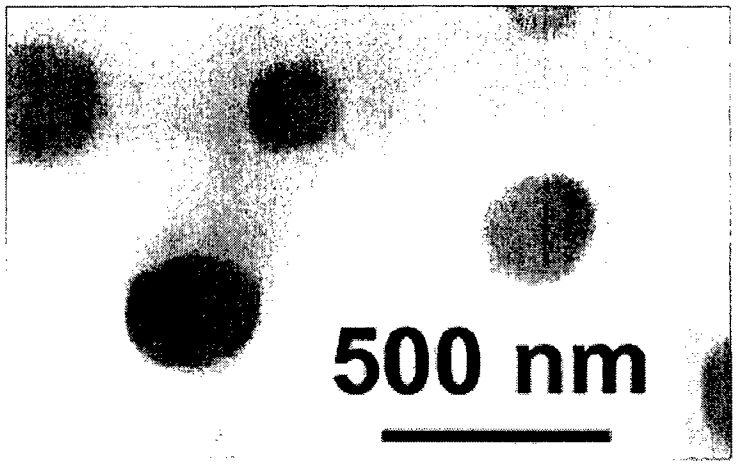

Figure 90: TEM image of zinc oxide nanoparticles that were functionalized with initiator (C).

The particles had a more homogenous appearance than the unfunctionalized zinc oxide nanoparticles. The surface modification with initiator (C) seemed to have a smoothening effect on the particles. The radius remained constant with 140 nm.

Elemental analysis of particles that were functionalized with initiator (A) obtained a carbon content of 5.0 %. Binding of photo-initiator molecules onto the surface led to a carbon content of 14.9 % in elemental analysis. The analysis of ATRP initiator (C) gave a carbon content of 16.9 %. Surprisingly the surface modification with initiator (D) resulted in a carbon content of only 6.6 % which was very low compared to results that were presented before. The carbon contents were in the same range as in case of the other metal oxide particles.

^{13}C CPMAS NMR analysis was performed on particles that were functionalized with initiator (C). The obtained spectrum and a comparison with the ^{13}C NMR of initiator (C) are shown in figure 91.

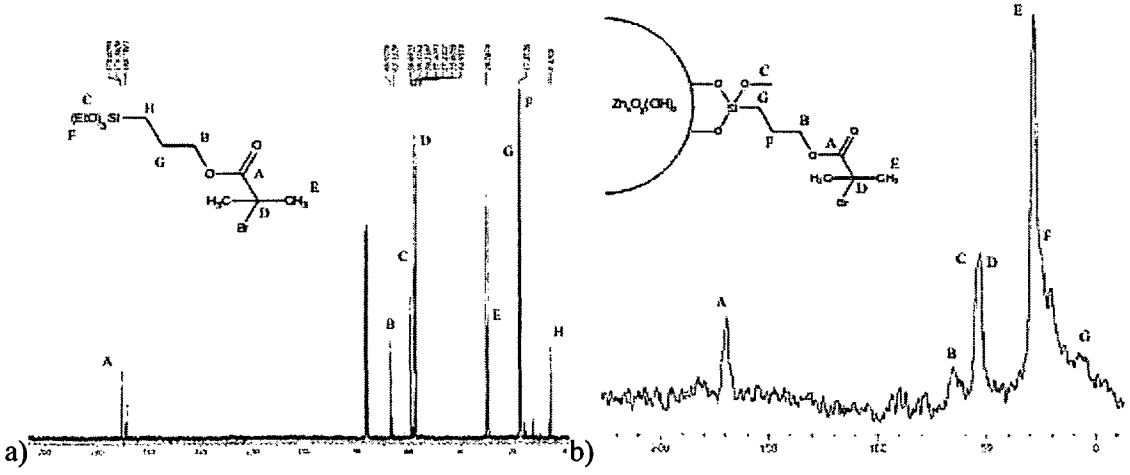

Figure 91: Comparison of the ^{13}C NMR of a) initiator (C) and b) zinc oxide particles that were functionalized with initiator (C).

At 171 ppm the signal of the carboxylate carbon atoms was detected followed by a signal at 66 ppm caused by the ester CH_2-group. From 50 to 60 ppm a broad peak was visible that was assigned to the tertiary carbon atom which is bound to the bromine and to absorbed ethanol or remaining ethoxy-groups. At 25 ppm the corresponding methyl-groups were detected, followed by the methyl groups of absorbed ethanol or unreacted ethoxy-groups. At 5 ppm a small peak that was assigned to the Si-CH_2-group was found.
The TGA results that were obtained if the modified nanoparticles were heated up to 800 °C are shown in table 11.

Table 11: TGA results of the functionalized zinc oxide nanoparticles and the calculated surface coverage.

Nanoparticle	**TGA Residue [%]**	**Modified Nanoparticle**	**TGA Residue [%]**	**Surface Coverage [mmol/g]**
$Zn_xO_y(OH)_z$	81.5	$Zn_xO_y(OH)_z$ + Subst. A	56.7	1.04
		+ Subst. B	52.2	1.23
		+ Subst. C	50.4	1.54
		+ Subst. D	64.4	0.94

The unmodified nanoparticles showed a mass loss of 28.5 %. In case of the zinc oxide particles, the functionalization process with initiator (A) led to a larger increase of mass loss of 43.3 % compared to all other modified metal oxide particles. This mass loss led to a calculated surface coverage of 0.60 mmol/g. Using initiator (B) for the surface modification resulted in a mass loss of 47.8 % which corresponded to a surface coverage of 0.81 mmol/g. The ATRP initiators (C) and (D) lost 45.6 % and 34.3 % of their mass, respectively which resulted in a surface coverage of 0.94 mmol/g in case of initiator (C) and 0.39 mmol/g in case of initiator (D). The revealed surface coverage with initiator (D) in case of the ZnO particles was the lowest compared to all other particles. The obtained results correspond to the carbon contents that were obtained in the elemental analyses.

The specific surface of the modified nanoparticles was measured via nitrogen sorption. The unmodified zinc oxide nanoparticles had a specific surface of 41 m^2/g which was a magnitude smaller than all others. This effect might have been caused by a different particle structure with lower porosity which was also observed by *Singal et al.*[259]
Functionalizing with initiator (A) led to a reduction of the specific surface to 32 m^2/g. Usage of initiator (B) reduced the specific surface to 26 m^2/g. The particles that were modified with the ATRP initiators (C) and (D) kept a measurable surface of 11 m^2/g and 22 m^2/g, respectively.

4.4.4.5. Functionalization of the aluminum oxide nanoparticles

Contrary to the other presented metal oxide nanoparticles, the functionalization approaches of aluminum oxide particles were not successful. A reason for this fact might be the increased zeta-potential of the surface OH-groups of the aluminum oxide particles. In general the zeta-potential can be seen as the overall charge a particle acquires in a specific medium and gives an indication of the stability of particle dispersions. In case of the aluminum oxide particles, eventually the high zeta-potential values of the surface OH-groups prevented significant functionalization with the ethoxy-silane derivates under the chosen conditions.

In figure 92 the zeta potentials of various metal alkoxides are presented.

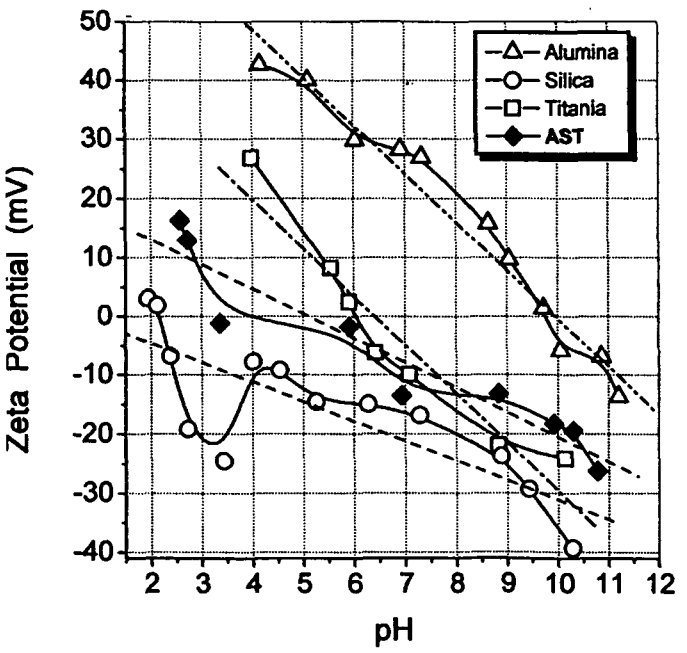

Figure 92: Zeta-potential of various metal oxides depending on the pH value.[278]

As shown in the diagram above, the zeta potential of Al_2O_3 is significantly higher compared to other metal oxides.[278, 279] The zeta potential curves of ZnO [280], ZrO_2 [281] and Fe_2O_3 [282] show slightly higher potential than the curve of TiO_2.

4.5. Photoluminescence spectroscopy of different types of TiO_2 nanoparticles

Photoluminescence spectroscopy is an extremely useful tool to obtain information about the electronic, optic and photoelectric properties of materials because it depends on electronic excitations. A number of photoluminescence studies on TiO_2 single crystals, polycrystalline powders, and thin films have been reported.[266-269] Recently, photoluminescence spectra of TiO_2 nanocrystals below the characteristic band-gap have also been measured, where the origin for the luminescence was ascribed to quantum confinement effect.[270, 271]

The luminescence properties of amorphous TiO_2 particles synthesized from metal salts (chapter 3.3.2.) and alkoxides modified with 3-chloro-pentane-2,4-dione (chapter 3.2.3.1.) were compared with crystalline samples, which were produced in a hydrothermal approach with a diameter of 19.5 nm (chapter 3.2.3.7), crystalline particles synthesized according to a literature procedure published by *Chemseddine et al.* [272] (diameter 13.5 nm), and crystalline TiO_2 nanoparticles, which were produced via chemical vapor deposition (CVD) by *Berger et al.*[273] These particles have an irregular shape, a diameter between 10 and 20 nm and a BET surface of 130 m^2/g.

In all cases, except the particles, which were synthesized via CVD, 30 mg of the nanoparticles were dispersed in 2 ml ethanol and treated for 20 minutes in an ultrasonic bath. The TiO_2 nanoparticles that were produced via CVD were measured in vacuum.
In a first step the diffuse reflectance spectra of the different TiO_2 nanoparticles were investigated via UV/VIS spectroscopy.

In figure 93 the obtained spectra are presented.

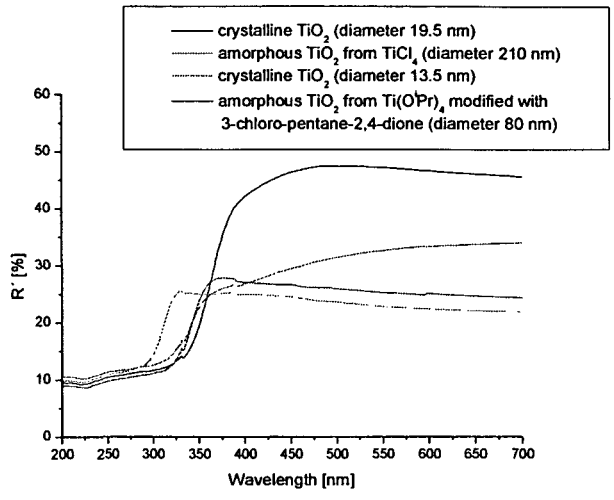

Figure 93: Diffuse reflectance spectra of the analyzed TiO_2 nanoparticles.

The crystalline particles with a diameter of 19.5 nm showed emission at a wavelength of 380 nm which corresponded to the band-gap of bulk anatase of 3.25 eV.[274] While the patterns normally showed a sharp decrease of the reflectance, in case of amorphous TiO_2 nanoparticles (prepared from $TiCl_4$ via a microemulsion approach), an additional absorption between 400 and 600 nm was observed. Both amorphous types of TiO_2 nanoparticles showed an equivalent band-gap of 360 nm which corresponded to 3.44 eV.[274] The crystalline TiO_2 nanoparticles with a diameter of 13.5 nm showed an increased band-gap energy, due to the presence of quantum size effects.

In figure 94 the photoluminescence spectra of the investigated TiO_2 nanoparticles are presented. The spectra were recorded at room temperature. The samples were excited at 270 nm.

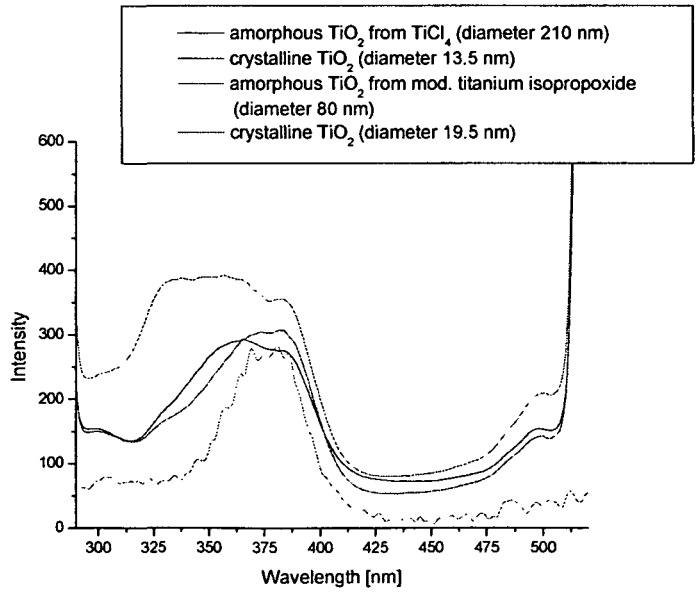

Figure 94: Photoluminescence spectra of the analyzed TiO_2 particles (slit excitation: 10, slit emission: 10, scan speed 500 without filter).

The emission wavelength of amorphous TiO_2 nanoparticles, synthesized from alkoxides modified with 3-chloro-pentane-2,4-dione, was 380 nm, while amorphous TiO_2 nanoparticles from $TiCl_4$ showed emission bands at 365 nm and 380 nm. The crystalline TiO_2 with a diameter of 19.5 nm showed a broad peak with maxima at 373 nm and 380 nm. Due to quantum effects, the smaller TiO_2 not only emitted light of a wavelength of 380 nm but also at higher energies between 327 nm and 372 nm. In case of very small particles, excited electrons not only emit light with energies, which match the difference between the lowest occupied energy level of the conduction band and the highest energy level of the valence band (band-gap) but also higher in energy. The same effect was observed by *Serpone et al.*, using anatase particles with a diameter of 13.3 nm, due to non communication of states within the conduction band.[275]

As titanium oxide is an indirect semiconductor some emissions might have been observable at room temperature because thermal quenching is highly likely. Therefore, the measurement was repeated at 77 K as the sample cell was cooled with liquid nitrogen. In figure 95 the obtained spectra are presented.

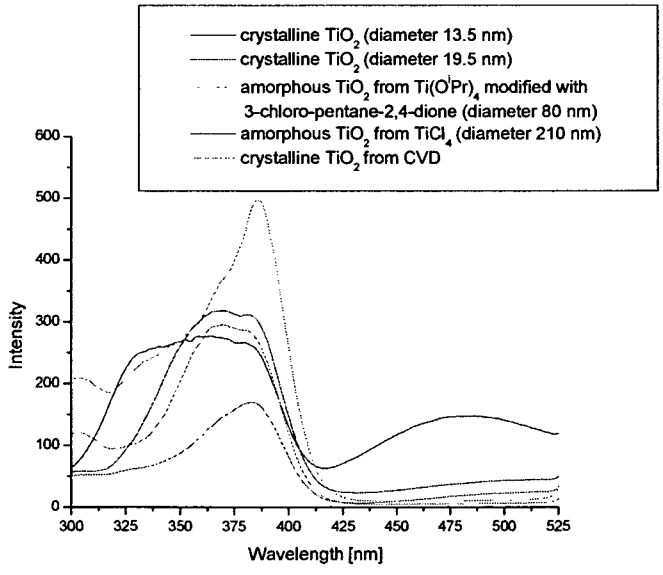

Figure 95: Photoluminescence spectra of the analyzed TiO_2 particles at 77 K (slit excitation: 10, slit emission: 10, scan speed 500, filter at 290 nm).

Additionally to the peaks that were observed at room temperature, the crystalline particles synthesized in solution showed a second excitation wavelength at 77 K as the occurrence of thermal quenching at low temperatures is highly unlikely. While in case of the particles with a diameter of 13.5 nm a second peak was observed at 482 nm, the crystalline particles with a diameter of 19.5 nm showed a second peak at 525 nm. The evolution of this second peak was analyzed in more detail in case of the crystalline particles that were produced in a hydrothermal approach with a diameter of 19.5 nm.
During the cooling phase, every 10 seconds a spectrum was recorded. In figure 96 the obtained spectra are presented.

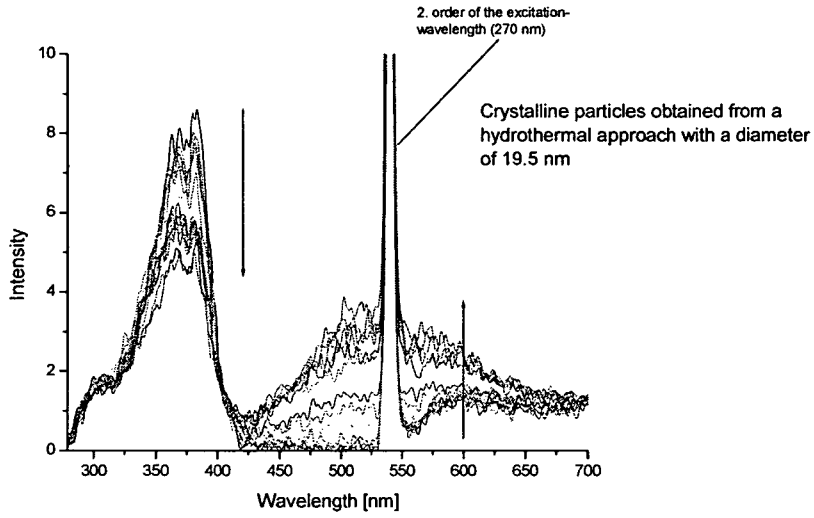

Figure 96: Photoluminescence spectra of TiO_2 particles with a diameter of 19.5 nm during the cooling with liquid nitrogen (slit excitation: 2.5, slit emission: 2.5, scan speed 500, filter at 290 nm).

In the presented spectra a noticeable increase of the peak at 525 nm during the cooling period was visible. The decrease of the peak at a wavelength of 375 might be caused by condensed water on the windows of the measuring cell.

The performed photoluminescence investigations revealed significant differences between the analyzed particles. Two parameters seemed to have great influence on the obtained photoluminescence wavelength. (i) The diameter of the particles, which has a direct influence

on the observed photoluminescence wavelength as a smaller particle diameter caused a shift to higher energies. (ii) Crystallinity combined with the size, led in case of the TiO_2 particles that were synthesized in solution to the evolution of a second emission band at lower energies at 77 K.

4.6. Photoluminescence spectroscopy of different types of ZrO_2 nanoparticles

Zirconia is an ideal medium for photonic applications, due to its high refractive index, wide energy band gap, low optical losses, and high chemical and photochemical stability, which makes photoluminescence spectroscopy an ideal method for characterization purposes.[276]
The two types of presented ZrO_2 nanoparticles, on the one hand using 3-chloro-pentane-2,4-dione modified zirconium alkoxides (chapter 3.2.3.2.) resulting in a diameter of 44 nm and on the other hand using zirconium salts (chapter 3.3.3.) resulting in a diameter of 640 nm, were analyzed via photoluminescence spectroscopy and compared to the spectra of commercially available crystalline ZrO_2 from Degussa (2094E, specific surface: 78 m^2/g). The amorphous particles were synthesized via a microemulsion approach. The sample preparation for the photoluminescence spectroscopy was performed as described in case of the investigated TiO_2 nanoparticles.
In a first step the diffuse reflectance spectra of all investigated ZrO_2 particles were measured (figure 97).

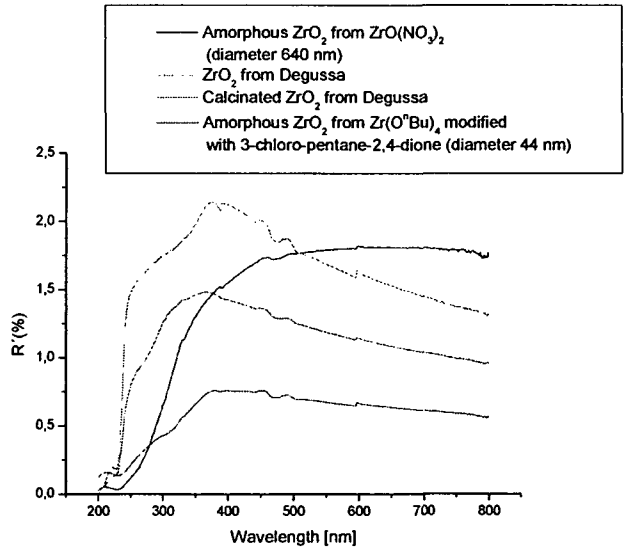

Figure 97: Diffuse reflectance spectra of the analyzed ZrO_2 nanoparticles.

Similar as in case of the amorphous TiO_2 nanoparticles, the recorded patterns of both types of amorphous ZrO_2 particles showed a rather smooth decrease of the reflectance, typical for amorphous samples. In case of 3-chloro-pentane-2,4-dione modified particles, eventually a second absorption at higher wavelength was observed. The crystalline sample obtained from Degussa, exposed a different curve progression. Both reflection patterns showed a sudden decrease at 235 nm corresponding to the bandgap energy.[277] Furthermore, they revealed a second decrease of the reflection pattern between 290 and 310 nm, eventually caused by the presence of quantum size effects.

The measured photoluminescence spectra of the different ZrO_2 nanoparticles were recorded in ethanol and are presented in figure 98.

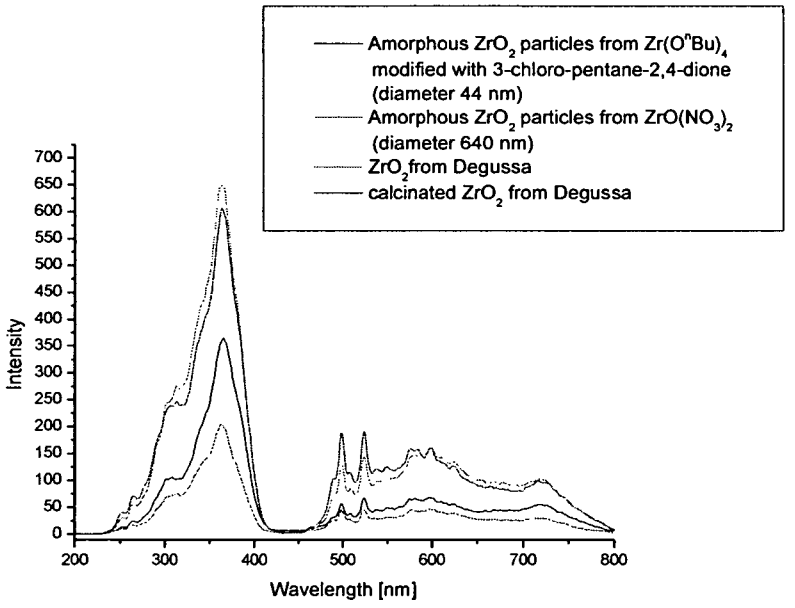

Figure 98: Photoluminescence spectra of the different ZrO_2 nanoparticles (slit excitation: 5.0, slit emission: 5.0, scan speed 500, filter excitation: UG5). The excitation wavelength was 220 nm.

Using an excitation wavelength of 220 nm, one fluorescence emission at 364 nm and three weak fluorescence emissions at 249 nm, 264 nm, and 313 nm could be observed, respectively. The emission patterns of all four samples looked very similar. Contrary to the emission spectra in case of TiO_2, no influence of crystallinity or size effects were observed. According to *Liang et al.* it can be attributed that emission appearing at 364 nm correspond to near band-

edge transitions.[277] The broad band between 460 nm and 800 nm corresponds to the second order of the discussed emissions.

The analyses were repeated at 77 K, to investigate, if the intensity of the fluorescence bands could be increased. In figure 99 the obtained emission patterns are presented.

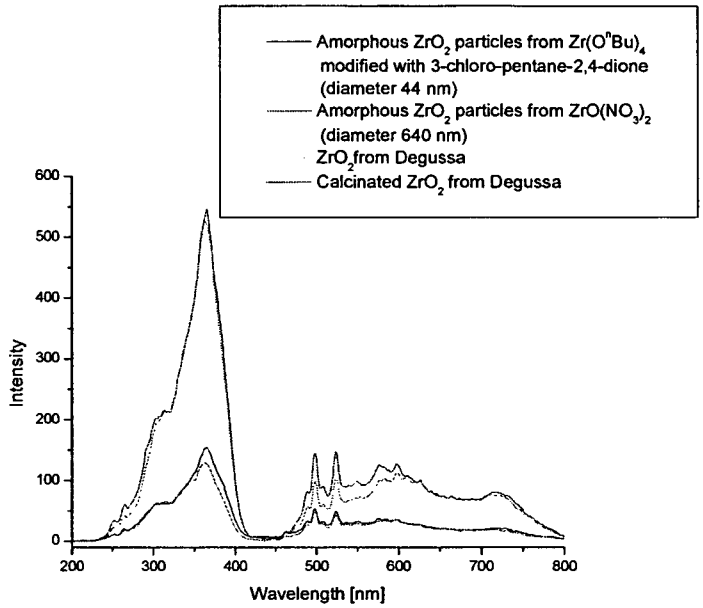

Figure 99: Photoluminescence spectra of the different ZrO_2 nanoparticles at 77 K (slit excitation: 5.0, slit emission: 5.0, scan speed 500, filter excitation: UG5). The excitation wavelength was 220 nm.

Compared to the investigation of the various TiO_2 particles at 77 K, which revealed additional emission bands in case of crystalline systems synthesized in solution, the observed emission patterns remained constant in case of ZrO_2. The change of intensity might have been caused by a different cuvette position.

4.7. Short summary

In this chapter the synthesis of various polymerization initiator molecules and their attachment to the surface of oxidic and metallic nanoparticles was discussed. Different types of initiators for free and controlled radical polymerization were presented that had, depending on the type of nanoparticle, either a thiol or a silane functionality, which allowed linkage to the corresponding surface. The success of the functionalization process was investigated via ^{13}C CPMAS NMR, TGA, nitrogen sorption, DLS, TEM, elemental analysis and FTIR. The

obtained results showed that there were several parameters which had an influence on the obtained degree of functionalization:

(i) The conditions during the functionalization process were of great importance. Taken into account that particles, which were functionalized at room temperature with initiator (A) had in general the lowest surface coverage, the influence of increased temperature was obvious. Furthermore, the particles that were functionalized at increased temperatures (initiator (C) and (D)) always showed the largest decrease of specific surface area in the nitrogen sorption analyses.

(ii) The zeta potential of the surface OH groups depended very strongly on the materials the particles were made of. Zinc oxide and zirconium oxide showed the highest degree of functionalization, while aluminum oxide particles did not allow any functionalization under the chosen conditions.

(iii) The different sizes of the initiator molecules also might have had influence on the surface coverage, which became visible if the surface coverage of initiator (A) and (B) were compared. It seemed as if surface functionalization was more difficult to perform in case of initiator (A) due to sterical hindrance.

FTIR-measurements revealed a decrease in the intensity of the broad OH-bands at 3200-3600 cm^{-1} after the functionalization of the surface was finished. However, OH-groups were still visible after the modification, which could have two reasons: (i) the particle core contained still uncondensed groups and/or (ii) the surface was not fully functionalized.

Furthermore, the photoluminescence properties of different functionalized titanium oxide nanoparticles were investigated. Depending on the diameter of the particles and their crystallinity, shifts of the photoluminescence wavelength were detected.

5. Aggregation of SiO_2 particles

The assembly of nanoparticles towards macroscopic materials are of both fundamental and technological interest. The two-phase synthesis of monolayer-protected nanoparticles[140, 195, 283], stepwise layer-by-layer construction[195, 284-286], ordering via DNA and other molecule assembling techniques[287-290] are investigated with high effort.

The functionalized SiO_2 nanoparticles presented earlier (chapter 4.1.) were used for the investigation of the aggregation behavior of nanoparticles caused by hydrogen bonds and

ionic interactions. First the dispersion capacity of various solvents was investigated to find a solvent which allows the dispersion of particles functionalized rather hydrophobic and hydrophilic.

5.1. Investigation of the influence of solvent effects on the redispersion of unmodified and surface functionalized silica nanoparticles

The influence of the solvent on the dispersing abilities was investigated via DLS. Exactly 3 mg of the different types of particles were dispersed in 3 ml solvent, ultrasonically treated for 3 hours and rested over night for these measurements.
In table 12 the obtained data for the unfunctionalized SiO_2 nanoparticles are presented.

Table 12: DLS results of the dispersion of unfunctionalized SiO_2 nanoparticles.

Solvent	Radius [nm]	Comment
Ethanol	42	No aggregates in solution; small amount of precipitate at the bottom of the cuvette
Water	51	No aggregates in solution; no precipitate at the bottom of the cuvette
Chloroform	---	No dispersion possible
Toluene	---	No dispersion possible
Methanol	42	No aggregates in solution; large amount of precipitate at the bottom of the cuvette
DMF	---	No dispersion possible
Acetonitrile	54	No aggregates in solution; large amount of precipitate at the bottom of the cuvette
THF	---	No dispersion possible

In chloroform, toluene, DMF and THF it was impossible to redisperse the unfunctionalized SiO_2 nanoparticles. Obviously the hydrophilic surface OH groups required more polar solvents to allow redispersion. In case of acetonitrile and methanol partial redispersion was obtained. DLS measurements obtained radii of 54 nm and 42 nm, respectively, but large amounts of undispersed particles were found at the bottom of the cuvette. These solvents did

not have the capacity to redisperse large amounts of SiO_2 nanoparticles. Better results were obtained with ethanol and water. In ethanol only a small amount of precipitate was found and DLS analysis revealed a radius of 42 nm. In water no precipitate at all was observed at the bottom of the cuvette and DLS analysis obtained a radius of 52 nm. Similar results were obtained by *Bertrand et al.*, who observed a strong influence of the used non-aqueous solvent on the electrostatic interactions between the particles and between the particles and the solvent.[291] The different radii that were observed in the DLS analyses might have been caused by different solvent-particle interactions.

In table 13 the obtained results for the SiO_2 nanoparticles functionalized with 3-amino-propyltriethoxysilane are shown.

Table 13: DLS results of the dispersion of SiO_2 nanoparticles functionalized with 3-amino-propyltriethoxysilane.

Solvent	**Radius [nm]**	**Comment**
Ethanol	51	No precipitate at the bottom; very little aggregate in solution (< 5 %)
Water	61	Large amount of precipitate at the bottom; much aggregated species in solution
Chloroform	---	No dispersion possible
Toluene	58	No precipitate at the bottom; no aggregate in solution
Methanol	241/365	Large amount of precipitate at the bottom of the cuvette; much aggregated species in solution
DMF	---	No dispersion possible
Acetonitrile	64/237	Large amount of precipitate at the bottom of the cuvette; 50 % of the particles aggregated in solution
THF	56/215	Large amount of precipitate at the bottom of the cuvette; 50 % of the particles aggregated in solution

In those cases where precipitate remained at the bottom of the cuvette, further addition of solvent led to dispersion of the residue. As the dispersing-ability of different solvents was compared, no additional solvent was added to the system.

As can be seen above, dispersion of the dried particles was obtained neither in chloroform nor in DMF because both solvents can not form hydrogen-bonds with the amino groups of the attached silane. The dispersion in methanol worked very poorly. Huge precipitates were still situated at the bottom of the cuvette and large aggregates were measured in solution. In acetonitrile and THF the dispersion of the functionalized particles did not work better because THF could not interact with the surface attached amino groups. Large amounts of precipitated particles were observed at the bottom of the cuvettes, but in solution isolated particles were detected despite the presence of aggregated particles as well. If water was used for the dispersion of the particles, a large amount of the particles remained precipitated at the bottom of the cuvette. During the measurement only dispersed particles and no aggregates were detected in the solution. In ethanol and toluene total dispersion of the particles was obtained, while in case of ethanol a small amount of precipitated particles was detected. In toluene all particles were dispersed as this hydrophobic solvent was able to form a solvation shell around the particles.

As shown in chapter 4.1, the pH value has a strong influence on the ionization state of surface functionalities. The influence of different pH values in various solvents was investigated. In each solvent the particles were dispersed, the pH value was adjusted either with ammonia or HCl, treated in the ultrasonic bath for several hours and rested over night. In table 14 the obtained results are given.

Table 14: DLS results of particles that were functionalized with 3-amino-propyltriethoxysilane in different solvents at different pH values.

Solvent	Radius in nm at pH 2	Radius in nm at pH 10
Ethanol	40 (Much precipitation at the bottom of the cuvette)	45
Water	122 (Much precipitation at the bottom of the cuvette; very low count rate)	37 (Much precipitation at the bottom of the cuvette)
Methanol	50	70 (Very broad peak)

The best dispersing medium at low pH value for particles that were functionalized with 3-amino-propyltriethoxysilane was methanol, where no precipitation was observed, possibly due to better interaction between the positively charged amino groups and the OH-groups of methanol. At higher pH values ethanol delivered the best dispersion.
These results are supported by a paper recently published by *Jesionowski*, who described the zeta potential of amino functionalized silica particles depending on the pH value.[292] He observed an increased zeta potential depending on the amount of surface amino-groups, which led to increased radii in DLS analysis.

The dispersion-abilities were also investigated with SiO_2 particles that were functionalized with 2-(carbomethoxy)ethyltrichlorosilane. The obtained results are shown in table 15.

Table 15: DLS results of the dispersion of SiO_2 nanoparticles which were functionalized with 2-(carbomethoxy)ethyltrichlorosilane.

Solvent	**Radius [nm]**	**Comment**
Ethanol	45	Small amount of precipitate at the bottom; no aggregate in solution
Water	55/213	Large amount of precipitate at the bottom
Chloroform	200	No precipitate at the bottom
Toluene	---	No dispersion
Methanol	56	Total dispersion
DMF	---	No dispersion
Acetonitrile	60	No aggregate in solution; small amount of precipitate at the bottom
THF	65/1500	No precipitate at the bottom

No dispersion at all was achieved with toluene and DMF as organic solvent. In water the dispersion did not work any better. At the bottom of the cuvette a large amount of precipitate was observed. In solution aggregated and free particles were measured as well. In chloroform only rather small aggregates (diameter 200 nm) were found, possibly due to weak interactions between carboxylate groups and the solvent. Nevertheless, no white precipitate was present in the cuvette. In case of THF just a small part of the particles was dispersed in suspension; most

of the functionalized SiO_2 nanoparticles were still aggregated in the suspension. The appropriate solvents for this type of functionalization seem to be acetonitrile, ethanol and methanol. Obviously the more hydrophilic carboxylate groups showed higher dispersion capacities in more polar solvents because the formation of hydrogen bonds was possible.

The influence of the solvent at different pH values was investigated while the particles were dispersed in the chosen solvent, the pH value was adjusted either with ammonia or HCl, treated in the ultrasonic bath for several hours and rested for 3 hours. In table 16 the obtained results are given.

Table 16: DLS results of particles that were functionalized with 2-(carbomethoxy)ethyltrichlorosilane in different solvents at different pH values.

Solvent	**Radius in nm at pH 2**	**Radius in nm at pH 10**
Ethanol	93 (Aggregation was observed)	65
Water	75 (Broad peak)	35 (Precipitation occurred at the bottom of the cuvette)
Methanol	43 (Precipitation occurred at the bottom of the cuvette; much aggregation in solution)	177 (Precipitation and aggregation were observed)

At low pH values the dispersion in methanol delivered the best results while high pH values led to aggregation. In ethanol the best dispersion was obtained at high pH values.

From these results different conclusions can be drawn. Depending on the type of functionalization, different solvents were appropriate for DLS investigations. It was shown that the measured particle radius depended very strongly on the used solvent due to different interaction of the functional groups on the particle surface with the solvent molecules.[292] The only solvent that allowed the dispersion of both types, ester and amine, was ethanol which was used for the DLS investigations of all other functionalized and unfunctionalized particles. A reason for this fact might be the balanced hydrophilicity and hydrophilicity of ethanol that

allows interaction, on the one hand with the still remaining OH-groups on the particle's surface or e.g. carboxyl-groups and on the other hand with more hydrophobic organic groups. Comparison of these results with literature data was difficult to perform as there is a lack of systematic studies of the interaction of different surface functionalities in various solvents at certain pH values.

5.2. Investigation of the aggregation behavior of the two types of functionalized silica nanoparticles

The interactions between the two types of functionalized SiO_2 particles were investigated via suspending them in ethanol, mixing them in different ratios at certain pH values, shaking for 30 seconds and then measuring the obtained suspension by DLS. When the samples were rested over night, the aggregated particles precipitated to the bottom of the cuvette due to the formation of large aggregates. For this approach, SiO_2 particles were used, which had a diameter of 93 nm in the unfunctionalized state. In table 17 the obtained results at a pH value of 5 are listed.

Table 17: DLS results of the aggregation of SiO_2 nanoparticles functionalized with 2-(carbomethoxy)ethyltrichlorosilane and 3-amino-propyltriethoxysilane respectively at a pH value of 5. The concentration of the two suspensions was 0.70 g particles/l. The given particle ratios are volumetric ratios.

Particle ratio	Radius / amount (non aggregated)	Radius / amount (aggregated)
SiO_2 particles functionalized with 2-(carbomethoxy)ethyltrichlorosilane (C)	46 nm 100 %	
10% A + 90 % C	138 nm 53 %	856 nm 47 %
20 % A + 80 % C		576 nm 100 %
30 % A + 70 % C		396 nm 100 %
40 % A + 60 % C		443 nm 100 %
50 % A + 50 % C		585 nm 100 %
60 % A + 40 % C		310 nm 100 %
70 % A + 30 % C	85 nm 7 %	400 nm 93 %
80 % A + 20 % C	164 nm 80 %	3910 nm 20 %

90 % A + 10 % C	175 nm 64 %	880 nm 36 %
SiO_2 particles functionalized with 3-amino-propyltriethoxysilane (A)	51 nm 100 %	

The amount of a certain species was obtained via integration of the peak area by the DLS software. At a pH value of 5 both functional groups should occur in a non-ionic form which should lead to particle-particle interactions via hydrogen bonds. The two types of functionalized particles in their pure form had a diameter of 92 nm (C: ester-functionality) and 102 nm (A: amino-functionality) in ethanol, respectively. If the amount of suspension (A) was raised, the particles began to aggregate. At a ratio of 10 % suspension (A) a single peak at 138 nm and a broader peak at 856 nm were visible. The second peak was a result of the aggregated species that had, at this point, a ratio of 47 %.

If the suspension was shaken, the obtained aggregate was destroyed easily, which led to the assumption that no ionic interactions took place. Raising the amount of suspension (A) the radius of the aggregates decreased until a minimum of 400 nm was reached. At a ratio of 50:50 the radius of the aggregated nanoparticles reached a maximum with a diameter of 585 nm. A possible explanation for this maximum was the balance of donor and acceptor molecules that were present in the system which led to the stabilization of larger structures. At ratios of 70:30 and 40:60, minima of the size of the aggregate were detected. In case of an excess of suspension (A), a second fraction was detected in the DLS measurements which indicated the presence of non-aggregated particles or smaller aggregates.

In figure 100 the normalized intensity correlation function and the DLS plots of the mixtures 10 % A + 90 % C, 50 % A + 50 % C and 90 % A + 10 % C are shown.

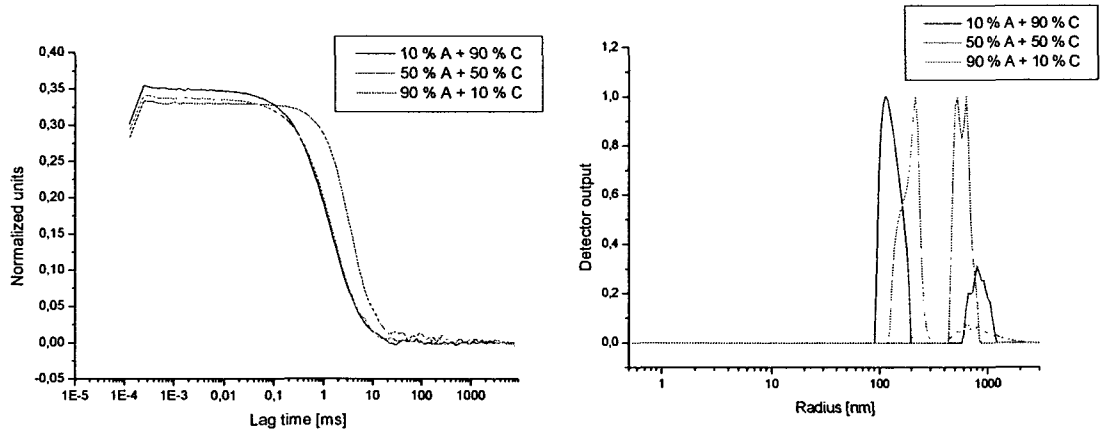

Figure 100: Normalized intensity correlation function and the DLS plots of the mixtures 10 % A + 90 % C, 50 % A + 50 % C and 90 % A + 10 % C.

As shown in figure 100 the normalized correlation intensity functions had the characteristic form of DLS correlation curves and showed only one step despite the massive presence of aggregated species which confirmed that the measured radii of aggregates were accurate and not falsified by too large sizes.[293]

The measurements were repeated with a pH value of 2 that was adjusted with 2 M HCl. The same particles as used at pH 5 were used for this investigation. The results are shown in table 18.

Table 18: DLS results of the aggregation of SiO_2 nanoparticles functionalized with 2-(carbomethoxy)ethyltrichlorosilane and 3-amino-propyltriethoxysilane, respectively, at a pH value of 2. The concentration of the two suspensions was 0.70 g particles/l. The given ratios are volumetric ratios.

Particle ratio	**Radius / amount (non aggregated)**	**Radius / amount (aggregated)**
SiO_2 particles functionalized with 2-(carbomethoxy)ethyltrichlorosilane (C)	46 nm 100 %	
10% A + 90 % C	101 nm 75 %	324 nm 25 %
20 % A + 80 % C	94 nm 100 %	
30 % A + 70 % C	228 nm 15 %	515 nm 80 %
40 % A + 60 % C	228 nm 10 %	650 nm 90 %
50 % A + 50 % C	80 nm 10 %	401 nm 75 %
60 % A + 40 % C	114 nm 15 %	1340 nm 85 %
70 % A + 30 % C	239 nm 100 %	
80 % A + 20 % C		660 nm 98 %
90 % A + 10 % C	249 nm 98 %	
SiO_2 particles functionalized with 3-amino-propyltriethoxysilane (A)	51 nm 100 %	

At a pH value of two, the aggregation process was mainly caused by ionic interactions as the amino derivate probably was positive charged due to protonation, while in case of the ester derivate protonation was rather unlikely under these conditions. The saponification of the ester group until the DLS experiment started was also unlikely as the period of time was too short and the conditions too mild. If the ratio of solution (A) was raised, aggregation was observed. At this pH value, up to 30 % solution (A), the interactions between the two functionalities seemed to be very weak and even at higher ratios particles that were not bond to the aggregates were observed.

At a pH value of 10 the measurement was repeated, in which the pH value was adjusted with 2M NH_3. The obtained results are shown in table 19.

Table 19: DLS results of the aggregation of SiO_2 nanoparticles functionalized with 2-(carbomethoxy)ethyltrichlorosilane and 3-amino-propyltriethoxysilane, respectively, at a pH value of 10. The concentration of the two suspensions was 0.70 g particles/l. The given ratios are volumetric ratios.

Particle ratio	Radius / amount (non aggregated)	Radius / amount (aggregated)
SiO_2 particles functionalized with 2-(carbomethoxy)ethyltrichlorosilane (C)	45 nm 100 %	
10% A + 90 % C	174 nm 86 %	883 nm 14 %
20 % A + 80 % C		313 nm 100 %
30 % A + 70 % C		484 nm 100 %
40 % A + 60 % C		680 nm 100 %
50 % A + 50 % C		641 nm 100 %
60 % A + 40 % C		541 nm 100 %
70 % A + 30 % C		464 nm 100 %
80 % A + 20 % C	204 nm 96 %	1230 nm 4 %
90 % A + 10 % C	74 nm 28 %	207 nm 26 %
SiO_2 particles functionalized with 3-amino-propyltriethoxysilane (A)	51 nm 100 %	

At a pH value of 10 the obtained results were quite similar to the measurements at a pH value of 5. At this pH value part of the ester groups probably became saponified, while no influence on the amino-functionality was expected. At small ratios of dispersion (A), small and large aggregates were detected by DLS. At higher amounts of dispersion (A), only one fraction was observed that showed a minimum at a ratio of 20:80 and 70:30. The largest aggregates were detected if the mixture consisted of 40 % of suspension (A) and 60 % of suspension (C). At 80 % and 90 % of suspension (A), two different types of aggregates were observed.
Taking in account the results at pH value 5, no big differences were observed. It seemed as if ionization was the determining force of the aggregation only at low pH values.[292]

The presented aggregates consisted of particles with nearly the same diameter. SiO_2 particles that were functionalized with 2-(carbomethoxy)ethyltrichlorosilane with a radius of 108 nm were mixed with SiO_2 particles that were functionalized with 3-amino-propyltriethoxysilane with a radius of 86 nm to investigate the influence of different particle diameters on the aggregation process. In table 20 the influence of the particle diameter was analyzed.

Table 20: DLS results of the aggregation of SiO_2 nanoparticles functionalized with 2-(carbomethoxy)ethyltrichlorosilane (108 nm) and 3-amino-propyltriethoxysilane (86 nm), respectively, at a pH value of 5. Both dispersions had a concentration of 0.70 g particles/l. The given ratios are volumetric ratios.

Particle ratio	Radius / amount (non aggregated)	Radius / amount (aggregated)
SiO_2 particles functionalized with 2-(carbomethoxy)ethyltrichlorosilane (E)	54 nm 100 %	
10% D + 90 % E	120 nm 85 %	1590 nm 15 %
20 % D + 80 % E	240 nm 84 %	1850 nm 15 %
30 % D + 70 % E		1660 nm 100 %
40 % D + 60 % E		910 nm 100 %
50 % D + 50 % E		1184 nm 100 %
60 % D + 40 % E		628 nm 100 %
70 % D + 30 % E		587 nm 100 %
80 % D + 20 % E	156 nm 4 %	665 nm 96 %
90 % D + 10 % E	54 nm	232-1000 nm

SiO_2 particles functionalized with 3-amino-propyltriethoxysilane (D)	43 nm 100 %

If two different particle diameters were utilized, the maximum size of the obtained aggregates was slightly larger than the size of the aggregates that contained particles with only one diameter. The reason for this observation might be that different particle sizes might have allowed closer particle contact which could have led to more surface to surface contact between the different types. Verification of the postulated explanation by literature data is difficult to perform, as no systematic studies of the aggregation behavior of surface functionalized particles with different diameters are published.
The technical limit in case of the measured radius of the used DLS instrument was 1.5 µm which was exceeded by various values given above. Therefore, the presented values have to be interpreted with care.

In figure 101 the normalized intensity correlation function and the DLS plots of the mixtures 10 % D + 90 % E, 50 % D + 50 % E and 90 % D + 10 % E were shown to demonstrate that the correlation functions are still regularly formed despite the large aggregates.

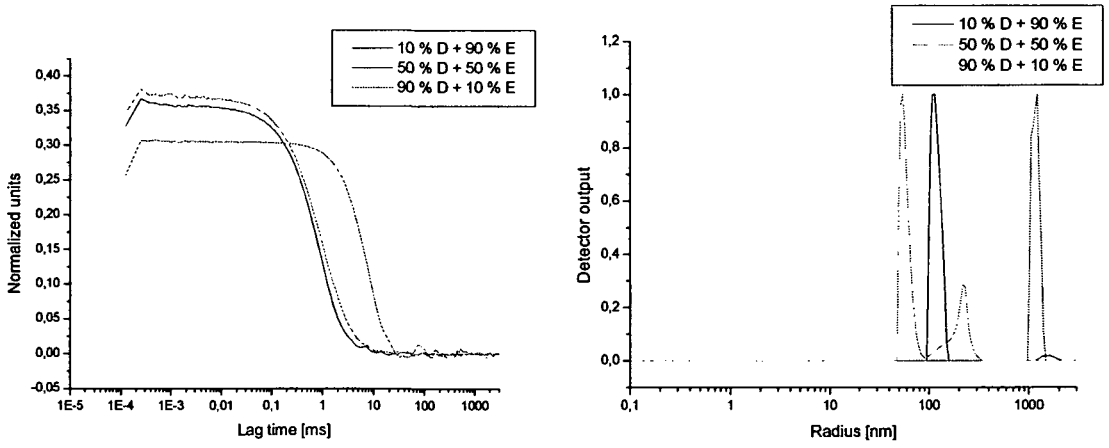

Figure 101: Normalized intensity correlation function and the DLS plots of the mixtures 10 % D + 90 % E, 50 % D + 50 % E and 90 % D + 10 % E.

Despite exceeding the technical limits of the instrument, the normalized correlation intensity functions had the characteristic form of DLS correlation curves and showed only one step despite the massive presence of aggregated species.

5.3. Short summary

In this chapter the dispersing capacity of different solvents was discussed. The obtained results confirmed that ethanol is a solvent that could disperse both unfunctionalized SiO_2, where the surface OH groups required rather hydrophilic conditions and functionalized particles as well, where the organic entities preferred more hydrophobic solvents, depending on the type of functionalization. Furthermore, the aggregation behavior of surface functionalized SiO_2 particles was investigated at different pH values. It seemed is if ionic interactions dominated the aggregation process rather at lower pH values, while hydrogen bondings were favored at higher pH values. Interpreting these results, it must be taken into account that one type of the particles was functionalized with an ester containing silane. In a controlling experiment these particles were dispersed in isopropanol and treated with a small amount of concentrated HCl. The particles were stirred for two days, isolated and washed. In the ^{13}C CPMAS NMR additional signals emerged at 56.2 ppm and 14.8 ppm, which led to the assumption that hydrolysis occurred. This chemical modification might have influenced the aggregation behavior of the particles.

6. Polymerization of the organic shell

In this work, the organic shell was formed via "grafting from" polymerization. The polymers that are presented here were synthesized via thermally or photochemically induced free radical polymerization and controlled radical polymerization (ATRP). Thus ATRP allows a better control over the polymer properties, e.g., the thickness of the organic shell, and avoids partially problems arising from termination reactions such as coupling of radicals located at different particles.

6.1. Polymerization of the organic shell around Au- and Au@SiO_2 nanoparticles

ATRP was chosen to make sure that polymerization was initiated only on the particle surface and not in solution like in the case of commonly applied free radical initiators.[145] Nevertheless, polymerization in solution can be thermally initiated but the thereby formed polymer can be separated easily by centrifugation in THF, due to the solubility of the free polymer in this solvent and the much lower density compared to the core-shell particles.

The "grafting from" polymerization was carried out using MMA, styrene, methacrylic acid trimethyloxysilyl-propylester and isoprene as monomers. The mentioned monomers were selected because ATRP of MMA and styrene is well investigated.[144, 294, 295] Additionally, the similarity of the molecular structure of the used initiator and of MMA supported the initiation process.[163] Methacrylic acid trimethyloxysilyl-propylester was chosen to induce a group capable to carry out the sol-gel process. Isoprene was used because it is a typical monomer for the industrial production of elastomers.

Two different catalytic active systems were used for the polymerizations. CuCl was used as metal species, because the catalytic activity was lower compared to other copper halides, which caused less termination reactions via recombination through the smaller amount of radicals in the system.[143] N,N,N′,N′,N′′-Pentamethyldiethylenetriamine (pmdeta)[172] and tris(2-(dimethylamino)ethyl)amine (Me_6Tren)[172] were used as ligands. Both catalysts had their assets and drawbacks. While pmdeta required increased temperatures (typically between 70 and 120 °C depending on the monomer) resulting in higher polymerization yield but also in polymerization in solution, Me_6Tren showed initiating activity at room temperature, which suppressed free polymerization but enlarged polymerization times and lowered the yield. Gold nanoparticles with a diameter of 15 nm synthesized in the presence of stabilizing citrate ions were used as macroinitiators for the polymerization of the organic shell. After the

synthesis they were functionalized with 2-sulfanylethyl-2-bromo-2-methylpropanoate as described in chapter 4.2.2.

The functionalized gold particles were mixed with CuCl and absolute toluene under an argon atmosphere. Afterwards, the monomer was added and the "freeze-pump-thaw" process was repeated three times to eliminate all oxygen. After the addition of the ligand, the catalyst complex formed and the polymerization was initiated at a certain temperature. When the polymerization was finished, the polymer was dissolved in THF and precipitated in methanol to eliminate unreacted monomer and the catalyst complex. The obtained core-shell particles were analyzed via TEM and DLS to investigate the morphology and the obtained size distribution.

In figure 102 TEM images of gold particles with a polymer shell are shown.

Figure 102: TEM pictures of a) Au nanoparticles with a diameter of 15 nm and a PS shell of 4 nm; b) Au nanoparticles with a diameter of 25 nm and a PS shell of 3 nm; c) Au particles with a PS shell of 11 nm (interface crystallization).

In the pictures above, gold particles were covered with a shell of polystyrene of different thickness. The core-shell particles were precipitated in ethanol. The precipitation led to agglomeration caused by physical interactions of polymer chains of different core-shell particles. Nevertheless, the core-shell character of the gained particles was still visible. In figure 102c) the particles that were shown in figure 102a) were redispersed in toluene. One drop of this dispersion was deposited onto a water surface in a beaker. After evaporation of the toluene the obtained particle monolayer was carefully grabbed with a TEM grid. The TEM sample that was prepared via the so called interface crystallization is presented in figure 102c). In this image the organic shell seemed to be larger in diameter which was probably

caused by the unfolding of the polymer chains. This unfolding process weakened the contrast of the polystyrene, which it difficult to recognize the border of the polymer-shell. The particles that were presented in figure 102a) were dissolved in THF, dispersed in the ultrasonic bath, and measured via DLS. The obtained plot is shown in figure 103.

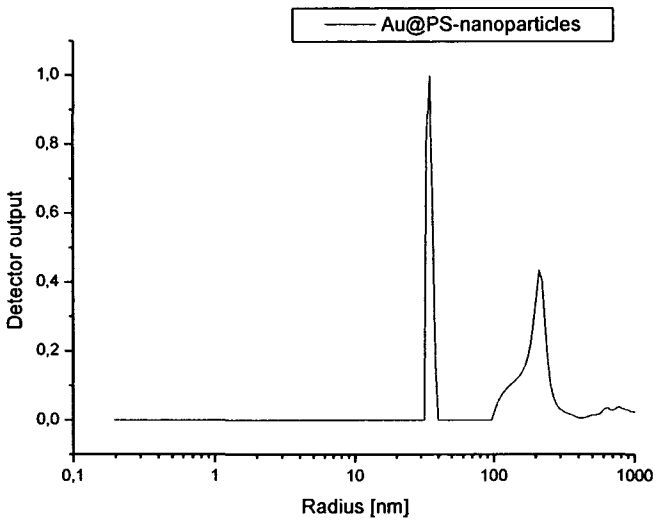

Figure 103: DLS plot of Au@PS particles recorded in THF.

A part of the Au@PS particles was redispersed in THF, where a particle diameter of 68 ± 8 nm was recorded. The rest of the particles was still aggregated, which is indicated by the second peak at higher radius in the DLS plot. Efforts were made to redisperse the core-shell particles in ethanol, to document the influence of the used solvent on the folding process of the polymer chains not only via TEM but also via DLS, but only aggregated particles were observed.

TGA analysis showed that 5.4 % of the mass of the obtained hybrid polymer consisted of gold cores. The incorporation of gold nanoparticles did not have an influence on the thermal stability which was observed in case of hybrid materials where metal oxide nanoparticles were incorporated (chapter 6.3.5.).

The surface functionalized Au@SiO_2 particles that were described in chapter 4.3. were used for the synthesis of Au@SiO_2@polymer particles. The diameter of the used Au@SiO_2 particles was 43 nm.
Figure 104 shows TEM images of Au@SiO_2 nanoparticles covered with a polymer shell.

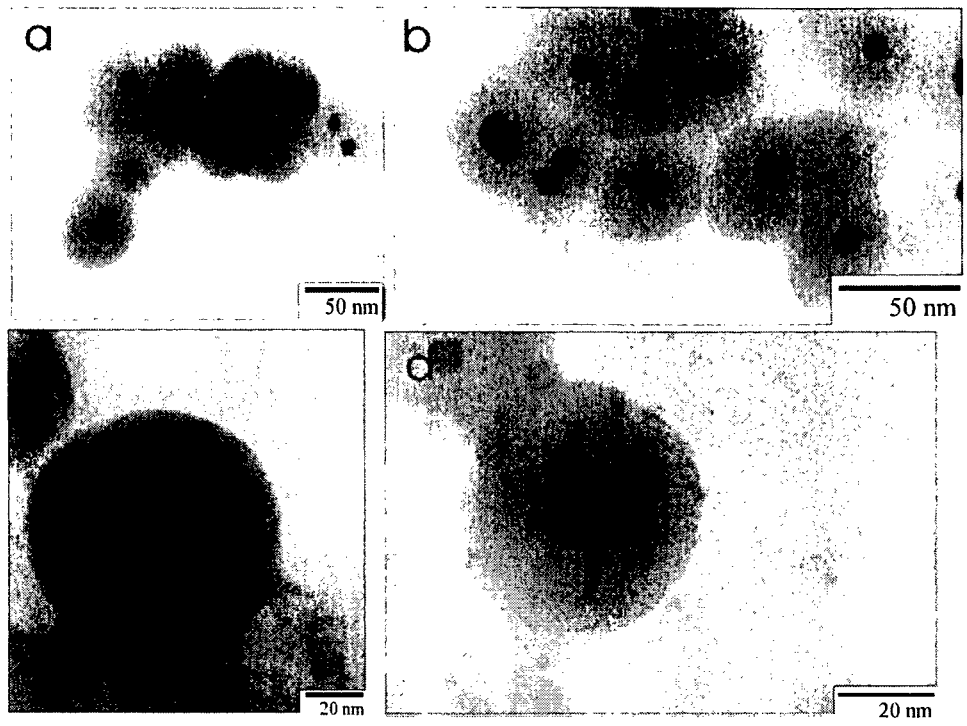

Figure 104: TEM pictures of $Au@SiO_2$ particles a) with a PS shell of 10 nm 20 hours; b) with a PS shell of 12 nm after 46 hours; c) with a polyisoprene shell of 20 nm after 44 hours; d) with a poly methacrylic acid trimethyloxysilyl propylester shell of 12 nm thickness.
In case of weak contrast between the silica shell and the polymer, the thickness of the polymer shell was calculated taking in account the diameter of the $Au@SiO_2$ particles.

Figure 104a) showed $Au@SiO_2$@polystyrene core-shell nanoparticles after 20 hours of polymerization. The three different materials that formed the composite particles were clearly visible whereby an overall diameter of 65 nm of the onion-like particles was estimated. Figure 104b) and 104c) showed $Au@SiO_2$ nanoparticles which were covered with a layer of polystyrene and polyisoprene after 46 and 44 hours, respectively. The contrast between the silica layer and the polyisoprene shell was much weaker than the contrast to polystyrene, which made it difficult to recognize the border of the polymer layer. After 46 hours of polymerization the SiO_2 layer was no longer visible because of the higher absorption of the thicker polymer shell. The obtained core-shell particles showed a diameter of about 90 nm. In figure 104d) methacrylic acid trimethyloxysilyl-propylester was used as monomer. The trimethoxysilyl groups showed a higher absorption ability, which made it impossible to differ between the silica and polymer layer. The overall diameter of the particles was about 70 nm.

TGA results revealed inorganic contents between 2.1 and 1.5 %. The core-shell particles were analyzed by DLS in THF. The corresponding plots are shown in figure 105.

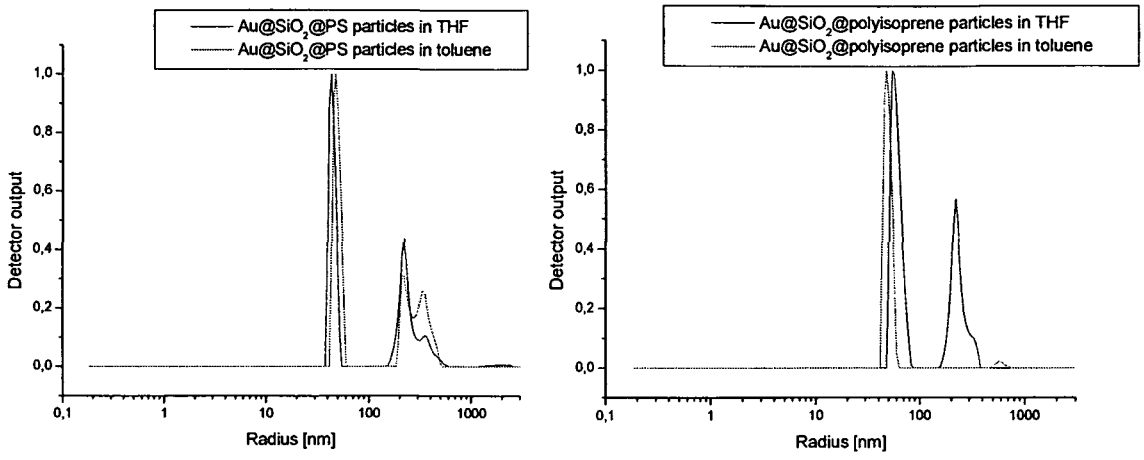

Figure 105: DLS plots of $Au@SiO_2$ particles that are covered with a polystyrene (after 46 hours) and polyisoprene shell (after 44 hours) respectively in THF and toluene.

No complete redispersion of the core-shell particles in THF was obtained in both cases. The $Au@SiO_2@PS$ particles showed a particle diameter of 88 ± 8 nm while the analysis of the $Au@SiO_2@$polyisoprene particles resulted in a diameter of 114 ± 12 nm. The DLS studies led to diameters that were slightly larger than the results that were estimated from the TEM images. A reason for this discrepancy was probably the use of different solvents. In case of the TEM images the particles were precipitated in ethanol, which led to a folding of the polymer chains. The DLS studies were performed in THF, where the polymer chains unfolded, and the measured hydrodynamic diameter became larger. It was tried to repeat the DLS analysis in ethanol to document the influence of the folding process of the polymer chains in different solvents, but only aggregated particles were observed. It was possible to redisperse the particles in toluene where the $Au@SiO_2@PS$ particles showed a particle diameter of 97 ± 10 nm while the analysis of the $Au@SiO_2@$polyisoprene particles resulted in a diameter of 100 ± 7 nm. These results showed that chains of polystyrene and polyisoprene reacted different when they were dispersed in THF and toluene. While in case of polyisoprene dispersion in toluene caused shrinkage, the polystyrene chains were unfolded further compared to the results that were obtained in THF. This observed effect was fully reversible within the inaccuracy of DLS and the size distribution of the particles. As the yield in case of isoprene was very low (6.1 % after 44 hours), the ATRP of isoprene was repeated with bromo-isobutyric acid, which is a well known ATRP initiator. After 44 hours a yield of

6.3 % was obtained. The theoretical degree of polymerization was 60; a molecular weight of 1240 g/mol (theoretical M_n 4080 g/mol) with MWD of 1.1 was revealed. These results showed that isoprene is not an effective monomer in ATRP.

6.1.1. Copolymerization of a second polymer-shell onto Au@SiO_2@PS particles

The second monomer was added after 24 hours of the styrene polymerization to receive block copolymers. In figure 106 TEM images of the obtained particles are shown.

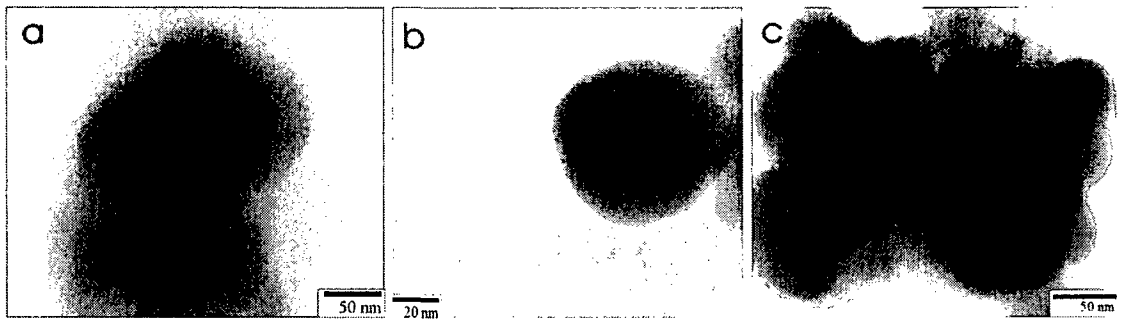

Figure 106: TEM images of Au@SiO_2@PS nanoparticles with a layer of a) polyisoprene, b) poly-methacrylic acid trimethyloxysilyl-propylester and c) poly(-methacrylic acid trimethyloxysilyl propylester), which was partly cross linked with water.

In figure 106a) isoprene was used as second monomer. The polyisoprene layer was visible having a thickness of approximately 40 nm, while the poly(-methacrylic acid trimethyloxysilyl propylester) layer in figure 106b) had nearly the same shade of grey as the silicate and the polystyrene layer. An enlargement of the diameter about 60 nm was calculated. In figure 106c) the trimethyloxysilyl groups were partly cross linked with water, which changed the contrast enormously. It was not possible to obtain DLS plots as the particles were highly crosslinked.

6.1.2. GPC analyses of the obtained Au and Au@SiO_2 core-shell systems

GPC analyses of various core-shell nanoparticles such as Au@PS, Au@SiO_2@PS, Au@SiO_2@PS@PMMA-R-$Si(OEt)_3$, and Au@SiO_2@PI were performed to investigate the principle usability of GPC in case of polymer-covered nanoparticles. The analyses were performed twice, once filtering the samples with a 200 nm Millipore filter and once without

using the filter, to investigate the presence of aggregated particles. The core-shell particles were dispersed in THF and treated 8 hours in a supersonic bath to minimize the amount of aggregates. In figure 107 the obtained GPC plots are presented.

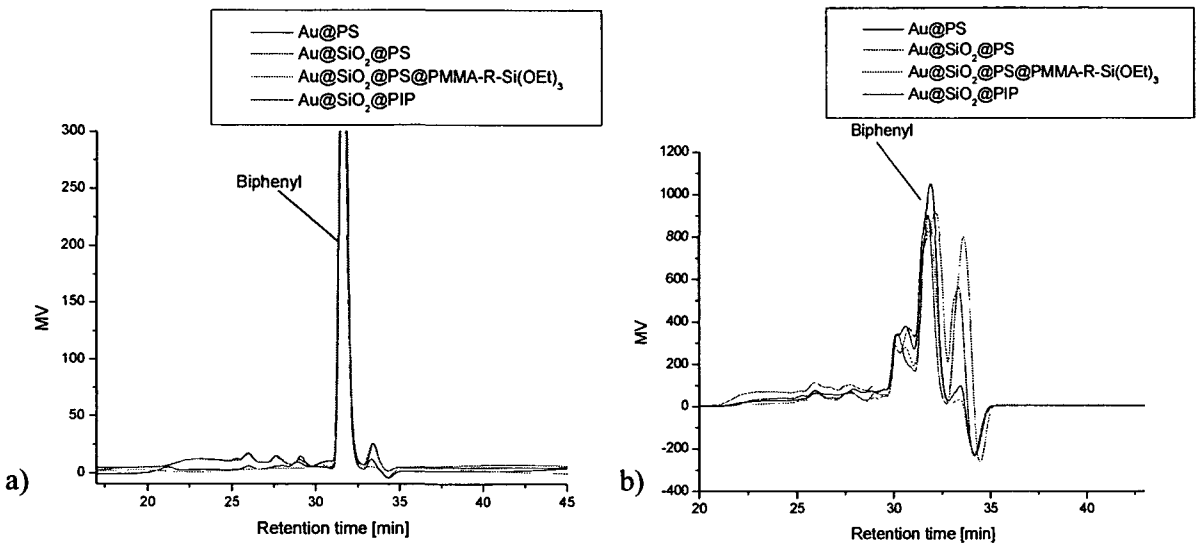

Figure 107: GPC plots of the various Au and Au@SiO_2 systems a) using a Millipore 200 filter and b) with filter using biphenyl as internal standard.

In all investigations biphenyl was used as internal standard. It seems as if the extensive treatment of the core-shell systems in the supersonic bath led to the cleavage of a minor amount of polymer, which was observed at retention times between 20 and 29 minutes. In both diagrams at a retention time of 33 minutes a signal was observed, which was assigned to the core-shell nanoparticles. Comparing the two diagrams, it seems as if the Millipore filter not only blocked aggregated species but also isolated core-shell particles, as the intensity of the corresponding signal is very small. If no filters were used, additional signals between retention times of 30 and 31 minutes were revealed, eventually due to the presence of aggregated species. Analyzing the signal of the dispersed particles in figure 107b) various observations can be made. The signal at a retention time of 33 minutes of the Au@SiO_2@PS@PMMA-R-Si(OEt)$_3$ core-shell particles was very small because the main part of the particles was crosslinked as the ethoxide groups were hydrolyzed. Furthermore, it was shown that the dispersion of larger systems (Au@SiO_2@Polymer) worked better as the dispersion of smaller systems (Au@PS) at similar concentration. The same effect was shown in case of the aggregation behavior of silica particles with different diameters in chapter 3.1.1.1.

6.1.3. Eliminating the silica shell of Au@SiO_2@polyisoprene particles

According to *Kamata et al.*, the silica layer of Au@SiO_2@polyisoprene core-shell particles was dissolved in HF.[296] The particles were stirred in concentrated HF for 24 hours and then washed with distilled water. Afterwards, a drop of the particles dispersed in water was deposited on a TEM copper grid. A TEM image of the obtained spheres is shown in figure 108.

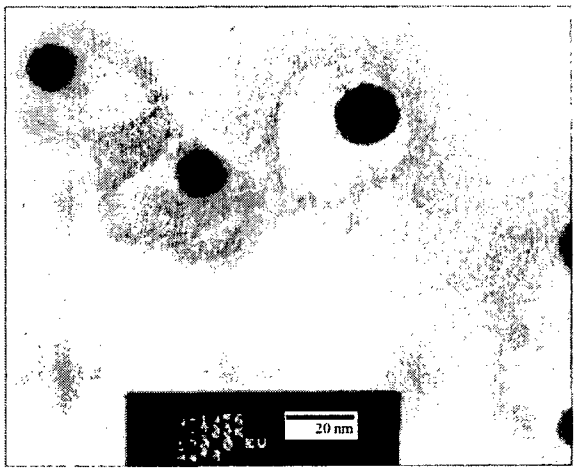

Figure 108: Au@SiO_2@polyisoprene nanoparticles, where the SiO_2-layer was dissolved in HF.

The concentrated HF penetrated the polyisoprene shell of the Au@SiO_2@polyisoprene nanoparticles and dissolved the silica shell. The remaining polyisoprene layers were still visible after the treatment with HF and the washing with water. A possible reason for the intactness of the shells could be physical coherence of the polystyrene chains. Verification of the obtained results is difficult as the attachment of a polyisoprene layer on an inorganic core was not described in literature.

6.1.4. Kinetic investigation of the polymerization process

The kinetic of the polymerization process was observed to investigate the degree of control of the polymerization process. ATRP, as a controlled radical polymerization, allows the adjusting of the molecular weight with low molecular weight distributions, which is important for the properties of the received composite materials. In figure 109 the kinetic plot, which

was recorded via UV/VIS spectroscopy at 370 nm, and the corresponding DLS plots of a styrene polymerization on $Au@SiO_2$ particles are shown.

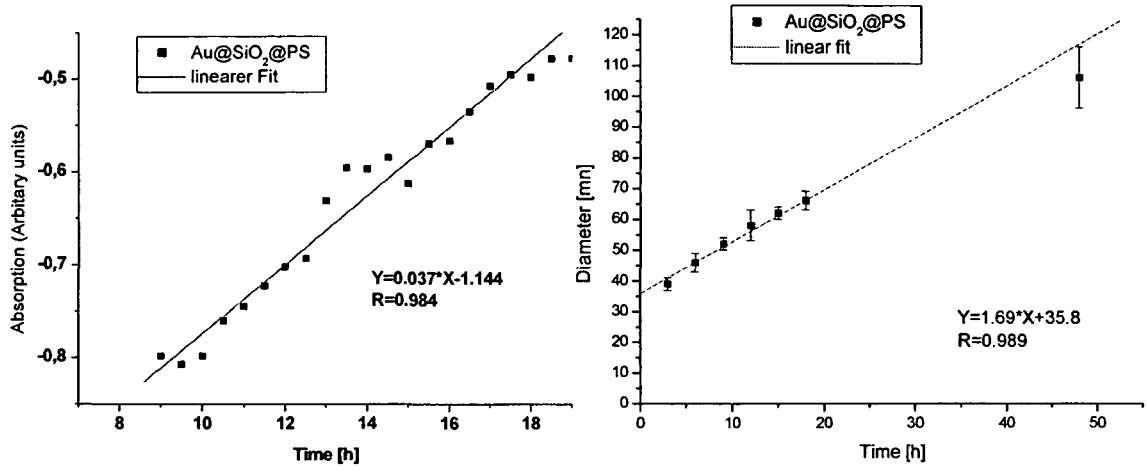

Figure 109: Kinetic of the styrene polymerization on $Au@SiO_2$-particles measured via UV/VIS spectroscopy and DLS [60 mg $Au@SiO_2$]:[15 mg CuCl]:[1.6 ml styrene]:[0.1 ml Me_6Tren] in 2 ml toluene at room temperature.

The growth of the intensity of the absorption of polystyrene at a wavelength at 370 nm was used to investigate the kinetic of the polymerization. The kinetic was recorded *in situ* in a cuvette that was equipped with a magnetic stirrer under nitrogen. It was demonstrated that the growth of the absorption of polystyrene was linear, which fulfilled the demands of an ATRP and resulted in a very homogenous material. The kinetic of the polymerization process was also investigated via DLS. Samples were taken every 3 hours and a final one after 48 hours where a conversion of 64.5 % was obtained via NMR analysis. The presented curve showed the controlled progression of the styrene ATRP from the surface of $Au@SiO_2$ nanoparticles. The diameter of the core-shell-particles increased from 40 nm to 105 nm.

As mentioned in the introduction, the production of 3 D lattices of core-shell nanoparticles is a major aim in material science. Core-shell particles are assembled into well-ordered 3 D structures via centrifugation, sedimentation, electrophoresis, pressing or via chemical interactions between the particles. In this work centrifugation and sedimentation were used for the investigation of aggregation phenomena.

The produced inorganic-organic core-shell nanoparticles showed a rather small size distribution of about ± 10 nm approved by DLS analysis. Although the particles showed rather similar diameters, it was not possible to crystallize the resulting product to ordered three dimensional structures. In figure 110 a scanning electron image of

Au@SiO_2@polystyrene particles is presented. The particles were dispersed in ethanol and one drop was placed on a SEM sample-carrier.

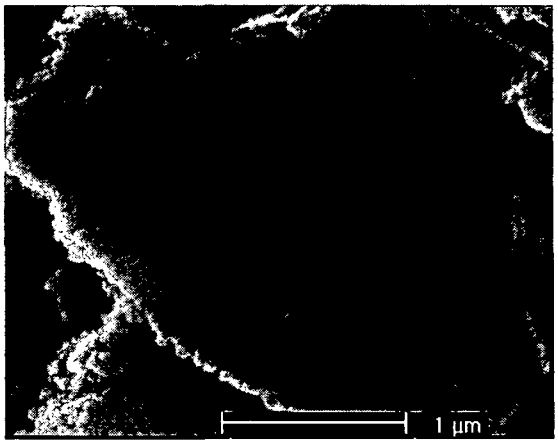

Figure 110: SEM image of Au@SiO_2@polystyrene nanoparticles.

There were several possible reasons for the mentioned difficulties of the crystallization process to ordered three dimensional structures. One could have been the diameter that was between 50 and 60 nm, which was fairly small for crystallization.[263] In these dimensions the Brownian molecular movement is a strong force, which works against the ordering process. Another reason that made ordering more difficult is the "softness" of the polymer layer, which allowed deformation of the organic shell. The combination of these two facts explained the difficulties in producing ordered structures.

6.2. Formation of core-shell nanoparticles from modified alkoxides

Functionalized alkoxides, containing bidentate ligands as described in chapter 3.2.3. that carry polymerization initiators, were used for the preparation of these particles. Depending on the initiator group different polymerization mechanisms were performed. In case of 3-bromo-2,4-pentane-dione and 3-chloro-2,4-pentane-dione, the polymerization capacities were investigated in solution and compared with well known systems.

6.2.1. Investigation of the polymerization capacities of 3-bromo-pentane-2,4-dione and 3-chloro-pentane-2,4-dione

Both 3-bromo-pentane-2,4-dione and 3-chloro-pentane-2,4-dione could initiate free radical polymerization thermally. Additionally, 3-bromo-pentane-2,4-dione could also be used as

initiator in photo-polymerizations due to the labile Br-C bond. In this chapter, their capabilities as ATRP initiators were investigated because in literature initiators with a similar chemical structure, such as halogen modified malonates with two geminal esters ($CH_3CBr(CO_2C_2H_5)_2$ are already described.[177] After the homolytical cleavage of the halogen atom, they formed stable radicals, which then reacted with the monomer molecules. Because of the structural affinity of the pentane-2,4-dione, it was assumed that they should be able to generate stable radicals as well and therefore allow ATRP. It was expected that the malonates would have higher polymerization efficiencies because of the attached methyl-group which stabilizes the formed radical.

If not otherwise mentioned, radical and controlled radical polymerizations were performed in bulk. In case of ATRP N,N,N′,N′,N′′-pentamethyldiethylenetriamine (pmdeta) was used as ligand for the catalyst system. CuCl and CuBr were used as copper salt to form the catalyst complex. The ratio between [initiator] : [CuX] : [Pmdeta] : [monomer] was kept constant at [$1.49*10^{-3}$] : [$1.49*10^{-3}$] : [$1.49*10^{-3}$]: [$2.99*10^{-2}$] mol. The given ratio resulted in a degree of polymerization (DP) of 20. In case of the free radical polymerizations the ratios were the same but without the copper catalyst. The temperatures were 80 °C for MMA and 110 °C for styrene polymerizations. Chloro- and bromo-propionic-acid-ethylester were taken as reference polymerization initiators. All polymerizations were terminated when they became solid or highly viscous.

In figure 111 the obtained plots for the system MMA and CuBr are shown, in table 21 the final polymerization results are summarized and in figure 112 the GPC plots are presented.

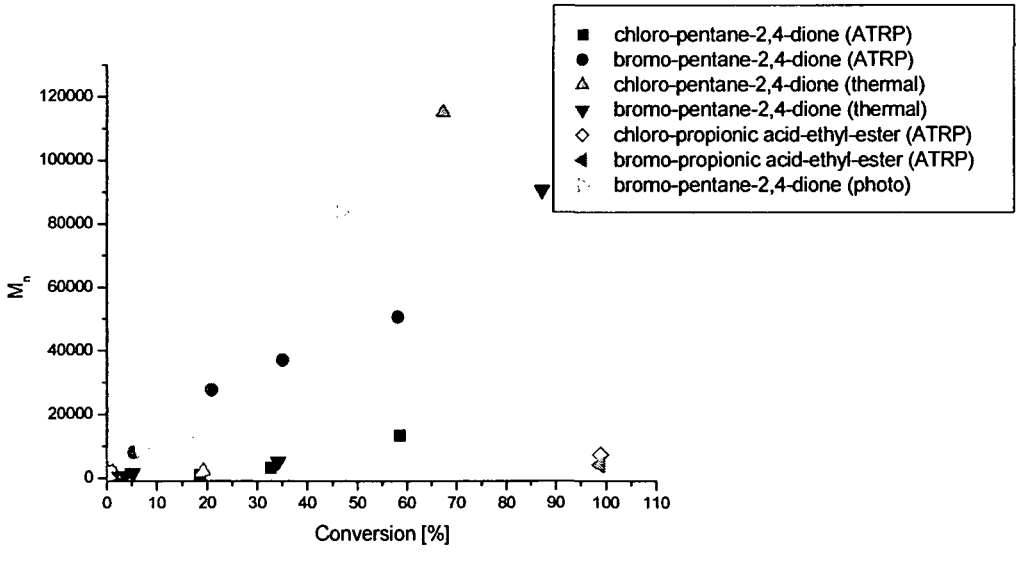

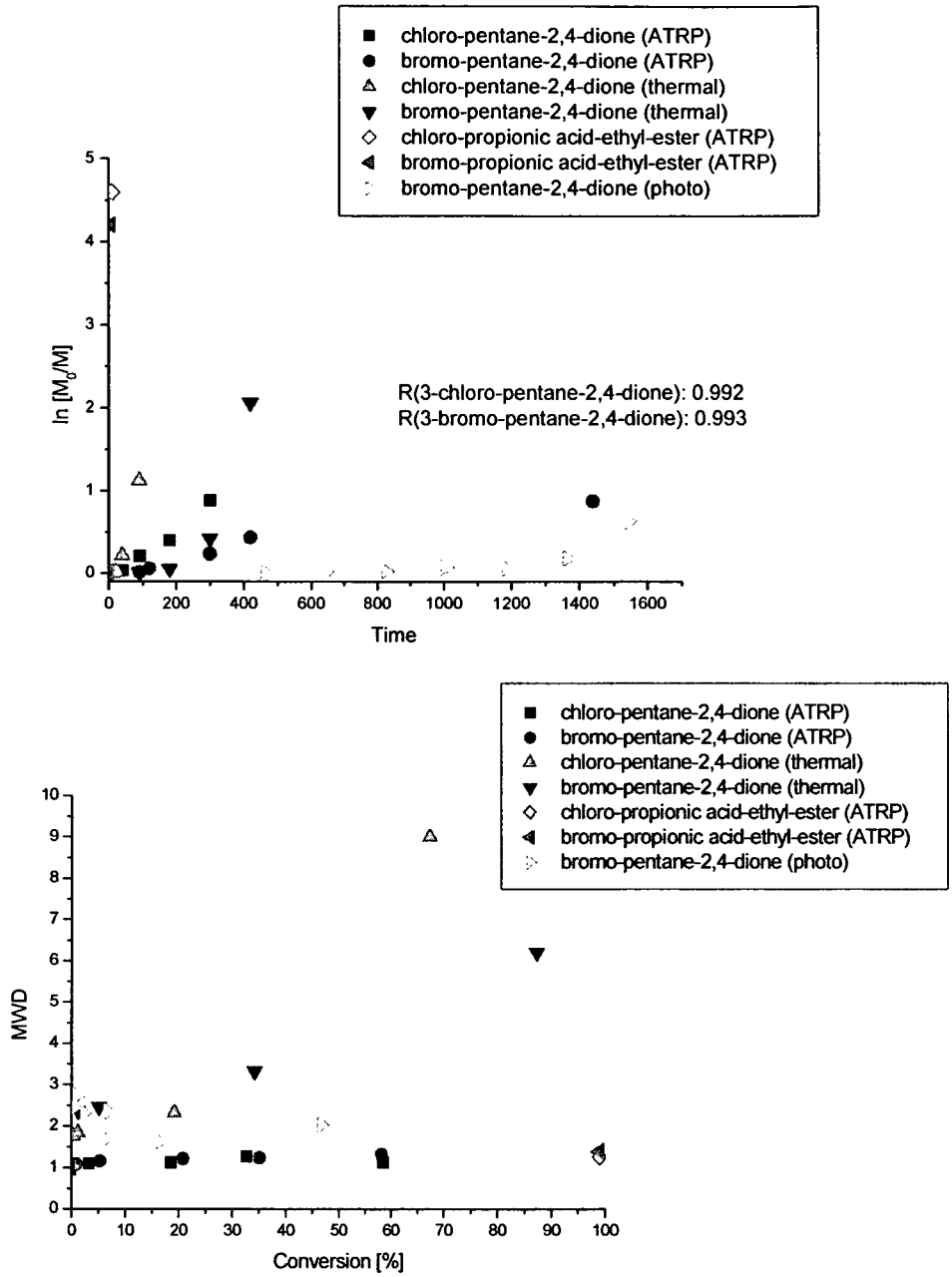

Figure 111: Conversion / molecular weight, time / ln (M_0/M) and conversion / PDI plot of the performed polymerizations using the system MMA as monomer and CuBr as metal center. The molar ratio between [initiator] : [CuBr] : [pmdeta] : [MMA] was kept constant [$1.49*10^{-3}$] : [$1.49*10^{-3}$] : [$1.49*10^{-3}$]: [$2.99*10^{-2}$] mol.

Table 21: Results of the polymerizations using MMA as monomer and CuBr as metal center. The molar ratio between [initiator] : [CuBr] : [pmdeta] : [MMA] was kept constant at [$1.49*10^{-3}$] : [$1.49*10^{-3}$] : [$1.49*10^{-3}$]: [$2.99*10^{-2}$] mol.

Initiator	Type	Time [min]	Conversion [%]	M_n [g/mol] MWD	M_{th}/M_n
Bromo-propionic acid-ethyl-ester	ATRP	5	99	4040 1.27	0.501
Chloro-propionic acid-ethyl-ester	ATRP	5	99	7240 1.37	0.283
3-Chloro-pentane-2,4-dione	ATRP	300	58.5	13410 1.12	0.101
3-Chloro-pentane-2,4-dione	therm. rad.	90	67.4	115000 9.0	0.012
3-Bromo-pentane-2,4-dione	ATRP	1440	58.2	50530 1.31	0.023
3-Bromo-pentane-2,4-dione	therm. rad.	420	87.3	90700 6.2	0.019
3-Bromo-pentane-2,4-dione	photo. rad.	1545	46.7	83750 2.01	0.011

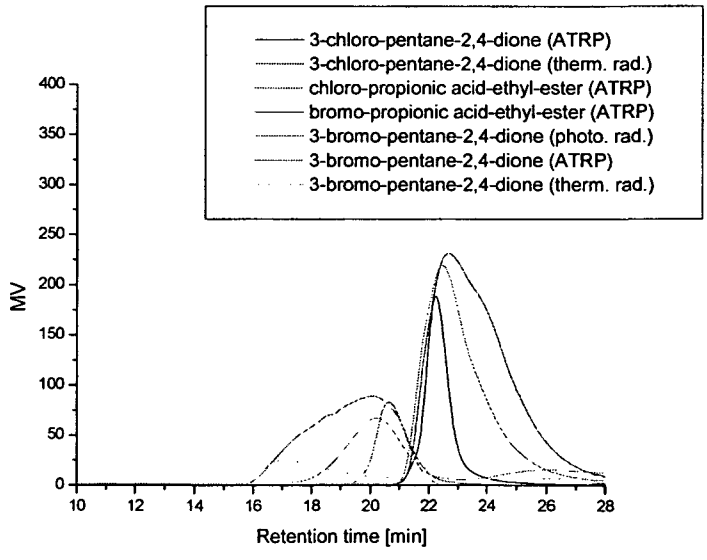

Figure 112: GPC-plots of the performed polymerizations using MMA as monomer and CuBr as metal center. The molar ratio between [initiator] : [CuBr] : [pmdeta] : [MMA] was kept constant at [$1.49*10^{-3}$] : [$1.49*10^{-3}$] : [$1.49*10^{-3}$]: [$2.99*10^{-2}$] mol.

The results of ATRP carried out in bulk strongly depended on the used initiator. Therefore, when the targeted degree of polymerization was 20, very different efficiencies were obtained. The well known ATRP initiators bromo-propionic acid-ethyl-ester and chloro-propionic acid ethyl-ester showed fairly low efficiencies of 0.501 and 0.283 under these rather extreme conditions in bulk. Normally, solvents would have been necessary to solubilize the forming PMMA, which had a glass transition temperature T_g > 100 °C. In addition, solution polymerization helps to keep the concentration of growing radicals low.[163] The obtained GPC plots confirmed the occurrence of termination reactions in some cases. Surprisingly, if bromo-propionic acid-ethyl ester was used as ATRP initiator, the corresponding GPC plots revealed a shoulder to lower molecular weight (M_n = 4040 g/mol; MWD = 1.27). The GPC curve of the chlorine-ester derivate also showed a tail to low molecular weight (M_n = 7240 g/mol; MWD = 1.37). The semilogarithmic kinetic plots showed for both esters a nearly linear dependence on time. Furthermore, the dependence of the increase of the molecular weight on time was also nearly linear. Such behavior indicates first-order kinetic with respect to the monomer and, therefore a constant concentration of active species during polymerization.[297]

The efficiency of 3-chloro-pentane-2,4-dione was 0.101 and therefore within the same range as the presented ethyl-esters. 3-bromo-pentane-2,4-dione showed a smaller efficiency in the polymerization of MMA. The obtained value of 0.023 was close to the values that were found in case of thermal initiated radical polymerization. This fact could be explained by the higher thermal instability of 3-bromo-pentane-2,4-dione compared to the chlorine derivative, which possibly caused a higher radical concentration. Nevertheless, both halo-pentane-2,4-derivates obtained a MWD < 1.35 in ATRP. The GPC plots of the ATRP that were initiated by a halo-pentane-2,4-dione did not show bimodality or significant tailoring. The semilogarithmic kinetic and the molecular weight plots showed for both pentane-2,4-dione derivatives a nearly linear dependence on time. *Ando et al.* used structural similar halogenated malonates as initiators of ruthenium catalyzed ATRP of MMA and obtained efficiencies of between 0.60 and 0.40.[177]

In case of free radical polymerization the efficiencies were lower compared to ATRP, which demonstrated the effect of the presence of the ATRP catalyst, especially, on the molecular weight, the MWD, and the linear progression of the polymerization process. While the GPC plot of the free radical polymerization initiated by 3-chloro-pentane-2,4-dione showed a shoulder to high molecular weight, possibly due to the occurrence of termination reactions,

the GPC plot of the polymerization initiated by 3-bromo-pentane-2,4-dione revealed a tail to low molecular weights. Furthermore, the GPC plot of the photo-polymerization showed a bimodal size distribution.

These kinetic investigations were repeated using CuCl instead of CuBr. In figure 113 the obtained kinetic plots are shown and in table 22 the collected results are summarized. The observed GPC curves are shown in figure 114.

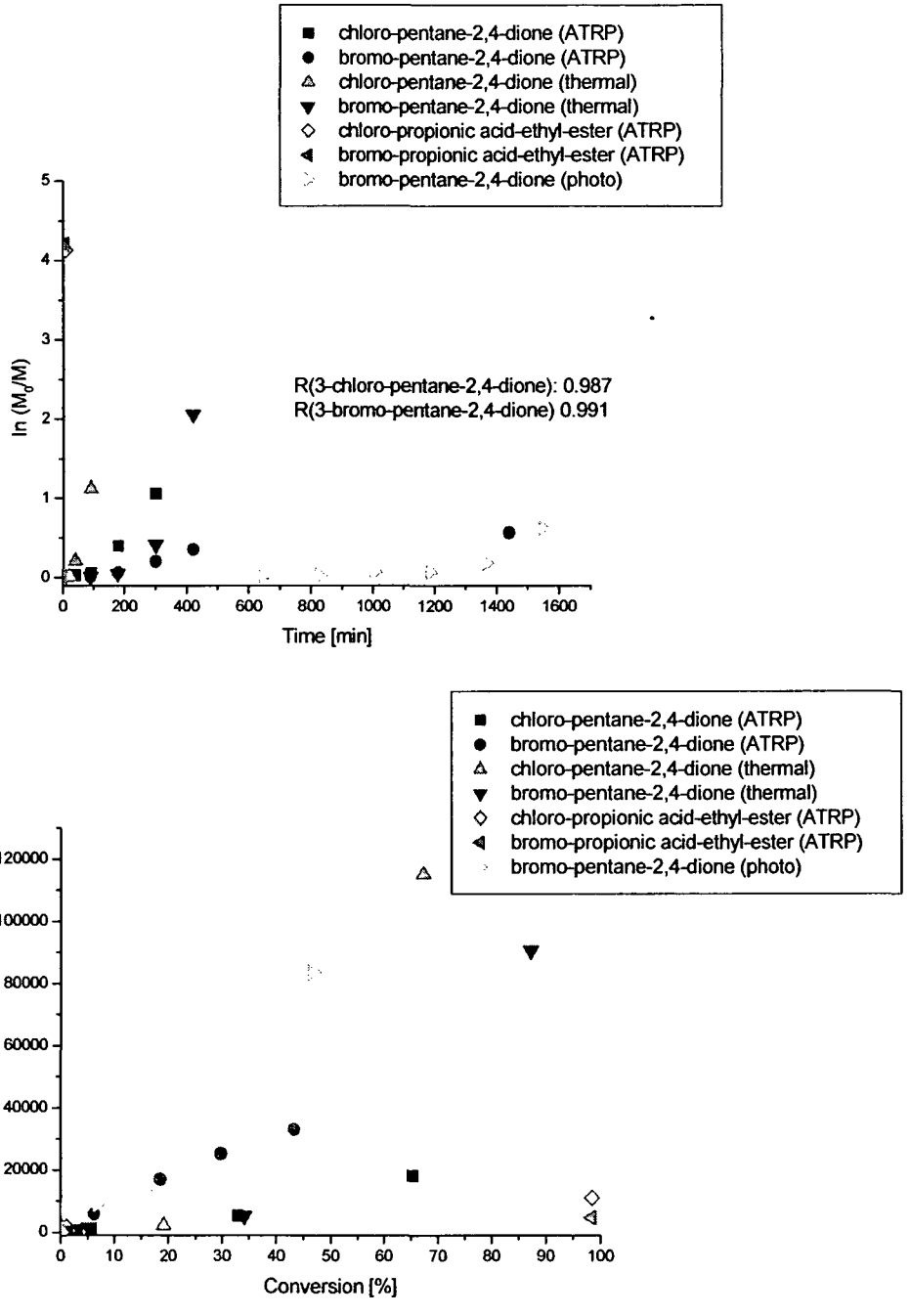

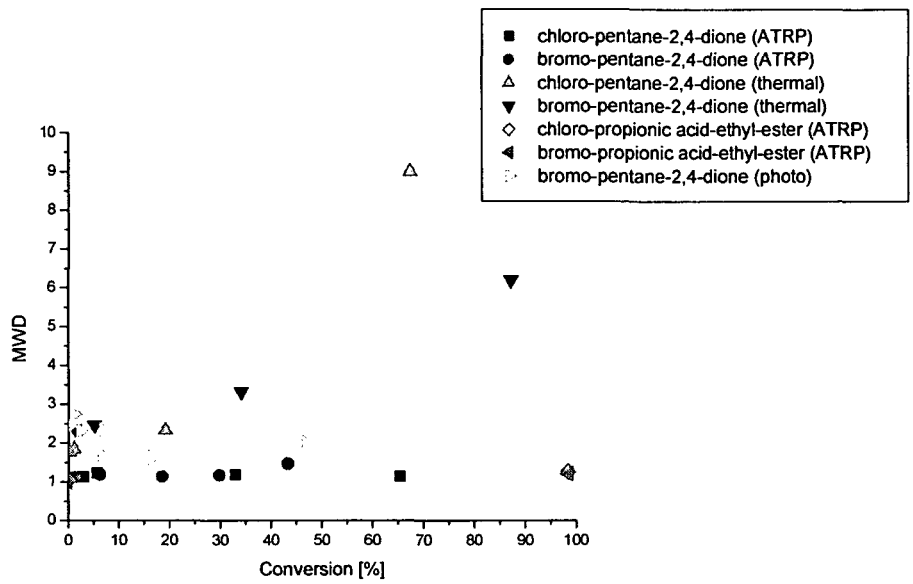

Figure 113: Conversion / molecular weight, time / ln (M_0/M) and conversion / PDI plot of the performed polymerizations using MMA as monomer and CuCl as metal center. The molar ratio between [initiator] : [CuCl] : [pmdeta] : [MMA] was kept constant at [$1.49*10^{-3}$] : [$1.49*10^{-3}$] : [$1.49*10^{-3}$]: [$2.99*10^{-2}$] mol.

Table 22: Results of the polymerizations using MMA as monomer and CuBr as metal center. The molar ratio between [initiator] : [CuCl] : [pmdeta] : [MMA] was kept constant at [$1.49*10^{-3}$] : [$1.49*10^{-3}$] : [$1.49*10^{-3}$]: [$2.99*10^{-2}$] mol. The results of the free radical polymerizations are described in table 21.

Initiator	Type	Time [min]	Conversion [%]	M_n [g/mol] MWD	M_{th}/M_n
Bromo-propionic acid-ethyl-ester	ATRP	10	98.5	11000 1.26	0.179
Chloro-propionic acid-ethyl-ester	ATRP	10	98.5	4690 1.20	0.421
3-Chloro-pentane-2,4-dione	ATRP	300	65.1	18050 1.14	0.073
3-Bromo-pentane-2,4-dione	ATRP	1440	43.3	32940 1.17	0.026

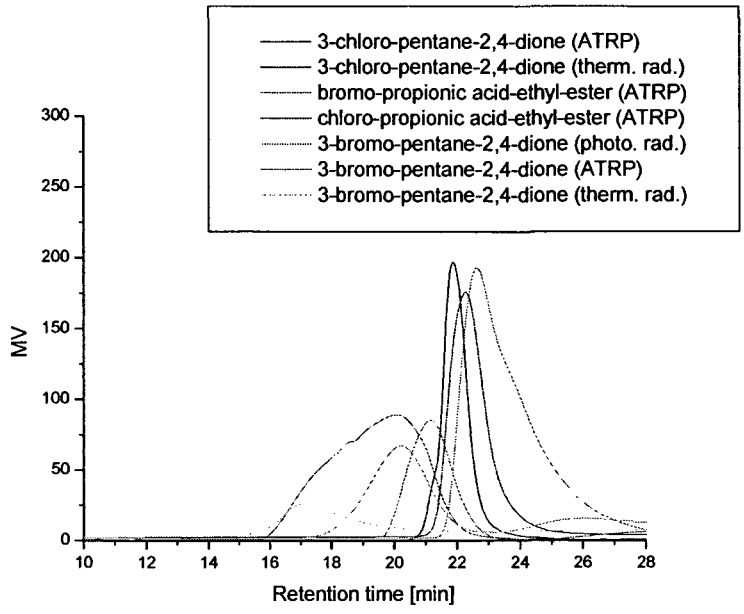

Figure 114: GPC plots of the performed polymerizations using MMA as monomer and CuCl as metal center. The molar ratio between [initiator] : [CuCl] : [pmdeta] : [MMA] was kept constant [$1.49*10^{-3}$] : [$1.49*10^{-3}$] : [$1.49*10^{-3}$]: [$2.99*10^{-2}$] mol.

The replacement of CuBr with CuCl led to increased efficiency in the polymerization initiated by bromo-propionic acid-ethyl-ester, while the efficiency of chloro-propionic acid-ethyl-ester decreased. This phenomenon was described by *Matyjaszewski et al.* who observed that the rate of initiation can be increased by using mixed halide initiating systems R-X/M_t-Y (X, Y = Br, Cl).[144] The GPC plot of the bromo-propionic acid-ethyl-ester initiated ATRP showed a shoulder to low molecular weight, possibly due to diffusion problems caused by the high viscosity during the polymerization process.

In general the efficiencies of the halo-pentane-2,4-diones decreased in case of the CuCl/pmdeta catalyzed ATRP due to the lower catalytic activity of CuCl compared to CuBr.[294] The GPC plots of the ATRPs that were initiated by the halo-pentane-2,4-diones did not show bimodality or significant tailoring, which resulted in MWDs < 1.17. The GPC plots of the free-radical polymerizations were discussed before. Furthermore, the semilogarithmic kinetic and the molecular weight plots showed a linear dependence on time. Such behavior indicated first-order kinetic with respect to the monomer and, therefore, a constant concentration of active species during polymerization.

The presented polymerizations were performed in bulk. Toluene was used as solvent to gain a higher degree of control of the polymerization process as the formed polymer was dissolved and the system was diluted, which led to a reduced radical concentration.

In figure 115 the $\ln(M_0/M)$ versus conversion plots of 3-chloro-pentane-2,4-dione using CuCl as metal center and 3-bromo-pentane-2,4-dione using CuBr as metal center for the polymerization of MMA are shown.

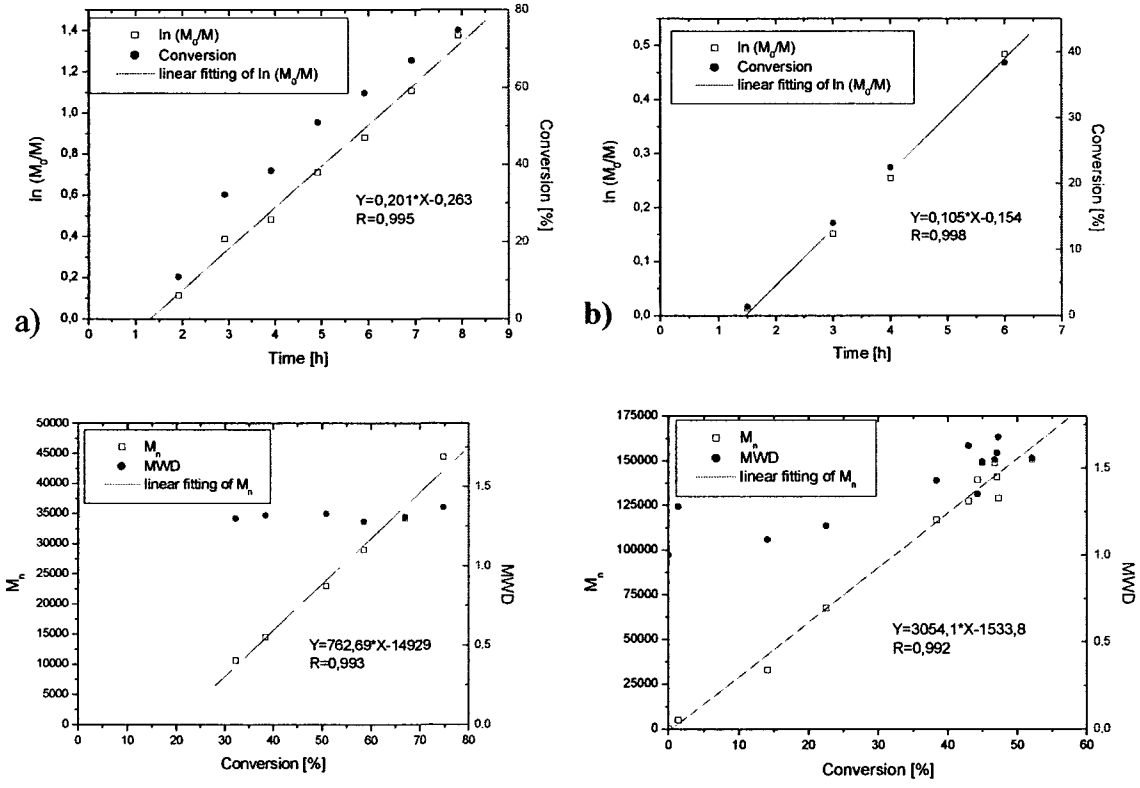

Figure 115: Kinetic plots of a) 3-chloro-pentane-2,4-dione using CuCl/CuBr as metal center and b) 3-bromo-pentane-2,4-dione with a molar ratio of [initiator] : [pmdeta] : [MMA] : [CuX] = $[2.5*10^{-4}] : [2.5*10^{-4}] : [5.0*10^{-2}] : [2.5*10^{-4}]$ in 5 ml toluene at 110 °C.

Compared to the polymerizations in bulk, the efficiency of the halo-pentane-2,4-diones increased if the ATRP was performed in toluene.[163] Efficiencies of 0.36 and 0.04 were obtained for 3-chloro- and 3-bromo-pentane-2,4-dione, respectively.

Methyl methacrylat is a very reactive monomer, which in this case reduced the control over the polymerization. The entire investigation was repeated to study the influence of the monomer using styrene instead of MMA.

In figure 116 the obtained kinetic plots for styrene as monomer and CuBr as metal center are shown. The polymerizations were performed without solvent at a temperature of 110 °C. The molar ratio between [initiator] : [CuX] : [pmdeta] : [styrene] was kept constant at [$1.49*10^{-3}$] : [$1.49*10^{-3}$] : [$1.49*10^{-3}$] : [$2.99*10^{-2}$]. In table 23 the obtained results are summarized and in figure 117 the measured GPC plots are presented.

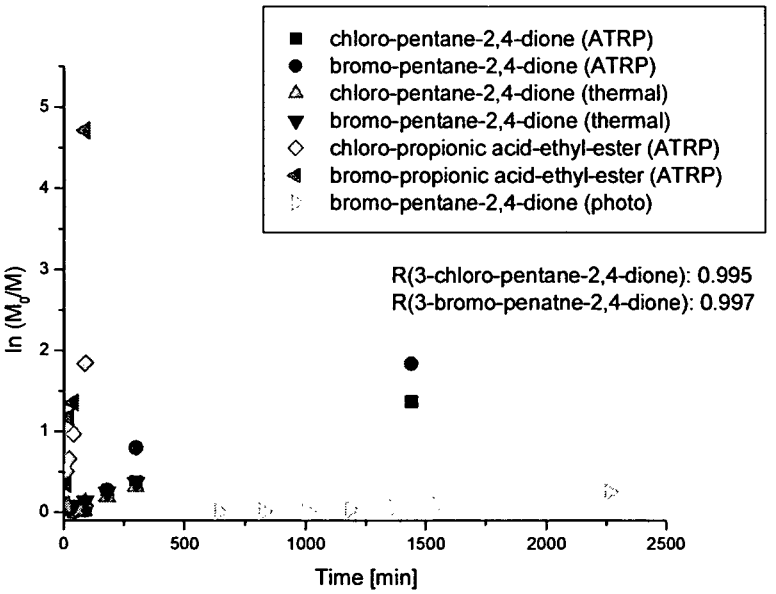

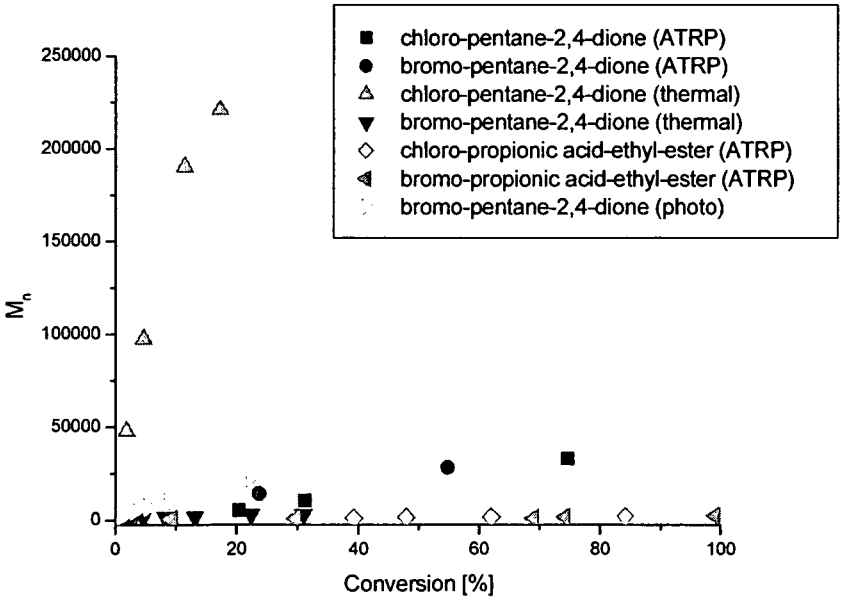

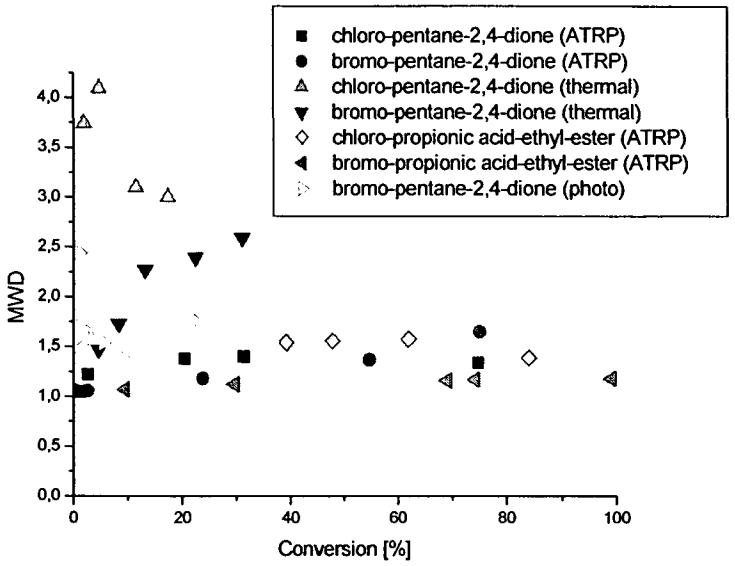

Figure 116: Conversion / molecular weight, time / ln (M_0/M) and conversion / PDI plot of the performed polymerizations using styrene as monomer and CuBr as metal center. The molar ratio between [initiator] : [CuBr] : [pmdeta] : [styrene] was kept constant at [1.49*10^{-3}] : [1.49*10^{-3}] : [1.49*10^{-3}]: [2.99*10^{-2}] mol.

Table 23: Results of the polymerizations using styrene as monomer and CuBr as metal center. The molar ratio between [initiator] : [CuBr] : [pmdeta] : [styrene] was kept constant at [1.49*10^{-3}] : [1.49*10^{-3}] : [1.49*10^{-3}]: [2.99*10^{-2}] mol.

Initiator	**Type**	**Time [min]**	**Conversion [%]**	**M_n [g/mol] MWD**	**M_{th}/M_n**
Bromo-propionic acid-ethyl-ester	ATRP	90	99.1	2440 1.18	0.845
Chloro-propionic acid-ethyl-ester	ATRP	90	84.1	2270 1.39	0.776
3-Chloro-pentane-2,4-dione	ATRP	1440	74.7	33160 1.36	0.047
3-Chloro-pentane-2,4-dione	therm. rad.	300	27.1	220900 3.0	0.003
3-Bromo-pentane-2,4-dione	ATRP	1440	75.1	61660 1.65	0.025

3-Bromo-pentane-2,4-dione	therm. rad.	300	31.0	3100 2.59	0.208
3-Bromo-pentane-2,4-dione	photo. rad.	2280	22.3	22350 1.76	0.021

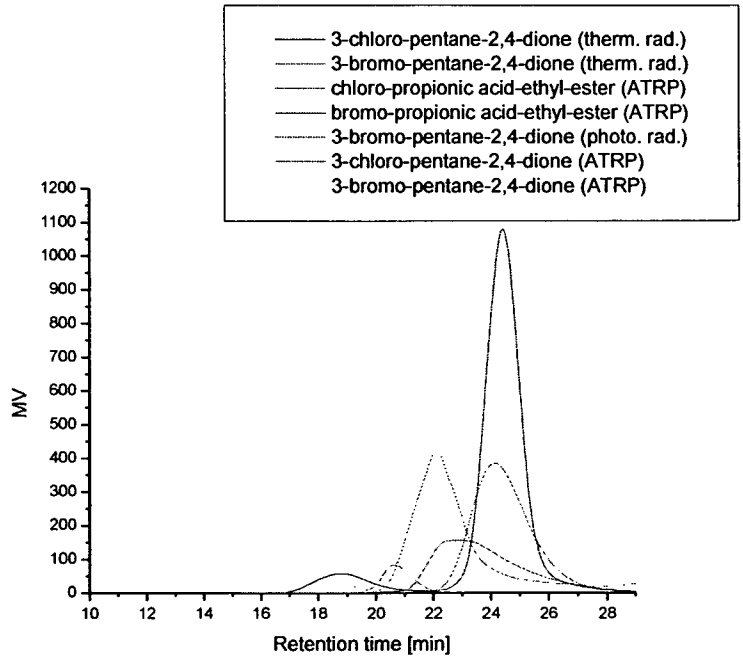

Figure 117: GPC plots of the performed polymerizations using styrene as monomer and CuBr as metal center. The molar ratio between [initiator] : [CuBr] : [pmdeta] : [styrene] was kept constant [$1.49*10^{-3}$] : [$1.49*10^{-3}$] : [$1.49*10^{-3}$]: [$2.99*10^{-2}$] mol.

If styrene was used as monomer, the initiation efficiency of the halo-propionic acid-ethyl-esters increased under these reaction conditions. The efficiencies were raised to 0.845 and 0.776. Nevertheless, due to structural dissimilarity between initiator and monomer, the initiation efficiency of the halo-pentane-2,4-dione dropped in case of styrene compared to MMA. For example, benzyl-substituted halides are useful initiators for the polymerization of styrene due to their structural resemblance.[295] The GPC plots of the ATRPs, initiated by the ester derivatives and the halo-pentane-2,4-diones, did not show significant tailoring or bimodality, which led to the assumption that termination reactions hardly occurred. The polymerization of styrene processed more controlled compared to the polymerization of MMA, which led to formation of shoulders and tails in the GPC plots, especially in case of the ester containing initiators. Furthermore, the semilogarithmic kinetic and the molecular

weight plots of all ATRPs had a linear dependence on time, which was characteristic for controlled radical polymerizations. The obtained molecular weights and the MWDs were also slightly decreased in case of the use of styrene as monomer. The free radical polymerization of styrene led to broad Gaussian formed peaks in the GPC plot, which is reflected by rather large MWDs, except in case of 3-bromo-pentane-2,4-dione initiated polymerizations, where thermal initiation led to a shoulder to low molecular weight, and in case of photo-initiation a tail to low molecular weight was observed.

These kinetic investigations were repeated using CuCl instead of CuBr as metal center. In figure 118 the obtained plots are given. In table 24 the results are summarized and the GPC plots are presented in figure 119.

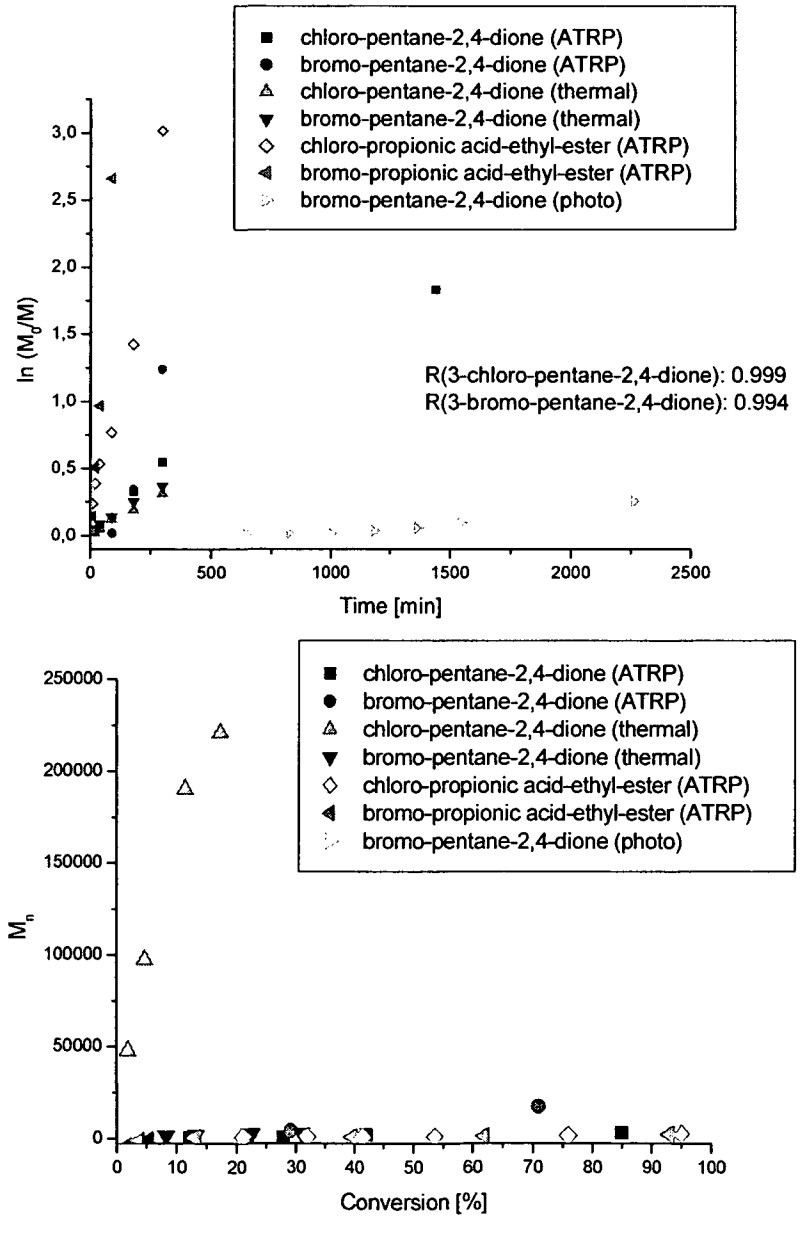

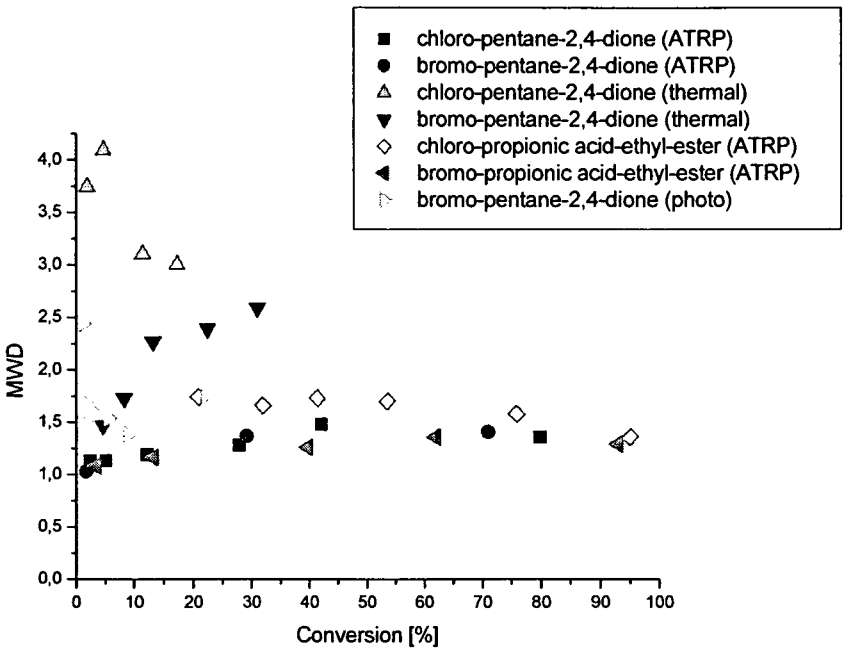

Figure 118: Conversion / molecular weight, time / ln (M_0/M) and conversion / PDI plot of the performed polymerizations using styrene as monomer and CuCl as metal center. The molar ratio between [initiator] : [CuCl] : [pmdeta] : [styrene] was kept constant at [$1.49*10^{-3}$] : [$1.49*10^{-3}$] : [$1.49*10^{-3}$]: [$2.99*10^{-2}$] mol.

Table 24: Results of the polymerizations using styrene as monomer and CuCl as metal center. The molar ratio between [initiator] : [CuCl] : [pmdeta] : [styrene] was kept constant at [$1.49*10^{-3}$] : [$1.49*10^{-3}$] : [$1.49*10^{-3}$]: [$2.99*10^{-2}$] mol. The results of the free radical polymerization are shown in table 23.

Initiator	**Type**	**Time [min]**	**Conversion [%]**	**M_n [g/mol] MWD**	**M_{th}/M_n**
Bromo-propionic acid-ethyl-ester	ATRP	300	95.0	2430 1.29	0.813
Chloro-propionic acid-ethyl-ester	ATRP	90	93.0	2470 1.36	0.783
3-Chloro-pentane-2,4-dione	ATRP	1440	84.9	3260 1.35	0.515

3-Bromo-pentane-2,4-dione	ATRP	300	71.0	17540 1.41	0.084

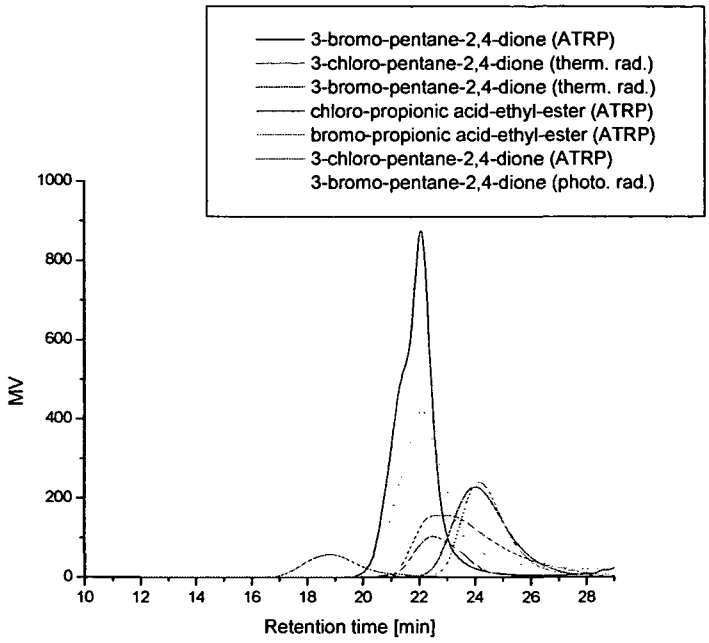

Figure 119: GPC plots of the performed polymerizations using styrene as monomer and CuCl as metal center. The molar ratio between [initiator] : [CuCl] : [pmdeta] : [styrene] was kept constant at [$1.49*10^{-3}$] : [$1.49*10^{-3}$] : [$1.49*10^{-3}$]: [$2.99*10^{-2}$] mol.

The replacement of CuBr with CuCl led to higher control over the ATRP because CuCl showed a lower catalytic activity. The efficiency of the two halo-pentane-2,4-diones increased to 0.515 and 0.084 in case of the chlorine- and bromine-derivative, respectively. The different efficiency of the two halo-pentane-2,4-dione was caused by their different thermal stability. Due to the lack of thermal stability of 3-bromo-pentane-2,4-dione, the GPC plot showed a shoulder to higher molecular weight, caused by occurring termination reactions via recombination. The GPC plot of the 3-chloro-pentane-2,4-dione initiated polymerization showed a small shoulder to low molecular weights.

All other GPC curves of ATRPs did not show bimodality or significant tailoring. The obtained semilogarithmic kinetic and molecular weight plots revealed for all ATRPs a linear dependence on time, which indicated first-order kinetic with respect to the monomer and therefore, a constant concentration of active species during the polymerization.

As the presented polymerizations were performed in bulk, they were repeated using toluene as solvent to investigate if the polymerization efficiency could be improved. In figure 120 the $\ln(M_0/M)$ versus conversion plots of 3-chloro-pentane-2,4-dione using CuCl as metal center and 3-bromo-pentane-2,4-dione using CuBr as metal center of the polymerization of styrene are shown.

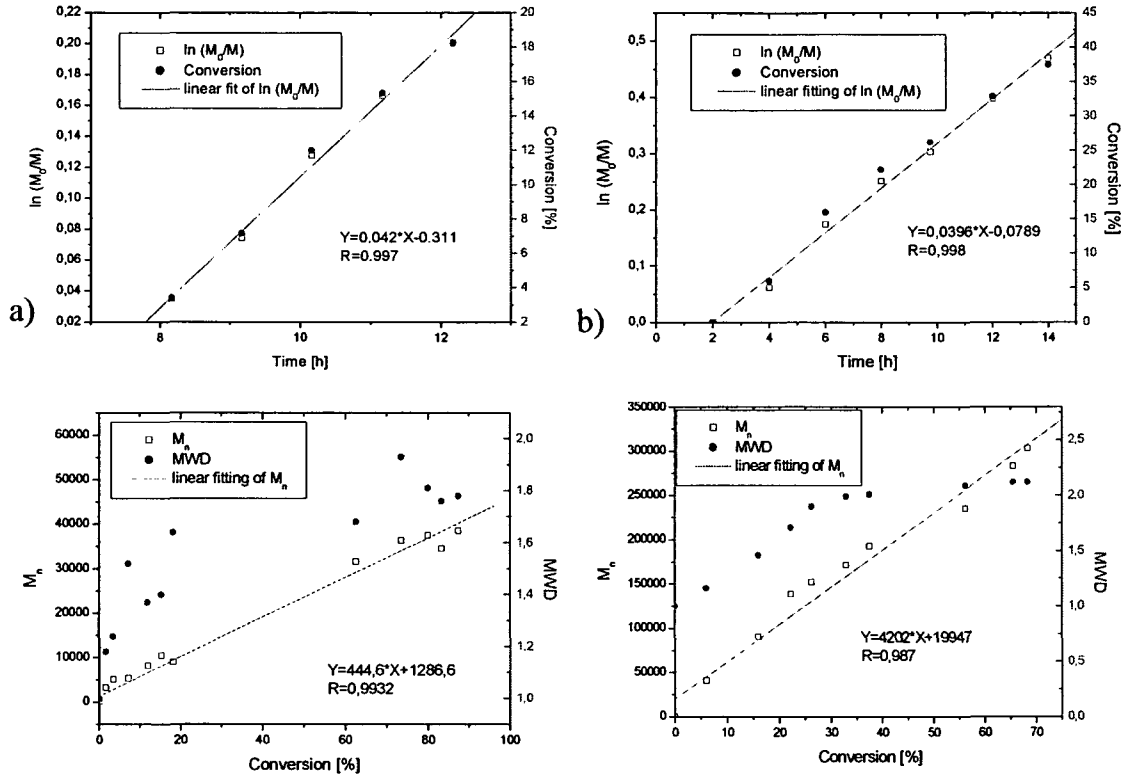

Figure 120: Kinetic plots of a) 3-chloro-pentane-2,4-dione using CuCl as metal center and b) 3-bromo-pentane-2,4-dione with [initiator] : [pmdeta] : [styrene] : [CuX] = $[2.5*10^{-4}]$: $[2.5*10^{-4}]$: $[5.0*10^{-2}]$: $[2.5*10^{-4}]$ in 5 ml toluene at 110 °C.

If styrene was used as monomer, no improvement of the degree of control in the polymerization process was obtained because the polymerization of styrene requires harsher conditions than MMA, such as higher radical concentration, increased temperature, etc. Therefore, the efficiency of the ATRPs dropped to 0.032 and 0.023.

The obtained polymerization results confirmed that both 3-halo-pentane-2,4-dions initiated ATRP. The efficiencies of the chloro- and bromo-derivative differed due to the lower thermal stability of the C-Br bond. The higher stability of the C-Cl bond prevented the uncontrolled cleavage of the carbon halogen bond and so reduced the radical concentration in the system.

In general, the efficiencies of the ATRPs were higher if styrene was used as monomer compared to MMA, which often led to the formation of higher molecular weights and higher MWD, possibly, due to the chosen reaction conditions. The replacement of CuBr with CuCl also increased the efficiency of the polymerization process due to reduced catalytic activity.[298]

Both halo-pentane-2,4-diones proved their ability to initiate free radical polymerization as well.

6.2.1.1. Investigation of the polymerization activity

The polymerization activity is an important parameter in order to characterize a certain polymerization initiator. The activity of 3-chloro-pentane-2,4-dione and 3-bromo-pentane-dione was investigated using 2,2,6,6-tetramethyl-piperidinyl-1-oxy (TEMPO) to trap the generated radicals. The change of the concentration of the corresponding halo-pentane-2,4-dione and the formation of the TEMPO-pentane-2,4-dione complex versus time was monitored using GPC, as published by *Matyjaszewski et al.* for several other systems.[299]

In scheme 35 the occurring reactions are presented.

Scheme 35

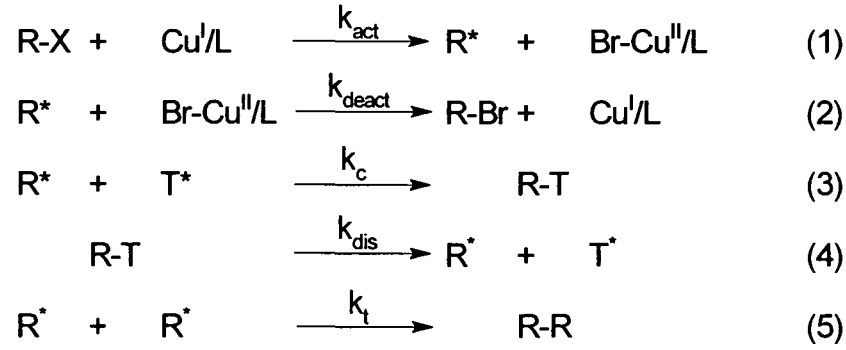

After the radical was generated through an atom transfer process (1), it was exclusively trapped with TEMPO (3), yielding an pentane-2,4-dione complex (R-T). The contributions of the deactivation step (2), thermal dissociation of R-T (4), and self coupling were negligible due to the low Cu(II)Br/L concentration.[300, 301]

Depending on the investigated halo-pentane-2,4-dione, CuCl or CuBr and TEMPO were mixed under an argon atmosphere in absolute toluene with pmdeta, which was used as ligand. After three freeze-pump-thaw cycles the mixture was stirred for 30 minutes at 40 °C and

mixed with a certain amount of the corresponding halo-pentane-dione and biphenyl, which served as internal standard in the GPC analysis. After certain periods of time, samples were drawn and analyzed via GPC. The areas under the peak, caused by the internal standard (biphenyl), were used for the normalization of the curves.

In figure 121 the obtained GPC plots using CuBr combined with 3-bromo-pentane-2,4-dione are presented. In the second plot the conversion of 3-bromo-pentane-2,4-dione obtained from the area decrease under the corresponding peak versus time, is shown.

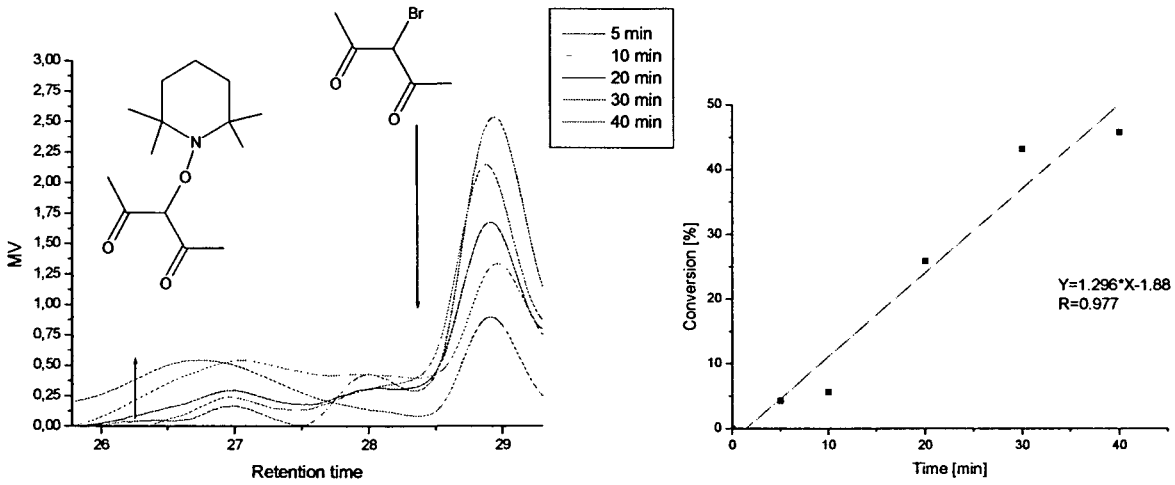

Figure 121: GPC traces in activation rate constant measurements $[Br\text{-}AcacH]_0 = [CuBr]_0 = [pmdeta]_0 = [TEMPO]_0 = 2.0*10^{-2}$ M in toluene at 40 °C. The analyses were performed using THF as eluent. In the second diagram the conversion of 3-bromo-pentane-2,4-dione versus time is shown.

The linear decrease of the amount of 3-bromo-pentane-2,4-dione was clearly visible in the GPC plots. The conversion plot of the pentane-dione-2,4-dione derivate was obtained by integrating the peak area and relating it to the normalized area at t = 0, using the area of the biphenyl peaks as internal standard for the normalization. The first-order kinetic plot of the consumption of 3-bromo-pentane-2,4-dione was almost linear, indicating that the change in concentration of the catalyst during the reaction was relatively small, while reactions 2 and 4 did not contribute significantly.

As CuBr is known as a very active catalyst, it was replaced via CuCl using the same molar ratios and the same concentrations as before. The obtained GPC traces and the conversion of 3-bromo-pentane-2,4-dione are shown in figure 122.

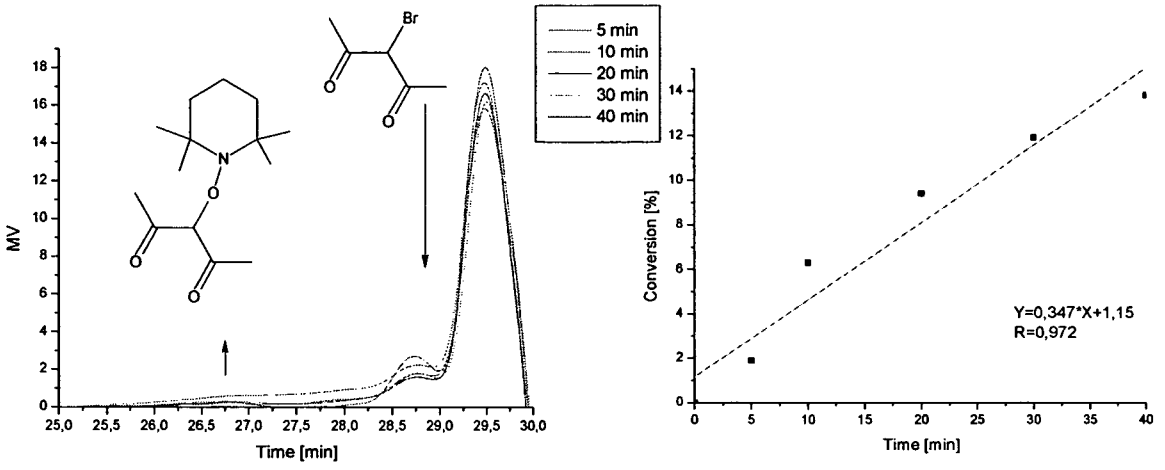

Figure 122: GPC traces in activation rate constant measurements $[Br\text{-}AcacH]_0 = [CuCl]_0 = [pmdeta]_0 = [TEMPO]_0 = 2.0*10^{-2}$ M in toluene at 40 °C. The analyses were performed using THF as eluent. In the second diagram the conversion of 3-bromo-pentane-2,4-dione versus time is shown.

Comparing the two activation rate analyses of 3-bromo-pentane-2,4-dione using CuBr/pmdeta and CuCl/pmdeta as catalyst, the conversion of 3-bromo-pentane-2,4-dione was dramatically reduced from 46 % to 14 % after 40 minutes if CuCl/pmdeta was used as catalyst. One reason leading to a smaller conversion rate of the halo-pentane-2,4-dione was the usage of CuCl, which is known as less effective catalyst. Furthermore, a halogen exchange between CuCl and 3-bromo-pentane-2,4-dione might have decreased the reaction rate.

The same analysis was repeated for 3-chloro-pentane-2,4-dione using CuCl/pmdeta as catalyst. As the signals in the GPC analysis were very weak, the concentrations were raised to $6.0*10^{-2}$ M.

In figure 123 the obtained GPC plots are presented.

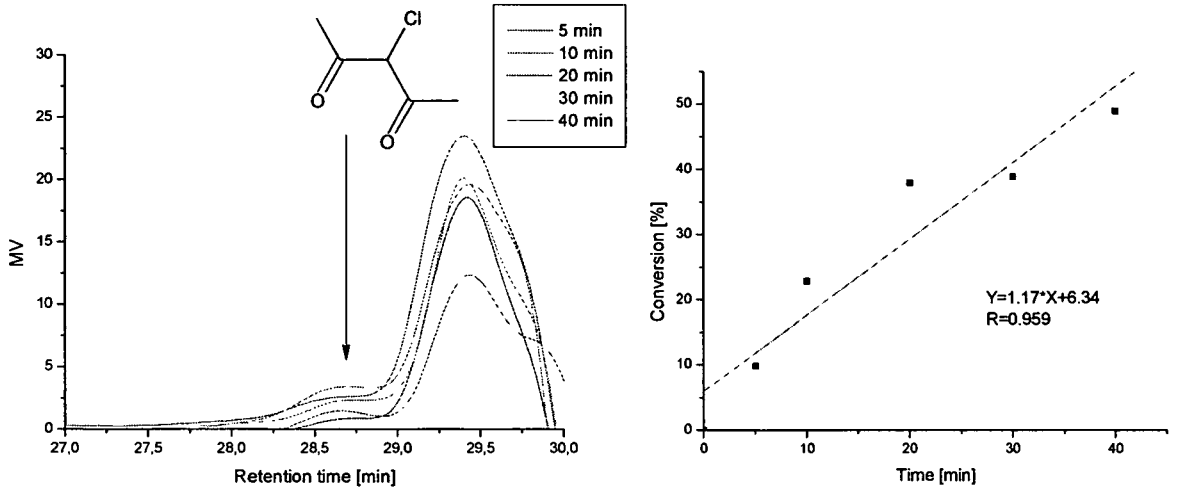

Figure 123: GPC traces in activation rate constant measurements $[Cl\text{-}AcacH]_0 = [CuCl]_0 = [pmdeta]_0 = [TEMPO]_0 = 6.0*10^{-2}$ M in toluene at 40 °C. The analyses were performed using THF as eluent. In the second diagram the conversion of 3-bromo-pentane-2,4-dione versus time is shown.

Contrary to the results presented in case of 3-bromo-pentane-2,4-dione, the formed TEMPO-pentane-2,4-dione complex could not be analyzed by GPC. Furthermore, the obtained GPC plots showed that the decrease of the present amount of 3-chloro-pentane-2,4-dione was not proceeding as steadily as in case of 3-bromo-pentane-dione. Eventually, the equilibrium of equation (1) was too far on the side of the dormant species. The slope of the linearized plot for the conversion of 3-chloro-pentane-2,4-dione was smaller compared to the slope if 3-bromo-pentane-dione was used. This reduction of the slope suggested a reduced amount of radicals present in the system. As the activation rate of mixed systems seemed to be very low, the system CuBr with 3-chloro-pentane-2,4-dione were not investigated.

Coordination of the pentane-2,4-dione derivatives to the copper catalyst can lead to a reduction of the catalytic activity. Whether coordination of the halo-pentane-2,4-diones to the CuBr/pmdeta and CuCl/pmdeta ATRP catalyst during polymerization occurred or not, was investigated with the following experiments. A stoichiometric amount of halo-pentane-2,4-dione was added to a [1]:[1] mol mixture of CuX and pmdeta. The mixture was analyzed via UV/VIS spectroscopy and compared to CuX/pmdeta and CuX/(Cl-Acac)Na. All spectra were recorded in toluene except the spectrum of CuX/(Cl-Acac)Na, which was recorded in ethanol (Figure 124).

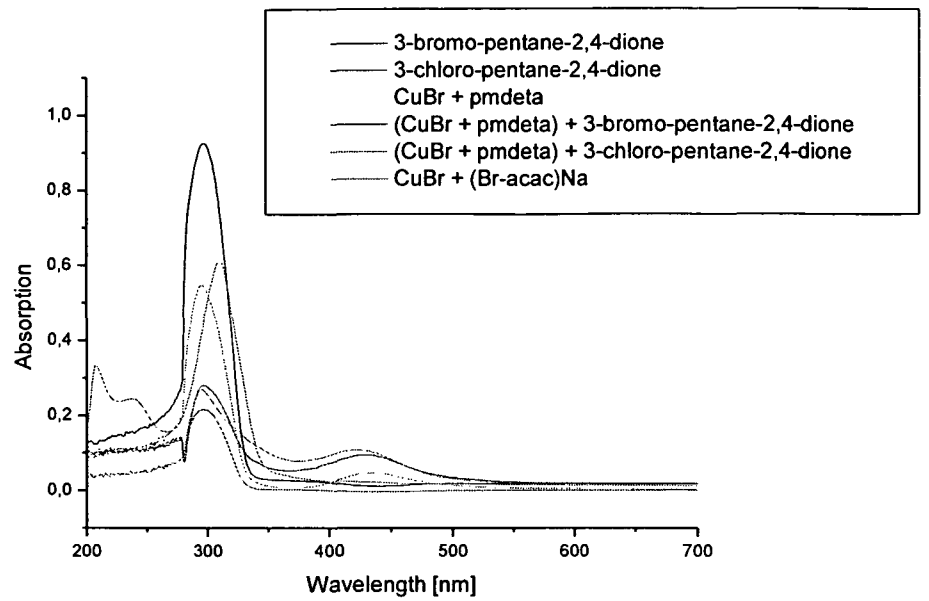

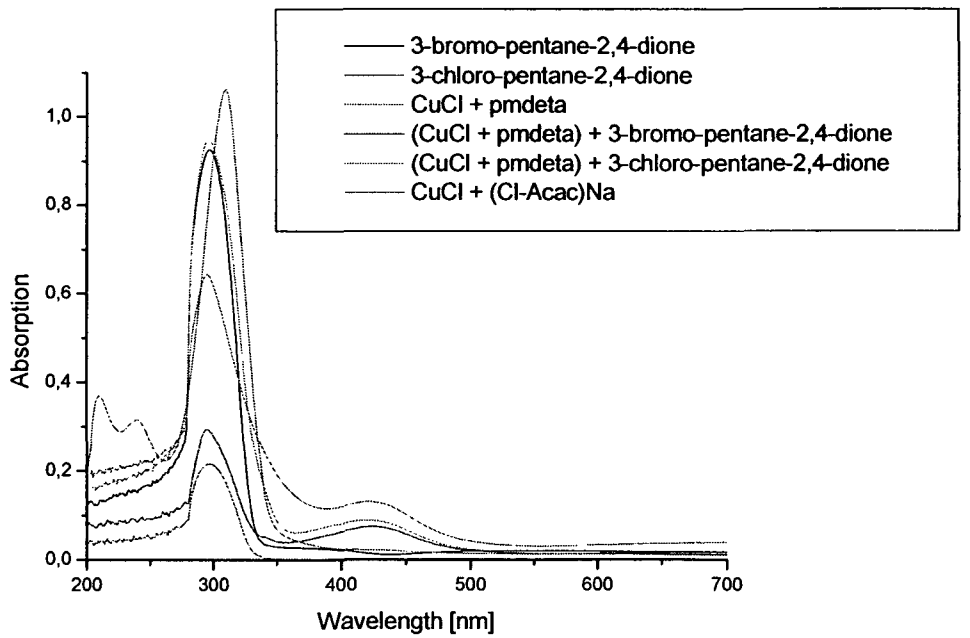

Figure 124: UV/VIS spectra of the produced pmdeta complexes.

The absorption spectra of the CuX/pmdeta complex did not change if one of the halo-pentane-2,4-diones was added. Signals were found at 298 nm and 428 nm. According to *David et al.*, these signals were assigned to intramolecular π–π^* transitions.[302] Compared to the CuX/(Br-acac)Na spectrum, where signals at 212 nm, 242 nm, and 311 nm were found, no coordination was observed.

From the obtained results, it can be concluded that both 3-chloro-pentane-2,4-dione and 3-bromo-pentane-2,4-dione are capable of initiating an ATRP. The occurrence of side reactions, which could reduce the activity of the initiator, such as coordination of the halo-pentane-2,4-diones to the copper catalyst, was not observed. Due to higher thermal stability of the halogen-carbon bond, 3-chloro-pentane-2,4-dione showed higher polymerization efficiencies.

6.2.2. Synthesis of titanium oxide core-shell nanoparticles

Functionalized nanoparticles that were synthesized from modified metal alkoxides, as described in chapter 3.2.3.1., were used for these polymerization experiments. Starting from modified titanium isopropoxide, particles with a diameter of 80 nm, in case of the 3-chloro-pentane-2,4-dione functionalization, and 200 nm, in case of 3-acetyl-5-bromo-5-methylhexane-2,4-dione functionalization, were used. As monomers MMA and styrene were polymerized. Depending on the utilized functionality different polymerization mechanisms were performed. The presented yields give the relation of the amount of isolated polymer to the amount of used monomer.

In case of 3-chloro-pentane-2,4-dione surface functionalized nanoparticles, thermal initiated free radical polymerization and ATRP were carried out. Free radical polymerization delivered a yield of 43.3 % in case of MMA as monomer and 12.2 % for the polymerization of styrene after 24 hours, respectively. The obtained yields were lower compared to the polymerization of MMA with uncoordinated 3-chloro-pentane-2,4-dione. If this initiator was used in an ATRP, yields of 32.4 % (after 48 hours) and 39.5 % (after 24 hours) were obtained in case of styrene and MMA, respectively.

The bromine derivative allowed initiation of the free radical polymerization, either by UV-irradiation or thermally. The highest reaction rate was observed for the photo-induced polymerization of MMA with 46.4 % compared to 13.3 %, which were received when styrene was utilized as monomer after 48 hours, respectively. Compared to uncoordinated bromo-pentane-2,4-dione, which obtained yields of 47 % (after 26 hours) in case of the photo-induced polymerization of MMA and 22 % (after 37 hours) in case of styrene as monomer, the received yields in case of the "grafting from" polymerization from the nanoparticles were slightly lower.

Thermal initiation led to polymerization rates after 24 hours of 36.3 % and 15.1 % for the reaction of MMA and styrene, respectively. ATRP resulted in yields of 12.8 % and 10.3 % for MMA and styrene after 24 hours.

Controlled radical polymerization of nanoparticles, which carried 1-acetyl-2-oxopropyl 2-bromo-2-methylpropanoate as initiating molecule resulted in a polymerization rate of 24.4 % (after 24 hours) for MMA and 19.3 % (after 48 hours) for styrene. This was slightly higher compared to macroinitiators containing 3-acetyl-5-bromo-5-methylhexane-2,4-dione that resulted in a yield of 22.1 % (after 24 hours) for the reaction of MMA and 15.3 % (after 48 hours) for using styrene as educt.

In figure 125 a TEM image of titanium oxide @ PMMA nanoparticles and the corresponding DLS-plot are shown.

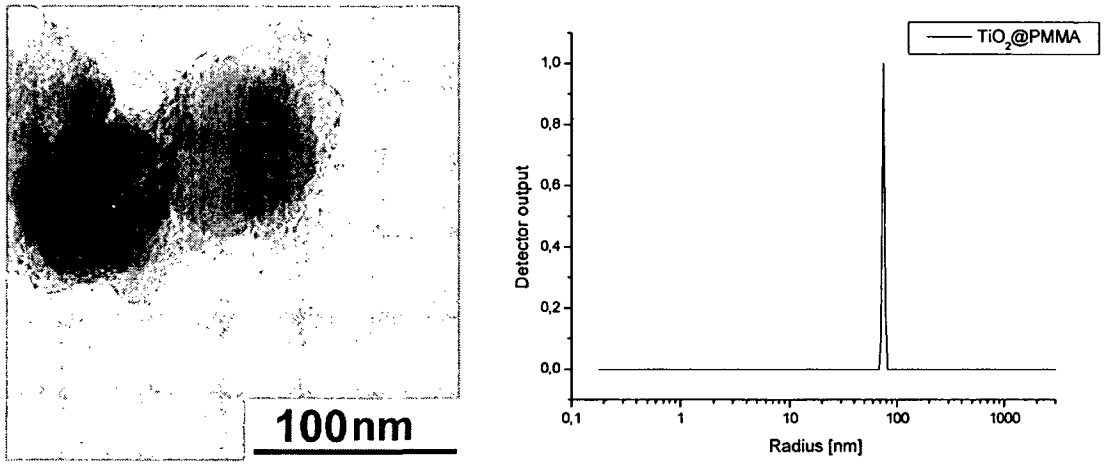

Figure 125: TEM image and the corresponding DLS-plot (recorded in toluene) of TiO_2 nanoparticles from the coordination product of $Ti(O^iPr)_4$ and 3-acetyl-5-bromo-5-methylhexane-2,4-dione covered with PMMA.

The diameter of the core-shell nanoparticles was with about 85 nm much smaller than the presented diameter of the TiO_2 nanoparticles alone, which had a diameter of 200 nm (chapter 3.2.3.1.). One possible reason might be that the structural integrity of the nanoparticles, synthesized from modified titanium alkoxides, was rather weak because of their high organic content, which may have prohibited complete cross-linking of the precursor molecules. The stability of the nanoparticles, functionalized with 3-acetyl-5-bromo-5-methylhexane-2,4-dione, was investigated via FTIR-spectrometry. The functionalized particles were suspended in toluene, which was the solvent that was used during the polymerization and rested for three days at room temperature. Afterwards, the particles were separated, and the toluene was investigated via FTIR. In the isolated toluene small amounts of precursor were found. The

weight loss of the modified nanoparticles was about 5 %, which proved that part of the particles was soluble in toluene.

The particles were also heated 3 days in toluene and afterwards analyzed via DLS. Only small fragments between 10 and 20 nm were observed, which led to the assumption that the particles are slightly soluble in cold toluene but remained stable during the polymerization because the particles presented in the TEM image were much larger.

In the TEM image the form of the inorganic core was not entirely spherical, which could be explained by the mentioned partial dissolving of the particles. This cleavage process could also explain the occurrence of free polymerization in solution which, had to be separated before TEM and DLS analyses were performed. The particles were suspended in THF, treated in a supersonic bath, centrifuged and dried in vacuo to separate the free polymer chains. About 10 % of the hybrid polymer was entirely soluble, which means that 10 % of the polymer chains were not grown from the surface of the nanoparticles but in free solution. It can not be excluded that a part of the polymer was cleaved from the particle surface in the ultrasonic bath.

The polymer shell, shown in the TEM image in figure 125, had a rather inhomogeneous appearance, caused both by the precipitation in ethanol for the preparation of the TEM-sample and the presence of polymer chains that were still adsorbed on the particles surface. The DLS plot was recorded by dispersing the hybrid material in toluene and showed a particle diameter of 150 ± 5 nm.

As these results were not satisfying, the core-shell particles from 3-chloro-pentane-2,4-dione functionalized precursors, were analyzed via TEM and DLS as well. In figure 126 the obtained TEM image and DLS plot are presented.

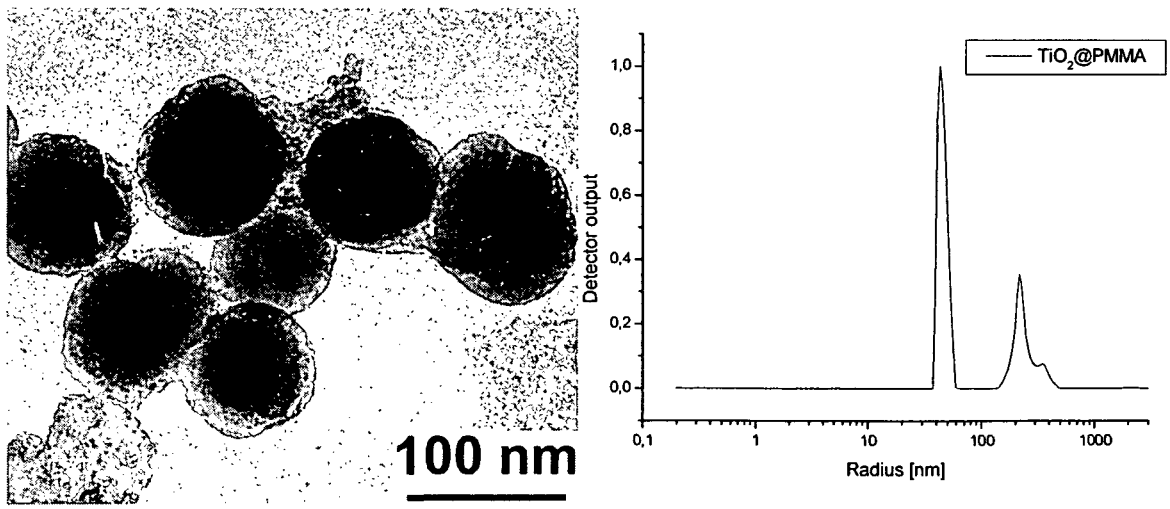

Figure 126: TEM image and DLS plot (recorded in THF) of TiO_2@PMMA nanoparticles from the coordination product of $Ti(O^iPr)_4$ and 3-chloro-pentane-2,4-dione.

The appearance of these particles was totally different. The TEM image suggested a diameter of the particles of 87 nm. The DLS investigation revealed a diameter of 95 ± 9 nm. The amount of free polymer was investigated by suspending the core-shell particles in THF, centrifuging the dispersion and measuring the weight loss. This analysis obtained an amount of free polymer of 4 %, which was significantly less, compared to the particles that were synthesized from particles that were functionalized with 3-acetyl-5-bromo-5-methylhexane-2,4-dione. Apparently particles that were functionalized with 3-chloro-pentane-pentane-2,4-dione showed a higher stability under polymerization conditions.

TGA investigation of all presented TiO_2 core-shell particles revealed that the incorporation rate of the nanoparticles into the polymer was rather small. The performed analyses resulted in inorganic contents between 0.6 % and 1.2 %. These results were obtained from the raw product without separating the polymer chains, which had grown in free solution.
The kinetic aspects of the polymerization process were investigated utilizing particles functionalized with 3-acetyl-5-bromo-5-methylhexane-2,4-dione as macro initiator for the polymerization of MMA. In figure 127 the obtained kinetic plots are shown.

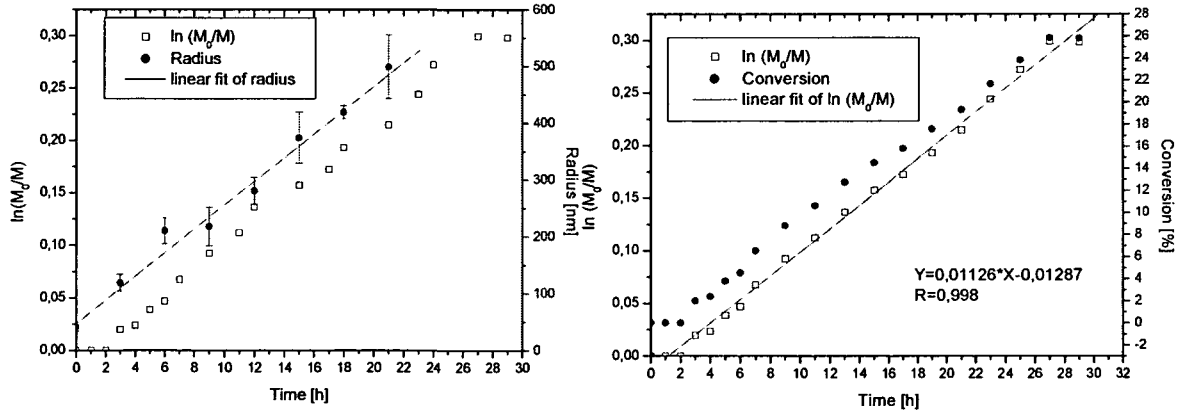

Figure 127: Kinetic plots of an ATRP initiated by 3-acetyl-5-bromo-5-methylhexane-2,4-dione modified nanoparticles with MMA as monomer in 6 ml toluene with 140 mg nanoparticles, [CuCl] : [Pmdeta] : [MMA] = $[1.99*10^{-3}]$: $[1.99*10^{-3}]$: $[9.99*10^{-2}]$ mol at 90 °C.

The $\ln(M_0/M)$ versus time plot revealed the typical linear dependence of a controlled/"living" polymerization. As shown in the second plot, the particle radius also changed linearly by time. The observed polymerization of unattached polymer-chains in solution might have influenced the measured radius of the core-shell particles as, possibly, the resulting polymer chains were partially adsorbed on the particle surface. The DLS investigation proved that in the beginning of the polymerization the diameter of the TiO_2 particles was slightly reduced but during the polymerization no further decay of the particles took place. Apparently the growing polymer shell protected the inorganic core from further decomposition.

.

A study of the polymers, grafted from the surface of the titania particles by GPC, was carried out by dissolving the particle cores in concentrated NaOH in an ultrasonic bath. The analysis of the molecular weights, eventually did not result in the correct length of single polymer chains because the solubility of TiO_2 in NaOH is limited.

The principle possibility for the cleavage of polymer-chains from inorganic surfaces was demonstrated by *Matyjaszewski et al.*, who performed ATRP on surface modified silica wafers.[298] The GPC analysis of the polystyrene polymers at 14 % conversion resulted in a molecular weight of 148000 g/mol and a molecular weight distribution of 1.4, while the polymerization of MMA revealed a molecular weight of 97500 g/mol and a polydispersity of 1.87 at 21 % conversion. The obtained results could be compared to the data published by *Patten et al.*, who grafted PMMA chains from surface modified silica particles and obtained conversions between 10 % and 30 % and MWDs between 1.9 and 1.6.[145] The obtained results showed that the grafting of the polymers seemed to be only in some degree controlled, which could be a result of the package density of the initiator molecules on the surface that could lead to termination reactions. In addition, a total dissolving of the inorganic core could not be guaranteed because of the higher protection of the core compared to, for example, the Au@SiO_2@PS core-shell particles, based on the higher degree of functionalization as a result of *in situ* functionalization. Taking in account the reduced solubility of titania compared to silica, it cannot be excluded that bonds between single polymer chains still existed. Furthermore, polymer chains that were initiated by separated precursor molecules, might also have falsified the values of the molecular weight, measured by GPC. An ATRP using pure TiO_2 nanoparticles was performed to prove that pure TiO_2 particles without functional groups do not act as initiator in a polymerization process. This experiment did not lead to any polymerization.

6.2.3. Synthesis of zirconium oxide core-shell nanoparticles

Particles functionalized with 1-acetyl-2-oxopropyl 2-bromo-2-methylpropanoate and 3-chloro-pentane-2,4-dione were chosen for the initiation of polymerization from zirconium oxide cores. Their synthesis was described in chapter 3.2.3.2. The obtained particles had diameters of 70 nm and 50 nm, respectively. Using 1-acetyl-2-oxopropyl 2-bromo-2-methylpropanoate functionalized zirconium oxide nanoparticles as macroinitiators for the polymerization of MMA, revealed a yield of 20.1 % (after 24 hours). In case of styrene a yield of 14 % (after 27 hours) was obtained. If particles that were functionalized with 3-chloro-pentane-2,4-dione were used, a yield of 19.1 % and 13.9 % in case of the polymerization of MMA and styrene, respectively, was obtained after 24 hours. The TGA analysis revealed inorganic contents between 1.5 and 4.0 %.

In figure 128 a TEM image and the corresponding DLS plot of the obtained ZrO_2@PMMA particles, synthesized from 1-acetyl-2-oxopropyl 2-bromo-2-methylpropanoate functionalized precursors, are presented after free polymer chains were separated.

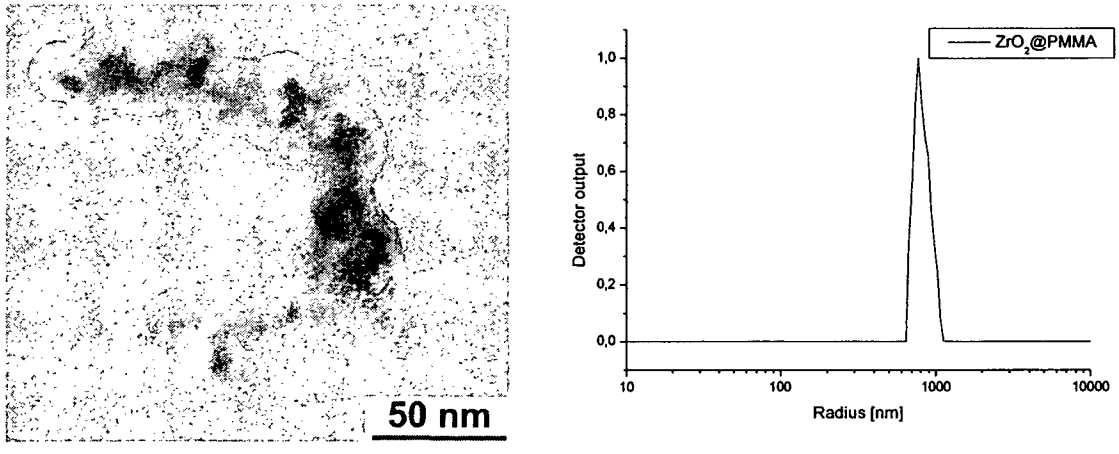

Figure 128: TEM image and the corresponding DLS plot of ZrO_2@PMMA nanoparticles.

The TEM image suggested that the zirconium oxide nanoparticles broke into smaller pieces in the beginning of the polymerization process. The fragments shown above, all initiated the polymerization process, which made the core-shell character of the particles clearly visible. Both single core and multi core hybrid particles were visible. The stability of the functionalized ZrO_2 particles was analyzed. The ZrO_2 particles were suspended in toluene and rested 3 days in the solvent. Afterwards the particles were isolated and the toluene was

analyzed via FTIR spectroscopy whereby small signals of the precursor molecules were observed. The particles were dried and the mass was compared to the mass before the dispersion in toluene. A weight loss of about 5 % was recorded. If the particles were heated in toluene for three days, total decomposition of the particles was observed via DLS because they were not protected by the growing polymer shell. As mentioned above, polymerization in solution took place as well initiated by dissolved initiator molecules. These polymer chains were separated by dissolving the obtained material in THF and centrifugation. About 11 % of the polymer chains were polymerized in free solution, initiated by dissolved precursor molecules.

As particles that are functionalized with 1-acetyl-2-oxopropyl 2-bromo-2-methylpropanoate seemed to be unstable in toluene, the core-shell particles that were obtained from 3-chloro-pentane-2,4-dione functionalized particles were investigated in more detail. In figure 129 a TEM image and the corresponding DLS-plot are presented.

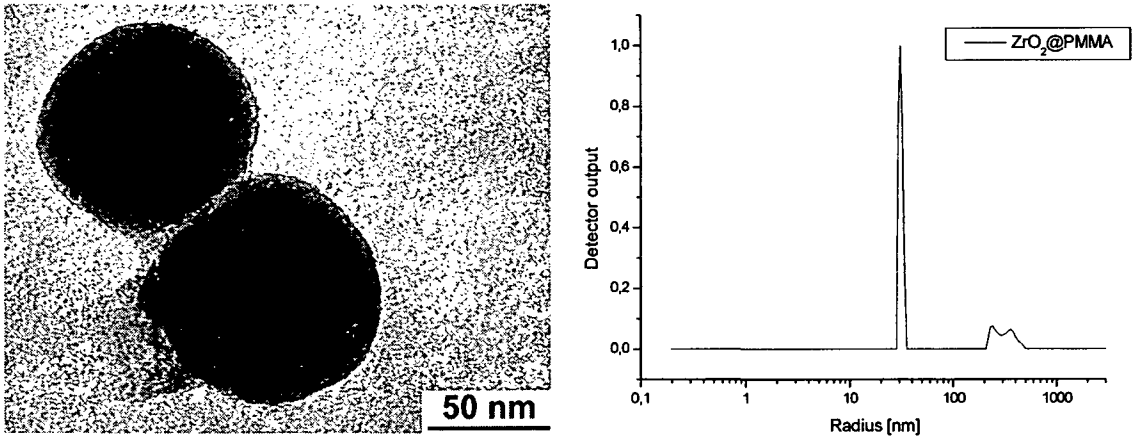

Figure 129: TEM image and DLS-plot (recorded in THF) of ZrO_2@PMMA nanoparticles from ZrO_2 nanoparticles that were functionalized with 3-chloro-pentane-2,4-dione.

According to the TEM image, the core-shell particles had a diameter of 58 nm, while DLS analysis resulted in a diameter of 64 ± 4 nm. The amount of free polymerization was investigated by dispersing the core-shell particles in toluene, separating the unattached polymer chains, and analyzing the weight loss, which showed that approximately 4 % of the polymerization was initiated in solution. As can be seen above, the surface of the zirconium oxide particles smoothened in the early phase of the polymerization.

The kinetic aspects of the polymerization were analyzed via NMR, GPC and DLS. The obtained diagrams are shown in figure 130.

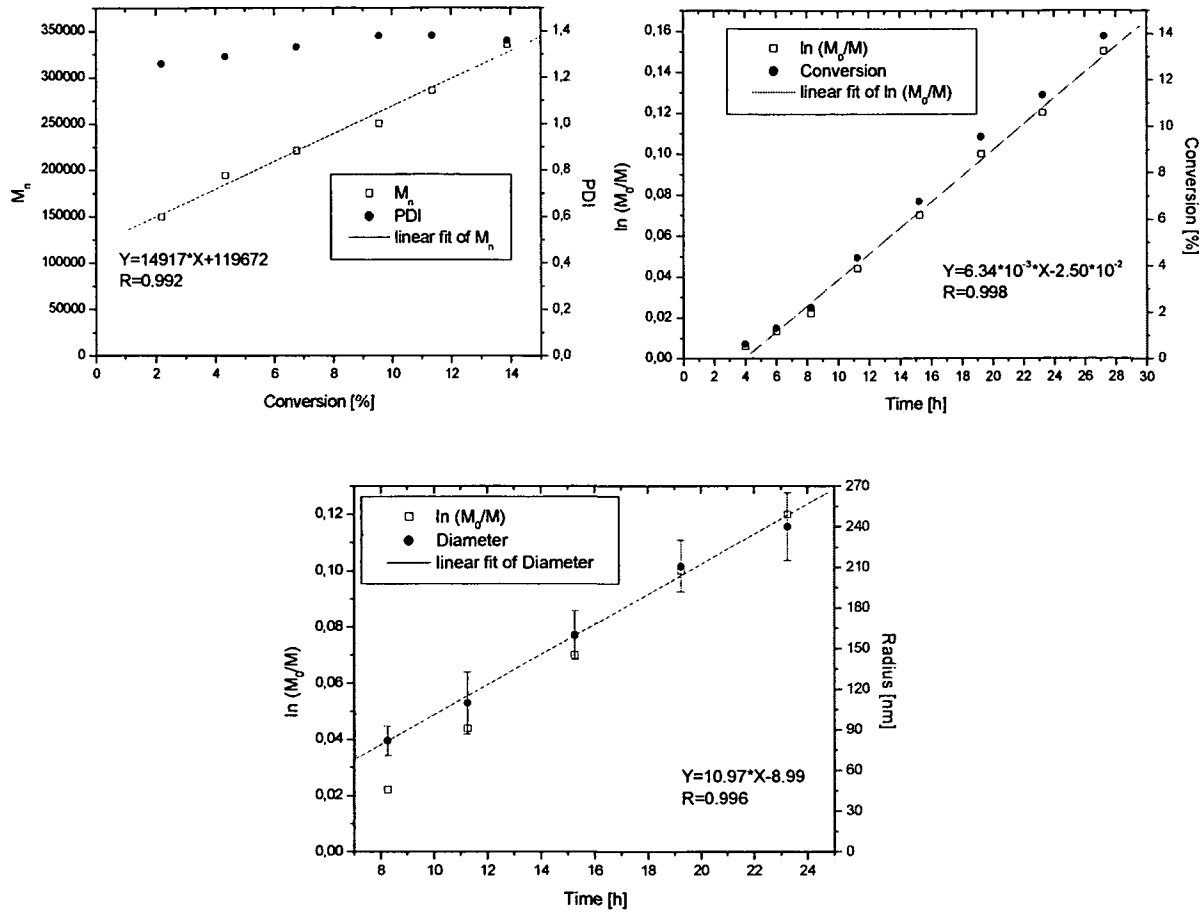

Figure 130: Kinetic plots of an ATRP initiated by modified zirconium oxide nanoparticles with styrene as monomer in 10 ml toluene with 67 mg nanoparticles, [CuCl] : [pmdeta] : [MMA] = [$1.99*10^{-3}$] : [$1.99*10^{-3}$] : [0.1] mol at 90 °C.

As can be seen above, a conversion of 14 % was reached after 27 hours of polymerization. The $\ln(M_0/M)$ values and the increase of the molecular weight showed the linear time dependence typical for an ATRP. The core-shell particles were treated with concentrated NaOH to dissolve the ZrO_2 core to obtain these results. The gained molecular weights were rather high, so that it could not be guaranteed that the actual weight of one single polymer chain was measured by GPC. The molecular weight distribution was about 1.4, which is within the typical range for ATRPs that are initiated with macro initiators. The time dependence of the growth of the diameter was also linear, which suggested that the

polymerization of styrene was much more controlled than the presented polymerization of MMA in case of the TiO_2 nanoparticles.

6.2.4. Synthesis of tantalum oxide core-shell nanoparticles

Functionalized 1-acetyl-2-oxopropyl 2-bromo-2-methylpropanoate and 3-chloro-pentane-2,4-dione precursors were used for the synthesis of tantalum oxide core-shell systems. The synthesis of these nanoparticles was described in chapter 3.2.3.5., whereby diameters of 11 nm and 4 nm, respectively, were obtained.

The 1-acetyl-2-oxopropyl 2-bromo-2-methylpropanoate functionalized tantalum oxide particles were used as macro initiators for the polymerization of MMA, whereby a yield of 27.6 % was obtained after 24 hours. Using styrene as monomer, a yield of 15.1 % was received after 24 hours. In case of tantalum oxide particles that were functionalized with 3-chloro-pentane-2,4-dione, yields of 8.1 % and 5.1 % for the polymerization of MMA and styrene were received after a polymerization time of 24 hours. TGA analysis revealed an incorporation rate of inorganic material between 2.0 % and 3.0 %. After the elimination of a small amount (4 %) of free polymer chains that were produced during the polymerization process, TEM and DLS analyses were performed. A TEM image and the corresponding DLS plot of tantalum oxide particles with a PMMA shell from a 1-acetyl-2-oxopropyl 2-bromo-2-methylpropanoate functionality are shown in figure 131.

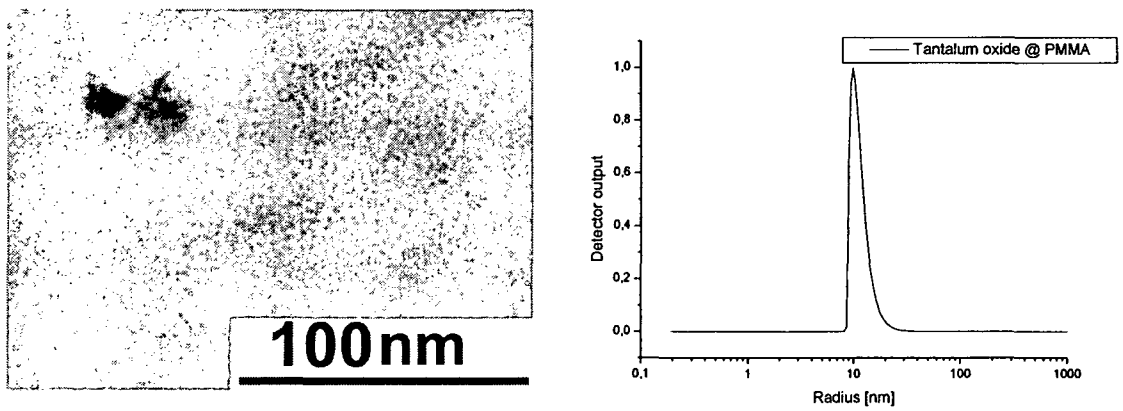

Figure 131: TEM image and the corresponding DLS plot (recorded in THF) of tantalum oxide that were functionalized with 1-acetyl-2-oxopropyl 2-bromo-2-methylpropanoate, covered with a PMMA shell.

Because of the small diameter of the tantalum oxide nanoparticles, the received polymer shell was very fragile. During the observation in the TEM the polymer shell of the particle on the left side was depolymerized by the irradiation of electrons. The particle at the right side still had an intact polymer shell. The diameter of the core-shell particles was about 14 nm according to the TEM image, compared to 6 nm of the original tantalum oxide particles. DLS analysis revealed a slightly larger diameter of 22 ± 4 nm. The shoulder on the right side of the peak suggests the occurrence of larger particles or small aggregates. The stability of the particles was investigated as described in case of the TiO_2 particles. The isolated toluene was analyzed via FTIR spectroscopy whereby small traces of the ν(CO) vibrations of the CO-groups of the coordinated pentane-dione derivates were observed. The weight loss was approximately 2 %.

DLS analysis of 1-acetyl-2-oxopropyl 2-bromo-2-methylpropanoate functionalized particles after 3 days at 100 °C in toluene revealed the decay of the particles. The amount of free polymer was investigated by dispersing the particles in THF, centrifugation and precipitation of the dissolved polymer in methanol. About 4 % of the polymer chains were not attached to the surface of the nanoparticles.

6.2.5. Synthesis of vanadium oxide core-shell nanoparticles

1-Acetyl-2-oxopropyl 2-bromo-2-methylpropanoate and 3-chloro-pentane-2,4-dione functionalized particles were used for the synthesis of vanadium oxide core-shell systems. The production of these particles was described in chapter 3.2.3.4. The particles had a diameter of 25 nm and 160 nm in case of functionalization with 1-acetyl-2-oxopropyl 2-bromo-2-methylpropanoate and 80 nm in case of 3-chloro-pentane-2,4-dione.

The 1-acetyl-2-oxopropyl 2-bromo-2-methylpropanoate functionalized particles were polymerized with MMA and styrene in an ATRP, whereby a yield of 26 % and 10 % was obtained, respectively, after a polymerization time of 24 hours. If particles that were functionalized with 3-chloro-pentane-2,4-dione were used, yields of 11.4 % and 6.2 % were obtained for the polymerization of MMA and styrene after a polymerization time of 24 hours. TGA analysis resulted in an inorganic residues between 0.9 and 2.3 %.

The obtained core-shell systems synthesized from particles that were functionalized with 1-acetyl-2-oxopropyl 2-bromo-2-methylpropanoate are presented in figure 132 and 133. Homopolymer obtained in solution was separated from the particles by dissolving the particles in THF and centrifugation. About 8 % of the polymers were not attached to the

surface of the nanoparticles. The particles shown in figure 132 were synthesized using functionalized vanadium oxide macroinitiators with a diameter of 25 nm.

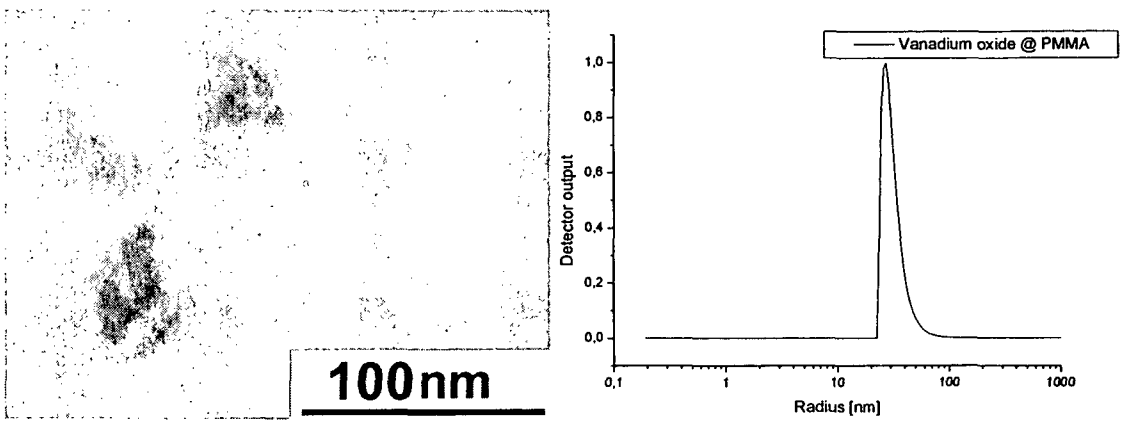

Figure 132: TEM image and corresponding DLS plot (recorded in THF) of vanadium oxide nanoparticles with a PMMA shell.

The vanadium oxide particles seemed to decompose in the beginning of the polymerization. In the obtained hybrid material the pieces of the original particles were still clearly visible. The DLS measurement showed a broad peak at 38 ± 8 nm for these aggregated systems. The stability of the modified particles was investigated by dispersing the functionalized particles in toluene and measuring the weight loss before the dispersing process and afterwards. About 4 % of the particles were dissolved during 3 days in toluene. Performing the same experiment at increased temperature led to further decay of the functionalized vanadium oxide particles according to DLS.

The particles that were used for the synthesis of the core-shell particles in figure 133 originally had a diameter of 160 nm.

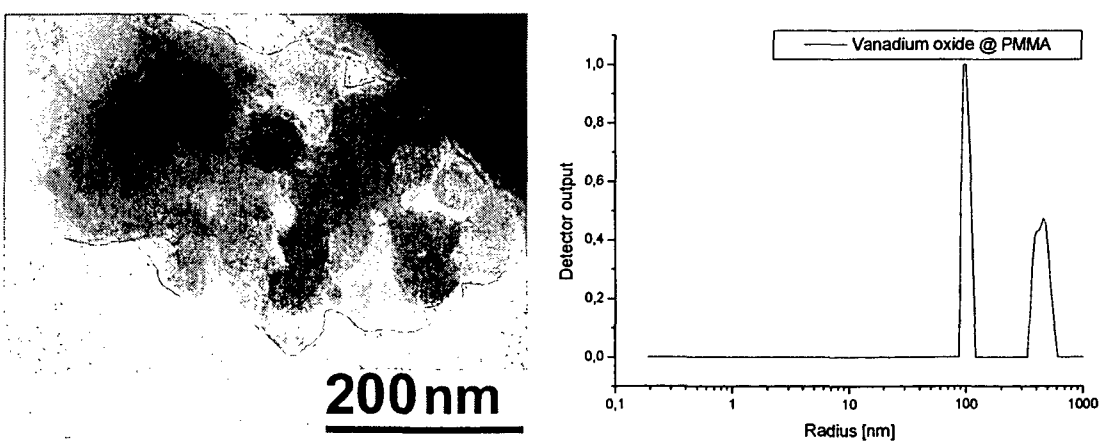

Figure 133: TEM image and corresponding DLS plot (recorded in THF) of vanadium oxide nanoparticles with a PMMA shell.

The core-shell particles that are shown above aggregated during the precipitation in ethanol. The TEM image suggests that the inorganic cores became smaller during polymerization, which could be explained by partially dissolving and/or aging processes in the beginning of the polymerization process. The DLS analysis revealed a diameter of 202 ± 8 nm for the single particles while aggregated systems with a larger diameter were also detected.

As the particles that were functionalized with 1-acetyl-2-oxopropyl 2-bromo-2-methylpropanoate seemed to be slightly unstable in toluene, the core-shell particles, which were synthesized using 3-chloro-pentane-2,4-dione functionalized particles, were analyzed in more detail.

In figure 134 a TEM image and the DLS plot of the observed particles are shown.

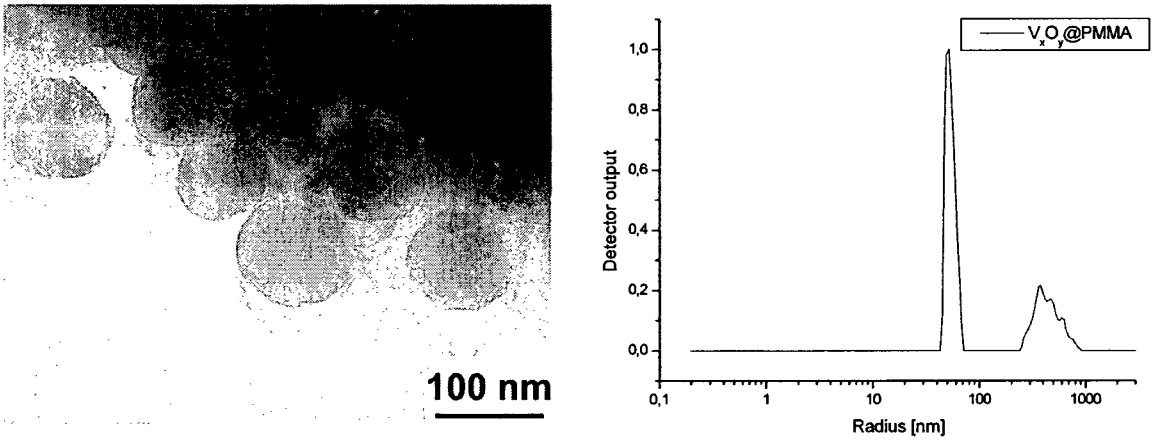

Figure 134: TEM image and corresponding DLS plot (recorded in THF) of vanadium oxide nanoparticles with a PMMA shell.

Contrary to the 1-acetyl-2-oxopropyl 2-bromo-2-methylpropanoate functionalized particles, the 3-chloro-pentane-2,4-dione modified system seemed to be more stable in the beginning of the polymerization process. According to the TEM image, the particles had a diameter of 95 nm, while DLS measurement obtained a diameter of 106 ± 10 nm. The amount of free polymer was measured as described before, which led to a fraction of 4 % polymer that was not attached to the surface of the particles.

6.2.6. Synthesis of yttrium oxide core-shell nanoparticles

1-Acetyl-2-oxopropyl 2-bromo-2-methylpropanoate (85 nm diameter) and 3-chloro-pentane-2,4-dione macroinitiators (200 nm diameter) were used for the synthesis of yttrium oxide core-shell nanoparticles particles. The synthesis of these systems was described in chapter 3.2.3.4. 1-Acetyl-2-oxopropyl 2-bromo-2-methylpropanoate functionalized yttrium oxide macroinitiators were used as for the polymerization of MMA and styrene, which led to a yield of respectively 6.5 % and 4.5 % after 24 hours. If 3-chloro-pentane-2,4-dione functionalized nanoparticles were used in the polymerization process, yields of respectively 11.4 % for MMA and 6.2 % for styrene were obtained after 24 hours. TGA analysis revealed an inorganic content between 2.0 % and 4.5 %. A TEM image of the obtained core-shell particles and the corresponding DLS plot are shown in figure 135.

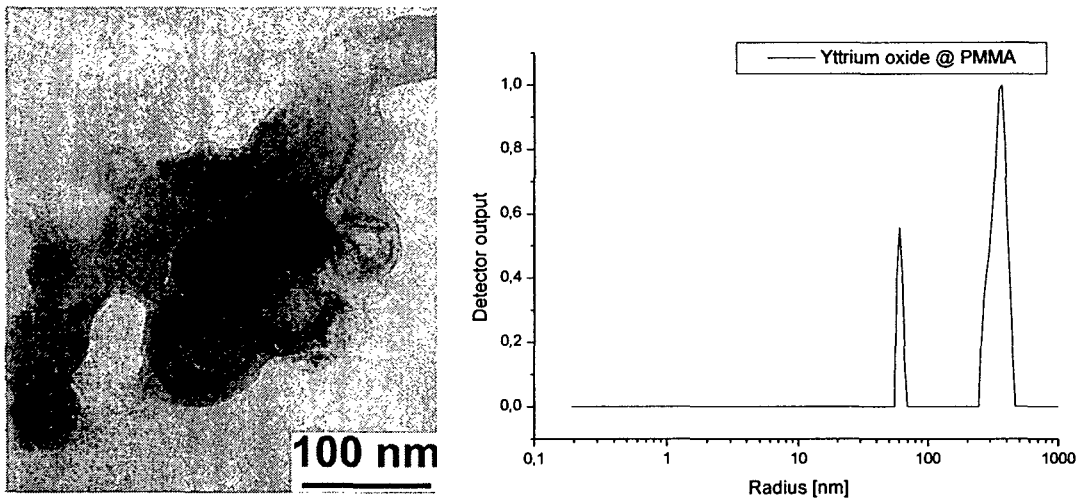

Figure 135: TEM image and DLS-plot (measured in THF) of yttrium oxide nanoparticles with a PMMA shell.

As observed before, the yttrium oxide particles slightly reduced their diameter in toluene. The dissolved precursor molecules initiated polymerization in solution as well. The stability of the functionalized particles was investigated as described as in case of the other metal oxide systems, which revealed a weight loss of the particles of 5 % in toluene. At increased temperatures in toluene, the particle diameter was decreased to about 30 nm. After the separation of free polymer chains, the particles were precipitated in ethanol to prepare the sample for the TEM analysis and redispersed in THF for the DLS analysis. About 12 % of the polymer chains were not attached on the surface of the particles as acquired gravimetrically.

The TEM image suggests that aggregation of the particles occurred during the precipitation procedure. Nevertheless, the core-shell character was still visible. DLS analysis revealed a diameter of 120 ± 8 nm which was slightly larger than the 90 nm observed by TEM analysis. If 3-chloro-pentane-2,4-dione functionalized particles were used in a polymerization process, the obtained core-shell systems were more stable. A TEM image and the corresponding DLS plot of the obtained particles are presented in figure 136.

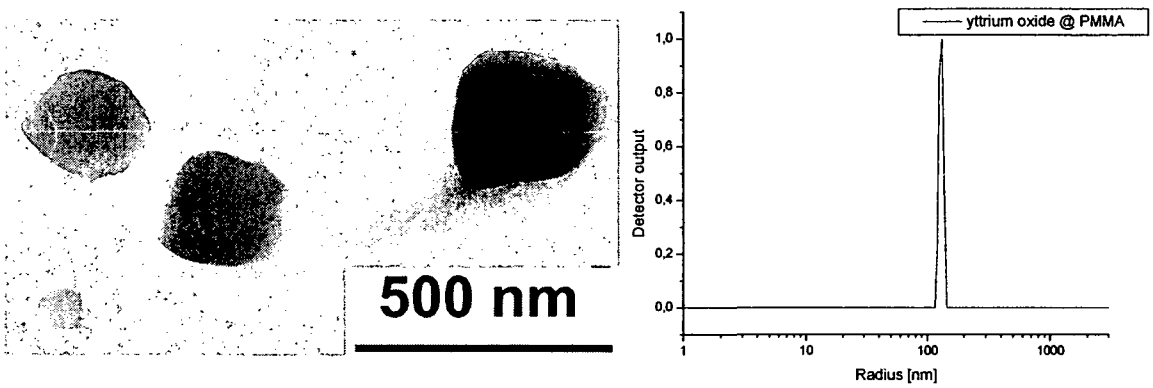

Figure 136: TEM image and corresponding DLS plot (recorded in THF) of yttrium oxide nanoparticles with a PMMA shell.

The TEM image suggests a diameter of about 240 nm of the non-spherical core-shell systems. The appearance of the inorganic core remained unchanged during the polymerization as the functionalized macroinitiators showed the same structure before the polymerization process. The DLS analysis resulted in a diameter of 250 ± 15 nm. The stability of the used surface functionalized particles was much higher compared to the 1-acetyl-2-oxopropyl 2-bromo-2-methylpropanoate functionalized system. About 4 % of the obtained polymer chains were not attached to the surface of the nanoparticles.

6.2.7. Synthesis of iron oxide core-shell nanoparticles

The synthesis of the used multifunctional initiators with a diameter of 90 nm was described in chapter 3.2.3.6. In the ATRP of MMA and styrene, functionalized 3-acetyl-5-bromo-5-methylhexane-2,4-dione particles served as macroinitiators, whereby yields of 14.1 % and 8.3 % were received after 24 hours. TGA analysis showed inorganic contents of 4.7 % (PMMA) and 5.3 % (PS). The free polymer chains were eliminated via suspending the particles in THF followed by centrifugation. About 10 % of the polymer chains were not attached to the surface of the nanoparticles.

In figure 137 a TEM image and the corresponding DLS plot of the obtained particles are presented.

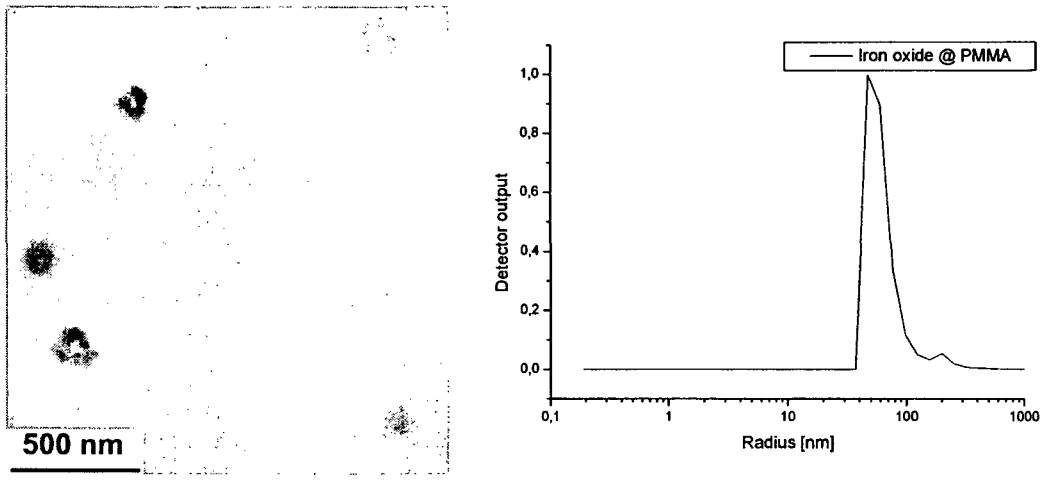

Figure 137: TEM image and the corresponding DLS plot (recorded in THF) of iron oxide nanoparticles with PMMA shell.

Both, the TEM image and the DLS plot suggest a fairly monodisperse size-distribution with a diameter of 110 nm according to the TEM image and 120 ± 25 nm incase of the DLS plot. The broad size distribution and the shoulder on the right side of the peak in the DLS plot were, possibly, caused by aggregated particles. The stability of the functionalized iron oxide particles was analyzed as described before in toluene. Stirring in toluene at room temperature for three days led to a weight loss of 4 %, while at 100 °C only fragments with a diameter about 30 nm were found in DLS. Dispersion in THF, centrifugation, drying and comparing the weight before and after the procedure showed that 9 % of the polymer chains were not attached to the iron oxide core. As mentioned in chapter 3.2.3.6., it was not possible to synthesize 3-chloro-pentane-2,4-dione functionalized iron oxide particles because within one week no particle formation took place.

It has to be mentioned that, in general, the stability of the particles that were produced from modified alkoxides was relatively low, which led to the unexpected occurrence of polymerization in the free solution as well, initiated by cleaved precursor molecules. The stability was improved by replacing 3-acetyl-5-bromo-5-methylhexane-2,4-dione and 1-acetyl-2-oxopropyl 2-bromo-2-methylpropanoate with 3-chloro-pentane-2,4-dione. Possibly the lower sterical demand allowed for a denser structure of the synthesized particles.

6.3. Grafting of a polymer shell from particles that were synthesized from metal salts

The "grafting from" polymerization applying the surface-functionalized metal oxide core was carried out using methyl methacrylate (MMA) and styrene as monomer. Depending on the initiating molecule that was immobilized on the particle surface, different polymerization mechanisms were available.

6.3.1. Synthesis of iron oxide core-shell nanoparticles

Iron oxide particles with a diameter of 110 nm (chapter 4.4.4.1.) were used for the synthesis of iron oxide core-shell systems. Depending on the utilized polymerization mechanism, different yields were received. The highest yield of 56 % was obtained if particles where initiator B was immobilized, were polymerized photo-chemically with styrene as monomer. All other polymerizations resulted in yields between 19 and 30 %.
In table 25 the obtained yields of the polymerizations after a polymerization time of 24 hours are shown with the exception of the photo-initiated polymerization, which was performed in 48 hours.

Table 25: Yields of the polymerizations with MMA and styrene grafted from iron oxide particles.

Modified Particle	Monomer	Isolated Yield
$Fe_xO_y(OH)_z$ + Subst. A	Styrene	0.67 g (33.5 %)
	MMA	0.38 g (18.9 %)
+ Subst. B	Styrene	1.11 g (55.8 %)
	MMA	0.23 g (11.5 %)
+ Subst. C	Styrene	0.38 g (19.2 %)
	MMA	0.59 g (29.7 %)
+ Subst. D	Styrene	0.44 g (22.4 %)
	MMA	0.46 g (22.9 %)

In figure 138 the obtained iron oxide core shell particles are presented. The polymerization of the polystyrene layer was performed using ATRP that was initiated by initiator C.

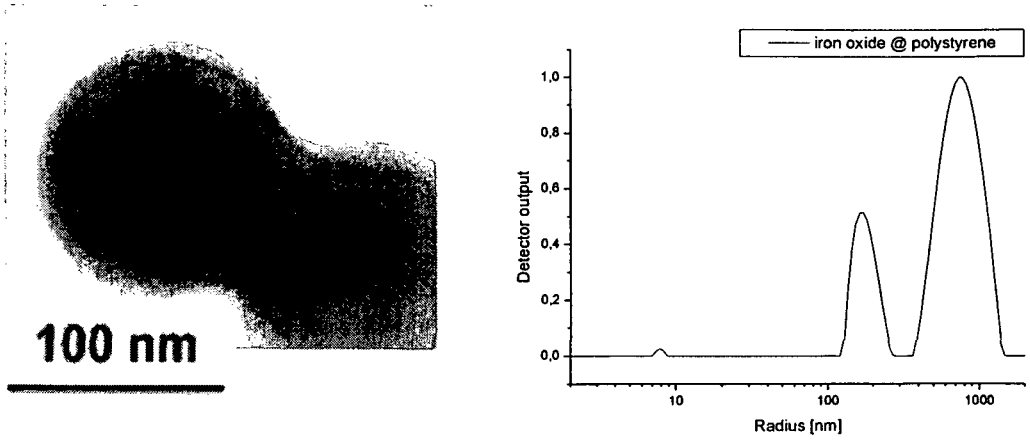

Figure 138: TEM image of iron oxide nanoparticles that are covered with polystyrene and the corresponding DLS plot recorded in THF.

The core-shell particles shown in the TEM image in figure 138 had a diameter of 120 nm while the DLS measurement suggests a diameter of 260 ± 44 nm. It has to be mentioned that the polymer-covered particles were precipitated in ethanol before TEM-analysis. Precipitation in ethanol caused a folding process of the polymer chains, which reduced the measurable diameter of the core-shell particles. The first peak in the DLS plot was rather broad, which might have been caused either by aggregation during the polymerization process of the core-shell particles or during the redispersion in THF. The second peak that was visible in the DLS-plot was obviously caused by aggregated particles because during the TEM analysis no larger structures were observed. The stability of the functionalized particles was analyzed like described in chapter 6.2., by dispersing them in toluene for three days. Neither a significant weight loss of the particles before and after the dispersion in toluene nor signals from cleaved initiator molecules in the FTIR analysis of the used toluene were found.

Contrary to the results obtained in case of the core-shell particles, which were synthesized from modified alkoxides, the polymerization of polymer chains that were not attached to the surface of the particles was not observed.

Different functionalized iron oxide particles were compared in their polymerization behavior using MMA and styrene as monomer. The inorganic core was modified with the different initiators and polymerization was initiated. After finishing the reaction after a certain period of time, the polymers were separated from the iron oxide core by dissolving the core in concentrated HCl. The obtained molecular weight and the MWD of the polymers are shown in table 26, and the resulting GPC plots are presented in figure 139.

Table 26: Comparison of the polymers received using iron oxide cores, functionalized with the various initiators. The polymerization time for initiator B was 48 h, while all other initiators were polymerized 24 h (MWD = molecular weight distribution).

PMMA	Initiator A	Initiator B	Initiator C	Initiator D
M_n [g/mol]	93300	118700	210000	195400
MWD	1.95	2.80	1.58	1.38
PS	**Initiator A**	**Initiator B**	**Initiator C**	**Initiator D**
M_n [g/mol]	125300	14800	286400	245100
MWD	1.78	2.85	1.54	1.32

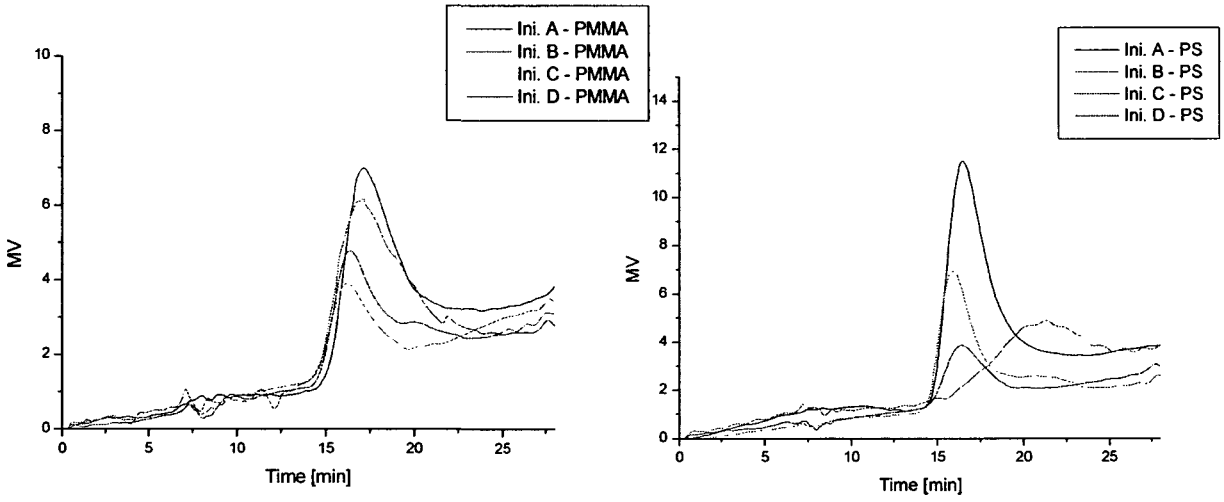

Figure 139: GPC-plots of the cleaved polymer chains.

All polymers showed monomodal molecular weight distributions with varying molecular weight. The photochemical polymerization with initiator B resulted in the highest molecular weight distribution (MWD) of about 2.8, further in very low molecular weights of 14800 g/mol for polystyrene (PS) and quite low molecular weights of 118700 g/mol for PMMA, indicating a low efficiency of this initiator. Surprisingly, the polymers formed by ATRP had the highest molecular weights between 286400 g/mol and 195400 g/mol keeping the polydispersity between 1.32 and 1.58 as expected. Possibly, the high density of initiator groups on the surface of the nanoparticles led to a high degree of polymer chain entanglement during polymerization, which seemed to be irreversible even after ultrasonic treatment.

Kamata et al. showed recently that it is possible to dissolve the inorganic core of a core-shell particle leaving the polymer shell intact.[246] Therefore, the measured values represented probably the intact polymer shell originally surrounding the iron oxide core. This assumption was also supported by DLS measurements before and after dissolving the Fe-oxide core, which revealed shrinkage of the radius of the objects in the solution from 160 nm (Fe-oxide@PS) to 136 nm (polymer after HCl treatment). In figure 140 the DLS plots before and after the HCl treatment are compared.

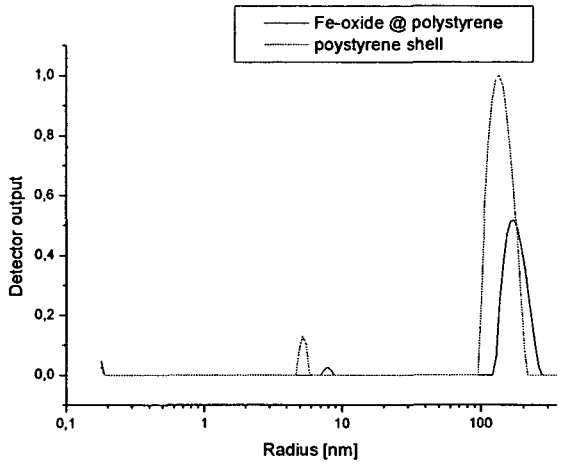

Figure 140: Comparison of the DLS-plots of iron oxide nanoparticles with a polystyrene shell before and after the dissolution of the iron oxide core with HCl measured in THF.

The radius of the Fe_2O_3@PS particles was reduced from 161 ± 23 nm to 135 ± 25 nm.[246] The shell was investigated via UV/VIS spectroscopy and no absorption of iron oxide was found. Furthermore, there might have occurred an interaction of the end groups of the polymers formally attached to the metal oxide core. In case of the free radical polymerization, the lower molecular weight suggested that only single polymer chains were measured because of the low initiator coverage of the iron oxide core, in case of the azo initiator, a good entanglement was less likely.

The kinetics of the grafting from polymerization of styrene using iron oxide nanoparticles modified with initiator D as macroinitiators was investigated in more detail. For this purpose, the polymers were cleaved from the core as described above. ATRP was carried out using CuCl/pmdeta as catalyst in toluene at 90°C with styrene and MMA as monomer. In figure 141 the kinetic plots for the polymerization of styrene are shown.

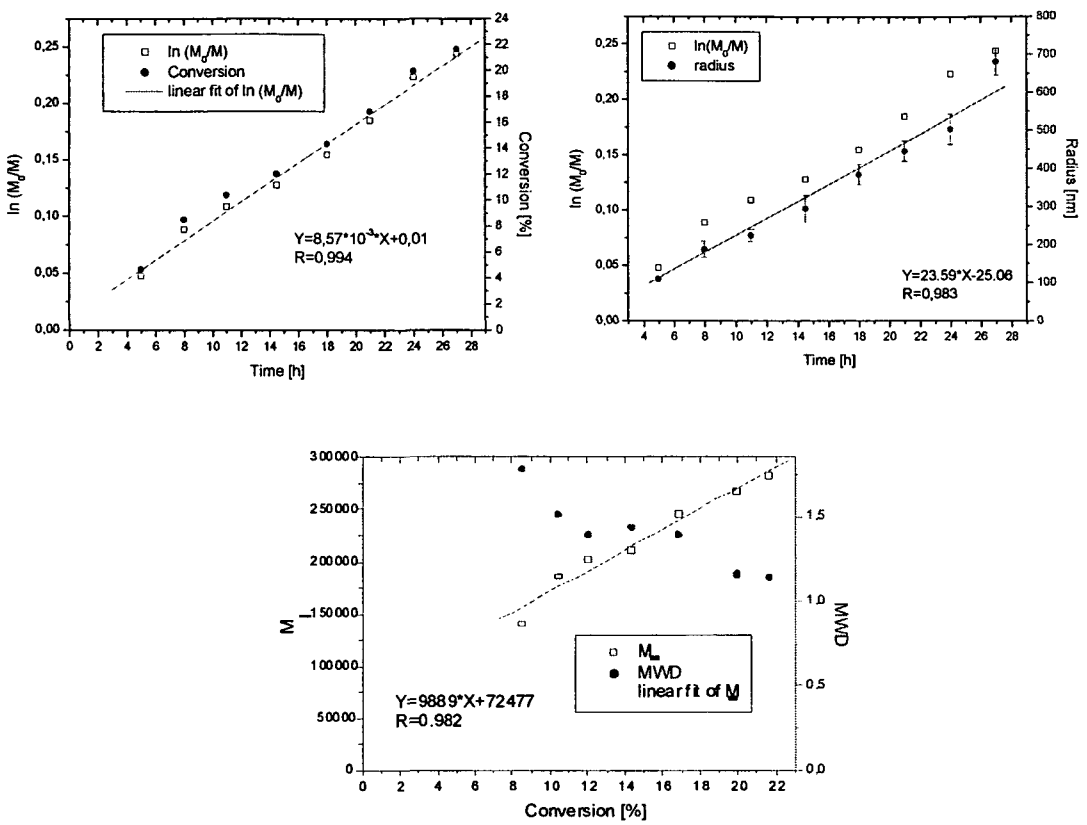

Figure 141: Kinetic plots of the polymerization of styrene from the surface of iron oxide particles functionalized with initiator D; [CuCl] : [pmdeta] : [styrene] = [1] : [1] : [10] mol in 10 ml toluene at 90 °C.

In the presented kinetic investigation a conversion of 21 % was obtained after 28 hours. This rather low conversion was caused by the large amount of solvent that was used to minimize termination reactions, such as coupling. The molecular weight of the polystyrene chains increased linearly up to 280000 g/mol at 21 % conversion, while the molecular weight distribution showed the usual progression for ATRP, starting at fairly high values and decreasing gradually during the polymerization process to 1.14 after 27 hours. The polymerization showed a first order kinetic with respect to monomer concentration. The diameter of the core-shell particles was measured by DLS that showed a linear growth from 110 nm to 660 nm.

The same kinetic investigation was performed using MMA as monomer (figure 142).

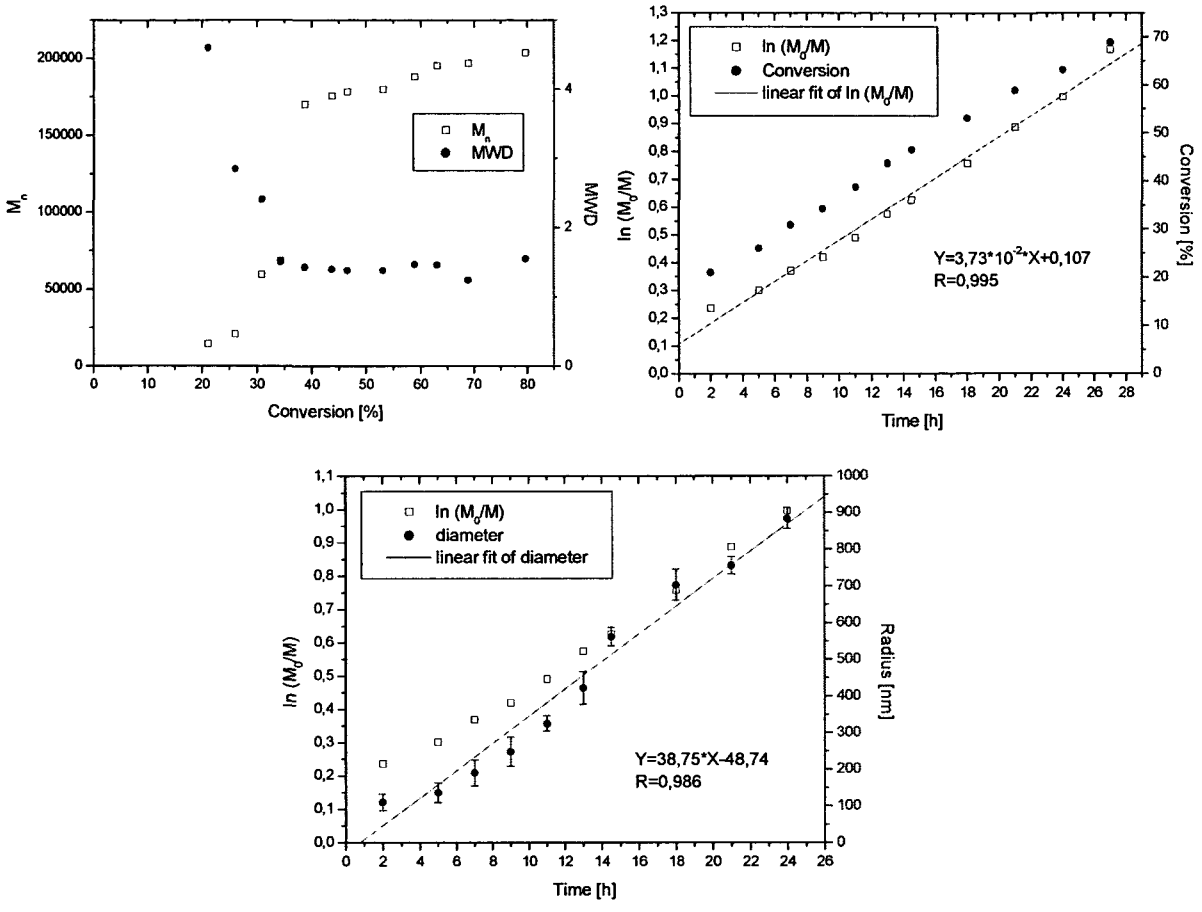

Figure 142: Kinetic plots of the polymerization of styrene onto the surface of iron oxide particles functionalized with initiator D; [CuCl] : [pmdeta] : [MMA] = [1] :[1] :[10] mol in 10 ml toluene at 90 °C.

The usage of MMA as monomer led to a measured molecular weight of 203000 g/mol, and a conversion of 72 % was obtained after 28 hours, compared to 21 % in case of styrene. Because of the higher reactivity under the chosen reaction conditions, the polydispersity of the molecular weight reached 1.55 after 28 hours, which was higher than in case of the styrene polymerization. The obtained semilogarithmic kinetic and molecular weight plots showed for all ATRPs a linear dependence on time, which indicated first-order kinetic with respect to the monomer and, therefore, a constant concentration of active species during the polymerization. The growth of the diameter of the core-shell particles proceeded very regularly, which was shown by the nearly linear dependence on time.

The obtained core-shell particles were analyzed via SEM to investigate if a self-organization process of the particles took place as in literature various examples of the formation of 3D-arrays of nanoparticles, such as silica, latex etc. are presented.[303] The particles were precipitated in ethanol. A drop of this dispersion was placed onto the SEM sample carrier. In figure 143 iron oxide particles covered with a polystyrene layer are shown.

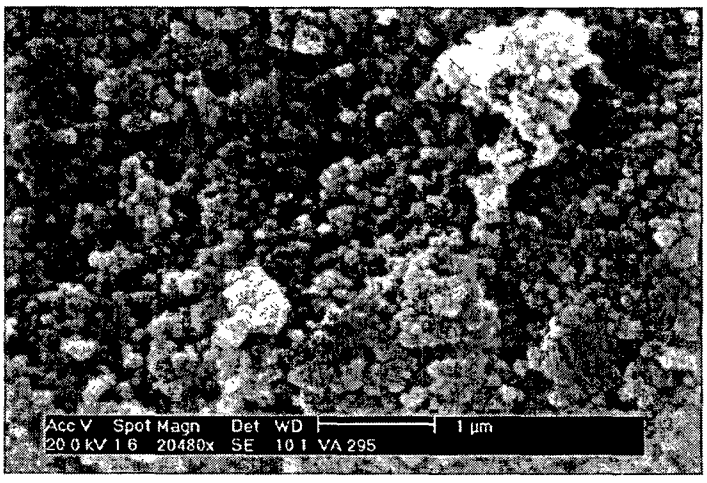

Figure 143: SEM image of iron oxide particles with a PS shell.

According to the SEM image presented above no ordering process took place. The core-shell particles were randomly arranged. Despite occurring entanglement of polymers distinct particles were observable. Comparison with literature is difficult because no description of the ordering process of such systems to 3D arrays could be found.

6.3.2. Synthesis of titanium oxide core-shell nanoparticles

Precursor systems with a diameter of 210 nm (chapter 4.4.4.2.) were used for the production of titanium oxide core-shell nanoparticles. In case of the functionalized titanium oxide nanoparticles, the obtained yields for all types of polymerization were higher than in case of using iron oxide particles for the initiation process, possibly due to influences of Fe(III) ions on the ATRP mechanism, which are known to deactivate initiating/growing radicals.[172] Initiator C showed conversions of 66 % for styrene being used as monomer and 56 % for MMA. Only polymerizations that were initialized by initiator A in a free radical polymerization gave rather small yields with 6 % with styrene as monomer and 18 % if MMA was used as monomer.

In table 27 the obtained yields are summarized. The polymerization time was in all polymerizations 24 hours except photo-initiated polymerization which was performed 48 hours.

Table 27: Obtained yields in the polymerization process of titanium oxide particles.

Modified Particle	Monomer	Isolated Yield
$Ti_xO_y(OH)_z$ + Subst. A	Styrene	0.12 g (6.0 %)
	MMA	0.37 g (18.4 %)
+ Subst. B	Styrene	0.44 g (22.0 %)
	MMA	1.27 g (63.7 %)
+ Subst. C	Styrene	1.33 g (66.5 %)
	MMA	1.12 g (56.2 %)
+ Subst. D	Styrene	1.10 g (55.2 %)
	MMA	0.63 g (31.7 %)

In figure 144 a TEM image of titanium oxide nanoparticles with a polystyrene layer is shown, polymerized with ATRP, initiated by initiator D.

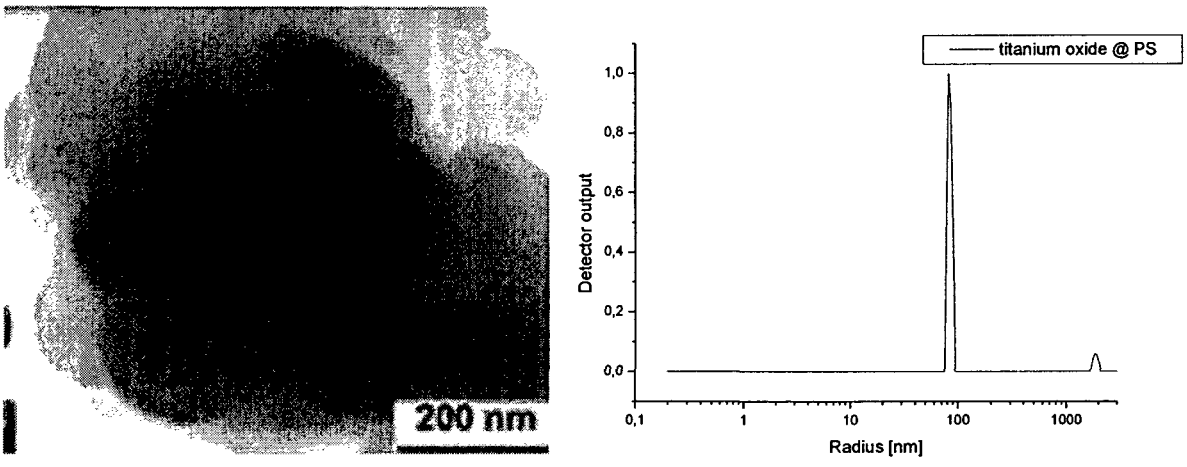

Figure 144: TEM image and the corresponding DLS-plot (recorded in CH_2Cl_2) of TiO_2@PS core-shell nanoparticles.

According to the TEM image and the DLS-plot, the obtained core-shell particles aggregated during the precipitation. In the TEM image the single core-shell particles were still visible with a diameter of approximately 180 nm but entangled. The DLS plot obtained a diameter of

170 ± 8 nm. The DLS analysis was performed in CH_2Cl_2 as redispersing in THF did not lead to acceptable results.

In figure 145 a SEM image of the isolated core-shell particles is shown.

Figure 145: SEM image of titanium oxide nanoparticles with a PS shell.

Again, the core-shell particles were randomly arranged and no ordering process was observed, however, the boundaries of the single particle structures were clearly visible, which excluded that the observed aggregation was caused by cross linking of polymer chains of different particles, taking in account the results from DLS. It rather seemed as if physical entanglement of polymer chains of different particles had occurred.

6.3.3. Synthesis of zirconium oxide core-shell nanoparticles

Zirconium oxide precursors with a diameter of 640 nm (chapter 4.4.4.3.) were used for the production of zirconium oxide core-shell nanoparticles.
Depending on the used initiator and monomer, different yields were obtained in the polymerization processes. Initiator A resulted in rather high polymerization rates with 65 % conversion in case of styrene and 63 %, if MMA was used as monomer, whereas photo-polymerizations showed rather small yields. ATRP resulted in conversion rates between 20 % and 50 %. All polymerizations were performed 24 hours except photo-polymerization, which was performed 48 hours. In table 28 the obtained results are summarized.

Table 28: Yields of the polymerization of zirconium oxide with MMA and styrene.

Modified Particle	Monomer	Isolated Yield
$Zr_xO_y(OH)_z$ + Subst. A	Styrene	1.31 (65.37 %)
	MMA	1.26 g (63.0 %)
+ Subst. B	Styrene	0.10 g (5.0 %)
	MMA	0.25 g (12.6 %)
+ Subst. C	Styrene	0.82 g (41.1 %)
	MMA	0.37 g (18.4 %)
+ Subst. D	Styrene	0.59 g (29.6 %)
	MMA	1.00 g (50.0 %)

In figure 146 a TEM image of zirconium oxide@PS nanoparticles and the corresponding DLS plot are shown. The polymerization process was initialized by initiator D, which was immobilized on the nanoparticles surface.

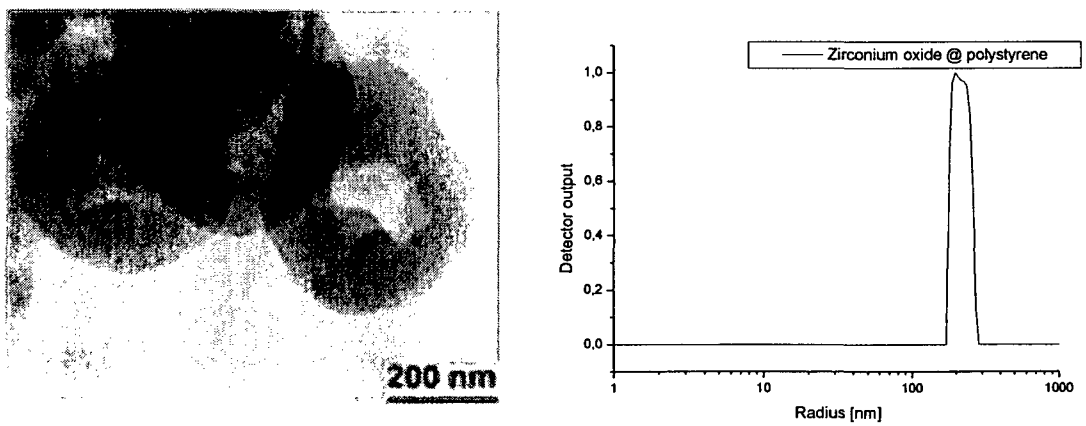

Figure 146: TEM image and the corresponding DLS-plot (recorded in THF) of zirconium oxide nanoparticles with a PS shell.

According to the TEM image, the core-shell particles had a diameter of approximately 400 nm. The appearance of the core-shell particles is slightly different compared to the other presented systems. Thus it seemed as if the inorganic cores had somehow disappeared but the TGA analyses, presented in chapter 6.3.5., proved that zirconium oxide cores were still incorporated. The DLS plot suggested a slightly larger diameter of 430 ± 30 nm, possibly due

to aggregation, which might be also the reason for the shoulder on the right hand side of the peak. Furthermore, the unfolding process of the polystyrene chains in THF might have increased the measured diameter. In figure 147 a SEM image of the gained core-shell particles is shown.

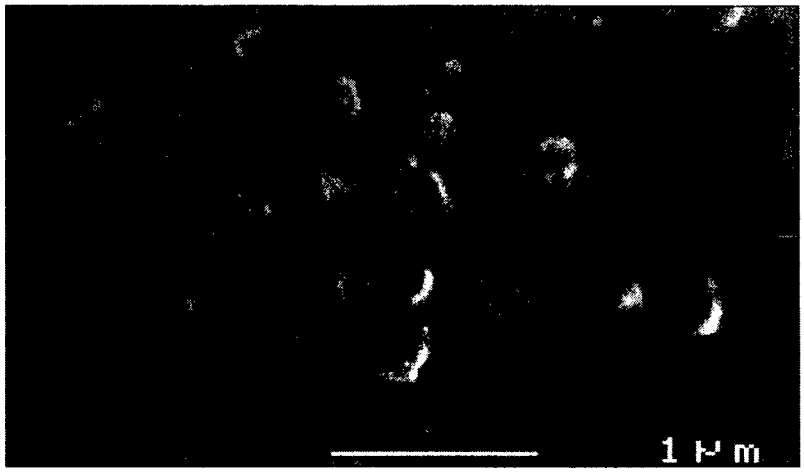

Figure 147: SEM image of the zirconium oxide particles with a polystyrene shell.

Compared to the other core-shell systems, the presented SEM image looks different, possibly, due to interactions between the zirconium oxide core and the electron beam. In the SEM image above, the boundaries of the core-shell particles were still visible. No self-organization was observed.

6.3.4. Synthesis of zinc oxide core-shell nanoparticles

Zinc oxide precursors with a diameter of 156 nm were used for the production of zinc oxide core-shell nanoparticles. The obtained yields, which were received if surface modified zinc oxide particles were used as macroinitiators in the polymerization process, were rather low compared to the other metal oxides. All yields were between 6 % and 30 %, in respect of the used amount of monomer, except free radical polymerization initiated by initiator (A) where above 70 % of the monomer were converted. The small yields of the ATRPs might have been caused by the small degree of surface functionalization of the ZnO particles with initiator (D) (chapter 4.4.4.4.). This theory is supported by the high yields obtained in free radical polymerization. In table 29 the obtained yields are summarized.

Table 29: Obtained yields of the polymerization of MMA and styrene on the surface of zinc oxide particles.

Modified Particle	Monomer	Isolated Yield
$Zn_xO_y(OH)_z$ + Subst. A	Styrene	0.30 g (15.2 %)
	MMA	1.45 g (72.3 %)
+ Subst. B	Styrene	0.47 (23.6 %)
	MMA	0.12 g (6.1 %)
+ Subst. C	Styrene	0.30 g (15.1 %)
	MMA	0.55 g (27.7 %)
+ Subst. D	Styrene	0.15 g (7.6 %)
	MMA	0.20 g (10.0 %)

In figure 148 a TEM image of ZnO@PS nanoparticles and the corresponding DLS plot are shown. The polymerization process was started by initiator C.

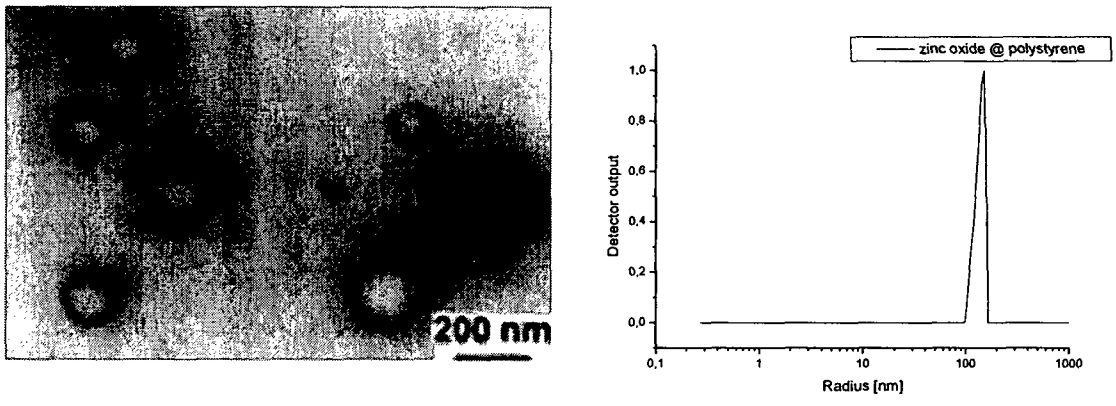

Figure 148: TEM image and the corresponding DLS-plot (measured in THF) of ZnO@PS nanoparticles.

Again, the diameter from DLS analysis was slightly larger than from the TEM image. The particles shown in the TEM image, had a diameter of 220 nm, compared to 260 ± 30 nm measured by DLS. The DLS curve showed a shoulder on the left side, possibly caused by smaller core-shell particles, which are also shown on the TEM image. The unfolding of the PS chains in THF also might have increased the by DLS measured diameter.

A SEM image of the core shell particles is shown in figure 149.

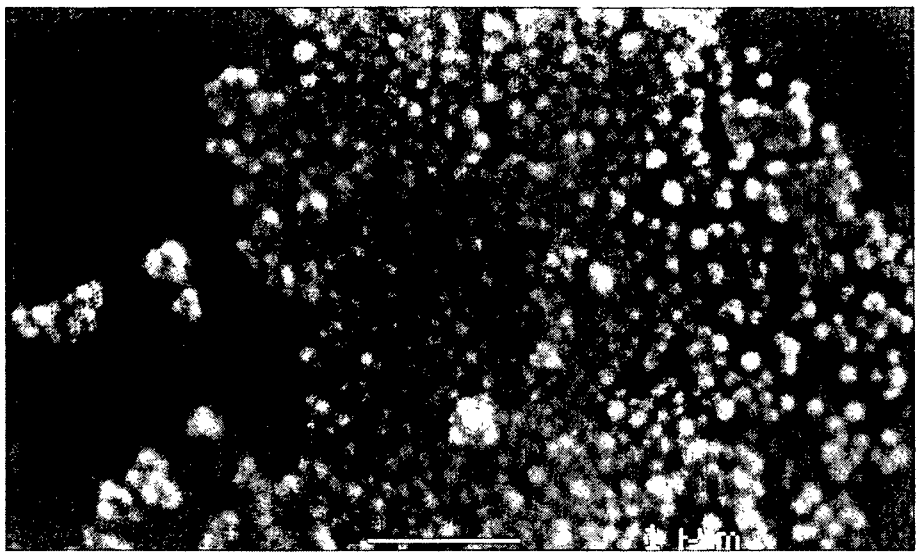

Figure 149: SEM image of ZnO@PS core-shell particles.

As shown in the SEM-image above, no ordering took place, however, the boundaries of the core-shell particles are visible. Compared to the other SEM investigations, isolated particles are observable especially on the right side of the image. Thus it can be excluded that cross-linking of polymer chains of different particles occurred during the polymerization process.

6.3.5. Thermal investigation of the obtained hybrid materials

Some polymers are degraded completely to low molecular products at increased temperatures, while other polymers additionally form crosslinked polymers.[304] PMMA depolymerizes at 300-450 °C completely to MMA, while PS forms crosslinked intermediate products. Whether a polymer degrades to monomers or forms intermediate crosslinked products, depends on the difference between the activation energy of a homolytical chain cleavage and the activation energy of crosslinking reactions. The form of the TGA curves heavily depends on the so called ZIP-length, i.e. to the number of cleaved monomer molecules per kinetic polymer chain. A low ZIP-length signifies a small number of cleaved monomer molecules, which does not automatically imply low polymer degradation. Depolymerization of polymers with a high ZIP-length results in a sudden mass reduction because the polymer mass remains constant until the temperature is high enough to deliver the activation energy for the depolymerization. In case of lower ZIP-length, at low temperatures, beside monomers, volatile oligomeres are

formed, while at higher temperatures only monomers are cleaved. The polymer mass starts to decrease slowly, but this fastens at higher temperatures.

The received core-shell systems were analyzed via TGA up to 800 °C in air. The recorded TGA plots of the hybrid materials that contained PMMA are shown in figure 150.

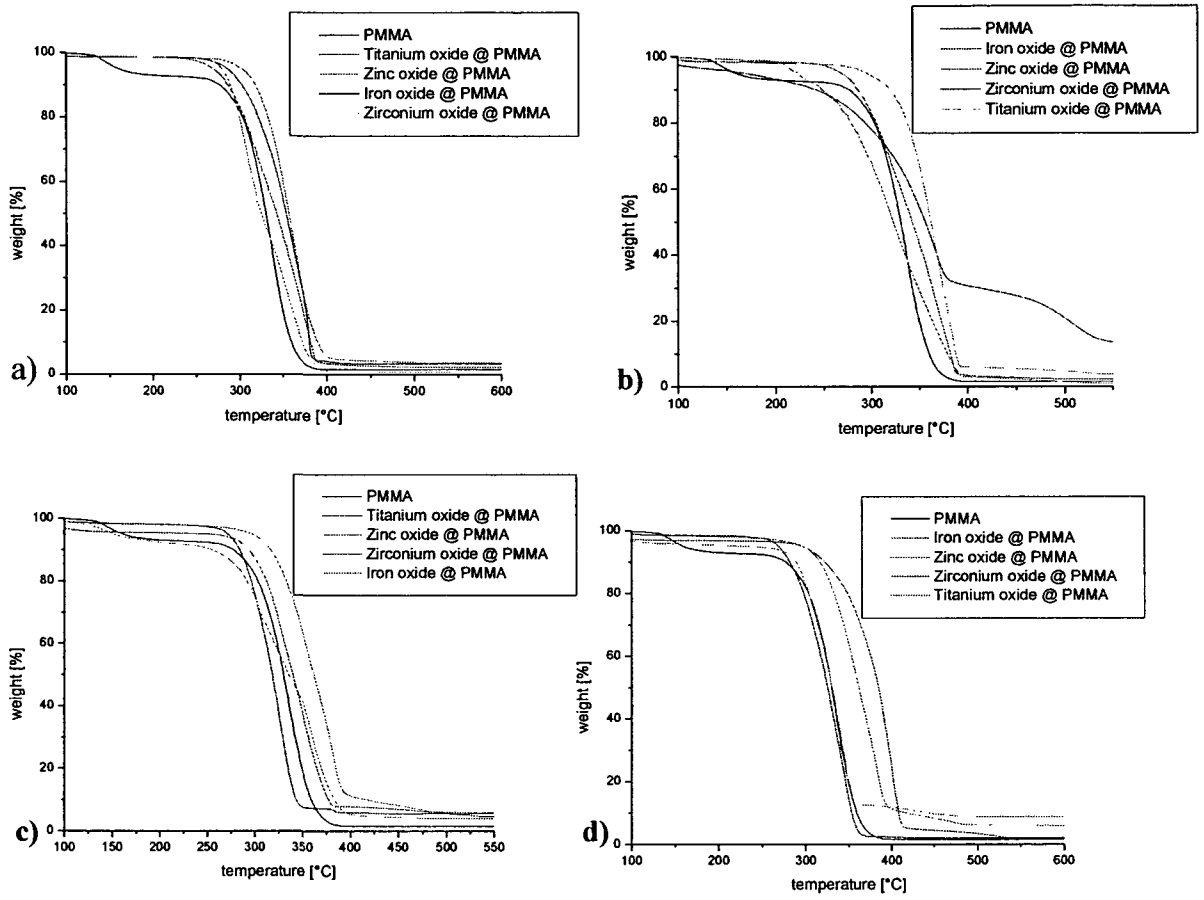

Figure 150: Diagrams of the TGA-analysis of the obtained PMMA hybrid materials, where the polymerization was initialized a) with initiator (A), b) with initiator (B), c) with initiator (C) and d) with initiator (D).

The diagrams shown in figure 150 revealed the typical degradation mechanism of PMMA. The mass loss started slow at low temperatures but fastened at higher temperatures, suggesting a low ZIP-length.

Furthermore, the polymerization mechanism, the amount of the inorganic species, and the kind of the incorporated metal oxide had a significant influence on the thermal stability of the synthesized hybrid materials. The curve of pure PMMA showed a weight loss of 5 % up to

150 °C, possibly due to remaining solvent, while all other curves showed smaller weight loss. In case of the particles, which were modified with the azo-initiator, the content of inorganic material in the hybrid material was between 2 % and 4 %. The highest improvement of the onset of the decomposition temperature was obtained if zinc oxide and iron oxide particles were incorporated. The thermal stability was increased about 30 °C. The amount of incorporated titanium- and zirconium oxide nanoparticles was rather small, which led to no improvement of the onset temperature of the degradation. In case of the utilization of particles that were functionalized with initiator (B), the obtained results were exactly the reverse. The rate of incorporated titanium- and zirconium oxide particle into the hybrid material was much larger, which resulted in a higher thermal stability. In case of the titanium oxide particles, the onset temperature of the decomposition was increased by about 40 °C. No significant increase of the onset of the decomposition temperature was observed for the other materials.

If ATRP initiators (C) and (D) initiated the polymerization process, the incorporation of zinc and iron oxide increased in both cases the onset temperature of the decomposition about 40 °C. The incorporation of zirconium oxide nanoparticles modified with initiator (C) had a negative effect on the decomposition temperature, while using particles modified with initiator (D) did not reveal an influence on the degradation temperature. An incorporation rate of 5-10 % was observed for these materials.

These analyses were repeated with the polystyrene containing hybrid materials. The measured TGA-diagrams are shown in figure 151.

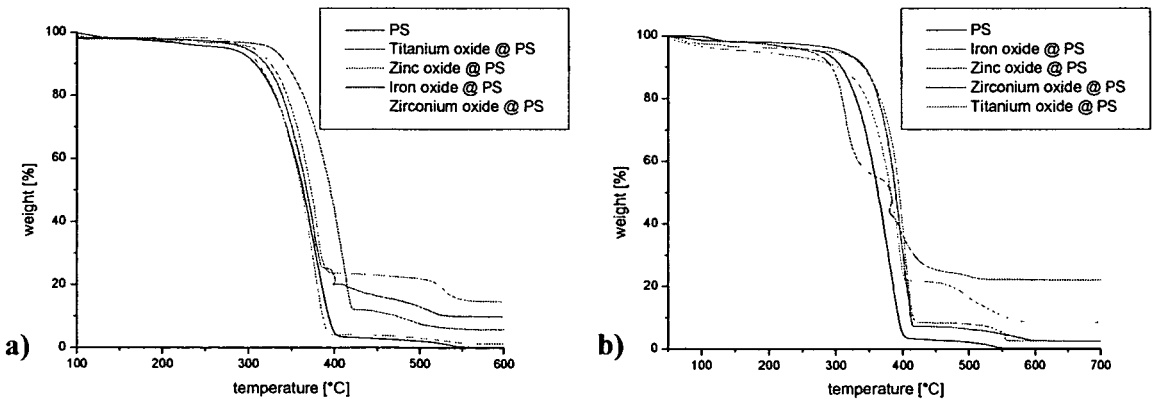

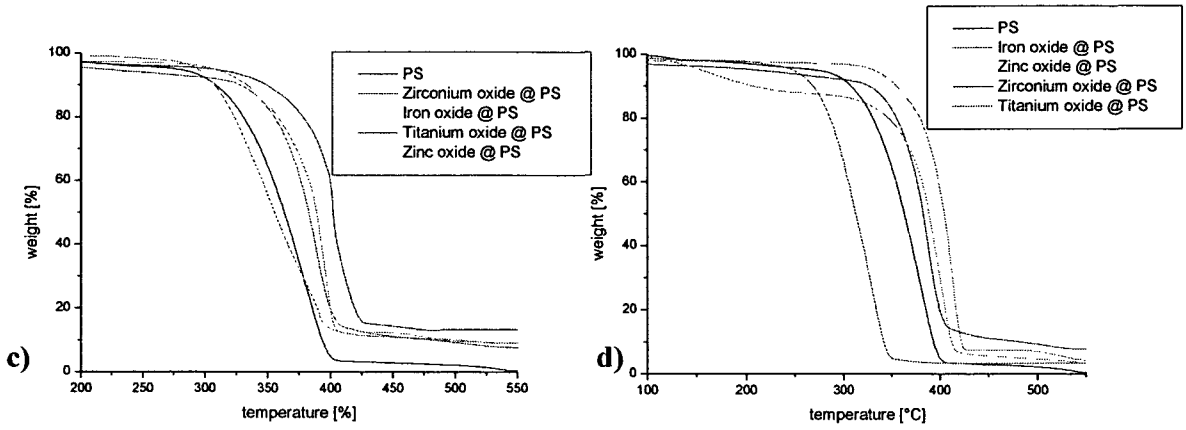

Figure 151: Diagrams of the TGA-analysis of the obtained PS hybrid materials where the polymerization was initialized a) with initiator (A), b) with initiator (B), c) with initiator (C) and d) with initiator (D).

The obtained TGA curves reflect the relatively high ZIP-length of PS (about 3.1), which led to a sudden mass loss at a certain temperature. Some curves showed mass loss up to 150 °C caused by the evaporation of solvent. If the core-shell particles were synthesized by thermally initiated free radical polymerization, only the incorporation of titanium oxide particles increased the onset temperature of the degradation temperature of the polystyrene layer significantly about 35 °C. All other materials showed just small effects or no effects at all. The incorporation of iron oxide particles led to a sudden increase of the temperature at about 400 °C, followed by a reduction of the temperature, despite the continuous heating in the thermogravimetric analysis, possibly caused by an exothermic oxidation process of the iron oxide particles. If the particles were functionalized with the presented photo-initiator, the obtained core-shell particles showed an increase of the onset temperature of the degradation when zinc and titanium oxide particles were incorporated in the hybrid material. In case of the iron oxide particles the same exothermic process was observed at about 400 °C, which was responsible for the erratic form of the curve. The obtained curves were repeatedly measured but the profile did not change.

If initiator (C) was used for the initiation process, all metal oxide particles increased the onset temperature of the decomposition of the polystyrene layer, except iron oxide. The highest increase was measured for the incorporation of titanium oxide nanoparticles with 50 °C, followed by zinc oxide with 30 °C, and zirconium oxide with 25 °C. In case of initiator (D)

the results were quite similar. Iron oxide did not improve the thermal stability of the produced hybrid material but decreased the onset temperature of the decomposition by about 50 °C. The highest improvement of the decomposition temperature was obtained if zinc oxide particles were used as macro initiator, which raised the decomposition temperature by about 45 °C, followed by titanium oxide, which increased the onset temperature of the degradation by about 30 °C, and zirconium oxide with 25 °C. Some of the curves showed an additional step after the decomposition of the polymer, possibly caused by the degradation of surface functionalities.

The thermal investigations were repeated under inert gas atmosphere. The obtained diagrams are shown in figure 152.

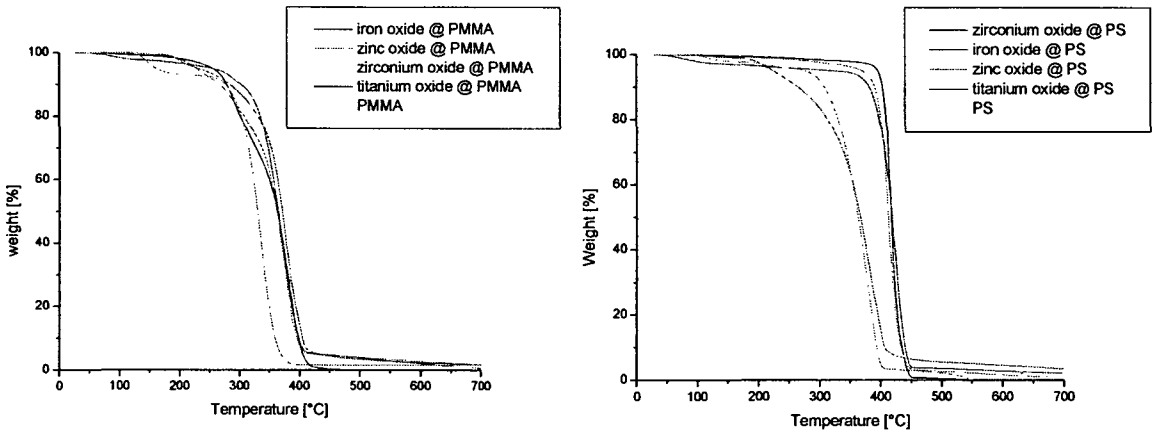

Figure 152: TGA analysis of the core-shell nanoparticles (polymerized using initiator (C)) under nitrogen atmosphere.

Both, in case of the polystyrene and the PMMA shell the shifts of the onset temperature of the degradation process were still visible. In case of the PMMA analyses, the onset temperatures of the degradation process of the polymer were slightly shifted to higher temperatures, but still volatile oligomeres were cleaved starting at low temperatures. A slight trend to increased temperatures was also observed in case of the PS covered nanoparticles. The degradation of the polymer started at higher temperatures leading to a quicker mass loss suggesting a higher ZIP-length. Only the incorporation of iron oxide had a negative impact on the onset temperature of the thermal degradation of the polystyrene shell. The second step at higher temperatures was not observed, if the TGA was performed under nitrogen. These analyses showed that the presence of oxygen did not provoke a thermal shift of the onset temperature of the degradation process of the polymer shell.

6.3.6. TG-FTIR analyses of representing core-shell nanoparticles performed at Netzsch-Gerätebau GmbH

TG-FTIR spectrometry was used to obtain information about the products formed during the decomposition process of the core-shell nanoparticles at varying temperatures. Furthermore, the progress of the decomposition was investigated. Two samples were analyzed via a TG-FTIR spectrometer at the Netzsch-Gerätebau GmbH by Dr. E. Füglein: (i) Titanium oxide nanoparticles covered with a shell of polystyrene and (ii) iron oxide nanoparticles covered with a shell of PMMA. The analyses were performed under nitrogen atmosphere.

In figure 153 the obtained TGA plots are presented. The maximum in the Gram Schmidt traces corresponds to the temperature which caused the highest intensity over all wavelengths in the FTIR analysis due to the highest mass loss.

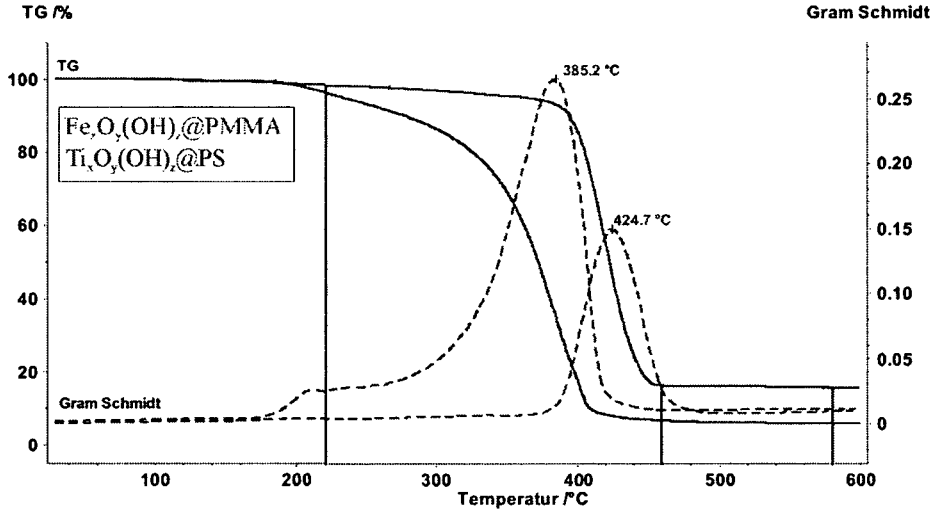

Figure 153: Comparison of the mass losses of the two investigated core-shell systems including the Gram Schmidt traces of both samples.

The decay temperatures of the two polymer-shells were calculated from the first deviation of the TGA curves. The $Ti_xO_y(OH)_z$@PS core-shell particles revealed a decomposition temperature of the PS-shell of 421 °C while the $Fe_xO_y(OH)_z$@PMMA lost the PMMA-shell at 384 °C. In case of the PMMA shell an additional decomposition step was detected at 210 °C, which is the reason for the smaller slope of the mass decay curve. The obtained results corresponded excellent to the results that were presented before (chapter 6.3.5.).

In figure 154, all performed FTIR spectra for both samples are shown as 3D-plot combined with the measured TG-signals.

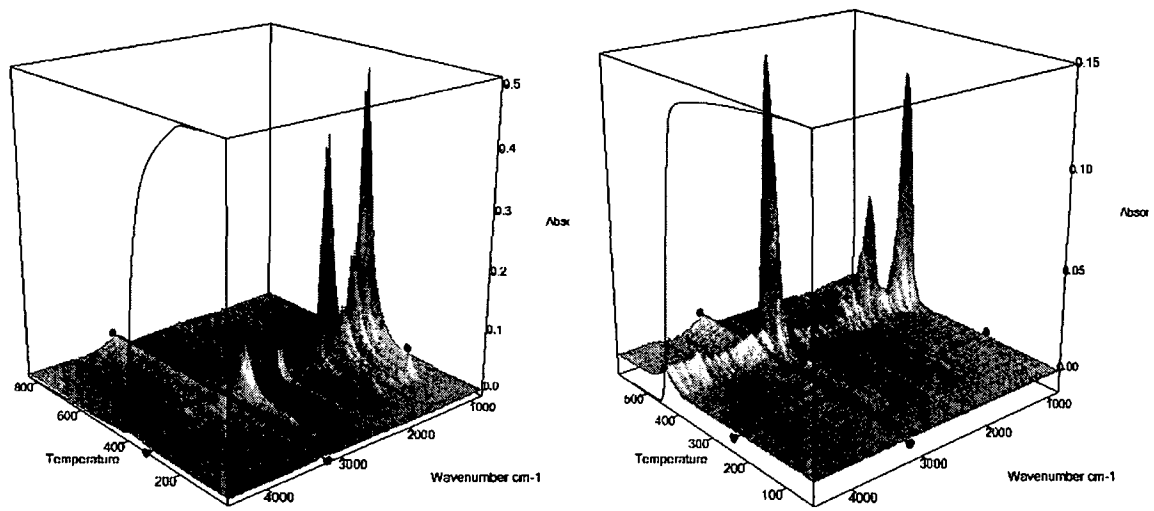

a) b)

Figure 154: 3D-plot of the recorded FTIR spectra with added TG-signal of a) $Fe_xO_y(OH)_z$@PMMA b) $Ti_xO_y(OH)_z$@PS.

The performed FTIR confirmed the decomposition temperatures which were obtained from TGA. Furthermore, the beginning of the decomposition of the PMMA shell (figure 154a) at 200 °C was affirmed by emerging signals in the FTIR plot (figure 155).

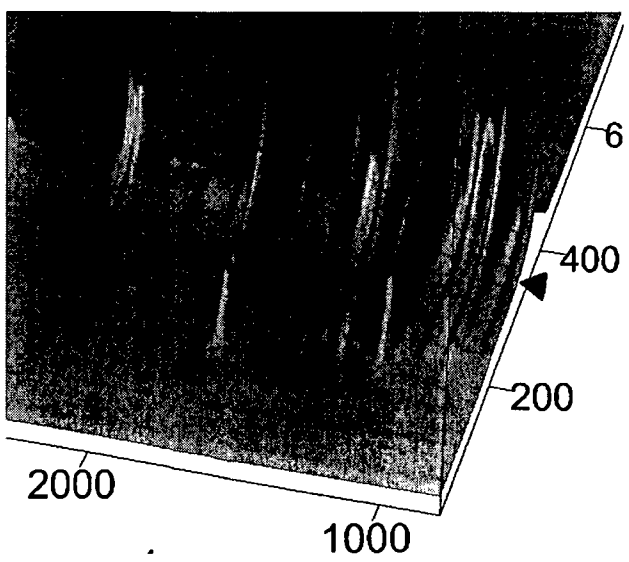

Figure 155: Zoom of the respective area of figure 154a).

The obtained FTIR spectra were compared with OPUS database spectra. In figure 156 the obtained FTIR spectrum at the maximum intensity of the Gram Schmidt trace of $Ti_xO_y(OH)_z$@PS is compared with the FTIR spectrum of PS.

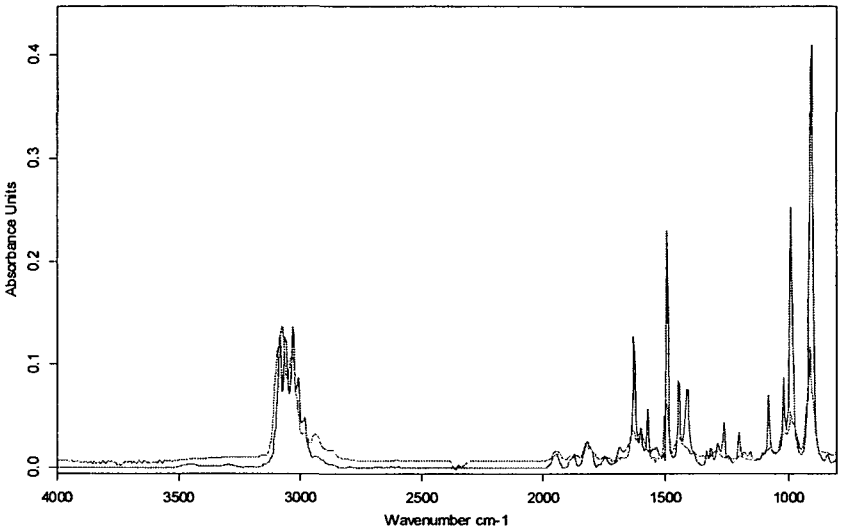

Figure 156: Comparison between the FTIR spectra of $Ti_xO_y(OH)_z$@PS (red) at the maximum intensity of the Gram Schmidt trace at 424 °C and PS from the OPUS database (blue).

In figure 157 the obtained FTIR spectrum at the maximum intensity of the Gram Schmidt trace of $Fe_xO_y(OH)_z$@PMMA is compared with the FTIR spectrum of PMMA.

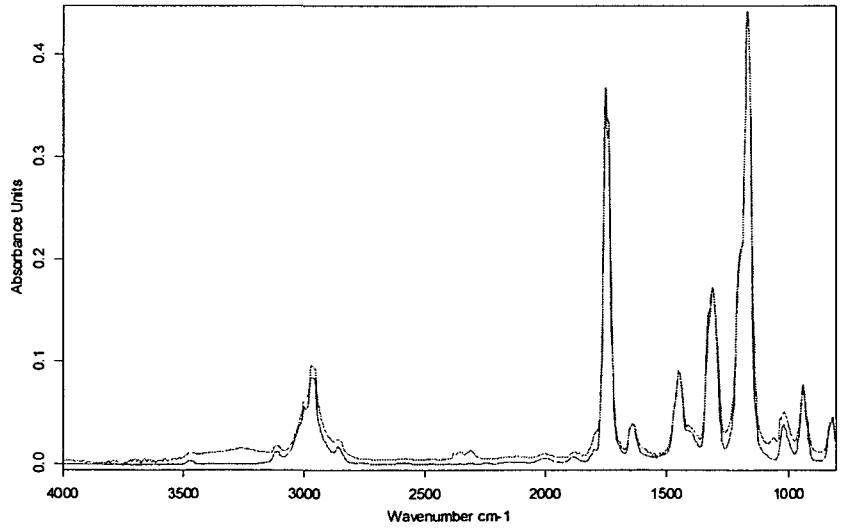

Figure 157: Comparison between the FTIR spectra of $Fe_xO_y(OH)_z$@PMMA (red) at the maximum intensity of the Gram Schmidt trace at 424 °C and PMMA from the OPUS database (blue).

FTIR analysis proved that only PS and PMMA were cleaved from the particle surface because no additional molecules, such as water or other degradation products, were detected. In case of the PMMA core-shell particles the enlargement of the FTIR spectrum at low temperatures showed that part of the PMMA was cleaved at lower temperatures, possibly caused by volatile oligomeric chains suggesting a lower ZIP-length. The recorded FTIR spectra of both analyzed samples corresponded very well to the spectra that were obtained from the OPUS database.

6.4. Short summary

In this chapter the polymerization capacities of 3-bromo-pentane-2,4-dione and 3-chloro-pentane-2,4-dione were analyzed. It was shown that both halo-pentane-2,4-dione derivatives were capable of initiating free radical and controlled radical polymerization reactions. The efficiency of the chlorine derivative was much higher compared to bromine-pentane-2,4-dione due to a higher thermal stability. Furthermore, the activation rate of the halo-pentane-diones was investigated proving the higher thermal instability of the bromine-derivate.

The polymerization of the organic shell in a "grafting from" approach, starting at the surface of the modified nanoparticles was discussed. In case of the nanoparticles that were synthesized from modified metal alkoxides, different stabilities of the particles depending on the contained functionality were observed. 1-Acetyl-2-oxopropyl 2-bromo-2-methylpropanoate and 3-acetyl-5-bromo-5-methylhexane-2,4-dione functionalized particles were slightly soluble in toluene, which caused a reduction of the diameter and/or decay of the functionalized metal oxide nanoparticles and led also to the occurrence of polymerization in solution. Apparently, the polymerization of polymer chains, which were not attached to the particle surfaces, was nearly entirely suppressed, if particles that contained 3-chloro-pentane-2,4-dione were used as macroinitiators.

In case of the inorganic-organic core-shell nanoparticles, which were produced from different metal salts, no polymerization in solution was found, but an increase of the thermal stability of the polymer shell was observed.

7. Experimental part

7.1. General techniques

All reactions that were sensitive to atmospheric conditions were carried out in an oxygen- and moisture free argon atmosphere applying Schlenk techniques or by working in a glove box. Standard procedures were used to purify all utilized solvents which were stored under an argon atmosphere afterwards. A mercury high pressure lamp TQ 150 (strongest resonance line at 366 nm) of Heraeus/Hanau with a quartz glass cooler was utilized for UV irradiation.

7.2. Materials

$Fe(OEt)_3$ was obtained from Vadim Kessler, Department of Chemistry, SLU, Uppsala, SLU, Sweden. The photoinitiator 2-hydroxy-1-[4-(2-hydroxyethoxy)phenyl]-2-methyl-1-propanone (IRGACURE 2959) was donated from CIBA Spezialchemikalien. All other chemicals were purchased from Sigma-Aldrich, Gelest and ABCR.
CuBr and CuCl were stirred in glacial acetic acid overnight, filtered, washed with absolute ethanol, dried in vacuo and stored in argon atmosphere. Monomers were distilled from CaH_2, degassed, and stored in a refrigerator prior to use. All alkoxides were stored in a moisture free environment at room temperature. All other chemicals were used without further purification.

7.3. Analytical techniques

Elemental analyses were carried out by Mag. Johannes Theiner at Microanalytical Laboratory at the Institute of Physical Chemistry, University of Vienna.

Liquid state NMR spectra were recorded on a 300 MHz DRX Avance Bruker or Bruker AC 250 instrument working at 300 (250), 75.43 (66.9) and 59.6 MHz for ^{1}H, ^{13}C and ^{29}Si, respectively. Solid state NMR spectra were recorded on a 300 MHz Bruker Avance 300 spectrometer, equipped with a 4 mm broad-band MAS probehead and ZrO_2 rotors. The rotor speed for all experiments was 8 kHz.

Relative size exclusion chromatography (SEC) measurements in THF were performed using a Waters system including a Waters 515 HPLC pump, a Waters 717 autosampler, a Waters

2410 differential refractive index detector, and Styragel columns (HR 0.5, 3, and 4, linear and GPC PHASE SDV 50/100/10E5A) at 40°C at a rate of 1 ml/min applying linear polystyrene standards. Molecular weight and polydispersity analysis was calculated with Waters Millennium software including the GPC/V option and related to an internal standard (diphenyl ether).

Dynamic light scattering (DLS) was used as a tool for studying the particle size in suspension. Because it is a non-routine technique a small introduction is given here.

The key step in a DLS measurement is determining the autocorrelation function, which relates the correlation of the system at one time with itself at a different time. Initially, envision setting up a very long line of microspheres and then releasing them simultaneously at time t_0 which would cause each of them to scatter the incident electric field of the laser. The superposition of the scattered fields at the detector results in an electric field of the value E_0. After a certain period of time the spheres have moved a sufficiently large distance. Afterwards, no coherence to the initial positions, where the spheres were lined up, is existing. The movement of the spheres results in an independence of the scattered electric fields superposition of the initiating position and so no correlation would be obtained. If the period of time is sufficiently short ($t = t_0 + \Delta t$), all of the spheres would have moved a small distance in a random direction due to Brownian motion. The correlation is still similar to the initial line of spheres. In this situation, the electric field at the detector is similar to E_0 which correlates the fields at t_0 and $t_0 + \Delta t$. The autocorrelation function describes the correlation of the system that can be written in the following form:

$$g_1(t) = e^{\frac{-t}{\tau}}$$

where τ is the decay time of the system.[305]

It has to be taken into account that it is not possible to align the microspheres straight and release them simultaneously. Furthermore this situation is referred to as an ensemble average, where many systems are taken and observed at one time.[306] Another complication is that light detectors can not measure electric fields but light impulses which are related to the electric field via the equation:

$$I = \left(\sum E^*\right) \cdot \left(\sum E\right)$$

where I is the intensity, Σ indicates a sum over all scatters, E is the electric field, and * indicates the complex conjugate. Normally the multiplication of a number by its complex conjugate results in a scalar and not a vector which would lead to the loss of the phase information. Siegert, however proved that the phase information is still retained and the autocorrelation function of the intensity obeys the relation

$$g_2(t) = < I_t^2 > \cdot g_1^2(t) + < I_t >^2$$

where < > indicates an average.[305] Instead of observing the intensity signal in the time domain, a spectrum analyzer will measure the signal in the frequency domain. After performing Fourier transformation, the diffusion coefficient can be calculated using the following equation

$$D^{-1} = \left[\frac{4n_0\pi \cdot \sin\frac{\theta}{2}}{\lambda} \right]^2 \cdot \tau$$

where n_0 is the refractive index of the solution, λ is the wavelength, τ is the decay time of the system and θ is the scattering angle.[305]

Finally the hydrodynamic radius can be calculated using the Stokes-Einstein relationship

$$R_h = \frac{kT}{6\pi\eta D}$$

where k is the Bolzmann's constant, T the absolute temperature, and η is the solvents viscosity.[307]

DLS measurements were performed applying a non-invasive backscattering technique by using an ALV NIBS/HPPS instrument in the first year. Furthermore, an ALV/CGS-3 Compact Goniometer System with an ALV/LSE-5003 Light Scattering Electronics and Multiple Tau Digital Correlator were used in the last two years. The determination of the particle diameter was performed via distribution function and cumulant analysis using the $g_2(t)$ method via a number weighted approach. If not otherwise mentioned a 90° angle was used for the measurements.

FTIR-spectra were measured on a Bruker Tensor 27 spectrometer in absorption or total reflection (ATR-technique). ATR measurements were performed using a Harrik MVP™ sample cell. The gained spectra were analyzed and interpreted with OPUS 4.0 software from Bruker. Until June 2002, IR spectra for solid samples were carried out with a Perkin Elmer 16 PC FT-IR instrument and with a Biorad FTS 135 for liquid samples.

A Shimadzu TA 50 WSI Thermal Analyzer was used for thermal analysis. Thermal gravimetric analyses were carried out with Shimadzu TG-50 instrument and with a heating rate of 5 °C/min under air. Furthermore a Netzsch TG209C with a Netzsch TASC 414/4 controller was used for measurements under nitrogen.
Several samples were analyzed at the Netzsch-Gerätebau GmbH. There a micro balance Netzsch-TG 209 C *Iris* with a heating rate of 10 °C and a Bruker FTIR TENSOR were used.

UV/VIS spectroscopy was measured in liquid and solid phase with a Perkin Elmer Lambda 15 UV/VIS spectrophotometer (Institute of Material Chemistry, Vienna University of Technology). Liquid samples and kinetics of gold particle formation, UV/VIS-spectra were recorded with an Agilent 8453 UV-visible spectrophotometer and a Varian Cary 5000 UV-VIS-NIR spectrophotometer (Institute of Physical Chemistry, University of Vigo).

Transmission electron microscope (TEM) measurements were performed on a JEOL JEM-200CX, a JEOL JEM-100CX (USTEM, Vienna University of Technology) and a JEOL JEM-1010 (Institute of Physical Chemistry, University of Vigo). The samples were prepared either via evaporation of the solvent of the particle suspension on a TEM Formvar grid or via interface crystallization. Applying the latter technique the particles were suspended in an organic solvent with a lower density than water and immiscible with water like toluene. A drop of the particle suspension was placed onto the water surface and the organic solvent evaporated. During this evaporation process the particles are forced to form ordered structures. Finally the particles were carefully deposited on the grid.

Scanning electron microscope (SEM) measurements were performed with a Philips XL-30 (Institute of Physical Chemistry, University of Vigo), a JEOL 6400 (USTEM, Vienna Technical University) and a Philips-FEI XL 30 with acceleration voltage of 0.5 - 30 kV (Institute of Inorganic Chemistry, University of Hanover). Samples for scanning electron microscopy were either prepared by ultrasonically dispersing the particles in ethanol before

depositing a drop of the suspension on an aluminum carrier or interface crystallization. The samples were sputtered with gold atoms.

Nitrogen sorption measurements were carried out on an ASAP-2010 M (Micrometrics) instrument. Prior to each measurement the samples were degassed at 60 °C for at least four hours to a remaining pressure lower than 10 μbar. A variety of theoretical methods for the interpretation of experimental data has been developed. Among them, the Brunauer, Emmett and Teller (BET) model is one of the most widely used.[256]

Luminescence spectra were recorded using a Perkin-Elmer LS-50B fluorespectrometer, equipped with a pulsed Xenon discharge lamp with the excitation wavelength of 270 nm. Low temperature measurements were performed using an accessory with liquid nitrogen cooling.

X-ray crystallography studies were carried out on a Bruker-AXS SMART diffractometer with an APEX CCD area detector. Graphite-monochromated Mo-K_α radiation (71.073 pm) was used for all measurements. The nominal crystal-to-detector distance was 5.00 cm. A hemisphere of data was collected by a combination of three sets of exposures at 173 K. Each set had a different ϕ angle for the crystal, and each exposure took 20 s and covered 0.3° in ω. The data were corrected for polarization and Lorentz effects, and an empirical absorption correction (SADABS)[308] was applied. The cell dimensions were refined with all unique reflections. The structure was solved by direct methods (SHELXS97).[309] Refinement was carried out with the full-matrix least-squares method based on F^2 (SHELXL97) with anisotropic thermal parameters for all non-hydrogen atoms.[309] Hydrogen atoms were inserted in calculated positions and refined riding with the corresponding atom.

High temperature X-ray powder diffraction spectroscopy was performed on a Phillips PW1050 powder diffraction spectrometer θ-2θ (Cu-K_α = 1.54178 Å) with a pair of HTK 1600 heating chambers with platinum filament (Institute of Chemical Technologies and Analytic, Vienna Technical University). The obtained diffractograms were assigned with the following program: Topas 2.0 (Bruker); the following databases were used: ICSD Datenbank Version 1.2.3. and PCPDFWIN version 2.2.

7.4. Synthesis procedures

7.4.1. Synthesis of SiO_2 nanoparticles

The SiO_2 nanoparticles were produced according to the so called "Stöber process".[56] 120 ml Ethanol were mixed with 6 ml of 25 % ammonia and stirred for 5 minutes. Afterwards, 4.2 ml ($1.88*10^{-2}$ mol) TEOS were added dropwise. The solution was stirred over night and the particles were isolated via centrifugation. The resulting SiO_2 nanoparticles were washed with ethanol and water several times.

Yield: 0.83 g (73.5 %) colorless powder

Diameter (TEM/DLS): 45 nm / 42 ± 18 nm

BET-surface: 117 m^2/g

Particles with a radius of 12.5 ± 0.6 nm were synthesized applying the following weight ratios; ethanol : water : NH_3 : TEOS = 157 : 77.6 : 12.43 (32 %) : 1.

BET-surface: 220 m^2/g

Particles with a radius of 78.5 ± 5.0 nm were synthesized applying the following weight ratios; ethanol : water : NH_3 : TEOS = 157 : 22.7 : 3.45 (32 %) : 1.

BET-surface: 51 m^2/g

7.4.2. Synthesis of gold nanoparticles[65]

In 500 ml distillated water 98 mg ($2.5*10^{-4}$ mol) $HAuCl_4*3H_2O$ were dissolved and heated up to the boiling point under vigorous stirring. Then 0.25 g ($8.5*10^{-4}$ mol) $C_6H_5O_7Na_3*2H_2O$ were dissolved in 25 ml distillated water and warmed up to 30°C. This solution was added to the first mixture and the heating process was continued under extensive stirring for 20 minutes.

Yield: 23 mg (47.0 %) red powder

Diameter (TEM/DLS): 15 nm / 15 ± 2 nm

UV/VIS (λ_{max}): 520 nm

FTIR (ν, ATR): 3452 ν(C-H);1587 ν(C-C) + ν(C-O); 1392 δ(CHR); 1069 ν(C-O); 830 γ(CHR) cm^{-1}.

7.4.3. Diameter enlargement of preformed gold nanoparticles[214]

40 ml Original gold particle solution containing particles with a diameter of 15 nm were added to 0.269 g ($8*10^{-4}$ mol) tetradecyltrimethylammonium bromide (TTAB) in 50 ml water at 30 °C under vigorous stirring. After 15 minutes 1 ml of a 0.1 M ascorbic acid solution was added and stirred for one minute. Then 25 mg ($6*10^{-4}$ mol) $HAuCl_4*3H_2O$ were dissolved in 10 ml water and added slowly under vigorously stirring.
Yield: 2 mg (≈ 40 %) red particles
Diameter (TEM/DLS) 25 nm / 27 ± 5 nm
UV/VIS (λ_{max}): 528 nm

7.4.4. Synthesis of gold@SiO_2 nanoparticles[214]

This synthesis was performed using the gold nanoparticle dispersion that described in chapter 7.4.2. After cooling down the original solution to room temperature 2.5 ml of a freshly prepared 10^{-3} M 3-aminopropyltrimethoxysilane solution (APS) were added slowly in 25 µl steps. 1 ml of a 27 % sodium silicate solution was diluted in 50 ml water. The pH value was adjusted with ion-exchange resin to 10-11. 20 ml of this solution were added slowly followed by ten minutes of stirring. Afterwards the mixture was stirred for 6 days. Then the particles were centrifuged and the residue was suspended in 50 ml ethanol. After the dilution in 200 ml ethanol, 15 ml (29 %) NH_3 and 0.1 ml ($4.5*10^{-4}$ mol) tetraethoxysilane were added slowly. After one day of stirring another 0.1 ml tetraethoxysilane (TEOS) were added.
Yield: 67 mg (76.2 %) red powder
Diameter (TEM/DLS): 43 nm / 38 ± 3 nm.
UV/VIS (λ_{max}): 528 nm

7.4.5. Synthesis of TiO_2 nanoparticles without additives

120 ml Ethanol were mixed with 6 ml of 25 % ammonia and stirred for 5 minutes. 4.0 ml ($1.35*10^{-2}$ mol) titanium isopropoxide were added dropwise. The solution was stirred over night and the resulting material was isolated via centrifugation. The resulting TiO_2 nanoparticles were redispersed and washed in ethanol and water various times. No further analyses were performed as the form of the particles was not spherical.
Yield: 3.4 g (88.6 %) colorless powder

7.4.6. Application of ethylenglycol in the synthesis of titanium oxide nanoparticles

0.25 ml ($6.5*10^{-4}$ mol) Titanium butoxide were added to 50 ml (0.87 mol) ethylene glycol under nitrogen atmosphere. The solution was magnetically stirred over night at room temperature and immediately poured into 750 ml acetone containing a small amount of water (~ 0.3 %) under vigorous stirring for ten minutes. After aging for 30 minutes the white precipitate was harvested by centrifugation, followed by washing with distilled water and ethanol to remove ethylene glycol from the surface of the titania glycolate particles.
Yield: 1.6 g (72.3 %)
Diameter (TEM/DLS): 95-110 nm / 101 ± 7 nm

^{13}C CPMAS NMR: 66 (OCH_2CH_2O), 10 (OCH_2CH_3) ppm.

7.4.7. General procedure for the coordination of 3-chloro-pentane-2,4-dione to metal alkoxides

A certain amount of the metal alkoxide was cooled to 0 °C under an argon atmosphere. In case of iron-, vanadium- and tantalum-alkoxide toluene was used as solvent to guarantee homogenous conditions. In case of the other alkoxides the usage of a solvent was used. Then a certain amount of 3-chloro-pentane-2,4-dione was added dropwise and stirred over night. If solvent was utilized during the synthesis it was removed in vacuo, otherwise the obtained product was used without any further purification. In table 30 the used ratios and the obtained results are presented. In table 31 the results of the elemental analyses are summarized and in table 32 the obtained bands of the FTIR spectroscopy are assigned.

Table 30: Coordination of 3-chloro-pentane-2,4-dione to various metal alkoxides and the obtained yields.

Metal alkoxide	Amount metal alkoxide	Amount initiator	Solvent	Yield
$Ti(O^iPr)_4$	3.16 g ($1.11*10^{-2}$ mol)	1.50 g ($1.11*10^{-2}$ mol)	---	4.3 g (95.5 %)
$Zr(O^nBu)_4$	5.32 g	1.50 g	---	4.1 g (91.9 %)

	($1.11*10^{-2}$ mol)	($1.11*10^{-2}$ mol)		
$Y(OEtOMe)_3$	1.00 g	0.43 g	---	0.87 g (86.8 %)
	($3.18*10^{-3}$ mol)	($3.18*10^{-3}$ mol)		
$Ta(OEt)_5$	1.00 g	0.33 g	toluene	1.08 g (88.5 %)
	($2.46*10^{-3}$ mol)	($2.46*10^{-3}$ mol)	(3 ml)	
$VO(OEt)_3$	1.00 g	0.55 g	toluene	1.11 g (91.6 %)
	($4.09*10^{-3}$)	($4.09*10^{-3}$)	(3 ml)	
$Fe(OEt)_3$	0.35 g	0.25 g	toluene	0.47 g (92.4 %)
	($1.83*10^{-3}$)	($1.83*10^{-3}$)	(3 ml)	

NMR analysis:

$Ti(O^iPr)_4$ + 3-chloro-pentane-2,4-dione

^{1}H NMR (δ, $CDCl_3$): 4.9 (sept., 1 H, free **CH**$(CH_3)_2$), 4.5 (broad., 1 H, bond **CH**$(CH_3)_2$), 2.0 (broad, 6 H, CO**CH$_3$**), 1.5-1.1 (broad, 18 H, CH(**CH$_3$**)$_2$) ppm.

^{13}C-NMR (δ, $CDCl_3$): 190 (**C**O), 111 (COCCO), 26 (**C**H_3) ppm.

$Zr(O^iPr)_4$ + 3-chloro-pentane-2,4-dione

^{1}H NMR (δ, $CDCl_3$): 3.8 (sept,1 H, bond **CH**$(CH_3)_2$), 1.7 (broad, 6 H, CO**CH$_3$**), 1.0 (s, 18 H, CH(**CH$_3$**)$_2$) ppm.

^{13}C-NMR (δ, $CDCl_3$): 187 (**C**O), 110 (COCCO), 69 ($CH(CH_3)_2$), 26-18 (**C**H_3) ppm.

$Y(OEtOMe)_3$+ 3-chloro-pentane-2,4-dione

^{1}H NMR (δ, $CDCl_3$): 4.0-3.2 (m, 9H, O**CH$_2$CH$_2$OCH$_3$**), 2.0 (s, 6 H, CO**CH$_3$**) ppm.

^{13}C-NMR (δ, $CDCl_3$):186 (**C**O), 110 (COCCO), 73 (OCH_2CH_2O), 61 (OCH_2CH_2O), 56 (OCH_3), 27 (CH_3CO) ppm.

$Ta(OEt)_5$ + 3-chloro-pentane-2,4-dione

^{1}H NMR (δ, $CDCl_3$): 4.6 (q, 4 H, free **CH$_2$**CH_3), 4.1 (q, 4 H, bond **CH$_2$**CH_3), 2.0 (s, 6 H, CO**CH$_3$**), 1.3 (m, 12 H, free CH_2**CH$_3$**) 1.1 (m, 12 H, bond CH_2**CH$_3$**) ppm.

^{13}C-NMR (δ, $CDCl_3$): 178 (**C**O), 110 (COCCO), 58 (**C**H_2CH_3), 26 (CH_3CO), 16 (CH_2**C**H_3) ppm.

$VO(OEt)_3$ + 3-chloro-pentane-2,4-dione

^{1}H NMR (δ, $CDCl_3$): 4.7 (broad, 2H, free **CH$_2$**CH_3), (broad, 1 H, bond **CH$_2$**CH_3), 2.4 (m, 6 H, CO**CH$_3$**), 1.5 (m, 12 H, free CH_2**CH$_3$**), 0.9 (m, 12 H, bond CH_2**CH$_3$**) ppm.

^{13}C-NMR (δ, $CDCl_3$): 170 (**C**O), 95 (COCCO), 55 (**C**H_2CH_3), 10 (CH_2**C**H_3) ppm.

Table 31: Elemental analysis of the obtained coordination products.

Coordination product containing	Calculated	Found
$Ti(O^iPr)_4$	43.5 % C, 7.2 % H	44.3 % C, 5.7 % H
$Zr(O^iPr)_4$	41.5 % C, 7.5 % H	42.7 % C, 7.0 % H
$Y(OEtOMe)_3$	35.2 % C, 6.2 % H	34.4 % C, 5.8 % H
$Ta(OEt)_5$	31.4 % C, 5.9 % H	31.4 % C, 4.5 % H
$VO(OEt)_3$	36.8 % C, 6.5 % H	37.0 % C, 2.0 % H
$Fe(OEt)_3$	34.3 % C, 6.8 % H	33.5 % C, 4.1 % H

Table 32: FTIR-analysis (ATR) of the obtained coordination products.

Coordination product containing	Assignment ν [cm^{-1}]
$Ti(O^iPr)_4$	2970 ν(C-H):Pr^iOH, Pr^iO, acac;1576 ν(C-C) + ν(C-O):acac;1460 δ(CH_3):Pr^iOH, Pr^iOH, Pr^iO, acac; 1414 δ(CH_3):Pr^iOH, Pr^iOH, Pr^iO, acac;1360 δ(CH_3):Pr^iOH, Pr^iOH, Pr^iO, acac;1346 ν(C-CH_3):Pr^iOH, Pr^iOH, Pr^iO;1286 ν(C-CH_3):acac; 1124 γ(CH_3):PrOH, Pr^iO; 1042 ν(C-O):Pr^iO; 1017 ν(C-O):Pr^iO; 944 ν(C-O):Pr^iO; 919 ν(C-O):Pr^iO; 846 γ(CH_3):Pr^iOH
$Zr(O^iPr)_4$	2960 ν(C-H):Pr^iOH, Pr^iO, acac; 2876 ν(C-H):Pr^iOH, Pr^iO, acac; 1586 ν(C-C) + ν(C-O):acac; 1460 δ(CH_3):Pr^iOH, Pr^iOH, Pr^iO, acac; 1416 δ(CH_3):Pr^iOH, Pr^iOH, Pr^iO, acac; 1361 δ(CH_3):Pr^iOH, Pr^iOH, Pr^iO, acac; 1135 γ(CH_3):PrOH, Pr^iO; 1049 ν(C-O):Pr^iO; 1016 ν(C-O):Pr^iO; 967 ν(C-O):Pr^iO; 920 ν(C-O):Pr^iO; 847 γ(CH_3):Pr^iOH
$Y(OEtOMe)_3$	2924 ν(C-H):MeOEtOH, MeOEtO, acac; 1589 ν(C-C) + ν(C-O):acac; 1421 δ(CH_3): MeOEtOH, MeOEtOH, MeOEtO, acac; 1341 δ(CH_3): MeOEtOH, MeOEtOH, MeOEtO, acac; 1281 ν(C-CH_3): MeOEtO; 1122 γ(CH_3): MeOEtOH, MeOEtO; 1065 ν(C-O):MeOEtO; 1031 ν(C-O):MeOEtO; 1014 ν(C-O):MeOEtO; 908 ν(C-O):MeOEtO; 835 γ(CH_3):MeOEtOH

$Ta(OEt)_5$	2970 ν(C-H):EtOH, EtO, acac; 2866 ν(C-H):EtOH, EtO, acac; 1583 ν(C-C) + ν(C-O):acac; 1460 δ(CH_3):EtOH, EtOH, EtO, acac; 1420 δ(CH_3):EtOH, EtOH, EtO, acac; 1364 δ(CH_3):EtOH, EtOH, EtO, acac; 1142 γ(CH_3):EtOH, EtO; 1298 ν(CH_3):acac; 1105 γ(CH_3): EtOH, EtO;1065 ν(C-O):EtO; 1046 ν(C-O):EtO; 914 ν(C-O):EtOH + *n*(C-CH_3) acac
$VO(OEt)_3$	2964 ν(C-H):Pr^iOH, Pr^iO, acac; 2933 ν(C-H):Pr^iOH, Pr^iO, acac; 2875 ν(C-H):Pr^iOH, Pr^iO, acac; 1574 ν(C-C) + ν(C-O):acac;1458 δ(CH_3):Pr^iOH, Pr^iOH, Pr^iO, acac; 1415 δ(CH_3):Pr^iOH, Pr^iOH, Pr^iO, acac;1345 δ(CH_3):Pr^iOH, Pr^iOH, Pr^iO, acac; 1295 ν(C-CH_3):acac; 1262 ν(C-CH_3):acac; 1044 ν(C-O):Pr^iO; 1017 ν(C-O):Pr^iO; 978 ν(C-O):Pr^iO; 902 ν(C-O):Pr^iO; 847 γ(CH_3):Pr^iOH
$Fe(OEt)_3$	3026 ν(C-H):EtOH, EtO, acac; 2925 ν(C-H):EtOH, EtO, acac; 1564 ν(C-C) + ν(C-O):acac; 1495 δ(CH_3):EtOH, EtOH, EtO, acac; 1454 δ(CH_3):EtOH, EtOH, EtO, acac; 1420 δ(CH_3):EtOH, EtOH, EtO, acac; 1360 δ(CH_3):EtOH, EtOH, EtO, acac; 1333 ν(C-CH_3):EtOH, EtO; 1289 ν(CH_3):acac; 1092 γ(CH_3): EtOH, EtO;1041 ν(C-O):EtO; 918 n(C-O):EtOH + *n*(C-CH_3) acac

7.4.8. Synthesis of 3-bromo-pentane-2,4-dione

10.1 g (0.101 mol) Pentane-2,4-dione, 60 ml of distilled water and 60 ml chloroform were mixed and cooled below 0 °C using a NaCl-ice bath. A mixture of 16.2 g (0.101 mol) bromine and 40 ml chloroform was added dropwise within 60 minutes under vigorous stirring. The stirring was continued for an additional hour. The phases were separated and the organic layer was dried with $MgSO_4$. Afterwards chloroform and unreacted pentane-2,4-dione were removed in vacuo.

Yield: 15.06 g (83.3 %) light yellow liquid.

Elemental analysis: calcd. 33.6 % C, 3.9 % H, 44.6 % Br; found 33.2 % C, 4.2 % H, 42.3 % Br.

^1H NMR (δ, $CDCl_3$): 2.22 (m, 3H, **CH_3CO**) ppm.

^{13}C-NMR (δ, $CDCl_3$): 190.1 (**C**O), 100.7 (COCCO), 27.6 (**C**H_3-CO) ppm.

FTIR (ν, chloroform): 3027 ν(C-H); 1717 ν(C-O) (keto-form); 1597 ν(C-O) (enol-form); 1417 δ(CH_3); 1360 δ(CH_3); 1273 ν(C-CH_3); 1273 ν(C-CH_3); 1226 ν(C-CH_3); 1195 γ(CH_3); 1172 γ(CH_3); 1142 γ(CH_3); 1006 ν(C-O); 911 ν(C-O) cm^{-1}.

7.4.9. Coordination of 3-bromo-pentane-2,4-dione to titanium isopropoxide

1.5 g ($6.7*10^{-3}$ mol) 3-Bromo-pentane-2,4-dione were cooled below 0 °C using a NaCl-ice bath and mixed with 1.905 g ($6.7*10^{-3}$ mol) dropwise added titanium isopropoxide under argon atmosphere. The mixture was stirred until it became solid. The resulting alcohol was not removed because it did not disturb the following synthesis.
Yield: 2.65 g (97.9 %) orange solid.

^{1}H NMR (δ, C_6D_6): 5.07 (sept., 1 H, free **CH**(CH_3)$_2$), 4.6 (broad., 1 H, bond **CH**(CH_3)$_2$), 2.2 (broad, 6 H, CO**CH$_3$**), 1.9 (s, 1 H, free CO**CH$_3$**), 1.6-1.2 (broad, 18 H, CH(**CH$_3$**)$_2$) ppm.

^{13}C-NMR (δ, $CDCl_3$): 190 (**C**O), 100 (COCCO), 80-77 (O**C**H(CH_3)$_2$), 29-22 (**C**H_3) ppm.

Elemental analysis: calcd. 38.3 % C, 6.3 % H; found 40.6 % C, 7.1 % H.

FTIR (ν, chloroform): 2971 ν(C-H):Pr^{i}OH, Pr^{i}O, acac; 1568 ν(C-C) + ν(C-O):acac; 1459 δ(CH_3):Pr^{i}OH, Pr^{i}OH, Pr^{i}O, acac; 1380 δ(CH_3):Pr^{i}OH, Pr^{i}OH, Pr^{i}O, acac;1360 δ(CH_3):Pr^{i}OH, Pr^{i}OH, Pr^{i}O, acac; 1220 ν(C-CH_3):acac; 1124 γ(CH_3):PrOH, Pr^{i}O; 1069 ν(C-O):Pr^{i}O; 1029 ν(C-O):Pr^{i}O; 946 ν(C-O):Pr^{i}O cm^{-1}.

7.4.10. Synthesis of 1-acetyl-2-oxopropyl 2-bromo-2-methylpropanoate

3.34 g (0.02 mol) 2-Bromo-2-methylpropionic acid and 6.79 g (0.02 mol) $(N(Bu)_4)HSO_4$ used as phase transfer catalyst were dissolved in 10 ml of 2 M NaOH and stirred for 30 minutes. The solution was extracted three times with 30 ml of dichloromethane and the combined organic phases were dried over $MgSO_4$. After filtration 4.04 g (0.03 mol) of 2-chloro-pentane-2,4-dione were added and the mixture was refluxed overnight. Afterwards the solution was

washed three times with 20 ml of 2.5 M H_2SO_4 and 20 ml of water. The organic phase was dried with $MgSO_4$ and the solvent was removed in vacuo.
Yield: 4.15 g (78.3 %) orange oil

Elemental analysis: calcd. 41.8 % C, 4.9 % H; found 42.4 % C, 5.7 % H.

^{1}H NMR (δ, $CDCl_3$): 2.10 (m, 6H, **CH_3**CO), 1.97 (m, 6H, **CH_3**C) ppm.

^{13}C NMR (δ, $CDCl_3$): 192.5 (CH_3**C**OC), 182.3 (O**C**OC), 111.6 (COCCO), 62.6 (Br**C**(CH_3)$_2$), 23.4 (**CH_3**CO) ppm.

FTIR (ν, chloroform): 3028 ν(C-H); 2940 ν(C-H); 2879 ν(C-H); 1730 ν(C-C) + ν(C-O) (keto-form); 1601 ν(C-C) + ν(C-O) (enol-form); 1483 δ(CH_3); 1463 δ(CH_3); 1384 δ(CH_3); 1361 ν(C-CH_3); 1273 ν(C-CH_3); 1243 ν(C-CH_3); 1170 γ(CH_3); 1112 γ(CH_3); 1037 ν(C-O); 973 ν(C-O) + n(C-CH_3), 913 γ(CH_3); 886 γ(CH_3-CO-C) cm^{-1}.

7.4.11. General procedure of the coordination of 1-acetyl-2-oxopropyl 2-bromo-2-methylpropanoate

1-Acetyl-2-oxopropyl 2-bromo-2-methylpropanoate was coordinated to various metal alkoxides. In general the 1-acetyl-2-oxopropyl 2-bromo-2-methylpropanoate was stirred in 20 ml absolute THF or toluene and mixed with the corresponding amount of metal alkoxide in a molar ratio of 1:1. The resulting mixture was refluxed over night. The solvent was evaporated in vacuo and the product was used for further reactions without additional purification. In table 33 the amounts of the educts and the obtained yields are given in more detail. In table 34 the results of the elemental analyses are summarized and in table 35 the measured FTIR spectra are assigned.

Table 33: Coordination of various metal alkoxides and the obtained yields.

Metal alkoxide	Amount metal alkoxide	Amount initiator	Solvent	Yield
Ti(O^{i}Pr)$_4$	1.067 g ($3.75*10^{-3}$ mol)	1 g ($3.75*10^{-3}$ mol)	THF	1.75 g (= 95.6 %)

$Zr(O^nBu)_4$	0.9 g (80%)	0.5 g	toluene	1.01 g
	($1.88*10^{-3}$ mol)	($1.88*10^{-3}$ mol)		(= 94.0 %)
$Y(OEtOMe)_3$	2.36 g	2.0 g	THF	3.76 g
	($7.51*10^{-3}$ mol)	($7.51*10^{-3}$ mol)		(= 96.2 %)
$Ta(OEt)_5$	1.53 g	1.0 g	THF	2.29 g
	($3.76*10^{-3}$ mol)	($3.76*10^{-3}$ mol)		(= 97.0 %)
$VO(OEt)_3$	1.52 g	2.0 g	THF	2.84 g
	($7.52*10^{-3}$ mol)	($7.52*10^{-3}$ mol)		(= 89.3 %)
$Fe(O^iPr)_3$	0.43 g	0.5 g	toluene	0.74 g
	($1.88*10^{-3}$ mol)	($1.88*10^{-3}$ mol)		(90.0 %)

$Ti(O^iPr)_4$ + 1-acetyl-2-oxopropyl 2-bromo-2-methylpropanoate

^{1}H NMR (δ, $CDCl_3$): 5.07 (sept., 1 H, free **CH**$(CH_3)_2$), 4.6 (broad., 1 H, bond **CH**$(CH_3)_2$), 2.0-1.7 (m, CO**CH$_3$** + C(**CH$_3$**)$_2$Br), 1.3 (broad, 18 H, CH(**CH$_3$**)$_2$) ppm.

^{13}C-NMR (δ, $CDCl_3$): 188-187 (**C**O,COO), 110 (COCCO), 69-58 (alkoxy-groups, Br**C**), 28-13 (**C**H_3) ppm.

$Zr(O^nBu)_4$ + 1-acetyl-2-oxopropyl 2-bromo-2-methylpropanoate

^{1}H NMR (δ, $CDCl_3$): 3.9 (broad, 6H, bond O**CH$_2$**), 3.3 (m, 2H, free HO**CH$_2$**), 1.6-1.4 (broad, 12 H, **CH$_2$CH$_2$**), 0.9 (s, 6H, BrC(**CH$_3$**)$_2$), 0.8 (s, 6H, **CH$_3$**CO) ppm.

^{13}C-NMR (δ, $CDCl_3$): 195-187 (**C**O,COO), 63 (Br**C**), 59 (OCH_2), 35 (OCH_2CH_2), 24-14 (CH_3) ppm.

$Y(OEtOMe)_3$ + 1-acetyl-2-oxopropyl 2-bromo-2-methylpropanoate

^{1}H NMR (δ, $CDCl_3$): 4.1-3.2 (m, 9H, O**CH$_2$CH$_2$OCH$_3$**), 1.5 (s, 6 H, CO**CH$_3$**), 0.9 (s, 6H, BrC(**CH$_3$**)$_2$) ppm

^{13}C-NMR (δ, $CDCl_3$): 187-186 (**C**O,COO), 111 (COCCO), 73 (OCH_2CH_2O), 65 (Br**C**) 61 (OCH_2CH_2O), 56 (OCH_3), 27-18 (CH_3) ppm.

$Ta(OEt)_5$ + 1-acetyl-2-oxopropyl 2-bromo-2-methylpropanoate

^{1}H NMR (δ, $CDCl_3$): 4.6 (q, 4 H, free **CH$_2$**CH_3), 4.1 (q, 4 H, bond **CH$_2$**CH_3), 2.0 (s, 6 H, CO**CH$_3$**), 1.3 (m, 12 H, free CH_2**CH$_3$**) 1.1 (m, 12 H, bond CH_2**CH$_3$**) 0.9 (s, 6H, **CH$_3$**C) ppm.

^{13}C-NMR (δ, $CDCl_3$): 187-186 (COO, **C**O), 115 ($(CO)_2$**C**O), 65 (BrC), 58 (**C**H_2CH_3), 27-13 (**C**H_3) ppm.

$VO(OEt)_3$+ 1-acetyl-2-oxopropyl 2-bromo-2-methylpropanoate

^{1}H NMR (δ, $CDCl_3$): 4.2-3.0 (broad, 10 H, bond **CH$_2$**CH_3), 2.4 (m, 6 H, CO**CH$_3$**), 2.0-1.0 (broad, 12 H, **CH$_3$**) ppm.

^{13}C-NMR (δ, $CDCl_3$): 192-189 (**C**OO, **C**O), 118 ($(CO)_2$**C**O), 65 (Br**C**), 58 ($\mathbf{C}H_2CH_3$), 27-13 ($\mathbf{C}H_3$) ppm.

Table 34: Elemental analysis of the obtained coordination products.

Coordination product containing	Calculated	Found
$Ti(O^iPr)_4$	46.7 % C, 7.4 % H, 16.4 % Br	47.9 % C, 9.1 % H, 15.9 % Br
$Zr(O^nBu)_4$	43.7 % C, 7.3 % H, 13.8 % Br	44.3 % C, 8.2 % H, 13.5 % Br
$Y(OEtOMe)_3$	41.5 % C, 6.9 % H, 15.4 % Br	29.3 C, 5.1 % H, 10.9 % Br
$Ta(OEt)_5$	34.6 % C, 5.7 % H, 12.8 % Br	35.6 % C, 6.8 % H, 11.7 % Br
$VO(OEt)_3$	41.3 % C, 6.5 % H, 17.2 % Br	40.3 % C, 7.2 % H, 16.5 % Br
$Fe(O^iPr)_3$	44.0 % C, 6.7 % H, 18.3 % Br	43.7 % C, 5.3 % H, 18.0 % Br

Table 35: FTIR spectra (ATR) of the obtained coordination products.

Coordination product containing	Assignments ν [cm^{-1}]
$Ti(O^iPr)_4$	2971 ν(C-H):Pr^iOH, Pr^iO, acac; 1577 ν(C-C) + ν(C-O):acac; 1461 δ(CH_3):Pr^iOH, Pr^iOH, Pr^iO, acac; 1415 δ(CH_3):Pr^iOH, Pr^iOH, Pr^iO, acac;1363 δ(CH_3):Pr^iOH, Pr^iOH, Pr^iO, acac; 1128 γ(CH_3):Pr^iOH, Pr^iO; 1050 ν(C-O):Pr^iO; 946 ν(C-O):Pr^iO; 919 ν(C-O):Pr^iO; 788 γ(CH_3):Pr^iOH
$Zr(O^nBu)_4$	2971 ν(C-H):BuOH, BuO, acac; 2933 ν(C-H):BuOH, BuO, acac; 2876 ν(C-H):BuOH, BuO, acac; 1588 ν(C-C) + ν(C-O):acac; 1465 δ(CH_3):BuOH, BuOH, BuO, acac; 1379 δ(CH_3):BuOH, BuOH, BuO, acac; 1344 δ(CH_3):BuOH, BuOH, BuO, acac; 1218 ν(C-CH_3):acac; 1145 γ(CH_3):BuOH,

	BuO; 1070 ν(C-O):BuO; 1050 ν(C-O):BuO; 1024 ν(C-O):BuO; 920 ν(C-O):BuO + *n*(C-CH_3); 898 γ(CH_3):BuOH
$Y(OEtOMe)_3$	2926 ν(C-H):MeOEtOH, MeOEtO, acac; 1529 ν(C-C) + ν(C-O):acac; 1443 δ(CH_3): MeOEtOH, MeOEtOH, MeOEtO, acac; 1330 δ(CH_3): MeOEtOH, MeOEtOH, MeOEtO, acac; 1285 ν(C-CH_3): MeOEtO; 1132 γ(CH_3): MeOEtOH, MeOEtO; 1045 ν(C-O):MeOEtO; 1031 ν(C-O):MeOEtO; 1013 ν(C-O):MeOEtO; 912 ν(C-O):MeOEtO; 835 γ(CH_3):MeOEtOH
$Ta(OEt)_5$	2975 ν(C-H):EtOH, EtO, acac; 1720 ν(C-O):acac (uncoordinated); 1650 ν(C-C) + ν(C-O):acac; 1464 δ(CH_3):EtOH, EtOH, EtO, acac; 1422 δ(CH_3):EtOH, EtOH, EtO, acac; 1360 δ(CH_3):EtOH, EtOH, EtO, acac; 1140 γ(CH_3):EtOH, EtO; 1298 ν(CH_3):acac; 1111 γ(CH_3): EtOH, EtO; 1046 ν(C-O):EtO; 932 n(C-O):EtOH + *n*(C-CH_3) acac; 833 γ(CH_3):OEt
$VO(OEt)_3$	1739 cm^{-1}, 1574 cm^{-1}2965 ν(C-H):Pr^iOH, Pr^iO, acac; 2933 ν(C-H):Pr^iOH, Pr^iO, acac; 2876 ν(C-H):Pr^iOH, Pr^iO, acac; 1739 ν(C-O):acac (uncoordinated); 1574 ν(C-C) + ν(C-O):acac; 1528 ν(C-C) + ν(C-O):acac; 1461 δ(CH_3):Pr^iOH, Pr^iOH, Pr^iO, acac; 1413 δ(CH_3):Pr^iOH, Pr^iOH, Pr^iO, acac;1380 δ(CH_3):Pr^iOH, Pr^iOH, Pr^iO, acac; 1047 ν(C-O):Pr^iO; 1000 ν(C-O):Pr^iO; 966 ν(C-O):Pr^iO; 953 ν(C-O):Pr^iO; 878 γ(CH_3):Pr^iOH; 738 γ(CH_3):Pr^iOH
$Fe(O^iPr)_3$	2875 ν(C-H):Pr^iOH, Pr^iO, acac; 1585 ν(C-C) + ν(C-O):acac; 1465 δ(CH_3):Pr^iOH, Pr^iOH, Pr^iO, acac; 1417 δ(CH_3):Pr^iOH, Pr^iOH, Pr^iO, acac; 1365 δ(CH_3):Pr^iOH, Pr^iOH, Pr^iO, acac; 1297 ν(C-CH_3):acac; 1182 γ(CH_3):Pr^iOH, Pr^iO;1109 γ(CH_3):Pr^iOH, Pr^iO; 1050 ν(C-O):Pr^iO; 838 γ(CH_3):Pr^iOH

7.4.12. Synthesis of 3-acetyl-5-bromo-5-methylhexane-2,4-dione

8.00 g (0.08 mol) Pentane-2,4-dione were mixed with 18.37 g (0.08 mol) 2-bromo-2-methylpropanoyl bromide and 11.04 g (0.08 mol) of K_2CO_3 in 80 ml absolute acetone and stirred over night. The mixture was filtered and the solvent was removed in vacuo.
Yield: 15.35 g (77.1 %) yellow oil

Elemental analysis: calcd. 43.4 % C, 5.3 % H, found 42.9 % C, 5.3 % H.

^{1}H NMR (δ, $CDCl_3$): 2.10 (m, 6H, **CH_3**CO), 1.97 (m, 6H, **CH_3**C) ppm.

^{13}C NMR (δ, $CDCl_3$): 188.5 (CH_3**C**OC), 177.6 (CH**C**OC), 171.5 (by-product), 100.8 (**C**$(CO)_3$), 30.9 ($(CH_3)_2$**C**-Br), 25.2 (**C**H_3COC) ppm.

FTIR (ν, chloroform): 2976 ν(C-H); 2670 ν(C-H); 1730 ν(C-O) (keto-form); 1589 ν(C-C) + ν(C-O) (enol-form); 1526 ν(C-C) + ν(C-O); 1464 δ(CH_3); 1375 δ(CH_3); 1238 ν(C-O) (small, by-product); 1127 γ(CH_3); 1062 ν(C-O); 1011 ν(C-O); 990 ν(C-O); 903 ν(C-O) + *n*(C-CH_3); 849 γ(CH_3); 814 γ(CH_3) cm^{-1}.

7.4.13. Coordination of 3-acetyl-5-bromo-5-methylhexane-2,4-dione

3-Acetyl-5-bromo-5-methylhexane-2,4-dione was dissolved in 20 ml absolute toluene and mixed with in a 1:1 stoichiometric ratio metal alkoxide under an argon atmosphere. The resulting mixture was refluxed over night. The solvent was evaporated in vacuo and the product was used for further reactions without additional purification.
The exact molar ratios are given in table 36. The results of the performed elemental analyses and the assignment of the FTIR spectra are shown in table 37 and 38, respectively.

Table 36: Coordination reactions and the obtained yield.

Metal alkoxide	Amount metal alkoxide	Amount initiator	Solvent	Yield
$Ti(O^iPr)_4$	1.00 g ($3.5*10^{-3}$ mol)	0.88 g ($3.5*10^{-3}$ mol)	toluene	1.51 g (= 91.0 %)
$Zr(O^nBu)_4$	8.44 g ($1.76*10^{-3}$ mol)	4.40 g ($1.76*10^{-3}$ mol)	toluene	9.32 g (= 94.9 %)
$Fe(O^iPr)_3$	0.5 g ($3.7*10^{-3}$ mol)	0.92 g ($3.7*10^{-3}$ mol)	toluene	1.25 g (= 97.3 %)

$Ti(O^iPr)_4$ + 3-acetyl-5-bromo-5-methylhexane-2,4-dione

^{1}H NMR (δ, $CDCl_3$): 4.8 (sept., 1 H, free **C**$H(CH_3)_2$), 4.4 (broad., 1 H, bound **C**$H(CH_3)_2$), 2.0-1.7 (m, CO**C**H_3 + C$(CH_3)_2$Br), 1.3 (broad, 18 H, CH$(CH_3)_2$) ppm.

^{13}C-NMR (δ, $CDCl_3$): 188/177 (CO), 101 (COCCO), 70-58 (alkoxy-groups, Br**C**), 31-20 (**C**H_3) ppm.

Zr(O^{n}Bu)$_4$+ 3-acetyl-5-bromo-5-methylhexane-2,4-dione

^{1}H NMR (δ, $CDCl_3$): 4 (q, 6H, bond O**C**H_2), 3.3 (m, 3H, free HO**C**H_2), 2.2-1.8 (broad, 12 H, **C**H_2**C**H_2), 1.5 (broad, 6H, BrC(**C**H_3)$_2$), 1.1 (s, 6H, **C**H_3CO) ppm.

^{13}C-NMR (δ, $CDCl_3$): 191-175 (**C**O,**C**OO), 101 (COCCO), 63 (Br**C**), 59 (O**C**H_2), 35 (OCH_2**C**H_2), 24-14 (**C**H_3) ppm.

Table 37: Elemental analysis of the obtained coordination products.

Coordination product containing	Calculated	Found
Ti(O^{i}Pr)$_4$	44.3 % C, 6.9 % H 16.7 % Br	46.9 % C, 7.7 % H 17.3 % Br
Zr(O^{n}Bu)$_4$	44.9 % C, 7.5 % H, 14.2 % Br	44.7 % C, 7.4 % H, 14.1 % Br
Fe(O^{i}Pr)$_3$	39.3 % C, 6.4 % H, 20.1 % Br	38.0 % C, 4.9 % H, 18.9 % Br

Table 38: FTIR spectra (ATR) of the obtained coordination products.

Coordination product containing	Assignment ν [cm^{-1}]
Ti(O^{i}Pr)$_4$	2976 ν(C-H):Pr^{i}OH, Pr^{i}O, acac; 2870 ν(C-H):Pr^{i}OH, Pr^{i}O, acac; 1731 ν(C-O):acac (3rd CO); 1582 ν(C-C) + ν(C-O):acac; 1526 ν(C-C) + ν(C-O):acac; 1464 δ(CH$_3$):Pr^{i}OH, Pr^{i}OH, Pr^{i}O, acac; 1417 δ(CH$_3$):Pr^{i}OH, Pr^{i}OH, Pr^{i}O, acac;1375 δ(CH$_3$):Pr^{i}OH, Pr^{i}OH, Pr^{i}O, acac; 1287 n(C-CH$_3$):acac; 1127 γ(CH$_3$):Pr^{i}OH, Pr^{i}O; 1062 ν(C-O):Pr^{i}O; 1011 ν(C-O):Pr^{i}O; 948 ν(C-O):Pr^{i}O; 903 ν(C-O):Pr^{i}O + *n*(C-CH$_3$); 849 γ(CH$_3$):Pr^{i}O; 818 γ(CH$_3$):Pr^{i}O; 768 γ(CH$_3$):Pr^{i}OH
Zr(O^{n}Bu)$_4$	2957 ν(C-H):BuOH, BuO, acac; 2930 ν(C-H):BuOH, BuO, acac; 2871 ν(C-H):BuOH, BuO, acac; 1738 ν(C-O):acac (3rd CO); 1592 ν(C-C) + ν(C-

	O):acac; 1526 ν(C-C) + ν(C-O):acac; 1463 δ(CH_3):BuOH, BuOH, BuO, acac; 1375 δ(CH_3):BuOH, BuOH, BuO, acac; 1280 δ(CH_3):BuOH, BuOH, BuO, acac; 1149 γ(CH_3):BuOH, BuO; 1105 ν(C-O):BuO; 1046 ν(C-O):BuO; 1046 ν(C-O):BuO
$Fe(O^iPr)_3$	2872 ν(C-H):Pr^iOH, Pr^iO, acac; 1738 ν(C-O):acac (3^{rd} CO); 1571 ν(C-C) + ν(C-O):acac; 1512 ν(C-C) + ν(C-O):acac; 1471 δ(CH_3):Pr^iOH, Pr^iOH, Pr^iO, acac; 1365 δ(CH_3):Pr^iOH, Pr^iOH, Pr^iO, acac; 1297 ν(C-CH_3):acac; 1246 ν(C-CH_3): Pr^iO; 1185 γ(CH_3):Pr^iOH, Pr^iO;1110 γ(CH_3):Pr^iOH, Pr^iO; 828 γ(CH_3):Pr^iOH

7.4.14. Synthesis of 1,3-diphenylpropane-1,3-dione derivatives

a) Synthesis of 2-bromo-1,3-diphenylpropane-1,3-dione

3.0 g ($1.34*10^{-2}$ mol) 1,3-Diphenylpropane-1,3-dione were dissolved in 20 ml water and 20 ml chloroform and cooled below 0 °C using a NaCl-ice bath. 2.13 g ($1.34*10^{-2}$ mol) Bromine were dissolved in 10 ml chloroform and added dropwise. The resulting mixture was stirred over night at room temperature. The phases were separated and the organic phase was dried over $MgSO_4$. The solvent was removed in vacuo.
Yield: 3.75 g (92.4 %) colorless crystals.

^1H NMR (δ, $CDCl_3$): 7.92 (m, 4H, **phenyl**), 7.40 (m, 6H, **phenyl**), 6.5 (s, 1H, **CH**Br) ppm.

^{13}C NMR (δ, $CDCl_3$): 188.9 (**C**O-phenyl), 134.3 (CO-**phenyl**), 129.1 (**phenyl**), 52.6 (**C**HBr) ppm.

Elemental analysis: calcd. 59.4 % C, 3.7 % H, 26.4 % Br, found: 58.7 % C, 3.8 % H, 26.9 % Br.

FTIR (ν, ATR): 1671 ν(C-O); 1593 ν(C-C) + ν(C-O); 1445 ν(C-C):phenyl; 1282 ν(C-phenyl); 1248 ν(C-phenyl); 1185 γ(CH); 996 ν(C-O); 803 γ(CH), 758 ν(C-Br); 683 γ(phenyl-C-O) cm^{-1}.

b) Synthesis of 2,2-dichloro-1,3-diphenylpropane-1,3-dione

3 g ($1.34*10^{-2}$ mol) 1,3-Diphenylpropane-1,3-dione were dissolved in 20 ml absolute toluene under an argon atmosphere. 3.61 g ($2.68*10^{-2}$ mol) SO_2Cl_2 were dissolved in 10 ml absolute toluene and added dropwise to the 1,3-diphenylpropane-1,3-dione solution. This mixture was stirred 4 days at room temperature. Then 30 ml of water were added followed by another day of stirring. The phases were separated and the organic phase was washed twice with 15 ml water. The solvent was removed and a crystalline product was obtained.
Yield: 3.63 g (92.3 %) colorless crystals

^{1}H NMR (δ, $CDCl_3$): 7.98 (m, 4H, **phenyl**), 7.45 (m, 6H, **phenyl**) ppm.

^{13}C-NMR (δ, $CDCl_3$): 185.4 (**C**O-phenyl), 134.3 (CO-**phenyl**), 128.7 (**phenyl**), 87.6 (**C**Cl_2) ppm.

Elemental analysis: calcd. 61.5 % C, 3.4 % H, 24.2 % Cl; found 61.7 % C, 4.0 % H, 23.2 % Cl.

FTIR (ν, ATR): 1694 ν(C-O); 1567 ν(C-C) + ν(C-O); 1443 ν(C-C):phenyl; 1282 ν(C-phenyl); 1248 ν(C-phenyl); 1192 γ(CH); 998 ν(C-O); 803 γ(CH), 799 ν(C-Cl); 687 γ(phenyl-C-O) cm^{-1}.

c) Synthesis of 2-chloro-1,3-diphenylpropane-1,3-dione

3 g ($1.34*10^{-2}$ mol) 1,3-Diphenylpropane-1,3-dione were dissolved in 20 ml absolute toluene under an argon atmosphere. 1.81 g ($1.34*10^{-2}$ mol) SO_2Cl_2 were dissolved in 10 ml absolute toluene and added dropwise to the 1,3-diphenylpropane-1,3-dione solution. This mixture was stirred over night at room temperature. Then 30 ml of water were added followed by another day of stirring. The phases were separated and the organic phase was washed twice with 15 ml water. The solvent was removed and a crystalline product was obtained.
Yield: 3.24 g (93.4 %) colorless crystals

^{1}H NMR (δ, $CDCl_3$): 7.98 (m, 4H, **phenyl**), 7.45 (m, 6H, **phenyl**), 6.45 (s, 1H, **CH**Cl) ppm.

^{13}C-NMR (δ, $CDCl_3$): 185.4 (**C**O-phenyl), 134.3 (CO-**phenyl**), 128.7 (**phenyl**), 78.3 (**C**HCl) ppm.

Elemental analysis: calcd. 69.6 % C, 4.3 % H, 13.7 % Cl; found 69.0 % C, 4.2 % H, 14.3 % Cl.

FTIR (ATR): 1690 ν(C-O); 1568 ν(C-C) + ν(C-O); 1444 ν(C-C):phenyl; 1283 ν(C-phenyl); 1249 ν(C-phenyl); 1192 γ(CH); 990 ν(C-O); 809 γ(CH), 791 ν(C-Cl); 689 γ(phenyl-C-O) cm^{-1}.

d) Crystallographic data of the obtained derivatives

Table 39: Crystal data of the obtained 1,3-diphylpropane-1,3-dione.

	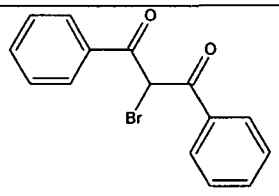	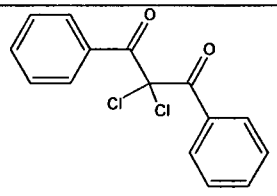	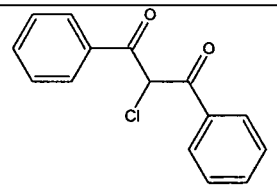
Empirical formula	$C_{15}H_{11}BrO_2$	$C_{15}H_{10}Cl_2O_2$	$C_{15}H_{11}ClO_2$
Formula weight	303.15 g/mol	293.13 g/mol	258.69 g/mol
Temperature	294(2) K	173(2) K	295(2) K
Crystal system	orthorhombic	triclinic	orthorhombic
space group	$Pca2_1$	P-1	$P2_12_12_1$
Unit cell dimensions [pm], [°]	a = 2841.3(4) α = 90 b = 573.43(9) β = 90 c = 1554.5(2) γ = 90	a = 882.04(9) α = 83.233(2) b = 916.09(9) β = 87.076(2) c = 922.95(9) γ = 63.897(2) °	a = 561.29(6) α = 90 b = 836.15(9) β = 90 c = 2707.3(3) γ = 90
Volume [pm^3]	$2.5327(7)*10^9$	$6.6504(11)*10^8$	$1.2706(2)*10^9$
Unit cells (Z)	4	2	4
Calculated	1.590	1.464	1.352

density [g/cm^3]			
Absorption coefficient	3.236 mm^{-1}	0.481 mm^{-1}	0.290 mm^{-1}
F(000)	1216	300	536
θ range for data collection [°]	1.94 - 28.29	2.22-28.32	2.55 - 28.39
Limiting indices	$-37 \leq h \leq 14$ $-7 \leq k \leq 5$ $-20 \leq l \leq 20$	$-11 \leq h \leq 11$ $-10 \leq k \leq 12$ $-12 \leq l \leq 12$	$-7 \leq h \leq 7$ $-11 \leq k \leq 10$ $-36 \leq l \leq 33$
Reflections collected / unique	7688 / 5407 [R(int) = 0.0282]	4641 / 3235 [R(int) = 0.0195]	8871 / 3158 [R(int) = 0.0255]
Completeness to θ [%]	95.8	97.6	98.7
Goodness-of-fit on F^2	0.998	1.112	1.145
Final R indices [$I > 2\sigma(I)$]	$R_1 = 0.0466$ $wR_2 = 0.1115$	$R_1 = 0.0493$ $wR_2 = 0.1210$	$R_1 = 0.0505$ $wR_2 = 0.1218$
R indices (all data)	$R_1 = 0.0679$ $wR_2 = 0.1267$	$R_1 = 0.0519$ $wR_2 = 0.1230$	$R_1 = 0.0615$ $wR_2 = 0.1271$
Largest diff. peak and hole [pm^{-3}]	$(5.16 \text{ and } -3.89)*10^{-7}$	$(4.93 \text{ and } -3.02)*10^{-7}$	$(3.09 \text{ and } -1.65)*10^{-7}$
crystal size [mm]	0.54 x 0.36 x 0.06	0.40 x 0.30 x 0.10	0.60 x 0.19 x 0.10

Table 40: Atomic coordinates ($*10^4$) and equivalent isotropic displacement parameters (A^2*10^3) for 2-bromo-1,3-diphenylpropane-1,3-dione.

	x	y	z	U(eq)
Br(1)	2624(1)	7119(1)	6870(1)	50(1)
C(1)	1639(2)	6014(9)	6819(3)	42(1)
O(1)	1791(2)	4120(7)	6606(3)	62(1)
O(2)	1706(1)	6503(6)	8519(2)	52(1)
C(2)	1976(2)	7887(9)	7175(3)	39(1)
C(3)	1948(2)	7965(9)	8169(3)	38(1)
C(4)	1133(2)	6587(8)	6764(3)	39(1)
C(5)	838(2)	4955(10)	6397(3)	51(1)
C(6)	353(2)	5356(11)	6378(4)	59(2)
C(7)	167(2)	7326(11)	6737(4)	58(2)
C(8)	461(2)	8962(10)	7099(4)	54(1)
C(9)	944(2)	8627(9)	7110(3)	43(1)
C(10)	2208(2)	9772(8)	8657(3)	36(1)
C(11)	2242(2)	9493(9)	9552(3)	44(1)
C(12)	2473(2)	11098(11)	10037(3)	53(1)
C(13)	2670(2)	13068(10)	9654(4)	52(1)
C(14)	2640(2)	13355(10)	8785(4)	49(1)
C(15)	2408(2)	11728(9)	8281(3)	42(1)

Table 41: Selected bond lengths [pm] and angels [°] of 2-bromo-1,3-diphenylpropane-1,3-dione.

Br(1)-C(2)	195.3(5)
C(1)-O(1)	121.4(6)
C(1)-C(4)	147.9(7)
C(1)-C(2)	154.1(7)
O(2)-C(3)	121.2(6)
C(2)-C(3)	154.7(6)
C(3)-C(10)	148.2(7)
O(1)-C(1)-C(4)	121.9(5)
O(1)-C(1)-C(2)	120.1(5)
C(4)-C(1)-C(2)	118.0(4)
C(1)-C(2)-C(3)	110.3(4)
C(1)-C(2)-Br(1)	109.9(3)
C(3)-C(2)-Br(1)	107.3(3)
O(2)-C(3)-C(10)	122.4(4)
O(2)-C(3)-C(2)	117.3(4)
C(10)-C(3)-C(2)	120.4(4)

Table 42: Atomic coordinates ($*10^4$) and equivalent isotropic displacement parameters (A^2*10^3) of 2,2-dichloro-1,3-diphenylpropane-1,3-dione.

	x	y	z	U(eq)
O(1)	3313(2)	5508(2)	2907(2)	35(1)
C(1)	3909(2)	6344(2)	2231(2)	23(1)
Cl(1)	587(1)	8376(1)	1609(1)	34(1)
O(2)	3108(2)	10277(2)	328(2)	33(1)
C(2)	2736(2)	7909(2)	1250(2)	23(1)
Cl(2)	3176(1)	7391(1)	-574(1)	34(1)
C(3)	2916(2)	9500(2)	1409(2)	23(1)
C(4)	5739(2)	5925(2)	2299(2)	23(1)
C(5)	6692(3)	4730(2)	3395(2)	30(1)
C(6)	8407(3)	4255(3)	3498(3)	39(1)
C(7)	9195(3)	4945(3)	2499(3)	38(1)
C(8)	8265(3)	6122(2)	1399(2)	32(1)
C(9)	6542(2)	6632(2)	1303(2)	26(1)
C(10)	2832(2)	10006(2)	2901(2)	23(1)
C(11)	3205(2)	11317(2)	3028(2)	31(1)
C(12)	3140(3)	11870(3)	4372(3)	39(1)
C(13)	2706(3)	11120(3)	5604(3)	41(1)
C(14)	2338(3)	9814(3)	5495(2)	37(1)
C(15)	2396(3)	9254(2)	4150(2)	29(1)

Table 43: Selected bond-lengths [pm] and angles [°] of 2,2-dichloro-1,3-diphenylpropane-1,3-dione.

O(1)-C(1)	120.8(2)
C(1)-C(4)	148.9(3)
C(1)-C(2)	155.9(3)
Cl(1)-C(2)	177.24(18)
O(2)-C(3)	120.5(2)
C(2)-C(3)	155.8(2)
C(2)-Cl(2)	178.04(18)
C(3)-C(10)	149.2(3)
O(1)-C(1)-C(4)	122.10(17)
O(1)-C(1)-C(2)	119.34(17)
C(4)-C(1)-C(2)	118.56(15)
C(3)-C(2)-C(1)	116.51(15)
C(3)-C(2)-Cl(1)	106.02(12)
C(1)-C(2)-Cl(1)	110.45(12)
C(3)-C(2)-Cl(2)	110.44(12)
C(1)-C(2)-Cl(2)	105.44(12)
Cl(1)-C(2)-Cl(2)	107.74(10)
O(2)-C(3)-C(10)	122.61(17)

O(2)-C(3)-C(2)	119.00(17)
C(10)-C(3)-C(2)	118.39(15)

Table 44: Atomic coordinates ($*10^4$) and equivalent isotropic displacement parameters (A^2*10^3) of 2-chloro-1,3-diphenylpropane-1,3-dione.

	x	y	z	U(eq)
Cl(1)	4443(1)	2178(1)	7826(1)	69(1)
O(1)	1330(3)	1078(3)	8592(1)	73(1)
C(1)	3287(4)	1301(3)	8763(1)	50(1)
C(2)	5158(4)	2240(3)	8466(1)	46(1)
O(2)	3634(4)	4405(2)	8930(1)	66(1)
C(3)	5124(4)	3999(3)	8635(1)	45(1)
C(4)	3961(4)	741(3)	9264(1)	47(1)
C(5)	6023(5)	1214(3)	9504(1)	57(1)
C(6)	6461(5)	745(3)	9981(1)	64(1)
C(7)	4860(5)	-225(4)	10228(1)	67(1)
C(8)	2828(6)	-718(4)	9991(1)	74(1)
C(9)	2379(5)	-258(3)	9516(1)	61(1)
C(10)	6906(4)	5140(3)	8435(1)	44(1)
C(11)	8845(5)	4685(3)	8152(1)	53(1)
C(12)	10429(5)	5819(4)	7985(1)	65(1)
C(13)	10137(5)	7400(4)	8101(1)	70(1)
C(14)	8221(6)	7861(4)	8384(1)	74(1)
C(15)	6620(5)	6754(3)	8554(1)	60(1)

Table 45: Selected bond-lengths [pm] and angles [°] of 2-chloro-1,3-diphenylpropane-1,3-dione.

Cl(1)-C(2)	178.0(2)
O(1)-C(1)	120.6(3)
C(1)-C(4)	148.4(3)
C(1)-C(2)	153.7(3)
C(2)-C(3)	154.1(3)
C(2)-H(2)	98.00
O(2)-C(3)	120.5(3)
C(3)-C(10)	148.4(3)
O(1)-C(1)-C(4)	122.2(2)
O(1)-C(1)-C(2)	120.1(2)
C(4)-C(1)-C(2)	117.7(2)
C(1)-C(2)-C(3)	108.92(18)
C(1)-C(2)-Cl(1)	109.85(16)
C(3)-C(2)-Cl(1)	108.30(15)

C(1)-C(2)-H(2)	109.9
C(3)-C(2)-H(2)	109.9
Cl(1)-C(2)-H(2)	109.9
O(2)-C(3)-C(10)	121.9(2)
O(2)-C(3)-C(2)	118.3(2)
C(10)-C(3)-C(2)	119.83(18)

7.4.15. Coordination of 2-bromo-1,3-diphenylpropane-1,3-dione to titanium isopropoxide

1 g ($3.30*10^{-3}$ mol) 2-Bromo-1,3-diphenylpropane-1,3-dione was dissolved in 10 ml absolute toluene and stirred for 15 minutes. Then 0.94 g ($3.30*10^{-3}$ mol) titanium isopropoxide were added dropwise and stirred over night at room temperature. The solvent was removed in vacuo and a mixture of products was obtained. The structure of the crystals is described below.

Yield: 1.56 g (89.6 %) colorless crystals in brown oil

Due to the received mixture no elemental analysis was performed.

^{1}H NMR (δ, $CDCl_3$):

Isopropoxide groups: 5.3 free O**C**H$(CH_3)_2$, 5.0 bound O**C**H$(CH_3)_2$, 4.5 bridging O**C**H$(CH_3)_2$ ppm.

Isopropyl benzoate: 8.0-7.4 (m, 5H, **phenyl**-ring), 4.31 (m, 1H, **C**H$(CH_3)_2$), 1.37 (m, 6H, CH$(\mathbf{CH_3})_2$) ppm.

1-isopropoxy-1-phenylethanone: 8.0-7.4 (m, 5H, **phenyl**-ring), 4.5 (s, 2H, CH_2), 4.31 (m, 1H, **C**H$(CH_3)_2$), 1.37 (m, 6H, CH$(\mathbf{CH_3})_2$) ppm.

^{13}C NMR (δ, $CDCl_3$):

Isopropoxide groups: 68.0 free O**C**H$(CH_3)_2$, 83.0-81.0 bound O**C**H$(CH_3)_2$, 77.5 bridging O**C**H$(CH_3)_2$ ppm.

Isopropyl benzoate: 164.2 (**C**O), 132-128 (**phenyl**-ring), 68.3 (O**C**$(CH_3)_2$), 22.2 (OC$(\mathbf{CH_3})_2$) ppm.

1-isopropoxy-1-phenylethanone: 186.0 (**C**O), 132-128 (**phenyl**-ring), 76.0 (**C**H_2) 68.3 (O**C**$(CH_3)_2$), 22.2 (OC$(\mathbf{CH_3})_2$) ppm.

Table 46: Molecular data of the obtained crystals.

Empirical formula	$C_{15}H_{35}BrO_6Ti_2$
Formula weight [g/mol]	487.14
Temperature	173(2) K
Crystal system	monoclinic
space group	$P2_1/n$
Unit cell dimensions	a = 987.34(8) $\alpha = 90$
[pm], [°]	b = 1916.04(16) $\beta = 102.710(2)$
	c = 1266.05(10) $\gamma = 90$
Volume [pm^3]	$2336.4(3)*10^9$
Unit cells (Z)	4
Calculated density [g/m^3]	1.385
Absorption coefficient [mm^{-1}]	2.416
F(000)	1008
θ range for data collection [°]	2.37-28.28
Limiting indices	$-13 \leq h \leq 11$
	$-25 \leq k \leq 22$
	$-16 \leq l \leq 16$
Reflections collected / unique	16160 / 5763 [R(int) = 0.0273]
Completeness to θ [%]	99.5
Goodness-of-fit on F^2	1.034
Final R indices [$I>2\sigma(I)$]	$R_1 = 0.0355$, $wR_2 = 0.0860$
R indices (all data)	$R_1 = 0.0520$, $wR_2 = 0.0941$
Largest diff. peak and hole [pm^{-3}]	$(8.86 \text{ and } -3.08)*10^{-7}$
Crystal size	0.40 x 0.38 x 0.24

Table 47: Atomic coordinates ($*10^4$) and equivalent isotropic displacement parameters (A^2*10^3) of the obtained crystals.

	x	y	z	U(eq)
Ti(1)	5176(1)	9222(1)	4821(1)	21(1)
Ti(2)	6386(1)	9461(1)	7301(1)	24(1)
Br(1)	6904(1)	10653(1)	8177(1)	38(1)
O(1)	6385(2)	8984(1)	4034(1)	31(1)
C(2)	8198(3)	8795(2)	3107(3)	68(1)

C(3)	6658(3)	8756(1)	3037(2)	37(1)
C(4)	6096(3)	8034(2)	2797(3)	58(1)
O(5)	3642(2)	8720(1)	4596(1)	33(1)
C(6)	2054(4)	8017(2)	5264(4)	87(1)
C(7)	2223(3)	8655(1)	4637(2)	40(1)
C(8)	1736(4)	9305(2)	5104(4)	75(1)
O(9)	4401(2)	10062(1)	4054(1)	25(1)
O(10)	6163(2)	8725(1)	6175(1)	28(1)
C(11)	6141(4)	7621(2)	7101(3)	71(1)
C(12)	6523(3)	7987(1)	6163(2)	44(1)
C(13)	8018(3)	7917(2)	6120(3)	62(1)
O(14)	5096(2)	9221(1)	7989(1)	38(1)
C(15)	5923(3)	9020(2)	9897(2)	54(1)
C(16)	4683(3)	9111(1)	8989(2)	39(1)
C(17)	3698(4)	8500(2)	8853(3)	61(1)
O(18)	8041(2)	9184(1)	8008(2)	42(1)
C(19)	9788(3)	8665(2)	9395(3)	62(1)
C(20)	9309(3)	9318(1)	8773(2)	46(1)
C(21)	10350(4)	9603(3)	8211(4)	99(2)

Table 48: Selected bond lengths [pm] and angles [°] of the obtained crystals.

Ti(1)-O(5)	176.36(16)	O(1)-Ti(1)-Ti(2)	116.38(5)
Ti(1)-O(1)	177.51(15)	O(9)-Ti(1)-Ti(2)	113.55(4)
Ti(1)-O(9)	194.75(14)	O(9A)-Ti(1)-Ti(2)	36.43(4)
Ti(1)-O(9A)	195.45(14)	O(10)-Ti(1)-Ti(2)	37.95(4)
Ti(1)-O(10)	201.44(15)	Ti(1A)-Ti(1)-Ti(2)	74.887(15)
Ti(1)-Ti(1A)	304.67(7)	O(14)-Ti(2)-O(18)	111.20(9)
Ti(1)-Ti(2)	313.74(6)	O(14)-Ti(2)-O(9A)	111.58(8)
Ti(2)-O(14)	175.49(16)	O(18)-Ti(2)-O(9A)	137.19(8)
Ti(2)-O(18)	176.32(18)	O(14)-Ti(2)-O(10)	101.04(7)
Ti(2)-O(9A)	194.84(14)	O(18)-Ti(2)-O(10)	95.47(7)
Ti(2)-O(10)	198.34(15)	O(9A)-Ti(2)-O(10)	74.95(6)
Ti(2)-Br(1)	254.18(5)	O(14)-Ti(2)-Br(1)	96.77(5)
O(1)-C(3)	141.7(2)	O(18)-Ti(2)-Br(1)	88.50(6)
C(2)-C(3)	150.5(4)	O(9A)-Ti(2)-Br(1)	88.05(4)
C(3)-C(4)	149.5(4)	O(10)-Ti(2)-Br(1)	158.89(5)
O(5)-C(7)	141.9(3)	O(14)-Ti(2)-Ti(1)	107.43(6)
C(6)-C(7)	148.6(4)	O(18)-Ti(2)-Ti(1)	124.80(6)
C(7)-C(8)	150.4(4)	O(9A)-Ti(2)-Ti(1)	36.56(4)
O(9)-Ti(2A)	194.84(14)	O(10)-Ti(2)-Ti(1)	38.65(4)
O(9)-Ti(1A)	195.45(14)	Br(1)-Ti(2)-Ti(1)	124.312(15)
O(10)-C(12)	145.8(3)	C(3)-O(1)-Ti(1)	149.69(16)
C(11)-C(12)	149.7(4)	O(1)-C(3)-C(4)	109.3(2)
C(12)-C(13)	149.5(4)	O(1)-C(3)-C(2)	108.7(2)
O(14)-C(16)	143.0(3)	C(4)-C(3)-C(2)	112.5(2)
C(15)-C(16)	149.3(4)	C(7)-O(5)-Ti(1)	149.49(15)
C(16)-C(17)	150.7(4)	O(5)-C(7)-C(6)	108.6(2)

O(18)-C(20)	142.7(3)	O(5)-C(7)-C(8)	110.2(2)
C(19)-C(20)	149.7(4)	C(6)-C(7)-C(8)	112.8(3)
C(20)-C(21)	147.8(5)	Ti(1)-O(9)-Ti(2A)	149.70(8)
		Ti(1)-O(9)-Ti(1A)	102.67(6)
O(5)-Ti(1)-O(1)	115.35(7)	Ti(2A)-O(9)-Ti(1A)	107.00(6)
O(5)-Ti(1)-O(9)	98.12(7)	C(12)-O(10)-Ti(2)	135.05(14)
O(1)-Ti(1)-O(9)	99.87(7)	C(12)-O(10)-Ti(1)	121.54(14)
O(5)-Ti(1)-O(9A)	122.66(7)	Ti(2)-O(10)-Ti(1)	103.40(6)
O(1)-Ti(1)-O(9A)	121.79(7)	O(10)-C(12)-C(13)	109.4(2)
O(9)-Ti(1)-O(9A)	77.33(6)	O(10)-C(12)-C(11)	110.0(2)
O(5)-Ti(1)-O(10)	96.73(7)	C(13)-C(12)-C(11)	114.2(3)
O(1)-Ti(1)-O(10)	95.56(7)	C(16)-O(14)-Ti(2)	149.11(18)
O(9)-Ti(1)-O(10)	151.45(6)	O(14)-C(16)-C(15)	110.7(2)
O(9A)-Ti(1)-O(10)	74.12(6)	O(14)-C(16)-C(17)	108.4(2)
O(5)-Ti(1)-Ti(1A)	115.88(6)	C(15)-C(16)-C(17)	113.4(2)
O(1)-Ti(1)-Ti(1A)	116.59(5)	C(20)-O(18)-Ti(2)	150.16(16)
O(9)-Ti(1)-Ti(1A)	38.75(4)	O(18)-C(20)-C(21)	109.8(3)
O(9A)-Ti(1)-Ti(1A)	38.58(4)	O(18)-C(20)-C(19)	109.6(2)
O(10)-Ti(1)-Ti(1A)	112.71(4)	C(21)-C(20)-C(19)	112.9(3)
O(5)-Ti(1)-Ti(2)	111.49(5)		

7.4.16. Synthesis of TiO_2 nanoparticles with the coordination product of titanium isopropoxide and 3-chloro-pentane-2,4-dione (without additives)

120 ml ethanol were mixed with 6 ml of 25 % ammonia and stirred for 5 minutes. 3.0 g ($8.36*10^{-3}$ mol) of the coordination product were added in small portions. The solution was stirred over night and the resulting material was isolated via centrifugation. The resulting TiO_2 nanoparticles were washed with ethanol and water various times.

Yield: 1.22 g (67.2 %) white powder

Diameter (TEM): 85 nm (non-spherical, highly aggregated)

FTIR (ν, ATR): 3254 ν(O-H); 2940 ν(C-H); 1580 ν(C-C) + ν(C-O); 1417 δ(CH_3); 1352 ν(C-CH_3); 1291 ν(C-CH_3); 1054 ν(C-O) cm^{-1}.

7.4.17. Formation of TiO_2 nanoparticles using the coordination product of titanium isopropoxide and 3-acetyl-5-bromo-5-methylhexane-2,4-dione (without additives)

120 ml Ethanol were mixed with 6 ml of 25 % ammonia and stirred for 5 minutes. 3.0 g ($5.02*10^{-3}$ mol) of the coordination product were added in small portions. The solution was stirred over night. Afterwards the particles were isolated by centrifugation and washed with ethanol and water a couple of times.

Yield: 1.53 g (74.3 %) white powder

Diameter (TEM/DLS): 185 nm / 172 ± 38 nm

FTIR (ν, ATR): 3337 ν(O-H), 1731 ν(C-O) (3rd CO); 1582 ν(C-C) + ν(C-O); 1345 n(C-CH_3); 1152 γ(CH_3);1050 ν(C-O); 668 γ(CH_3-CO-C) cm^{-1}.

7.4.18. General procedure for the synthesis of metal oxide nanoparticles from modified metal alkoxides in microemulsion

14.5 g (58.0 %) Cyclohexane were mixed with 3.75 g (15.0 %) of n-hexanol and 4.75 g (19.0 %) of Triton X-100 and stirred for 5 minutes. Afterwards 2.0 g (8.0 %) water were added and stirred for 20 minutes until the microemulsion was formed. Under vigorous stirring the modified alkoxide was added and stirred over night. The nanoparticles were centrifuged and washed several times with a 1:1 mixture of chloroform and methanol, methanol and finally with ethanol. In table 49 the obtained yields are presented. The assignment of the FTIR spectra is presented in table 50 and in table 51 the performed elemental analyses and the measured diameter are summarized.

Table 49: Yields of the synthesized metal oxide nanoparticles.

Alkoxide	Ligand	Used amount	Yield
$Ti(O^iPr)_4$	+ 3-chloro-pentane-2,4-dione	0.25 g	0.15 g (84.2 %)
	+ 3-bromo-pentane-2,4-dione	0.25 g	0.13 g (69.1 %)
	+ 1-acetyl-2-oxopropyl 2-bromo-2-methylpropanoate	0.25 g	0.14 g (63.3 %)
	+ 3-acetyl-5-bromo-5-methylhexane-2,4-dione	0.25 g	0.11 g (49.7 %)
$Zr(O^iPr)_4$	+ 3-chloro-pentane-2,4-dione	0.25 g	0.15 g (79.5 %)
	+ 1-acetyl-2-oxopropyl 2-bromo-2-methylpropanoate	0.25 g	0.12 g (53.2 %)
	+ 3-acetyl-5-bromo-5-methylhexane-2,4-dione	0.25 g	0.12 g (54.2 %)

$VO(OEt)_3$	+ 3-chloro-pentane-2,4-dione	0.25 g	0.16 g (74.6 %
	+ 1-acetyl-2-oxopropyl 2-bromo-2-methylpropanoate	0.25 g	0.14 g (67.3 %)
$Y(OEtOMe)_3$	+ 3-chloro-pentane-2,4-dione	0.25 g	0.16 g (79.3 %)
	+ 1-acetyl-2-oxopropyl 2-bromo-2-methylpropanoate	0.25 g	0.13 g (62.3 %)
$Ta(OEt)_5$	+ 3-chloro-pentane-2,4-dione	0.25 g	0.19 g (91.0 %)
	+ 1-acetyl-2-oxopropyl 2-bromo-2-methylpropanoate	0.25 g	0.14 g (68.5 %)
$Fe(OEt)_3$	+ 3-acetyl-5-bromo-5-methylhexane-2,4-dione	0.25 g	0.16 g (79.3 %)

Table 50: FTIR analyses of the synthesized nanoparticles.

Alkoxide	**Ligand**	**Assignments** ν [cm^{-1}]
$Ti(O^iPr)_4$	+ 3-chloro-pentane-2,4-dione	3237 ν(O-H); 2930 ν(C-H); 1576 ν(C-C) + ν(C-O); 1417 $\delta(CH_3)$; 1361 ν(C-CH_3); 1294 ν(C-CH_3); 1051 ν(C-O); 1022 ν(C-O)
	+ 3-bromo-pentane-2,4-dione	3240 ν(O-H); 2928 ν(C-H); 1568 ν(C-C) + ν(C-O); 1452 $\delta(CH_3)$; 1422 $\delta(CH_3)$; 1333 ν(C-CH_3); 1290 ν(C-CH_3); 1030 ν(C-O)
	+ 1-acetyl-2-oxopropyl 2-bromo-2-methylpropanoate	3245 ν(O-H); 2946 ν(C-H);1651 ν(C-C) + ν(C-O); 1576 ν(C-C) + ν(C-O); 1455 $\delta(CH_3)$; 1417 $\delta(CH_3)$; 1379 $\delta(CH_3)$; 1337 ν(C-CH_3);1261 ν(C-CH_3); 1202 ν(C-CH_3); 1173 $\gamma(CH_3)$; 1025 ν(C-O); 801 $\gamma(CH_3)$
	+ 3-acetyl-5-bromo-5-methylhexane-2,4-dione	3191 ν(O-H); 2925 ν(C-H); 1731 ν(C-O) (3rd CO); 1582 ν(C-C) + ν(C-O); 1529 ν(C-C) + ν(C-O);

		1455 $\delta(CH_3)$; 1376 $\delta(CH_3)$; 1203 $\gamma(CH_3)$; 1115 $\gamma(CH_3)$; 1028 ν(C-O); 987 ν(C-O)
$Zr(O^iPr)_4$	+ 3-chloro-pentane-2,4-dione	3250 ν(O-H); 2925 ν(C-H); 1550 ν(C-C) + ν(C-O); 1432 $\delta(CH_3)$; 1360 $\nu(C-CH_3)$; 1294 $\nu(C-CH_3)$; 1050 ν(C-O); 1025 ν(C-O)
	+ 1-acetyl-2-oxopropyl 2-bromo-2-methylpropanoate	3243 ν(O-H); 1649 ν(C-C) + ν(C-O); 1588 ν(C-C) + ν(C-O); 1450 $\delta(CH_3)$; 1417 $\delta(CH_3)$; 1379 $\delta(CH_3)$; 1346 $\nu(C-CH_3)$; 1263 $\nu(C-CH_3)$; 1202 $\nu(C-CH_3)$; 1174 $\gamma(CH_3)$; 1027 ν(C-O)
	+ 3-acetyl-5-bromo-5-methylhexane-2,4-dione	3203 ν(O-H); 2953 ν(C-H); 1731 ν(C-O) (3^{rd} CO); 1591 ν(C-C) + ν(C-O); 1535 ν(C-C) + ν(C-O); 1456 $\delta(CH_3)$; 1378 $\delta(CH_3)$; 1208 $\gamma(CH_3)$; 1115 $\gamma(CH_3)$; 1026 ν(C-O); 987 ν(C-O)
$VO(OEt)_3$	+ 3-chloro-pentane-2,4-dione	3300 ν(O-H); 2987 ν(C-H); 1672 δ(O-H); 1627 ν(C-C) + ν(C-O); 1462 $\delta(CH_3)$; 1388 $\delta(CH_3)$; 1258 $\nu(C-CH_3)$, 1080 ν(C-O); 987 ν(C-O)
	+ 1-acetyl-2-oxopropyl 2-bromo-2-methylpropanoate	3298 ν(O-H); 1610 ν(C-C) + ν(C-O); 1574 ν(C-C) + ν(C-O); 1457 $\delta(CH_3)$; 1379 $\delta(CH_3)$; 1266 $\nu(C-CH_3)$; 1174 $\gamma(CH_3)$; 1050 ν(C-O); 986 ν(C-O)
$Y(OEtOMe)_3$	+ 3-chloro-pentane-2,4-dione	3445 ν(O-H); 3159 ν(O-H); 1594 ν(C-C) + ν(C-O); 1450 $\delta(CH_3)$; 1418 $\delta(CH_3)$; 1386 $\delta(CH_3)$; 1361 $\nu(C-CH_3)$; 1264 $\nu(C-CH_3)$; 1038 ν(C-O); 910 ν(C-O); 705 $\gamma(CH_3)$
	+ 1-acetyl-2-oxopropyl 2-bromo-2-methylpropanoate	3350 ν(O-H); 2954 ν(C-H); 1560 ν(C-C) + ν(C-O); 1455 $\delta(CH_3)$; 1372 $\nu(C-CH_3)$; 1267 $\nu(C-CH_3)$; 1111 $\gamma(CH_3)$; 1050 ν(C-O); 785 $\gamma(CH_3)$;
$Ta(OEt)_5$	+ 3-chloro-pentane-2,4-dione	3289 ν(O-H); 2966 ν(C-H); 1583 ν(C-C) + ν(C-O); 1472 $\delta(CH_3)$; 1419 $\delta(CH_3)$; 1145 $\gamma(CH_3)$; 1045 ν(C-O); 1021 ν(C-O)
	+ 1-acetyl-2-oxopropyl 2-bromo-2-methylpropanoate	3360 ν(O-H); 2924 ν(C-H); 2878 ν(C-H); 1723 ν(C-O) (absorbed); 1659 ν(C-C) + ν(C-O); 1461 $\delta(CH_3)$; 1377 $\nu(C-CH_3)$; 1256 $\nu(C-CH_3)$; 1202

		γ(CH_3); 1122 γ(CH_3); 1055 ν(C-O); 797 γ(CH_3)
$Fe(OEt)_3$	+ 3-acetyl-5-bromo-5-methylhexane-2,4-dione	3430 ν(O-H); 1732 ν(C-O) (3rd CO); 1573 ν(C-C) + ν(C-O); 1512 ν(C-C) + ν(C-O); 1471 δ(CH_3); 1365 ν(C-CH_3); 1297 ν(C-CH_3); 1246 ν(C-CH_3); 1185 γ(CH_3); 1111 γ(CH_3); 828 γ(CH_3)

Table 51: Elemental analysis and diameter of the obtained nanoparticles.

Alkoxide	Ligand	Elemental analysis	Diameter (DLS) [nm]
$Ti(O^iPr)_4$	+ 3-chloro-pentane-2,4-dione	26.9 % C, 3.8 % H, 5.1 % Cl	92 ± 4
	+ 3-bromo-pentane-2,4-dione	27.2 % C, 3.5 % H, 7.2 % Br	210 ± 4
	+ 1-acetyl-2-oxopropyl 2-bromo-2-methylpropanoate	28.7 % C, 3.9 % H, 4.9 % Br	106 ± 15
	+ 3-acetyl-5-bromo-5-methylhexane-2,4-dione	35.0 % C, 6.4 % H, 4.1 % Br	156 ± 25
$Zr(O^iPr)_4$	+ 3-chloro-pentane-2,4-dione	15.6 % C, 3.8 % H, 3.0 % Cl	49 ± 7
	+ 1-acetyl-2-oxopropyl 2-bromo-2-methylpropanoate	14.0 % C, 2.9 % H, 2.7 % Br	65 ± 7
	+ 3-acetyl-5-bromo-5-methylhexane-2,4-dione	16.6 % C, 3.1 % H, 2.6 % Br	0.6 ± 0.1
$VO(OEt)_3$	+ 3-chloro-pentane-2,4-dione	14.9 % C, 2.0 % H, 1.2 % Cl	76 ± 5
	+ 1-acetyl-2-oxopropyl 2-bromo-2-methylpropanoate	25.2 % C, 3.9 % H, 3.1 % Br	25 ± 2 160 ± 31
$Y(OEtOMe)_3$	+ 3-chloro-pentane-2,4-dione	30.2 % C, 3.3 % H, 13.4 % Cl	222 ± 25
	+ 1-acetyl-2-oxopropyl 2-bromo-2-methylpropanoate	13.0 % C, 3.0 % H, 3.6 % Br	80 ± 11
$Ta(OEt)_5$	+ 3-chloro-pentane-2,4-dione	12.2 % C, 1.8 % H, 1.3 % Cl	11 ± 6
	+ 1-acetyl-2-oxopropyl 2-bromo-2-methylpropanoate	21.2 % C, 3.4 % H, 1.2 % Br	4 ± 0.2
$Fe(OEt)_3$	+ 3-acetyl-5-bromo-5-methylhexane-2,4-dione	21.3 % C, 3.2 % H, 1.9 % Br	120 ± 17

7.4.19. General procedure for the synthesis of crystalline TiO_2 nanoparticles in a microemulsion approach at increased temperature and pressure

5 ml Triton X-100 were mixed with 8 ml cyclohexane and 3 ml n-hexanol and stirred inside a glass reactor. Afterwards $4.92*10^{-3}$ mol titanium alkoxide were dissolved in 4 ml 5 M HNO_3 and added dropwise to the surfactant mixture inside the glass reactor and stirred until no turbidity was visible. The reactor was sealed and heated up to 120 °C in an oil bath. After 18 hours the particles were isolated via centrifugation and washed with water and ethanol.

Table 52: Diameter, FTIR-assignments and elemental analysis of the obtained nanoparticles.

Precursor	Yield	Assignments FTIR (ATR) [cm^{-1}]	Elemental analysis	Diameter (DLS) [nm]
titanium n-butoxide	0.95 g (79.5 %)	3238 ν(O-H); 1692 ν(C-H); 1414 δ(CH_3)	---	19 ± 2
titanium isopropoxide + 3- bromo-2,4-pentane-dione	0.71 g (51.6 %)	3683 ν(O-H); 1714 ν(C-H); 1691 ν(C-H); 1394 δ(CH_3); 1044 γ(CH_3)	3.6 % C, 2.0 % H, < 0.2 % Br	12 ± 2
titanium isopropoxide + 3-chloro-2,4-pentane-dione	0.65 g (56.1 %)	3696 ν(O-H); 1718 ν(C-H); 1694 ν(C-H); 1397 δ(CH_3); 1034 γ(CH_3)	4.9 % C, 2.0 % H, < 0.2 % l	82 ± 7
titanium isopropoxide + 3-acetyl-5-bromo-5-methylhexane-2,4-dione	0.85 g (49.4 %)	3460 ν(O-H); 3070 ν(O-H); 2919 ν(C-H); 1716 ν(C-H); 1695 ν(C-H); 1045 γ(CH_3)	5.8 % C, 3.7 % H, < 0.2 % Br	42 ± 1

7.4.20. General procedure for the synthesis of metal oxide nanoparticles using metal salts

The nanoparticles were prepared by mixing two water-in-oil microemulsions (A+B) one containing the metal salt (A) and the other an ammonia solution (B). All used microemulsions were formed according to the following procedure: 14.50 g (58 %) cyclohexane were mixed with 3.75 g (15 %) n-hexanol and 4.75 g (19 %) Triton-X100 and stirred at room temperature

for 20 minutes. Microemulsion A was prepared by adding 2.00 g (8 %) water, which contained 0.3 mol metal salt. In case of the titanium- and zirconium-salt solution the salt was dissolved in 0.4 ml conc. HCl and then diluted with water. Microemulsion B was formed by addition of the necessary amount of NH_4OH to the basic solution. After 24 h of excessive stirring the microemulsions were centrifuged and sequentially redispersed two times with 20 ml of a chloroform and methanol 1:1 mixture, methanol, water, and ethanol.

Table 53: Diameter of the obtained particles.

Metal Salt (0.3 mol/l)	Ammonia Concentration	Obtained Particles	Diameter (DLS) [nm]
119 mg $FeCl_2*4H_2O$	70.3 mg (0.6 mol/l)	red-brown (15 mg) (26 %)	112 ± 18
113 mg $TiCl_4$	400 mg (3.4 mol/l)[#]	White (12 mg) (25 %)	210 ± 15
138 mg $ZrO(NO)_3$	187 mg (1.6 mol/l)[#]	White (11 mg) (13 %)	658 ± 81
135 mg $ZnBr_2$	70.3 mg (0.6 mol/l)	White (10 mg) (17 %)	135 ± 6
482 mg $AlCl_3*6H_2O$[##]	545 mg (4.6 mol/l)	White (111 mg) (84 %)	8 ± 0.4

[#] higher than the stoichiometric ammonia concentration was necessary because the metal salt solutions showed a very low pH value (< 1).

[##] in case of the aluminum oxide nanoparticles a concentration of 1 mol/l was used.

7.4.21. General procedure for the functionalization of the surface of the SiO_2 particle

Half of the SiO_2 nanoparticles suspension in ethanol which was received from the Stöber process was utilized per functionalization reaction.

First the NH_3 was removed in vacuo until a pH value between 7 and 9 was reached. In a second step the silane was added dropwise in high excess under an argon atmosphere to guarantee total reaction of the surface OH-groups. The mixture was stirred for at least 3 days at 50 °C. Afterwards the particles were isolated by centrifugation and washed with ethanol to

eliminate physically absorbed silane molecules. The obtained particles were dispersed in 250 ml ethanol.

Table 54: Used silanes and obtained diameter (DLS).

Utilized silane	Amount	Diameter [nm]
2-(Carbomethoxy)ethyltrichlorosilane	2 ml ($1.31*10^{-2}$ mol)	90 ± 17
3-Amino-propyltriethoxysilane	2 ml ($1.29*10^{-2}$ mol)	102 ± 8

CPMS NMR:

2-(Carbomethoxy)ethyltrichlorosilane:
^{13}C CPMS NMR: 164.5 (**C**OO), 50.6 (O**C**H$_3$), 39.5 (OC**C**H$_2$), 8.3 (Si**C**H$_2$) ppm.
^{29}Si CPMAS: T-units at -66.9, -75.3 ppm; Q-units: -101.0, -110.6, -119.2 ppm.

3-Amino-propyltriethoxysilane:
^{13}C CPMS NMR: 54.3 (**C**H$_2$NH$_2$), 35.4 (CH$_2$**C**H$_2$CH$_2$), 8.4 (**C**H$_2$Si) ppm.
^{29}Si CPMAS: T-units at -67, -76 ppm; Q-units: -101.0, -110.5, -119.5 ppm.

7.4.21.1. Hydrolysis of methoxy-ester group of the functionalized silica nanoparticles

0.25 g 2-(Carbomethoxy)ethyltrichlorsilane functionalized particles were suspended in 10 ml isopropanol in the presence of 2 drops concentrated HCl and stirred for 48 hours. Afterwards the particles were isolated via centrifugation and washed several times with ethanol.
^{13}C CPMS NMR: 167.5 (**C**OO), 56.2 (OCH(CH$_3$)$_2$), 49.7 (OC**C**H$_2$), 14.8 (**C**H$_3$), 7.9 (Si**C**H$_2$) ppm.
^{29}Si CPMAS: T-units at -66.9, -75.3 ppm; Q-units: -101.0, -110.6, -119.2 ppm.

7.4.22. Synthesis of 2-sulfanylethyl 2-bromo-2-methylpropanoate

a) Ratio 1:1.2
6.4 g ($8.21*10^{-2}$ mol) Sulfanylethanol were mixed with 10.0 g ($9.88*10^{-2}$ mol) triethylamine. After the mixture was cooled below 0°C, using a NaCl-ice bath, 22.72 g ($9.88*10^{-2}$ mol) 2-bromo-2-methyl-propionic acid bromide were added slowly and stirred over night. Hydrolysis

was carried out adding 65 g of water. The resulting ester was extracted 3 times with 50 ml diethyl ether. The unified organic phases were extracted three times with 50 ml saturated $NaHCO_3$ solution, three times with 25 ml water and dried over $MgSO_4$. The diethyl ether was removed in vacuo and the resulting product was distilled in vacuum (5 mm Hg) whereby fractions were drawn at 80 °C and 123 °C, respectively.
Yield: 4.320 g (23.25 %) colorless oil (fraction at 123 °C)

Elemental analysis: calcd. 33.9 C, 4.7 H, 41.0 Br; found: 32.9 C, 4.2 H, 40.1 Br.

^{1}H NMR (δ, $CDCl_3$): 4.30 (m, 2H, $SCH_2\mathbf{CH_2}O$), 3.21 (m, 2H, $S\mathbf{CH_2}CH_2O$), 1.93 (s, 6H $CBr(\mathbf{CH_3})_2$) ppm.

^{13}C NMR (δ, $CDCl_3$): 199.07 (**C**SO), 171.0 (**C**OO), 63.8 ($SCH_2\mathbf{C}H_2O$), 55.5 ($\mathbf{C}Br(CH_3)_2$), 301.0 ($CBr(\mathbf{C}H_3)_2$), 28.6 ($S\mathbf{C}H_2CH_2O$) ppm.

b) Ratio 1:5
20.4 g (0.261 mol) Sulfanylethanol were diluted with 30 ml diethyl ether and mixed with 5.28 g ($5.22*10^{-2}$ mol) triethylamine. 12 g ($5.22*10^{-2}$ mol) 2-Bromo-2-methyl-propionic acid bromide were added slowly after the mixture was cooled below 0 °C, using a NaCl-ice bath, and stirred over night. Hydrolysis was carried out adding 40 g of water. The resulting ester was extracted 2 times with 35 ml diethyl ether. The organic phase was extracted three times with 30 ml saturated $NaHCO_3$ solution, two times with water and dried over $MgSO_4$. The diethyl ether was removed in vacuo and the resulting product was distilled in vacuum (7 mm Hg) at 108 °C.
Yield: 9.89 g (83.07 %) of slightly yellow oil.

Elemental analysis: calcd. 34.9 C, 5.4 H, 33.1 Br; found: 32.6 C, 4.6 H, 34.5 Br.

^{1}H NMR (δ, $CDCl_3$): 4.22 (m, 2H, $HSCH_2\mathbf{CH_2}O$), 2.79 (m, 2H, $HS\mathbf{CH_2}CH_2O$), 1.85 (s, 6H $CBr(\mathbf{CH_3})_2$).

^{13}C NMR (δ, $CDCl_3$): 171.0 (COO), 66.8 ($HSCH_2\mathbf{C}H_2O$), 55.5 ($\mathbf{C}Br(CH_3)_2$), 30.5 ($CBr(\mathbf{C}H_3)_2$), 22.8 ($HS\mathbf{C}H_2CH_2O$) ppm.

7.4.23. Functionalization of gold nanoparticles with 2-sulfanylethyl-2-bromo-2-methylpropanoate

The gold nanoparticle dispersion was centrifuged twice at 6000 rpm. 2-sulfanylethyl-2-bromo-2-methylpropanoate was added to an aqueous suspension of the gold nanoparticles in large excess and refluxed over night, whereas the color changed instantaneously from red to black. The particles were washed with water and ethanol in an ultrasonic bath to remove free initiator and transferred into toluene.

Specific surface area: 22.9 m^2/g

Surface coverage (estimated from TGA): 0.88 mmol/g

7.4.24. Synthesis of 2-bromo-2-methyl-propionic acid allyl ester

9.534 g (0.164 mol) Allyl alcohol were mixed with 19.63 g (0.194 mol) triethylamine and cooled to 0 °C. 44.6 g (0.194 mol) 2-Bromo-2-methyl-propionic acid bromide were added dropwise. A white precipitate formed; this suspension was stirred over night. Hydrolysis was carried out adding 130 g (7.22 mol) of water. The resulting ester was extracted with 130 ml diethyl ether. The organic phase was washed three times with saturated sodium hydrogen carbonate solution and three times with water and afterwards dried over $MgSO_4$. The diethyl ether was evaporated in vacuo and the resulting ester was distilled in vacuum (4 mm Hg) at 55 °C.

Yield: 24.85 g (61.9 %) yellow oil

Elemental analysis: calcd. 40.6 C, 5.3 H, found 40.7 C, 5.5 H.

^{1}H NMR (δ, $CDCl_3$): 5.95 (m, 1H, $CH_2\mathbf{C}\mathbf{H}CH_2O$), 5.35 (m, 2H, $\mathbf{CH_2}CHCH_2O$), 4.66 (m, 2H, CH_2CHCH_2O), 2.0 (s, 6H $CBr(\mathbf{CH_3})_2$) ppm.

^{13}C NMR (δ, $CDCl_3$): 171.4 (COO), 131.6 ($CH_2\mathbf{C}HCH_2O$), 118.7 ($\mathbf{C}H_2CHCH_2O$), 66.5 (CH_2CHCH_2O), 55.8 ($\mathbf{C}Br(CH_3)_2$), 31.0 ($CBr(\mathbf{C}H_3)_2$) ppm.

7.4.25. Hydrosilation of 2-bromo-2-methyl-propionic acid allyl ester

12.00 g (57.9 mmol) 2-Bromo-2-methyl-propionic acid allyl ester were diluted with 10 ml absolute toluene under an argon atmosphere. Three drops of a Karstedt catalyst solution and 14.26 g (86.9 mmol) triethoxy silane were added via a syringe through a septum and refluxed over night. After removing the solvent and the excess of triethoxy silane in vacuo, 20.98 g (98 %) of yellow oil were obtained.

Elemental analysis: calc. 42.2 C, 7.2 H; found 41.3 C, 7.5 H.

^{1}H NMR (δ, $CDCl_3$): 4.07 (m, 2H, $O\mathbf{CH_2}CH_2CH_2Si$), 3.80 (q, 6H, $SiO\mathbf{CH_2}CH_3$), 1.85 (s, 6H, $C(\mathbf{CH_3})_2Br$), 1.72 (m, 2H, $OCH_2\mathbf{CH_2}CH_2Si$), 1.85 (s, 9H, $SiOCH_2\mathbf{CH_3}$) 0.93 (m, 2H, $OCH_2CH_2\mathbf{CH_2}Si$) ppm.

^{13}C NMR (δ, $CDCl_3$): 170.6 (**C**OO), 66.9 ($O\mathbf{C}H_2CH_2CH_2Si$), 59.0 ($\mathbf{C}(CH_3)_2Br$), 58.5 ($SiO\mathbf{C}H_2CH_3$), 29.8 ($C(\mathbf{C}H_3)_2Br$), 17.3 ($SiOCH_2\mathbf{C}H_3$), 14.4 ($OCH_2\mathbf{C}H_2CH_2Si$), 5.2 ($OCH_2CH_2\mathbf{C}H_2Si$) ppm.

^{29}Si NMR (δ, $CDCl_3$): -46.8 ($(EtO)_3\mathbf{Si}C$) ppm.

7.4.26. Functionalization of the Au@SiO_2 nanoparticles with 2-bromo-2-methyl-propionic acid propane -(3′-triethoxy-silane)-ester

2-Bromo-2-methyl-propionic acid propane -(3′-triethoxy-silane)-ester was added to a suspension of Au@SiO_2 nanoparticles in toluene in great excess. The mixture was refluxed over night and then centrifuged and washed with toluene to eliminate excessive initiator.
Specific surface area: 35.6 m^2/g
Surface coverage (estimated from TGA): 1.1 mmol/g

7.4.27. Synthesis of the asymmetric azo-initiator[16]

First step: 300 ml Water were mixed with 27.79 g (0.43 mol) KCN and 27.97 g (2.15 mol) hydrazine sulfate and heated up to 50 °C. 24.96 g (0.215 mol) laevulin acid were mixed with 12.47 g (0.215 mol) acetone and 8.6 g (0.215 mol) NaOH in 75 ml water. The obtained

laevulin salt mixture was added dropwise to the KCN solution and stirred for 3 hours at 50 °C. After cooling down the solution to room temperature the pH value was adjusted to 4 with conc. HCl. Then bromine was added in excess which was detected through the permanent orange color of the solution. The excessive bromine was destroyed with sodium hydrogen sulfite. The obtained white precipitate was stirred 30 minutes in 125 ml 1 N NaOH and separated. The filtrate was acidified with concentrated HCl and the obtained white precipitate was isolated and dried.
Yield: 1.85 g (4.1 %) white powder

^{1}H NMR (δ, $CDCl_3$): 2.50 (m, 2H, HOOC**C**$\mathbf{H_2}$$CH_2$C), 2.35 (m, 2H, HOOC$CH_2$**C**$\mathbf{H_2}$C), 1.67 (s, 12H, C(**C**$\mathbf{H_3}$)$_2$) ppm.

^{13}C NMR (δ, $CDCl_3$): 178.9 (**C**OOH), 119.2-117.9 (**C**N-groups), 71.9 (CH_2**C**CNCH_3N), 68.9 (**C**CN(CH_3)$_2$N), 38.0 (HOOC**C**H_2CH_2C), 29.3 (HOOCCH_2**C**H_2C), 26.3 (CH_2CCN**C**H_3N), 24.7 (NC(CN)(**C**H_3)$_2$) ppm.

FTIR (ν, KBr): 3210 ν(O-H); 2294 ν(C-H); 2242 ν(CN), 1800 ν(C-O); 1712 ν(C-H) + ν(C-O); 1453 δ(CH_3); 1438 δ(CH_3); 1420 δ(CH_3); 1366 δ(CH_3); 1305 ν(C-CH_3); 1226 ν(C-CH_3); 1166 γ(CH_3); 1127 γ(CH_3); 949 ν(C-O); 876 γ(CH_3) cm^{-1}.

Second step: 8.0 g (38.4 mmol) PCl_5 were mixed with 10 ml dichloromethane under an argon atmosphere and cooled to 0°C. 1.852 g (8.81mmol) of the compound that was received in the first part were dissolved in 10 ml dichloromethane and added dropwise to the PCl_5 suspension. This suspension was stirred overnight and filtered afterwards. The solvent was removed in vacuo and 0.876 g (40.63 %) of a colorless product were obtained.

^{1}H NMR (δ, $CDCl_3$): 2.86 (m, 2H, ClOC**C**$\mathbf{H_2}$$CH_2$CO), 2.47 (m, 2H, ClOC$CH_2$**C**$\mathbf{H_2}$C), 1.67 (s, 12H, C(**C**$\mathbf{H_3}$)$_2$) ppm.

^{13}C NMR (δ, $CDCl_3$): 172.6 (**C**OCl), 119.2-117.9 (**C**N-groups), 71.9 (CH_2**C**CNCH_3N), 69.1 (**C**CN(CH_3)$_2$N), 42.1 (ClOC**C**H_2CH_2C), 33.3 (ClOCCH_2**C**H_2C), 25.6 (CH_2CCN**C**H_3N), 24.1 (NC(CN)(**C**H_3)$_2$) ppm.

FTIR (ν, KBr): 3210 ν(O-H); 2294 ν(C-H); 2242 ν(CN), 1800 ν(C-O); 1715 ν(C-H) + ν(C-O); 1453 δ(CH_3); 1438 δ(CH_3); 1425 δ(CH_3); 1366 δ(CH_3); 1300 ν(C-CH_3); 1226 ν(C-CH_3); 1166 γ(CH_3); 1127 γ(CH_3); 950 ν(C-O); 876 γ(CH_3) cm^{-1}.

Third step: 0.704 ml (8,67 mmol) Pyridine and 0.25 g (4.34 mmol) allyl alcohol were mixed with 5.5 ml dichloromethane and cooled to 0 °C. 0.867 g (3.58 mmol) Acid chloride of the second reaction step were dissolved in 5.5 ml dichloromethane under an argon atmosphere. This solution was added slowly to the allyl alcohol / pyridine mixture and stirred for three days. The obtained solution was extracted with 2N H_2SO_4 whereby the obtained organic phase was washed with saturated $NaHCO_3$ solution and water. The solution was dried with $MgSO_4$ and filtered and after removal of the solvent 1.127 g (95 %) of a yellow oil.

^1H NMR (δ, $CDCl_3$): 5.85 (m, 1H, CH_2**CH**CH_2O), 5.28 (m, 2H, **CH_2**$CHCH_2O$), 4.52 (m, 2H,CH_2CH**CH_2**O), 2.86 (m, 2H, OC**CH_2**CH_2C), 2.47 (m, 2H, $OCCH_2$**CH_2**C), 1.67 (s, 12H, C(**CH_3**)$_2$) ppm.

^{13}C NMR (δ, $CDCl_3$): 169.9 (**C**OO), 130.7 (CH_2**C**HCH_2O und **C**H_2CHCH_2O) 117.2-116.9 (**C**N-groups), 70.5 (CH_2**C**$CNCH_3N$), 67.5 (CH_2CH**C**H_2O), 64.6 (**C**$CN(CH_3)_2N$), 52.1 (OO**C**CH_2CH_2C), 32.1 ($OOCCH_2$**C**H_2C), 28.0 (CH_2CCN**C**H_3N), 24.1 (NC(CN)(**C**H_3)$_2$) ppm.

FTIR (ν, KBr): 3240 ν(O-H); 2296 ν(C-H); 2243 ν(CN), 1713 ν(C-O); 1660 ν(C-H) + ν(C-O); 1450 δ(CH_3); 1440 δ(CH_3); 1421 δ(CH_3); 1366 δ(CH_3); 1309 ν(C-CH_3); 1226 ν(C-CH_3); 1166 γ(CH_3); 1127 γ(CH_3); 955 ν(C-O); 870 γ(CH_3) cm^{-1}.

7.4.28. Hydrosilation of the asymmetric azo initiator

1.74 g (6.9 mmol) Asymmetric azo initiator were dissolved in 15 ml absolute toluene under an argon atmosphere. Three drops of a Karstedt catalyst solution were added via a syringe through a septum and the mixture was vigorously stirred for 5 minutes. After the dropwise addition of 3.41 g (20.8 mmol) triethoxy silane the mixture was heated to 40°C and stirred for four days (the reaction was carried out until no further changes in the NMR spectrum were visible). The solvent and the excess of silane were evaporated in vacuo, and 2.46 g (86 %) colorless oil were obtained. No elemental analysis was performed because of the thermal instability of the resulting product.

^{1}H NMR (δ, $CDCl_3$): 5.85 (m, traces, CH_2**C**HCH_2O), 5.28 (m, traces, **C**H_2CHCH_2O), 4.52 (m, 2H,CH_2CH**C**H_2O), 4.27 (m, 2H, CH_2CH_2**C**H_2O), 3.82 (t, 6H, CH_3**C**H_2OSi), 3.47 (m, 2H, OC**C**H_2CH_2C), 2.47 (m, 2H, $OCCH_2$**C**H_2C), 1.67 (s, 6H, NNC(CN)(**C**$H_3)_2$) 1.47 (s, 3H, $CH_2C(CN)$**C**H_3NN) 1.19 (m, 9H, **C**H_3CH_2OSi) 1.17 (m, 2H, Si**C**H_2) ppm.

^{13}C NMR (δ, $CDCl_3$): 169.9 (**C**OO), 130.7 (traces of CH_2**C**HCH_2O and **C**H_2CHCH_2O) 117.2-116.9 (**C**N-groups), 67.5 (CH_2CH**C**H_2O), 58.1 (CH_3**C**H_2OSi), 57.3 (CH_2**C**$(CN)CH_3NN$), 38.3 ($OCCH_2$), 24.1 ($SiCH_2$**C**H_2CH_2O), 22.4 (**C**$H_2C(CN)CH_3NN$), 17.1 (**C**H_3CH_2O), 17.0 ($NNCCH_3$**C**N)), 0.0 (Si**C**H_2) ppm.

^{29}Si NMR (δ, $CDCl_3$): -42.4 ($(EtO)_3$**Si**C) ppm.

FTIR (ν, ATR): 3240 ν(O-H); 2294 ν(C-H); 2243 ν(CN), 1713 ν(C-O); 1680 ν(C-H) + ν(C-O); 1454 δ(CH_3); 1463 δ(CH_3); 1421 δ(CH_3); 1369 δ(CH_3); 1345 ν(C-CH_3); 1221 ν(C-CH_3); 1161 γ(CH_3); 1126 γ(CH_3); 956 ν(C-O); 871 γ(CH_3) cm^{-1}.

7.4.29. Etherification of 2-hydroxy-1-[4-(2-hydroxyethoxy)phenyl]-2-methyl-1-propanone with allyl bromide

6.65 g (0.055 mol) Allyl bromide and 0.608 g (1.11 mmol) tetraoctylammonium bromide as phase transfer catalyst were added to a mixture of 11.3 g (0.05 mol) 2-hydroxy-1-[4-(2-hydroxyethoxy)phenyl]-2-methyl-1-propanone and 2.2 g (0.055 mol) NaOH in 150 ml toluene, and stirred for 24 hours at 50 °C. Afterwards the precipitate was separated and dried in vacuo.
Yield: 14.58 g (81.2%) colorless powder

^{1}H NMR (δ, $CDCl_3$): 7.96-7.02 (m, 4H, phenyl), 5.80 (m, 1H, CH_2**C**HCH_2O), 5.23-5.08 (q, 2H, **C**H_2CHCH_2O), 4.22 (s, 1H, **OH**), 4.06 (t, 2H, O**C**H_2CH_2O), 3.95 (t, 2H, OCH_2**C**H_2O), 3.67 (t, 1H, CH_2CH**C**H_2O), 1.49 (s, 6H, HOC(**C**$H_3)_2$) ppm.

^{13}C NMR (δ, $CDCl_3$): 201.6 (CO), 161.7/131.4/113.2 (phenyl), 138.2 (CH_2CHCH_2O), 125.7 (CH_2CHCH_2O) 78.03 ($OCC(CH_3)_2OH$), 72.4 (CH_2CHCH_2O), 67.8 (OCH_2CH_2O), 66.7 (OCH_2CH_2O), 27.7 ($OCC(CH_3)_2OH$) ppm.

7.4.30. Hydrosilation of the modified photo-initiator

2.00 g (7.57 mmol) Allyl-modified photoinitiator (chapter 7.4.29) were diluted in 15 ml absolute toluene under light exclusion and an argon atmosphere. Three drops of a Karstedt catalyst solution and 3.72 g (22.7 mmol) triethoxy silane were added via a syringe through a septum and stirred for four days at 40°C. After evaporation of the solvent and the excess of triethoxy silane, 2.93 g (90 %) yellow oil were obtained. No elemental analysis was performed because of the instability of the resulting product.

^{1}H NMR (δ, $CDCl_3$): 7.20-6.80 (m, 4H, aromatic), 4.82 (s, 1H, **OH**), 4.06 (t, 2H, OCH_2CH_2O), 3.95 (t, 2H, OCH_2CH_2O), 3.78 (m, 6H, CH_3CH_2OSi) 3.67 (t, 2H, $CH_2CH_2CH_2O$), 1.49 (s, 6H, $HOC(CH_3)_2$), 1.43 (m, 2H, $SiCH_2CH_2CH_2$), 1.17 (m, 2H, CH_3CH_2OSi), 0.82 ($SiCH_2$) ppm.

^{13}C NMR (δ, $CDCl_3$): 201.6 (CO), 161.7/131.4/113.2 (aromatic), 83.6 ($OCC(CH_3)_2OH$), 72.7 (OCH_2CH_2O), 72.3 (OCH_2CH_2O), 68.1 ($SiCH_2CH_2CH_2O$), 57.3 ($SiOCH_2CH_3$), 21.9 ($C(OH)(CH_3)_2$), 17.3 ($SiOCH_2CH_3$), 13.0 ($SiCH_2CH_2CH_2O$), 5.4 ($SiCH_2CH_2CH_2O$) ppm.

^{29}Si NMR (δ, $CDCl_3$): -46.8 ($(EtO)_3SiC$), -107 ($(EtO)_3SiO$ (by-product)) ppm.

7.4.31. Hydrosilation of 4-vinyl-benzyl-chloride with triethoxysilane

6.00 g (39.3 mmol) 4-Vinyl-benzyl chloride were diluted in 10 ml toluene under an argon atmosphere. Three drops of a Karstedt catalyst solution and 9.68 g (58.9 mmol) triethoxy silane were added and the mixture was heated under reflux for 48 h. After evaporation of the toluene and the excess of silane in vacuo, 9.45 g (87.2 %) yellow oil were obtained.

Elemental analysis: calc. 56.9 C, 7.8 H; found 56.8 C, 7.9 H.

^{1}H NMR (δ, $CDCl_3$): 7.3-7.2 (m, 5H, phenyl), 4.44 (s, 2H, $ClCH_2$-phenyl), 3.77 (q, 6H, $SiOCH_2CH_3$), 2.66 (t, 2H, $SiCH_2CH_2$-phenyl), 1.14 (m, 9H, $SiOCH_2CH_3$), 0.91 (t, 2H, $SiCH_2CH_2$-phenyl) ppm.

^{13}C NMR (δ, $CDCl_3$): 140, 135, 127.6-127.4 (phenyl), 58.5 ($SiOCH_2CH_3$), 50.2 ($ClCH_2$-phenyl), 27.7 (phenyl-CH_2CH_2Si), 20.4 (phenyl-CH_2CH_2Si), 17.3 ($SiOCH_2CH_3$) ppm.

^{29}Si NMR (δ, $CDCl_3$): - 46.8 ($(EtO)_3SiC$) ppm.

7.4.32. General procedure for the functionalization of metal oxide nanoparticles

Depending on the triethoxy silane-functionalized polymerization initiator different reaction conditions were chosen. The metal oxide particles were mixed with absolute ethanol under an argon atmosphere and the modified initiator was added in high excess. In case of the azo and photoinitiator the mixture was stirred at room temperature for four days under light exclusion while the ATRP initiator containing mixtures were refluxed for 48 hours.

Elemental analysis:

The diction @ shows that the particle core is modified with the following initiator.

Iron oxide nanoparticles functionalized with: $Fe_xO_y(OH)_z$@(**A**): 2.8 C, 2.0 H, 0.1 N; $Fe_xO_y(OH)_z$@(**B**): 15.4 C, 2.9 H; $Fe_xO_y(OH)_z$@(**C**): 10.9 C, 2.4 H; $Fe_xO_y(OH)_z$@(**D**): 18.2 C, 3.4 H.

Titanium oxide nanoparticles functionalized with: $Ti_xO_y(OH)_z$@(**A**): 3.3 C, 3.0 H, 2.7 N; $Ti_xO_y(OH)_z$@(**B**): 9.3 C, 3.0 H; $Ti_xO_y(OH)_z$@(**C**): 15.2 C, 2.9 H; $Ti_xO_y(OH)_z$@(**D**): 12.0 C, 2.0 H.

Zirconium nanoparticles functionalized with: $Zr_xO_y(OH)_z$@(**A**): 4.2 C, 2.0 H, 2.2 N; $Zr_xO_y(OH)_z$@(**B**): 13.9 C, 2.7 H; $Zr_xO_y(OH)_z$@(**C**): 8.4 C, 2.3 H; $Zr_xO_y(OH)_z$@(**D**): 13.0 C, 2.5 H.

Zinc oxide nanoparticles functionalized with: $Zn_xO_y(OH)_z$@(**A**): 5.0 C, 2.2 H, 2.3 N; $Zn_xO_y(OH)_z$@(**B**): 14.9 C, 3.0 H; $Zn_xO_y(OH)_z$@(**C**): 16.9 C, 3.5 H; $Zn_xO_y(OH)_z$@(**D**): 6.6 C, 2.1 H.

^{13}C CPMAS NMR:

$Fe_xO_y(OH)_z$@(**D**): 140, 135, 127-127 (phenyl), 58 (traces, $SiO\mathbf{C}H_2CH_3$), 44 ($Cl\mathbf{C}H_2$-phenyl), 27 (phenyl-$\mathbf{C}H_2CH_2Si$), 20 (phenyl-$CH_2\mathbf{C}H_2Si$), 17 (traces, $SiOCH_2\mathbf{C}H_3$) ppm.

$Ti_xO_y(OH)_z$@(**C**): 181, 171 (COO), 77-73 ($O\mathbf{C}H_2CH_2$), 59 ($\mathbf{C}(CH_3)_2Br$) , 31 ($C(\mathbf{C}H_3)_2Br$), 17.3 ($SiOCH_2CH_3$) ppm.

$Ti_xO_y(OH)_z$@(**D**): 127 (phenyl), 58 ($SiO\mathbf{C}H_2CH_3$), 27 (phenyl-$\mathbf{C}H_2CH_2Si$), 20 (phenyl-$CH_2\mathbf{C}H_2Si$), 17 ($SiOCH_2\mathbf{C}H_3$) ppm.

$Zr_xO_y(OH)_z$@(**C**): 179 (COO), 70-50 ($O\mathbf{C}H_2CH_2$)/($\mathbf{C}(CH_3)_2Br$)/($SiO\mathbf{C}H_2CH_3$), 31 ($C(\mathbf{C}H_3)_2Br$), 17 ($SiOCH_2\mathbf{C}H_3$) ppm.

$Zn_xO_y(OH)_z$@(**C**): 171 (COO), 66 ($O\mathbf{C}H_2CH_2$), 60-50 ($\mathbf{C}(CH_3)_2Br$)/($SiO\mathbf{C}H_2CH_3$), 25 ($C(\mathbf{C}H_3)_2Br$), 17 ($SiOCH_2\mathbf{C}H_3$), 5 ($OCH_2CH_2\mathbf{C}H_2Si$) ppm.

7.4.33. General procedure for atom transfer radical polymerization[15]

The macroinitiator was placed with the copper salt in a flask that was closed with a septum which was fixed with copper wire. The flask is evacuated and refilled three times with the help of a steel canula. Afterwards the solvent (toluene) and the utilized monomer are added and stirred vigorously until the particles are suspended in the solution. Now three "freeze-pump-thaw" cycles were performed. The ligand was added under vigorous stirring. The mixture was heated up to the polymerization temperature in a pre-heated oil-bath. After the polymerization the obtained polymer was dissolved in THF, precipitated in methanol and dried in vacuo.

7.4.33.1. Polymerization results using Au- and Au@SiO_2-particles as macroinitiators

The following monomers were used: MMA, styrene, isoprene and methacrylic acid trimethyloxysilyl propylester (MMA-R'-SiR_3).

Table 55: Results of the performed polymerizations using Au- and Au@SiO_2-particles as macroinitiators.

Nanoparticle	Toluene	CuCl	Monomer	Temp. [°C]	Ligand	Time	Yield
Au (10 mg)	5 ml	7.3 mg	MMA 0.2 g ($2*10^{-3}$ mol)	75	Pmdeta (13 mg)	21.5 h	0.1 g 50.0 %
Au@SiO_2 (10 mg)	5 ml	6.5 mg	MMA 0.2 g ($2*10^{-3}$ mol)	75	Pmdeta (11.4 mg)	22.5 h	0.13 g 65.1 %
Au (30 mg)	3 ml	21 mg	Styrene 1.5 g ($1.4*10^{-2}$ mol)	80 °C	Pmdeta (158 mg)	22 h	0.78 g 52.0 %
Au@SiO_2 (60 mg)	3 ml	15 mg	Styrene 1.6 g ($1.5*10^{-2}$ mol)	80°C	Pmdeta (104 mg)	46 h	0.97 g 60.6 %
Au@SiO_2 (60 mg)	3 ml	15 mg	MMA-R'-SiR_3 1.6 g	80 °C	Pmdeta (104 mg)	45 h	1.2 g 75.0 %
Au@SiO_2 (60 mg)	3 ml	15 mg	Isoprene 1.6 g ($2.3*10^{-2}$ mol)	80°C	Pmdeta (104 mg)	44 h	0.10 g 6.1 %
Au (35 mg)	4 ml	25 mg	Styrene 1.6 g ($1.5*10^{-2}$ mol)	R_T	Me_6Tren (104 mg)	24 h	0.31 g 19.4 %
Au@SiO_2 (60mg)	2 ml	15 mg	Styrene 1.6 g ($1.5*10^{-2}$ mol)	R_T	Me_6Tren (104 mg)	24 h	0.52 g 32.5 %
Au@SiO_2 (30 mg)	3 ml	26 mg	Isoprene 2.0 g ($2.9*10^{-2}$ mol)	R_T	Me_6Tren (208 mg)	46 h	0.11 g 5.5 %

Bromo-isobutyric-acid	3 ml	77.4 mg	Isoprene 3.0 g ($4.4*10^{-2}$ mol)	80 °C	Pmdeta (76.3 mg)	48 h	0.19 g 6.3 %

a) General procedure for the copolymerization of Au@SiO_2@PS core-shell-nanoparticles.

Isoprene and methacrylic acid trimethyloxysilyl propylester were used as monomers for the copolymerization. After 24 h of styrene polymerization 1 ml of the other monomer was added and polymerized for another 24 h.

b) Elimination of the SiO_2 layer in Au@SiO_2@Polyisopren core-shell nanoparticles.

After precipitating the nanoparticles in methanol, they were stirred for 24 h in concentrated HF, then centrifuged with 1500 rpm and washed with water.

7.4.33.2. General procedure for free radical polymerization

The modified nanoparticles were dispersed in the monomer either with solvent or without. The mixture was either heated to 90°C for 24 h (thermal initiated) or UV-irradiated for 48 h (initiator B). The resulting particles were precipitated in methanol and dried in vacuo.

7.4.33.3. Results of the polymerizations initiated by halo-pentane-2,4-diones

Table 56: Results of the polymerizations initiated by 3-chloro-pentane-2,4-dione and 3-bromo-pentane-2,4-dione.

Initiator	**Type**	**M_n [g/mol] / MWD MMA**		**M_n [g/mol] / MWD Styrene**	
		CuCl	**CuBr**	**CuCl**	**CuBr**
Bromo-propionic acid-ethyl-ester	ATRP	11000 1.26	4040 1.27	2430 1.29	2440 1.18
Chloro-propionic acid-ethyl-ester	ATRP	4690 1.20	7240 1.37	2470 1.36	2270 1.39

3-Chloro-pentane-2,4-dione	ATRP	18050	13410	3260	33160
		1.14	1.12	1.35	1.36
3-Chloro-pentane-2,4-dione	therm. rad.	115000		220900	
		9.0		3.0	
3-Bromo-pentane-2,4-dione	ATRP	32940	50530	17540	61660
		1.17	1.31	1.41	1.65
3-Bromo-pentane-2,4-dione	therm. rad.	90700		3100	
		6.2		2.59	
3-Bromo-pentane-2,4-dione	photo. rad.	83750		22350	
		2.01		1.76	

7.4.33.4. General procedure for the investigation of the activation rate of 3-bromo-pentane-2,4-dione and 3-chloro-pentane-2,4-dione in ATRP

CuX was mixed with the corresponding amount of 2,2,6,6,-teramethyl-piperidinyl-1-oxy (TEMPO) under an argon atmosphere. Afterwards 2 ml toluene and pmdeta were added. After three freeze-pump-thaw cycles the mixture was stirred 30 minutes at 40 °C and the corresponding amounts of the halo-pentane-2,4-dione and biphenyl were added dissolved in 0.5 ml toluene. In table 57 the used ratios are presented.

Table 57: Used ratios for the activity measurements.

CuBr *CuCl*	**Pmdeta**	**TEMPO**	**BrAcacH** *ClAcacH*	**Biphenyl**
7.2 mg	8.66 mg	7.8 mg	**8.95 mg**	4.25 mg
0.05 mmol	0.05 mmol	0.05 mmol	**0.05 mmol**	0.03 mmol
4.95 mg	8.66 mg	7.8 mg	**8.95 mg**	4.25 mg
0.05 mmol	0.05 mmol	0.05 mmol	**0.05 mmol**	0.03 mmol
14.8 mg	26.0 mg	23.4 mg	20.18 mg	1.76 mg
0.15 mmol	0.15 mmol	0.15 mmol	0.15 mmol	0.007 mmol

7.4.33.5. Synthesis of pmdeta-complexes

In 40 ml absolute toluene the copper salt was suspended under an argon atmosphere. The ligand was added to 4 ml of the prior synthesized suspension. After 30 minutes of stirring the halo-pentane-2,4-dione was added. In table 58 the utilized ratios and the results of the UV/VIS spectroscopy are presented.

Table 58: Signals of the UV/VIS spectra of the obtained pmdeta complexes.

CuCl *CuBr*	**Pmdeta**	**3-chloro-pentane-2,4-dione**	**3-bromo-pentane-2,4-dione**	**Signals UV/VIS λ [nm]**
0.015 g	0.026 g			295
1.49*10^{-4} mol	1.49*10^{-4} mol			421
0.021 g	0.026 g			295
*1.49*10^{-4} mol*	1.49*10^{-4} mol			426
0.015 g	0.026 g	0.020 g		296
1.49*10^{-4} mol	1.49*10^{-4} mol	1.49*10^{-4} mol		424
0.021 g	0.026 g	0.020 g		296
*1.49*10^{-4} mol*	1.49*10^{-4} mol	1.49*10^{-4} mol		434
0.015 g	0.026 g		0.031 g	295
1.49*10^{-4} mol	1.49*10^{-4} mol		1.49*10^{-4} mol	427
0.021 g	0.026 g		0.031 g	297
*1.49*10^{-4} mol*	1.49*10^{-4} mol		1.49*10^{-4} mol	429
0.050 g		0.079 g		211
5.05*10^{-4} mol		5.05*10^{-4} mol		240
				310
0.050 g		0.055 g		208
*3.50*10^{-4} mol*		3.50*10^{-4} mol		238
				310

7.4.33.6. Polymerization of the organic shell using metal oxide particles synthesized from modified metal alkoxides as macroinitiators

Table 59: Obtained results of the performed polymerizations using metal oxide particles synthesized from modified metal alkoxides as macroinitiators.

Precursor for the nanoparticles	amount	**MMA** */Styrene*	**CuCl** */CuBr*	pmdeta	ratio [m:s]	temp.	time	yield [%]
$Ti(O^iPr)_4$ + 3-chloro-pentane-2,4-dione	15 mg	**3.0 g (30.0 mmol)**	---	---	---	90 °C	24 h	43.3
$Ti(O^iPr)_4$ + 3-chloro-pentane-2,4-dione	15 mg	*3 g (29.9 mmol)*	---	---	---	90 °C	24 h	12.2
$Ti(O^iPr)_4$ + 3-chloro-pentane-2,4-dione	20 mg	**3.0 g (30.0 mmol)**	*21.4 mg (0.15 mmol)*	26.0 mg (0.15 mmol)	1:1	75 °C	24 h	39.5
$Ti(O^iPr)_4$ + 3-chloro-pentane-2,4-dione	20 mg	*3.0 g (29.9 mmol)*	*21.4 mg (0.15 mmol)*	26 mg (0.15 mmol)	1:1	75 °C	48 h	32.4
$Ti(O^iPr)_4$ + 3-bromo-pentane-2,4-dione	10 mg	**3.0 g (30.0 mmol)**	---	---	---	90 °C	24 h	36.3
$Ti(O^iPr)_4$ + 3-bromo-pentane-2,4-dione	10 mg	*3.0 g (29.9 mmol)*	---	---	---	90 °C	24 h	15.1
$Ti(O^iPr)_4$ + 3-bromo-pentane-2,4-dione	25 mg	**3.0 g (30.0 mmol)**	---	---	---	UV	48 h	46.4

$Ti(O^iPr)_4$ + 3-bromo-pentane-2,4-dione	25 mg	*3.0 g (29.9 mmol)*	---	---	---	UV	48 h	13.3
$Ti(O^iPr)_4$ + 3-bromo-pentane-2,4-dione	15 mg	**3.0 g (30.0 mmol)**	**29.6 mg (0.30 mmol)**	54.0 mg (0.30 mmol)	1:1	75 °C	24 h	12.8
$Ti(O^iPr)_4$ + 3-bromo-pentane-2,4-dione	15 mg	*3.0 g (29.9 mmol)*	**29.6 mg (0.30 mmol)**	54.0 mg (0.30 mmol)	1:1	75 °C	24 h	10.3
$Ti(O^iPr)_4$ + 1-acetyl-2-oxopropyl 2-bromo-2-methylpropanoate	15 mg	**3.0 g (30.0 mmol)**	**29.6 mg (0.30 mmol)**	54.0 mg (0.30 mmol)	1:1	90 °C	24 h	24.4
$Ti(O^iPr)_4$ + 1-acetyl-2-oxopropyl 2-bromo-2-methylpropanoate	15 mg	*3.0 g (29.9 mmol)*	**29.6 mg (0.30 mmol)**	54.0 mg (0.30 mmol)	1:1	90 °C	48 h	19.3
$Ti(O^iPr)_4$ + 3-acetyl-5-bromo-5-methylhexane-2,4-dione	15 mg	**3.0 g (30.0 mmol)**	**29.6 mg (0.30 mmol)**	54.0 mg (0.30 mmol)	1:1	90 °C	24 h	22.1
$Ti(O^iPr)_4$ + 3-acetyl-5-bromo-5-methylhexane-2,4-dione	15 mg	*3.0 g (29.9 mmol)*	**29.6 mg (0.30 mmol)**	54.0 mg (0.30 mmol)	1:1	90 °C	48 h	15.3
$Zr(O^nBu)_4$ + 3-chloro-pentane-2,4-dione	40 mg	**3.0 g (30.0 mmol)**	**29.6 mg (0.30 mmol)**	54.0 mg (0.30 mmol)	1:1	90 °C	24 h	19.1
$Zr(O^nBu)_4$ + 3-chloro-pentane-2,4-dione	40 mg	*3.0 g (29.9 mmol)*	**29.6 mg (0.30 mmol)**	54.0 mg (0.30 mmol)	1:1	90 °C	24 h	13.9
$Zr(O^nBu)_4$ + 1-acetyl-2-oxopropyl 2-bromo-2-methylpropanoate	40 mg	**3.0 g (30.0 mmol)**	**29.6 mg (0.30 mmol)**	54.0 mg (0.30 mmol)	1:1	90 °C	24 h	20.1
$Zr(O^nBu)_4$ + 1-acetyl-2-oxopropyl 2-	67 mg	*10.4 g*	**0.197 g**	0.34 g	1:1	90 °C	27 h	14.0

bromo-2-methylpropanoate		*(0.1 mol)*	**(2.0 mmol)**	(2.0 mmol)				
$Ta(OEt)_5$ + 3-chloro-pentane-2,4-dione	20 mg	**3.0 g**	**29.6 mg**	54.0 mg	1:1	90 °C	24 h	8.1
		(30.0 mmol)	**(0.30 mmol)**	(0.30 mmol)				
$Ta(OEt)_5$ + 3-chloro-pentane-2,4-dione	20 mg	*3.0 g*	**29.6 mg**	54.0 mg	1:1	90 °C	24 h	5.1
		(29.9 mmol)	**(0.30 mmol)**	(0.30 mmol)				
$Ta(OEt)_5$ + 1-acetyl-2-oxopropyl 2-bromo-2-methylpropanoate	20 mg	**3.0 g**	**29.6 mg**	54.0 mg	1:1	90 °C	24 h	27.6
		(30.0 mmol)	**(0.30 mmol)**	(0.30 mmol)				
$Ta(OEt)_5$ + 1-acetyl-2-oxopropyl 2-bromo-2-methylpropanoate	20 mg	*3.0 g*	**29.6 mg**	54.0 mg	1:1	90 °C	24 h	15.1
		(29.9 mmol	**(0.30 mmol)**	(0.30 mmol)				
$VO(OEt)_3$ + 3-chloro-pentane-2,4-dione	20 mg	**3.0 g**	**29.6 mg**	54.0 mg	1:1	90 °C	24 h	9.4
		(30.0 mmol)	**(0.30 mmol)**	(0.30 mmol)				
$VO(OEt)_3$ + 3-chloro-pentane-2,4-dione	20 mg	*3.0 g*	**29.6 mg**	54.0 mg	1:1	90 °C	24 h	6.2
		(29.9 mmol)	**(0.30 mmol)**	(0.30 mmol)				
$VO(OEt)_3$ + 1-acetyl-2-oxopropyl 2-bromo-2-methylpropanoate	20 mg	**3.0 g**	**29.6 mg**	54.0 mg	1:1	90 °C	24 h	26.0
		(30.0 mmol)	**(0.30 mmol)**	(0.30 mmol)				
$VO(OEt)_3$ + 1-acetyl-2-oxopropyl 2-bromo-2-methylpropanoate	20 mg	*3.0 g*	**29.6 mg**	54.0 mg	1:1	90 °C	24 h	10.1
		(30.0 mmol)	**(0.30 mmol)**	(0.30 mmol)				
$Y(O^iPr)_3$ + 3-chloro-pentane-2,4-dione	20 mg	**3.0 g**	**29.6 mg**	54.0 mg	1:1	90 °C	24 h	11.4
		(30.0 mmol)	**(0.30 mmol)**	(0.30 mmol)				
$Y(O^iPr)_3$ + 3-chloro-pentane-2,4-dione	20 mg	*3.0 g*	**29.6 mg**	54.0 mg	1:1	90 °C	24 h	6.2
		(29.9 mmol)	**(0.30 mmol)**	(0.30 mmol)				

$Y(O^iPr)_3$ + 1-acetyl-2-oxopropyl 2-bromo-2-methylpropanoate	20 mg	**3.0 g (30.0 mmol)**	**29.6 mg (0.30 mmol)**	54.0 mg (0.30 mmol)	1:1	90 °C	24 h	6.5
$Y(O^iPr)_3$ + 1-acetyl-2-oxopropyl 2-bromo-2-methylpropanoate	20 mg	*3.0 g (30.0 mmol)*	**29.6 mg (0.30 mmol)**	54.0 mg (0.30 mmol)	1:1	90 °C	24 h	4.5
$Fe(O^iPr)_3$ + 3-acetyl-5-bromo-5-methylhexane-2,4-dione	20 mg	**3.0 g (30.0 mmol)**	**29.6 mg (0.30 mmol)**	54.0 mg (0.30 mmol)	1:1	90 °C	24 h	14.1
$Fe(O^iPr)_3$ + 3-acetyl-5-bromo-5-methylhexane-2,4-dione	20 mg	*3.0 g (30.0 mmol)*	**29.6 mg (0.30 mmol)**	54.0 mg (0.30 mmol)	1:1	90 °C	24 h	8.3

7.4.33.7. Polymerization of the organic shell using metal oxide particles synthesized from metal salts as macroinitiators

Table 60: Results of the polymerizations with 25 mg of the nanoparticles are reacted under the following conditions: Initiator A and B: free radical polymerization; thermal and photochemically initiated and initiator C and D: ATRP with the following ratios [CuCl]:[pmdeta]:[monomer]=1:1:5 in 3 ml toluene for 24 h at 90 °C.

Modified Particle	Monomer	Isolated Yield
$Fe_xO_y(OH)_z$ + Subst. A	Styrene	0.67 g (33.5 %)
	MMA	0.38 g (18.9 %)
+ Subst. B	Styrene	1.11 g (55.8 %)
	MMA	0.23 g (11.5 %)
+ Subst. C	Styrene	0.38 g (19.2 %)
	MMA	0.59 g (29.7 %)
+ Subst. D	Styrene	0.44 g (22.4 %)
	MMA	0.46 g (22.9 %)
$Ti_xO_y(OH)_z$ + Subst. A	Styrene	0.12 g (6.0 %)
	MMA	0.37 g (18.4 %)
+ Subst. B	Styrene	0.44 g (22.0 %)
	MMA	1.27 g (63.7 %)
+ Subst. C	Styrene	1.33 g (66.5 %)
	MMA	1.12 g (56.2 %)
+ Subst. D	Styrene	1.10 g (55.2 %)
	MMA	0.63 g (31.7 %)
$Zr_xO_y(OH)_z$ + Subst. A	Styrene	1.31 (65.37 %)
	MMA	1.26 g (63.0 %)
+ Subst. B	Styrene	0.10 g (5.0 %)
	MMA	0.25 g (12.6 %)
+ Subst. C	Styrene	0.82 g (41.1 %)
	MMA	0.37 g (18.4 %)
+ Subst. D	Styrene	0.59 g (29.6 %)
	MMA	1.00 g (50.0 %)
$Zn_xO_y(OH)_z$ + Subst. A	Styrene	0.30 g (15.2 %)

	MMA	1.45 g (72.3 %)
+ Subst. B	Styrene	0.47 (23.6 %)
	MMA	0.12 g (6.1 %)
+ Subst. C	Styrene	0.30 g (15.1 %)
	MMA	0.55 g (27.7 %)
+ Subst. D	Styrene	0.15 g (7.6 %)
	MMA	0.20 g (10.0 %)

8. Summary

Hybrid inorganic-organic core-shell nanoparticles, consisting of an organic polymer shell and an inorganic core, such as a metal or a metal oxide, are nanocomposites, which can act as building blocks for many applications.

A simple classification based on the nature of links between the organic and the inorganic component was proposed by *Judeinstein et al.*, who defined two main classes.[312] Class I corresponds to systems in which the components only interact weakly and class II materials represent systems in which the inorganic and organic parts are linked together through strong chemical bonds. The properties of such materials depend not only on the chemical nature of their components, but also on their synergistic properties.

In the present work class II materials, prepared in a multi-step approach, are presented. Different approaches were used for the synthesis of the inorganic core. Inorganic nanoparticles were synthesized in free solution stabilized by ions and in water-in-oil microemulsions where the inorganic nanoparticles were synthesized inside the stabilized water droplets. These water droplets worked as so called nanoreactors where the particles were formed either via reduction or coprecipitation reactions.

As precursors for the nanoparticles synthesis modified metal alkoxides or metal salts were used. The metal alkoxide were coordinated with pentane-2,4-dione derivatives, which could initiate controlled or free radical polymerization. In addition, they allowed for a higher control in the particle formation due to a reduction of the hydrolysis and condensation velocities. As these precursors already carried a functional group which was still present in the final material, no additional functionalization after the particle formation was necessary.

In another approach, non-functionalized nanoparticles were synthesized using metal salts as precursors. These nanoparticles had to be surface functionalized in an additional step. Silane or thiol coupling agents, which allowed for the attachment of a polymerization initiator directly onto the particles surface, were used in this methode.

The organic shell was synthesized in a so called "grafting from" approach growing the polymer chains directly from the surface, covalently bond via the initiating group. Different types of initiating mechanisms were used for the polymerization process, depending on the type of initiator molecules. Thermally or photochemically initiated free radical polymerization and controlled radical polymerization via the atom transfer radical polymerization mechanism (ATRP) were applied.

In figure 158 the different steps of the synthesis of core-shell nanoparticles are shown.

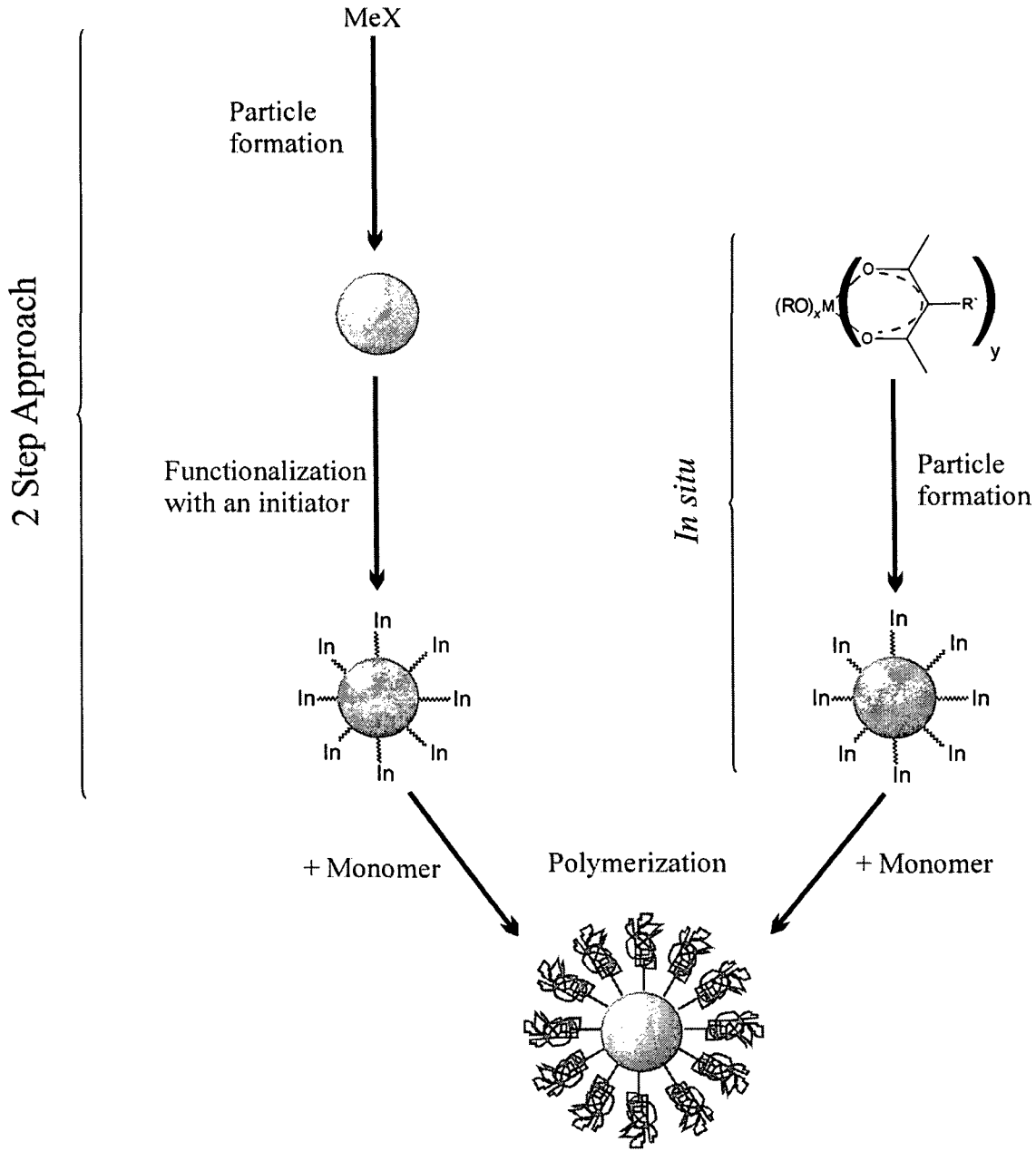

Figure 158: Formation of inorganic-organic core-shell nanoparticles from metal salts (left) and from modified metal alkoxides (right).

SiO_2 nanoparticles were prepared and functionalized, and served as a model system for the synthesis of other metal oxide nanoparticles. Silica was produced according to the so called Stöber process, without the use of stabilizing additives.[56] Starting from tetraethoxysilane (TEOS), nanoparticles were synthesized in various diameters between 20 and 150 nm in ammonia containing ethanol. The kinetic of the particle formation, which was investigated via

DLS, revealed that the particle formation was quite fast, while the size distribution of the particles kept narrow.

In addition, gold nanoparticles were synthesized due to their interesting optical properties using stabilizing additives. Citrate stabilized gold nanoparticles were synthesized in various sizes by the reduction of gold salts.[65, 214] Two different approaches for their surface coverage were used. On the one hand, they were covered with a silica shell by replacing the citrate ions with aminopropyltrimethxysilane (APS) and sodium silicate.[214] The thickness of the silica layer was easy to control by adding a certain amount of TEOS, which formed a stable silica shell. On the other hand, thiol-modified polymerization initiator molecules were attached onto the gold nanoparticle surface.

Metal oxide particles are a major focus of investigation because interesting properties, e.g. electric, magnetic, optic, quantum size effects, etc., can be induced into a hybrid material, if oxidic systems are incorporated. Furthermore, oxidic particles show higher stability against environmental influences compared to metallic particles.

Different metal salts served as precursors for the synthesis of metal oxide nanoparticles. Iron oxide, titanium oxide, zirconium oxide, zinc oxide and aluminum oxide nanoparticles were synthesized from $FeCl_2*4H_2O$, $TiCl_4$, $ZrO(NO_3)_2$, $ZnBr_2$ and $AlCl_3*3H_2O$ as precursors. In this approach, two microemulsions, one containing the dissolved metal salt the other containing ammonia, were unified and particle formation took place inside the new formed micelles. As surfactant Triton X-100 was used, the organic phase consisted of cyclohexane, and n-hexanol served as cosurfactant. In figure 159 TEM images of the synthesized particles are presented.

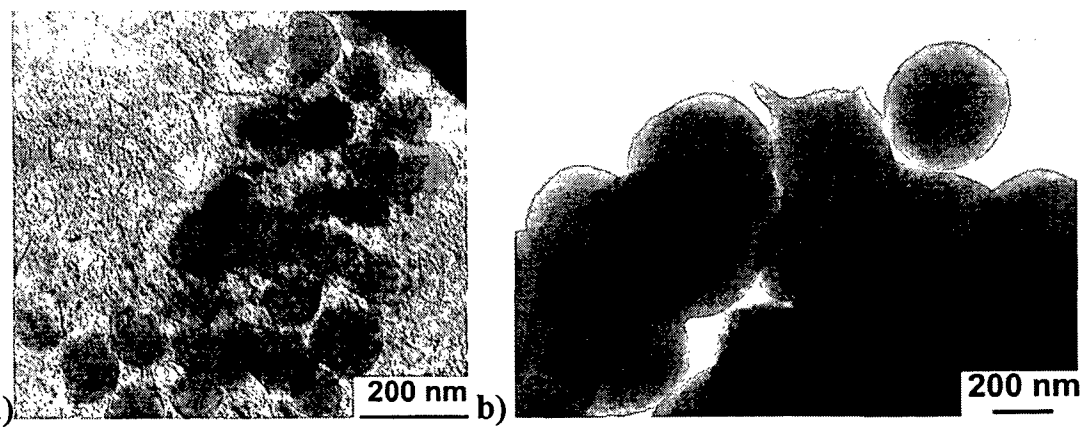

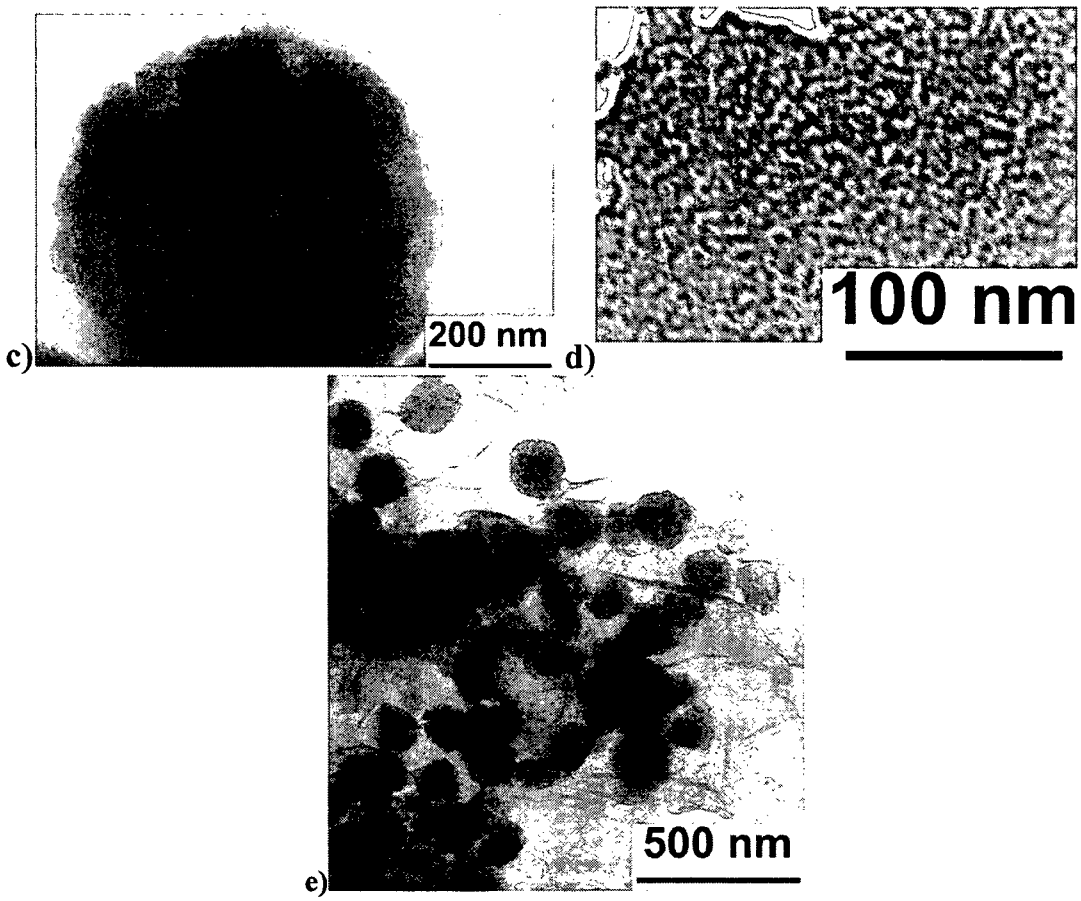

Figure 159: Nanoparticles made of a) $Fe_xO_y(OH)_z$ with a diameter of 112 ± 18 nm; b) $Ti_xO_y(OH)_z$ with a diameter of 210 ± 15 nm; c) $Zr_xO_y(OH)_z$ with a diameter of 660 ± 70 nm; d) $Al_xO_y(OH)_z$ with a diameter of 8 ± 0.4 nm; e) $Zn_xO_y(OH)_z$ with a diameter of 135 ± 6 nm. The presented diameters were obtained from DLS measurements in ethanol at room temperature.

It was observed that the particle formation mechanism depends very strongly on the used metal salt. The obtained TEM images suggested different particle formation mechanisms. In principle, it was possible to differ between two basic formation mechanisms. If the nucleation velocity is much faster than the growing velocity, many nucleation cores are formed in one micelle, which constantly grow and afterwards aggregate to form the final particle. The other possible mechanism is the formation of one or a few nucleation cores in one micelle and a homogenous growth of the formed core. In case of titanium oxide growing of the core was the determining step, while in case of the zinc oxide and zirconium oxide nanoparticles aggregation of many preformed and slightly grown cores was observed.

In table 61 the characteristic properties of the nanoparticles are summarized.

Table 61: Results of the nanoparticles obtained from metal salts.

	Yield [%]	Weight loss TGA [%]	Specific BET-surface [m^2/g]	Diameter (TEM) [nm]	Diameter DLS [nm]
$Ti_xO_y(OH)_z$	25	24.0	459	245	210 ± 15
$Zr_xO_y(OH)_z$	13	25.8	396	642	658 ± 71
$Fe_xO_y(OH)_z$	26	19.0	351	103	112 ± 18
$Zn_xO_y(OH)_z$	17	18.5	41	156	135 ± 6
$Al_xO_y(OH)_z$	84	45.0	200	6	8 ± 0.4

Not only metal salts can be used as precursor for the preparation of metal oxide nanoparticles, but also metal alkoxides.

In a first approach, it was tried to synthesize the particles using a sol-gel approach according to the Stöber process without stabilizing additives. Due to the higher reactivity of the metal alkoxides compared to TEOS these experiments were not successful and led to immediate precipitation of metal oxides. Two different approaches were applied to overcome uncontrolled particle formation: either (i) reducing the reactivity of the metal alkoxide via coordination of a bidentate ligand and/or (ii) a microemulsion technique was applied, which allowed for a more controlled formation process, due to the diffusion barrier built by the surfactant layer and the synthesis in a confined space serving as nanoreactor.

The molecules, which were used as bidentate ligand, were chemically adapted pentane-2,4-dione derivatives prepared by the modification of the highly acid hydrogen atom bond to the 3C-carbon atom. Removing this hydrogen atom enables the attachment of polymerization initiator molecules. These diones coordinate to the metals as diketonates. The synthesized pentane-2,4-dione derivatives are presented in figure 160.

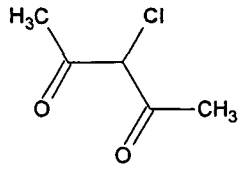

3-Chloro-pentane
2,4-dione

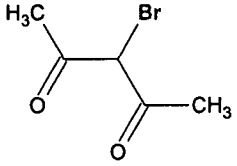

3-Bromo-pentane
2,4-dione

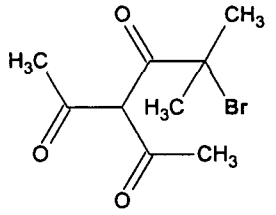

3-Acetyl-5-bromo-5-methyl-
hexane-2,4-dione

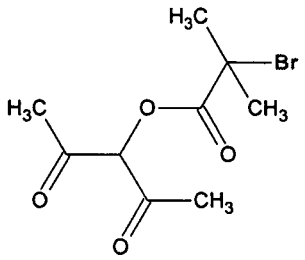

1-Acetyl-2-oxopropyl 2-bromo-
methylproponate

Figure 160: Synthesized pentane-2,4-dione derivates.

The initiation activity of the different diones is based on the cleavage of the C-X bonds in the molecules. Depending on the stability of this bond, different polymerization mechanisms, such as UV-light and thermal induced free radical polymerization and controlled radical polymerization (ATRP) were applied.

Furthermore, several functionalized 1,3-diphenly-propane-1,3-dione derivates were synthesized enabling additional modification of the phenyl-rings. The obtained crystals revealed that the molecules only occurred in the corresponding diketo-form, contrary to the pentane-2,4-diones, which occurred in both tautomeric forms.

The presented pentane-2,4-dione derivates were coordinated to various metal alkoxide molecules such as $Ti(O^iPr)_4$, $Zr(O^nBu)_4$, $Y(OEtOMe)_3$, $Ta(OEt)_5$, $VO(OEt)_3$ and $Fe(O^iPr)_3/Fe(OEt)_3$ in a molar ratio of 1 : 1. The obtained coordination products were characterized via elemental analysis, ^1H and ^{13}C NMR and FTIR analysis. These methods proved that coordination was reached. However this coordination was in some cases only partially and hence, not only one coordination product but a mixture of mono and multiple coordinated alkoxide molecules was obtained. FTIR analysis confirmed coordination in all cases, as new signals of coordinated CO-groups emerged. Depending on the used metal

alkoxide and the coordinated pentane-2,4-dione derivate, the observed ν(C-O) signals of the coordinated CO-group were found between 1500 and 1650cm^{-1}. NMR analysis showed quite complicated spectra due to the obtained mixture of various coordination products.
It was not possible to obtain coordination of the various 1,3-diphenyl-propane-1,3-dione derivatives to metal alkoxides because the halogen-carbon bond was cleaved and the formation of a metal-halogen cluster occurred.

As the particle formation using the modified metal alkoxide precursors in ammonia containing ethanol without additives did not lead to controlled particle formation, further experiments were performed in microemulsions. In figure 161 various different nanoparticles are presented.

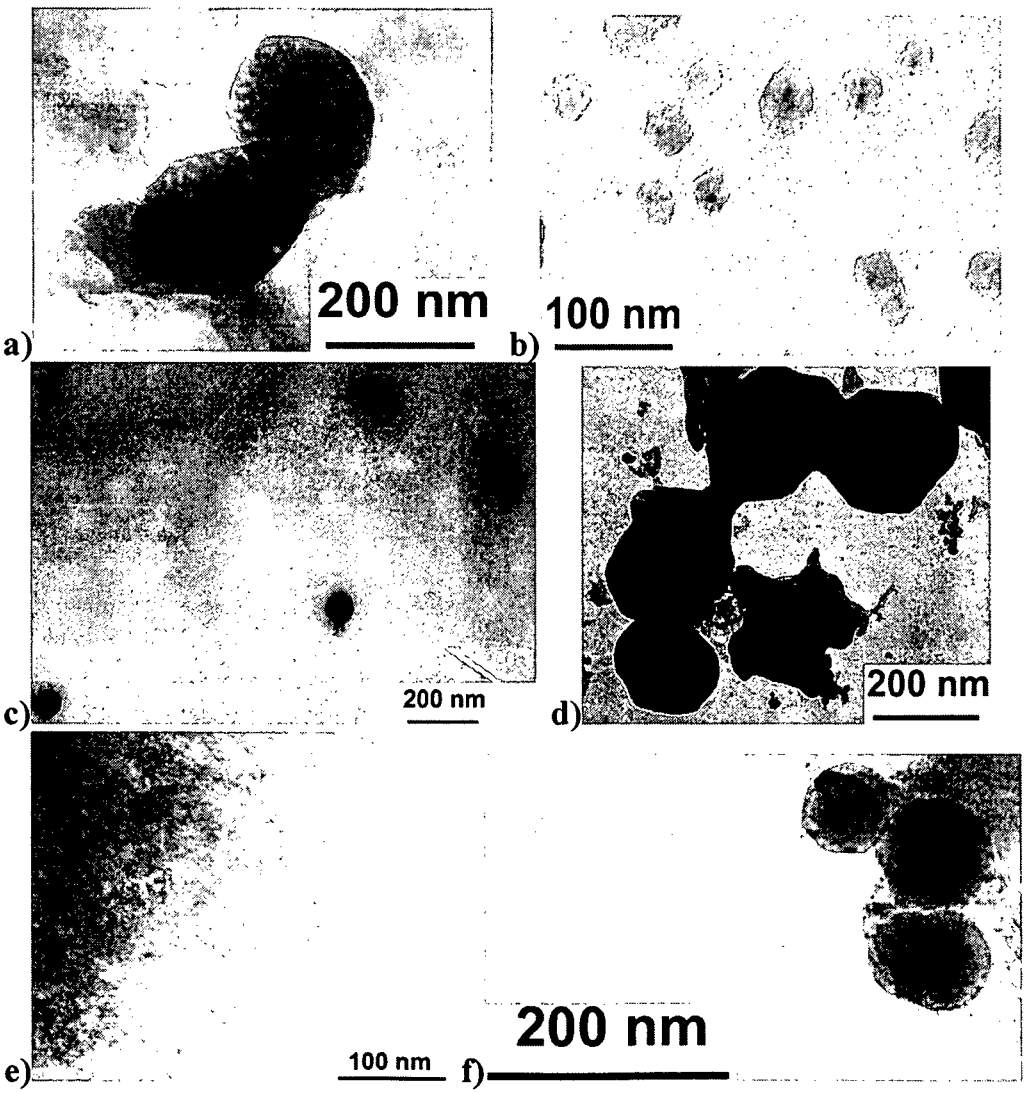

Figure 161: Nanoparticles of a) $Ti_xO_y(OH)_z$ functionalized with 3-acetyl-5-bromo-5-methylhexane-2,4-dione (diameter: 210 ± 4m); b) $Zr_xO_y(OH)_z$ functionalized with 3-chloro-pentane-2,4-dione (diameter: 49 ± 7 nm); c) $V_xO_y(OH)_z$ functionalized with 3-chloro-pentane-2,4-dione (diameter: 76 ± 5 nm); d) $Y_xO_y(OH)_z$ functionalized with 3-chloro-pentane-2,4-dione (diameter: 222 ± 25 nm); e) $Ta_xO_y(OH)_z$ functionalized with 1-acetyl-2-oxopropyl 2-bromo-methylpropanate (diameter: 4 ± 0.2 nm); f) $Fe_xO_y(OH)_z$ functionalized with 3-acetyl-5-bromo-5-methylhexane-2,4-dione (diameter: 120 ± 17 nm). The presented diameters were obtained from DLS analyses recorded in ethanol at room temperature.

Similar as in case of metal salt precursors, it was observed that the particle formation mechanism depended very strongly on the used metal alkoxide and the coordinated ligand. For example, in case of 3-acetyl-5-bromo-5-methylhexane-2,4-dione functionalized titanium oxide particles, the formed nucleation cores were still visible in the final particles (figure 161a). The formation of the 3-acetyl-5-bromo-5-methylhexane-2,4-dione functionalized iron oxide particles followed the second formation mechanism where growth is the determining process (figure 161e).

In case of titanium isopropoxide the influence of the different ligands on the kinetic of the particle formation process was investigated in more detail. It was demonstrated that differences of the electronical structure and sterical hindrance of the coordinated ligands had a great influence on the particle growth. Compared to silica nanoparticles formed according to the Stöber process in free solution, the different titanium oxide nanoparticles showed an initiation phase, mostly likely due to the diffusion process through the surfactant layer. The time of this initiation phase varied from approximately 100 minutes in case of 3-acetyl-5-bromo-5-methylhexane-2,4-dione to more than 600 minutes in case of 3-chloro-pentane-2,4-dione modification.

Furthermore, the influence of different parameters like precursor concentration, water content and pH value on the formation was investigated for 3-chloro-pentane-2,4-dione and 1-acetyl-2-oxopropyl 2-bromo-methylpropanate functionalized particles. It was shown that up to a precursor concentration of 2.5 %, the diameter of the produced particles increased nearly linearly. Due to partially incomplete hydrolysis and condensation reactions of the precursor, the diameter of the particles decreased at higher concentration, although a great excess of water was used in the microemulsion.

Variation of the water contents revealed a maximum particle diameter at a water content of 6 % in case of the 3-chloro-pentane-2,4-dione functionalized system and at 13 % in case of

the 1-acetyl-2-oxopropyl 2-bromo-2-methylpropanoate functionality. At lower contents particle formation was not favored as most of the water molecules were bond to surfactant molecules, while higher contents than the optimal also led to a decrease of the diameter.
Both H^+ and OH^- ions seemed to catalyze the hydrolysis and condensation process of the functionalized titanium isopropoxide precursors. Both investigated precursors showed a maximum of the obtained diameter at low pH value (around pH 3) and at high pH value (around pH 12). The particle diameter reached a minimum around pH 7.

All particles formed with this process were non-crystalline; however, interesting properties arise from crystallinity, such as different refractive indices. As all presented nanoparticles were X-ray amorphous at room temperature, the onset temperature of the crystallization process was studied via X-ray powder diffraction which corresponded to literature-known values.
According to a method presented by *Andersson et al.*[105], crystalline titanium oxide nanoparticles were formed at increased temperatures. Depending on the used functionality either anatase or a mixture of rutile and anatase was obtained. FTIR experiments showed that the functional groups were decomposed during the particle formation and could not initiate a polymerization process.

Contrary to metal oxide particles synthesized from modified metal alkoxides, particles obtained from metal salts were functionalized in a second step. Polymerization initiators were attached onto the particle's surface via molecules containing alkoxy silane groups (in case of oxidic nanoparticles) or thiol groups (in case of gold nanoparticles) to allow "grafting from" polymerization directly from the surface (figure 162).

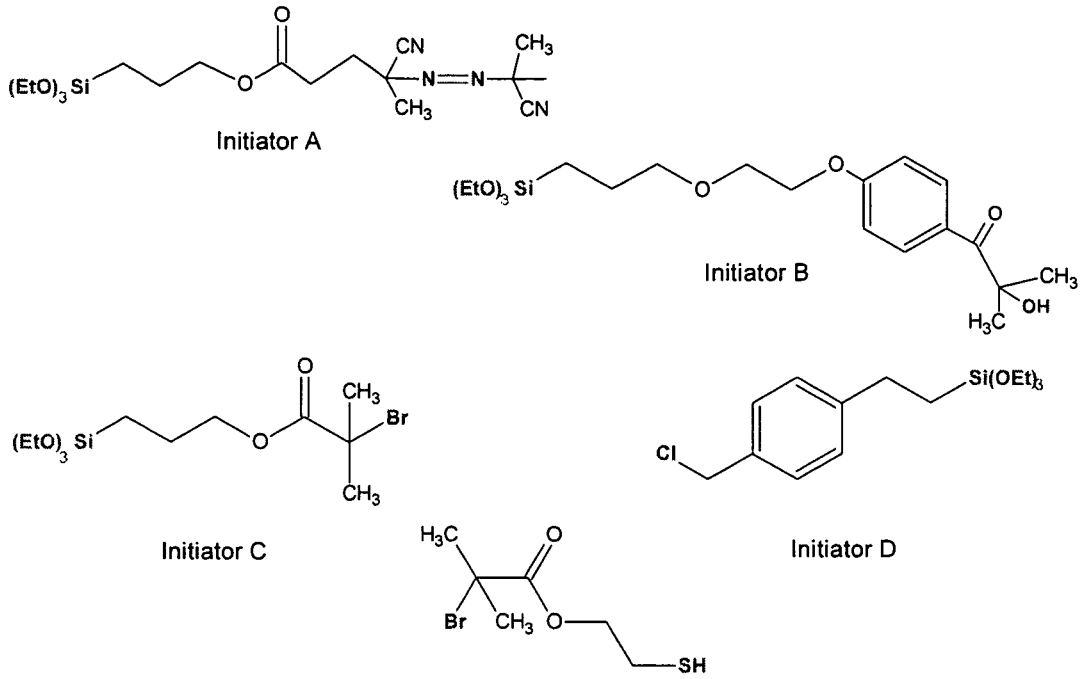

Figure 162: Synthesized polymerization molecules for oxidic and gold nanoparticles.

The presented initiators allowed the initiation of the polymerization process using different mechanisms. Initiator (A) and (B) were able to start free radical polymerization, thermally or photo-initiated, respectively. Initiator (C) and (D) were capable to start controlled radical polymerizations (ATRP). The gold nanoparticles were functionalized with 2-sulfanylethyl-2-bromo-2-methylpropanoate to initiate ATRP. The oxidic nanoparticles carried OH groups at the surface, which were reacted with ethoxide groups under the elimination of ethanol. With this approach surface initiator-coverages between 0.05 and 1.13 mmol/g were obtained, depending on the used initiator and the applied metal oxide. The BET-surface area of the particles decreased significantly after the functionalization process. ^{13}C CPMAS NMR proved that initiator molecules were attached to the surface of the nanoparticles and no degradation of the functionalities occurred. The obtained results demonstrated that several parameters had an influence on the obtained degree of functionalization. (i) The conditions during the functionalization process. Particles, which were functionalized at room temperature with initiator (A) and (B), had the lowest surface coverage, while those functionalized at increased temperatures reached a higher degree of functionalization. (ii) The zeta-potential of the surface OH groups depended very strongly on the materials the particles were made of. Zinc oxide and zirconium oxide showed the highest degree of functionalization while aluminum

oxide particles did not allow any functionalization under the chosen conditions. (iii) The different size of the initiator molecules also might have influence on the surface coverage, which became observable, if the surface coverage of initiator (A) and (B) were compared. It seemed as if surface functionalization was more difficult to perform in case of initiator (A) due to sterical hindrance.

In case of the titanium oxide and zirconium oxide nanoparticles the photoluminescence capacities were analyzed. Significant differences between crystalline and amorphous TiO_2 particles were observed as crystalline systems showed an additional fluorescence band at 77 K. Furthermore, small particle diameters led to a shift of the emission band to higher energy due to the appearance of quantum size effects. In case of zirconium oxide such effects were not observed.

The assembly of nanoparticles towards macroscopic materials is of both fundamental and technological interest. Surface functionalization plays a major role as the particle interactions are determined by the functional groups situated at the particle surface. As a model system, silica particles, which were synthesized according to the Stöber process, were used, containing attracting functional groups, such as the commercially available 3-amino-propyltriethoxysilane and 2-(carbomethoxy)ethyltrichlorosilane. The aggregation process was dominated either by electrostatic interactions or hydrogen-bonds, depending on the pH value. In a primarily investigation the influence of the used dispersing medium was analyzed. It was demonstrated that ethanol has the ability to disperse both, unfunctionalized SiO_2 particles, where the surface OH groups required rather hydrophilic conditions and functionalized particles as well, where the organic entities preferred, depending on the type of functionalization, more hydrophobic solvents. Furthermore, the aggregation behavior of surface functionalized SiO_2 particles was investigated at different pH values. It seemed as if ionic interactions dominated the aggregation process low pH values, while hydrogen bonds were preferred at high pH values. The obtained aggregates were not ordered and only weak interactions were observed. The size of the aggregates depended strongly on the used pH value and on the ratio between to two types of functionalized silica, whereby the largest aggregates were observed, if a volumetric ratio of 2 : 1 was used.

As mentioned before, polymerization was initiated via free radical or controlled radical polymerization (ATRP), which reduced the polydispersity of the molecular weight

distribution and if successful, a prediction of molecular weight was possible. ATRP as a quasi living polymerization allowed the formation of block copolymers. MMA, styrene, isoprene and methacrylic acid trimethyloxysilyl propylester were used as monomer.

In case of Au and Au@SiO_2 particles only ATRP was performed. The kinetic of the polymerization process showed a nearly linear dependence between monomer conversion and the increase of the particle diameter.

Metal oxide particles were synthesized from modified metal alkoxides and metal salts. In case of the precursors containing a modified alkoxide, new pentane-2,4-dione derivates, which can initiate polymerization, were created. All presented molecules were able to initiate an ATRP. Additionally, 3-chloro-pentane-2,4-dione and 3-bromo-pentane-2,4-diones were capable of initiating thermally initiated radical polymerization. 3-Bromo-pentane-2,4-dione could also start a photo-induced radical polymerization process.

In case of both halo-pentane-2,4-diones, the polymerization capacities were investigated and compared with well known systems. The polymerization efficiency of the two pentane-2,4-diones in ATRP differed, most likely due to their different thermal stability. While 3-chloro-pentane-dione reached efficiencies between 0.51 and 0.05, depending on the used catalyst and monomer, the efficiency of 3-bromo-pentane-2,4-dione was between 0.08 and 0.02. Halo-propionic acid-ethyl-esters, which are well-known ATRP initiators, reached under the same reaction conditions polymerization efficiencies between 0.85 and 0.28.

If the functionalized nanoparticles were used as macroinitiators, between 2 % and 15 % of the obtained hybrid material consisted of inorganic nanoparticles. In general, it can be stated that ATRP obtained higher yields compared to free radical polymerization. Furthermore, the molecular weight of the synthesized polymer chains was closer to theoretical value in case of ATRP. ATRP also delivered lower molecular weight distributions (< 1.5) compared to free radical polymerization resulting in MWD up to 3.5.

In theory, no free polymerization in solution should have occurred as the initiators were covalently bond to the particles. In case of particles, which were formed from modified metal alkoxides, a minor solubility of the particles under polymerization conditions was observed, which led to the occurrence of polymer chains that were not attached to the surface of the nanoparticles. This effect was reduced by using particles, which contained 3-chloro-pentane-2,4-dione. In figure 163 TEM images of the synthesized core-shell nanoparticles are shown.

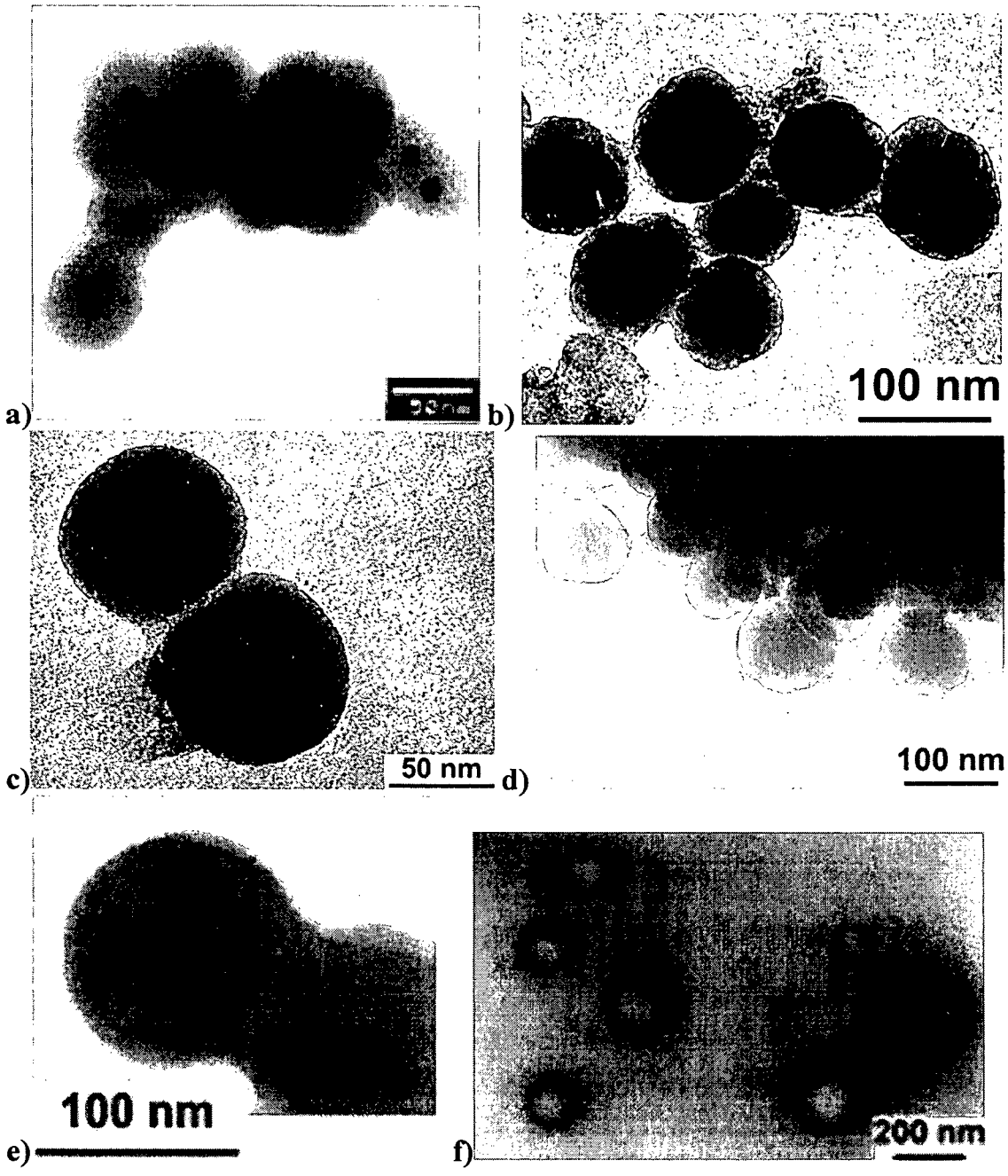

Figure 163: a) $Au@SiO_2@PS$ with diameter of 88 ± 8 nm; b) $Ti_xO_y(OH)_z$(Cl-acac)@PMMA with a diameter of 95 ± 9 nm; c) $Zr_xO_y(OH)_z$(Cl-acac)@PMMA with a diameter of 64 ± 4 nm; d) $V_xO_y(OH)_z$(Cl-acac)@PMMA with a diameter of 106 ± 10 nm; e) $Fe_xO_y(OH)_z$(Ini. C)@PS with a diameter of 260 ± 24 nm; f) $Zn_xO_y(OH)_z$(Ini. C) with a diameter of 260 ± 30 nm. The presented diameters were obtained from DLS analyses in THF or toluene at room temperature.

In case of the ATRP initiators the kinetic of the polymerization process was investigated via ^{1}H NMR, GPC and DLS. The obtained semilogarithmic kinetic and molecular weight plots showed a linear dependence on time. Such behavior indicates first-order kinetic with respect to the monomer and, therefore a constant concentration of active species during polymerization.

Thermal analysis of the produced core-shell particles showed an increased onset temperature of the degradation process of the polymer chains that were attached to the inorganic core in case of particles that were produced from metal salts. Contrary, this effect was not observed in case of particles, which were synthesized from modified alkoxides, possibly due to occurring polymerization in solution and lower incorporation rate of inorganic particles.
The shift of the onset temperature of the decomposition process of the polymer to higher temperatures was also accomplished by TG-FTIR analyses which allowed for estimation of the onset temperature of the polymer degradation and identification of the cleaved entities.

9. Literature

1: F. Caruso, *Adv. Mater.* **2001**, *13*, 11.

2: D. Kang, N. A. Clark, *J. Korean Chem. Soc.*, **2002**, *41*, 817.

3: E. Matijevic, *Progr. Colloid Polym. Sci.* **1976**, *61*, 24.

4: Y. Xia, B. Gates, S. H. Park, *J. Lightwave Technol.* **1999**, *17*, 1956.

5: S. Huang, G. Tsutsui, H. Sakaue, S. Shingubara, T. Takahagi, *J. Vac. Sci. Technol.* **2000**, *18*, 2653.

6: C. L. Huang, E. Matijevic, *J. Mater. Res.* **1995**, *10*, 1327.

7: F. Corcos, E. Bourgeat-Lami, C. Novat, J. Lang, *Colloid Polym. Sci.* **1999**, *277*, 1142.

8: T. Von Werne, T. E. Patten, *Polym. Prep.*, **2001**, *42(Am. Chem. Soc., Polym. Div.)*, 479.

9: H. Mori, D. C. Seng, M. Zhang, A. H. E. Müller, *Langmuir*, **2002**, *18*, 3682.

10: T. S. Lee, C. Yang, W.-H. Park, *Macromol. Rapid Commun.* **2000**, *21*, 951.

11: E. Matijevic, in *Fine Particle Science and Technology*, Kluwer, Dordrecht, **1996**, pp. 1-16.

12: L. M. Liz-Marzan, M. Giersig, P. Mulvaney, *Langmuir*, **1996**, *12*, 4329.

13: C. H. M. Hoffman-Caris, *New J. Chem.* **1994**, *18*, 1087.

14: R. Partch, in *Materials Synthesis and Characterisation*, Plenum, New York, **1997**, pp. 1-17.

15: K. Matyjaszewski, P. J. Miller, J. Pyun, G. Kickelbick, S. Damanti, *Macromolecules*, **1999**, *32*, 6526.

16: O. Prucker, J. Rühe, *Langmuir*, **1998**, *14*, 6893.

17: G. Kickelbick, U. Schubert, *Monatsh. Chem.*, **2001**, *132*, 13.

18: A. van Blaadern, A. Vrij, *J. Colloid Interface Sci.*, **1993**, *156*, 1.

19: G. Kickelbick, L. M. Liz-Marzan, *Encyclopedia of Nanoscience and Nanotechnology*, **2003**, *10*, 1.

20: J. Sinzig, U. Radtke, M. Quinten, U. Kreibig, *Z. Phys. D*, **1993**, *26*, 242.

21: L. Rivas, S. Sánchez-Cortez, J. V. Garziá-Ramos, G. Morzillo, *Langmuir*, **2000**, *16*, 9722.

22: M. Schierhorn, L. M. Liz-Marzán, *Nanoletters*, **2002**, *2*, 13.

23: S. L. Westcott, S. J. Oldenburg, L. Randall, N. J. Halas, *Langmuir*, **1988**, *14*, 5396.

24: S. J. Oldenburg, R. D. Averitt, S. L. Westcott, N. J. Halas, *Chem. Phys. Lett.*, **1988**, *288*, 243.

25: G. Kickelbick, *Prog. Polym. Sci.*, **2003**, *28*, 83.

26: D. Holzinger, G. Kickelbick, *Chem. Mater.*, **2004**, *14*, 217.

27: G. Kickelbick, D. Holzinger, C. Brick, G. Trimmel, E. Moons, *Chem. Mater.*, **2002**,

14, 4382.

28: S. C. Farmer, T. E. Patten, *Chem. Mater.*, **2001**, *13*, 3920.

29: M. Husseman, E. E. Malström, M. McNamara, M. Mate, D. Mecerreyes, D. G. Benoit, J. L. Hedrick, P. Mansky, E. Huang, T. P. Russel, C. J. Hawker, *Macromolecules*, **1999**, *32*, 1424.

30: J.-E. Jönsson, H. Hassander, B. Törnell, *Macromolecules*, **1994**, *27*, 1932.

31: D. B. Cairns, S. P. Armes, L. G. B. Bremer, *Langmuir*, **1999**, *15*, 8052.

32: C. Lu, R. Pelton, *Colloids Surf. A*, **2002**, *201*, 161.

33: M. Okaniwa, *Polymer*, **1999**, *41*, 453.

34: S. Kirsch, A. Doerk, E. Bartsch, H. Sillescu, K. Landfester, H. W. Spiess, W. Maechtle, *Macromolecules*, **1999**, *32*, 4508.

35: A. Imhof, *Langmuir*, **2001**, *17*, 3579.

36: R. Langer, *Science*, **1990**, *249*, 1527.

37: N. Kawahashi, E. Matijevic, *J. Mater. Chem.*, **1991**, *1*, 577.

38: H. Shiho, N. Kawahashi, *Colloid Polym. Sci.*, **2000**, *278*, 270.

39: H. Shiho, N. Kawahashi, *J. Colloid Interface Sci.*, **2000**, *226*, 91.

40: C. H. Niemeyer, *Angew. Chem., Int. Ed.*, **2001**, *40*, 4128.

41: S. Mann, W. Shenton, M. Li, S. Connolly, D. Fitzmaurice, *Adv. Mater.*, **2000**, *12*, 147.

42: H. Mattoussi, J. M. Mauro, E. R. Goldman, G. P. Anderson, V. C. Sundar, F. V. Mikulec, M. G. Bawendi, *J. Am. Chem. Soc.*, **2000**, *122*, 12142.

43: A. P. Alivisatos, K. P. Johnsson, X. Peng, T. E. Wilson, C. J. Loweth, M. P. Bruchez Jr., P. G. Schulz, *Nature*, **1996**, *382*, 609.

44: E. Bourgeat-Lami, P. Espiard, A. Guyot, *Polymer*, **1995**, *36*, 4385.

45: P. Espiard, A. Guyot, *Polymer*, **1995**, *36*, 4391.

46: E. Bourgeat-Lami, P. Espiard, Guyot, C. Gauthier, L. David, G. Vigier, *Angew. Makromol. Chem.*, **1996**, *242*, 105.

47: E. Bourgeat-Lami, J. Lang, *J. Colloid Interface Sci.*, **1998**, *197*, 293.

48: E. Bourgeat-Lami, J. Lang, *J. Colloid Interface Sci.*, **1999**, *210*, 281.

49: Z. Li, Y. Zhu, *Appl. Surf. Sci.*, **2003**, *211*, 215.

50: G. L. Li, G. H. Wang, *Nanostruct. Mater.*, **1999**, *11*, 663.

51: M. P. Pileni, *Reactivity in Reverse Micelles*, New York, Elsevier, **1989**.

52: E. Matijevic, *Chem. Mater.*, **1995**, *5*, 412.

53: V. K. LaMer, *Ind. Eng. Chem.*, **1952**, 44, 1270.

54: V. K. LaMer, R. Dinegar, *J. Am. Chem. Soc.*, **1950**, *72*, 4847.

55: T. Sugimoto, *J. Colloid Interface Sci.*, **1992**, *150*, 208.

56: W. Stöber, A. Fink, E. Bohn, *J. Colloid Interface Sci.*, **1968**, *26*, 62.

57: R. Brace, E. Matijevic, *J. Inorg. Nucl. Chem.*, **1973**, *35*, 3691.

58: R. Demchak, E. Matijevic, *J. Inorg. Nucl. Chem.*, **1969**, *31*, 257.

59: E. Matijevic, P. Schreiner, *J. Colloid Interface Sci.*, **1978**, *63*, 509.

60: B. Aiken, W. P. Hsu, E. Matijevic, *J. Amer. Ceram. Soc.*, **1988**, *71*, 845.

61: S. Kratohvil, E. Matijevic, *J. Mater. Res.*, **1991**, *6*, 766.

62: E. Matijevic, D. Murphy-Wilhelmy, *J. Colloid Interface Sci.*, **1982**, *86*, 476.

63: S. K. Park, K. D. Kim, H. T. Kim, *Colloids Surf. A*, **2002**, *197*, 7.

64: X. Jiang, T. Herricks, Y. Xia, *Adv. Mater.*, **2003**, *15*, 1205.

65: B. V. Enüstün, J. Turkevitch, *J. Am. Chem. Soc.* **1963**, *85*, 3317.

66: G. Frens, *Nature, Phys. Sci.* **1973**, *273*, 20 .

67: J. Legrand, C. Petit, D. Bazin, M. P. Pileni, *Appl. Surf. Sci.*, **2000**, *164*, 186.

68: C. Petit, A. Taleb, M. P. Pileni, *J. Phys. Chem. B*, **1999**, *103*, 1805.

69: W. Zhang, *J. Nanoparticle Res.*, **2003**, *5*, 323.

70: S. Veintemillas-Verdaguer, O. Bomati, M. P. Morales, P. E. Di Nunzio, S. Martelli, *Mater. Lett.*, **2003**, *57*, 1184-1189.

71: H. Yin, T. Yamamoto, Y. Wada, S. Yanagida, *Mater. Chem. Phys.*, **2004**, *83*, 66.

72: M. J. Rosemary, T. Pradeep, *J. Colloid Interface Sci.*, **2003**, *268*, 81.

73: Y. Hou, S. Gao, *J. Mater. Chem.*, **2003**, *13*, 1510.

74: S.-H. Wu, D.-H. Chen, *J. Colloid Interface Sci.*, **2003**, *259*, 282.

75: N. Toshiba, T. Yonezawa, *New. J. Chem.*, **1998**, *22*, 1179.

76: T. Yonezawa, N. Toshima, *J. Chem. Soc., Faraday Trans.*, **1995**, *91*, 4111.

77: M. Danek, K. F. Jensen, C. B. Murray, M. G. Bawendi, *Chem. Mater.*, **1996**, *8*, 173.

78: E. Bourgeat-Lami, *J. Nanosci. Nanotechnol.*, **2002**, *2*, 1.

79: V. Pillai, D. O. Shah, *Surfactant Sci. Ser.*, **1997**, *66 (Ind. App. Microemulsions)*, 227.

80: E. Joselevich, I. Willner, *J. Phys. Chem.*, **1994**, *98*, 7628.

81: F. J. Arriagada, K. Osseo-Asare, *J. Colloid Interface Sci.*, **1999**, *211*, 210.

82: M. A. Lopez-Quintela, *Curr. Opin. Colloid Interface Sci.*, **2003**, *8*, 137.

83: K. Landfester, *Adv. Mater.*, **2001**, *13*, 765.

84: T. Hellweg, *Curr. Opin. Colloid Interface Sci.*, **2001**, *7*, 50.

85: A. K. Panda, S. P. Moulik, B. B. Bhowmik, *J. Colloid Interface Sci.*, **2001**, *235*, 218.

86: J. Ning, J. Zhang, Y. Pan, J. Guo, *Ceram. Int.*, **2004**, *30*, 63.

87: K. Hayase, S. Hayano, *Bull. Chem. Soc. Jpn.*, **1977**, *50*, 83.

88: Y. Miyagishi, S. Hayano, *J. Colloid Interface Sci.*, **1982**, *86*, 344.

89: S. P. Moulik, G. C. De, B. B. Bhowmik, A. R. Das, *Langmuir*, **1999**, *15*, 8391.

90: Y. He, B. Yang, G. Cheng, *Mater. Lett.*, **2003**, *57*, 1880.

91: T. Hanaoka, T. Hatsuta, T. Tago, M. Kishida, *Appl. Catal. A Gen.*, **2000**, *190*, 291.

92: P. Lianos, R. Zana, *J. Colloid Interface Sci.*, **1984**, *101*, 587.

93: K. J. Schweighofer, U. Essmann, M. Berkovic, *J. Phys. Chem. B*, **1997**, *101*, 10775.

94: J. C. Brinker, G. W. Scherer, *Sol-Gel Science*, Academic Press, New York, **1990**.

95: N. Hüsing, U. Schubert, *Angew. Chem*,. **1998**, *110*, 22.

96: K. L. Walther, A. Waukaun, B. E. Handy, A. Baiker, *J. Non-Cryst. Solids*, **1991**, *143*, 47.

97: D. C. M. Dutoit, M. Schneider, A. Baiker, *J. Catal.*, **1995**, *153*, 167.

98: D. C. M. Dutoit, M. Schneider, P. Fabrigioli, A. Baiker, *Chem. Mater.*, **1996**, *8*, 734.

99: S. S. Kistler, *Nature*, **1931**, *127*, 741.

100: S. S. Kistler, *J. Phys. Chem.*, **1932**, *36*, 52.

101: P. Espiard, J. E. Mark, A. Guyot, *Polym. Bull.*, **1990**, *24*, 173.

102: P. Espiard, A. Guyot, J. E. Mark, *Inorg. J. Organomet. Polym.*, **1995**, *5*, 391.

103: G. Kickelbick, U. Schubert, *Chem. Ber.*, **1997**, *130*, 473.

104: Y. Berkovich, A. Aserin, E. Wachtel, N. Garti, *J. Colloid Interface Sci.*, **2002**, *245*, 58.

105: M. Andersson, L. Österlund, S. Ljungström, A. Palmqvist, *J. Phys. Chem. B.*, **2002**, *106*, 10674.

106: F. J. Arriagada, K. Osseo-Asare, *Colloids Surf.*, **1992**, *69*, 105.

107: F. J. Arriagada, K. Osseo-Asare, *J. Colloid Interface Sci.*, **1995**, *170*, 8.

108: J. Esquena, T. F. Tadros, K. Kostarelos, C. Solans, *Langmuir*, **1997**, *13*, 6400.

109: P. D. Moran, J. R. Bartlett, J. L. Woolfrey, G. A. Bowmaker, R. P. Cooney, *Ceram. Trans.*, **1995**, *51 (Ceram. Processing Sci. Technol.)*,27.

110: V. Chhabra, V. Pillai, B. K. Mishra, A. Morrone, D. O. Shah, *Langmuir*, **1995**, *11*, 3307.

111: M. Wu, J. Long, A. Huang, Y. Luo, S. Feng, R. Xu, *Langmuir*, **1999**, *15*, 8822.

112: H. Schmidt, C. Kropf, T. Schiestel, H. Schirra, S. Sepeur, C. Lesniak, *Ceram. Trans.*, **1998**, *95*, 49.

113: P. A. Dresco, V. S. Zaitsev, R. J. Gambino, B. Chu, *Langmuir*, **1999**, *15*, 1945.

114: L. M. Liz-Marzan, M. A. López-Quintela, J. Rivas, J. Mira, *J. Mater. Sci.*, **1994**, *29*, 3797.

115: C. Y. Tai, B. Y. Hsiao, H. Y. Chiu, *Colloids Surf., A*, **2004**, *237*, 105.

116: M. L. Curri, G. Palazzo, G. Colafemmina, M. Della, A. Ceglie, *Prog. Colloid Polym.*

Sci., **1998**, *110 (Trends Colloid Interface Sci. XII)*, 188.

117: H. H. Ingelsten, R. Bagwe, A. Palmqvist, M. Skoglundh, C. Svanvberg, K. Holmberg, D. O. Shah, *J. Colloid Interface Sci.*, **2001**, *241*, 104.

118: J. Lin, W. Zhou, C. J. O'Conner, *Mater. Chem. Lett.*, **2001**, *49*, 282.

119: P. Van Der Voort, E. F. Vansant, *J. Liq. Chromatogr. Relat. Technol.*, **1996**, *19*, 2723.

120: G. N. Zaitseva, V. V. Strelko, in *Fundamental and Applied Aspects of Chemically Modified Surfaces*, Springer Verlag, New York, **1999**.

121: A. P. Philipse, A. Vrij, *J. Colloid Interface Sci.*, **1989**, *128*, 121.

122: M. Z. Rong, L. Q. Ji, M. Q. Zhang, K. Friedrich, *Eur. Polym. J.*, **2002**, *38*, 1573.

123: W. Yoshida, R. P. Castro, J.-D. Jou, Y. Cohen, *Langmuir*, **2001**, *17*, 5882.

124: S. Y. Chang, L. Lui, S. A. Asher, *J. Am. Chem. Soc.*, **1994**, *116*, 739.

125: T. Rajh, L. X. Chen, K. Lukas, T. Lui, M. C. Thurnauer, D. M. Tiede, *J. Phys. Chem. B*, **2002**, *106*, 10543.

126: Z. L. Liu, Z. H. Ding, K. L. Yao, J. Tao, G. H. Du, Q. H. Lu, X. Wang, F. L. Gong, X. Chen, *J. Magnetism Magnetic Mater.*, **2003**, *265*, 98.

127: W. W. Weare, S. M. Reed, M. G. Warner, J. E. Hutchison, *J. Am. Chem. Soc.*, **2000**, *122*, 12890.

128: M. Yamamoto, M. Nakamoto, *Chem. Lett.*, **2003**, *32*, 452.

129: J. R. Heat, L. Brandt, D. V. Leff, *Langmuir*, **1996**, *12*, 4723.

130: J. R. Heat, J. R. Knobler, D. V. Leff, *J. Phys. Chem. B*, **1997**, *101*, 189.

131: P. R. Selvakannan, S. Mandal, S. Phadtare, R. Pasricha, M. Sastry, *Langmuir*, **2003**, *19*, 3545.

132: M. C. Daniel, D. Astruc, *Chem. Rev.*, **2004**, *104*, 293.

133: J. C. Debsikar, *J. Mater. Sci.*, **1985**, *20*, 44.

134: J. C. Debsikar, *J. Non-Cryst. Solids*, **1986**, *86*, 231.

135: M. Emili, L. Incoccia , S. Mobilio, G. Fagherazzi, M. Gugliemi, *J. Non-Cryst. Solids*, **1985**, *74*, 11.

136: C. Sanchez, F. Babonneau, F. Doeuff, A. Léaustic, *Ultrastructure processing of advanced ceramics*, (Ed: J. D. Mackenzie, D. R. Ulrich); Wiley: New York, **1988**, pp. 77.

137: A. Léaustic, F. Babonneau, J. Livage, *Chem. Mater.*, **1989**, *1*, 240.

138: T. Shono, S. Kashimura, M. Sawamura, T. Soejima, *J. Org. Chem.*, **1988**, *53*, 907.

139: A. J. Poss, R. K. Belter, *J. Org. Chem.*, **1988**, *53*, 891.

140: M. Brust, M. Walker, D. Bethell, D. J. Schiffrin, R. J. Whyman, *J. Chem. Soc., Chem.*

Commun., **1994**, *7*, 801.

141: M. Green, P. O'Brian, *Chem. Commun.*, **2001**, *19*, 1912.

142: K. Matyjaszewski, T. E. Patten, J. Xia, T. Albernathy, *Science*, **1996**, *272*, 866.

143: K. Matyjaszewski, T. E. Patten, J. Xia, *J. Am. Chem. Soc.*, **1997**, *119*, 674.

144: K. Matyjaszewski, D. A. Shipp, J. L. Wang, T. Grimaud, T. E. Patten, *Macromolecules*, **1998**, *31*, 6836.

145: T. Von Werne, T. E. Patten, *J. Am. Chem. Soc.* **2001**, *123*, 7497.

146: K. Yoshinaga, R. Horie, F. Saigoh, T. Kito, N. Enomoto, H. Nishida, M. Komatsu, *Polym. Adv. Technol*, **1992**, *3*, 91.

147: K. Yoshinaga, K. Sueishi, H. Karakawa, *Polym. Adv. Technol.*, **1995**, *7*, 53.

148: B. Erdem, D. Sudol, V. L. Dimione, M. El-Aasser, *J. Polym. Sci., A*, **2000**, *38*, 4431.

149: B. Erdem, D. Sudol, V. L. Dimione, M. El-Aasser, *J. Polym. Sci., A*, **2000**, *38*, 4441.

150: N. Bechthold, F. Tiarks, M. Willert, K. Landfester, M. Antonietti, *Macromol. Symp.*, **2000**, *151*, 549.

151: D. Hoffmann, K. Landfester, M. Antonietti, *Magnetohydrodynamics*, **2001**, *37*, 217.

152: F. Tiarks, K. Landfester, M. Antonietti, *Macromol. Chem. Phys.*, **2001**, *202*, 51.

153: F. Tiarks, K. Landfester, M. Antonietti, *Langmuir*, **2001**, *17*, 5775.

154: C. S. Chern, Y. C. Liou, *Polymer*, **1998**, *9*, 3767.

155: B. R. Saunders, B. Vincent, *Adv. Colloid Interface Sci.*, **1999**, *80*, 1.

156: N. Tsubokawa, A. Kogure, Y. Sone, *J. Polym. Sci., A*, **1990**, *28*, 1923.

157: H. Skaff, M. F. Ilker, E. B. Coughlin, T. Emrick, *J. Am. Chem. Soc.*, **2002**, *124*, 5729.

158: G. Odian, *Principles of Polymerization,* Wiley, New York, **1991**, pp. 286.

159: N. Tsubokawa, H. Ishida, *J. Polym. Sci.*, **1992**, *30,* 2241.

160: O. Prucker, J. Rühe, *Macromolecules*, **1998**, *31*, 592.

161: J. Bai, K.-Y. Qiu, Y. Wei, *Polym. Intern.*, **2003**, *52*, 853.

162: T. E. Patten, K. Matyjaszewski, *Adv. Mater.*, **1998**, *10*, 901.

163: K. Matyjaszewski, J. Xia, *Chem. Rev.*, **2001**, *101*, 2921.

164: J. A. M. Brandts, P. van de Geijn, E. E. Van Faassen, J. Börsma, G. van Koten, *J. Organomet. Chem.*, **1999**, *584*, 246.

165: M. A. Stump, D. M. Haddelton, A. McCamly, D. Duncalf, J. A. Segal, D. J. Irvin, *Polym. Prepr.*, **1997**,*38 (Am. Chem. Soc., Div. Polym. Chem.)*, 508.

166: Y. Kotani, M. Kamigaito, M. Sawamoto, *Macromolecules*, **1999**, *32*, 2420.

167: M. Kato, M. Kamigaito, M. Sawamoto, T. Higashimura, *Macromolecules*, **1995**, *28*, 1721.

168: T. Ando, M. Kamigaito, M. Sawamoto, *Macromolecules*, **1997**, *30*, 4507.

169: V. Percec, B. Barboiu, A. Neumann, B. Ronda, *Macromolecules*, **1996**, *29*, 3665.

170: T. Otsu, T. Tazaki, M. Yoshioka, *Chem. Express*, **1990**, *5*, 801.

171: P. Lecomte, I. Drapier, P. Dubois, P. Teyssié, R. Jéróm, *Macromolecules*, **1997**, *30*, 7631.

172: V. Coessens, K. Matyjaszewski, *J. Macromol. Sci.*, **1999**, *A36 (Pure Appl. Chem.)*, 653.

173: F. Simal, A. Demonceau, A. F. Noels, *Angew. Chem., Int. Ed. Engl.*, **1999**, *38*, 538.

174: H. Takahshi, T. Ando, M. Kamigaito, M. Sawamoto, *Macromolecules*, **1999**, *32*, 3820.

175: T. Ando, M. Kamigaito, M. Sawamoto, *Macromolecules*, **2000**, *33*, 5825.

176: J.-S. Wang, K. Matyjaszewski, *Macromolecules*, **1995**, *28*, 7901.

177: T. Ando, M. Kamigaito, M. Sawamoto, *Tetrahedron*, **1997**, *53*, 15445.

178: H. Uegaki, M. Kamigato, M. Sawamoto, *J. Polym. Sci., A*, **1999**, *37*, 3003.

179: K. Matyjaszewski, S. M. Jo, H.-J. Paik, S. G. Gaynor, *Macromolecules*, **1997**, *30*, 6398.

180: V. Percec, B. Barboiu, *Macromolecules*, **1995**, *28*, 7970.

181: J. Pyun, S. Jia, T. Kowalewski, G. D. Patterson, K. Matyjaszewski, *Macromolecules* **2003**, *36*, 5094.

182: T. Von Werne, T. E. Patten, *J. Am. Chem. Soc.*, **1999**, *121*, 7409.

183: H. Böttcher, M. L. Hallensleben, S. Nuß, H. Wurm, *Polym. Bull.*, **2000**, *44*, 223.

184: Y. Wang, X. Teng, J.-S. Wang, H. Yang, *Nano Lett.*, **2003**, *3*, 789.

185: Y. Zhang, L. R. Sita, *J. Am. Chem. Soc.*, **2004**, *126*, 7776.

186: Y. K. Chong, P. T. Tam, G. Moad, E. Rizzardo, S. H. Thang, *Macromolecules*, **1999**, *32*, 2071.

187: G. B. Fiels, C. Fields, *J. Am. Chem. Soc.*, **1991**, *113*, 4202.

188: A. R. Szkurhan, M. K. Georges, *Macromolecules*, **2004**, *37*, 4776.

189: F. Burmeister, C. Schafle, B. Keilhofer, C. Bechinger, J. Boneberg, P. Leiderer, *Chem. Eng. Technol.*, **1998**, *21*, 761.

190: Y. Yin, Y. Lu, B. Gates, Y. Xia, *J. Am. Chem. Soc.*, **2001**, *123*, 8718.

191: Q. Guo, C. Arnoux, R. E. Palmer, *Langmuir*, **2001**, *17*, 7150.

192: S. H. Park, Y. Xia, *Langmuir*, **1999**, *15*, 266.

193: A. Taleb, C. Petit, M. P. Pileni, *J. Phys. Chem. B*, **1998**, *102*, 2214.

194: M. Hilgendorff, B. Tesche, M. Giersig, *Aust. J. Chem.*, **2001**, *54*, 497.

195: Z. L. Wang, *Adv. Mater.*, **1998**, *10*, 13.

196: R. P. Andres, J. D. Bielefeld, J. I. Henderson, D. B. Janes, V. R. Kolagunta, C. P.

Kubiak, W. J. Mahoney, R. G. Osifchin, *Science*, **1996**, *273*, 1690.

197: C. Beck, W. Härtl, R. Hempelmann, *Angew. Chem.*, **1999**, *111*, 1381.

198: L. Han, J. Luo, N. N. Kariuki, M. M. Maye, V. W. Jones, C. J. Zhong, *Chem. Mater.*, **2003**, *15*, 29.

199: J. J. Storhoff, R. Mucic, C. A. Mirkin, *J. Clust. Sci.*, **1997**, *8*, 179.

200: A. K. Boal, F. Ilhan, J. E. DeRouchey, T. Thurn-Albrecht, T. P. Russel, V. M. Rotello, *Nature*, **2000**, *404*, 746.

201: H. Mori, M. G. Lanzendörfer, A. H. E. Müller, J. E. Klee, *Langmuir*, **2004**, *20*, 1934.

202: A. P. Philipse, A. Vrij, *J. Chem. Phys.*, **1987**, *87*, 5634.

203: S. K. Park, K. D. Kim, H. T. Kim, *Colloids Surf., A*, **2002**, *197*, 7.

204: M. Szekeres, J. Toth, I. Dekany, *Langmuir*, **2002**, *18*, 2678.

205: N. Baccile, D. Grosso, C. Sanchez, *J. Mater. Chem.*, **2003**, *13*, 3011.

206: N. Kallay, S. Zalac, *J. Colloid Interface Sci.*, **2002**, *253*, 70.

207: J. N. Brønsted, *Z. Physik. Chem.*, **1922**, *102,* 169.

208: J. A. Christiansen, *Z. Physik. Chem.*, **1924**, *113*, 35.

209: D. L. Green, J. S. Lin, Y. F. Lam, M. Z.-C. Hu, D. W. Schaefer, M. T. Harris, *J. Colloid Interface Sci.*, **2003**, *266*, 346.

210: J. Björnström, A. Martinelli, J. R. T. Johnson, A. Matic, I. Panas, *Chem. Phys. Lett.*, **2003**, *380*, 165.

211: S. Nuss, H. Böttcher, H. Wurm, M. L. Hallensleben, *Angew. Chem.*, **2001**, *40*, 4016.

212: G. Frens, *Nature,* **1973,** *273*, 20 .

213: T. Ung, L. M. Liz-Marzan, P. Mulvaney, *J. Phys. Chem. B.*, **2001**, *105*, 3441.

214: J. Wagner,T. Kirner, G. Mayer, J. Albert, J. M. Kohler, *Chem. Eng. J.*, **2004**, *101*, 251.

215: Personal communication from Luis M. Liz-Marzán.

216: C. Graf, D. L. J. Vossen, A. Imhof, A. v. Blaadern, *Langmuir*, **2003**, *19*, 6693.

217: V. Salgueirino-Maceira, F. Caruso, L. M. Liz-Marzan, *J. Phys. Chem. B* **2003**, *107*, 10990.

218: S. Kratohvil, E. Matijevic, *Adv. Ceramic Mater.*, **1987**, *2*, 798.

219: B. Aiken, E. Matijevic, *J. Colloid Interface Sci.*, **1988**, *126*, 645.

220: A. Garg, E. Matijevic, *Langmuir*, **1988**, *4*, 38.

221: A. Garg, E. Matijevic, *J. Colloid Interface Sci.*, **1988**, *126*, 243.

222: M. Ohmori, E. Matijevic , *J. Colloid Interface Sci.*, **1992**, *150*, 594.

223: L. M. Liz-Marzán, A. P. Philipse, *J. Colloid Interface Sci.*, **1995**, *176*, 459.

224: L. M. Liz-Marzán, M. Giersig, P. Mulvaney, *J. Chem. Soc., Chem. Commun.*, **1996**, 731.

225: J. H. Jean, T. A. Ring, *Langmuir*, **1986**, *2*, 251.

226: E. Scolan, C. Sanchez, *Chem. Mater.*, **1998**, *10*, 3217.

227: A. Leaustic, F. Babonneau, J. Livage, *Chem. Mater.*, **1989**, *1*, 248.

228: C. Catviela, C. L. Serrano, M. M. Surbano, *J. Org. Chem.*, **1995**, *60*, 3074.

229: U. B. Saxena, A. K. Rai, V. K. Mathur, R. C. Mehrotra, D. Radford, *J. Chem. Soc., A*, **1970**, *6*, 904.

230: B. Moraru, N. Huesing, G. Kickelbick, U. Schubert, P. Fratzl, H. Peterlik, *Chem. Mater.*, **2002**, *14*, 2732.

231: H. Z. Zhang, J. F. Banfield, *J. Mater. Chem.* **1998**, *8*, 2073.

232: A. A. Gribb, J. F. Banfield, *Am. Mineral.* **1997**, *82*, 717.

233: Y. Hwu, Y. D. Yao, N. F. Cheng, C. Y. Tung, H. M. Lin, *Nanostruct. Mater.* **1997**, *9*, 355.

234: M. D. Wiggins, M. C. Nelson, C. R. Aita, *J. Vac. Sci. Technol. A*, **1996**, *14*, 772.

235: K. V. R. Krishna, N. S. V. Nagender, I. Leela, *J. Am. Ceram. Soc.*, **1970**, *53*, 124.

236: R. Restori, D. Schwarzenbach, J. R. Schneider, *Acta Cryst. B*, **1987**, *43*, 251.

237: K. T. Lim, H. S. Hwang, *Langmuir*, **2004**, *20*, 2466.

238: J. Zhai, L. Zhang, X. Yao, *J. Non-Cryst. Solids*, **1999**, *260*, 160.

239: J.-P Hsu, A. Nacu, *Langmuir*, **2003**, *19*, 4448.

240: A. K. Van Helden, J. W. Jansen, A. Vrij, *J. Colloid Interface Sci.*, **1981**, *81*, 354.

241: C.-C. Wang, J. Y. Ying, *Chem. Mater.*, **1999**, *11*, 3113.

242: L. Li, W. Wang, *Solid State Commun.*, **2003**, *127*, 639.

243: J. Malek, L. Benes, T. Mitsuhashi, *Powder Diffr.*, **1997**, *12*, 96.

244: V. F. Petrunin, V. V. Popov, H. Zhu, A. A. Timofeev, *Inorg. Mater.*, **2004**, *40*, 251.

245: P. Van der Voort, I. V. Babitch, P. J. Grobet, A. A. Verberckmoes, E. F. Vansant, *J. Chem. Soc., Faraday Trans.*, **1996**, *92*, 3635.

246: W. Bruckner, H. Oppermann, W. Reichelt, J. I. Terukow, W. A. Tschudnowski, E. Wolf *Vanadiumoxide*, Akademie, Berlin, **1993**.

247: A. M. Chippindale, P. G. Dickens, A. V. Powell, *J. Solid State Chem.*, **1991**, *93*, 526.

248: D. B. McWahn, M. Marezio, J. P. Remeika, P. D. Dernier, *Phys. Rev. B*, **1974**, *10*, 490.

249: R. Enjalbert, J. Galy, *Acta Cryst. C*, **1986**, *42*, 1467.

250: M. Mitric, A. Kremenovic, R. Dimitrijevic, D. Rodic, *Solid State Ionics*, **1997**, *101*, 495.

251: P. S. Dobal, R. S. Katiyar, R. Guo, A. S. Bhalla, *J. Raman Spectrosc.*, **2000**, *31*, 1061.

252: A. S. Brown, M. A. Spackman, R. J. Hill, *Acta Cryst. A*, **1993**, *49*, 513.

253: E. Riedel, *Anorganische Chemie*, de Gruyter, Berlin, New York, **1994**.

254: X. Y. Zhou, X. J. Wei, M. V. Fedkin, K. H. Strass, S. N. Lvov, *Rev. Sci. Instr.*, **2003**, *74*, 2501.

255: X. Liao, J. Zhu, W. Zhong, H.-Y. Chen, *Mater. Lett.*, **2001**, *50*, 341.

256: S. Brunauer, P. H. Emmett, E. Teller, *J. Am. Chem. Soc.*, **1938**, *60*, 309.

257: S. Förster, V. Abetz, A. H. E. Müller, *Adv. Polym. Sci.*, **2004**, *166*, 173.

258: K. Matsui, M. Ohgai, *J. Am. Ceram. Soc.*, **1997**, *80*, 1949.

259: M. Singhal, V. Chhabra, P. Kang, D. O. Shah, *Mater. Res. Bull.*, **1997**, *32*, 239.

260: E. H. Kisi, M. M. Elcombe, *Acta Cryst. C*, **1989**, *45*, 1867.

261: X. Sun, J. Li, F. Zhang, X. Qin, Z. Xiu, H. Ru, Y. You, *J. Am. Ceram. Soc.*, **2003**, *86*, 1321.

262: E. T. Lippmaa, M. A. Alla, T. J. Pehk, *J. Am. Chem. Soc.*, **1978**, *100*, 1929.

263: C. Perruchot, M. A. Khan, A. Kamitsi, A. P. Armes, T. von Werne, T. E. Patten, *Langmuir*, **2001**, *17*, 4479.

264: D. Holzinger, G. Kickelbick, *Polym. Sci. A*, **2002**, *40*, 3858.

265: G. C. Armatas, C. E. Salmas, M. Louloudi, G. P. Androutsopoulos, P. J. Pomonis, *Langmuir*, **2003**, *19*, 3128.

266: L. G. J. Haart, G. Blasse, *J. Solid State Chem.*, **1986**, *61*, 135.

267: H. Tang, H. Berger, P. E. Schmid, F. Lévy, *Solid State Commun.*, **1993**, *87*, 847.

268: S. K. Poznyak, V. V. Sviridov, A. I. Kulak, M. P. Samtsov, *J. Electroanal. Chem.*, **1992**, *340*, 73.

269: L. Forss, M. Schubnell, *Appl. Phys. B*, **1993**, *56*, 363.

270: L. D. Zhang, C. M. Mo, *Nanostruct. Mater.*, **1995**, *6*, 831.

271: W. F. Zhang, M. S. Zhang, Z. Yin, *Phys. Stat. Sol. A*, **2000**, *179*, 319.

272: A. Chemseddine, T. Moritz, *Eur. J. Inorg. Chem.*, **1999**, 235.

273: Personal communication from T. Berger.

274: J. J. Sene, W. A. Zeltner, M. A. Anderson, *J. Phys. Chem. B*, **2003**, *107*, 1597.

275: N. Serpone, D. Lawless, R. Khairutdinov, *J. Phys. Chem.*, **1995**, *99*, 16646.

276: F. Ramos-Brito, M. Garcia-Hipolito, R. Martinez-Martinez, E. Martinez-Sanchez, C. Falcony, *J. Phys. D: Appl. Phys.*, **2004**, *37*, L13.

277: J. Liang, X. Jiang, G. Liu, Z. Deng, J. Zhuang, F. Li, Y. Li, *Mater. Res. Bull.*, **2003**, *38*, 161.

278: V. M. Gun'ko, V. I. Zarko, R. Leboda, E. Chibowski, *Adv. Colloid Interface Sci.*, **2001**, *91*, 1.

279: R. Wäsche, M. Naito, V. A. Hackley, *Powder Technol.*, **2002**, *123*, 275.

280: S. Liufu, H. Xiao, Y. Li, *Powder Technol.*, **2004**, *145*, 20.

281: J. Cordelair, P. Greil, *J. Colloid Interface Sci.*, **2003**, *265*, 359.

282: S. Chibowski, W. Janusz, *Appl. Surf. Sci.*, **2002**, *196*, 343.

283: F. P. Zamborini, M. S. Gross, R. W. Murray, *Langmuir*, **2001**, *17*, 481.

284: T. Baum, D. Bethell, M. Brust, D. J. Schiffrin, *Langmuir*, **1999**, *15*, 866.

285: M. D. Musick, D. J. Pena, S. L. Botsko, T. McEvoy, J. N. Richardson, M. J. Natan, *Langmuir*, **1999**, *15*, 844.

286: F. P. Zamborini, J. F. Hicks, R. W. Murray, *J. Am. Chem. Soc.*, **2000**, *122*, 4514.

287: R. Elghanian, J. J. Storhoff, R. C. Mucic, C. A. Mirkin, *Science*, **1997**, *277*, 1078.

288: M. Bruchez, M. Moronne, P. Gin, S. Weiss, A. P. Alivisatos, *Science*, **1998**, *281*, 2013.

289: J. K. N. Mbindo, B. D. Reiss, B. R. Martin, C. D. Keating, M. J. Natan, T. E. Mallouk *Adv. Mater.*, **2001**, *13*, 249.

290: A. K. Boal, V. M. Rotello, *J. Am. Chem. Soc.*, **1999**, *121*, 4914.

291: I. L. Bertrand, U. Paik, *Ceram. Int.*, **1993**, *19*, 241.

292: T. Jesionowski, *Colloids Surf., A*, **2003**, *222*, 87.

293: S. Takata, T. Norisuye, N. Tanaka, M. Shibayama, *Macromolecules*, **2000**, *33*, 5470.

294: D. Holzinger, G. Kickelbick, *J. Polym. Sci., A*, **2002**, *40*, 3858.

295 K. Matyjaszewski, D. A. Shipp, J. L. Wang, T. Grimaud, *Macromolecules*, **1998**, *31*, 1527.

296: K. Kamata; Y. Lu, Y. Xia, *J. Am. Chem. Soc.* **2003**, *125*, 2384.

297: T. Sabru, T. Pintauer, B. McKenzie, K. Matyjaszewski, *J. Polym. Sci., A,* **2002**, *40*, 3153.

298: K. Matyjaszewski, P. J. Miller, N. Shukla, B. Immaraporn, A. Gelman, B. B. Luokala, T. M. Siclovan, G. Kickelbick, T. Vallant, H. Hoffmann, T. Pakula, *Macromolecules*, **1999**, *32*, 8716.

299: K. Matyjaszewski, H. Paik, P. Zhou, S. J. Diamanti, *Macromolecules*, **2001**, *34*, 5125.

300: W. G. Skene, S. T. Belt, T. J. Conolly, P. Hahn, J. C. Scaiano, *Macromolecules*, **1998**, *31*, 9103.

301: S. Marque, C. L. Mercier, P. Tordo, H. Fischer, *Macromolecules*, **2000**, *33*, 4403.

302: L. David, C. Cracium, O. Cozar, V. Chris, C. Agut, D. Rusu, M. Rusu, *J. Mol. Struct.*, **2001**, *563*, 573.

303: Y. Xia, B. Gates, Y. Yin, Y. Lu, *Adv. Mater.*, **2000**, *12*, 693.

304: H.-G. Elias, *Makromoleküle, Band 1: Chemische Struktur und Synthesen*, Wiley-VCH, Weinheim, Ney York, **1998**.

305: N. C. Santos, M. A. R. B. Castanho, *Biophysical. J.*, **1996**, *71*, 1641.

306: B. J. Bernes, *Dynamic Light Scattering*, Wiley, 1976, pp. 16.

307: P. Pershan, *Harvard Physics 191r lab manual.* pp. A-7-1.

308: G. M. Sheldrick, **1996**, University of Göttingen, Germany.

309: G. M. Sheldrick, **1997**, University of Göttingen, Germany.

310: K. Lehovec, *J. Comm. Metals*, **1964**, *27*, 1037.

311: E. N. Maslen, V. A. Streltsov, N. R. Streltsova, N. Ishizawa, *Acta Cryst. B*, **1994**, *50*, 435.

312: P. Judeinstein, C. Sanchez, *J. Mater. Chem.*, **1996**, *6*, 511.

Curriculum Vitae

Personal Data:

NAME:	Dieter HOLZINGER
ADDRESS:	Lorenz-Müller-Gasse 1A/5406 1200 Vienna Austria
DATE OF BIRTH:	27th March 1976
CITIZENSHIP:	Austrian
PLACE OF BIRTH:	Gmunden
MARTIAL STATUS:	Single

Higher Education:

December 2001-November 2004	PhD thesis under the guidance of Dr. Guido Kickelbick at the Vienna University of Technology (Austria)
September 2003-November 2003	Research project in the Department of Physical Chemistry, University Vigo, Spain under the guidance of Dr. Luis Liz-Marzán.
16th October 2001	Master degree exam with distinction
February 2001-October 2001	Master project under the guidance of Dr. Guido Kickelbick at the Vienna University of Technology (Austria)
July 2000-December 2000	Erasmus exchange term at the Chalmers University, Gothenburg, Sweden
Since October 1996	Study of technical chemistry at the Vienna University of Technology

Military Service:

October 1995-May 1996	BetrRVKp/FlFMB, Hörsching

School Education:

June 1995	High school diploma exam with distinction (Reifeprüfung)
1990-1995	HTL Wels, Abteilung für chemische Betriebstechnik
1986-1990	Lower grammer school in Gmunden (Bundes-Gymnasium)
1982-1986	Primary School in Gmunden